TECHNISCHE UNIVERSITÄT MÜNCHEN

Wissenschaftszentrum Weihenstephan für Ernährung, Landnutzung und Umwelt
Lehrstuhl für Experimentelle Genetik

Characterization of the novel human aldo-keto reductase AKR1B15 and the 17beta-hydroxysteroid dehydrogenase 17beta-HSD12 and analysis of vitamin D metabolism in cells

Susanne Weber

Vollständiger Abdruck der von der Fakultät Wissenschaftszentrum Weihenstephan für Ernährung, Landnutzung und Umwelt der Technischen Universität München zur Erlangung des akademischen Grades eines

Doktors der Naturwissenschaften

genehmigten Dissertation.

Vorsitzender:	Prof. Dr. Harald Luksch
Prüfer der Dissertation:	1. apl. Prof. Dr. Jerzy Adamski 2. Prof. Dr. Johannes Buchner 3. Prof. Dr. Michael Rychlik

Die Dissertation wurde am 22.02.2017 bei der Technischen Universität München eingereicht und durch die Fakultät Wissenschaftszentrum Weihenstephan für Ernährung, Landnutzung und Umwelt am 27.06.2017 angenommen.

Charakterisierung der neuen humanen Aldo-Keto Reduktase AKR1B15 und der 17beta-Hydroxysteroiddehydrogenase 17beta-HSD12 und Analyse des Vitamin D Metabolismus in Zellen

Susanne Weber

TABLE OF CONTENTS

TABLE OF CONTENTS I

SUMMARY VII

ZUSAMMENFASSUNG IX

I. INTRODUCTION 1

I.1. ALDO-KETO REDUCTASES (AKRS) 1

I.1.1. GENERAL CHARACTERISTICS OF AKRS 2

I.1.2. HUMAN AKR MEMBERS AND THEIR ROLE IN METABOLISM AND DISEASE 4

I.2. SHORT-CHAIN DEHYDROGENASE/REDUCTASES (SDRS) 8

I.2.1. GENERAL CHARACTERISTICS OF SDRS 8

I.2.2. HUMAN 17β-HYDROXYSTEROID DEHYDROGENASES (17β-HSDS) BELONGING TO THE SUPERFAMILY OF SDRS 9

I.3. FATTY ACID AND STEROL/STEROID METABOLISM 12

I.3.1. SHORT-CHAIN VS. LONG-CHAIN FATTY ACID ELONGATION 12

I.3.2. THE ROLE OF MITOCHONDRIA IN FATTY ACID METABOLISM 14

I.3.3. SEX STEROID METABOLISM 17

I.3.4. CYTOCHROME P450 ENZYMES (CYPS) AND THEIR ROLE IN VITAMIN D METABOLISM 19

I.4. AIMS OF THIS THESIS 21

II. MATERIAL AND METHODS 22

II.1. WORKING WITH *ESCHERICHIA COLI* (*E. COLI*) 22

II.1.1. CULTIVATION OF *E. COLI* 22

II.1.2. TRANSFORMATION OF CHEMICALLY COMPETENT *E. COLI* 23

II.1.3. AMPLIFICATION OF PLASMIDS IN *E. COLI* 23

II.1.4. CULTIVATION OF *E. COLI* CLONES FOR COLONY SCREENS 24

II.1.5. RECOMBINANT EXPRESSION OF PROTEINS IN *E. COLI* 24

II.2. WORKING WITH *PICHIA PASTORIS* (*P. PASTORIS*) 24

II.2.1. CULTIVATION OF *P. PASTORIS* 25

II.2.2. ELECTROPORATION OF *P. PASTORIS* 25

II.2.3. RECOMBINANT EXPRESSION OF PROTEINS IN *P. PASTORIS* 26

II.3. WORKING WITH HUMAN CELL LINES 27

II.3.1. CULTIVATION AND STORAGE OF HUMAN CELL LINES 27

II.3.2. TRANSIENT TRANSFECTION OF HUMAN CELL LINES 29

II.3.3. HARVEST OF HUMAN CELL LINES 30

II.3.4. ISOLATION OF MITOCHONDRIA FROM BEWO CELLS 30

II.4. WORKING WITH DNA AND RNA 31

II.4.1. ISOLATION OF PLASMIDS FROM *E. COLI* 31

II.4.2. ISOLATION OF GENOMIC DNA FROM *P. PASTORIS* 32

II.4.3. ISOLATION OF RNA FROM HUMAN CELL LINES 32

II.4.4. CDNA SYNTHESIS VIA REVERSE TRANSCRIPTION OF RNA 33

II.4.5. Application of polymerase chain reaction (PCR) 33
II.4.5.1. Amplification of DNA sequences for cloning 33
II.4.5.2. Site-specific mutagenesis of plasmid DNA 34
II.4.5.3. Analysis of cloning results by colony screen PCR 35
II.4.5.4. Detection of *AKR1B15* transcripts in cDNA samples 36
II.4.5.5. Sequencing of DNA 37
II.4.6. Analysis or purification of DNA via agarose gel electrophoresis 37
II.4.7. Purification of linear DNA 38
II.4.8. Determination of DNA / RNA concentration 38
II.4.9. Cloning of DNA into plasmids 39
II.4.9.1. Restriction digestion of DNA 39
II.4.9.2. Ligation of DNA 39
II.5. Working with proteins 40
II.5.1. Purification of human AKR1B15 from *E. coli* 40
II.5.2. Purification of human 17β-HSD12 from *P. pastoris* 41
II.5.2.1. Test of detergents for solubilization 41
II.5.2.2. Preliminary purification methods for 17β-HSD12 43
II.5.3. Determination of protein concentrations 44
II.5.4. Cofactor binding studies with AKR1B15 isoforms 45
II.5.5. Separation of proteins via polyacrylamide gel electrophoresis (PAGE) 46
II.5.6. Detection of proteins via Western blotting 47
II.5.6.1. Blotting of proteins via semi-dry blot 47
II.5.6.2. Immunochemical detection of proteins using chemiluminescence 48
II.5.6.3. Immunochemical detection of proteins using infrared (IR) fluorescence 48
II.6. Establishment of monoclonal anti-AKR1B15 antibodies 49
II.7. Subcellular localization studies using HeLa cells and fluorescence microscopy 50
II.8. Activity tests 52
II.8.1. Enzymatic activity assays using ^{3}H-labeled steroids 52
II.8.2. Enzymatic activity assays using unlabeled substrates 55
II.8.2.1. Assays using product fluorescence 55
II.8.2.2. Assays using cofactor fluorescence 55
II.8.2.3. Assays using cofactor absorption 56
II.8.2.4. Assays using retinoids and HPLC-UV analysis 57
II.8.3. Determination of mitochondria integrity 58
II.9. Generation of TALENs for an AKR1B15 knock-out in cell lines via TALEN technology 59
II.9.1. Design of TALENS for AKR1B15 knock-outs 60
II.9.2. Assembly of AKR1B15 TALEN pairs 61
II.9.3. Cloning of selection marker for TALEN transfection 64
II.9.4. Test of AKR1B15 TALEN efficiencies 64
II.9.4.1. Cloning of pCMV-Duplirep reporter plasmids 66
II.9.4.2. Preparation of samples for the determination of TALEN pair efficiencies 66
II.9.4.3. Determination of TALEN pair efficiencies 68
II.9.5. Enrichment of *ΔLNGFR* (over)expressing cells 69
II.10. *In silico* analyses 70
II.10.1. Prediction of splice sites 70
II.10.2. Prediction of subcellular localization 70
II.10.3. Prediction of post-translational modifications 70

II.11. ANALYSIS OF VITAMIN D METABOLITES 71
II.11.1. PREPARATION OF BIOLOGICAL SAMPLES FOR VITAMIN D ANALYSES 71
II.11.1.1. Harvest of samples from cell culture experiments 72
II.11.1.2. Homogenization of mouse tumor samples 72
II.11.1.3. Preprocessing of human plasma samples 73
II.11.1.4. Solid phase extraction (SPE) of vitamin D metabolites 73
II.11.2. CHROMATOGRAPHIC ANALYSES OF VITAMIN D METABOLITES 74
II.11.2.1. Analysis of vitamin D_3 metabolites via UV detection 74
II.11.2.2. Analysis of ^{3}H-labeled vitamin D_3 metabolites 75
II.11.2.3. Analysis of vitamin D metabolites and itraconazole via LC-MS/MS 76
II.11.3. VALIDATION OF THE VITAMIN D LC-MS/MS METHOD 79

II.12. MATERIAL, EQUIPMENT AND SOFTWARE 81
II.12.1. CELL STRAINS AND CELL LINES 81
II.12.1.1. *Escherichia coli* (*E.coli*) strains (chemically competent) 81
II.12.1.2. *Pichia pastoris* (*P. pastoris*) strains 81
II.12.1.3. Human cell lines and cell strains 81
II.12.2. MEDIA, SUPPLEMENTS, AND ANTIBIOTICS 81
II.12.2.1. Media and media supplements 81
II.12.2.2. Antibiotics 82
II.12.3. BIOLOGICAL SAMPLES 82
II.12.4. PLASMIDS 83
II.12.4.1. Purchased and donated plasmids 83
II.12.4.2. Generated plasmids 83
II.12.5. ANTIBODIES 85
II.12.6. ENZYMES 85
II.12.7. KITS, REAGENTS, AND STAINS 86
II.12.8. CHEMICALS, COMPOUNDS, AND SOLVENTS 87
II.12.8.1. Cofactors and unlabeled substrates for activity tests 87
II.12.8.2. Vitamin D metabolites 87
II.12.8.3. Radiochemicals 88
II.12.8.4. HPLC solvents and chemicals 88
II.12.8.5. Other chemicals 88
II.12.9. COLUMNS, RESINS, AND SPE CARTRIDGES 89
II.12.10. EQUIPMENT 89
II.12.10.1. Chromatography systems 89
II.12.10.2. Detection systems 90
II.12.10.3. Centrifuges, incubators, shakers, and laminar flows 90
II.12.10.4. Other equipment 91
II.12.11. CONSUMABLES 92
II.12.12. DATABASES AND SOFTWARE 92

III. RESULTS 94

III.1. CHARACTERIZATION OF THE HUMAN ALDO-KETO REDUCTASE 1B SUBFAMILY MEMBER 15 (AKR1B15) 94
III.1.1. *AKR1B15* TRANSCRIPT ANALYSIS 94
III.1.1.1. Results from *in silico AKR1B15* splice site prediction 95
III.1.1.2. Design of *AKR1B15* transcript specific primers 96
III.1.1.3. Transcript analysis in human tissues and cell lines 97

III.1.2. GENERATION OF MONOCLONAL ANTIBODIES AGAINST AKR1B15 99
III.1.2.1. Target sequences for the generation of monoclonal anti-AKR1B15 antibodies 100
III.1.2.2. Analysis of putative positive monoclonal antibodies 100
III.1.2.3. Analysis of established monoclonal antibodies concerning specificity and sensitivity 102
III.1.2.4. Analysis of established antibodies with HEK-293 lysates 103
III.1.3. SUBCELLULAR LOCALIZATION OF AKR1B15 ISOFORMS 104
III.1.3.1. Subcellular localization of full length AKR1B15 isoforms 104
III.1.3.2. *In silico* subcellular localization prediction 107
III.1.3.3. Effect of N-termini on the subcellular localization 108
III.1.4. ENZYMATIC ACTIVITY OF AKR1B15 ISOFORMS 110
III.1.4.1. Identification of AKR1B15 substrates 110
III.1.4.2. Cofactor preference of AKR1B15 isoforms substrates 115
III.1.4.3. Position selectivity of AKR1B15.1 with steroidal substrates 117
III.1.4.4. Kinetic parameters of AKR1B15.1 118
III.1.5. DETECTION OF ENDOGENOUS AKR1B15 ISOFORMS 120
III.1.5.1. Western blotting with human total tissue and cell lysates 120
III.1.5.2. Prediction of post-translational modification sites in AKR1B15 isoforms 122
III.1.5.3. Western blotting with enriched mitochondria from BeWo cell line 123
III.1.6. PROPERTIES OF THE AKR1B15.1 S8R MUTANT 125
III.1.7. GENERATION OF TALENS FOR AKR1B15 KNOCK-OUTS IN CELL LINES/STRAINS VIA TALEN TECHNOLOGY 126
III.1.7.1. Design and cloning of TALENs 127
III.1.7.2. Analysis of AKR1B15 TALEN efficiencies 128
III.1.7.3. Enrichment of cells via *ΔLNGFR* expression 131
III.2. EXPRESSION AND PURIFICATION OF THE HUMAN 17β-HYDROXYSTEROID DEHYDROGENASE TYPE 12 (17β-HSD12) 134
III.2.1. EXPRESSION OF HUMAN *HSD17B12* IN *PICHIA PASTORIS* (*P. PASTORIS*) 134
III.2.2. SOLUBILIZATION OF HUMAN 17β-HSD12 FROM *P. PASTORIS* EXPRESSION CULTURES 135
III.2.3. PURIFICATION OF HUMAN 17β-HSD12 FROM *P. PASTORIS* EXPRESSION CULTURES VIA THE HIS_6 TAG 138
III.3. METHOD DEVELOPMENT FOR THE ANALYSIS OF VITAMIN D METABOLITES IN BIOLOGICAL SAMPLES 142
III.3.1. DEVELOPMENT OF A HPLC-UV METHOD FOR THE ANALYSIS OF VITAMIN D_3 METABOLITES 142
III.3.2. DEVELOPMENT OF A RADIOACTIVE HPLC METHOD FOR THE ANALYSIS OF ^{3}H-LABELED VITAMIN D_3 METABOLITES 144
III.3.3. DEVELOPMENT OF A LC-MS/MS METHOD FOR THE ANALYSIS OF VITAMIN D METABOLITES 145
III.3.3.1. Optimization of MRM parameters for the MS/MS detection of vitamin D metabolites 146
III.3.3.2. Adaptation of the HPLC method for the MS/MS analysis of vitamin D metabolites 146
III.3.4. EXTRACTION OF VITAMIN D METABOLITES FROM CELL CULTURE SAMPLES 151
III.3.4.1. Optimizing and testing of solid phase extraction (SPE) 151
III.3.4.2. Testing of suitable cell harvest protocols 154
III.3.4.3. Imbedding an internal standard: 25-(OH)-D_2 [25,26,27-$^{13}C_3$] 157
III.3.4.4. Final method for cell culture sample preparation 158
III.3.5. VALIDATION OF THE VITAMIN D LC-MS/MS METHOD FOR CELL CULTURE SAMPLES 159
III.3.5.1. Design of a quantification method for vitamin D metabolites 159
III.3.5.2. Limits of detection (LOD) and quantification (LOQ) 160
III.3.5.3. Selectivity of the LC-MS/MS method 162
III.3.5.4. Injection reproducibility 163
III.3.5.5. Linearity of the quantification method 164
III.3.5.6. Precision of the LC-MS/MS method 165

III.3.5.7. Recovery of the internal standard 25-(OH)-D_2 [25,26,27-$^{13}C_3$] 168
III.3.5.8. Recovery of vitamin D metabolites 168
III.3.5.9. Stability of vitamin D metabolites in cell culture samples 171
III.3.5.10. Summary of the validation results 172
III.3.6. BIOLOGICAL APPLICATION OF THE VITAMIN D LC-MS/MS METHOD 173
III.3.6.1. Detection of vitamin D_3 metabolites in cell culture samples 173
III.3.6.2. Detection of vitamin D metabolites and itraconazole (ITZ) in mouse tumor samples 177
III.3.6.3. Detection of vitamin D metabolites in human plasma 179

IV. DISCUSSION 182

IV.1. HUMAN *AKR1B15*: A GENE ENCODING FOR TWO ISOFORMS WITH DIFFERENT CHARACTERISTICS 182
IV.1.1. EXPRESSION OF TWO VARIANTS *IN VIVO* 182
IV.1.2. TWO ISOFORMS WITH DIFFERENT SUBCELLULAR LOCALIZATION 184
IV.1.3. TWO ISOFORMS WITH DIFFERENT ENZYMATIC PROPERTIES 186
IV.1.4. WHAT PROVOKES THE SEVERE PHENOTYPE OF THE AKR1B15.1 S8R MUTANT? 189
IV.1.5. HYPOTHESES FOR THE BIOLOGICAL ROLES OF AKR1B15 ISOFORMS *IN VIVO* 191

IV.2. HUMAN 17β-HSD12: ON THE WAY TO EFFICIENT PROTEIN PURIFICATION AND CHARACTERIZATION 194
IV.2.1. SOLUBILIZATION OF 17β-HSD12 EXPRESSED IN *P. PASTORIS* 194
IV.2.2. LIMITATIONS OF *P. PASTORIS* AS EXPRESSION SYSTEM FOR HUMAN PROTEINS 196
IV.2.3. HOW TO CLARIFY THE PHYSIOLOGICAL ROLE OF 17β-HSD12 IN HUMAN IN FUTURE? 197

IV.3. VITAMIN D ANALYSIS: MONITORING THE VITAMIN D STATUS IN BIOLOGICAL SAMPLES 198
IV.3.1. ADVANTAGES AND LIMITATIONS OF THE DEVELOPED VITAMIN D LC-MS/MS METHOD 199
IV.3.2. CRITICAL ISSUES IN SAMPLE PREPARATION AND VITAMIN D ANALYSIS 201
IV.3.3. APPLICABILITY OF THE VITAMIN D LC-MS/MS METHOD WITHIN THE IN-HOUSE METABOLOMIC ANALYSES POOL 205

V. REFERENCES 207

VI. APPENDIX 233

VI.1. PUBLICATIONS, PRESENTATIONS, AND AWARDS 233
VI.1.1. SCIENTIFIC PUBLICATIONS 233
VI.1.2. SCIENTIFIC PRESENTATIONS 233
VI.1.3. SCIENTIFIC AWARDS 234

VI.2. ABBREVIATIONS 235

VI.3. MONOCLONAL ANTIBODY CLONES 239

VI.4. ALIGNMENT OF AKR1B15.1, AKR1B15.2, AND AKR1B10 CDNA SEQUENCES 240

VI.5. OUTPUTS FROM LOCALIZATION PREDICTIONS 241
VI.5.1. MITOPROT II (V1.101) PREDICTION 241
VI.5.2. IPSORT PREDICTION 241
VI.5.3. PSORT II PREDICTION 241
VI.5.4. PREDISI PREDICTION 242
VI.5.5. SIGNALP 4.1 SERVER 242
VI.5.6. TARGETP 1.1 SERVER 242

VI.6. CONSTRUCTED *AKR1B15* TALEN PAIRS 243

VI.7. PRIMERS 244
VI.7.1. VECTOR PRIMERS 244
VI.7.2. CLONING PRIMERS 245
VI.7.2.1. Cloning of full length protein encoding sequences 245
VI.7.2.2. Cloning of N-termini encoding sequences into pAcGFP-N1 246
VI.7.2.3. Cloning of TALEN target sites into pCMV-Univ-Duplirep 247
VI.7.3. SITE-DIRECTED MUTAGENESIS PRIMERS 248
VI.7.4. SEMI-QUANTITATIVE RT-PCR PRIMERS 248
VI.7.5. OTHER PRIMERS 249
VI.8. PARAMETERS OF MRMS USED WITHIN THE VITAMIN D LC-MS/MS METHOD DEVELOPMENT 250

DANKSAGUNG (ACKNOWLEDGEMENTS) i

LEBENSLAUF (CURRICULUM VITAE) iii

SUMMARY

Enzymes belonging to the superfamilies of aldo-keto reductases (AKRs), short-chain dehydrogenases/reductases (SDRs), and cytochromes P450 (CYPs) play important roles in various physiological pathways, such as the steroid, fatty acid, or vitamin D pathway, and in the genesis of different diseases, including cancer.

This thesis covers the analysis of single enzymes belonging to these superfamilies as well as associated metabolites in order to increase the knowledge of their roles in physiological processes, their importance in the development of diseases, and their potential as targets for therapies.

In 2011, a novel human AKR, called AKR1B15, was identified. This at that time only little explored AKR was extensively characterized within this thesis. Database search revealed that alternative splicing gives rise to two AKR1B15 isoforms, AKR1B15.1 and AKR1B15.2, differing in their N-terminus. Both *AKR1B15* transcripts were mainly found in adipose tissue, skeletal muscle, and reproductive tissues. Using newly generated monoclonal antibodies, it was possible to show the endogenous occurrence of both predicted AKR1B15 proteins. These two isoforms differed in their subcellular localization. Whereas the longer AKR1B15 variant AKR1B15.2 located in the cytosol, AKR1B15.1 colocalized surprisingly with mitochondria. Mutagenesis experiments demonstrated that, when compared to the cytosolic AKR1B10, in AKR1B15.1 the amino acid residue Leu24 is responsible for its mitochondrial localization. In activity assays, AKR1B15.1 appeared to be a reductive enzyme and catalyzed NADP(H)-dependent redox reactions on sex steroids (estrogens and androgens), retinoids, and acetoacetyl-CoA. Thereby, AKR1B15.1 represented a selective 17β-hydroxysteroid dehydrogenase. In contrast, AKR1B15.2 turned out to be an enzymatically inactive protein due to a lack of NAD(P)(H) cofactor binding. Analysis of the S8R mutation in AKR1B15.1, which was reported to be responsible for an infantile mitochondrial phenotype, showed no clear discrepancy in activity and localization when compared with the wild type enzyme. Finally, the basic tools for a knock-out of AKR1B15 via the TALEN technology were generated, serving for further functional analysis in the future. Conclusively, a role of AKR1B15.1 in the mitochondrial function is assumed but it is unclear which of its actions are of importance: those in the steroid, retinoid, and/or fatty acid metabolism or yet not analyzed protein-protein interactions.

Besides, this doctoral thesis dealt with the closer characterization of the human 17β-HSD12, a membrane-bound SDR. This enzyme is considered to play an essential role in the elongation of (very) long fatty acids *in vivo* by acting as 3-keto-acyl reductase. In order to proof this hypothesis in *in vitro* experiments, a method for the purification of enzymatically active His_6-tagged 17β-HSD12, using *P. pastoris* for recombinant protein expression, was developed. Via the developed procedure it will be possible to perform comparative *in vitro* activity assays with the purified enzyme in the future.

Finally, this thesis included also the development of an analytical method for the parallel detection and quantification of several vitamin D metabolites in biological samples. The

generated novel vitamin D LC-MS/MS method enables the concurrent analysis of the eight vitamin D metabolites: 24,25-$(OH)_2$-D_3, 1α,25-$(OH)_2$-D_3, 25-(OH)-D_3, 1α-(OH)-D_3, vitamin D_3, 1α,25-$(OH)_2$-D_2, 25-(OH)-D_2, and vitamin D_2. The validation of this method revealed good detection limits as well as recovery and stability parameters for all vitamin D metabolites with cells as matrix. Besides, the vitamin D LC-MS/MS method was already successfully applied in a research project. Finally, the established method has the potential to form the basis for the analysis of these eight vitamin D metabolites in other matrices, such as human plasma, too.

In summary, this doctoral thesis describes for the first time a more detailed characterization of the novel human aldo-keto reductase AKR1B15 and newly established tools for its further analysis, a method for the expression and purification of the membrane-bound 17β-hydroxy-steroid dehydrogenase 17β-HSD12 as enzymatically active protein, and, finally, a selective method for the analysis of up to eight different vitamin D metabolites in biological samples. These findings and tools can significantly contribute to the elucidation of pathological processes as well as to the identification and implementation of new treatment options in the future.

ZUSAMMENFASSUNG

Enzyme aus den Superfamilien der Aldo-Keto Reduktasen (AKRs), Short-Chain Dehydrogenasen/Reduktasen (SDRs), und Cytochrome P450 (CYPs) spielen wichtige Rollen in unterschiedlichsten physiologischen Stoffwechselwegen, wie zum Beispiel dem Steroid-, Fettsäure- oder Vitamin D-Stoffwechsel, und in der Genese verschiedenster Krankheiten, inklusive Krebserkrankungen.

Diese Arbeit befasst sich mit der Untersuchung einzelner Enzyme dieser Superfamilien sowie assoziierter Stoffwechselprodukte, um ein besseres Verständnis für ihre Funktionen in physiologischen Prozessen, ihre Bedeutungen in der Entstehung von Krankheiten und ihr Potenzial als mögliche Therapie-Targets zu gewinnen.

Innerhalb dieser Doktorarbeit wurde die 2011 neu entdeckte und bis dato wenig untersuchte humane AKR, AKR1B15, umfassend charakterisiert. Datenbankrecherchen zeigten, dass durch alternatives Spleißen zwei AKR1B15 Isoformen (AKR1B15.1 und AKR1B15.2) resultieren, welche sich N-terminal unterscheiden. Beide *AKR1B15* Transkripte wurden vor allem in Fettgewebe, Skeletmuskel und reproduktiven Geweben nachgewiesen. Mit Hilfe von neu generierten monoklonalen Antikörpern konnte zudem gezeigt werden, dass die AKR1B15 Isoformen auch als endogene Proteine exprimiert werden. In Lokalisationsstudien wiesen die zwei Isoformen eine unterschiedliche subzelluläre Lokalisation auf; während die längere Proteinvariante AKR1B15.2 im Zytosol zu finden war, kolokalisierte AKR1B15.1 unerwartet mit Mitochondrien. Über Mutagenese-Experimente konnte in AKR1B15.1, im Vergleich zum cytosolischen AKR1B10, die Aminosäure Leu24 als Grund für dessen mitochondriale Lokalisation identifiziert werden. AKR1B15.1 zeigte sich in Aktivtitätsassays als reduktives Enzym und katalysierte NADP(H)-abhängige Redoxreaktionen an Sex-steroiden (Estrogenen und Androgenen), Retinoiden und Acetoacetyl-CoA. Hierbei stellte AKR1B15.1 eine selektive 17β-Hydroxysteroiddehydrogenase dar. Im Gegensatz dazu erwies sich AKR1B15.2 aufgrund mangelnder NAD(P)(H)-Kofaktorbindung als enzymatisch inaktives Protein. Untersuchungen zu einem Aminosäurenaustausch (S8R) in AKR1B15.1, welcher mit einem infantilen mitochondrialen Phänotyp assoziiert sein soll, zeigten bezüglich der Aktivität und subzellulären Lokalisation keine wesentlichen Unterschiede zum Wildtyp. Für künftige weiterführende funktionelle Analysen wurden schließlich Basiswerkzeuge zur Erzeugung eines AKR1B15 Knock-outs per TALEN-Technologie konstruiert. Schlussfolgernd aus den Erkenntnissen wird für AKR1B15.1 eine Rolle in der Mitochondrien-Funktion angenommen, wobei unklar ist, ob diese in Form einer Beteiligung am Steroid-, Retinoid- und/oder Fettsäuren-Metabolismus oder aber in Form bislang nicht untersuchter Protein-Protein-Interaktionen übernommen wird.

Im Zuge der Dissertation wurde zudem an der näheren Charakterisierung der humanen 17β-HSD12, einer membranständige SDR, gearbeitet. Für dieses Enzym wird eine essentielle Funktion als 3-Keto-Acyl-Reduktase bei der Elongation von (sehr) langen Fettsäuren *in vivo* angenommen. Um diese Hypothese in *in vitro* Experimenten beweisen zu können, wurde unter Verwendung des rekombinanten Expressionssystems *P. pastoris* eine Methode für die

Aufreinigung von enzymatisch aktivem His_6-getaggtem 17β-HSD12 entwickelt. Über das hier entwickelte Verfahren kann künftig das gereinigte Enzym für vergleichende *in vitro* Aktivitätsassays genutzt werden.

Schließlich umfasste diese Doktorarbeit auch eine Methodenentwicklung zur parallelen Detektion und Quantifizierung mehrerer Vitamin D Metabolite in biologischen Proben. Die neu erschaffene Vitamin D LC-MS/MS Methode ermöglicht die simultane Analyse von acht Vitamin D Metaboliten: 24,25-$(OH)_2$-D_3, 1α,25-$(OH)_2$-D_3, 1α,25-$(OH)_2$-D_2, 25-(OH)-D_3, 25-(OH)-D_2, 1α-(OH)-D_3, Vitamin D_2, und Vitamin D_3. Die Validierung der Methode zeigte gute Nachweisgrenzen sowie Wiederfindungs- und Stabilitätsparameter für alle Vitamin D Metabolite mit Zellen als Matrix. Darüber hinaus konnte die Methode bereits erfolgreich für ein Forschungsprojekt eingesetzt werden. Abschließend besitzt die eingeführte Methode das Potenzial nach geringfügigen Modifikationen auch für die Analyse der genannten Vitamin D Metabolite in weiteren Matrices, wie zum Beispiel humanem Plasma, eingesetzt werden zu können.

Zusammenfassend beschreibt diese Doktorarbeit zum ersten Mal eine vertiefte und detailliertere Charakterisierung der neuen humanen Aldo-Keto Reduktase AKR1B15 sowie neu erschaffene Werkzeuge zu deren weiteren Analyse, eine Methode zur Expression und Aufreinigung der membranständingen 17β-Hydroxysteroiddehydrogenase 17β-HSD12 als enzymatisch aktives Protein und schließlich eine selektive Methode zur gleichzeitigen Bestimmung von bis zu acht verschiedenen Vitamin D Metaboliten in biologischen Proben. Die daraus erhaltenen Erkenntnisse und Werkzeuge können in Zukunft signifikant zur Aufklärung von pathologischen Prozessen sowie zur Identifizierung und Analyse von Behandlungsmöglichkeiten beitragen.

I. INTRODUCTION

Cardiovascular diseases (CVDs) and malignant neoplasms (cancers) are the most frequent death causes in Germany, Europe, and other developed countries worldwide (sources: Destatis, Eurostat, CDC/NCHS, and WHO). In Germany, for example, CVDs and cancers caused 39 % and 26 % of all death cases in 2014, respectively [1]. Although the incidences of CVDs and cancers stayed more or less constant or even increased the last decades, the morbidity and age-standardized mortality rates of these diseases have tended to decline in Germany and the majority of developed (high-income) countries within the last years [1–8]. Intense studies have led to progress in the elucidation of different risk factors, pathways, and mechanisms triggering and promoting these and other widespread diseases [9–13]. Beside other factors, enzymes of different pathways have been identified to play important roles in the development and/or progression of these diseases; among them are several proteins belonging to the superfamilies of aldo-keto reductases (AKRs), short-chain dehydrogenase/ reductases (SDRs), or cytochromes P450 (CYPs) which are, for example, involved in the sterol/steroid and fatty acid/lipid metabolism [14–16]. Some of these enzymes and related pathways are already targets for treatments (e.g., inhibition of steroid synthesis by the anticancer drug abiraterone or inhibition of fatty acid oxidation by the anti-anginal drug trimetazidine [17, 18]). However, in order to further improve treatment and screening options for diseases, it is crucial to enlarge the knowledge of both enzymes and metabolic pathways as well as to identify new enzyme targets.

I.1. ALDO-KETO REDUCTASES (AKRS)

Aldo-keto reductases (AKRs) are members of a rapidly growing superfamily of proteins belonging to the group of phase I metabolizing oxidoreductases [19]. By the end of 2015, more than 190 AKR superfamily members occurring in various phyla (archaea, bacteria, fungi, plants, and vertebrates) had been annotated and confirmed [14, 20]. According to their sequence identity, the members of the AKR superfamily are subdivided into 16 families (≤ 40 % amino acid sequence identity to other families) and these families are further subdivided into subfamilies (> 60 % amino acid sequence identity) [14, 20, 21]. In this way, the mammalian AKRs including the 15 human AKR members, which have been annotated and verified so far, appear only in the AKR families 1 (subfamilies A-E), 6, and 7 [14, 20].

As pointed out in the phylogenetic tree of human AKRs, the human members belong to the groups of aldehyde reductases (AKR1A subfamily), aldose reductases (AKR1B subfamily), hydroxysteroid dehydrogenases (AKR1C subfamily), steroid reductases (AKR1D subfamily), 1,5-anhydro-D-fructose reductases (AKR1E subfamily), potassium voltage-gated channel β-subunits (AKR6 family), and aflatoxin aldehyde reductases (AKR7 family) [Figure I-1]. Here, AKR1B15, which was annotated by Salabei *et al.* in 2011, represents the most recently identified human AKR [22].

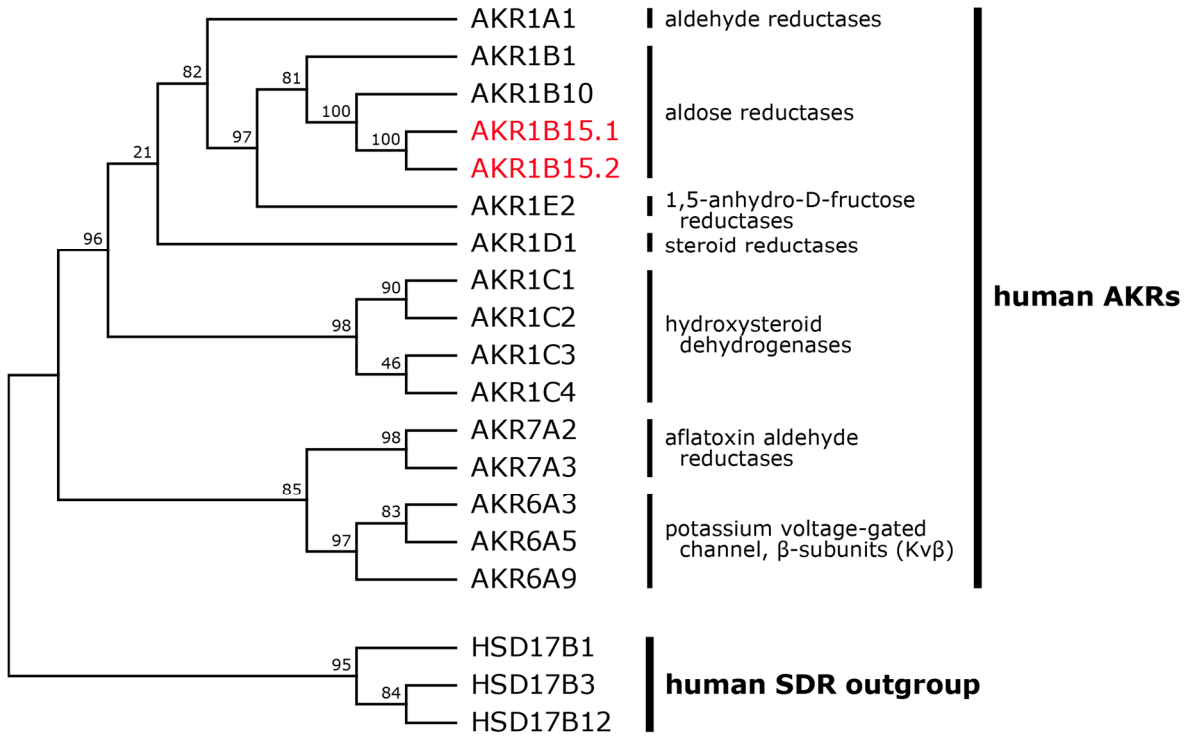

Figure I-1: AKR1B15 clusters with AKR1B10 in phylogenetic analysis of human AKRs.
Shown is the herein constructed Maximum Likelihood tree for human AKRs. The phylogenetic analysis of verified human AKRs (and human SDR representatives as outgroup) was performed by using the MEGA6 software [23]. For this, the respective protein sequences (source: UniProtKB database) were aligned via ClustalW alignment and analyzed via phylogenetic reconstruction applying the Maximum Likelihood (ML) statistical method with Bootstrap testing (1000 replications, log likelihood = -7632). The Jones-Taylor-Thornton (JTT) model was used as amino acid substitution model, whereas the Nearest-Neighbor-Interchange (NNI) ML heuristic method with Neighbor Joining initial tree and Moderate branch swap filter was chosen for calculating the tree interference options. The calculated bootstrap values of branches in the phylogenetic tree are listed at the respective branches. The two isoforms of AKR1B15 were analyzed separately and are highlighted in red.

I.1.1. General characteristics of AKRs

Although members of the superfamily of AKRs are present in various phyla and divided in different families, all AKRs share common characteristics. The characteristics of AKR concerning their three-dimensional structure and reaction mechanisms had been reviewed in several articles in the past [14, 19, 24–27]. In general, AKRs are polypeptides of about 280-420 amino acid in length and a molecular weight of 30-45 kDa. With the exception of some members of the AKR2, AKR6, and AKR7 families which form dimers or multimers, AKRs are considered to be cytosolic and monomeric proteins. All AKRs share a $(\alpha/\beta)_8$-barrel structure (also known as TIM barrel structure) with a N-terminal β-sheet, forming the bottom of the barrel, and three flexible and variable loops for the binding of substrates and NAD(P)(H) cofactors in an extended anti-conformation as well as a conserved catalytic tetrad consisting typically of Asp44, Tyr49, Lys78, and His111 (human AKR1B10 numbering) [19, 24, 26, 28]. These characteristic AKR features are shown in Figure I-2 on the example of the human AKR1B10.

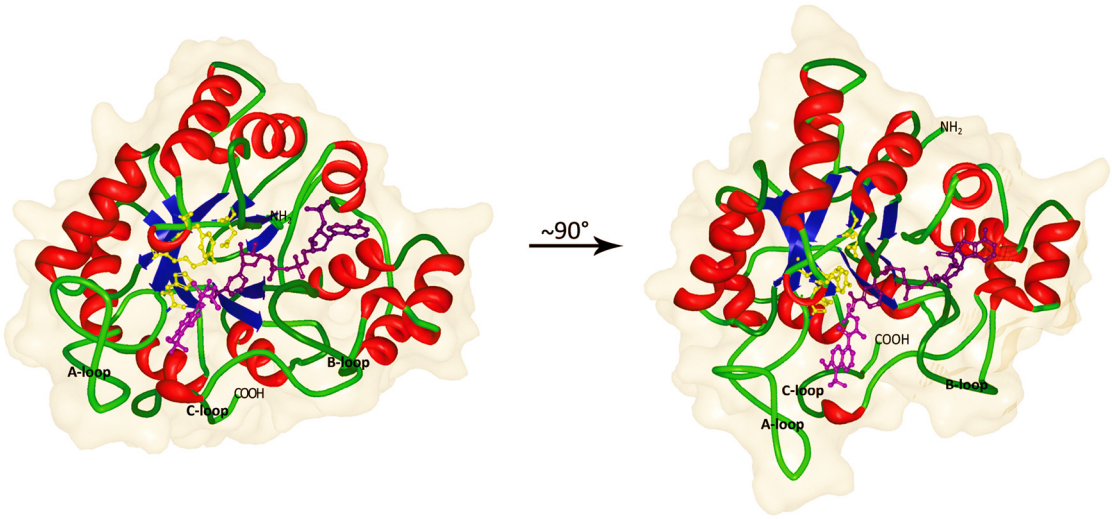

Figure I-2: Three dimensional structure of AKRs on the example of human AKR1B10.
Back and 90° rotated orientation view of the 1.25 Å X-ray structure of human AKR1B10 in complex with $NADP^+$ and tolrestat (PDB: 1ZUA) [29]. The bound cofactor $NADP^+$ (purple) and ligand tolrestat (bright purple) as well as the residues of the catalytic tetrad: Asp44, Tyr49, Lys78, and His111 (yellow) are shown in atoms and bonds style, whereas the AKR backbone is shown as secondary ribbon structure showing the typical AKR $(\alpha/\beta)_8$-barrel structure with its three loops A-C. Thereby, α-helices are colored in red, β-sheets in blue, turns in bright green, and coils in dark green.

AKRs predominantly catalyze the NAD(P)H-dependent reduction of a broad range of biogenic and xenobiotic carbonyl groups to primary and secondary alcohols. However, the AKR1D family members are exceptions: they have an altered catalytic tetrad, where the catalytic active Glu120 replaces the catalytic His present in other AKRs, and thus function as double bond reductases [30–32]. In general, the amino acid sequences of the C-terminal domains of AKRs, especially those residues building up the variable loops, are considered to define the substrate specificity [24, 26, 33]. As a result, the substrate spectrum of AKRs covers aliphatic and (poly)cyclic aldehydes or ketones, monosaccharides, steroids, prostaglandins, bile acid precursors, and isoflavinoids as well as endogenous oxidation by-products (e.g., advanced glycation end products (AGEs) or lipid peroxidation-derived aldehydes) and exogenous carcinogens including their metabolites (e.g., polycyclic aromatic hydrocarbons, nicotine-derived 4-(methylnitrosamino)-1-(3-pyridyl)-1-butanone, or aflatoxin dialdehydes) [14, 19, 26, 27].

All AKRs are presumed to follow the same reaction mechanism which is mediated by the conserved catalytic tetrad and the $(\alpha/\beta)_8$-barrel structure forming an oxyanion binding site for the nicotinamide ring of NAD(P)(H) cofactors. In this ordered bi-bi reaction the cofactor binds first to the apo-enzyme before the respective substrate binds to the resulting holo-enzyme [14, 26]. The reductive 4-pro-R hydride transfer from the C4 of the cofactor nicotinamide ring and the concomitant proton transfer to the substrate as well as the reverse oxidative reaction are accomplished by a push-pull mechanism triggered by the catalytic tetrad. Here, the catalytic tyrosine serves as a general acid, facilitated by the catalytic histidine residue (or the superacid glutamate in the AKR1D family), or as a general base, facilitated by the catalytic lysine and aspartate residues, in reductive or oxidative reactions, respectively [14, 26, 34]. For most AKRs the release of cofactor, which leaves last, is the rate-determining step of the redox reactions. However, in some cases the chemical catalysis step or the release of both products are the rate determining steps [35–37].

I.1.2. HUMAN AKR MEMBERS AND THEIR ROLE IN METABOLISM AND DISEASE

As mentioned above, 15 AKR members belonging to the AKR1, 6, and 7 families have been identified in humans so far [14, 20], and previous studies on human AKRs and mammalian orthologs reported a crucial role of various human AKRs in health and disease [Table I-1].

The majority of human AKRs belong to the AKR1 family which is subdivided in the subfamilies A-E. AKR1A1, also known as aldehyde reductase, is the only human member of the AKR1A subfamily. This enzyme catalyzes the reduction of a broad spectrum of carbonyls, like aromatic and aliphatic aldehydes and ketones, quinones, isocorticosteroids, or D-glucuronic acid, as well as the oxidation of polycyclic aromatic hydrocarbons (PAH) trans-dihydrodiols [38–41]. At the moment, the real physiological role of AKR1A1 in humans can only be supposed. One hypothesis for its function is the involvement in the myo-inositol catabolism (glucuronate-xylulose pathway) by catalyzing the reduction of D-glucuronic acid [42]. Although this function has not been shown *in vivo* so far, it is likely because of results gained from studies on the murine and porcine AKR1A1 orthologs [43, 44]. However, AKR1A1 might also play a role in the development of cancerous diseases, like lung cancer, by catalyzing the oxidation and thus activation of pro-cancerogenic PAH trans-dihydrodiols [41, 45]. The most extensively studied human AKR is the AKR1B family founding member AKR1B1, also known as aldose reductase. AKR1B1 enzymes of different mammalians were early described as aldose reducing enzymes of the polyol pathway reducing hexoses to their respective alcohols. Possessing only low binding affinities towards hexoses, like especially glucose, AKR1B1 catalyzes the basal reduction of glucose into sorbitol in healthy individuals and regulates thereby osmotic imbalances [27, 46–48]. However, under hyperglycemic conditions, AKR1B1 reduces excess glucose leading to higher levels of sorbitol [27, 46]. This increased glucose conversion rate induces both osmotic and oxidative stress in hyperglycemic diabetics and promotes the development of secondary diabetic complications, like cataractogenesis, retinopathy, nephropathy, neuropathy, or cardiovascular diseases [49–52]. Besides, AKR1B1 is also involved in the detoxification of physiologically significant and harmful aldehydes, like lipid peroxidation-derived aldehydes (e.g., 4-hydroxy-2-nonenal (4-HNE)) or advanced glycation end-product (AGE) precursors (e.g., methylglyoxal), *in vivo* [27, 53–56]. In addition, recent studies showed that human AKR1B1 is able to catalyze the NADPH-dependent reduction and in absence of NADP(H) cofactors the isomerization of prostaglandin H_2 (PGH_2) [57, 58]. By doing so, AKR1B1 is involved in the formation of prostaglandin D_2 (PGD_2) or prostaglandin $F_{2\alpha}$ ($PGF_{2\alpha}$), respectively, and thus in ischemic and inflammatory processes *in vivo* [59]. Another well characterized member of the AKR1B subfamily is AKR1B10. Due to its close relationship to AKR1B1 (71 % amino acid identity and similar substrate specificity) and its high abundance in the small intestine [60, 61], the AKR1B10 enzyme was also called small intestine aldose reductase. In contrast to AKR1B1, AKR1B10 seems to play a major role in the cytosolic retinoid metabolism by catalyzing the reduction of retinaldehydes and thus regulating the generation of the biologically active retinoic acid [62, 63]. Besides, different studies indicate that AKR1B10, like AKR1B1, reduces xenobiotic ketones (e.g., the antiemetic drug dolasetron or anticancer drugs daunorubicin and idarubicin) as well as toxic aldehydes (e.g., the cancerogenic acrolein, crotonaldehyde, or 4-HNE) *in vivo* [64–66]. Because AKR1B10 was reported to be strongly overexpressed in hepatocellular carcinomas (HCC), cholangiocarcinomas, lung squamous cell carcinomas

(SCC), lung adenocarcinomas, as well as uterine and esophageal cancers, it additionally represents a potential tumor marker [60, 67–69]. The negative effect of AKR1B10 activity on the progression of cancers and their therapeutic prognosis has been shown in several studies, defining AKR1B10 as potential target for cancer intervention due to its role in the inhibition of oncotic cell death, the promotion of cell proliferation syntheses, and the degradation of anticancer drugs [66, 69–71]. Another AKR1 family subfamily, intensely studied due to its pivotal role in sex steroid hormone metabolism [I.3.3, Figure I-6] and its correlation with cancers in humans, is the AKR1C subfamily. *In vivo*, the four human AKR1C subfamily members AKR1C1, AKR1C2, AKR1C3, and AKR1C4 catalyze mainly redox reactions on 3(α/β)-, 17(β)-, and 20(α)-keto- or hydroxysteroids, however, with discriminative preferences [72–74]. Beside these major physiological activities, all AKR1C subfamily enzymes oxidize pro-cancerogenic PAH trans-dihydrodiols to their respective redox-active o-quinones [35, 45, 75]. The human AKR1C1 is also known as 20α-hydroxysteroid dehydrogenase (20α-HSD) and catalyzes predominantly the reduction of progesterone and (allo)pregnanolone to 20α-hydroxyprogesterone and (allo)pregnanediol, respectively [72, 76]. In doing so, AKR1C1 regulates the levels of the biologically active progesterone, which binds to the progesterone receptors with high affinity, and thus the physiological action of progesterone in target tissues [73, 77, 78]. In addition, AKR1C1 is involved in the metabolism of the neurosteroidal $GABA_A$ receptor modulator (allo)pregnanolone, where AKR1C1 either reduces the formation of active neurosteroids by the reduction of the precursor progesterone or catalyzes the inactivation of these neurosteroids [73, 79]. Burczynski *et al.* reported also a potential role of AKR1C1 in the elimination of toxic aldehydes and Matsunaga *et al.* presented protective effects against reactive oxygen species (ROS) *in vivo* [80, 81]. Another human AKR1C subfamily member is the 3α-hydroxysteroid dehydrogenase (3α-HSD) AKR1C2 which catalyzes redox reactions at position 3(α) of gestagens and androgens [72, 73, 82]. Like AKR1C1, AKR1C2 plays a role in the neurosteroid metabolism by catalyzing the reduction of dihydroprogesterone to (allo)pregnanolone in the brain [73, 82]. Thus, contrary to AKR1C1, AKR1C2 is responsible for the generation of active $GABA_A$ receptor modulators *in vivo* [79]. AKR1C2 additionally possesses enzymatic activity on androgens and catalyzes the reduction of dihydrotestosterone (DHT) to 3α,17β-androstanediol [72, 83]. However, the function of AKR1C2 in the androgen metabolism seems to be of minor importance *in vivo* since its activity with androgens is much lower when compared with AKR1C4 [72]. Because initial studies showed that AKR1C2 binds bile acids with high affinity but possesses only little enzymatic activity with them, AKR1C2 is also called bile acid binding protein. This feature suggests a predominant role in the intracellular bile acid transport and the monitoring of intracellular bile acid levels *in vivo* [84, 85]. As indicated above, AKR1C4, also known as chlordecone reductase, is the most potent 3α-hydroxysteroid reductase among the human AKR members and exhibits high enzymatic activities with androgens, like androstanedione and DHT, but also with bile acid precursors [72, 86, 87]. Since *AKR1C4* is mainly expressed in liver, the major physiological role of AKR1C4 lies in the hepatic steroid metabolism (inactivation of biologically active steroids and synthesis of bile acids) and thus in the regulation of circulating steroid hormone levels [72]. The fourth human member of the AKR1C subfamily is AKR1C3. *In vitro* studies on AKR1C3 demonstrated that the enzyme is able to catalyze bi-directional redox reactions at positions C3(α), C17(β), and C20(α) of androgens, estrogens, and gestagens [88–91]. However, under physiological conditions AKR1C3 (alias 17β-HSD5) strongly prefers the reduction of 17-ketosteroids, like the reduction of Δ4-androstenedione or androstanedione to testosterone or DHT, respectively

[88, 92, 93]. Thus, AKR1C3 is involved in the androgen metabolism *in vivo* [73, 78]. But not only ketosteroids are biological substrates of AKR1C3. In fact, human AKR1C3 possesses much higher catalytic activities in the reduction of prostaglandins, like prostaglandin D_2 (PGD_2) and prostaglandin H_2 (PGH_2) [94, 95]. Due to this favored activity, AKR1C3 is also called prostaglandin F synthase and considered to play an important role in prostaglandin metabolism and signaling [47, 96]. Several studies demonstrated an altered expression (mostly upregulation) of *AKR1C* genes in cancers linked to sex steroid metabolism, like prostate, breast, endometrial, and cisplatin resistant colon cancers but also in endometriosis [73, 81, 92]. As a result, members of the AKR1C subfamily are considered to represent potential targets for the treatment of cancer and inflammatory diseases [14, 97]. AKR1D1, alias Δ4-3-ketosteroid 5β-reductase, is the only human member of the AKR1D subfamily. Whereas all other enzymatically active AKRs catalyze the reduction or oxidation of carbonyls or alcohols, respectively, members of the AKR1D subfamily selectively reduce Δ4 double bonds in 3-ketosteroids belonging to the class of bile acid precursors, gestagens, and androgens [30, 98]. Thus, AKR1D1 plays a pivotal role in hepatic bile acid synthesis *in vivo* and its deficiency results in cholestasis, hepatitis, and liver failure [87, 99–101]. Within the steroid hormone metabolism, AKR1D1 does not only trigger the inactivation and degradation of androgens by catalyzing the reduction of Δ4-3-ketoandrogens (e.g., testosterone) to their respective 5β-3-ketoandrogens (e.g., 5β-dihydrotestosterone) but also regulates 5β-pregnane mediated hormone receptor activation [47, 74].

Another AKR family occurring in humans is the AKR7 family. Two human AKR7 members are known: AKR7A2 and AKR7A3 (alias aflatoxin B1 aldehyde reductase 1 and aflatoxin B1 aldehyde reductase 2, respectively). Both enzymes catalyze the successive reduction of aflatoxin dialdehydes to mono- and dialcohols and are, thus, the predominant enzymes involved in the detoxification of hepatotoxic and cancerogenic aldehydes *in vivo* [102–104]. The ubiquitously expressed AKR7A2 represents also a potent succinic semialdehyde reductase catalyzing the formation of the neuromodulator (γ-aminobutyrate agonist) γ-hydroxybutyrate from succinic semialdehyde [40, 102, 105]. Picklo *et al.* showed that patients with neurodegenerative diseases, e.g., Alzheimer's disease, exhibited significantly elevated AKR7A2 levels, which was either connected to an altered neuromodulation or an increased detoxification of oxidized toxic species [106].

In contrast to the AKR1 and AKR7 family members, the three human AKR6 family members (AKR6A3, AKR6A5, and AKR6A9) which are also called voltage-gated potassium channel β-subunits (1, 2, and 3, respectively) are rather regulatory than enzymatically active proteins [107, 108]. *In vivo*, tetrameric AKR6 family member complexes interact selectively with the base of a subset of voltage-gated potassium channels expressed, e.g., in the brain or heart, and thereby regulate most likely the excitability of cells in dependence of their metabolic state by acting as intracellular redox-sensors [107, 109–117].

Whereas the above described AKRs are mostly well characterized, the physiological function of the testis specific human AKR1 family member AKR1E2 (also known as 1,5-anhydro-D-fructose reductase) is yet unclear, as it only showed low activity with the common AKR substrate 9,10-phenanthrenequinone but no activity with other substrates (e.g., androgens, estrogens, gestagens, and prostaglandins) tested [118, 119]. Moreover, the most recently annotated human AKR, AKR1B15, represented a rather poorly characterized enzyme prior to this thesis [22]. For this reason AKR1B15 was intensely studied herein.

Table I-1: Human AKRs and their biological roles.

AKR member (locus) alternative name(s)	biological roles references
AKR1A1 (1p33-p32) aldehyde reductase	reduction of aromatic and aliphatic aldehydes to alcohols; oxidation of PAH trans-dihydrodiol metabolites [38–41]
AKR1B1 (chr. 7q35) aldose reductase	reduction of hexoses (e.g., glucose) into sugar alcohols (e.g., sorbitol) in the polyol pathway; reduction and isomerization of prostaglandins (e.g., PGH_2); reduction of lipid peroxidation-derived aldehydes (e.g., 4-HNE) or AGE precursors (e.g., methylglyoxal) [27, 50, 52–56, 58]
AKR1B10 (7q33) small intestine reductase	reduction of xenobiotic and toxic carbonyls (e.g., acrolein); reduction of retinaldehydes to retinols [62, 64–66]
AKR1B15 (7q33)	**unknown** [22]
AKR1C1 (10p15-p14) 20α-hydroxysteroid dehydrogenase	reduction of progesterone to 20α-hydroxyprogesterone or (allo)pregnanolone to (allo)pregnanediol [72, 76]
AKR1C2 (10p15-p14) 3α-HSD3 / bile acid binding protein	reduction of dihydroprogesterone to (allo)pregnanolone; reduction of dihydrotestosterone to 3α,17β-androstanediol [72, 82, 83]
AKR1C3 (10p15-p14) 17β-HSD5 / 3α-HSD2 / PGF synthase	reduction of 17-ketosteroids (e.g., Δ4-androstenedione) to 17β-hydroxysteroids (e.g., testosterone); reduction of prostaglandins (e.g., PGD_2 or PGH_2) in prostaglandin synthesis [72, 88, 89, 94, 95]
AKR1C4 (10p15) 3α-HSD1 / chlordecone reductase	reduction of 3-ketosteroids (e.g., dihydrotestosterone) to 3-hydroxysteroids (e.g., 3α,17β-androstanediol) in the clearance of steroids and bile acid synthesis; [72, 86, 87]
AKR1D1 (7q32-q33) Δ4-3-ketosteroid 5β-reductase	reduction of Δ4 double bonds in Δ4-3-ketosteroids (e.g., 7α-hydroxy-Δ4-cholestene-3-one) to the respective 5β-dihydrosteroids (e.g., 7α-hydroxy-5β-cholestan-3-one) in bile acid synthesis or sex steroid metabolism [27, 30, 98]
AKR1E2 (10p15) 1,5-anhydro-D-fructose reductase	low enzymatic activity with 9,10-phenanthrenequinone; unclear function [118, 119]
AKR6A3 (3q26) voltage-gated K^+ channel β-subunit 1	regulation of voltage-dependent potassium channels (e.g., inactivation) [109–111, 114, 117]
AKR6A5 (1p36) voltage-gated K^+ channel β-subunit 2	regulation of voltage-dependent potassium channels (e.g., hyperpolarization) [109, 114, 117]
AKR6A9 (17p13) voltage-gated K^+ channel β-subunit 3	regulation of voltage-dependent potassium channels (e.g., inactivation) [112, 117]
AKR7A2 (1p36) aflatoxin B1 aldehyde reductase 1	reduction of succinic semialdehyde to the neuromodulator gamma-hydroxybutyrate; reduction of the dialdehydic form of aflatoxin B1 to its respective dialcohol form [40, 102, 105]
AKR7A3 (1p36) aflatoxin B1 aldehyde reductase 2	reduction of the dialdehydic form of aflatoxin B1 to its respective dialcohol form [103, 104]

I.2. SHORT-CHAIN DEHYDROGENASE/REDUCTASES (SDRS)

Another superfamily of proteins, mostly belonging to the class of oxidoreductases, is the steadily growing superfamily of short-chain dehydrogenases/reductases (SDRs). SDRs are present in all species and build up one of the oldest and largest superfamily with already more than 163000 members identified in 2012 [120, 121]. Because SDRs show only amino acid sequence identities between 20 % and 30 % in pairwise comparisons but high 3D structural identities, subclassifications of SDRs into types and families were made by Hidden Markov Models assigning 122940 proteins to 464 SDR families [120]. The 78 human SDR members, which had been annotated in the UniProtKB database by the end of 2015, are distributed in 47 SDR families [121, 122]. Like AKRs, SDRs possess high functional diversities and are involved in numerous metabolic pathways and cellular processes, like the detoxification of endogenous metabolites, ethanol, and xenobiotics, the pre-receptor regulation of lipid-, isoprenoid-, or steroid signaling through the metabolism of prostaglandins, retinoids, or steroids, respectively, the lipid, carbohydrate, amino acid, and cofactor metabolism, the sensing of intracellular redox states, and the regulation of gene transcription and RNA processing [121, 123].

I.2.1. GENERAL CHARACTERISTICS OF SDRS

SDRs possess only little pairwise and overall sequence identity, but share some structural and mechanistic characteristics. The majority of SDRs are enzymes of 250-350 amino acids in length and form oligomeric (mostly homodimeric or homotetrameric) quarternary structures [123]. But there are also SDRs occurring as monomers [123]. One basic feature of SDRs is a central Rossmann fold structure for NAD(P)(H) cofactor binding. This structural element is built up by a central, twisted parallel β-sheet structure (consisting of 6-7 strands) which is flanked by 3-4 α-helices at each side [123]. The enzymatic activity of SDRs follows in general an ordered bi-bi reaction mechanism, where the NAD(P)(H) cofactor binds first [123]. In most SDRs, the proton transfer is accomplished by a catalytic triad or tetrad consisting of (Asn114,) Ser142, Tyr155, and Lys159 (17β-HSD1 numbering) [124, 125]. The preference for NAD(H) or NADP(H) cofactors is defined by acidic amino acid residues approximately 20 amino acids downstream of the glycine-rich (Gly-rich) cofactor binding motif or basic amino acids within this motif, respectively [123]. In contrast, the variable C-terminus is responsible for substrate selectivity and binding [123].

According to the subunit sizes and sequence motifs responsible for cofactor binding and catalytic activity, SDRs can be subdivided into seven types: classical (C), extended (E), intermediate (I), complex (X), atypical (A), divergent (D), and unassigned (U) [Table I-2]. The huge majority of SDR enzymes, covering the classes of oxidoreductases, epimerases, and dehydratases, belong to classical and extended type of SDRs [122, 126]. These two types differ in their Gly-rich cofactor binding motif as well as an additional C-terminal domain in the extended type [122, 126, 127]. Intermediate SDRs, which resemble the alcohol dehydrogenase (ADH) in *Drosophila*, are similar to classical SDRs with the exception that the Gly-rich cofactor binding motif is more like in the extended type and richer in alanine

content [120, 123, 126]. SDRs which are part of multifunctional enzyme complexes, belong to the complex SDR type and possess an YxxxN active site motif instead of the general YxxxK motif found in classical, extended, and intermediate SDRs. In contrast, SDRs of the divergent type have an irregular active site motif by possessing an additional methionine or hydrophobic amino acid residue and appear as enoyl reductases in plants and bacteria [123, 126]. Atypical SDRs feature variable Gly-rich cofactor binding motifs as well as altered active sites, mostly lacking the catalytic tyrosine and represent proteins with unknown or none enzymatic activity, similar to the fungal transcription regulator NmrA [121, 122]. Finally, SDR members which cannot be assigned to the aforementioned types (yet) are classified as unassigned SDRs [120].

Table I-2: Types of SDRs and their characteristics.

SDR type	Gly-rich cofactor binding motif	active site motif	number of human SDRs
classical (C)	TGxxx[A/G]xG	YxxxK	56
extended (E)	[S/T]GxxGxxG	YxxxK	18
intermediate (I)	[G/A]xxGxx[G/A]	YxxxK	-
complex (X)	GGxGxxG	YxxxN	1
divergent (D)	GxxxxxSxA	YxxMxxxK	-
atypical (A)	variable	variable	1
unassigned (U)	-	-	2

Listed are the seven types of SDRs and their characteristic cofactor and active site motifs. The given numbers of human SDRs within the different types result from their classification into SDR families according to the SDR nomenclature initiative and can differ from other experimental records [120–123]. Square brackets indicate possible amino acid residues at this position and any amino acid residues or gaps within the motifs are shown as "x".

I.2.2. Human 17β-Hydroxysteroid Dehydrogenases (17β-HSDs) belonging to the superfamily of SDRs

The superfamily of SDRs includes members of numerous enzyme families belonging to the class of, e.g., oxidoreductases, epimerases, dehydratases, or lyases [122, 126]. One family is the family of 17β-hydroxysteroid dehydrogenases (17β-HSDs), which covers enzymes belonging to either the protein superfamily of AKRs or SDRs and catalyzing redox reactions at position C17 of steroid nuclei [128, 129]. In general, 17β-HSDs are multifunctional enzymes with a broad substrate spectrum, since most of them do not only oxidize or reduce steroids but also (some of them preferentially) other substrate classes, like retinoids, fatty acids, or bile acids. One feature of 17β-HSDs of the SDR superfamily is that they possess several conserved amino acid sequence motifs [Table I-3] and a high structural similarity but only low amino acid sequence identity (approx. 20 %) outside of the conserved regions [129, 130]. An especially high variability in amino acid residues is found in the C-terminal regions which define the substrate selectivity of 17β-HSDs [130].

Table I-3: Conserved SDR sequence motifs in 17β-HSDs.

conserved SDR sequence motif	position within the protein	function
TGxxxGxG	N-terminal, part of Rossmann-fold	cofactor binding
NAG	between cofactor binding & active site	structure stabilization
YxxSK	catalytic center	active site
PGxxxT	C-terminal of active site	definition of reaction direction

Up to now, 14 human 17β-HSD family members (13 SDRs and 1 AKR) have been annotated and more or less intensely studied. The results of these studies, especially the characteristics and biological roles of 17β-HSDs, have been summarized in several reviews [129, 131–134]. Looking at the substrate spectrum and promoted reactions *in vitro* and *in vivo* it can be seen that, although classified as 17β-HSDs, these enzymes do not only catalyze redox reactions at position C17 but also at position C3 of steroid nuclei and that steroids are not necessarily their biological substrates. Whereas some of the human 17β-HSD members belonging to the superfamily of SDRs are well characterized, the detailed enzymatic and structural parameters as well as the actual roles *in vivo* of other members (e.g., 17β-HSD6, 17β-HSD11, 17β-HSD12, 17β-HSD13, 17β-HSD14) are still more or less unclear [Table I-4]. It has been shown that several 17β-HSDs play an important role in various biological processes, like the pre-receptor-regulated steroid signaling and homeostasis (17β-HSD1, 17β-HSD2, 17β-HSD3, and 17β-HSD10), the cholesterol biosynthesis (17β-HSD7), the bile acid metabolism (17β-HSD4), or the fatty acid metabolism (17β-HSD4, 17β-HSD8, and 17β-HSD10), as well as in the development of diseases, like cancer (17β-HSD1, 17β-HSD2, and 17β-HSD3), pseudo-hermaphroditism (17β-HSD3), metabolic diseases (17β-HSD4, 17β-HSD8, and 17β-HSD10), or neurological diseases (17β-HSD1, 17β-HSD10) [129, 133–138].

One human 17β-HSD family member with yet ambiguous function *in vivo* is the 17β-HSD type 12 (17β-HSD12, SDR12C1). 17β-HSD12 is encoded on chromosome 11p11 by the *HSD17B12* gene. This gene covers 11 exons and is ubiquitously expressed [139–141]. The translated protein is 312 amino acid residues in length (molecular weight of 34.3 kDa) and possesses high similarity (72 % and 40 % amino acid residue similarity and identity, respectively) to the androgen metabolizing 17β-HSD3, its closest relative [129, 139, 142]. Like 17β-HSD3, 17β-HSD12 is anchored to the membrane of the endoplasmic reticulum (ER) [140, 142, 143]. However, 17β-HSD12 shows only very low activity with androgens and estrogens indicating a minor role in steroid metabolism [139, 144]. Instead, Moon and Horton showed that the reductive 17β-HSD12 might play an important role in the elongation of (very) long-chain fatty acids ((V)LCFA), and therefore they called 17β-HSD12 also 3-keto-acyl-CoA reductase (KAR) or very-long-chain 3-oxoacyl-CoA reductase [140]. This presumed biological function is supported by the its homologs in *Saccharomyces cerevisiae* (Ybr159p) and *Caenorhabditis elegans* (LET-767) as well as by the fact that 17β-HSD12 is capable of curing the phenotype of *ΔYbr159* mutant yeasts and shows higher expression levels in differentiated adipocytes when compared with undifferentiated preadipocytes [145, 146]. Yet, up to now, no in-depth characterization of 17β-HSD12, concerning, e.g., its substrate spectrum, kinetic parameters, interaction partners, and structure, which could clarify the question if 17β-HSD12 is a steroid or fatty acid metabolizing enzyme, have been reported.

Table I-4: Human 17β-HSDs belonging to the superfamily of SDRs.

17β-HSD (SDR family) member	subcellular localization	preferred cofactor *(reaction direction)*	substrate (classes)	references
17β-HSD1 (SDR28C1)	cytosol	NADP(H) *(reductive)*	**estrogens**, androgens, retinoids	[147, 148]
17β-HSD2 (SDR9C2)	ER *(membrane-bound)*	NAD(H) *(oxidative)*	**estrogens**, **androgens**, **gestagens**	[149, 150]
17β-HSD3 (SDR12C2)	ER *(membrane-bound)*	NADP(H) *(reductive)*	**androgens**, estrogens	[135, 143]
17β-HSD4 (SDR8C1)	peroxisomes *(membrane-bound)*	NAD(H) *(oxidative)*	(very long)- and branched-chain **fatty acid thioesters**, androgens, estrogens, bile acid intermediates	[151–156]
17β-HSD6 (SDR9C6)	ER *(membrane-bound)*	NAD(H) *(oxidative)*	**androgens**, **gestagens**, retinoids	[157–160]
17β-HSD7 (SDR37C1)	ER *(membrane-bound)*	NADP(H) *(reductive)*	**zymosterone**, estrogens, androgens	[136, 161]
17β-HSD8 (SDR30C1)	mitochondria *(matrix)*	NAD(H) *(oxidative)*	**fatty acid thioesters**, estrogens, androgens	[162, 163]
17β-HSD9 (SDR9C5)	ER *(membrane-bound)*	NAD(H) *(oxidative)*	**retinoids**, androgens	[164, 165]
17β-HSD10 (SDR5C1)	mitochondria *(matrix)*	NAD(H) *(oxidative)*	(methylated) short-chain **fatty acid thioesters**, estrogens, androgens, glucocorticoids, gestagens, bile acids	[137, 138, 166, 167]
17β-HSD11 (SDR16C2)	ER / lipid droplets *(membrane-bound)*	NAD(H) *(oxidative)*	androgens, estrogens, lipids?	[168–171]
17β-HSD12 (SDR12C1)	ER *(membrane-bound)*	NADP(H) *(reductive)*	(very) long-chain **fatty acid thioesters**, estrogens, androgens	[139, 140]
17β-HSD13 (SDR16C3)	lipid droplets *(membrane-bound?)*	NAD(H)?	lipids?	[172, 173]
17β-HSD14 (SDR47C1)	cytosol	NAD(H) *(oxidative)*	androgens, estrogens	[174]

Listed are fundamental biological characteristics of the 13 validated human 17β-HSD members belonging to the SDR superfamily. Of the accepted substrate classes identified in *in vitro* or/and *in vivo* analyses, the substrates playing very probably the most important role *in vivo* are highlighted in bold characters. Unclear features are labeled by a question mark.

I.3. FATTY ACID AND STEROL/STEROID METABOLISM

The short-/medium- and very long-chain fatty acid metabolism as well as the vitamin D and the steroid metabolism are central pathways covered within this thesis. Because of this, the basics of these pathways, which all originate from the common precursor acetoacetyl-CoA [Figure I-3], are described in the following sections.

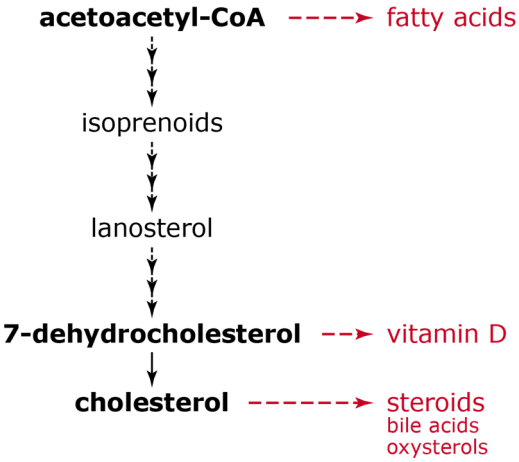

Figure I-3: Precursors of fatty acids, vitamin D metabolites, and other sterols/steroids.

I.3.1. SHORT-CHAIN VS. LONG-CHAIN FATTY ACID ELONGATION

The mechanisms of short-chain fatty acid (SCFA) and (very) long-chain fatty acid ((V)LCFA) synthesis have been intensely studied by researchers in the past. These studies led to a comprehensive knowledge of successive basic steps in the SCFA and (V)LCFA elongation as described below and illustrated in Figure I-4.

Whereas the SCFA elongation (acyl chain length up to C16) takes place in the cytosol of eukaryotic organisms and is mainly catalyzed by the fatty acid synthase I (FAS I) – a dimeric multi-domain protein system with six different catalytic centers (malonyl/acetyl transferase, β-keto-acyl-ACP synthase, β-keto-acyl-ACP reductase, β-hydroxyl-acyl-ACP dehydrase, 2-enoyl-ACP reductase, and thioesterase) –, the elongation of LCFAs and VLCFAs (acyl chain length of C16 and longer) takes place in the endoplasmic reticulum (ER) and covers four steps which are catalyzed by discrete ER membrane associated enzymes [175–178]. The process of (V)LCFA elongation was first analyzed in detail in yeasts [177, 179]. In yeast, the steps of malonyl-CoA condensation to acyl-CoA chains, 3-keto-acyl-CoA reduction, 3-hydroxy-acyl-CoA dehydration, and 2-enoyl-CoA reduction are catalyzed by the members of the Elo family, Ybr159p, Phs1p, and Tsc13p, respectively [Figure I-4]. In humans, seven elongases (ELOVL1-7) with variable substrate specificities, catalyzing the first step of (very) long-acyl fatty acid elongation and being homologous to the yeast Elo family members, have been identified between the late 1990s and 2000s [177, 180]. Moon and Horton described 2003 a single human 3-keto-acyl-CoA reductase (KAR), representing the human homolog of the Ybr159p in *Saccharomyces cerevisiae* (*S. cerevisiae*) and catalyzing the NADPH-dependent

reduction of 3-keto-acyl-CoA conjugates within the second step in (V)LCFA elongation [140]. This KAR had high sequence homology to members of the family of 17β-HSDs and was found to be identical to the human 17β-HSD12, an ubiquitous enzyme with up to that date unclear function [129, 140]. The subsequent dehydration of 3-hydroxy-acyl-CoA conjugates generating the respective trans-2-acyl-CoA conjugates is catalyzed in humans by the four members of the human 3-hydroxy-acyl-CoA dehydratase family: HACD1-4 [178, 181]. The four HACDs display distinct expression pattern and possess more or less sequence identity with the single yeast homolog Phs1p catalyzing the third step in (V)LCFA elongation [181]. Finally, the last step in (V)LCFA elongation, namely the NADPH-dependent reduction of the unsaturated trans-2-acyl-CoA conjugates to the saturated acyl-CoA conjugates, is catalyzed by the ubiquitous human trans-2,3-enoyl-CoA reductase TER, a homolog of the yeast Tsc13p [140, 178].

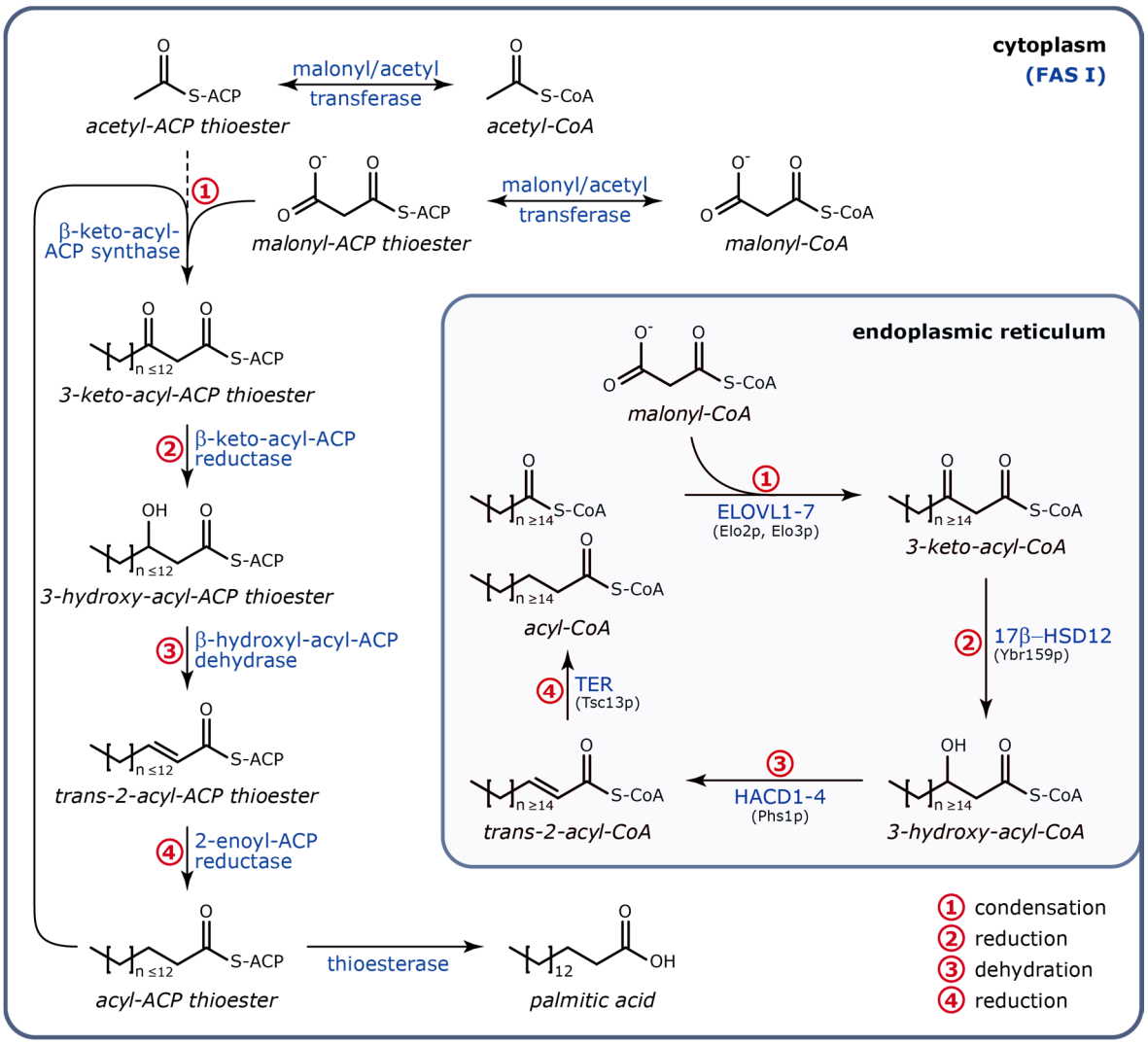

Figure I-4: Short-chain fatty acid (SCFA) and (very) long-chain fatty acid ((V)LCFA) elongation. Illustrated are the basic cycling steps of SCFA and (V)LCFA elongation and their compartmentalization. The SCFA elongation generally takes place in the cytosol and is mediated by a homodimer of the soluble fatty acid synthase I (FAS I), a single enzyme with six different catalytic centers. In contrast, four discrete non-soluble transmembrane enzymes catalyze the elongation of (V)LCFAs in the endoplasmic reticulum (ER). The domains of the FAS I as well as the human enzymes involved in (V)LCFA elongation are shown in blue and the yeast homologs of human enzymes are listed in brackets.

Although the basic steps of the (V)LCFA synthesis (as well as the above not specified introduction of double bonds or side chains) are well analyzed and described, the single enzymes involved in the elongation process are poorly characterized because of their multiple transmembrane regions which anchor them to the membrane of the ER and allow widely only for their analysis in a microsomal environment.

I.3.2. THE ROLE OF MITOCHONDRIA IN FATTY ACID METABOLISM

Mitochondria are known to perform multiple crucial functions *in vivo* including, among others, the first steps of steroid synthesis and parts of the urea cycle (detoxification of ammonia) as well as the induction of the cell death via apoptosis. Besides, mitochondria are especially famous for being the energy machineries of eukaryotic cells. Thereby, the citric cycle, which is a central pathway within the mitochondrial matrix, generates redox equivalents (in form of NADH and $FADH_2$) but also the energy carrier molecules ATP and GTP. In successive electron transfer reactions, these redox equivalents drive the oxidative phosphorylation pathway and thus the synthesis of the major ATP pool in the cells. The citric cycle is primarily fed by acetyl-CoA, a small molecule which results either from the oxidative decarboxylation of the glycolysis end-product pyruvate by the pyruvate dehydrogenase complex (PDC) or from the β-oxidation of fatty acids in the mitochondrial matrix [Figure I-5].

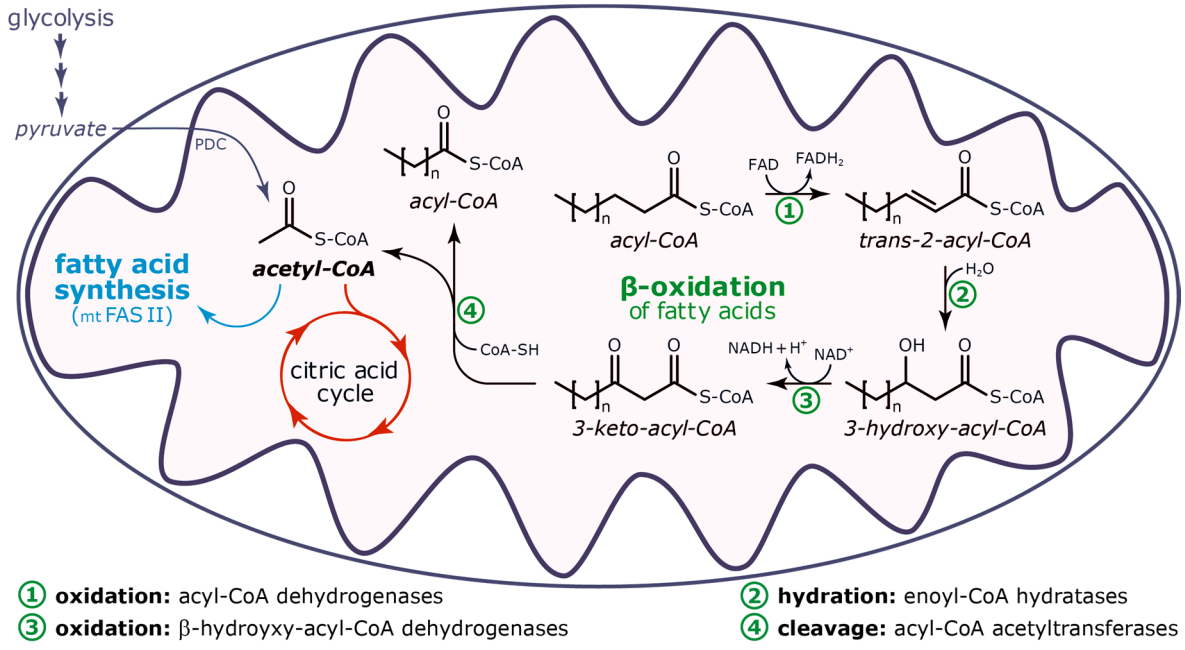

Figure I-5: Mitochondrial β-oxidation of fatty acids generates the central metabolite acetoacetyl-CoA.
Shown are the basic steps of the β-oxidation of fatty acids in the mitochondria (recently reviewed in more detail by Houten *et al.* [182]). Each β-oxidation cycle reduces the acyl chain of fatty acids by two carbon atoms and generates acetyl-CoA as well as $FADH_2$ and NADH redox equivalents. A high portion of the resulting acetyl-CoA feeds the citric cycle and some of the acetyl-CoA is used for the mitochondrial *de novo* fatty acid synthesis, a process in which the enzymes of the mitochondrial fatty acid synthesis type II (mtFAS II) complex are involved [Table I-5].
PDC, pyruvate dehydrogenase complex.

However, mitochondria do not only host the machinery for the catabolism of fatty acids via β-oxidation but also enzymes for the anabolism of fatty acids. This mitochondrial fatty acid synthesis complex (mtFAS II) resembles the cytosolic fatty acid synthesis type II complex occurring, for example, in bacteria and catalyzes the *de novo* synthesis of fatty acids [183–185]. The fatty acid elongation process in mitochondria follows in principle the same catalytic steps as the cytosolic fatty acid synthase type I (FAS I) [Figure I-4]. Though, in contrast to the cytosolic FAS I of eukaryotes which is a homodimer of a multifunctional polypeptide chain, the mtFAS II complex comprises discrete nuclear encoded proteins/ enzymes [Table I-5].

Table I-5: Members of the mitochondrial fatty acid synthesis type II complex.

mtFAS II complex members (protein / molecular function)	encoding genes	
	yeast	**human**
mitochondrial acyl carrier protein	*ACP1*	*NDUFAB1*
phosphopantetheine:protein transferase	*PPT2*	*AASDHPPT*
acetyl-CoA carboxylase	*HFA1*	*ACACB?*
malonyl-CoA:ACP transferase	*MCT1*	*MCAT*
3-keto-acyl-ACP synthase	*CEM1*	*OXSM*
3-keto-acyl-ACP reductase	*OAR1*	*HSD17B8+CBR4*
3-hydroxy-acyl-ACP dehydratase	*HTD2*	*RPP14*
2-enoyl-ACP reductase	*ETR1*	*MECR*

Listed are the basic components of the mitochondrial fatty acid synthesis (mtFAS II) complex, which resembles the type II fatty acid synthase complexes found in bacteria, as well as the corresponding genes encoding for these components in the yeast *S. cerevisiae* and in humans [184–188]. Please note that the role of acetyl-CoA carboxylase 2 (encoded by *ACACB*) in the mtFAS II is only supposed because of its subcellular localization and enzymatic properties [187, 188] and has not been validated so far (indicated by "?").

Whereas the pathway of mitochondrial fatty acid synthesis as well as the involved proteins are well explored in *S. cerevisiae*, the human counterparts are less characterized [184]. Similar to the cytosolic fatty acid synthesis by the FAS I, the elongation of fatty acids in mitochondria takes place by being attached to a phosphopantetheine arm which is covalently linked to the mitochondrial acyl carrier protein (mtACP). In humans, the mtACP is a non-catalytic subunit of the respiratory chain complex I and encoded by the *NDUFAB1* gene [184, 189]. The post-translational association of the phosphopantetheine arm to the mitochondrial apo-ACP, resulting in its holo-form, is most likely catalyzed by the L-aminoadipate-semialdehyde dehydrogenase-phosphopantetheinyl transferase (AASDHPPT) [184, 186]. Like in the cytosolic pathway, malonyl-ACP thioester units are the building blocks for the prolongation of the growing acyl chain. Those units result from the carboxylation of acetyl-CoA and the successive trans-esterification of the resulting malonyl-CoA to the mtACP [184]. The enzymes catalyzing these reactions, namely the mitochondrial acetyl-CoA carboxylase and the mitochondrial malonyl-CoA-acyl carrier protein transacylase, are well

known in yeast (encoded by the genes *HFA1* and *MCT1*, respectively) [184]. Although, literary researches indicate that the acetyl-CoA carboxylase 2 (encoded by *ACACB*) is the human mitochondrial acetyl-CoA carboxylase involved in the mtFAS II, the role of this enzyme in mtFAS II still needs to be validated [187, 188]. The human mitochondrial malonyl-CoA-acyl carrier protein transacylase is known and encoded by the gene *MCAT* which is a homolog of the yeast *MCT1* [184, 190]. Within the elongation process, the condensation of an acetyl unit (from malonyl-ACP) to the growing acyl-ACP chain is catalyzed by the mitochondrial 3-keto-acyl-ACP synthase which is encoded by *OXSM* in humans [184]. The human 3-keto-acyl-ACP reductase (mtKAR) catalyzing the subsequent reduction of 3-keto-acyl-ACP towards 3-hydroxy-acyl-ACP had been completely unknown for a long time [184]. While a single short-chain dehydrogenase/reductase (SDR), the 3-oxo-acyl-ACP reductase (encoded by *OAR1*), carries out this reaction in yeast, more recent studies indicate that the human mtKAR is built up by a heterotetramer of the 17β-HSD8 and the carbonyl reductase family member 4, encoded by the human genes *HSD17B8* and *CBR4*, respectively [162, 184, 185, 191]. The last two steps of mitochondrial fatty acid elongation, the dehydration of the 3-hydroxy-acyl chain and the reduction of the resulting enoyl-chain, are catalyzed by 3-hydroxy-acyl-ACP dehydratases and 2-enoyl-ACP reductases which are represented by the mitochondrial hydroxyacyl-thioester dehydratase type 2 (encoded by *RPP14*) and the mitochondrial trans-2-enoyl-CoA reductase (encoded by *MECR*) in humans, respectively [184].

As a result, the mtFAS II provides octanoic acid, the direct precursor for the synthesis of lipoic acid, but also fatty acids with acyl chains counting up to 14-16 carbon atoms [183–185]. The importance of the mitochondrial fatty acid synthesis for the mitochondrial function has been shown in several studies [184, 185]. Thus, the disruption of parts of the mtFAS II machinery in yeast resulted in phenotypes exhibiting small rudimentary mitochondria, deficient mitochondrial respiration, a loss of mitochondrial cytochromes, and low cellular lipoic acid levels which could be reversed by the complementation with the respective human homologs [184, 185]. The mtFAS II effects not only the mitochondrial respiration via the generation of the precursor of lipoic acid, which is necessary for the lipoylation and thus the integrity of mitochondrial proteins, and probably of additional medium- and long-chain fatty acids [184, 185, 192]. Moreover, it was shown that an impaired mtFAS II function is linked to an inefficient RNaseP cleavage in mitochondria which negatively effects the maturation of mitochondrial tRNAs and by this reduces the rate of mitochondrial protein synthesis [184, 193].

Although first insights into the *de novo* fatty acid synthesis in mitochondria and its effect on the integrity and functionality of mitochondria were received in the past, the complete role of mtFAS II on cell metabolism and potential further enzymes involved in mtFAS II remain interesting research topics in the future.

I.3.3. SEX STEROID METABOLISM

Sex steroid hormones (gestagens, androgens, and estrogens) play a central role in life and represent extremely effective signaling molecules, e.g., for the sex steroid hormone receptor-regulated transcription of target genes. Because of their vital role in health (e.g., sexual differentiation and reproduction or modulation of the immune system) but also in diseases (e.g., cancer or autoimmune diseases), the metabolism of sex steroids, which is basically described in the following and illustrated in Figure I-6, was and is intensely studied and reviewed by many researchers [78, 194–197].

The first steps of steroidogenesis start from the precursor cholesterol (**1**) and take place in mitochondria by the action of the mitochondrial type I cytochrome P450 enzyme CYP11A1 which catalyzes the formation of the C21-steroid (gestagen) pregnenolone (**2**) through successive hydroxylation and oxidation reactions [198]. The subsequent oxidation of the pregnenolone's 3β-hydroxyl group and isomerization of the Δ5 double bond into a Δ4 double bond by a 3β-hydroxysteroid dehydrogenase/Δ5→4-isomerase (3β-HSD) in the mitochondria or endoplasmic reticulum (ER) results in progesterone (**3**), the physiologically most active gestagen. Here, it should be noted that the pregnenolone exits the mitochondria in an unaided way for the subsequent steps of sex steroidogenesis in the ER [198]. In the ER, pregnenolone and progesterone become hydroxylated at position C17 of the steroid nucleus by the type II cytochrome P450 enzyme CYP17A1 leading to 17α-hydroxypregnenolone (**4**) and 17α-hydroxyprogesterone (**5**), respectively. Via the additional 17,20-lyase activity of the CYP17A1, the 17α-hydroxylated gestagens are converted into androgens (C19-steroids) in the ER. Thereby, the cleavage of the C20-C21 side chain from 17α-hydroxypregnenolone and 17α-hydroxyprogesterone results in the generation of dehydroepiandrosterone (DHEA) (**8**) and Δ4-androstenedione (**9**), respectively. Beside the 3β-HSDs, which catalyze the oxidation and Δ5→4-isomerization of Δ5-androgens, several enzymes belonging to the class of 3α-HSDs and 17β-HSDs, which catalyze redox reactions on the positions C3 and C17 of the steroid nucleus, respectively, are involved in the activation and inactivation of androgens [Figure I-6]. By doing so, the most physiological active androgens testosterone (**11**) and dihydrotestosterone (DHT) (**12**) are built from but also inactivated to the less potent androgens Δ4-androstenedione, Δ5-androstene-3β,17β-diol (**10**), 3β,17β-androstanediol (**13**), 3α,17β-androstanediol (**14**), androstanedione (**15**), and androsterone (**16**). A key enzyme within the androgen pathway is the 5α-reductase 2 (S5AR2). S5AR2 catalyzes the reduction of the Δ5 double bond in testosterone resulting in the even more potent saturated androgen DHT. However, active androgens can not only be synthesized via the classical pathway described above but also by a so-called backdoor pathway [Figure I-6]. Here, the Δ5 double bond of 17α-hydroxypregnenolone is reduced by the Δ5-reductase 1 (S5AR1) leading to 17α-hydroxypregnane-3,17-dione (**6**) which is further reduced by 3α-HSDs. The resulting pregnane-3α,17α-diol-20-one (**7**) is like the other 17α-hydroxygestagens a good substrate for the CYP17A1 which catalyzes the generation of the androgen androsterone via its 17,20-lyase activity [194, 195]. *In vivo*, the estrogens estrone (**17**) and the highly physiologically active estradiol (**18**) are generated from Δ4-androstenedione and testosterone, respectively. These reactions are catalyzed by the aromatase CYP19A1, which belongs also to the type II cytochrome P450 enzymes, and takes place in the ER as all steps in sex steroidogenesis with the exception of the initial gestagen formation.

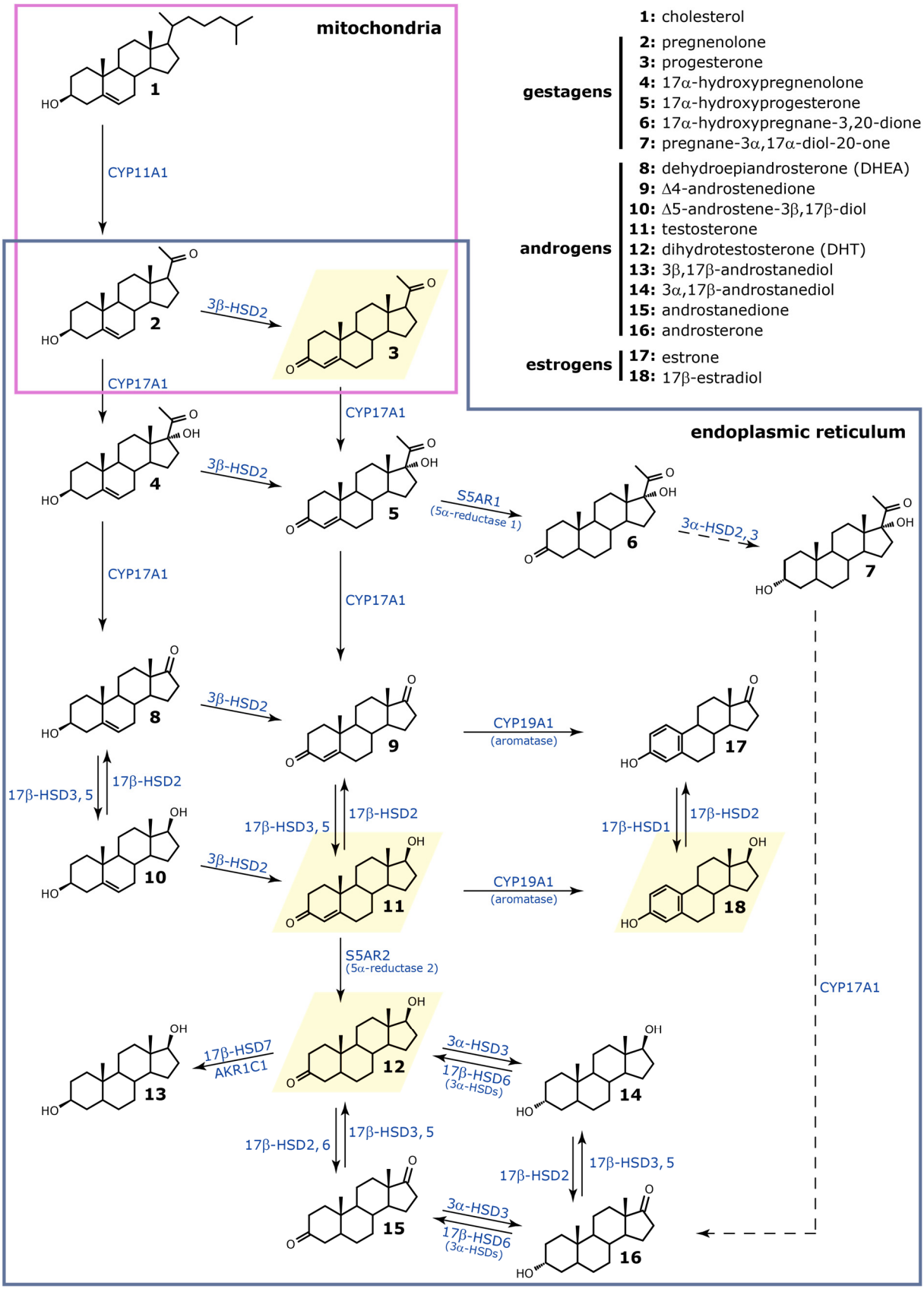

Figure I-6: Sex steroid metabolism pathway.
Shown are the fundamental steps for the activation and inactivation of sex steroids together with the major enzymes catalyzing those reactions [78, 194–196]. Reactions of the so-called backdoor pathway are indicated by dashed lines and the most physiologically active sex steroids are highlighted in yellow.

I.3.4. CYTOCHROME P450 ENZYMES (CYPS) AND THEIR ROLE IN VITAMIN D METABOLISM

The vitamin D metabolism and signaling represents another physiologically important pathway in mammalians in general and particularly in humans.

In humans, the metabolic vitamin D pathway [Figure I-7], which can be divided into an activation and an inactivation (catabolic) sequence and is well described in literature, is mainly catalyzed by five enzymes belonging to the cytochrome P450 superfamily [199–201]. As shown in Figure I-7, the endogenous vitamin D molecule vitamin D_3 (**3**), which is like the nutritional vitamin D_2 (**4**) a direct precursor for all subsequent enzymatic vitamin D activation and inactivation steps of the vitamin D pathway, is formed in the skin from the vitamin D_3 precursor 7-dehydrocholesterol (**1**) by two successive non-enzymatic reactions. Here, 7-dehydrocholesterol is first transformed to provitamin D (**2**) by an UV-light triggered photochemical reaction. This intermediate is then isomerized to vitamin D_3 by an isothermal reaction. For the generation of the major biologically active vitamin D derivatives 1α,25-dihydroxyvitamin D_3 (**7**) and 1α,25-dihydroxyvitamin D_2 (combined in the term 1α,25-dihydroxyvitamin D), vitamin D_3 as well as vitamin D_2 are generally in the liver first hydroxylated at position C25 by the 25-hydroxylases CYP27A1, CYP2R1, and CYP3A4 forming the vitamin D storage forms 25-hydroxyvitamin D_3 (**5**) and 25-hydroxyvitamin D_2. In the second activation step which takes place in the kidneys but also other target tissues, these storage forms are further hydroxylated at position C1 by the 1α-hydroxylase CYP27B1 to generate the potent 1α,25-dihydroxyvitamin D. However, 25-hydroxyvitamin D_3 and 25-hydroxyvitamin D_2 can also become hydroxylated at position C24 by the 24-hydroxylase CYP24A1 which results in 24,25-dihydroxyvitamin D_3 (**6**) and 24,25-dihydroxyvitamin D_2, respectively. The active vitamin D metabolites are inactivated and catabolized by successive hydroxylation and/or oxidation reactions, again catalyzed by the CYP24A1. Thereby, the initial hydroxylation occurs either at position C24 (**8**) or at position C23 (**10**) and initiates the calcitroic acid (**9**) or lactone (**11**) degradation pathway, respectively. Besides, the C3 epimerization of vitamin D metabolites via a yet unknown mechanism seems to be another pathway for the modulation of vitamin D signaling *in vivo* [202–205].

The major biologically active vitamin D metabolite 1α,25-dihydroxyvitamin D is involved in a plethora of physiological processes in a vitamin D receptor dependent or independent manner. Thus, for example, 1α,25-dihydroxyvitamin D effects the bone health by regulating the calcium and phosphorus homeostasis, increases the muscle strength and mass via neuromuscular effects, mediates favorable immunomodulatory effects in diseases (e.g., in multiple sclerosis, type 1 diabetes, psoriasis, rheumatoid arthritis, or asthma), mediates cardiovascular effects via the regulation of the renin-angiotensin system and an increased insulin sensitivity, and reduces the risk of cancer by antiproliferative, antiangiogenetic, prodifferentiative, and apoptotic effects [206–208]. Although 1α,25-dihydroxyvitamin D had been considered to be the most important biologically active vitamin D metabolite for a long time, recent studies predicted also a physiological role for the vitamin D metabolite 24,25-dihydroxyvitamin D [209, 210]. Because of the deep impact of the levels of vitamin D metabolites in health and disease, cytochrome P450 enzymes of the metabolic vitamin D pathway as well as vitamin D metabolites themselves are promising targets in the therapy of multiple diseases, like osteoporosis, inflammatory diseases, and cancer [199, 206, 211].

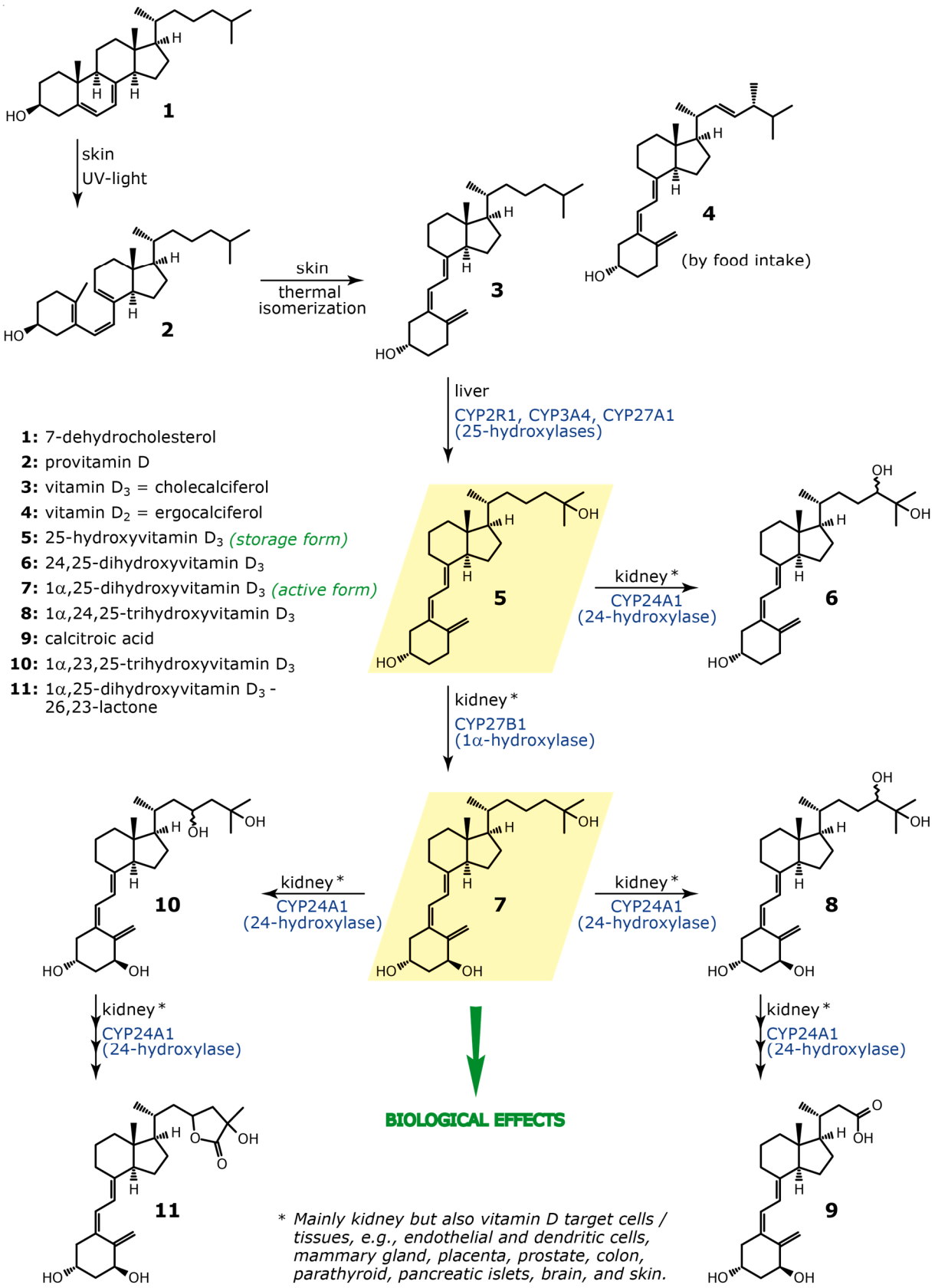

Figure I-7: Vitamin D metabolism pathway.
The vitamin D pathway is exemplarily shown for endogenous vitamin D_3 metabolites; but it is also valid for nutritional vitamin D_2 derivatives [199–201]. The major vitamin D_3 storage form 25-hydroxyvitamin D_3 (**5**) and the most potent biologically active metabolite 1α,25-dihydroxyvitamin D_3 (**7**) are highlighted in yellow.

I.4. AIMS OF THIS THESIS

AKRs and SDRs are large and steadily growing superfamilies which are characterized by their typical cofactor binding structures: $(\alpha/\beta)_8$-barrel structure and Rossmann fold, respectively. Despite these central, conserved structures, members of both superfamilies reveal highly variable and mostly broad substrate spectra [14, 122]. Because of their crucial roles *in vivo* and their association with numerous diseases, members of these superfamilies have been intensely studied for a long time.

Bioinformatic improvements lead to the permanent identification of novel family members. Thus, a novel human AKR member with unknown features and biological roles – called *AKR1B15* – was identified and annotated in 2011 [22]. This thesis aimed to characterize the novel human *AKR1B15* fundamentally in order to get an idea about its function *in vivo*. For this, the expression of *AKR1B15* on transcript and protein level as well as the subcellular localization of AKR1B15 isoforms, demanding also the generation of specific antibodies, were analyzed. Furthermore, substrates belonging mainly to the group of steroids or fatty acids were identified and enzymatic parameters determined. Finally, as starting point for future *in vivo* analyses, all necessary constructs for an AKR1B15 knock-out in cell lines expressing *AKR1B15* endogenously via the TALEN technology were prepared and tested.

In contrast, some members belonging to the AKR or SDR family have been known for a long time, however, their actual functions *in vivo* are still unclear. One of those family members is the human SDR *HSD17B12*. Although there is strong evidence that the human 17β-HSD12 is involved in the fatty acid metabolism *in vivo*, a role in the steroid metabolism cannot be completely excluded [139, 140]. Here, a method for the solubilization and purification of the presumed membrane-bound protein from the heterologous expression system *Pichia pastoris* was established, allowing for a closer characterization of its enzymatic activities.

Vitamin D metabolites, especially 1α,25-dihydroxyvitamin D, are known to have numerous effects *in vivo*. Because of its assumed anticancer effects, 1α,25-dihydroxyvitamin D itself but also enzymes belonging to the superfamily of CYPs, which catalyze the metabolism of vitamin D metabolites and thus control the levels of active vitamin D metabolites *in vivo*, represent promising targets for cancer therapy [208]. A comprehensive determination of the levels of all metabolites of the vitamin D pathway in biological samples could enable an in-depth assessment of the vitamin D status in samples but would also help to answer open questions of basis research. Thus, an analytical tool which could measure more than only one or two vitamin D metabolites at a time (as it is common for most commercially available methods at the moment) would facilitate such diagnostic and research.

Hence, another aim of this thesis was to develop, establish, and validate a LC-MS/MS based method for the simultaneous detection and quantification of as many important components of the vitamin D metabolism pathway as possible in biological samples, especially in samples from cell culture experiments. By the use of this novel method, it was aimed to explore the uptake and metabolism of vitamin D metabolites in cultured cells as well as to analyze the effect of azoles (e.g., itraconazole), which are known to be CYP inhibitors, on the vitamin D metabolism (especially on the inactivation of 1α,25-dihydroxyvitamin D).

II. MATERIAL AND METHODS

II.1. WORKING WITH *ESCHERICHIA COLI* (*E. COLI*)

All work with *E. coli* was performed in a semi-sterile manner, which means using only sterile materials and acting next to a Bunsen burner flame.

II.1.1. CULTIVATION OF *E. COLI*

E. coli cells (see II.12.1.1) were cultured either in liquid LB medium or on LB agar plates, both containing the appropriate selection antibiotic [Table II-1].

Table II-1: Final concentrations of antibiotics in culture media.

antibiotic		final concentration
ampicillin	(Amp)	100 $\mu g/ml$
kanamycin	(Kan)	50 $\mu g/ml$
spectinomycin	(Spec)	50 $\mu g/ml$
tetracycline	(Tet)	10 $\mu g/ml$
Zeocin	(Zeo)	25 $\mu g/ml$

Liquid *E. coli* cultures were used for colony screens, plasmid amplifications, or recombinant protein expressions. Colony screen and plasmid amplification cultures were incubated at 37 °C with gentle agitation (180-200 rpm). In contrast, cultures for recombinant protein expression were initially grown at 37 °C and after induction incubated at 30 °C, both with gentle agitation (180-200 rpm). Cultivation of *E. coli* on LB-agar plates was used for the selection of transformed *E. coli* cells or for the isolation of single *E. coli* clones from agar stabs as well as glycerol stocks. For this, the plates were incubated at 37 °C overnight. Glycerol stocks were prepared for the long-term storage of *E. coli* clones by mixing 1 ml of liquid overnight cultures with 500 µl of sterile 80 % glycerol and freezing them at -80 °C.

LB medium:	2.5 % (w/v)	LB-medium (Luria/Miller) powder in MilliQ-H_2O
LB-agar plates:	4 % (w/v)	LB-agar (Luria/Miller) powder in MilliQ-H_2O
80 % glycerol	80 % (v/v)	glycerol in MilliQ-H_2O

LB medium, LB-agar, and 80 % glycerol were autoclaved at 121°C for 20 min. Antibiotics were added to the chilled medium or agar.

II.1.2. TRANSFORMATION OF CHEMICALLY COMPETENT *E. COLI*

According to downstream applications, 50-100 µl of the respective chemically competent *E. coli* strains (see II.12.1.1) were thawed on ice and 1-10 µl of either plasmid solutions or ligation reactions were added. The transformation batches were incubated on ice for 30 min before a heat shock using a bench incubator at 42 °C was carried out for 1 min. Thereby, the incubation on ice allows the plasmids to adhere on the cell membranes, while the heat-shock enables the inclusion of the plasmids into the *E. coli* cells. The heat-shocked cells were immediately cooled on ice before 400 µl LB medium or S.O.C. medium (Invitrogen) were added. Afterwards, the transformation reactions were incubated with gentle agitation (180-200 rpm) at 37 °C for 60 min. Finally, 50-350 µl of the transformation reactions were plated on LB-agar plates containing the appropriate antibiotic and incubated at 37 °C overnight. If plasmids allowing for blue-white screening of cells were transformed, the transformation reactions were streaked out together with 50 µl X-Gal/IPTG.

Plates showing colonies were wrapped with Parafilm M and kept at 4 °C for long-term storage.

X-Gal/IPTG:	5 1	volumes volume	X-Gal solution IPTG solution
X-Gal solution:	20	$^{mg}/_{ml}$	X-Gal in dimethyl formamide
IPTG solution:	0.5	M	IPTG in MilliQ-H_2O

IPTG solution was sterile filtrated using sterile syringe filters with a 0.22 µm pore size.

II.1.3. AMPLIFICATION OF PLASMIDS IN *E. COLI*

Plasmids were amplified in transformed *E. coli* cells of the strain DH5α, TOP10, or Stellar [II.12.1.1].

For mini-scale plasmid amplification 2-5 ml LB medium containing the appropriate antibiotic were inoculated with either 100-300 µl of a colony screen culture, one single colony from a LB-agar plate, or 5-20 µl of a frozen glycerol stock culture and incubated with gentle agitation (180-200 rpm) at 37 °C overnight.

For midi-scale plasmid amplification 5 ml LB medium containing the appropriate antibiotic were inoculated with 5-20 µl of a frozen glycerol stock culture and grown with gentle agitation (180-200 rpm) at 37 °C for 8-16 h. This pre-culture was transferred to 50-100 ml LB medium containing the appropriate antibiotic and further incubated with gentle agitation (180-200 rpm) at 37 °C overnight.

II.1.4. CULTIVATION OF *E. COLI* CLONES FOR COLONY SCREENS

In order to identify *E. coli* clones including the requested plasmids after the cloning process, single colonies grown on LB-agar plates were screened by PCR. To amplify single *E. coli* clones for the screening process and the downstream glycerol stock preparation and plasmid isolation steps, wells of a 96-well square-deep-well plate (Macherey-Nagel) containing 400 µl LB medium supplemented with the appropriate antibiotic were inoculated with single *E. coli* colonies from the LB-agar plates, closed with an adhesive gas permeable membrane (Thermo Scientific) and incubated with gentle agitation (180-200 rpm) at 37 °C for 2-3 h. During the analysis of the colonies and before initiating the downstream processes, the colony screen cultures in the 96-well plates were tightly closed and kept at 4 °C for short-term storage.

II.1.5. RECOMBINANT EXPRESSION OF PROTEINS IN *E. COLI*

Different AKRs were recombinantly expressed in *E. coli*. For this purpose, *E. coli* BL21(DE3) cells which were transformed with pET28a(+)-based plasmids (encoding for N-terminally His_6-tagged AKRs under the control of a T7*lac* promoter, see also II.12.4) were used. 5-20 ml LB-Kan(50) medium were inoculated with the respective *E. coli* BL21(DE3) - pET28a(+)-AKR glycerol stock culture and incubated with gentle agitation (180-200 rpm) at 37 °C overnight. The next day, the pre-culture was transferred into 100-1000 ml LB-Kan(50) medium and further incubated at 37 °C with gentle agitation (180-200 rpm) until the OD_{600} reached 0.5-0.8. At that time, the expression was induced by adding IPTG in a final concentration of 0.5 mM. The addition of IPTG to *E. coli* BL21(DE3) cultures initiates the expression of the T7 RNA polymerase encoded by the host genome and inhibits the *lac* repressor (*lac*I) encoded on pET28a(+) plasmids. As a result the T7 RNA polymerase binds to the T7 promoter on the pET28a(+)-AKR plasmids and promotes the expression of the respective AKR. After the induction, cultures were incubated with gentle agitation (180-200 rpm) at 30 °C overnight. The next day, the expression cultures were harvested by centrifugation (3800-15000 x *g*, 4 °C, 15-30 min). The resulting pellets were either directly used for downstream protein purification [II.5.1] or resuspended in PBS, aliquoted, once more pelleted (10000 x *g*, 4 °C, 10 min) before they were stored at -20 °C for downstream Western blotting analysis [II.5.6].

IPTG solution:	0.5 M	IPTG in MilliQ-H_2O

IPTG solution was sterile filtrated using sterile syringe filters with a 0.22 µm pore size.

II.2. WORKING WITH *PICHIA PASTORIS* (*P. PASTORIS*)

All work with *P. pastoris* was performed in a semi-sterile manner, which means using only sterile materials and acting next to a Bunsen burner flame. Because Zeocin is light sensitive, medium and plates containing Zeocin were stored and incubated protected from light.

II.2.1. CULTIVATION OF *P. PASTORIS*

P. pastoris cells (see II.12.1.2) were cultured either in liquid YPD medium or on YPDS agar plates, both, if required, supplemented with various concentrations (100-1000 $^{ng}/_{ml}$) of Zeocin (Gibco) as selection antibiotic.

Liquid *P. pastoris* cultures were used for the generation of competent cells for transformation, colony screens, or recombinant protein expression. All cultures were grown with gentle agitation (180-200 rpm) at 30 °C. Cultivation of *P. pastoris* on YPDS agar plates was used for the selection of transformed *P. pastoris* cells or for the isolation of single clones from glycerol stocks. The plates were incubated at 30 °C for 3-5 days before single colonies appeared.

For long-term storage of *P. pastoris* clones, 1 ml of liquid overnight YPD cultures was mixed with 500 µl of sterile 80 % glycerol and frozen at -80 °C.

YPD medium:	5 % ($^{w}/_{v}$)	YPD medium powder in MilliQ-H_2O
YPDS agar plates:	5 % ($^{w}/_{v}$) 1 M 2 % ($^{w}/_{v}$)	YPD medium powder sorbitol agar granulate in MilliQ-H_2O
80 % glycerol	80 % ($^{v}/_{v}$)	glycerol in MilliQ-H_2O

YPD medium, YPDS agar, and 80 % glycerol were autoclaved at 121°C for 20 min. Zeocin was added to the chilled medium or agar in concentrations of 100-1000 $^{\mu g}/_{ml}$.

II.2.2. ELECTROPORATION OF *P. PASTORIS*

For the expression of human *HSD17B12* in *P. pastoris*, different *P. pastoris* strains (KM71 and X33) were electroporated with *Sac*I linearized pPICZ-A-HSD17B12 (encoding for the human 17β-HSD12 followed by a TEV protease recognition site, cloned into pPICZ-A, Invitrogen, via *Eco*RI/*Not*I restriction sites, see also II.12.4.2, Figure IV-4). When in the cell, the linearized pPICZ-A-HSD17B12 can be integrated into the *Pichia* genome via homologous recombination and allows for the selection of recombined clones on Zeocin plates as well as for the expression of C-terminally His_6-tagged 17β-HSD12 under the control of an *AOX1* promoter.

The generation of electro-competent *P. pastoris* cells, which were always freshly prepared, was performed as described in the following: 5 ml YPD medium were inoculated with *P. pastoris* strains from YPD plates or glycerol stocks and incubated overnight. The next day, 100 ml YPD medium were inoculated with 50-5000 µl of the pre-culture and further incubated until the OD_{600} reached a value of 1.5-2.5 (5 h to overnight). The cultures were pelleted at 1500 x *g*, 4 °C for 5 min and the cell pellets were washed with 100 ml ice-cold MilliQ-H_2O (1500 x *g*, 4 °C for 5 min). The wash step was repeated twice, however, using first 50 ml ice-cold MilliQ-H_2O and then 4 ml ice-cold 1 M sorbitol. Here, the cells were kept on ice between each centrifugation step. The resulting electro-competent cell pellets were finally resuspended in 200 µl ice-cold 1 M sorbitol and kept on ice until electroporation (1-3 h).

The pPICZ-A-HSD17B12 plasmids were linearized by digesting up to 10 µg plasmid in 1x CutSmart Buffer with 20 U *Sac*I-HF (NEB) at 37 °C for 4 h up to overnight.

For electroporation, GenePulser/MicroPulser 0.2 cm gap electroporation cuvettes (Bio-Rad) were prechilled on ice before 80 µl of the freshly prepared cell suspensions and 5-10 µg of the linearized pPICZ-A-HSD17B12 were added. The electroporation reactions were incubated on ice for 1 min and then pulsed using a GenePulser II electroporation system (Bio-Rad) and the following settings: 1500 V, 200 Ω, 25 µF. After addition of 1 ml ice-cold 1 M sorbitol, the cell suspensions were incubated at 30 °C for 1-3 h. Finally, 50-200 µl of the cell suspensions were plated on YPDS-Zeocin agar plates and incubated at 30 °C until colonies appeared (3-5 days).

1 M sorbitol:	1 M	sorbitol in MilliQ-H_2O

1 M sorbitol was autoclaved at 121°C for 20 min.

II.2.3. RECOMBINANT EXPRESSION OF PROTEINS IN *P. PASTORIS*

For the recombinant expression of human *HSD17B12* in *P. pastoris*, clones of the *P. pastoris* strains X33 or KM71 which had been successfully transformed with pPICZ-A-HSD17B12 were used. For this, 5 ml YPD-Zeocin(100-200) medium were inoculated with either single colonies from YPDS-Zeocin agar plates or cells from glycerol stocks and incubated with gentle agitation (180-200 rpm) at 30 °C overnight. Since dextrose represses the *AOX1* promoter and thus has to be removed for an efficient expression, the pre-cultures were pelleted at 8000 x *g* for 5 min the next day and the cell pellet was resuspended in 1 ml MM medium. 50-100 ml MM medium were inoculated with this cell suspension and the cultures were further incubated (180-200 rpm, 30 °C) overnight. The expression of *HSD17B12* was induced every 24 h by the addition of methanol in a final concentration of 0.5 %. Thereby, methanol activates the *AOX1* promoter in the absence of glucose or dextrose which enables yeasts to use methanol as carbohydrate source. The expression cultures were incubated with gentle agitation (180-200 rpm) at 30 °C for 2-5 days. Finally, the expression cultures (OD_{600}: 2-12) were harvested by centrifugation at 4000 x *g*, 4 °C for 15 min and the cell pellets were frozen at -80 °C until they were used for expression analysis or protein purification [II.5.2].

MM medium:	1.34 % ($^w/_v$)	YNB with ammonium sulfate
	1 % ($^v/_v$)	histidine stock solution
	0.2 % ($^v/_v$)	biotin stock solution
		in MilliQ-H_2O
histidine stock solution:	0.4 % ($^w/_v$)	L-histidine
		in MilliQ-H_2O
biotin stock solution:	0.02 % ($^w/_v$)	biotin
		in MilliQ-H_2O

MM medium was autoclaved at 121°C for 20 min. The biotin and histidine stock solutions were sterile filtrated using sterile syringe filters with a 0.22 µm pore size and added to the chilled medium.

II.3. WORKING WITH HUMAN CELL LINES

Within this thesis, different human cell lines (see II.12.1.3) were cultured for various purposes. The human embryonic kidney cell line HEK-293 was used for the overexpression of proteins and downstream activity or protein assays because they feature a minor background activity in steroid metabolism and a lacking expression of *AKR1B15*. Since the human cervix adenocarcinoma cell line HeLa grows in stretched epithelial-like monolayers, HeLa cells were used for localization studies with overexpressed proteins. In contrast, the human placental choriocarcinoma cell line BeWo and the human Simpson-Golabi-Behmel syndrome (SGBS) preadipocyte cell strain SGBS [212] were used for the analysis of endogenous AKR1B15 isoforms, as both showed endogenous expression of *AKR1B15*. The human keratinocyte cell line HaCaT [213, 214], which represents a model cell line for vitamin D metabolism, was used for the development of the vitamin D LC-MS/MS method. Cultivation and subcultivation of human cell lines were performed in a semi-sterile manner which means using only sterile materials and semi-sterile incubators as well as working under a tissue culture hood.

II.3.1. CULTIVATION AND STORAGE OF HUMAN CELL LINES

For setting up new cultures, cryopreserved cultures were rapidly thawed in a water bath at 37 °C and transferred to a falcon tube containing 8-10 ml of the appropriate pre-warmed culture medium [Table II-2]. After pelleting the cells at 550 x *g* for 5 min, the cell pellet was resuspended in 10 ml culture medium, transferred to a 25 cm^2 culture flask, and incubated in a humidified incubator at 37 °C with 5 % CO_2 (culturing conditions) until the cells reached 70-80 % confluency.

Table II-2: Composition of culture and freezing media used for the cultivation and cryo-preservation of different cell lines, respectively.

cell line	culture medium	freezing medium
BeWo	10 % FBS Superior in F-12K Nutrient Mixture	5 % dimethyl sulfoxide in BeWo culture medium
HaCaT	10 % FBS Superior in DMEM	10 % dimethyl sulfoxide in HaCaT culture medium
HEK-293	10 % FBS Superior in DMEM	10 % dimethyl sulfoxide in HEK-293 culture medium
HeLa	10 % FBS Superior in MEM	10 % dimethyl sulfoxide in HeLa culture medium
SGBS	10 % FBS Superior 1 % pan/biotin stock solution in DMEM/F-12 (1:1)	10 % glycerol 20 % FBS Superior 1 % pan/biotin stock solution in DMEM/F-12 (1:1)

Confluent cultures were subcultured by aspirating the medium and washing the cell layers once with pre-warmed PBS. The cells were then detached by using 0.5-2 ml of 0.05 % Trypsin-EDTA (Gibco) and the trypsinization reaction was stopped by the addition of the respective culture medium [Table II-2] in at least 5-fold excess. With the exception of SGBS cells, appropriate ratios of the cell suspensions (BeWo: 1:3-1:5, HaCaT: 1:8-1:12, HEK-293: 1:10-1:14, HeLa: 1:8-1:10) were directly transferred to 75 cm^2 culture flasks containing already pre-warmed culture medium to reach a final culture volume of 20 ml. SGBS cells needed an extra centrifugation step to deplete the Trypsin from the culture medium. Thus, SGBS cell suspensions were transferred to a falcon tube, pelleted, and afterwards resuspended in 12 ml of culture medium. Finally, ratios of 1:6-1:8 were transferred to 75 cm^2 culture flasks containing again pre-warmed culture medium to reach a final culture volume of 20 ml.
The cultures were further incubated at culturing conditions (37 °C, 5 % CO_2) until they reached 70-80 % confluency. In case of BeWo cultures the culture medium was exchanged the day after splitting and every 2-3 days, whereas the medium of SGBS cultures was only exchanged every 2-3 days.

For the cryopreservation of cells cultured in 75 cm^2 culture flasks, the medium was aspirated and the cell layers were washed once with 10 ml pre-warmed PBS. The cells were trypsinized with 2 ml of 0.05 % Trypsin-EDTA (Gibco) and after detachment resuspended in 8 ml culture medium [Table II-2]. Afterwards, the resuspended cells were counted by using Fast-Read 102® counting chambers (Biosigma) and the cell suspensions were centrifuged at 550 x *g* for 5 min. The cell pellets were resuspended in an appropriate volume of freezing medium [Table II-2] before aliquots of 0.5-2x10^6 cells (in maximum 1.8 ml cell suspension) were rapidly transferred to labeled cryo tubes (Nunc) and placed in a CoolCell® LX alcohol-free cell freezing container (Bioscision). Putting the container at -80 °C allowed for a standardized cooling rate of -1 °C per min while freezing the cells.
The frozen cultures were transferred to liquid nitrogen tanks for long-term storage.

pan/biotin stock solution:	1.5 mM	D-pantothenic acid
	3 mM	biotin
		in DMEM/F-12 (1:1)
PBS (pH 7.4):	140 mM	sodium chloride
	2.7 mM	potassium chloride
	10 mM	disodium hydrogen phosphate
	2 mM	potassium dihydrogen phosphate

PBS was autoclaved at 121°C for 20 min. The pantothenate/biotin stock solution was sterile filtrated using sterile syringe filters with a 0.22 µm pore size and stored at -20 °C.

II.3.2. TRANSIENT TRANSFECTION OF HUMAN CELL LINES

For the overexpression of proteins in human cell lines and downstream analysis, HEK-293, HeLa, BeWo, or SGBS were transiently transfected using either the X-tremeGENE 9 DNA Transfection Reagent (Roche), the Lipofectamine 3000 Reagent (Life Technologies), or the ViaFect Transfection Reagent (Promega). The day before transfection, an appropriate number of cells were sown in 75 cm^2 culture flasks, 6-well plates, 12-well plates, or 10 cm dishes [Table II-3] and afterwards incubated at 37 °C and 5 % CO_2. The transient transfection of the cells was accomplished according to the manufacturer's recommendations. For this, appropriate DNA - transfection reagent reactions were mixed [Table II-3], incubated at room temperature for the generation of DNA-lipid complexes, and finally added dropwisely to the cultured cells.

After the addition of transfection reactions, the cells were incubated at 37 °C and 5 % CO_2 for two more days in order to express the proteins of interest. Finally, the cultures were either harvested [II.3.3] or directly used in subcellular localization [II.7] or sorting [II.9.5] studies.

Table II-3: Cell numbers, transfection reagents, DNA amounts, and reagent volumes used for the transient transfection of human cell lines.

cell line	plate size (growth area)	number of cells	transfection reagent	DNA amount [µg]	reagent volume [µl]	serum free medium [µl]
HEK-293	T-75 flask (75 cm^2)	$2 \cdot 10^6$	X-tremeGENE 9	10	30	ad 1000
HEK-293	12-well plate (3.8 cm^2)	$2 \cdot 10^5$	Lipofectamine 3000	2	4	ad 100
HEK-293	12-well plate (3.8 cm^2)	$2 \cdot 10^5$	ViaFect	2	4	ad 100
HeLa	6-well plate (9.6 cm^2)	$4 \cdot 10^4$	X-tremeGENE 9	1	3	ad 100
BeWo	10 cm dish (60 cm^2)	$2 \cdot 10^6$	ViaFect	10	30	ad 1000

In addition, HEK-293 cells were transiently transfected via electroporation according to Wefers *et al.* [215]: 10^6 HEK-293 cells were pelleted at 200 x *g* for 4 min and the cell pellets were washed with 2 ml PBS. After a second centrifugation step (200 x *g*, 4 min), the cells were resuspended in 100 µl of the respective plasmid DNA mixture dilution in PBS. The cells-DNA mixtures were transferred to GenePulser/MicroPulser 0.2 cm gap electroporation cuvettes (Bio-Rad) and pulsed using a GenePulser II electroporation system (Bio-Rad) with the following settings: 250 V, 1000 Ω, 250 µF. Immediately after electroporation, the cells were resuspended in 9 ml pre-warmed culture medium [Table II-2] and finally distributed into three wells of a 12-well plate. For the expression of transfected plasmids, the cultures were incubated at 37 °C and 5 % CO_2 for two days.

II.3.3. HARVEST OF HUMAN CELL LINES

Generally, human cell lines were harvested by trypsinization for downstream applications, such as activity assays [II.8], protein analysis [II.5.6], or RNA isolation [II.4.3].

For cell harvest via trypsinization, the medium supernatants were aspirated and the cell layers washed with 2-10 ml PBS. The cells were then detached with 0.5-2 ml of 0.05 % Trypsin-EDTA (Gibco) and the trypsinization reactions were stopped by the addition of culture medium [Table II-2] in at least 5-fold excess. The cell suspensions were transferred to Eppendorf or falcon tubes and centrifuged at 550 x *g* for 5 min. The cell pellets were resuspended in PBS and again pelleted at 550 x *g* for 5 min. If required, the cell suspensions were counted using Fast-Read® 102 counting chambers (Biosigma) prior centrifugation and after centrifugation resuspended in an appropriate volume PBS. Counted cell suspensions were either directly used for downstream applications or aliquoted in defined cell numbers and once more centrifuged at 10000 x *g* and 4 °C for 10 min. The resulting cell pellets were immediately frozen at -80 °C for long-term storage.
Besides harvesting cells via trypsinization, cells were also harvested via cell lysis (e.g., for luciferase and β-galactosidase assays [II.9.4.2]), EDTA (for MACS selection [II.9.5]), and scraping (for the analysis of vitamin D metabolites [II.11.1.1]). The detailed procedures for these harvest methods are described within the respective method sections.

II.3.4. ISOLATION OF MITOCHONDRIA FROM BEWO CELLS

The isolation of mitochondria from BeWo cells based technically on the procedure published by Schmitt *et al.* [216].

Prior to the isolation of mitochondria, the cells were harvested via trypsinization, counted, and centrifuged at 500 x *g* for 5 min. The resulting cell pellets were resuspended in pre-cooled isolation buffer yielding a cell density of $5x10^{6}$ $^{cells}/_{ml}$. Immediately afterwards, the cell suspensions were homogenized via a pre-cooled pump-controlled cell rupture system (PCC) consisting of a Pump 11 Plus high-precision pump (Harvard), two 1 ml Luer Lock gas tight syringes (Supelco), and a cell homogenizer with 10 µm clearance (Isobiotech) which was purged with suspension buffer to minimize air in the system [Figure II-1].

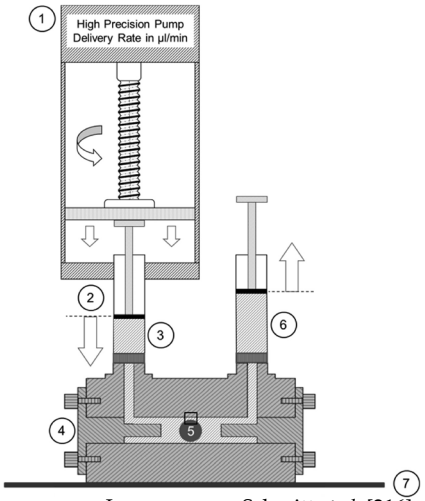

Image source: Schmitt *et al.* [216]

Figure II-1: Set-up of the pump-controlled cell rupture system.
A pump-controlled cell rupture system (PCC) according to Schmitt *et al.* [216] was applied for the isolation of functional mitochondria from BeWo cells. Mitochondria were isolated from $2x10^{7}$ cells per isolation batch using BeWo cell suspensions of $5x10^{6}$ $^{cells}/_{ml}$ in suspension buffer, a clearance of 10 µm, a flow rate of 700 $^{µl}/_{min}$, and three passages.
1) High-precision pump; 2) gas tight syringe; 3) sample delivery pool; 4) cell homogenizer; 5) clearance; 6) gas tight syringe; 7) cooling plate.

For cell homogenization and fractionation, 1 ml of cell suspension in isolation buffer was drawn into a syringe and passed three times through the PCC system with a constant flow of 700 $\mu l/_{min}$. The cell homogenate was transferred to a 2 ml Eppendorf tube and put on ice. The system was rinsed once with 1 ml isolation buffer to reduce losses through the death volumes of the system and the wash was added to the cell homogenate. Here, $2x10^7$ cells (corresponding to four homogenization runs) were processed within one isolation batch. Afterwards, the pooled cell homogenates were centrifuged at 800 x *g* and 4 °C for 5 min. Thereby, nuclei as well as cell debris were pelleted and removed from the homogenate. The supernatant was transferred into a new tube and centrifuged at 9000 x *g* and 4 °C for 10 min. By that centrifugation step, the mitochondria were pelleted and isolated from the remaining cell homogenate, containing only few impurities with other cell organelles [216].

For downstream analysis, the pellets containing nuclei and cell debris (800x*g* pellet) were resuspended in 100 µl isolation buffer each and combined, whereas the pellets containing mitochondria (9000x*g* pellet) were successively resuspended and combined in 40 µl isolation buffer (uniquely added). Please note that all fractions were kept on ice during the isolation process to reduce the functional loss of mitochondria. Finally, the concentration of total protein in each fraction was determined (see II.5.3) and the integrity of mitochondria in the mitochondrial fraction was tested as described in II.8.3. All fractions were stored at ≥ -20 °C until Western blot analysis [II.5.6].

isolation buffer:	5 mM	Tes / KOH (pH 7.2)
	300 mM	sucrose
	200 µM	EGTA
		in MilliQ-H_2O

II.4. WORKING WITH DNA AND RNA

II.4.1. ISOLATION OF PLASMIDS FROM *E. COLI*

Plasmids were isolated from mini-scale *E. coli* cultures (2-4 ml) via the NucleoSpin Plasmid (Macherey-Nagel) kit. The isolation was basically performed according to the manufacturer's instructions for high-copy plasmids from *E. coli* using an Eppendorf Centrifuge 5415 D; however, with the exception that bacterial cells were harvested at 11000 x *g* for 1 min (instead of 30 sec) and that the plasmids were eluted with 30-50 µl MilliQ-H_2O (instead of Buffer AE).

The isolation of plasmids from midi-scale *E. coli* cultures (50-100 ml) was performed via the NucleoBond Xtra Midi (Macherey-Nagel) kit according to the manufacturer's instructions with little modifications. All centrifugation steps were carried out at maximum speed (3800 x *g*) with a Hettich Universal 32R centrifuge. In doing so, the centrifugation steps concerning the precipitation and wash of plasmid DNA were extended to 30-60 min. The final plasmid DNA pellet was dissolved in 100-400 µl MilliQ-H_2O.

Plasmid DNA was kept at 4 °C for short-term storage and at -20 °C for long-term storage.

II.4.2. ISOLATION OF GENOMIC DNA FROM *P. PASTORIS*

Genomic DNA of *P. pastoris* clones was isolated from 4 ml overnight cultures following a protocol based on the procedure "Total DNA Isolation from Pichia" described by Invitrogen. For this, overnight cultures were pelleted at 1500 x *g* for 10 min and the cell pellets washed with 2 ml MilliQ-H_2O (1500 x *g*, 10 min) before the cells were resuspended in 700 µl SAED buffer. In order to generate spheroblasts, 100 µl lyticase solution were added and the reactions were incubated at 37 °C for 60 min. The spheroblasts were mixed with 700 µl SDS solution and incubated on ice for 5 min before 500 µl KAc solution were added. The cell lysates were centrifuged at 10000 x *g* and 4 °C for 10 min and 500 µl of the resulting supernatants were transferred to a fresh 1.5 ml Eppendorf tube. The genomic DNA was precipitated by the addition of 1000 µl ethanol and pelleted at 10000 x *g* and 8 °C for 30 min, after an incubation period at room temperature for 15 min. The resulting pellet was washed with 1000 µl 70 % ethanol (10000 x g, 10 °C, 30 min), dried, and, finally, dissolved in 200 µl MilliQ-H_2O. The isolated genomic DNA was stored at -20 °C.

SAED buffer:	10 mM	sodium acetate
	10 mM	EDTA
	10 mM	dithiothreitol
	1 M	sorbitol
		in MilliQ-H_2O
lyticase solution:	3 $^{mg}/_{ml}$	lyticase
		in MilliQ-H_2O
SDS solution:	1 % ($^{w}/_{v}$)	sodium dodecyl sulfate
		in MilliQ-H_2O
KAc solution:	5 M	potassium acetate
		in MilliQ-H_2O
70 % ethanol:	70 % ($^{v}/_{v}$)	ethanol
		in MilliQ-H_2O

II.4.3. ISOLATION OF RNA FROM HUMAN CELL LINES

The RNeasy Mini Kit (Qiagen) was used for the isolation of total RNA from harvested BeWo and SGBS cell pellets (< $5x10^6$ cells). The applied procedure followed the manufacturer's protocol "Purification of Total RNA from Animal Cells using Spin Technology" and included an on-column DNase treatment step using the RNase-free DNase I Set (Qiagen). The homogenization of the samples prior to the RNA isolation was performed by applying the cell lysates onto QIAshredder spin columns and centrifuging them at 16000 x *g* for 2 min using an Eppendorf Centrifuge 5415 D. All other centrifugation steps were carried out at 10000 x *g*. Finally, the RNA was eluted once with 40 µl RNase-free water.

This method yielded RNA with high purity ($^{260}/_{280}$ > 2.03; $^{260}/_{230}$ > 1.9). The isolated RNA samples were stored at -80°C.

II.4.4. cDNA SYNTHESIS VIA REVERSE TRANSCRIPTION OF RNA

1 µg of total RNA was reverse transcribed into cDNA using the AffinityScript qPCR cDNA Synthesis Kit (Agilent). The applied RNA was either isolated from human cell lines via the RNeasy Mini Kit (Qiagen) (see II.4.3) or purchased (Human Total RNA Panel, see II.12.3). The cDNA synthesis was in principle carried out according to the manufacturer's recommendations. However, within the first strand synthesis, an anchored Oligo(dT)$_{18}$ primer (# 2005, 20 µM) was used instead of the primers provided in the kit. In addition, the incubation temperatures and times for first strand synthesis varied from the standard protocol [Table II-4].

Table II-4: PCR program used for cDNA first strand synthesis.

25 °C	➞ 5 min
42 °C	➞ 30 min
55 °C	➞ 15 min
95 °C	➞ 5 min

II.4.5. APPLICATION OF POLYMERASE CHAIN REACTION (PCR)

Polymerase chain reactions (PCRs) are a potent tool to detect, analyze, amplify, and modify specific DNA sequences *in vitro* by amplification reactions using DNA polymerases. Within this thesis, PCRs were used for different purposes, such as cloning, mutagenesis, transcript analysis, and sequencing. All cycling reactions, covering denaturation, annealing, and elongation steps, were conducted with a RoboCycler 96 (Stratagene) PCR machine.

II.4.5.1. AMPLIFICATION OF DNA SEQUENCES FOR CLONING

The amplification of DNA sequences necessary for cloning was performed in 50 µl reactions using the Phusion High-Fidelity DNA Polymerase (NEB). Due to its 3'➞5'-exonuclease activity, the Phusion DNA polymerase possesses proof-reading activity and enables high accuracy within the DNA amplification. The reactions contained either 20-300 ng of plasmid DNA or 50-70 ng of cDNA as template, dNTPs in a final concentration of 200 µM each, the respective forward (FW, for) and reverse (RV, rev) primers in a final concentration of 200 nM each, and 1 U of the Phusion High-Fidelity DNA Polymerase (NEB) in 1x Phusion HF Buffer (NEB). The DNA was amplified in 38 cycles running the PCR program listed in Table II-5.

Table II-5: PCR program using the Phusion High-Fidelity DNA Polymerase.

98 °C	➞ 30-60 sec	
98 °C	➞ 20-30 sec	38 cycles
T_M+3 °C	➞ 30-45 sec	
72 °C	➞ 30 $^{sec}/_{kb}$	
72 °C	➞ 5 min	

T_M, highest salt adjusted melting temperature of primers (given by Metabion).

The PCR products were either immediately employed for downstream processes (analysis, purification, cloning) or stored at -20 °C.

II.4.5.2. SITE-SPECIFIC MUTAGENESIS OF PLASMID DNA

Two different set-ups were used for site-specific single nucleotide exchanges in the coding sequences in plasmids. In both cases, the mutation was generated by the amplification of complete plasmids via PCR. For this, complementary primer pairs carrying the mutation in the middle of the sequence were used.

To insert a mutation in the Ensembl *AKR1B15-201* (ENST00000423958.1) transcript sequence encoding for AKR1B15.1 which results in the AKR1B15.1 S8R mutant, a protocol derived from Sawano & Miyawaki [217] was followed. The 50 µl reactions contained 50 ng of the wild type plasmid DNA template, dNTPs in a final concentration of 200 µM each, the 5'-phosphorylated mutagenesis primer pair # 2680 and # 2681 in a final concentration of 300 nM each, as well as 1 U of the Phusion High-Fidelity DNA Polymerase (NEB), necessary for the amplification of the plasmid DNA strand after primer annealing, and 20 U of the *Taq* DNA Ligase (NEB), necessary for the ring closure of plasmid DNA. In order to provide optimal buffer conditions, the reactions were carried out in a mixture of 0.5x Phusion HF Buffer (NEB) and 0.5x *Taq* DNA Ligase Buffer (NEB). The PCR program applied for the amplification of mutated plasmids is shown in Table II-6.

Table II-6: PCR program for site-specific mutagenesis of AKR1B15.1 according to Sawano & Miyawaki [217]**.**

65 °C	5 min	
98 °C	2 min	
98 °C	30 sec	17 cycles
62 °C	30 sec	
65 °C	5.5 min	
72 °C	7 min	

Subsequently, 20 U of *Dpn*I (NEB) were added to the mutagenesis reactions and the reactions were incubated at 37 °C for 90 min. In doing so, *Dpn*I digested the methylated wild type plasmid DNA template which was originally purified from in *E. coli*.

After the *Dpn*I treatment, potentially arisen strand breaks in the mutated plasmids were repaired by two PCR cycles [Table II-7].

Table II-7: PCR program for strand break repair after mutagenesis.

98 °C	2 min	
98 °C	30 sec	2 cycles
60 °C	1 min	
72 °C	7 min	

Finally, 10 µl of the mutagenesis reactions were transformed into chemically competent *E. coli* DH5alpha (see II.1.2).

For the mutagenesis of the N-terminal sequence in AKR1B10 fused to AcGFP the QuikChange Lightning Site-Directed Mutagenesis Kit (Agilent) was used. According to the manufacturer's instructions, 50 ng of the wild type pAcGFP-AKR1B10 (Met1-Ala38) plasmid DNA template, the respective mutagenesis primer pair (# 2919 + # 2920 or # 2921 + # 2922) in a final concentration of 200 nM each, 1 µl of the provided dNTP mix, as well as 1.5 µl of the QuikSolution reagent were mixed in 50 µl 1x reaction buffer before 1 µl of the QuikChange Lightning Enzyme was added. The mutagenesis was carried out using the slightly modified PCR program listed in Table II-8.

Table II-8: PCR program for the site-directed mutagenesis of AKR1B10 (Met1-Ala38) via the QuikChange Lightning Site-Directed Mutagenesis Kit.

95 °C →	2 min	
95 °C →	30 sec	18 cycles
55 °C →	45 sec	
68 °C →	2.5 min	
68 °C →	5 min	

After mutagenesis 2 µl of the provided *Dpn*I restriction enzyme were directly added to each amplification reaction. The reactions were mixed and incubated at 37 °C for 10 min to digest the methylated wild type plasmid DNA template which was originally purified from *E. coli*.

Finally, 2 µl of the reactions were transformed into chemically competent *E. coli* TOP10 cells (see II.1.2).

II.4.5.3. Analysis of cloning results by colony screen PCR

Colony screen PCRs served for the identification of potentially "positive *E. coli* clones" resulting from cloning reactions and were performed in 22 µl reactions. 20 µl of a master mix, containing dNTPs in a final concentration of 200 µM each, the respective forward and reverse primer pair in a final concentration of 250 nM each, and 0.5 µl of a lab-made *Taq* polymerase in 1.1x Standard *Taq* buffer, were added to 2 µl of the colony screen cultures. The amplification was conducted with 30 cycles using the PCR program listed in Table II-9. Afterwards, PCR products were analyzed via agarose gel electrophoresis [II.4.6].

Table II-9: PCR program used for colony screen PCRs.

95 °C →	3-5 min	
95 °C →	1 min	30 cycles
T_M-3 °C →	1 min	
72 °C →	1 $^{min}/_{kb}$	
72 °C →	5 min	

10x Standard *Taq* buffer:	100 mM	Tris / HCl (pH 9.0)
	500 mM	potassium chloride
	15 mM	magnesium chloride
		in MilliQ-H_2O

II.4.5.4. DETECTION OF *AKR1B15* TRANSCRIPTS IN CDNA SAMPLES

In order to determine the abundance of *AKR1B15* splice variants (Ensembl transcripts *AKR1B15-001* [ENST00000457545.2] and *AKR1B15-201* [ENST00000423958.1]; referred to as *AKR1B15.2* and *AKR1B15.1*, respectively) in comparison to that of the *AKR1B10* transcript in different human tissues as well as cell lines, semi-quantitative end-point RT-PCR was carried out. The 20 µl reactions included 50 ng of the respective cDNA sample, dNTPs in a final concentration of 200 µM each, the transcript specific primer pairs [Table II-10, Figure III-1, VI.4] in a final concentration of 250 nM each, and 1.25 U of the commercial available DreamTaq DNA Polymerase (Thermo Scientific) in 1x DreamTaq Green Buffer (Thermo Scientific). The amplification of human *GAPDH* (h*GAPDH*) served as control [Table II-10].

Table II-10: Transcript specific primer pairs used for semi-quantitative RT-PCR.

transcript	primer pair	T_M	product size
AKR1B15.2	AKR1B15.2-TK-FW (# 2715) AKR1B15-TK-LocR1 (# 2713)	58 °C 59 °C	423 bp
AKR1B15.1	AKR1B15.1-TK-FW (# 2714) AKR1B15-TK-LocR1 (# 2713)	60 °C 59 °C	409 bp
AKR1B10	AKR1B15.1-TK-FW (# 2714) AKR1B10-TK-RV (# 2716)	60 °C 65 °C	409 bp
h*GAPDH*	hGAPDH qRT for 1 (# 1728) hGAPDH qRT rev 1 (# 1727)	56 °C 55 °C	186 bp

The PCR programs applied for the amplification of the human *AKR1B15* and *AKR1B10* transcripts (h*AKR1B*'s) or h*GAPDH* are listed in Table II-11.

Table II-11: PCR programs used for the amplification of human *AKR1B15.1*, *AKR1B15.2*, and *AKR1B10* as well as *GAPDH* transcripts by semi-quantitative RT-PCR.

h*AKR1B*'s		h*GAPDH*	
95 °C → 3 min		95 °C → 3 min	
95 °C → 45 sec	38 cycles	95 °C → 45 sec	25 cycles
57 °C → 30 sec		50 °C → 45 sec	
72 °C → 45 sec		72 °C → 45 sec	
72 °C → 10 min		72 °C → 10 min	

The PCR products were analyzed by gel electrophoresis using 2.5 % agarose gels. In addition, the specificity of *AKR1B15* primer pairs was verified by Sanger sequencing of the respective PCR products.

II.4.5.5. SEQUENCING OF DNA

The sequencing of plasmid DNA was conducted in-house. To enable the in-house DNA sequence analysis according to Sanger [218, 219], sequencing PCR reactions were set up with the BigDye3.1 Terminator v3.1 Cycle Sequencing Kit (Applied Biosystems). For this, 1 µl of plasmid DNA (≥ 150 $^{ng}/_{\mu l}$) or 2 µl of plasmid DNA (≤ 150 $^{ng}/_{\mu l}$) were mixed with 1 µl of the respective primer (10 µM), 1 µl of 5x Buffer (Applied Biosystems), 1 µl of BigDye Terminator v3.1 Ready Reaction Mix (Applied Biosystems), and MilliQ-H_2O to a reach final volume of 5 µl. Afterwards, the PCR program listed in Table II-12 was applied resulting in single-stranded fluorophore-labeled DNA amplicons.

Table II-12: PCR program used for Sanger sequencing.

95 °C	→	1 min	
95 °C	→	30 sec	⎫
T_M-3 °C	→	45 sec	⎬ 36 cycles
60 °C	→	4 min	⎭

The PCR products were purified via the Montage SEQ_{96} Sequencing Reaction Cleanup Kit (Merck Millipore) according to the manufacturer's instructions and, finally, analyzed by an ABI 3730 DNA Analyzer (Applied Biosystems).

II.4.6. ANALYSIS OR PURIFICATION OF DNA VIA AGAROSE GEL ELECTROPHORESIS

PCR products and restriction digestions of DNA were analyzed or separated for downstream purification by agarose gel electrophoresis. For this, the DNA samples were mixed with an appropriate volume of 6x loading-dye and loaded on agarose gels containing either 0.025 ‰ ($^{v}/_{v}$) Midori Green Advance DNA stain (Nippon Genetics) or 0.1 ‰ ($^{v}/_{v}$) ethidium bromide solution (500 $^{\mu g}/_{ml}$, Sigma-Aldrich). Depending on the size of DNA fragments and purpose, 1-2.5 % ($^{w}/_{v}$) agarose in 1x TBE buffer gels were applied [Table II-13].

Table II-13: Percentages, application, and run time of agarose gels.

agarose gel	fragment / purpose	run time
1 %	PCR products > 1000 bp	20-30 min
	colony screen analysis	20-30 min
	analysis of digestions	30-60 min
	purification of linear DNA	20-60 min
1.5 %	PCR products < 1000 bp	20-30 min
	colony screen analysis	
2.5 %	PCR products < 500 bp	20-30 min
	transcript analysis	30 min

The gels were run in a (Mini-)Sub-Cell GT (Bio-Rad) horizontal electrophoresis chamber filled with 1x TBE buffer at 100 mA for 20-60 min. Afterwards, the separated DNA was visualized upon UV illumination using a Bio-Vision Gel Documentation system (PeqLab).

When DNA was purified via agarose gels, only 70 % UV-light intensity were used for the visualization of DNA bands. Appropriate bands were cut from the gel and the gel slices subjected to the "Purification of linear DNA" [II.4.7] using the Wizard SV Gel and PCR Clean-Up System (Promega).

5x TBE buffer:	445 mM	Tris
	12.5 mM	EDTA
	445 mM	boric acid
		in MilliQ-H_2O
6x loading-dye	15 % ($^w/_v$)	Ficoll® 400
	0.25 % ($^w/_v$)	bromophenol blue
	0.25 % ($^w/_v$)	xylene cyanol FF
		in MilliQ-H_2O

II.4.7. PURIFICATION OF LINEAR DNA

Linear DNA was purified in order to reduce or eliminate enzymes, buffer salts, and small DNA fragments (< 20-30 bp), such as primers or multiple cloning site fragments of plasmids, in products resulting from PCR or restriction digestion reactions. The purification was performed with the Wizard SV Gel and PCR Clean-Up System (Promega) according to the manufacturer's instructions. Elution was performed with 20-50 µl MilliQ-H_2O.

II.4.8. DETERMINATION OF DNA / RNA CONCENTRATION

The concentration and purity of DNA or RNA samples was determined by spectrophotometric analysis using a NanoDrop ND-1000 (PeqLab) spectrophotometer. For this, the absorption spectrum (220 nm to 350 nm) of a sample was recorded. The absorption value at 260 nm was used for the quantification [Equation II-1]. In contrast, the quality of the sample was estimated on the basis of the absorption value at 280 nm by calculating the $^{260}/_{280}$ ratios. Samples with $^{260}/_{280}$ ratios ≥ 1.8 were considered to be of high quality.

DNA:	$c\ [^{ng}/_{\mu l}] = A\text{-}260_{(10\ mm\ path)} \cdot 50\ [^{ng}/_{\mu l}]$
RNA:	$c\ [^{ng}/_{\mu l}] = A\text{-}260_{(10\ mm\ path)} \cdot 40\ [^{ng}/_{\mu l}]$

Equation II-1: Equations used for the calculation of DNA and RNA concentrations, based on the Lambert-Beer law.
The extinction coefficients ($\varepsilon_{260\ nm}$) used for DNA and RNA were 0.02 µl · ng^{-1} · cm^{-1} and 0.025 µl · ng^{-1} · cm^{-1}, respectively.
$A\text{-}260_{(10\ mm\ path)}$, absorption at λ = 260 nm per 1 cm path length.

II.4.9. CLONING OF DNA INTO PLASMIDS

The cloning of DNA into plasmids was primarily carried out by conventional cloning using restriction enzymes. The only exceptions were the cloning of selection marker for TALEN transfection, the cloning of TALEN-RVDs into pcGoldyTALEN plasmids, as well as the cloning of TALEN target sequences into pCMV-Univ-Duplirep reporter plasmids. All exceptions are described in detail in "Generation of TALENs for an AKR1B15 knock-out in cell lines via TALEN technology" [II.9].

The conventional cloning procedure covers basically two steps. Within the first step, plasmids and linear double-stranded DNA sequences (inserts) were digested with restriction enzymes [II.4.9.1], thereby, generating compatible DNA ends (mostly complementary sticky ends). In the second step, the T4 DNA ligase catalyzes the ligation of compatible DNA ends of digested plasmids and inserts [II.4.9.2]. The cloning process ends with the transformation of ligation reactions into *E. coli* cells [II.1.2].

II.4.9.1. RESTRICTION DIGESTION OF DNA

Restriction digestions of plasmid DNA as well as PCR products were performed in 50 µl reactions. 1-5 µg of purified plasmids or up to 43 µl of purified PCR products and 10-20 U of each required restriction enzyme were mixed in the appropriate 1x restriction buffer (see II.12.6) and incubated at 37 °C for 2-18 h.

Afterwards, in order to eliminate restriction enzymes, salts of the buffer system, and interfering DNA digestion by-products, the digestion reactions were either directly purified (DNA by-products < 30 bp) or separated via agarose gel electrophoresis and the cut gel slices were purified (DNA by-products > 30 bp), both times using the Wizard SV Gel and PCR Clean-Up System (Promega) [II.4.6, II.4.7]. The purified digestion reactions were mostly immediately used for ligation reactions or kept at -20 °C for storage.

II.4.9.2. LIGATION OF DNA

Digested plasmids and inserts possessing compatible DNA ends were ligated in 20 µl reactions. The ligation reactions contained 50-100 ng of the digested plasmid, the digested double-stranded DNA insert in a 3- to 10-fold molar excess, as well as 400 U of the T4 DNA Ligase (NEB) in 1x T4 DNA Ligase Buffer (NEB).

The ligation reactions were incubated at room temperature for 15 min up to 16 h before they were transformed into chemically competent *E. coli* DH5α or *E. coli* TOP10 [II.1.2].

II.5. WORKING WITH PROTEINS

II.5.1. PURIFICATION OF HUMAN AKR1B15 FROM *E. COLI*

In order to have pure protein for, e.g., activity tests [II.8] or cofactor binding assays [II.5.4], both AKR1B15 isoforms were purified via the fused His_6 tag from pellets of 1000 ml *E. coli* BL21(DE3) – pET28a(+)-AKR1B15.1 or *E. coli* BL21(DE3) – pET28a(+)-AKR1B15.2 overnight expression cultures (see II.1.5). The applied purification procedure is described below.

Firstly, the *E. coli* expression culture cell pellets were resuspended in an appropriate volume of ice-cold lysis buffer and lysed via four 30 sec ultrasonication – 30 sec ice bath cycles using a VirSonic 475 sonicator (Virtis) combined with an ultrasonic converter CL4 (Virtis) at level 7. The lysates were centrifuged at 13000 x *g* and 4 °C for 30 min and the supernatants were filtrated through sterile syringe filters with a 0.22 µm pore size before 10 % Triton X-100 solution was added to reach a final concentration of 2 % Triton X-100. Afterwards, the Triton X-100 supplemented supernatants were subjected to an automated purification of His_6-tagged proteins using a Profinia Affinity Chromatography Protein Purification System (Bio-Rad) in combination with a 1 ml Bio-Scale Mini Profinity IMAC cartridge (Bio-Rad) and a downstream 10 ml Bio-Scale Mini Bio-Gel P-6 Desalting Cartridge (Bio-Rad). The chromatographic purification was performed at 4 °C according to the preassigned Profina method "Native IMAC + Desalting" (Bio-Rad). However, instead of the standard buffers recommended for the IMAC purification, a modified set of buffers (i.e., buffers containing the detergent N-lauroylsarcosine) was used for the purification of AKR1B15 isoforms.

The eluates were analyzed via PAGE [II.5.5] and the protein concentrations were determined [II.5.3]. Finally, the purified proteins were stored at 4 °C.

lysis buffer:	50 mM	KP_i (pH 8.0)
	300 mM	potassium chloride
	5 mM	imidazole
	1 % ($^w/_v$)	N-lauroylsarcosine
		in MilliQ-H_2O
2x wash buffer (1):	100 mM	KP_i (pH 8.0)
	600 mM	potassium chloride
	10 mM	imidazole
	0.5 % ($^w/_v$)	N-lauroylsarcosine
		in MilliQ-H_2O
2x wash buffer (2):	100 mM	KP_i (pH 8.0)
	600 mM	potassium chloride
	20 mM	imidazole
	0.5 % ($^w/_v$)	N-lauroylsarcosine
		in MilliQ-H_2O
2x elution buffer:	100 mM	KP_i (pH 8.0)
	600 mM	potassium chloride
	500 mM	imidazole
	0.1 % ($^w/_v$)	N-lauroylsarcosine
		in MilliQ-H_2O

1x desalting buffer:	20 mM	KP_i (pH 8.0)
	1 mM	EDTA
		in MilliQ-H_2O

All buffers used for purification were sterile filtered (0.22 μm pore size).
N-lauroylsarcosine was added after filtration.

II.5.2. PURIFICATION OF HUMAN 17β-HSD12 FROM *P. PASTORIS*

II.5.2.1. TEST OF DETERGENTS FOR SOLUBILIZATION

In order to find suitable solubilizing agents for the purification of human 17β-HSD12 from *P. pastoris*, different detergents (Anameg-7, Brij-35, 2,6-dimethyl-4-heptyl-β-D-malto-pyranoside, dodecyl-β-D-maltoside, MEGA-8, n-octyl-β-D-glucopyranoside, NP-40, sodium cholate, and Tween20R) were tested.

To test whether Anameg-7, MEGA-8, n-octyl-β-D-glucopyranoside, NP-40, or sodium cholate are proper additives, pellets from *P. pastoris* – pPICZ-A-HSD17B12 expression cultures (see II.2.3) were resuspended in SAED buffer (1-2 ml per OD_{600} of harvested culture) before 10 μl of lyticase solution (final lyticase concentration: 3-7.5 $^{\mu g}/_{ml}$) were added for spheroblasting. The mixtures were incubated on a CAT RM 5 (CAT M. Zipperer) roller mixer at room temperature for 3 h and then centrifuged at 600 x *g* for 10 min. The spheroblast pellets were resuspended in 1 M sorbitol solution using the same volume as used for the cell pellets and divided into appropriate aliquots. After an centrifugation step at 600 x *g* for 10 min, the resulting spheroblast pellets were resuspended either in MilliQ-H_2O+PI, in NP-40 solution, or in breaking buffer which was supplemented with 10 % detergent stock solution (from Solution Master Detergent Kit, Affimetrix). Here, the taken volumes were again comparable to the volumes of the initial cell suspension. The spheroblasts were lysed via three freeze-thaw cycles using liquid nitrogen for freezing and lukewarm water for thawing. Finally, the lysates were centrifuged at 450 x *g* and 4 °C for 2 min. Samples of all steps were separated by PAGE [II.5.5] and subjected to Western blotting [II.5.6] in order to monitor the presence of His_6-tagged 17β-HSD12 in each fraction. In addition, supernatants from the last centrifugation step were frozen at -80 °C for storage and analyzed via activity tests with ^{3}H-labeled substrates [II.8.1] at a later date.

To test whether 2,6-dimethyl-4-heptyl-β-D-maltopyranoside, Brij-35, dodecyl-β-D-maltoside, or Tween20R are proper additives, pellets from *P. pastoris* KM71 – pPICZ-A-HSD17B12 expression cultures (see II.2.3) were resuspended in 8 ml suspension buffer (0.8 ml per OD_{600} of harvested culture) before adding 500 μl of lyticase solution for spheroblasting. The mixtures were incubated on a CAT RM 5 (CAT M. Zipperer) roller mixer at room temperature for 1 h. The spheroblasts were subsequently lysed via two freeze-thaw cycles (liquid nitrogen – lukewarm water) and two sonication-ice cycles (15 sec ultrasonic bath – 15 sec ice bath) without any centrifugation step in between. The lysates were transferred into ultracentrifugation tubes (Beckman) and centrifuged at 125000 x *g* and 4 °C for 1 h using an OptimaMAX ultracentrifuge with MLA-80 rotor (Beckman Coulter). The resulting pellets

were resuspended in 5 ml solubilization buffer and split into 900 µl aliquots. 100 µl of the respective 10 % detergent solution were added to the 900 µl aliquots (final detergent concentration 1 %) and incubated at 4 °C while rotating on a LD79 test-tube rotator (Labinco) to solubilize membrane proteins, including the 17β-HSD12. Afterwards, the mixtures were centrifuged in the OptimaMAX ultracentrifuge with TLA-55 rotor (Beckman Coulter) at 55000 x *g* and 4 °C for 30 min. Samples of all steps were frozen at -80 °C until they were analyzed via PAGE [II.5.5] followed by Western blotting [II.5.6] and activity tests with ^{3}H-labeled substrates [II.8.1] at a later time point.

SAED buffer:	10 mM	sodium acetate
	10 mM	EDTA
	10 mM	dithiothreitol
	1 M	sorbitol
		in MilliQ-H_2O
lyticase solution:	3 $^{mg}/_{ml}$	lyticase
		in MilliQ-H_2O
1 M sorbitol solution:	1 M	sorbitol
		in MilliQ-H_2O
MilliQ-H_2O+PI	1 $^{tablet}/_{10\ ml}$	cOmplete Mini, EDTA-free Protease Inhibitor Cocktail (Roche)
		in MilliQ-H_2O
NP-40 solution:	2 % ($^{v}/_{v}$)	NP-40
		in MilliQ-H_2O
breaking buffer:	50 mM	NaP_i (pH 7.7)
	10 % ($^{v}/_{v}$)	glycerin
	1 mM	EDTA
	1 $^{tablet}/_{10\ ml}$	cOmplete Mini, EDTA-free Protease Inhibitor Cocktail (Roche)
		in MilliQ-H_2O
suspension buffer:	20 mM	NaP_i (pH 7.4)
	500 mM	sodium chloride
		in MilliQ-H_2O
solubilization buffer:	20 mM	NaP_i (pH 7.4)
	500 mM	sodium chloride
	20 mM	imidazole
	1 $^{tablet}/_{10\ ml}$	cOmplete Mini, EDTA-free Protease Inhibitor Cocktail (Roche)
		in MilliQ-H_2O
10 % Brij-35 solution:	10 % ($^{w}/_{v}$)	Brij-35
		in solubilization buffer
10 % maltoside solution:	10 % ($^{w}/_{v}$)	dodecyl-β-D-maltoside
		in solubilization buffer
10 % pyranoside solution:	10 % ($^{w}/_{v}$)	2,6-dimethyl-4-heptyl-β-D-maltopyranoside
		in solubilization buffer
10 % Tween20R solution:	10 % ($^{v}/_{v}$)	Tween20R
		in solubilization buffer

II.5.2.2. PRELIMINARY PURIFICATION METHODS FOR 17β-HSD12

Two widely differing methods were used for the small-scale purification of His_6-tagged 17β-HSD12 from *P. pastoris* KM71 – pPICZ-A-HSD17B12 expression cultures (see II.2.3). Method A describes the detergent-free purification of 17β-HSD12 from supernatants of ultracentrifuged cell lysates and the solubilization of active 17β-HSD12 from the remaining pellets. In contrast, method B combines the lysis of spheroblasts and the solubilization of 17β-HSD12 through the addition of Brij-35 prior to the purification.

METHOD A: DETERGENT-FREE 17β-HSD12 PURIFICATION METHOD

Cell pellets resulting from 50 ml expression cultures (OD_{600}: 5-10) were resuspended in 10 ml suspension buffer before 500 µl lyticase solution were added for spheroblasting. The mixtures were incubated on a CAT RM 5 (CAT M. Zipperer) roller mixer at room temperature for 1 h and the spheroblasts were subsequently lysed via two freeze-thaw cycles (liquid nitrogen – lukewarm water) and three sonication-ice cycles (15 sec ultrasonic bath – 15 sec ice bath) without any centrifugation step in between. To reduce the presence of cell debris or nuclei in the subsequent ultracentrifugation and solubilization steps, the cell lysates were at first centrifuged at 500 x *g* and 4 °C for 2 min before the resulting supernatants were transferred into ultracentrifugation tubes (Beckman Coulter) and centrifuged at 125000 x *g* and 4 °C for 1 h using an OptimaMAX ultracentrifuge with MLA-80 rotor (Beckman Coulter). The supernatants were taken, supplemented with 2 M imidazole solution to reach a final concentration of 20 mM, and manually loaded onto a 1 ml HisTrap HP column (GE Healthcare Life Sciences). The loaded columns were washed with 5 column volumes 20 mM wash buffer to reduce weak bound proteins before His_6-tagged 17β-HSD12 was eluted with 300 mM elution buffer in fractions of 1 ml, 1.5 ml, 1 ml, and 3 ml. In order to solubilize 17β-HSD12 from the pellet of the first ultracentrifugation step, pellets were resuspended in either 1 ml 1 % Brij-35 or 1 ml 1 % Tween20R suspension solution and afterwards incubated on a LD79 test-tube rotator (Labinco) at 4 °C for at least 60 min. The suspensions were once more centrifuged using the OptimaMAX ultracentrifuge with TLA-55 rotor at 55000 x *g* and 4 °C for 30 min and analyzed for the solubilization of His_6-tagged 17β-HSD12 from the pellet.

METHOD B: BRIJ-35 CONTAINING PURIFICATION METHOD

Cell pellets resulting from 100 ml expression cultures (OD_{600}: 15) were resuspended in 15 ml suspension buffer before 1650 µl lyticase solution were added for spheroblasting. These mixtures were incubated on a CAT RM 5 (CAT M. Zipperer) roller mixer at room temperature for 1 h without any lysis step afterwards. The spheroblast suspensions were mixed with 10 % Brij-35 solution to reach a final concentration of 1 % Brij-35 and then incubated on a LD79 test-tube rotator (Labinco) at 4 °C for at least 60 min in order to lyse spheroblasts and solubilize 17β-HSD12. Alternatively, prior to the addition of Brij-35, the spheroblast suspensions were centrifuged at 40 x *g* and 4 °C for 3 min and the supernatants, including the spheroblasts, were taken. Finally, the solubilization reactions were centrifuged using an OptimaMAX ultracentrifuge with TLA-55 rotor (Beckman Coulter) at 35500 x *g* and 4 °C for 1 h. For the purification of His_6-tagged 17β-HSD12, the resulting supernatants were supplemented with 2 M imidazole solution to reach a final concentration of 20 mM and loaded onto a 1 ml Ni Sepharose High Performance (GE Healthcare Life Science) resin bed in an Econo-Pac Chromatographic column (Bio-Rad). The loaded resin was washed three times with 2 ml 20 mM wash buffer and once more with 6 ml 20 mM wash buffer before the bound His_6-tagged 17β-HSD12 was eluted three times with 2 ml 300 mM elution buffer.

All fractions gained from the purification and solubilization procedure were collected and subjected to activity tests with ^{3}H-labeled estrone [II.8.1] and PAGE [II.5.5] followed by Western blotting [II.5.6].

suspension buffer:	20 mM 500 mM	NaP_i (pH 7.4) sodium chloride in MilliQ-H_2O
lyticase solution:	3 $^{mg}/_{ml}$	lyticase in MilliQ-H_2O
2 M imidazole solution:	2 M	imidazole in MilliQ-H_2O
20 mM wash buffer:	20 mM 500 mM 20 mM	NaP_i (pH 7.4) sodium chloride imidazole in MilliQ-H_2O
300 mM elution buffer:	20 mM 500 mM 300 mM	NaP_i (pH 7.4) sodium chloride imidazole in MilliQ-H_2O
1 % Brij-35 suspension solution:	10 % ($^{v}/_{v}$)	10 % Brij-35 solution in suspension buffer
1 % Tween20R suspension solution:	1 % ($^{v}/_{v}$)	Tween20R in suspension buffer
10 % Brij-35 solution:	10 % ($^{w}/_{v}$)	Brij-35 in MilliQ-H_2O

II.5.3. Determination of protein concentrations

The concentration of proteins in cell lysates or protein solutions were determined via the DC Protein Assay (Bio-Rad). This Lowry assay based protein assay kit was chosen since it is not affected by detergents which could be present in the samples as well. The assay was performed according to the manufacturer's "Standard Assay Protocol", however, using only a quarter of the volumes listed there.

Bovine serum albumin (BSA) was used as standard protein for creating the calibration curve. For this, BSA was diluted with MilliQ-H_2O to gain a final concentration of 0.2 $^{mg}/_{ml}$, 0.4 $^{mg}/_{ml}$, 0.6 $^{mg}/_{ml}$, 0.8 $^{mg}/_{ml}$, and 1.0 $^{mg}/_{ml}$ BSA in 25 µl. 25 µl MilliQ-H_2O served as blank. The samples were prepared by diluting 2-10 µl of cell lysate or protein solution with MilliQ-H_2O to reach a final volume of 25 µl. The prepared protein dilutions were mixed with 125 µl Reagent A' (100 volumes Reagent A + 2 volumes Reagent S) before 1000 µl Reagent B were added. The samples were immediately vortexed and incubated for 15 min before they were transferred into semi-micro disposable plastic cuvettes (Brand). Finally, the calibration curve was created from the absorption of the standard dilutions at 750 nm and the concentrations of the samples were determined using an UV/Vis spectrophotometer DU530 (Beckman Coulter).

II.5.4. COFACTOR BINDING STUDIES WITH AKR1B15 ISOFORMS

The capability of AKR1B15 isoforms to bind pyridine nucleotide cofactors was studied fluorometrically via quenching of protein fluorescence upon cofactor binding as described earlier [220]. For this, 14 µg of purified His_6-tagged AKR1B15.1 or AKR1B15.2 (correspond to approx. 362 pmol or 336 pmol, respectively) were diluted with 20 mM KP_i (pH 7.4) buffer to reach a final volume of 2 ml in a Quartz SUPRASIL cuvette (Hellma). The protein dilutions were equilibrated while steering at room temperature for 15-20 min in a RF-5000 (Shimadzu) fluorimeter before nucleotide solutions in 20 mM KP_i (pH 7.4) buffer were titrated. The initial protein fluorescence and the protein fluorescence after each addition of nucleotides were recorded twice using an excitation wavelength λ_{ex} of 280/3 nm and monitoring an emission spectrum λ_{em} of 300-500/5 nm. The recorded fluorescence signals were corrected by the increase in volume and the inner filter effect resulting from the titration of nucleotides [220]. Finally, the dissociation constants K_d for the respective cofactors and the maximum quenching in protein fluorescence ΔF_{max} were calculated by fitting Equation II-2 to the data using the SigmaPlot 12 software (Systat Software).

$$\Delta F = \Delta F_{max} \cdot \frac{[E] + [N] + K_d - \sqrt{([E] + [N] + K_d)^2 - 4 \cdot [E] \cdot [N]}}{2 \cdot [E]}$$

Equation II-2: Quadratic Morison equation used in cofactor titration studies for the determination of cofactor dissociation constants.
$\Delta F_{(max)}$, (maximum) decrease in fluorescence; [E], total concentration of enzyme; K_d, dissociation constant; [N], total concentration of cofactor.

In order to have the exact concentration of cofactor in solutions, the concentrations of the prepared cofactor stock solutions were determined spectrophotometrically prior to the titration. For this, the absorption of appropriate dilutions of the cofactor stock solutions in 20 mM KP_i (pH 7.4) buffer were measured using a Cary50 UV-Visible spectrophotometer (Varian) which was controlled by the Cary WinUV software (see also II.8.2.3) and the concentrations were calculated according to Equation II-3. For the titration of cofactors, the nucleotide solutions were further diluted in 20 mM KP_i (pH 7.4) buffer allowing the addition of small amounts of cofactors.

$$c_{(cofactor)} = \text{dilution factor} \cdot A_\lambda \; / \; (\varepsilon_\lambda \cdot d_{path})$$

Equation II-3: Lambert-Beer law based equation used for the calculation of pyridine nucleotide cofactor stock solution concentrations.
The extinction coefficient used for NAD(P)H was $\varepsilon_{340\,nm} = 6.22\ mM^{-1} \cdot cm^{-1}$, whereas for $NAD(P)^+$ an $\varepsilon_{260\,nm} = 18\ mM^{-1} \cdot cm^{-1}$ was used.
A_λ, absorption at measured wavelength; d_{path}, path length; ε_λ, extinction coefficient at measured wavelength.

20 mM KP_i (pH 7.4) buffer	20 mM	KP_i (pH 7.4) in MilliQ-H_2O

II.5.5. SEPARATION OF PROTEINS VIA POLYACRYLAMIDE GEL ELECTROPHORESIS (PAGE)

Polyacrylamide gel electrophoresis (PAGE) is a simple technique to separate proteins according to their molecular properties. Here, the denaturing SDS-PAGE was applied to analyze the presence of proteins in cell lysates or to analyze the purity of samples during and after the protein purification process.

Samples subjected to SDS-PAGE were prepared either by adding 1 volume of 5x Laemmli buffer to 4 volumes of protein solution/cell lysate or by resuspending cell pellets in an appropriate volume of 1x Laemmli buffer. Afterwards, the samples were incubated at 95 °C for 10-15 min. Denatured samples were loaded on self-made Tris-SDS-PAGE mini gels (5 % stacking gel, 12 % resolving gel) or on 12 % Criterion TGX precast midi gels (Bio-Rad). Self-made mini gels were run at constant 25-30 mA (per mini gel) in a Mini-PROTEAN cell (Bio-Rad) filled with 1x SDS-running buffer for 45-60 min. In contrast, precast midi gels were run at constant 200 V in a Criterion cell (Bio-Rad) filled with 1x SDS-running buffer for 45-55 min. To estimate the molecular weight of proteins, the PageRuler Prestained Protein Ladder (Thermo Scientific) was always applied as molecular weight marker.

After electrophoretic separation, the protein gels were either subjected to Western blotting [II.5.6] or stained with Coomassie Brilliant Blue. For the Coomassie Brilliant Blue staining of proteins, the separated gels were shortly boiled in Coomassie staining solution and then incubated on a horizontal shaker with moderate agitation until the intensity of the staining was sufficient. Afterwards, the staining solution was replaced by destaining solution and a piece of tissue paper and the gel was incubated therein until the background staining of the gel matrix was removed. The gels were rinsed with MilliQ-H_2O, scanned, and dried between two sheets of GelAir cellophane (Bio-Rad) for documentation and long-term storage.

5x Laemmli buffer:	300 mM	Tris / HCl (pH 6,8)
	50 % ($^v/_v$)	glycerin
	10 % ($^w/_v$)	sodium dodecyl sulfate
	25 % ($^v/_v$)	β-mercaptoethanol
	0.05 % ($^w/_v$)	bromophenol blue
		in MilliQ-H_2O
1x Laemmli buffer:	1 volume	5x Laemmli buffer
	4 volumes	MilliQ-H_2O
5 % stacking gel:	17 % ($^v/_v$)	Rotiphorese Gel 30
	125 mM	Tris / HCl (pH 6.8)
	0.125 % ($^w/_v$)	sodium dodecyl sulfate
	0.1 % ($^v/_v$)	TEMED
	1 % ($^v/_v$)	APS solution (10 %)
		in MilliQ-H_2O
12 % resolving gel:	40 % ($^v/_v$)	Rotiphorese Gel 30
	375 mM	Tris / HCl (pH 8.8)
	0.125 % ($^w/_v$)	sodium dodecyl sulfate
	0.1 % ($^v/_v$)	TEMED
	1 % ($^v/_v$)	APS solution (10 %)
		in MilliQ-H_2O

10 % APS	10 % ($^{w}/_{v}$)	ammonium persulfate in MilliQ-H_2O
1x SDS-running buffer:	25 mM 192 mM 0.1 % ($^{w}/_{v}$)	Tris glycine SDS in MilliQ-H_2O
Coomassie staining solution:	0.1 % ($^{w}/_{v}$) 40 % ($^{v}/_{v}$) 1 % ($^{v}/_{v}$)	Coomassie Brilliant Blue G250 methanol acetic acid in MilliQ-H_2O
destaining solution:	10 % ($^{v}/_{v}$)	acetic acid in MilliQ-H_2O

II.5.6. Detection of proteins via Western blotting

Western blotting was applied to detect His_6- and/or myc-tagged as well as untagged proteins in various cell lysates and fractions resulting from purification or enrichment steps. In principle, the Western blotting covered two steps. Within the first step, the SDS-PAGE separated proteins were transferred to a PVDF membrane by following a semi-dry blot protocol [II.5.6.1]. In the second step, selected proteins or protein tags blotted onto the membranes were immunochemically stained and detected via either chemiluminescence [II.5.6.2] or infrared fluorescence [II.5.6.3].

II.5.6.1. Blotting of proteins via semi-dry blot

Before blotting, the SDS-PAGE gels were incubated in blot buffer on a horizontal shaker with moderate agitation for 15 min. Meanwhile, the Immobilon FL PVDF membranes (Merck Millipore) were activated with methanol for 15 sec and subsequently also incubated in blot buffer. Shortly before blotting, per membrane, six pieces of filter paper (Gel Blotting Paper GB003, Whatman) were soaked with blot buffer. The filter papers, membranes, and gels were assembled as shown in Figure II-2 and the proteins were blotted at 20 V for 45-90 min using a Trans-Blot SD semi-dry transfer cell (Bio-Rad).

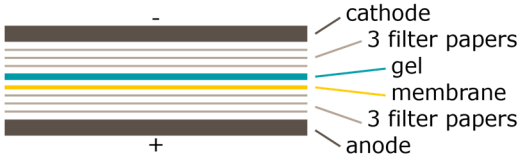

Figure II-2: Assembly of Western blot stacks for semi-dry blot.

blot buffer:	48 mM 39 mM 1.3 mM 20 % ($^{v}/_{v}$)	Tris glycine SDS methanol in MilliQ-H_2O

II.5.6.2. IMMUNOCHEMICAL DETECTION OF PROTEINS USING CHEMILUMINESCENCE

For the immunochemical detection of tagged and untagged proteins via chemiluminescence, the blotted membranes were incubated in 5 % milk solution for 60 min in order to block nonspecific binding valences on the membranes and thus to reduce background and nonspecific signals. The 5 % milk solution was replaced by dilutions of the respective primary antibodies [II.12.5] in 0.5 % milk solution and the membranes were incubated therein either at room temperature for 1.5-4 h or at 4 °C overnight. Here, the incubation times depended on the assumed target protein amounts. Excess primary antibodies, which had not bound to the blotted proteins, were removed by three washing steps, each for 10 min, using PBS. Afterwards, the membranes were incubated at room temperature for 1-4 h in dilutions of the appropriate HRP-conjugated secondary antibodies [II.12.5] in 0.5 % milk solution. Finally, the membranes were again washed three times with PBS for 10 min. Please note that all incubation or washing steps described above were done on a horizontal shaker with moderate agitation.

The staining of tagged and untagged proteins, which were recognized by the primary and HRP-conjugated secondary antibodies, was performed with the Pierce ECL Plus Western Blotting Substrate (Thermo Scientific) according to the manufacturer's instructions. The resulting chemiluminescence signals were visualized by the Fusion FX7 (Vilber Lourmat) imaging system.

5 % milk solution:	5 % ($^{w}/_{v}$)	powdered milk in PBS
0.5 % milk solution:	10 % ($^{v}/_{v}$)	5 % powdered milk solution in PBS
PBS (pH 7.4):	140 mM 2.7 mM 10 mM 2 mM	sodium chloride potassium chloride disodium hydrogen phosphate potassium dihydrogen phosphate in MilliQ-H_2O

II.5.6.3. IMMUNOCHEMICAL DETECTION OF PROTEINS USING INFRARED (IR) FLUORESCENCE

Immunochemical detection of proteins via infrared (IR) fluorescence was used for the verification of low abundant endogenous AKR1B15 isoforms in biological samples.

In contrast to the detection of proteins via chemiluminescence, the membranes used for the detection via IR fluorescence were blocked through an incubation in IR blocking solution for 60 min. The blocking solution was replaced by appropriate dilutions of monoclonal anti-AKR1B15 antibodies [II.12.5] in antibody solution. After the incubation in primary antibody dilution solutions at 4 °C overnight, the membranes were washed three times with PBS-T for 10 min to remove unbound primary antibodies. Afterwards, the membranes were

incubated in appropriate dilutions of the respective IR dye-conjugated secondary antibodies [II.12.5] in antibody solution for 2-3 h. Finally, the membranes were washed three times with PBS-T for 10 min and once more with PBS. Please note that all incubation or washing steps described above were done on a horizontal shaker with moderate agitation and protected from light. In general, membranes were dried between sheets of tissue papers for higher signal intensities and storage.

The detection of IR fluorescence signals was performed with an Odyssey infrared imaging system (LI-COR) by analyzing both wet and dry membranes.

IR blocking solution:	50 % (v/v)	Odyssey Blocking Buffer (PBS) in PBS (pH 7.4)
antibody solution:	50 % (v/v)	Odyssey Blocking Buffer (PBS) in PBS-T
PBS-T:	0.05 % (v/v)	Tween20R in PBS (pH 7.4)
PBS (pH 7.4):	140 mM	sodium chloride
	2.7 mM	potassium chloride
	10 mM	disodium hydrogen phosphate
	2 mM	potassium dihydrogen phosphate in MilliQ-H_2O

II.6. ESTABLISHMENT OF MONOCLONAL ANTI-AKR1B15 ANTIBODIES

Monoclonal anti-AKR1B15 antibodies were generated in cooperation with Dr. med. Elisabeth Kremmer (Service Unit Monoclonal Antibodies of the Helmholtz Zentrum München).

In order to identify peptide sequences within the both human AKR1B15 isoforms which are surface exposed and at the same time possess high immunogenic potential, the protein sequence of AKR1B15.2 was scanned for these features by the technical support of the Peps4LS GmbH. Out of the identified protein regions three epitopes with highest heterogeneity to the human AKR1B10 were selected as targets for the generation of monoclonal antibodies [Table II-14, Figure III-4]. These peptides were both synthesized and coupled to ovalbumin or biotin by Peps4LS GmbH.

Table II-14: Peptides (coupled to ovalbumin, C-) used for the immunization of Lou/c rats and C57/BL6 mice.

antibody	antigenic peptide
AKB-1	C-PQVNSTNNFHQGPL
AKB-2	C-QGFKTGDDFFPKDDKGNMISGKGTF
AKB-3	C-NRNWRAFDFKEFSHLEDFPFDAEY-COOH

The production and initial testing of monoclonal antibodies was performed in the group of Elisabeth Kremmer (Service Unit Monoclonal Antibodies, HMGU) according to their standard procedures. In short, a mixture of 50 µg antigenic peptide coupled to ovalbumin (Peps4LS) [Table II-14], 5 nmol CPG oligonucleotides (TIB MOLBIOL), 500 µl PBS, and 500 µl Freund's adjuvant was used for the subcutaneous and intraperitoneal immunization of Lou/c rats and C57/BL6 mice. Six weeks after the primary injection, a boost without adjuvant was given. Immune spleen cells of rats and mice were taken and fused with the myeloma cell line P3X63Ag8.653 (CRL-1580™, ATCC®) for the generation of monoclonal hybridoma cells. Supernatants of the hybridoma cultures were initially tested in differential ELISAs, using avidin coated ELISA plates and biotinylated AKR1B15 peptides or biotinylated irrelevant off-target peptides.

The specificity of monoclonal antibodies which bound to the respective AKR1B15 but not to the off-target peptides in the initial ELISAs (see VI.3) was further analyzed by Western blotting in our lab. Since the supernatants resulting from the primary hybridoma clones possibly included also nonspecific IgM antibodies, the Western blots for the identification of clones producing IgG antibodies that recognize only the AKR1B15 isoforms (but not other human AKRs) were performed with subclass specific HRP-conjugated secondary antibodies.

The herein identified AKR1B15 specific hybridoma clones were established by the group of Elisabeth Kremmer (Service Unit Monoclonal Antibodies, HMGU) and the supernatants of the established hybridoma clones were used for the detection of AKR1B15 isoforms.

II.7. SUBCELLULAR LOCALIZATION STUDIES USING HELA CELLS AND FLUORESCENCE MICROSCOPY

Confocal fluorescence microscopy was used for the analysis of the subcellular localization of AKR1B15 isoforms overexpressed in HeLa cells.

The day before transient transfection, $4x10^4$ HeLa cells (in 2 ml culture medium per well) were sown on 6-well plates containing ethanol and flame treated cover slips. The next day, the cells were transiently transfected with plasmids encoding untagged, N-terminally myc-tagged, or C-terminally myc-tagged AKR1B15.1, AKR1B15.1 S8R, or AKR1B15.2. For this, the coding sequences of the wild type AKR1B15 isoforms had been cloned into pcDNA3.1(+) (Invitrogen), N-myc-pcDNA3 (Ferdinand Haller), and pcDNA4-myc/His B (Invitrogen) via the *Hind*III/*Xho*I, *Not*I/*Xho*I, and *Not*I/*Hind*III restriction sites, respectively [II.12.4.2]. The plasmids encoding for the AKR1B15.1 S8R mutant were obtained by the mutagenesis of the wild type plasmids [II.12.4.2]. In addition, plasmids encoding for variable long N-terminal sequences of AKR1B15.1, AKR1B15.2, and AKR1B10 fused to AcGFP were also transiently transfected to HeLa cells in order to analyze the influence of the N-terminal amino acid sequence of AKR1B15 on its subcellular localization. Here, the coding sequences of the N-termini were cloned into pAcGFP-N1 (Clontech) via the *Hind*III/*Age*I restriction sites [Table II-15, II.12.4.2]. For counterstaining of the endoplasmic reticulum (ER) or cytosol, HeLa cells were co-transfected with pDsRed2-ER (Clontech) or pCMV DsRed-Express2 (Clontech), respectively.

Table II-15: Plasmid constructs used in subcellular localization studies with AKR1B10 or AKR1B15 N-termini-AcGFP fusion proteins.

	plasmid	N-terminus	template	primers for cloning / mutagenesis
pAcGFP-N1 -	AKR1B15.1	Met1-Gly26	pET28a(+)-AKR1B15.1	# 2541 + # 2711
	AKR1B15.1	Met1-Glu30	pET28a(+)-AKR1B15.1	# 2541 + # 2705
	AKR1B15.1	Met1-Ala38	pET28a(+)-AKR1B15.1	# 2541 + # 2708
	AKR1B15.2	Met1-Leu30	pET28a(+)-AKR1B15.2	# 2542 + # 2704
	AKR1B15.2	Met1-Glu58	pET28a(+)-AKR1B15.2	# 2542 + # 2705
	AKR1B15.2	Met1-Ala66	pET28a(+)-AKR1B15.2	# 2542 + # 2708
	AKR1B10	Met1-Glu30	pET28a(+)-AKR1B10	# 2541 + # 2707
	AKR1B10	Met1-Ala38	pET28a(+)-AKR1B10	# 2541 + # 2708
	AKR1B10 K22R	Met1-Ala38	pAcGFP-AKR1B10 (Met1-Ala38)	# 2921 + # 2922
	AKR1B10 P24L	Met1-Ala38	pAcGFP-AKR1B10 (Met1-Ala38)	# 2919 + # 2920

The detailed amino acid sequences of the different N-termini can be seen from the alignment of the AKR1B15 isoforms and AKR1B10 in Figure III-4.

The transfections were carried out as described in II.3.2 via the X-tremeGENE 9 DNA Transfection Reagent. The cells were incubated at 37 °C and 5 % CO_2 for two days in order to express the transfected plasmids. In contrast to the counterstaining of ER and cytosol, the counterstaining of mitochondria was performed prior to the fixation of cells on the cover slips. For this, the culture medium was replaced by 300 nM MitoTracker Orange CMTMRos (Molecular Probes) in serum-free medium. The cells were incubated therein at culturing conditions for 30 min. Thereby, the MitoTracker Orange CMTMRos cationic dye accumulates in the mitochondria of living cells due to their membrane potential and allows for the permanent staining of mitochondria after fixation.

To prepare objects for microscopy, the cell layers were washed twice with 3 ml/well PBS before they were incubated in 2 ml/well fixation solution at 37 °C, 5 % CO_2 for 10 min to fix the cells on the cover slips. After fixation, the cell layers were washed once with 3 ml/well PBS and were then incubated in 2 ml/well permeabilization solution at room temperature for 5 min. For the immunocytochemical staining of proteins or protein tags, the cell layers were washed twice with 3 ml/well PBS before free valences were blocked with 2 ml/well blocking solution for 30-60 min. The cell layers were washed once with 3 ml/well PBS and were afterwards incubated in 1 ml/well of the respective primary antibody [II.12.5] dilution in blocking solution at room temperature for 1.5-3 h. Before and after the subsequent incubation in 1 ml/well of the respective secondary antibody [II.12.5] dilution in blocking solution at room temperature for 1-2 h, the cell layers were washed twice with 3 ml/well PBS.

In contrast to the immunocytochemical staining, cell layers for the subcellular localization analysis of N-termini-AcGFP fusion proteins were only washed twice with 3 ml/well PBS after the permeabilization step without any blocking or antibody staining afterwards.

In the end, nuclei were stained by Hoechst 33342 (Molecular Probes), a dye emitting blue fluorescence when bound to the double-stranded (chromosomal) DNA. For this cell layers were incubated in 1 ml/well Hoechst 33342 dilution (1:5000 in PBS) for 1 min before the cell

layers were once more washed twice with 3 ml/well PBS. Finally, the cover slips were taken out of the wells, dipped into MilliQ-H_2O to reduce salt remains, and mounted on SuperFrost Plus microscope slides (Thermo Scientific) with VectaShield mounting medium (VectorLabs). The cover slips were fixed with nail polish and the objects were stored at -20 °C.

The subcellular localization data were collected and analyzed by confocal fluorescence microscopy using a Zeiss AxioImager Z1/ApoTome confocal microscope with a 63x water immersion objective and a Zeiss AxioCam MRm camera. The recording was controlled and processed by the AxioVision Rel. 4.8 software.

MitoTracker Orange (stock solution):	1 mM	MitoTracker Orange CMTMRos in dimethyl sulfoxide
fixation solution:	10 % (v/v)	formaldehyde solution (≥ 36.0 %) in PBS (pH 7.4)
permeabilization solution:	0.5 % (v/v)	Triton X-100 in PBS (pH 7.4)
blocking solution:	3 % (w/v)	albumin fraction V in PBS (pH 7.4)
PBS (pH 7.4):	140 mM	sodium chloride
	2.7 mM	potassium chloride
	10 mM	disodium hydrogen phosphate
	2 mM	potassium dihydrogen phosphate
		in MilliQ-H_2O

II.8. ACTIVITY TESTS

II.8.1. ENZYMATIC ACTIVITY ASSAYS USING ^{3}H-LABELED STEROIDS

Enzymatic activity assays with tritium (^{3}H)-labeled steroids [II.12.8.3] served for the identification of AKR1B15 substrates, the analysis of cofactor preferences of AKR1B15, and the determination of kinetic parameters. The assays based on end-point measurements and analyzed the conversion of steroids at a certain time point.

Assays with ^{3}H-labeled steroids were performed either with 10^6 HEK-293 cells (transiently transfected with plasmids overexpressing *AKR1B15* variants or non-transfected controls) in reaction buffer or with 1.1 µg purified AKR1B15 isoform (correspond to approx. 28 pmol and 26 pmol of His_6-tagged AKR1B15.1 and AKR1B15.2, respectively) in reaction buffer + BSA. HEK-293 cells or purified enzymes, ^{3}H-labeled steroids in a final concentration of 15-40 nM, and, in the case of assays determining kinetic parameters, the respective unlabeled steroid solutions up to a final concentration of 10-15 µM were mixed with reaction buffer (+ BSA) in glass vials to reach a final reaction volume of 500 µl. In order to have less variability in the volumes pipetted, cells or purified enzymes as well as steroids were pre-diluted in reaction buffer (+ BSA). The reactions were initiated by the addition of the respective cofactor solution

(NAD(P)H for reductive and $NAD(P)^+$ for oxidative reactions) in a final concentration of 300-350 µM (in some cases up to l050 µM) in reaction buffer (+ BSA). These mixtures were immediately vortexed and incubated in a water bath at 37 °C for various periods. In the end, the enzymatic reactions were stopped by the addition of 100 µl stop solution and thoroughly vortexing.

Steroids were extracted from the reaction mixture by solid phase extraction (SPE) using Strata C18-E 55 µm reversed phase (100 $^{mg}/_{ml}$) tubes (Phenomenex) and a VacElut 20 manifold (Varian). For this, the cartridges were preconditioned with two times 1 ml methanol and two times 1 ml MilliQ-H_2O before the reaction mixtures were loaded. The test tubes were washed with 500 µl MilliQ-H_2O and the wash was loaded onto the cartridge. Finally, steroids were eluted into 1.1 ml micro vials PP (Zinsser Analytics) with two times 200 µl methanol. The vials were capped and stored at -20 °C until analysis.

The conversion of steroids was analyzed on a Beckman Coulter HPLC system, comprising of a LC-502E autosampler with 20 µl sample loop and a System Gold 125 Solvent Module as binary pump, coupled to a Berthold LB 506 D Radioactivity Monitor and controlled by the 32 Karat software Version 3.0 (Beckman Coulter). 25 µl of the eluate were injected and the steroids were separated on a Luna 5 µm C18(2) 100 Å 125 mm x 4 mm (Phenomenex) reversed phase column with SecurityGuard Standard C18 4 mm x 2 mm (Phenomenex) cartridge using an isocratic method (43 % acetonitrile in MilliQ-H_2O) with a constant flow of 1 $^{ml}/_{min}$ [Table II-16]. Downstream the chromatographic separation of steroids on the column, before entering the scintillation detector, the mobile phase was mixed with 1 $^{ml}/_{min}$ Ready Flow III (Beckman Coulter) scintillation cocktail supplied by a MCP-Z Standard gear pump (Ismatec). As a result, the random decay of tritium atoms in the mobile phase excites organic compounds in the scintillation cocktail, whose de-excitation is coupled to the emission of light flashes. These flashes are recorded by the scintillation detector which enables the detection and analysis of eluting ^{3}H-labled steroids.

The conversion of substrate in the reactions was calculated from the percentage ratios of the peak areas of substrate and product peaks [Table II-17] given by the 32 Karat software Version 3.0 (Beckman Coulter). The Michaelis constants K_M and the maximum reaction velocities v_{max} or turnover rates k_{cat} were determined from the mean conversion of replicates by fitting the Michaelis-Menten ("Hyperbola, Single Rectangular, 2 Parameter") equation to the data using the SigmaPlot 12.0 software (Systat Software).

Table II-16: "Radioactive" HPLC method for the separation of ^{3}H-labeled steroids.

total time [min]	**module**	**function**	**value**	**duration**
0.0	pump	% B	43	
0.0	Pump	Relay on	2	0.1
0.0	Pump	Relay on	1	0.1
up to 25.0	Pump	Relay on	2	0.1

^{3}H-labeled steroids were separated on a Luna 5 µm C18(2) 100 Å 125 mm x 4 mm column with SecurityGuard Standard C18 4 mm x 2 mm cartridge using a Beckman Coulter Gold HPLC system with Berthold scintillation detector. Please note that the total run time of the method varied according to the retention times of steroids [Table II-17] from 10 min to 25 min. Mobile phase A = MilliQ-H_2O; mobile phase B = acetonitrile.

Table II-17: Retention times of steroids using the "radioactive" HPLC method for the separation of ^{3}H-labeled steroids.

steroid		retention time
estrone	(E1)	7.9 min
17β-estradiol	(E2)	5.4 min
17α-estradiol	(17α-E2)	5.4 min
progesterone	(P)	18.9 min
androsterone	(AN)	13.8 min
3α,17β-androstanediol	(A-diol)	8.8 min
Δ4-androstenedione	(Δ4-AE)	8.0 min
dehydroepiandrosterone	(DHEA)	7.0 min
dihydrotestosterone	(DHT)	9.2 min
testosterone	(T)	5.7 min
cortisol	(C-ol)	15.3 min
cortisone	(C-one)	12.1 min

Please note that for the analysis of enzymatic activity of 17β-HSD12 in fractions resulting from the solubilization or purification of 17β-HSD12 from *P. pastoris* expression cultures additional enzymatic activity assays with ^{3}H-labeled steroids (^{3}H-estrone) were performed in an analogous manner.

reaction buffer:	100 mM 1 mM	NaP_i (pH 7.4) EDTA in MilliQ-H_2O
reaction buffer + BSA:	100 mM 1 mM 0.05 % ($^{w}/_{v}$)	NaP_i (pH7.4) EDTA albumin fraction V in MilliQ-H_2O
NADH solution:	2.5 $^{mg}/_{ml}$	NADH in reaction buffer
NAD^+ solution:	2.5 $^{mg}/_{ml}$	NAD^+ in reaction buffer
NADPH solution:	2.5 $^{mg}/_{ml}$	NADPH in reaction buffer (+ BSA)
$NADP^+$ solution:	2.5 $^{mg}/_{ml}$	$NADP^+$ in reaction buffer (+BSA)
steroid solution:	10 mM	steroid in ethanol
stop solution:	210 mM 1 % ($^{v}/_{v}$)	ascorbic acid acetic acid in methanol
autosampler wash solution:	100 %	methanol

II.8.2. ENZYMATIC ACTIVITY ASSAYS USING UNLABELED SUBSTRATES

Enzymatic activity assays with unlabeled substrates were performed with purified AKR1B15 isoforms in order to identify non-steroidal AKR1B15 substrates or to determine the kinetic parameters of acetoacetyl-CoA. The read-out systems used here were substrate fluorescence, cofactor fluorescence, cofactor absorption, and, in the case of retinoids, UV absorption after HPLC separation.

II.8.2.1. ASSAYS USING PRODUCT FLUORESCENCE

To check whether AKR1B15.1 and/or AKR1B15.2 possess enzymatic activity with the Δ4-androstenedione substitute 8-acetyl-2,3,5,6-tetrahydro-1h,4h-11-oxa-3α-aza-benzo[de]-anthracen-11-one (= fluorogenic substrate) [221], reactions with purified AKR1B15 isoforms were carried out. Mixtures of 5.5 µg His_6-tagged AKR1B15.1 or 11 µg His_6-tagged AKR1B15.2 and 20 µl of a fluorogenic substrate dilution in reaction buffer (total volume: 230 µl) were pre-incubated at 37 °C for 5 min in a Safire II plate-reader (Tecan) which was controlled by the XFluorSafireII (Version: V4.62n) software (Tecan). Afterwards, the reactions were initiated by the addition of 15 µl NADPH solution corresponding to a final NADPH concentration of 185 µM and a total reaction volume of 245 µl. Respective controls contained either no enzyme or no fluorogenic substrate. The kinetics of the reaction (accumulation of the fluorescent product) at 37 °C was monitored in intervals of 2 min for up to 60 min. The wavelengths for excitation λ_{ex} and emission λ_{em} were set to 440/20 nm and 510/20 nm, respectively [221].

fluorogenic substrate dilution:	1 % ($^{v}/_{v}$)	4 mM fluorogenic substrate (in ethanol) in reaction buffer
NADPH solution:	2.5 $^{mg}/_{ml}$	NADPH in reaction buffer
reaction buffer:	100 mM 1 mM	NaP_i (pH 7.4) EDTA in MilliQ-H_2O

II.8.2.2. ASSAYS USING COFACTOR FLUORESCENCE

Different substrates, which were connected to the mitochondrial metabolism (acetoacetyl-CoA, DL-3-hydroxy-butyryl-CoA, DL-3-hydroxy-3-methyl-glutaryl-CoA, methyl-malonyl-CoA, and succinyl-CoA), were tested for being substrates of AKR1B15.1in assays using NADPH fluorescence. Those assays were performed in 96-well format (MicroWell 96-Well Optical-Bottom Plates, Nunc) using a Safire II plate reader (Tecan) with XFluorSafireII (Version: V4.62n) software (Tecan) and a total reaction volume of 250 µl.

For the analysis of potential AKR1B15 substrates, mixtures of His_6-tagged AKR1B15.1 and cofactor in reaction buffer were pre-incubated at 37 °C for 15-30 min before the respective substrate was added. The final reactions contained 5.5 µg His_6-tagged AKR1B15.1, 20 µM cofactor (NADPH for reductive and $NADP^+$ for oxidative reactions), as well as 50-100 µM "mitochondrial" substrate or 10 µM androsterone (positive control) in 250 µl reaction buffer. Negative controls contained either no enzyme or no substrate. After cofactor addition, the change in NADPH fluorescence was analyzed at 37 °C in 1 min intervals for 60 min using an excitation wavelength λ_{ex} of 340/10 nm and monitoring an emission wavelength λ_{em} of 450/10 nm. In order to ease the comparison of changes in fluorescence, the fluorescence signals at each time point were corrected by the respective initial fluorescence signals.

reaction buffer:	100 mM 1 mM	NaP_i (pH 7.4) EDTA in MilliQ-H_2O
NADP(H) solution:	2.5 $^{mg}/_{ml}$	NADPH or $NADP^+$ in reaction buffer
"mitochondrial" substrate solution:	5 mM	"mitochondrial" substrate in MilliQ-H_2O
androsterone dilution:	0.5 % ($^{v}/_{v}$)	10 mM androsterone (in ethanol) in reaction buffer

II.8.2.3. ASSAYS USING COFACTOR ABSORPTION

Activity assays with unlabeled "mitochondrial" substrates using the change in cofactor (NADPH) absorption at 340 nm as read-out were performed in a Cary50 UV-Visible spectrophotometer (Varian) which was controlled by the Cary WinUV software at 37 °C [27]. The reactions were carried out in Quartz SUPRASIL UV/Vis cuvettes in a final volume of 250 µl. For this, purified His_6-tagged AKR1B15 isoforms as well as NADP(H) cofactors were diluted in reaction buffer to reach a final concentration of 6 µM and 100 µM, respectively. These mixtures were pre-incubated at 37 °C for 5-15 min before the reactions were started by the addition of substrate in appropriate final concentrations (0-1000 µM). The usage or generation of NADPH through substrate conversion was continuously monitored at 340 nm for 30 min. The kinetic parameters were calculated from the initial reaction velocities of the first order reactions via Michaelis-Menten fit ("Hyperbola, Single Rectangular, 2 Parameter" equation) using the SigmaPlot 12 software (Systat Software).

reaction buffer:	100 mM 1 mM	NaP_i (pH 7.4) EDTA in MilliQ-H_2O
NADP(H) solution:	x $^{mg}/_{ml}$	NADPH or $NADP^+$ in reaction buffer
"mitochondrial" substrate solution:	5 mM	"mitochondrial" substrate in MilliQ-H_2O

Concentrations of NADP(H) stock solutions were spectrophotometrically determined [II.5.4].

II.8.2.4. ASSAYS USING RETINOIDS AND HPLC-UV ANALYSIS

End-point HPLC-UV detection was used for activity assays testing the enzymatic activity of AKR1B15 isoforms (either overexpressed in HEK-293 cells after transient transfection with pIRES-hrGFP-1α-AKR1B15.1 / -AKR1B15.2 or purified from *E. coli*) with retinoids (all-trans retinol, all-trans retinal) as substrates.

500 µl reactions were set up in glass test tubes containing either 10^6 HEK-293 cells or 1.1 µg purified protein (correspond to approx. 28 pmol or 26 pmol of His_6-tagged AKR1B15.1 or AKR1B15.2, respectively) as well as 10 µM retinoid and 650-700 µM cofactor (NADPH for reductive or $NADP^+$ for oxidative reactions) in reaction buffer. Negative controls contained either non-transfected HEK-293 cells or no enzyme. The mixtures were incubated at 37 °C with gentle agitation (300-400 rpm) for up to 2 h before the reactions were stopped by the addition of 100 µl stop solution and thoroughly vortexing.

Retinoids were extracted via solid phase extraction (SPE) using Strata C18-E 55 µm reversed phase (100 $^{mg}/_{ml}$) tubes (Phenomenex) in combination with a Visiprep 24DL vacuum manifold (Supelco). For this, the SPE cartridges were conditioned with 1 ml methanol and two times 1 ml 40 % acetonitrile in MilliQ-H_2O before the cartridges were loaded with the stopped reaction solutions (see above). The test tubes were washed with 1 ml 40 % acetonitrile in MilliQ-H_2O and the wash was loaded on the tubes. After one washing step using 1 ml of 40 % acetonitrile in MilliQ-H_2O, the samples were eluted twice with 150 µl 5 % methanol in acetonitrile. The eluates were collected in glass vials with insert (Crimp µ-vials 350 µl, Glastechnik Gräfenroda) and directly employed for HPLC-UV analysis.

The conversion of all-trans retinal and all-trans retinol was analyzed on a Perkin Elmer Series 200 HPLC system, comprising of a Series 200 Autosampler with 50 µl sample loop, a Series 200 Vacuum Degasser, two Series 200 Micro Pumps, a Series 200 Mixer, and a Series 200 UV/Vis Detector, which was controlled by the TotalChrom Workstation Version 6.3.2 (Perkin Elmer) software. 50 µl of sample were injected and the retinoids were separated on a Synergy 4 µm Fusion-RP 80 Å 150 mm x 4.6 mm (Phenomenex) reversed phase column with SecurityGuard Standard C18 4 mm x 2 mm (Phenomenex) cartridge using an isocratic method (92 % acetonitrile in MilliQ-H_2O) with a constant flow of 1 $^{ml}/_{min}$ [Table II-18]. The elution of retinoids was monitored at 345 nm with a sampling rate of 10 $^{pts}/_{s}$. Comparable to the analysis of HPLC runs with ^3H-labeled substrates, the conversion of substrates was determined by the percentage ratios of substrate and product peak areas.

Since retinoids are light sensitive, all steps were performed with minimal light exposure or protected from light.

Table II-18: HPLC-UV method for the separation all-trans retinol and all-trans retinal.

step	time interval [min]	mobile phase A [%]	mobile phase B [%]	curve
0	1.0	100	0	0.0
1	7.0	100	0	0.0

All-trans retinol and all-trans retinal were separated on a Synergy 4 µm Fusion-RP 80 Å 150 mm x 4.6 mm column with SecurityGuard Standard C18 4 mm x 2 mm cartridge using a Perkin Elmer 200 HPLC system with UV-detector (set to 345 nm).

reaction buffer:	100 mM 1 mM	NaP_i (pH 7.4) EDTA in MilliQ-H_2O
all-trans retinal stock solution:	500 µM	all-trans retinal in dimethyl formamide
all-trans retinol stock solution:	500 µM	all-trans retinol in dimethyl formamide
NADPH solution:	2.5 $^{mg}/_{ml}$	NADPH in reaction buffer
$NADP^+$ solution:	2.5 $^{mg}/_{ml}$	$NADP^+$ in reaction buffer
SPE eluent:	5 % ($^{v}/_{v}$)	methanol in acetonitrile
mobile phase A:	92 % ($^{v}/_{v}$)	acetonitrile in MilliQ-H_2O
autosampler wash solution:	100 %	methanol

II.8.3. DETERMINATION OF MITOCHONDRIA INTEGRITY

The integrity of isolated/enriched mitochondria was analyzed via the relative membrane potential ($\Delta\Psi_m$) after the inhibition of complex I by the addition of rotenone, using the quenching of Rhodamine 123 fluorescence as read-out (described in [222, 223]). The analysis based on the accumulation of lipophilic cations, like Rhodamine 123, in the mitochondrial matrix due to the electrochemical gradient generated by intact and functional mitochondria. In contrast to other lipophilic and cationic fluorophores, $\Delta\Psi_m$-dependent enrichment of Rhodamine 123 in mitochondria implicates a quenching of its fluorescence. However, the break-down of $\Delta\Psi_m$, e.g., by leakage of the mitochondrial membranes or by the addition of the ionophor carbonyl cyanide-4-(trifluoromethoxy)-phenylhydrazone (FCCP), leads to a release of Rhodamine 123 into the surroundings and thus prevents fluorescence quenching.

The determination of the relative $\Delta\Psi_m$ was performed in a 96-well format (MicroWell 96-Well Optical-Bottom Plate, Nunc) using an assay volume of 200 µl. 25 µl mitochondria suspension (2 $^{µg}/_{µl}$ total protein in isolation buffer) and 50 µl Rhodamine 123 solution were mixed with 125 µl swelling buffer. A mixture of 25 µl mitochondria suspension (2 $^{µg}/_{µl}$ total protein in isolation buffer), 50 µl Rhodamine 123 solution, and 10 µl FCCP solution in 115 µl swelling buffer served as negative control by featuring a decoupled $\Delta\Psi_m$. The plate was placed in a Synergy 2 Multi-Mode Microplate reader (BioTek) which was controlled by the Gen5 (version 1.11) software (BioTek) and the Rhodamine 123 fluorescence was measured at 37 °C in intervals of 1 min for 60 min. The wavelengths for excitation λ_{ex} and emission λ_{em} were set to 485/20 nm and 528/20 nm, respectively. Afterwards, 10 µl FCCP solution were added to each sample in order to decouple the respiratory chain and destroy the electrochemical gradient before measuring the Rhodamine 123 fluorescence for another period of 5 min. Finally, the relative $\Delta\Psi_m$ was determined by calculating the ratio of Rhodamine 123 fluorescence after and before FCCP addition [Equation II-4]. Ratios higher than 1.5 (better 1.7) indicated intact mitochondria of sufficient high purity.

$$\text{relative } \Delta\Psi_m = RFU_{(+FCCP)} / RFU_{(-FCCP)}$$

Equation II-4: Calculation of relative membrane potential ($\Delta\Psi_m$). $\Delta\Psi_m$, membrane potential; + FCCP, after FCCP addition; - FCCP, before FCCP addition; RFU, relative fluorescence units.

swelling buffer:	10 mM	Mops / 2 M Tris (pH 7.4)
	200 mM	sucrose
	5 mM	succinate
	1 mM	phosphoric acid
	10 µM	EGTA
	2 µM	rotenone
		in MilliQ-H_2O
Rhodamine 123 solution:	500 nM	Rhodamine 123 (Invitrogen) in swelling buffer
FCCP solution:	10 µM	FCCP in swelling buffer

II.9. GENERATION OF TALENS FOR AN AKR1B15 KNOCK-OUT IN CELL LINES VIA TALEN TECHNOLOGY

Transcription activator-like effector nucleases (TALENs) are a potent tool for manipulating genomes [224–226].

These TALENs consist of a transcription activator-like (TAL) domain which had its origin in the plant pathogen *Xanthomonas spp.* and a *Fok*I nuclease effector (EN) domain from *Flavobacterium okeanokoites*. The TAL domain binds specifically to DNA sequences via 33-35 amino acid repeats with repeat-variable di-residues (RVDs) at positions 12 and 13. Here, adenine is recognized by the RVD NI, guanine by NH, cytosine by HD, and thymine by NG. In contrast, the catalytic domain of the *Fok*I nuclease serves as effector and induces a DNA double-strand break upon dimerization.

By combining two TALENs, one binding to the sense and the other one binding to the antisense strand in close distance (15-35 bp), *Fok*I nucleases dimerize and cleave the double-stranded DNA at a defined position between the recognition sites in a sequence independent manner [224, 227, 228]. This double-strand break activates the highly conserved cellular repair mechanisms. As a result, the double-strand break is repaired by either homologous recombination (HR) or non-homologous end joining (NHEJ). However, whereas HR leads to an accurate DNA repair, NHEJ is often associated with insertions or deletions affecting reading frames or regulatory domains and thus manipulating genomes [Figure II-3] [229, 230].

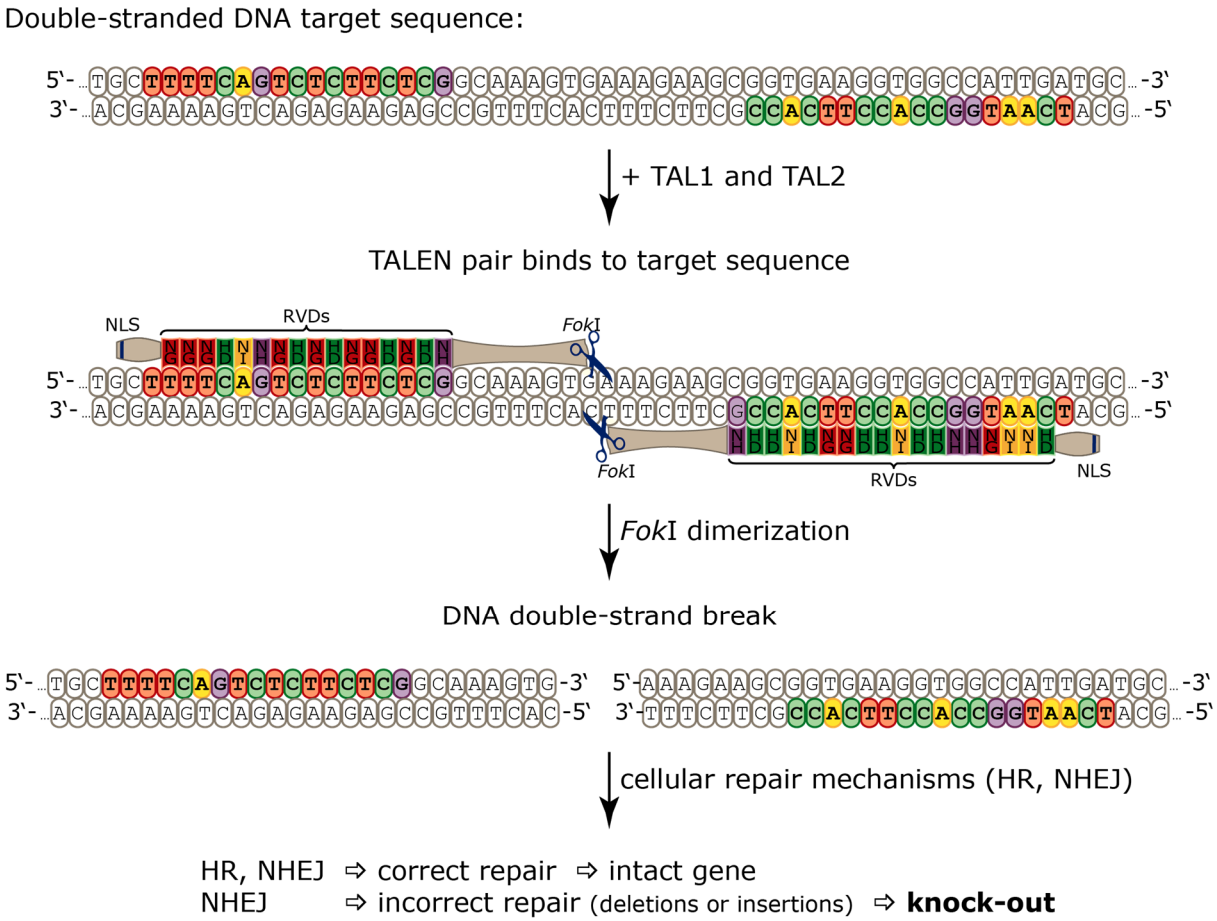

Figure II-3: Schematic illustration of a gene knock-out via the TALEN technology, shown on the example of the TALEN pair AKR1B15-E2(26).
The nucleotides of the double-stranded target DNA sequence which are recognized by the respective RVD sequences of the TALEN pairs (HD binds to C, NG binds to T, NH binds to G, and NI binds to A) together with the thymine 5' upstream of the target sequence are highlighted in green, red, purple, and yellow, respectively. Binding of TALEN pairs in close proximity leads to a DNA double-strand break due to an active *Fok*I dimer. This double-strand break is repaired either by HR or by error-prone NHEJ.
HR, homologous recombination; NHEJ, non-homologous end joining; NLS, nuclear localization signal; RVDs, repeat-variable di-residues.

II.9.1. Design of TALENs for AKR1B15 knock-outs

In this study, TALEN pairs targeting three different regions of the *AKR1B15* gene (exon 3 of *AKR1B15.2*, exon 1 of *AKR1B15.1*, and the first common exon (4/2) of both *AKR1B15* variants [Table III-4]) were designed by the TAL effector Nucleotide Targeter 2.0 algorithm (https://tale-nt.cac.cornell.edu). For this, the respective target region sequence was pasted into the form and the TALEN architecture established by Miller *et al.* (2011) using 15-20 bp spacer and 15-20 RVDs was selected [227]. The RVD "NH" was selected as G substitute, encoding for an Asn-His dipeptide which binds more specifically to guanine [231, 232], however, the Streubel *et al.* (2012) guidelines were ignored [232]. The predicted targets were blasted against the human genome/promoterome and counted. Finally, "T only" was selected as upstream base. TALEN pairs with the highest specificity were selected for assembly.

II.9.2. ASSEMBLY OF AKR1B15 TALEN PAIRS

The cloning of the TALEN constructs aimed for the knock-out of either one or both of the AKR1B15 isoforms (AKR1B15.1, AKR1B15.2, or AKR1B15-E2) was performed with the Golden Gate TALEN and TAL Effector Kit 2.0 (Addgene). This kit consists of plasmids enabling the position specific assembly of any custom TALEN pair and is based on the technique developed by Cermak *et al.* [224]. The assembly of the final TALEN pairs covered in principle two cloning steps and was mainly carried out according to the protocol used by the Voytas lab (Golden_Gate_TALEN_assembly_v5.doc) with slightly modifications. The procedure with all alterations is described in the following and illustrated in Figure II-4.

Before starting the cloning, all plasmids necessary for the assembly of AKR1B15 TALEN constructs [Table II-19] were purified from mini-scale *E. coli* cultures carrying the respective plasmid using the NucleoSpin Plasmid (Macherey Nagel) kit.

Table II-19: Plasmids necessary for the assembly of TALEN constructs against *AKR1B15* targets.

module vectors	intermediate target vectors	last repeat vectors	final target vector
pHD1 - pHD2 - pHD3 - pHD4 pHD5 - pHD6 - pHD7 - pHD8 pHD9 - pHD10	pFUS-A	pLR-HD pLR-NG pLR-NH pLR-NI	pcGoldyTALEN
pNG1 - pNG2 - pNG3 - pNG4 pNG5 - pNG6 - pNG7 - pNG8 pNG9 - pNG10	pFUS-B4 pFUS-B5 pFUS-B6 pFUS-B7 pFUS-B8 pFUS-B9		
pNH1 - pNH2 - pNH3 - pNH4 pNH5 - pNH6 - pNH7 - pNH8			
pNI1 - pNI2 - pNI3 - pNI4 - pNI5 pNI6 - pNI7 - pNI9 - pNI10			

On the first day, the pFUS-A/B intermediate target vectors were digested with the restriction enzyme *Bsa*I. *Bsa*I cuts the *LacZ* selection marker out of the pFUS-A/B plasmids which allows the insertion of the RVDs into the vector backbones. The digestion reactions were separated on a 1 % agarose gel and the pFUS-A/B vector backbone (2500 bp) was purified from the gel using the Wizard SV Gel and PCR Clean-Up System (Promega). For the first cloning step, 20 µl reactions (called Golden Gate Reaction #1) were set up. The reactions comprised of either 150 ng of the purified pFUS-A vector backbone and 150 ng of each of the first ten module vectors (position 1-10) or 150 ng of the purified pFUS-B(n-11) vector backbone and 150 ng of each of the remaining module vectors (position 11-(n-1)) as well as 10 U of the restriction enzyme *Bsa*I (NEB) and 400 U of the T4 DNA Ligase (NEB) in 1x T4 DNA Ligase Buffer. *Bsa*I is a restriction enzyme that cuts outside of the recognition sites (one bp downstream of the 3' base and five bp upstream of the 5' base of the recognition site) and, therefore, allows for the generation of variable overhangs for ligation reactions and the elimination of restriction sites after ligation. The overhangs of *Bsa*I restriction sites in the module vectors are designed in a way that enables the sequential assembly of RVDs. The concerted digestion (at 37 °C) and ligation (at 16 °C) of plasmids was performed in a RoboCycler 96 (Stratagene) using the program listed in Table II-20.

Table II-20: PCR program used for the Golden Gate Reaction #1.

37 °C	➞	5 min	10 cycles
16 °C	➞	10 min	
50 °C	➞	5 min	
80 °C	➞	5 min	

Subsequently, in order to get rid of all linear and unligated DNA fragments, the reactions were treated with 1 µl Plasmid-Safe ATP-dependent DNase (Epicentre Biotechnologies) and 0.5 µl ATP (25 mM) at 37 °C for 60 min. Afterwards, the DNase treatment was stopped by an incubation step at 70 °C for 30 min. These reactions were then transformed into chemically competent *E. coli* DH5α cells and streaked out together with X-Gal/IPTG on LB-agar-Spec(50) plates allowing for blue-white screening (see II.1.2).

The next day, a colony screen using the pCR8_F1 forward (# 2698) and pCR8_R1 reverse (# 2698) primer pair was performed with white colonies from the plate. Plasmids of potential positive clones were amplified in overnight cultures, isolated, and sequenced using the primers pCR8_F1 (# 2698) and pCR8_R1 (# 2698).

For the second cloning step, resulting in the final TALEN constructs, 20 µl reactions (called Golden Gate Reaction #2) were set up. These reactions included 150 ng of each intermediate pFUS-A (RVD 1-10) and pFUS-B (RVD 11-(n-1)) vector, 150 ng of the respective pLR vector, which encodes for the final RVD, and 75 ng of the pcGoldyTALEN destination vector. The successive digestion of RVD encoding plasmids as well as the final target vector and the ligation reactions of the resulting linear DNA fragments were catalyzed by the addition of 10 U of *Bsm*BI (NEB) and 400 U of the T4 DNA Ligase (NEB) in 1x T4 DNA Ligase Buffer. Just as *Bsa*I, *Bsm*BI is a restriction enzyme that cuts outside the recognition sites (one bp downstream of the 3' base and five bp upstream of the 5' base of the recognition site). The restriction sites are again designed in a way that leads to variable overhangs allowing for the correct assembly of the TALEN fragments and eliminating the restriction site. The reactions were performed in a RoboCycler 96 (Stratagene) using the program listed in Table II-21.

Table II-21: PCR program used for the Golden Gate Reaction #2.

37 °C	➞	5 min	10 cycles
16 °C	➞	10 min	
37 °C	➞	15 min	
80 °C	➞	5 min	

Afterwards, the products resulting from the Golden Gate Reaction #2 were transformed into chemically competent *E. coli* DH5α cells and streaked out together with X-Gal/IPTG on LB-agar-Amp(100) plates allowing for blue-white screening (see II.1.2).

The next day, a colony screen using the TAL_F1 forward (# 2700) and TAL_R2 reverse (# 2701) primer pair was performed with white colonies from the plate. Plasmids of potential positive clones were amplified in overnight cultures, isolated, and sequenced using the forward primers TAL_F1 (# 2700) or SeqTALEN_5-1 (# 2702) as well as the reverse primer TAL_R2 (# 2701).

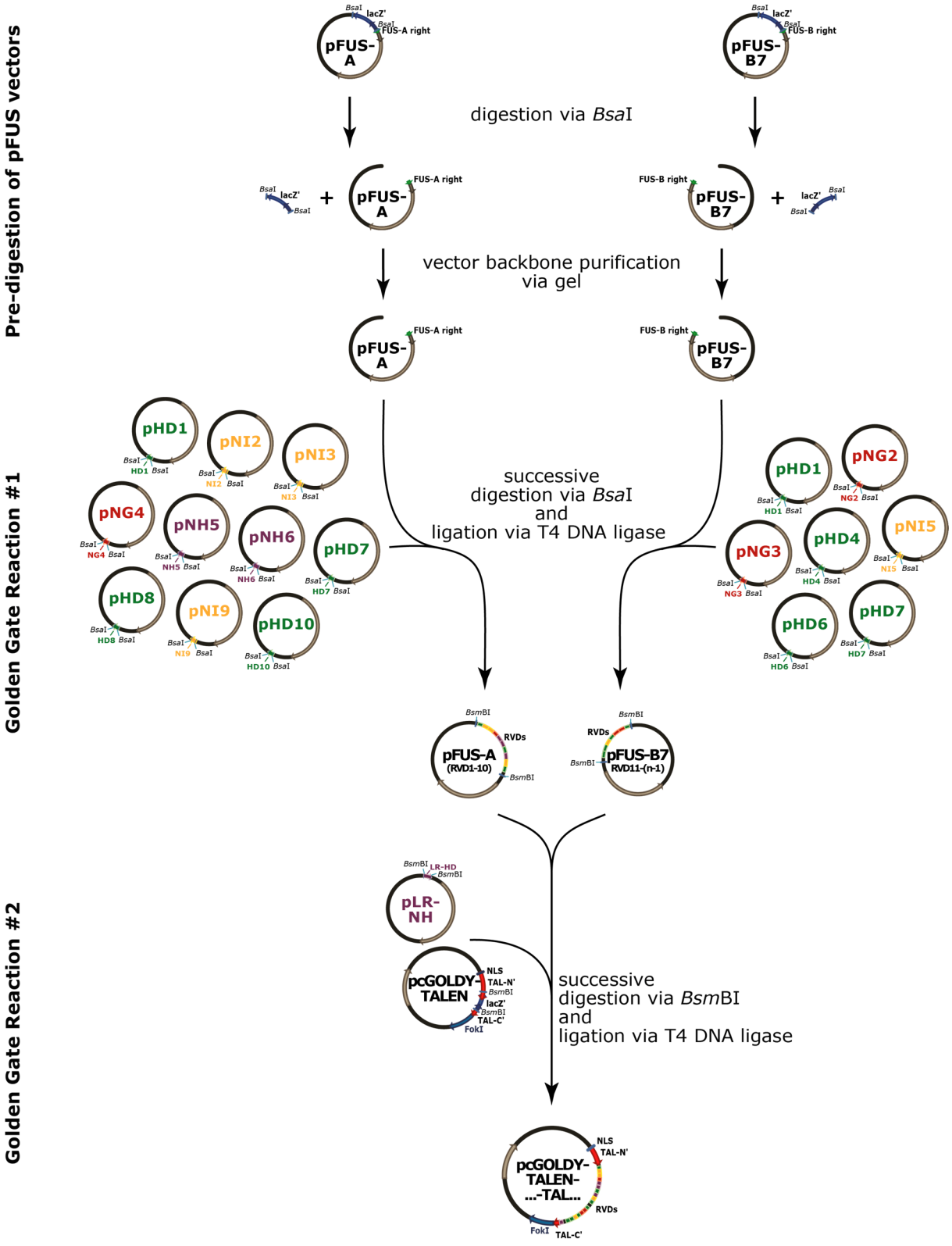

Figure II-4: Schematic illustration of the cloning procedure for AKR1B15 TALENs.
The assembly of TALENs was performed in two cloning steps (Golden Gate Reaction #1 and Golden Gate Reaction #2) via concerted restriction digestions (using the *Bsa*I and *Bsm*BI enzymes, respectively) and ligation reactions (using the T4 DNA ligase).
HD, His-Asp di-residue; NG, Asn-Gly di-residue; NH, Asn-His di-residue, NI, Asn-Ile di-residue; NLS, nuclear localization signal; pFUS-A/B, intermediate target vectors; pHD, pNG, pNH, and pNI, module vectors; pcGoldyTALEN, final target vector; RVD, repeat-variable di-residue.

II.9.3. CLONING OF SELECTION MARKER FOR TALEN TRANSFECTION

Selection markers are a good tool for the identification of successfully transfected cells. Here, different selection markers under the control of a CMV promoter (CMV-*AcGFP*, CMV-*DsRed*, and CMV-*ΔLNGFR*) [Table II-22] were cloned the into pcGoldyTALEN target and effector vectors via the *Dra*III restriction site using the In-Fusion HD Cloning Plus (Clontech) kit.

Table II-22: Primers and templates used for the amplification of selection marker.

selection marker	primers for cloning	template
CMV-*AcGFP*	# 2945 + # 2946	pAcGFP-N1
CMV-*DsRed*	# 2945 + # 2946	pCMV DsRed-Express2
CMV-*ΔLNGFR*	# 2943 + # 2944	pMACS-ΔLNGFR

The cloning was largely carried out according to the manufacturer's instructions, however, taking only half of the volumes recommended. The procedure is described briefly in the following.

Following the manufacturer's recommendations, the selection markers were amplified in 25 µl reactions containing 90 ng plasmid template, primers in a final concentration of 200 nM each, as well as the 2x CloneAmp HiFi PCR-Mix (Clontech) [Table II-22]. In order to enable the In-Fusion recombination reactions, 5 µg of the respective pcGoldyTALEN plasmids were linearized in 1x CutSmart Buffer with 20 U of *Dra*III-HF (NEB) at 37 °C overnight. Both, PCR products as well as linearized plasmids, were purified via the NucleoSpin Gel and PCR Clean-Up Kit (Macherey-Nagel) before 35-40 ng linearized plasmid and 40 ng PCR product were applied in 5 µl In-Fusion cloning reactions containing also 1 µl of the 5x In-Fusion HD Enzyme Premix. Differing from the recommendations of the manufacturer, these cloning reactions were incubated at 50 °C for 30 min before 1.2 µl were transformed into 50 µl Stellar Competent Cells (Clontech) and plated on LB-agar-Amp(100) plates for selection [II.1.2].

II.9.4. TEST OF AKR1B15 TALEN EFFICIENCIES

The functionality of the generated TALEN pairs was basically determined according to Wefers *et al.* [215].

This procedure used a reporter system which allows the determination of TALEN pair efficiencies through the detection/quantification of active β-galactosidase products resulting from the homologous recombination (used here as double-strand repair mechanism in HEK-293 cells) of TALEN pair induced DNA double-strand breaks in the respective TALEN pair reporter plasmids. The reporter plasmids based on the universal pCMV-Univ-Duplirep plasmid but included appropriate target sequences for the respective TALEN pairs which were inserted via the *Bst*BI/*Nru*I restriction sites [Table II-23, Figure II-5].

Table II-23: Primers used for the generation of TALEN pair specific reporter plasmids.

reporter plasmid target sequence primers	target sequence for TALEN pair
pCMV-Duplirep-AKR1B15.2	
AKR1B15.2_Sense (# 2816)	pcGoldyTALEN-AKR1B15.2(66)_TAL1/TAL2
+ AKR1B15.2_AntiSense (# 2817)	pcGoldyTALEN-AKR1B15.2(67)_TAL1/TAL2
pCMV-Duplirep-AKR1B15.1	
AKR1B15.1_Sense (# 2818)	pcGoldyTALEN-AKR1B15.1(36)_TAL1/TAL2
+ AKR1B15.1_AntiSense (# 2819)	pcGoldyTALEN-AKR1B15.1(40)_TAL1/TAL2
pCMV-Duplirep-AKR1B15-E2	
AKR1B15-E2_Sense (# 2820)	pcGoldyTALEN-AKR1B15-E2(25)_TAL1/TAL2
+ AKR1B15-E2_AntiSense (# 2821)	pcGoldyTALEN-AKR1B15-E2(26)_TAL1/TAL2

Using the *Bst*BI/*Nru*I restriction sites, the TALEN target sequences are 5′ flanked by the coding sequence of the inactive N-terminus (Met1-Leu135) of the β-galactosidase followed by a TAA stop codon and 3′ flanked by the coding sequence of the complete (Ala3-Lys1024) active enzyme [Figure II-5]. Upon double-strand break within the target sequence, caused by efficient TALEN pairs, the 5′ and 3′ flanking sequences recombine due to their homology. Since the inactivating stop codon is eliminated within this homologous recombination, the resulting plasmid encodes solely for the active full length β-galactosidase [Figure II-5].

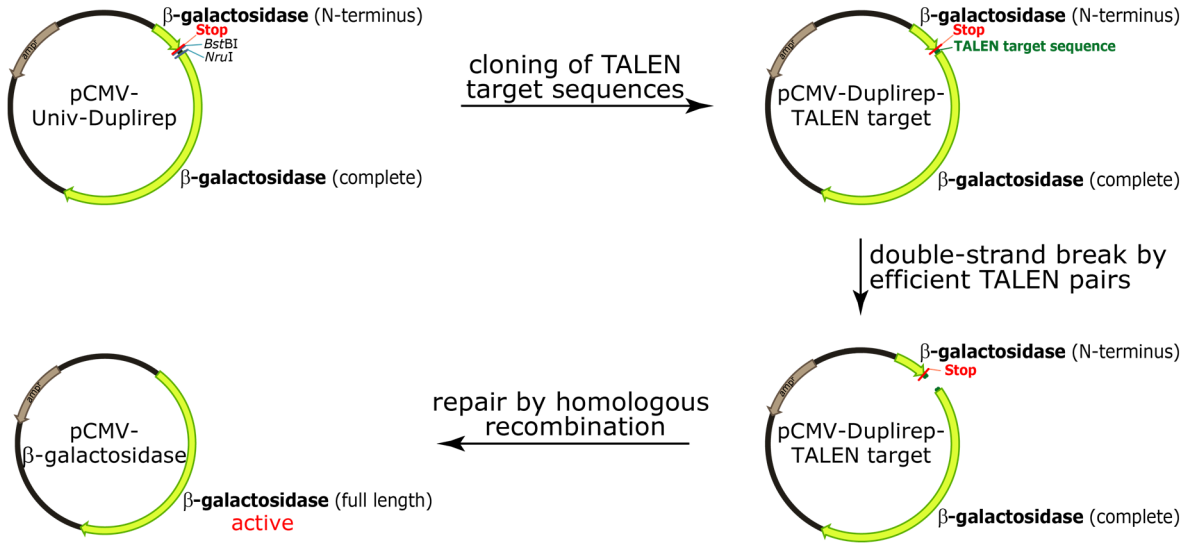

Figure II-5: Schematic illustration of TALEN reporter plasmid generation and reporter mechanism.
The pCMV-Duplirep plasmid encodes for both an inactive N-terminal (Met1-Leu135) and an active complete (Ala3-Lys1024) β-galactosidase sequence. Because of the stop codon after the β-galactosidase (N-terminus) sequence, only the inactive form is translated in the original Duplirep plasmids. However, upon homologous recombination, which serves as repair mechanism for efficient TALEN pair mediated DNA double-strand breaks, the stop codon is eliminated and the coding sequence for the active full length β-galactosidase is expressed.
The coding sequences of β-galactosidase (N-terminus and complete) are shown as bright green arrows, the position of the stop codon as red line and the TALEN pair target sequence as dark green bar.

II.9.4.1. CLONING OF PCMV-DUPLIREP REPORTER PLASMIDS

In order to generate the respective pCMV-Duplirep reporter plasmids for the testing of TALEN pair efficiencies, universal pCMV-Univ-Duplirep plasmids were first digested at 65 °C for 90 min in 50 µl 1x CutSmart Buffer (NEB) using 40 U of the *Bst*BI (NEB) restriction enzyme. The linearized plasmids were purified via the Wizard SV Gel and PCR Clean-Up System (Promega) before they were digested with 40 U of *Nru*I (NEB) in 50 µl 1x NEB3.1 Buffer (NEB) at 37 °C for 90 min. Since the second digestion cuts a DNA fragment of 55 bp from pCMV-Univ-Duplirep plasmids which cannot be efficiently depleted by direct DNA purification, the digestion reactions were separated on a 1 % agarose gel and the about 7300 bp long vector backbone was purified from the gel using the Wizard SV Gel and PCR Clean-Up System (Promega).

The double-stranded DNA inserts of the TALEN target sequences were generated by the annealing of the respective HPLC purified primer pairs [Table II-23]. For this, 50 pmol of the sense primer and 50 pmol of the antisense primer were diluted in 100 µl TE buffer. These mixtures were incubated at 99 °C for 5 min and afterwards slowly cooled down to room temperature. This step enables the correct annealing of the primers and generates a double-stranded DNA fragment with 5'-CG overhang on the one side and a blunt end on the other side, suitable for the cloning into *Bst*BI and *Nru*I digested target vectors. For the ligation of the TALEN target sequences into the digested pCMV-Univ-Duplirep vector, 100 ng of the digested target vector, 1.5 pmol of the respective double-stranded DNA fragment insert, and 400 U of T4 DNA Ligase (NEB) were incubated in 50 µl 1x T4 DNA Ligase Buffer at room temperature overnight. The next day, the ligation reactions were transformed into chemically competent *E. coli* DH5α cells and plated on LB-agar-Amp(100) plates [II.1.2].

The colonies grown on the plates were analyzed by sequencing [II.4.5.5]. For this, plasmids were isolated from LB-Amp(100) overnight cultures of single colonies and sequenced using the pCMV-DsRed-FW primer (# 2776).

TE buffer:	10 mM	Tris / HCl (pH 7.4)
	0.1 mM	EDTA
		in MilliQ-H_2O

II.9.4.2. PREPARATION OF SAMPLES FOR THE DETERMINATION OF TALEN PAIR EFFICIENCIES

In order to estimate the efficiencies of different AKR1B15 TALEN pairs, HEK-293 cells were transiently co-transfected with a TALEN pcGoldyTALEN effector plasmid pair, the appropriate pCMV-Duplirep reporter plasmid, and for normalization reasons a plasmid encoding for a humanized luciferase (pCMV-hLuci) [Table II-24]. HEK-293 cells transiently co-transfected with the respective pCMV-Duplirep reporter, pCMV-hLuci, and pPICZ-A plasmids served as negative control [Table II-24]. In doing so, the yeast expression plasmid pPICZ-A was used for balancing the DNA amount in the transfection reactions and should not have any influence on the expression profile of HEK-293 cells. In contrast, HEK-293 cells transiently co-transfected with a plasmid encoding for a functional β-galactosidase

(pCMV-βGal), pCMV-hLuci, and pPICZ-A served as positive control [Table II-24]. Similar to the reactions with TALEN pairs, HEK-293 cells were also co-transfected with a Zinc-finger nuclease (ZFN) pair featuring a good efficiency (pCAG-Rab-ZFN-A + pCAG-Rab-ZNF-B), the respective reporter plasmid (pCMV-Rab-Reporter), and pCMV-hLuci as well as with the respective negative control. These transfections served as reference standard and control for the complete test system, including the level of homologous recombination in HEK-293 cells after the DNA double-strand break in the β-galactosidase reporter plasmids [215].

Transfections of HEK-293 cells were performed in 12-well plate dimensions using either electroporation or chemical transfection with the Lipofectamine 3000 (Life Technologies) or ViaFect (Promega) transfection reagents. For this, the plasmid DNA mixtures listed in Table II-24 were transfected in triplicates by applying the standard procedures described in II.3.2 and the transfected cells were incubated at 37 °C and 5 % CO_2 for two days.

Table II-24: Composition of plasmid DNA mixtures which were transiently transfected into HEK-293 cells for the determination of TALEN pair efficiencies.

plasmid DNA	chemical transfection			electroporation		
	negative control	TALEN test	positive control	negative control	TALEN test	positive control
pCMV-Duplirep-AKR1B15…	0.5	0.5	-	5.0	5.0	-
pcGoldyTALEN-AKR1B15…_TAL1	-	0.5	-	-	5.0	-
pcGoldyTALEN-AKR1B15…_TAL2	-	0.5	-	-	5.0	-
pCMV-hLuci	0.5	0.5	0.5	5.0	5.0	5.0
pCMV-βGal	-	-	0.5	-	-	5.0
pPICZ-A	1.0	-	1.0	10.0	-	10.0
∑ plasmid DNA	2.0	2.0	2.0	20.0	20.0	20.0

Listed are the used plasmid DNA amounts in μg per well (chemical transfections) or per 10^6 HEK-293 cells (electroporation). The transfection reactions were prepared by diluting appropriate volumes of plasmid stock solutions (concentration = 1 $^{\mu g}/_{\mu l}$) in either 98 μl serum-free DMEM medium per well (chemical transfections) or 80 μl PBS per 10^6 HEK-293 cells (electroporation).

For the analysis of TALEN efficiencies, the transiently transfected cell layers were washed twice with 3 ml PBS before 700 μl of 1x Lysis Buffer (Roche) were added to each well. The cells were lysed at room temperature for 30 min by putting the plates on a horizontal shaker with moderate agitation. The lysates were centrifuged at 16000 x *g* and 4 °C for 2 min. The obtained supernatants were put on ice and immediately used for the determination of TALEN efficiencies via β-galactosidase and luciferase assays (described below).

PBS (pH 7.4):	140 mM	sodium chloride
	2.7 mM	potassium chloride
	10 mM	disodium hydrogen phosphate
	2 mM	potassium dihydrogen phosphate
		in MilliQ-H_2O
1x Lysis Buffer:	20 % ($^v/_v$)	5x Lysis Buffer (Roche)
	1 $^{tablet}/_{10\ ml}$	cOmplete Mini, EDTA-free Protease Inhibitor Cocktail (Roche)
		in MilliQ-H_2O

II.9.4.3. DETERMINATION OF TALEN PAIR EFFICIENCIES

The efficiency of TALEN pairs was determined via β-galactosidase and luciferase assays [215]. Here, β-galactosidase assays served as read-out for the expression of enzymatically active β-galactosidase and thus for the occurrence of TALEN pair mediated DNA double-strand breaks in the TALEN target sequence of the respective reporter plasmids [Figure II-5], whereas luciferase assays were used for the normalization with respect to different cell numbers, transfection efficiencies, and expression levels in the reactions.

The β-galactosidase activity in lysate supernatants (see II.9.4.2) was analyzed in triplicates using the β-Gal Reporter Gene Assay, chemiluminescent kit (Roche) and a GloMax-Multi Detection System with Dual Injector System (Promega). For this, 20 µl of lysate supernatant were pipetted per well of a white 96-well plate (F96 MicroWell White Polystyrene Plate, Nunc) before 40 µl of the β-Gal Substrate Reagent were added and the samples were incubated at room temperature, protected from light on a horizontal shaker with moderate agitation for 30 min. The 96-well plate was transferred to the GloMax-Multi Detection system and 25 µl of Initiation Reagent were automatically injected to each sample via the GloMax Dual Injector System. After a delay time of 2 sec, the intensity of luminescence, resulting from the β-galactosidase reaction product, was measured for 5 sec.

The luciferase activity in the supernatants of lysates was also determined in triplicates, however, using the Luciferase Assay System (Promega) in combination with the GloMax-Multi Detection System with Dual Injector System (Promega). The assay was again carried out with 20 µl of lysate supernatant per well of a white 96-well plate (F96 MicroWell White Polystyrene Plate, Nunc). The plated 96-well plate was directly transferred to the GloMax-Multi Detection system and 100 µl of Luciferase Assay Reagent were automatically injected to each sample via the GloMax Dual Injector System. After a delay time of 2 sec, the intensity of luminescence, resulting from the luciferase reaction product, was measured for 5 sec.

The TALEN pair efficiencies were calculated from the β-galactosidase luminescence signal intensities in the TALEN test samples and the appropriate negative controls after normalization by the respective luciferase signal intensities. For this, the average intensity of β-galactosidase luminescence of each sample measured in triplicates was normalized by the average luciferase luminescence in the respective sample. The resulting luminescence ratios were averaged for sample triplicates before the average luminescence ratio of samples containing TALEN pairs (TALEN test) was divided by the average luminescence ratio of the respective negative control. TALEN pairs with efficiencies comparable to the reference standard (Rab reporter system) or higher provide a good tool for gene knock-out [215].

β-Gal Substrate Reagent:	1 % (v/v)	β-Gal Substrate in Assay Buffer (Roche)
Initiation Reagent:	1 volume 5 volumes	Enhancer Initiation Solution (Roche)
Luciferase Assay Reagent:	1 vial 10 ml	Luciferase Assay Substrate, lyophilized Luciferase Assay Buffer (Promega)

II.9.5. ENRICHMENT OF *ΔLNGFR* (OVER)EXPRESSING CELLS

Cells expressing either endogenous human *LNGFR*, like cells of the human BeWo cell line, or exogenous *ΔLNGFR* (after transient transfection with plasmids encoding for ΔLNGFR) were selected via the MACSelect LNGFR System (Miltenyi Biotec).

For this, cultured cells were harvested and magnetically labeled with MACSelect LNGFR MicroBeads (Miltenyi Biotec) according to the manufacturer's instructions for "Procedure A: Harvest and magnetic labeling of transfected adherent cells with EDTA". In short, the culture medium was aspired and the cell layers were washed once with PBS before appropriate volumes of PBE and MicroBeads (e.g., 600 µl PBE and 80 µl MicroBeads per 10 cm dish) were added and the cells were incubated therein at 4 °C for 15 min. During this incubation step, the cells were detached by the action of EDTA provided by the PBE buffer and selectively magnetically labeled via the binding of MACSelect LNGFR MicroBeads (Miltenyi Biotec) to the extracellular LNGFR domain. Afterwards, the cells were carefully suspended in a final volume of 2 ml PBE and subjected to the magnetic separation. The magnetic separation of labeled and unlabeled cells was performed according to the manufacturer's instructions for "Magnetic separation with MS Column". For this, MACS Separation (MS) Columns (Miltenyi Biotec) were put on a µMACS Separator (Miltenyi Biotec) magnet and rinsed with PBE before the cell suspensions were applied in aliquots of 500 µl. The loaded columns were washed four times with 500 µl PBE. Finally, the retained labeled cells were eluted by removing the columns from the magnet and applying 1 ml PBE.

All fractions from the separation process were collected for downstream analysis (e.g., counting of cells via Cellometer or semi-quantitative RT-PCR). In addition, the enriched cells were further cultivated with the appropriate culture medium at standard conditions [II.3.1].

PBE:	5 mM 0.5 % (w/v)	EDTA albumin fraction V in PBS
PBS (pH 7.4):	140 mM 2.7 mM 10 mM 2 mM	sodium chloride potassium chloride disodium hydrogen phosphate potassium dihydrogen phosphate in MilliQ-H_2O

PBE was sterile filtrated using sterile syringe filters with a 0.22 µm pore size prior to use and stored at 4 °C.

II.10. *IN SILICO* ANALYSES

II.10.1. PREDICTION OF SPLICE SITES

Splice site predictions within *AKR1B15* were accomplished with the whole *AKR1B15* gene sequence (Ensembl: ENSG00000227471; Chr. 7: 134549136-134579875) using the NetGene2 Server (CBS) (http://www.cbs.dtu.dk/services/NetGene2) and the Alternative Splice Site Predictor – ASSP (http://wangcomputing.com/assp/index.html) [233, 234]. In both cases, the prediction was performed for human genes. Within the prediction using the ASSP algorithm, false splice site cutoff values of 4.0 for acceptor sites and 6.0 for donor sites were chosen.

II.10.2. PREDICTION OF SUBCELLULAR LOCALIZATION

Different prediction algorithms [Table II-25] were used for the *in silico* analysis of subcellular localizations. For this, protein sequences published in the UniProtKB database or protein sequences of the respective mutants were pasted into the entry masks and the predictions were performed using the parameter settings listed in Table II-25.

Table II-25: Algorithms / programs and parameters used for the prediction of subcellular localizations and signal peptide cleavage sites.

algorithm / program	references	parameter settings
MitoProt II (v1.101)	[235]	-
PrediSi	[236]	*organism group:* eukaryotic *truncation:* 300
iPSORT Prediction	[237]	non-plant protein
PSORT II		*source input:* yeast/animal
SignalP 4.1 Server	[238]	*organism group:* eukaryotes *D-cutoff values:* default *method:* … include TM regions
TargetP 1.1 Server	[239, 240]	*organism group:* non-plant *prediction scope:* yes *cutoffs:* no cutoffs

II.10.3. PREDICTION OF POST-TRANSLATIONAL MODIFICATIONS

The prediction of sites of various post-translational modifications, such as phosphorylation, glycation, glycosylation, sulfation, SUMOylation, or ubiquitination was performed by the use of different online tools and the parameter settings listed in Table II-26.

Table II-26: Algorithms / programs and parameters used for the prediction of phosphorylation, glycation, glycosylation, sulfation, SUMOylation, and ubiquitination sites in the AKR1B15 isoforms.

algorithm / program	references	parameter settings
KinasePhos 2.0	[241]	*specificity:* 80 % *prediction on:* all kinases
NetPhos 2.0 Server	[242]	*prediction on:* Ser, Tyr, Thr
NetPhosK 1.0 Server	[243]	*method:* … without filtering *threshold:* 0.5
NetGlycate 1.0 Server	[244]	-
NetNGlyc 1.0 Server	[245]	-
NetOGlyc 4.0 Server	[246]	-
Sulfinator	[247]	-
GPS-SUMO	[248, 249]	*thresholds:* low *console:* sumoylation
SUMOplot		*organism group:* non-plant *prediction scope:* yes *cutoffs:* no cutoffs
CKSAAP_UbSite	[250, 251]	*organism:* H. sapiens
UbPred	[252]	-

II.11. ANALYSIS OF VITAMIN D METABOLITES

II.11.1. PREPARATION OF BIOLOGICAL SAMPLES FOR VITAMIN D ANALYSES

The preparation of biological samples for subsequent chromatographic analysis of vitamin D metabolites (and itraconazole) covered basically two steps.

Within the first step either culture samples were harvested, mouse tumor samples were homogenized, or human plasma samples were preprocessed. In either case, this step included also the addition of an internal standard (IS) for subsequent normalization purposes. The second step covered the extraction of these samples for the downstream analysis of vitamin D metabolites (and itraconazole) via mainly LC-MS/MS using solid phase extraction (SPE).

II.11.1.1. HARVEST OF SAMPLES FROM CELL CULTURE EXPERIMENTS

Cell culture experiments with subsequent LC-MS/MS analysis of vitamin D metabolites (and itraconazole) in medium or cells were performed in 6-well plates.

For the generation of medium samples, medium was collected and centrifuged at 1000 x *g* and 4 °C for 10 min. 1600 µl of the resulting supernatant were transferred into a fresh 2 ml Eppendorf tube, supplemented with 200 µl IS solution for medium, and vortexed before the samples were either immediately extracted or stored at -80°C until SPE (see II.11.1.4).

For cell harvest, the cell layers were washed with PBS and afterwards harvested via speedy scraping using 750 µl IS solution for cells. The resulting cell lysate suspension was transferred into a 1.5 ml safe-lock Eppendorf tube and put on dry ice. Wells of the plate were rewashed with 500 µl 40 % methanol in MilliQ-H_2O. The wash was combined with the cell lysate suspension, vortexed, and stored at -80 °C until SPE (see II.11.1.4). Please note that alternative cell harvest methods with poorer performance were additionally used within the method development. These procedures are not described here but in the respective results section (see III.3.4.2).

IS solution for medium:	200 $^{ng}/_{ml}$	25-(OH)-D_2 [25,26,27-$^{13}C_3$] (CIL) in methanol
IS solution for cells:	40 $^{ng}/_{ml}$ 60 % ($^{v}/_{v}$)	25-(OH)-D_2 [25,26,27-$^{13}C_3$] (CIL) methanol in MilliQ-H_2O

II.11.1.2. HOMOGENIZATION OF MOUSE TUMOR SAMPLES

Allograft tumor samples of NMRI-*Foxn1*^{nu} nude mice (prepared by Benedikt Linder Tumor Genetics Group, UMG) were weighted (14 mg – 120 mg) and transferred to Precellys ceramic kit 1.4/2.8 mm 2.0 ml tubes (PEQLAB).

For homogenization and normalization reasons, 500 µl methanol and an appropriate volume IS solution for tumors (10 µl IS solution per 100 mg tumor) were added. The use of the low-priced 1α,25-(OH)$_2$-D_2 as IS for mouse tumor samples was possible since its precursor vitamin D_2 is not built endogenously in mice and the feed of the mice was not supplemented with vitamin D_2 or any other vitamin D_2 metabolite. The homogenization of tumors was performed with a Precellys 24 tissue homogenizer (Bertin Technologies) operating three cycles of 20 sec homogenization at 5500 rpm and 30 sec pausing in between. During the homogenization the temperature was kept constant at 4 °C using a Cryolys temperature controller (Bertin Technologies).

The tumor homogenates were centrifuged at 5000 x *g* and 4 °C for 5 min before 500 µl of the resulting homogenate supernatants were immediately loaded onto conditioned Strata-X SPE cartridges. To reduce the loss of metabolites in the tumor homogenate pellets, the remaining pellets were washed with 500 µl methanol which was followed by another centrifugation step (5000 x *g* and 4 °C for 5 min). The resulting wash supernatants were also loaded onto the respective SPE cartridges before the SPE was performed (see II.11.1.4).

IS solution for tumors:	1 $^{\mu g}/_{ml}$	1α,25-(OH)$_2$-D$_2$ in methanol

II.11.1.3. PREPROCESSING OF HUMAN PLASMA SAMPLES

Human plasma was thawed on ice, vortexed, and split into Eppendorf tubes in appropriate aliquots (50 µl to 500 µl). After the addition of 750 µl IS solution for cells and up to 500 µl 40 % methanol in MilliQ-H_2O (the volume of 40 % methanol in MilliQ-H_2O was reduced by the volume of plasma added), the plasma samples were briefly vortexed, incubated at room temperature for 15-30 min, and finally centrifuged at 4000 x *g* and room temperature for 1 min. In doing so, the addition of IS solution and 40 % methanol in MilliQ-H_2O triggered the precipitation of plasma proteins. The resulting supernatants, which still contained small aggregates of precipitated proteins, were subjected to SPE (see II.11.1.4).

IS solution for cells:	40 $^{ng}/_{ml}$ 60 % ($^{v}/_{v}$)	25-(OH)-D$_2$ [25,26,27-$^{13}C_3$] (CIL) methanol in MilliQ-H_2O

II.11.1.4. SOLID PHASE EXTRACTION (SPE) OF VITAMIN D METABOLITES

Although the herein described solid phase extraction (SPE) procedure was initially optimized and validated for the extraction of vitamin D metabolites from cell culture samples, it was also used for the extraction of vitamin D metabolites (and itraconazole) from mouse tumor homogenates and preprocessed human plasma samples.

Strata-X 33 µm polymeric reversed phase (30 $^{mg}/_{ml}$) tubes (Phenomenex) and either a Visiprep 24DL vacuum manifold (Supelco) or, for a higher number of samples, a nitrogen-driven Positive Pressure-96 Processor (Waters) teamed with a 96-Well Tab-less Tube Holder (Phenomenex) were used for the SPE of vitamin D metabolites (and itraconazole).

For SPE the Strata-X cartridges were conditioned with 1 ml methanol and 1 ml MilliQ-H_2O. Samples from cell culture experiments [II.11.1.1] were (if necessary) thawed at room temperature and well vortexed before either two times 900 µl IS-supplemented medium supernatants or one times approximately 1200 µl cell suspensions were directly loaded onto the conditioned cartridges, whereas plasma sample supernatants [II.11.1.3] were loaded without any preceding vortexing step. In contrast, 500 µl tumor homogenate supernatants as well as 500 µl of their wash supernatants [II.11.1.2] were successively loaded onto SPE tubes containing each time already 400 µl MilliQ-H_2O.

After loading the samples, the cartridges were successively washed with 1 ml 10 % methanol in MilliQ-H_2O, 1 ml 30 % methanol in MilliQ-H_2O, and 1 ml 50 % methanol in MilliQ-H_2O. In order to increase the purity of extracts, the process included an additional fourth washing step using 500 µl of 55 % methanol in MilliQ-H_2O when medium and mouse tumor samples were extracted.

Vitamin D metabolites (and itraconazole) were eluted from the SPE sorbent with 2 % formic acid in methanol (SPE eluent) in two steps. In case of SPE by using the vacuum manifold, the samples were eluted into glass vials with insert (Crimp µ-vials) with 200 µl and 175 µl SPE eluent and evaporated in an UniVapo 150 ECH (UniEquip) rotational vacuum concentrator, whereas in case of SPE by using the positive pressure unit, the samples were eluted into 96 DeepWell PP plates (Nunc) with two times 250 µl SPE eluent and evaporated under constant nitrogen flow. ^{3}H-labeled vitamin D metabolites were eluted into micro vials PP (Zinsser Analytic) with two times 200 µl SPE eluent and directly used for the analysis via radioactive HPLC. The evaporated eluates were generally reconstituted in 150 µl methanol and diluted with 75 µl MilliQ-H_2O (100 µl methanol and 50 µl MilliQ-H_2O with human plasma samples) for subsequent LC-MS/MS analysis, whereas eluates for HPLC-UV analysis were reconstituted in 100 µl methanol and diluted with 100 µl MilliQ-H_2O. The reconstituted samples were stored at 4 °C and generally analyzed within the next 24-48 hours.

SPE eluent:	2 % ($^{v}/_{v}$)	formic acid in methanol

II.11.2. Chromatographic analyses of vitamin D metabolites

In the following, the finally optimized and established methods for the separation and detection of vitamin D metabolites in prepared samples via HPLC coupled to UV detection (HPLC-UV), HPLC coupled to scintillation detection (radioactive HPLC), and HPLC coupled to tandem mass spectrometry (LC-MS/MS) are described.

II.11.2.1. Analysis of vitamin D_3 metabolites via UV detection

In order to develop a basic HPLC method for the separation of different vitamin D_3 metabolites (vitamin D_3, 25-(OH)-D_3, 1α-(OH)-D_3, 24,25-$(OH)_2$-D_3, 1α,25-$(OH)_2$-D_3) a Perkin Elmer Series 200 HPLC system comprising of a Series 200 Autosampler with 50 µl sample loop, two Series 200 Micro Pumps, a Series 200 Mixer, a Series 200 Vacuum Degasser, and a Series UV/Vis Detector was used. 30-50 µl of sample, which was reconstituted with methanol and diluted with MilliQ-H_2O (1:1), were injected. The metabolites were separated on a Kinetex 2.6 µm C18 100 Å 50 mm x 4.6 mm (Phenomenex) reversed phase column with SecurityGuard Standard C18 4 mm x 2 mm (Phenomenex) cartridge using a gradient of mobile phase A (5 mM ammonium acetate, 0.1 % formic acid, and 80 % methanol in MilliQ-H_2O) and mobile phase B (5 mM ammonium acetate and 0.1 % formic acid in methanol) at a constant flow of 1 $^{ml}/_{min}$. The total HPLC run time was 23 min and covered a column equilibration step (step 0; 5 min) prior to the sample injection as well as the gradient steps necessary for the separation of vitamin D_3 metabolites (step 1-3; 18 min). Details of the HPLC program are listed in Table II-27. The elution of the vitamin D_3 metabolites was monitored at 265 nm with a sampling rate of 50 $^{pts}/_{s}$. The HPLC runs were controlled and analyzed by the TotalChrom Workstation Version 6.3.2 (Perkin Elmer) software.

Table II-27: HPLC-UV method for the separation of vitamin D_3 metabolites.

step	time interval [min]	mobile phase A [%]	mobile phase B [%]	curve
0	5.0	100	0	0.0
1	6.0	100	0	0.0
2	7.0	50	50	0.0
3	5.0	10	90	0.0

Vitamin D_3 metabolites were separated on a Kinetex 2.6 µm C18 100 Å 50 mm x 4.6 mm column with SecurityGuard Standard C18 4 mm x 2 mm cartridge using a Perkin Elmer Series 200 HPLC system with UV-detection at 265 nm.

mobile phase A:	5 mM	ammonium acetate
	0.1 % ($^v/_v$)	formic acid
	80 % ($^v/_v$)	methanol
		in MilliQ-H_2O
mobile phase B:	5 mM	ammonium acetate
	0.1 % ($^v/_v$)	formic acid
		in methanol
autosampler wash solution:	100 %	methanol

II.11.2.2. Analysis of ^{3}H-labeled vitamin D_3 metabolites

Since UV-detection of vitamin D_3 metabolites possesses only limited sensitivity, a method analyzing commercially available ^{3}H-labeled vitamin D_3 metabolites (1α,25-$(OH)_2$-D_3 and 25-(OH)-D_3,) or possible cellular derivatives (e.g., 24,25-$(OH)_2$-D_3) was also generated.

As with ^{3}H-labeled steroids, ^{3}H-labeled vitamin D_3 metabolites were analyzed on a Beckman Coulter HPLC system, comprising of a LC-502E autosampler with 20 µl sample loop and a System Gold 125 Solvent Module as binary pump, but coupled to an in-line connected System Gold 166 UV detector (Beckman Coulter) and Berthold LB 506 D Radioactivity Monitor. This system was controlled by the 32 Karat software Version 3.0 (Beckman Coulter). 20 µl of sample in 2 % formic acid in methanol were injected and the metabolites were separated on a Kinetex 2.6 µm C18 100 Å 50 mm x 4.6 mm (Phenomenex) reversed phase column with SecurityGuard Standard C18 4 mm x 2 mm (Phenomenex) cartridge using a gradient of mobile phase A (0.05 % formic acid in MilliQ-H_2O) and mobile phase B (5 mM ammonium acetate and 0.1 % formic acid in methanol) at a constant flow of 1 $^{ml}/_{min}$. The total run time was 22 min. Details of the HPLC program are listed in Table II-28. For the detection of ^{3}H-labeled metabolites via the scintillation detector, the mobile phase was mixed with the Ready Flow III (Beckman Coulter) scintillation cocktail, supplied by a MCP-Z Standard gear pump (Ismatec) with a constant flow of 1 $^{ml}/_{min}$ before entering the detection chamber. For the determination of the retention times of vitamin D_3 metabolites not available as ^{3}H-labeled compounds, ^{3}H-labeled metabolites were spiked with unlabeled metabolites and also analyzed via UV absorption at 265 nm using the in-line System Gold 166 UV detector (Beckman Coulter).

Table II-28: "Radioactive" HPLC method for the separation of vitamin D_3 metabolites.

total time [min]	**module**	**function**	**value**	**duration**
0.0	Pump	% B	70	
0.0	Pump	Relay on	1	0.0
0.0	Pump	Relay on	2	0.0
0.0	Det166-2	Autozero		
1.0	Pump	% B	80	0.1
7.0	Pump	% B	90	0.1
14.0	Pump	% B	98	0.1
18.0	Pump	% B	70	0.1
22.0	Pump	Relay on	1	0.0
22.0	Pump	Relay on	2	0.0
22.0	Det166-2	Stop Data		

Vitamin D_3 metabolites were separated on a Kinetex 2.6 µm C18 100 Å 50 mm x 4.6 mm column with SecurityGuard Standard C18 4 mm x 2 mm cartridge using a Beckman Coulter Gold HPLC system with in-line 166 UV detector and Berthold scintillation detector.

mobile phase A:	0.05 % (v/v)	formic acid in MilliQ-H_2O
mobile phase B:	5 mM	ammonium acetate
	0.1 % (v/v)	formic acid in methanol
autosampler wash solution:	100 %	methanol

II.11.2.3. Analysis of vitamin D metabolites and itraconazole via LC-MS/MS

Within this doctoral thesis, a liquid chromatography coupled to tandem mass spectrometry (LC-MS/MS) method was finally developed and applied as a potent tool for the analysis of vitamin D metabolites (vitamin D_3, 25-(OH)-D_3, 1α-(OH)-D_3, 24,25-$(OH)_2$-D_3, 1α,25-$(OH)_2$-D_3, vitamin D_2, 25-(OH)-D_2, and 1α,25-$(OH)_2$-D_2) as well as itraconazole in cell culture, mouse tumor, or human plasma samples with high sensitivity and specificity.

Using this technique, compounds are first separated on a HPLC column and then directly passed into a mass spectrometer that allows for the detection of specific mother-daughter-ion pairs (multiple reaction monitorings = MRMs). For MRM detection, molecules entering the mass spectrometer are initially ionized in the source and then directed to a quadrupole (Q_1) that filters the molecules according to their mass-to-charge ratio (m/z). Selected mother ions become fragmented in the collision cell (Q_2) and the resulting daughter ions are once more filtered according to their m/z in another quadrupole (Q_3). Finally, the daughter ions are conducted to a pulse-counting channel electron multiplier (CEM) detector and the detected signals are processed by the software.

The LC-MS/MS method used a HPLC system consisting of a HTC-xt autosampler (CTC-PAL) with a 20 µl sample loop, a 1260 Infinity degasser (Agilent), a 1260 Infinity binary pump model G1312B (Agilent), and a 1260 TCC column oven model G1316A (Agilent) for the LC separation of vitamin D metabolites on a Kinetex 2.6 µm C18 column, whereas a QTrap 5500 mass spectrometer (AB Sciex) was used for MS/MS analysis. The complete LC-MS/MS set-up [Figure II-6] was controlled by the Analyst 1.6 software (AB Sciex).

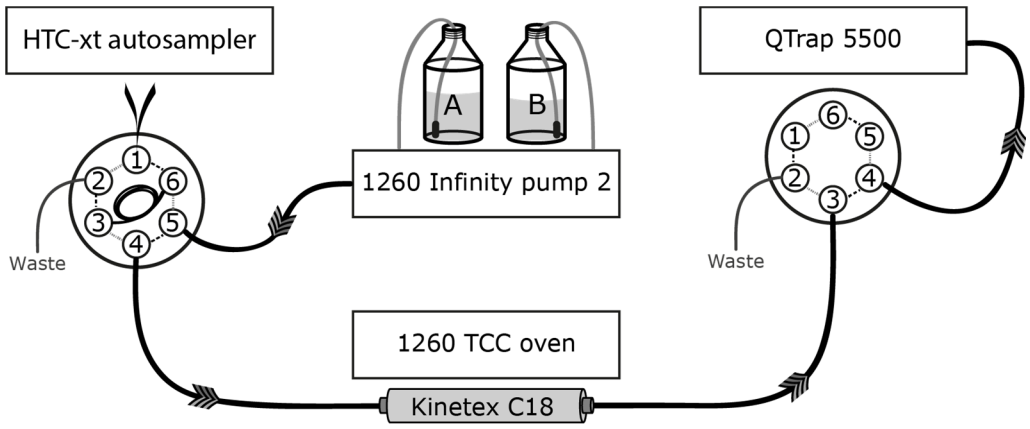

Figure II-6: Schematic illustration of the LC-MS/MS set-up.
The LC-MS/MS set-up used for the analysis of vitamin D metabolites included a HTC-xt autosampler with a 20 µl sample loop, a 1260 Infinity degasser, a 1260 Infinity binary pump, and a 1260 TCC column oven as well as a QTrap 5500 mass spectrometer.

For the analysis of vitamin D metabolites via LC-MS/MS, 25 µl of sample, which was reconstituted in methanol and diluted with MilliQ-H_2O (2:1) [II.11.1.4] were injected and separated on a Kinetex 2.6 µm C18 100 Å 50 mm x 2.1 mm (Phenomenex) reversed phase column with SecurityGuard Standard C18 4 mm x 2 mm (Phenomenex) cartridge using a gradient of mobile phase A (0.05 % formic acid and 0.15 mM lithium acetate in MilliQ-H_2O) and mobile phase B (0.05 % formic acid in methanol) at a constant flow of 0.3 $^{ml}/_{min}$. The total HPLC run time for the separation of vitamin D metabolites was 13 min. The HPLC method (described in detail in Table II-29) included a column equilibration step (auto-equilibration step: 5 min) which was followed by the sample injection and the gradient steps for the chromatographic separation of metabolites (step 1-4: 8 min). The column oven temperature was constantly set to 30 °C.

To reduce the carryover of hydrophobic vitamin D metabolites, after each sample a 5 min washing step was performed. For this, 25 µl of 100 % methanol were injected and the LC gradient method listed in Table II-29 was run.

MS/MS analysis was performed via ESI in positive-ion mode and MRM detection using the optimized parameter settings listed in Table II-30. These parameters resulted from infusion (flow: 7 $^{µl}/_{min}$) and FIA optimization analyses with single compounds in appropriate dilutions (< 1 $^{µg}/_{ml}$) in either 100 % methanol or 0.5-1 mM lithium acetate in methanol using the "Automatic Optimization tool" of the Analyst 1.6 software (see III.3.3.1). To increase the number of reading points per peak, at least when more than ten vitamin D MRMs were simultaneously monitored, scheduled MRM detection was applied [Table II-30].

The results from LC-MS/MS runs were visualized and analyzed by the Analyst 1.6 software (AB Sciex). Thereby, the three times ^{13}C isotope labeled 25-(OH)-D_2 [25,26,27-$^{13}C_3$] was used as internal standard (IS) for the normalization of signals and quantification (either relative or quantitative via calibration curves using a linear fit without weighting) of vitamin D metabolites in cell culture samples (see III.3.5.1).

Table II-29: HPLC methods for the analysis of vitamin D metabolites via LC-MS/MS.

	step	total time [min]	flow [µl/min]	mobile phase A [%]	mobile phase B [%]
separation method	auto-equilibration	5.0	300	20.0	80.0
	0	0.0	300	20.0	80.0
	1	0.1	300	20.0	80.0
	2	1.1	300	20.0	80.0
	3	2.5	300	0.0	100.0
	4	8.0	300	0.0	100.0
wash method	auto-equilibration	0	0	0	0
	0	0.0	300	0.0	100.0
	1	4.0	300	0.0	100.0
	2	4.5	300	20.0	80.0
	3	5.0	300	20.0	80.0

Vitamin D metabolites were separated using a Kinetex 2.6 µm C18 100 Å 50 mm x 2.1 mm column with SecurityGuard Standard C18 4 mm x 2 mm cartridge and an Agilent Infinity 1260 HPLC system coupled to a QTrap 5500 mass spectrometer [Figure II-6].

mobile phase A:	0.15 mM	lithium acetate
	0.05 % (v/v)	formic acid
		in MilliQ-H_2O
mobile phase B:	0.1 % (v/v)	formic acid
		in methanol
autosampler wash solution -I:	50 % (v/v)	acetonitrile
	20 % (v/v)	methanol
	15 % (v/v)	2-propanol
	0.25 % (v/v)	formic acid
		in MilliQ-H_2O
autosampler wash solution -II:	50 % (v/v)	methanol
		in MilliQ-H_2O

Please note that, beside the final mobile phase A (0.15 mM lithium acetate and 0.05 % formic acid in MilliQ-H_2O) and the MRMs listed in Table II-30, different other MRMs as well as an initial mobile phase A without lithium ions (0.05 % formic acid in MilliQ-H_2O) were used within the method development process. The ionization parameter settings of MRMs not used for the final method but mentioned in the results are listed in the appendix [VI.8].

Table II-30: MRMs and ionization parameter settings for the analysis of vitamin D metabolites (and itraconazole) on a QTrap 5500 via LC-MS/MS.

compound	adduct	Q_1 [m/z]	Q_3 [m/z]	$t_{scheduled}$ [min]	DP [V]	EP [V]	CE [V]	CXP [V]
24,25-$(OH)_2$-D_3 & 1α,25-$(OH)_2$-D_3	Li^+	423.174	91.000	2.3	110	10	100	14
	Li^+	423.323	77.000	2.3	181	10	127	12
	Li^+	423.174	128.000	2.3	110	10	120	14
25-(OH)-D_3 & 1α-(OH)-D_3	H^+	401.289	90.900	4.5	101	10	79	12
	Li^+	407.185	105.000	4.5	230	10	50	12
	Li^+	407.326	90.900	4.5	186	10	101	14
vitamin D_3	H^+	385.300	259.200	6.5	86	10	21	6
1α,25-$(OH)_2$-D_2	Li^+	435.314	91.000	2.3	141	10	99	14
	Li^+	435.314	77.100	2.3	141	10	123	6
25-(OH)-D_2	Li^+	419.323	361.300	4.5	181	10	35	26
	Li^+	419.323	77.000	4.5	181	10	127	12
vitamin D_2	H^+	397.325	91.100	6.5	61	10	83	10
	H^+	397.325	105.100	6.5	61	10	51	12
internal standard (25-(OH)-D_2 [25,26,27-$^{13}C_3$])	Li^+	422.323	361.300	4.5	181	10	35	26
	Li^+	422.323	77.000	4.5	181	10	127	12
itraconazole	H^+	705.203	392.200	-	41	10	47	16
	H^+	705.203	256.000	-	41	10	51	32

source = TurboSpray **CUR** = 40 **CAD** = Medium **IS** = 5500 **TEM** = 600 **GS1** = 40 **GS2** = 50

The MRM detection window for scheduled MRMs was set to 120 sec. If continuous MRM monitoring was performed, the time was set to 150 msec.
CAD, collision gas; CE, collision energy; CUR, curtain gas; CXP, collision cell exit potential; DP, declustering potential; EP, entrance potential; GS1, ion source gas 1; GS2, ion source gas 2; IS, ion spray voltage; source, ion source; TEM, temperature; $t_{scheduled}$, scheduled time.

II.11.3. VALIDATION OF THE VITAMIN D LC-MS/MS METHOD

The final vitamin D LC-MS/MS method was validated in combination with the SPE sample preparation method for cell culture samples. Thereby, basic method validation parameters covering the limits of detection (LODs) and quantification (LOQs), linearity, selectivity, precision, recovery/accuracy, reproducibility, and stability were determined.

For the validation of the method, principally two kinds of reference solutions were prepared: First, vitamin D mixes in 350 µl 2 % formic acid in methanol which were evaporated and reconstituted without any SPE processing, and second, vitamin D mixes in 52 % methanol in MilliQ-H_2O which were processed by SPE [II.11.1.4]. All reference solutions were prepared in triplicates by serial dilutions and contained each vitamin D metabolite (24,25-$(OH)_2$-D_3, 1α,25-$(OH)_2$-D_3, 1α,25-$(OH)_2$-D_2, 25-(OH)-D_3, 25-(OH)-D_2, 1α-(OH)-D_3, vitamin D_3, and vitamin D_2) in an amount of 1-100 pmol as well as 30 ng of the IS 25-(OH)-D_2 [25,26,27-$^{13}C_3$]. Whereas reference mixes without SPE processing were only used for the determination of the injection reproducibility [III.3.5.4] and the recovery of vitamin D metabolites from the

SPE process [III.3.5.8], SPE processed reference mixes were used for the generation of the quantification method (including the calibration curves) [III.3.5.1], the analysis of the LODs and LOQs [III.3.5.2], the selectivity [III.3.5.3], and the linearity [III.3.5.5] of the method, as well as for comparison reasons within the determination of all other parameters [III.3.5.6, III.3.5.7, III.3.5.8, III.3.5.9].

Since the studies on vitamin D metabolism in cell culture experiments concentrated mainly on four cell lines, namely HaCaT, ASZ001, $Ptch^{WT}$, and $Ptch^{-/-}$, these cell lines as well as the respective culture media were additionally included in the validation process [Table II-31]. For the validation of the vitamin D LC-MS/MS method in cell culture samples [III.3.5.6, III.3.5.7, III.3.5.8, III.3.5.9], triplicates of harvested, untreated cell lysate suspensions as well as medium aliquots [Table II-31] were spiked with vitamin D metabolites (2.5-10 pmol and 2.5-100 pmol each for cells and medium, respectively), vortexed, and incubated at room temperature for approximately 30 min before they were extracted via SPE [II.11.1.4]. Please note that the culturing of cells used in the validation process and the harvest of these cells were performed by Benedikt Linder (Tumor Genetics Group, UMG) in Göttingen according to the established protocols described in II.11.1.1 and Linder [253]. The harvested cell lysate suspensions (containing due to the harvest protocol already theoretically 30 ng of the IS) and fresh culture media were subsequently shipped to our lab on dry ice and stored at -80 °C until further processing and analysis.

All prepared reference and cell culture samples (each reconstituted in 150 µl methanol and 75 µl MilliQ-H_2O) were first analyzed on the day of the sample preparation (day 0) via the established LC-MS/MS method using scheduled MRM detection [II.11.2.3]. In order to determine the stability of vitamin D metabolites in the extracts and the LC-MS/MS method, the same samples were measured once more six days after the first analysis (day 6).

Table II-31: Cell lines and media considered within the validation process.

cell line / medium	characteristics	references
HaCaT	human keratinocyte cell line; control cell line for vitamin D metabolism	[254]
ASZ001	murine BCC cell line; basal cell carcinoma cell line possessing inactivated copies of the *Ptch* gene	[255, 256]
$Ptch^{WT}$	murine *Ptch*$^{flox/flox}$*ERT2*$^{+/-}$ fibroblast cell line (internal name: B9); fibroblast control cell line expressing wild type *Ptch*, derived from dermis of *Ptch*$^{flox/flox}$*ERT2*$^{+/-}$ mice	[257]
$Ptch^{-/-}$	murine *Ptch* deficient fibroblast cell line; *Ptch* knock-out cell line, derived from tamoxifen treated *Ptch*$^{flox/flox}$*ERT2*$^{+/-}$ fibroblasts	[258]
DMEM	DMEM (4.5 g/l D-glucose) medium + 1 % PenStrep; for the cultivation of HaCaT, $Ptch^{WT}$, and $Ptch^{-/-}$ cell lines	
154CF	154CF medium + 0.05 mM calcium chloride + 1 % PenStrep; for the cultivation of the ASZ001 cell line	

The listed cell lines were cultured and harvested by Benedikt Linder (Tumor Genetics Group, UMG) in Göttingen. The harvested cells as well as freshly prepared media were shipped on dry ice to our lab and stored at -80 °C until their use in the method validation analyses. All steps were performed according to the (here) established protocols described in II.11.1.1, II.11.1.4, II.11.2.3, and Linder [253].

II.12. MATERIAL, EQUIPMENT, AND SOFTWARE

II.12.1. CELL STRAINS AND CELL LINES

II.12.1.1. *ESCHERICHIA COLI* (*E.COLI*) STRAINS (CHEMICALLY COMPETENT)

E. coli strain	genotype	supplier
DH5α	F- Φ80*lac*ZΔM15 Δ(*lac*ZYA-*arg*F) U169 *rec*A1 *end*A1 *hsd*R17 (rk-, mk+) *pho*A *sup*E44 *thi*-1 *gyr*A96 *rel*A1 λ-	Invitrogen™
One Shot® TOP10	F- Φ80*lac*ZΔM15 Δ*lac*X74 *rec*A1 *end*A1 *ara*D139 Δ(*ara leu*)7697 *gal*U *gal*K *rps*L (StrR) *nup*G Δ(*mrr-hsd*RMS-*mcr*BC) *mcrA*	Invitrogen™
Stellar™	F– Φ80d*lac*ZΔM15 Δ(*lac*ZYA-*arg*F) U169 *rec*A1 *end*A1 *pho*A *sup*E44 *thi*-1 *gyr*A96 *rel*A1 Δ(*mrr-hsd*RMS-*mcr*BC) Δ*mcr*A λ–	Clontech Laboratories, Inc.
BL21(DE3)	F– *fhu*A2 *[lon] omp*T *gal [dcm] (λ sBam*HIo *ΔEco*RI-B *int::(lac*I::*Plac*UV5::*T7 gene*1*) i*21 *Δnin*5*) Δhsd*S	Stratagene®

II.12.1.2. *PICHIA PASTORIS* (*P. PASTORIS*) STRAINS

P. pastoris strain	genotype	phenotype	supplier
KM71	*arg4 his4 aox1::ARG4*	Mut^S, Arg^+	Invitrogen™
X33	wild type	Mut^+	Invitrogen™

II.12.1.3. HUMAN CELL LINES AND CELL STRAINS

human cell line/strain	description	supplier	number / references
BeWo	human choriocarcinoma cell line	ATCC®	CCL-98™
HaCaT	human keratinocyte cell line	Dr. A. Uhmann, UMG	[213, 214]
HEK-293	human embryonic kidney cell line	ATCC®	CRL-1573™
HeLa	human cervix carcinoma cell line	DSMZ GmbH	ACC-57
SGBS	human preadipocyte cell strain	Prof. Dr. M. Wabitsch	[212]

II.12.2. MEDIA, SUPPLEMENTS, AND ANTIBIOTICS

II.12.2.1. MEDIA AND MEDIA SUPPLEMENTS

media for bacteria	supplier
LB-Agar (Luria/Miller), for molecular biology	Carl Roth® GMBH + CO. KG
LB-Medium (Luria/Miller), for molecular biology	Carl Roth® GMBH + CO. KG
S.O.C. medium	Invitrogen™

media or supplements for yeasts	supplier
agar granulate	Difco™
L-histidine	Sigma-Aldrich® Co. LLC.
YNB with ammonium sulfate	Invitrogen™
YPD medium powder	Clontech Laboratories, Inc.

media or supplements for human cell lines / strains	supplier
biotin	Sigma-Aldrich® Co. LLC.
DMEM (4.5 g/l D-glucose, with L-glutamine)	Gibco®
DMEM/F-12 (1:1) (with L-glutamine and 15 mM HEPES)	Gibco®
D-pantothenic acid	Sigma-Aldrich® Co. LLC.
F-12K Nutrient Mixture Kaighn's Modification (with L-glutamine)	Gibco®
FBS Superior	Biochrom GmbH
MEM with Earle's salts (with L-glutamine)	PAA Laboratories GmbH

II.12.2.2. ANTIBIOTICS

antibiotic	supplier
ampicillin sodium salt, BioReagent	Sigma-Aldrich® Co. LLC.
kanamycin solution from *Streptomyces kanamyceticus*, BioReagent, sterile-filtered, 50 mg/ml in 0.9 % NaCl	Sigma-Aldrich® Co. LLC.
spectinomycin dichloride pentahydrate	Sigma-Aldrich® Co. LLC.
tetracycline hydrochloride, BioReagent	Sigma-Aldrich® Co. LLC.
Zeocin™ Selection Reagent (100 mg/ml)	Gibco®

II.12.3. BIOLOGICAL SAMPLES

human total RNA	supplier
Human Total RNA Master Panel II (Lot. No.: 1112058A)	Clontech Laboratories, Inc.
Human Adipose Total RNA (Lot. No.: 1206519A)	Clontech Laboratories, Inc.
Human Ovary Total RNA (Lot. No.: 1203295A)	Clontech Laboratories, Inc.
Human Testis Total RNA (Lot. No.: 1105041)	Clontech Laboratories, Inc.

human protein lysate	supplier
Adipose (Human) Total Protein Lysate (Lot. No.: GR135207-1)	Abcam® plc.
Human Placenta Protein Medley (Lot. No.: 1302243A)	Clontech Laboratories, Inc.
Human Testis Protein Medley (Lot. No.: 1207139A)	Clontech Laboratories, Inc.
Human Thymus Protein Medley (Lot. No.: 1002151A)	Clontech Laboratories, Inc.
Placenta (Human) Tissue Lysate (Lot. No.: GR138837-5)	Abcam® plc.
Prostate (Human) Tissue Lysate (Lot. No.: GR79390-2)	Abcam® plc.
Skeletal Muscle (Human) Tissue Lysate (Lot. No.: GR68330-8)	Abcam® plc.

II.12.4. PLASMIDS

II.12.4.1. PURCHASED AND DONATED PLASMIDS

purchased plasmid	supplier
Golden Gate TALEN and TAL Effector Kit 2.0	Addgene, Inc.
pAcGFP-N1	Clontech Laboratories, Inc.
pcDNA4-myc/His B	Invitrogen™
pcGoldyTALEN	Addgene, Inc.
pCMV DsRed-Express2	Clontech Laboratories, Inc.
pDsRed2-ER	Clontech Laboratories, Inc.
pPICZ-A	Invitrogen™

donated plasmid	cloning sites (CDS)	supplier
N-myc-pcDNA3	-	Ferdinand Haller, HMGU (IEG)
pCAG-Rab-ZFN-A / -ZFN-B	-	Ralf Kühn, HMGU (IDG)
pcDNA3.1(+)-AKR1B15.1	*Hind*III / *Xho*I	Oleg Barski, U of L
pcDNA3.1(+)-AKR1B15.2	*Hind*III / *Xho*I	Oleg Barski, U of L
pcDNA4-myc/His B-HSD17B12	*Bam*HI / *Eco*RI	Ferdinand Haller, HMGU (IEG)
pCMV-hLuci	-	Ralf Kühn, HMGU (IDG)
pCMV-Rab-Reporter	-	Ralf Kühn, HMGU (IDG)
pCMV-Univ-Duplirep	-	Ralf Kühn, HMGU (IDG)
pCMV-βGal	-	Ralf Kühn, HMGU (IDG)
pET16b(+)-3αHSD2 (= AKR1C3)	*Nco*I / *Bam*HI	Trevor Penning, UPenn
pET28a(+)-AKR1B1	*Nde*I / *Xho*I	Oleg Barski, U of L
pET28a(+)-AKR1B10	*Nde*I / *Xho*I	Oleg Barski, U of L
pET28a(+)-AKR1B15.1	*Nde*I / *Xho*I	Oleg Barski, U of L
pET28a(+)-AKR6A3	*Nde*I / *Xho*I	Oleg Barski, U of L
pIRES-hrGFP-1α-AKR1B15.1	*Not*I / *Xho*I	Oleg Barski, U of L
pMACS-ΔLNGFR	-	Ralf Kühn, HMGU (IDG)

II.12.4.2. GENERATED PLASMIDS

generated plasmid	cloning sites (CDS)	template (CDS)	insert/mutagenesis primers
N-myc-pcDNA3-AKR1B15.1	*Not*I / *Xho*I	pcDNA3.1(+)-AKR1B15.1	# 2544 + # 2546
N-myc-pcDNA3-AKR1B15.1 S8R	-	N-myc-pcDNA3-AKR1B15.1	# 2680 + # 2681
N-myc-pcDNA3-AKR1B15.2	*Not*I / *Xho*I	pcDNA3.1(+)-AKR1B15.2	# 2545 + # 2546
pAcGFP-N1-AKR1B10 (Met1-Ala38) alias: pAcGFP-AKR1B10_1015-RV-3	*Hind*III / *Age*I	pET28a(+)-AKR1B10	# 2541 + # 2708
pAcGFP-N1-AKR1B10 (Met1-Glu30) alias: pAcGFP-AKR1B10_10-RV-1	*Hind*III / *Age*I	pET28a(+)-AKR1B10	# 2541 + # 2707
pAcGFP-N1-AKR1B10 K22R alias: pAcGFP-AKR1B10 K22R (Met1-Ala38)	-	pAcGFP-AKR1B10_1015-RV-3	# 2921 + # 2922
pAcGFP-N1-AKR1B10 P24L alias: pAcGFP-AKR1B10 P24L (Met1-Ala38)	-	pAcGFP-AKR1B10_1015-RV-3	# 2919 + # 2920
pAcGFP-N1-AKR1B15.1 (Met1-Ala38) alias: pAcGFP-AKR1B15.1_1015-RV-3	*Hind*III / *Age*I	pcDNA3.1(+)-AKR1B15.1	# 2541 + # 2708
pAcGFP-N1-AKR1B15.1 (Met1-Glu30) alias: pAcGFP-AKR1B15.1_15sl-RV-1	*Hind*III / *Age*I	pcDNA3.1(+)-AKR1B15.1	# 2541 + # 2705
pAcGFP-N1-AKR1B15.1 (Met1-Gly26) alias: pAcGFP-AKR1B15.1_15s-RV-4	*Hind*III / *Age*I	pcDNA3.1(+)-AKR1B15.1	# 2541 + # 2711
pAcGFP-N1-AKR1B15.2 (Met1-Ala66) alias: pAcGFP-AKR1B15.2_1015-RV-3	*Hind*III / *Age*I	pcDNA3.1(+)-AKR1B15.2	# 2542 + # 2708

generated plasmid	cloning sites (CDS)	template (CDS)	insert/mutagenesis primers
pAcGFP-N1-AKR1B15.2 (Met1-Glu58) alias: pAcGFP-AKR1B15.2_15sl-RV-1	*Hind*III / *Age*I	pcDNA3.1(+)-AKR1B15.2	# 2542 + # 2705
pAcGFP-N1-AKR1B15.2 (Met1-Leu30) alias: pAcGFP-AKR1B15.2_15l-RV-2	*Hind*III / *Age*I	pcDNA3.1(+)-AKR1B15.2	# 2542 + # 2704
pcDNA3.1(+)-AKR1B15.1 S8R	-	pcDNA3.1(+)-AKR1B15.1	# 2680 + # 2681
pcDNA4-myc/His B-AKR1B15.1	*Not*I / *Hind*III	pcDNA3.1(+)-AKR1B15.1	# 2541 + # 2543
pcDNA4-myc/His B-AKR1B15.1 S8R	-	pcDNA4-myc/His B-AKR1B15.1	# 2680 + # 2681
pcDNA4-myc/His B-AKR1B15.2	*Not*I / *Hind*III	pcDNA3.1(+)-AKR1B15.2	# 2542 + # 2543
pcGoldyTALEN-AcGFP	*Dra*III	pAcGFP-N1	# 2945 + # 2946
pcGoldyTALEN-AcGFP-AKR1B15-E2(26)_TAL1	*Dra*III	pAcGFP-N1	# 2945 + # 2946
pcGoldyTALEN-DsRed-AKR1B15-E2(26)_TAL2	*Dra*III	pCMV DsRed-Express2	# 2943 + # 2944
pcGoldyTALEN-ΔLNGFR-AKR1B15-E2(26)_TAL2	*Dra*III	pMACS-ΔLNGFR	# 2945 + # 2946
pCMV-Duplirep-AKR1B15.1	*Bst*BI / *Nru*I	-	# 2818 + # 2819
pCMV-Duplirep-AKR1B15.2	*Bst*BI / *Nru*I	-	# 2816 + # 2817
pCMV-Duplirep-AKR1B15-E2	*Bst*BI / *Nru*I	-	# 2820 + # 2821
pET28a(+)-AKR1B15.2	*Nde*I / *Xho*I	pcDNA3.1(+)-AKR1B15.2	# 2799 + # 2546
pET28a(+)-AKR1C3	*Nde*I / *Xho*I	pET16b(+)-3αHSD2	# 2914 + # 2913
pET28a(+)-hAKR1A1	*Nde*I / *Xho*I	human liver cDNA	# 2883 + # 2884
pIRES-hrGFP-1α-AKR1B15.2	*Not*I / *Xho*I	pcDNA3.1(+)-AKR1B15.2	# 2533 + # 2534
pPICZ-A-HSD17B12	*Eco*RI / *Not*I	pcDNA4-myc/His B-HSD17B12	# 2242 + # 2243

generated TALEN plasmid (RVD assembly)	TALEN modules / intermediates
pcGoldyTALEN-AKR1B15.1(36)_TAL1	pLR-NH, pFUS-A_AKR1B15.1_TAL1, pFUS-B5_AKR1B15.1(36)_TAL1
pcGoldyTALEN-AKR1B15.1(36)_TAL2	pLR-NI, pFUS-A_AKR1B15.1_TAL2, pFUS-B9_AKR1B15.1(36)_TAL2
pcGoldyTALEN-AKR1B15.1(40)_TAL1	pLR-NI, pFUS-A_AKR1B15.1_TAL1, pFUS-B9_AKR1B15.1(40)_TAL1
pcGoldyTALEN-AKR1B15.1(40)_TAL2	pLR-NH, pFUS-A_AKR1B15.1_TAL2, pFUS-B6_AKR1B15.1(40)_TAL2
pcGoldyTALEN-AKR1B15.2(66)_TAL1	pLR-NI, pFUS-A_AKR1B15.2_TAL1, pFUS-B8_AKR1B15.2(66)_TAL1
pcGoldyTALEN-AKR1B15.2(66)_TAL2	pLR-NG, pFUS-A_AKR1B15.2_TAL2, pFUS-B5_AKR1B15.2(66)_TAL2
pcGoldyTALEN-AKR1B15.2(67)_TAL1	pLR-NI, pFUS-A_AKR1B15.2_TAL1, pFUS-B9_AKR1B15.2(67)_TAL1
pcGoldyTALEN-AKR1B15.2(67)_TAL2	pLR-NH, pFUS-A_AKR1B15.2_TAL2, pFUS-B4_AKR1B15.2(67)_TAL2
pcGoldyTALEN-AKR1B15-E2(25)_TAL1	pLR-HD, pFUS-A_AKR1B15-E2_TAL1, pFUS-B4_AKR1B15-E2(25)_TAL1
pcGoldyTALEN-AKR1B15-E2(25)_TAL2	pLR-HD, pFUS-A_AKR1B15-E2_TAL2, pFUS-B8_AKR1B15-E2(25)_TAL2
pcGoldyTALEN-AKR1B15-E2(26)_TAL1	pLR-NH, pFUS-A_AKR1B15-E2_TAL1, pFUS-B5_AKR1B15-E2(26)_TAL1
pcGoldyTALEN-AKR1B15-E2(26)_TAL2	pLR-NH, pFUS-A_AKR1B15-E2_TAL2, pFUS-B7_AKR1B15-E2(26)_TAL2
pFUS-A_AKR1B15.1_TAL1	pNH1, pNH2, pHD3, pHD4, pNI5, pHD6, pNH7, pNG8, pNG9, pNG10
pFUS-A_AKR1B15.1_TAL2	pNH1, pHD2, pHD3, pHD4, pNI5, pNH6, pNH7, pHD8, pHD9, pHD10
pFUS-A_AKR1B15.2_TAL1	pHD1, pNI2, pNI3, pHD4, pNG5, pNI6, pNI7, pHD8, pNI9, pNI10
pFUS-A_AKR1B15.2_TAL2	pHD1, pNI2, pNI3, pNI4, pNH5, pNH6, pNH7, pHD8, pHD9, pNI10
pFUS-A_AKR1B15-E2_TAL1	pNG1, pNG2, pNG3, pHD4, pNI5, pNH6, pNG7, pHD8, pNG9, pHD10
pFUS-A_AKR1B15-E2_TAL2	pHD1, pNI2, pNI3, pNG4, pNH5, pNH6, pHD7, pHD8, pNI9, pHD10
pFUS-B4_AKR1B15.2(67)_TAL2	pNI1, pHD2, pNH3, pNH4
pFUS-B4_AKR1B15-E2(25)_TAL1	pNG1, pNG2, pHD3, pNG4
pFUS-B5_AKR1B15.1(36)_TAL1	pNH1, pNG2, pNH3, pNH4, pNI5
pFUS-B5_AKR1B15.2(66)_TAL2	pNI1, pHD2, pNH3, pNH4, pNH5
pFUS-B5_AKR1B15-E2(26)_TAL1	pNG1, pNG2, pHD3, pNG4, pHD5
pFUS-B6_AKR1B15.1(40)_TAL2	pNI1, pHD2, pNI3, pNI4, pNG5, pNH6
pFUS-B7_AKR1B15-E2(26)_TAL2	pHD1, pNG2, pNG3, pHD4, pNI5, pHD6, pHD7
pFUS-B8_AKR1B15.2(66)_TAL1	pHD1, pNG2, pNG3, pHD4, pHD5, pNI6, pHD7, pHD8
pFUS-B8_AKR1B15-E2(25)_TAL2	pHD1, pNG2, pNG3, pHD4, pNI5, pHD6, pHD7, pNH8
pFUS-B9_AKR1B15.1(36)_TAL2	pNI1, pHD2, pNI3, pNI4, pNG5, pNH6, pNH7, pNH8, pHD9
pFUS-B9_AKR1B15.1(40)_TAL1	pNH1, pNG2, pNH3, pNH4, pNI5, pNH6, pHD7, pNG8, pHD9
pFUS-B9_AKR1B15.2(67)_TAL1	pHD1, pNG2, pNG3, pHD4, pHD5, pNI6, pHD7, pHD8, pNI9

II.12.5. ANTIBODIES

primary antibody	from	working dilution	supplier
Anti-c-Myc clone 9E10 (# 11667203001)	mouse	1:1000	Roche Diagnostics GmbH
His-Tag Monoclonal Antibody	mouse	1:4000 - 1:5000	Novagen®
His-Tag Antibody (# 2365)	rabbit	1:1000 - 1:2000	Cell Signaling Technology, Inc.
mouse-anti-AKR1B15.2 clone 29D4	mouse	1:10 - 1:40	Elisabeth Kremmer, HMGU (IMI)
rabbit-anti-AKR1B15 (polyclonal)	rabbit	1:200 - 1:2000	21st Century Biochemicals, Inc.
rat-anti-AKR1B15 clone 19E5	rat	1:10 - 1:20	Elisabeth Kremmer, HMGU (IMI)
rat-anti-AKR1B15 clone 7B1	rat	1:10 - 1:20	Elisabeth Kremmer, HMGU (IMI)
rat-anti-AKR1B15 clone 9A5	rat	1:10 - 1:40	Elisabeth Kremmer, HMGU (IMI)
*+ other tested monoclonal antibody clones listed in **VI.3**:*			
mouse-anti-AKR1B15	*mouse*	*1:10*	*Elisabeth Kremmer, HMGU (IMI)*
rat-anti-AKR1B15	*rat*	*1:10*	*Elisabeth Kremmer, HMGU (IMI)*

secondary antibody	from	working dilution	supplier
anti-mouse IgG1 - HRP	rat	1:1000	Elisabeth Kremmer, HMGU (IMI)
anti-mouse IgG2A - HRP	rat	1:1000	Elisabeth Kremmer, HMGU (IMI)
anti-mouse IgG2B - HRP	rat	1:1000	Elisabeth Kremmer, HMGU (IMI)
anti-rabbit IgG (whole molecule) - Peroxidase (# A-6154)	goat	1:5000	Sigma-Aldrich® Co. LLC.
anti-rat IgG1 - HRP	mouse	1:1000	Elisabeth Kremmer, HMGU (IMI)
anti-rat IgG2A - HRP	mouse	1:1000	Elisabeth Kremmer, HMGU (IMI)
anti-rat IgG2B - HRP	mouse	1:1000	Elisabeth Kremmer, HMGU (IMI)
anti-rat IgG2C - HRP	mouse	1:1000	Elisabeth Kremmer, HMGU (IMI)
goat-anti-mouse IgG (H+L) - Alexa Fluor® 488 (# A-11029)	goat	1:2000	Molecular Probes®
goat-anti-mouse IgG (H+L) - IRDye® 800CW (# 926-32210)	goat	1:20000	LI-COR® Biosciences GmbH
goat-anti-mouse IgG + IgM (H+L) - HRPO (# 115-035-068)	goat	1:10000 - 1:15000	Dianova GmbH
goat-anti-rabbit IgG (H+L) - HRP (# A16104)	goat	1:1000 - 1:5000	Life Technologies / Novex®
goat-anti-rabbit IgG (H+L) - Alexa Fluor® 488 (# A-11008)	goat	1:2000	Molecular Probes®
goat-anti-rat IgG (H+L) - Alexa Fluor® 488 (# A-11006)	goat	1:2000	Molecular Probes®
goat-anti-rat IgG (H+L) - Alexa Fluor® 790 (# 112-655-143)	goat	1:200000	Dianova GmbH
goat-anti-rat IgG + IgM (H+L) - HRPO (# 112-035-068)	goat	1:8000	Dianova GmbH

II.12.6. ENZYMES

enzyme + buffer / enzyme mixture / enzyme kit	supplier
AffinityScript qPCR cDNA Synthesis Kit	Agilent Technologies, Inc.
BigDye3.1® Terminator v3.1 Cycle Sequencing Kit	Applied Biosystems®
*Bsa*I (10000 U/ml) + 10x CutSmart Buffer	New England BioLabs, Inc.
*Bsm*BI (10000 U/ml)	New England BioLabs, Inc.
*Bst*BI (20000 U/ml) + 10x CutSmart Buffer	New England BioLabs, Inc.

enzyme + buffer / enzyme mixture / enzyme kit	supplier
CloneAmp™ HiFi PCR Premix (2x)	Clontech Laboratories, Inc.
*Dpn*I (20000 U/ml)	New England BioLabs, Inc.
*Dra*III-HF (20000 U/ml) + 10x CutSmart Buffer	New England BioLabs, Inc.
DreamTaq DNA Polymerase (5 U/µl) + 10x DreamTaq Green Buffer	Thermo Scientific
DreamTaq Green PCR Master Mix (2x)	Thermo Scientific
House-*Taq* + 10x Standard *Taq* Buffer	in-house (lab-made)
Lyticase from *Arthrobacter luteus*, lyophilized, ≥ 2000 u/mg protein	Sigma-Aldrich® Co. LLC.
*Nde*I (20000 U/ml) + 10x CutSmart Buffer	New England BioLabs, Inc.
*Nru*I (10000 U/ml) + 10x NEB3.1 Buffer	New England BioLabs, Inc.
Phusion® High-Fidelity DNA Polymerase (2000 U/ml) + 5x Phusion® HF Buffer	New England BioLabs, Inc.
Plasmid-Safe™ ATP-dependent DNase (10 U/µl) + 25 mM ATP solution	Epicentre® Biotechnologies
QuikChange Lightning Site-Directed Mutagenesis Kit	Agilent Technologies, Inc.
RNase-Free DNase I Set	Qiagen GmbH
*Sac*I-HF (20000 U/ml) + 10x CutSmart Buffer	New England BioLabs, Inc.
T4 DNA Ligase (400000 U/ml) + 10x T4 DNA Ligase Buffer	New England BioLabs, Inc.
Taq DNA Ligase (40000 U/ml) + 10x *Taq* Ligase Buffer	New England BioLabs, Inc.
Trypsin-EDTA (0.05 %), phenol red	Gibco®

II.12.7. KITS, REAGENTS, AND STAINS

product	supplier
albumin fraction V, protease-free , ≥ 98 %	Carl Roth® GMBH + CO. KG
β-Gal Reporter Gene Assay, chemiluminescent	Roche Diagnostics GmbH
cOmplete Mini, EDTA-free Protease Inhibitor Cocktail	Roche Diagnostics GmbH
DC™ Protein Assay	Bio-Rad Laboratories GmbH
ethidium bromide, BioReagent, 500 µg/ml in H_2O	Sigma-Aldrich® Co. LLC.
Golden Gate TALEN and TAL Effector Kit 2.0	Addgene, Inc.
Hoechst 33342, 10 mg/ml solution in water	Molecular Probes®
In-Fusion HD Cloning Plus kit	Clontech Laboratories, Inc.
Lipofectamine® 3000 Reagent	Life Technologies
Luciferase Assay System	Promega GmbH
MACSelect LNGFR MicroBeads	Miltenyi Biotec GmbH
Midori Green Advance DNA stain	Nippon Genetics Europe GmbH
MitoTracker® Orange CMTMRos	Molecular Probes®
Montage SEQ96 Sequencing Reaction Cleanup Kit	Merck Millipore
NucleoBond® Xtra Midi	Macherey-Nagel GmbH & Co. KG
NucleoSpin® Gel and PCR Clean-Up Kit	Macherey-Nagel GmbH & Co. KG
NucleoSpin® Plasmid	Macherey-Nagel GmbH & Co. KG
Odyssey™ Blocking Buffer (PBS)	LI-COR® Biosciences GmbH
PageRuler Prestained Protein Ladder	Thermo Scientific
Pierce ECL Plus Western Blotting Substrate	Thermo Scientific
Ready Flow™ III	Beckman Coulter, Inc.
RNeasy® Mini + QIAshredder spin columns	Qiagen GmbH Qiagen GmbH
Solution Master Detergent Kit	Affimetrix
VectaShield® mounting medium	VectorLabs Ltd. / Biozol GmbH
ViaFect™ Transfection Reagent	Promega GmbH
Wizard® SV Gel and PCR Clean-Up System	Promega GmbH
X-tremeGENE 9 DNA Transfection Reagent	Roche Diagnostics GmbH

II.12.8. CHEMICALS, COMPOUNDS, AND SOLVENTS

II.12.8.1. COFACTORS AND UNLABELED SUBSTRATES FOR ACTIVITY TESTS

cofactor	supplier
β-nicotinamide adenine dinucleotide	Serva Electrophoresis GmbH
β-nicotinamide adenine dinucleotide, reduced, disodium salt	Sigma-Aldrich® Co. LLC.
β-nicotinamide adenine dinucleotide phosphate, sodium salt hydrate	Sigma-Aldrich® Co. LLC.
β-nicotinamide adenine dinucleotide phosphate, reduced, tetrasodium salt	Serva Electrophoresis GmbH

substrate	supplier
2-oxobutyric acid, ≥ 95 %	Sigma-Aldrich® Co. LLC.
4-androstene-3,17-dione, analytical standard	Sigma-Aldrich® Co. LLC.
5α-androstane-3α,17β-diol, ≥ 98 %	Sigma-Aldrich® Co. LLC.
17β-estradiol, ≥ 98.0 %	Sigma-Aldrich® Co. LLC.
acetoacetyl coenzyme A, sodium salt hydrate	
all-trans retinal, ≥ 95 %	Sigma-Aldrich® Co. LLC.
all-trans retinol, > 95.0 % (HPLC)	Sigma-Aldrich® Co. LLC.
androsterone, 98 %	Sigma-Aldrich® Co. LLC.
5-androstene-3β-ol-17-one, ≥ 99.0 %	Sigma-Aldrich® Co. LLC.
DL-3-hydroxy-3-methylglutaryl coenzyme A, sodium salt hydrate, ≥ 90 % (HPLC)	Sigma-Aldrich® Co. LLC.
DL-glyceraldehyde, ≥ 90 % (GC)	Sigma-Aldrich® Co. LLC.
DL-β-hydroxybutyryl coenzyme A, lithium salt, ≥ 90 %	Sigma-Aldrich® Co. LLC.
estrone, ≥ 99.0 %	Sigma-Aldrich® Co. LLC.
8-acetyl-2,3,5,6-tetrahydro-1h,4h-11-oxa-3α-aza-benzo[de]-anthracen-11-one (= fluorogenic substrate)	Solvay Pharmaceuticals GmbH
methylmalonyl coenzyme A, lithium salt hydrate, ≥ 90 % (HPLC)	Sigma-Aldrich® Co. LLC.
oxaloacetic acid, ≥ 97 % (HPLC)	Sigma-Aldrich® Co. LLC.
succinyl coenzyme A, sodium salt, ≥ 85 %	Sigma-Aldrich® Co. LLC.
testosterone, analytical standard	Sigma-Aldrich® Co. LLC.

II.12.8.2. VITAMIN D METABOLITES

vitamin D metabolite	supplier
1α,25-dihydroxy vitamin D_2, ≥ 97.0 % (HPLC)	Sigma-Aldrich® Co. LLC.
25-hydroxy vitamin D_2, ≥ 98.0 % (HPLC)	Sigma-Aldrich® Co. LLC.
ergocalciferol, ≥ 98.0 % (HPLC)	Sigma-Aldrich® Co. LLC.
hydroxy-25-vitamin D_2 [25,26,27-$^{13}C_3$], 99 %	Cambridge Isotope Laboratories, Inc.
(24R)-24,25-dihydroxy vitamin D_3, ≥ 98.0 % (HPLC)	Sigma-Aldrich® Co. LLC.
(24S)-24,25-dihydroxy vitamin D_3, ≥ 99.0 % (HPLC)	Sigma-Aldrich® Co. LLC.
1α-hydroxyvitamin D_3, ≥ 97.0 % (HPLC)	Sigma-Aldrich® Co. LLC.
cholecalciferol, ≥ 98.0 % (HPLC)	Sigma-Aldrich® Co. LLC.
vitamin D_3, 1α,25-dihydroxy, ≥ 99.0 % (HPLC)	Calbiochem®
vitamin D_3, 25-hydroxy, ≥ 99.0 % (LC-MS)	Calbiochem®

II.12.8.3. RADIOCHEMICALS

^{3}H-labeled radiochemical	specific activity	supplier
androst-4-ene-3,17-dione [1,2,6,7-^{3}H]	98.2 $^{Ci}/_{mmol}$	PerkinElmer®, Inc.
5α-androstane-3α,17β-diol [9,11-^{3}H]	50 $^{Ci}/_{mmol}$	Hartmann Analytic GmbH
androsterone [9,11-^{3}H]	50 $^{Ci}/_{mmol}$	Hartmann Analytic GmbH
corticosterone [1,2,6,7-^{3}H]	70 $^{Ci}/_{mmol}$	PerkinElmer®, Inc.
cortisol = hydrocortisone [1,2,6,7-^{3}H]	73.5 $^{Ci}/_{mmol}$	PerkinElmer®, Inc.
cortisone [1,2-^{3}H]	60 $^{Ci}/_{mmol}$	Hartmann Analytic GmbH
11-dehydrocorticosterone [1,2-^{3}H]	50 $^{Ci}/_{mmol}$	Hartmann Analytic GmbH
dehydroepiandrosterone [1,2,6,7-^{3}H]	70.5 $^{Ci}/_{mmol}$	PerkinElmer®, Inc.
dihydrotestosterone [1,2,4,5,6,7-^{3}H]	110 $^{Ci}/_{mmol}$	PerkinElmer®, Inc.
dihydroxyvitamin D_3, 1α,25-[26,27-^{3}H]	155 $^{Ci}/_{mmol}$	PerkinElmer®, Inc.
17α-estradiol [6,9-^{3}H]	27 $^{Ci}/_{mmol}$	Amersham plc.
17β-estradiol [6,7-^{3}H]	40 $^{Ci}/_{mmol}$	PerkinElmer®, Inc.
estrone [2,4,6,7-^{3}H]	94 $^{Ci}/_{mmol}$	PerkinElmer®, Inc.
hydroxyvitamin D_3, 25-[26,27-^{3}H]	140 $^{Ci}/_{mmol}$	PerkinElmer®, Inc.
progesterone [1,2,6,7-^{3}H]	90 $^{Ci}/_{mmol}$	PerkinElmer®, Inc.
testosterone [1,2,6,7-^{3}H]	83.4 $^{Ci}/_{mmol}$	PerkinElmer®, Inc.

II.12.8.4. HPLC SOLVENTS AND CHEMICALS

HPLC solvent / chemical	supplier
2-propanol, for HPLC	PanReac AppliChem GmbH
acetonitrile, Rotisolv®, HPLC gradient grade,	Carl Roth® GMBH + CO. KG
ammonium acetate, for mass spectrometry, ≥ 99.0 %	Sigma-Aldrich® Co. LLC.
ethanol, LiChrosolv®, gradient grade for LC	Merck Millipore
formic acid, for mass spectrometry, ~ 98.0 %	Sigma-Aldrich® Co. LLC.
lithium acetate dehydrate, SigmaUltra	Sigma-Aldrich® Co. LLC.
methanol, for HPLC, supergradient grade	PanReac AppliChem GmbH
MilliQ-H_2O	in-lab ultrapure water device

II.12.8.5. OTHER CHEMICALS

chemical	supplier
5-bromo-4-chloro-3-indolyl-β-D-galactopyranoside (= X-Gal)	BioTech Trade & Service GmbH
acetic acid (glacial), EMSURE®, anhydrous for analysis	Merck Millipore
dimethyl sulfoxide, BioScience grade, ≥ 99.5 %	Carl Roth® GMBH + CO. KG
DNA agarose	Biozym Scientific GmbH
carbonyl cyanide 4-(trifluoromethoxy)phenyl-hydrazine, ≥ 98.0 % (TLC)	Sigma-Aldrich® Co. LLC.
formaldehyde solution, for molecular biology, ≥ 36.0 %	Sigma-Aldrich® Co. LLC.
IPTG, BioScience grade, ≥ 99 %, dioxane free	Carl Roth® GMBH + CO. KG
L(+)-ascorbic acid, for analysis	Merck Millipore
powdered milk, blotting grade, low fat	Carl Roth® GMBH + CO. KG
Rhodamine 123	Molecular Probes®
Rotenone, ≥ 95.0 %	Sigma-Aldrich® Co. LLC.
Rotiphorese® Gel 30 (37.5:1)	Carl Roth® GMBH + CO. KG
TEMED, ~ 99 %, for electrophoresis	Sigma-Aldrich® Co. LLC.

All other chemicals (molecular biology grade or higher) were purchased from BioMol GmbH, Carl Roth® GMBH + CO. KG, Merck Millipore, PanReac AppliChem GmbH, or Sigma-Aldrich® Co. LLC.

II.12.9. COLUMNS, RESINS, AND SPE CARTRIDGES

columns, resins, and SPE cartridges	producer / supplier
Bio-Scale Mini Bio-Gel P-6 Desalting cartridge (10 ml)	Bio-Rad Laboratories GmbH
Bio-Scale Mini Profinity IMAC cartridge (1 ml)	Bio-Rad Laboratories GmbH
Econo-Pac Chromatography column	Bio-Rad Laboratories GmbH
HisTrap HP (1 ml)	GE Healthcare Life Science GmbH
Kinetex 2.6 µm C18 100 Å 50 mm x 2.1 mm	Phenomenex®, Inc.
Kinetex 2.6 µm C18 100 Å 50 mm x 4.6 mm	Phenomenex®, Inc.
Luna 5 µm C18(2) 100 Å 125 mm x 4 mm	Phenomenex®, Inc.
MACS® Separation Columns	Miltenyi Biotec GmbH
Ni Sepharose High Performance resin	GE Healthcare Life Science GmbH
SecurityGuard Standard C18 4 mm x 2 mm	Phenomenex®, Inc.
Synergy 4 µm Fusion-RP 80 Å 150 mm x 4.6 mm	Phenomenex®, Inc.
Strata C18-E 55 µm reversed phase (100 $^{mg}/_{ml}$) tube	Phenomenex®, Inc.
Strata-X 33 µm polymeric reversed phase (30 $^{mg}/_{ml}$) tube	Phenomenex®, Inc.

II.12.10. EQUIPMENT

II.12.10.1. CHROMATOGRAPHY SYSTEMS

FPLC system	producer
Profinia™ Affinity Chromatography Protein Purification System	Bio-Rad Laboratories GmbH

HPLC-UV autosampler, pump, degasser, and detector	producer
Series 200 Autosampler	Perkin Elmer®, Inc.
Series 200 Micro Pump	Perkin Elmer®, Inc.
Series 200 Mixer	Perkin Elmer®, Inc.
Series 200 UV/Vis Detector	Perkin Elmer®, Inc.
Series 200 Vacuum Degasser	Perkin Elmer®, Inc.

radioactive HPLC autosampler, pump, degasser, and detector	producer
LB 506 D Radioactivity Monitor	Berthold GmbH & Co. KG
LC-502E Autosampler	Beckman Coulter, Inc.
MCP-Z Standard gear pump	Ismatec®
System Gold® 125 Solvent Module	Beckman Coulter, Inc.
System Gold® 166 Detector	Beckman Coulter, Inc.

LC-MS/MS autosampler, pump, degasser, and detector	producer
1260 Infinity degasser	Agilent Technologies, Inc.
1260 Infinity binary pump model G1312B	Agilent Technologies, Inc.
1260 TCC column oven model G1316A	Agilent Technologies, Inc.
HTC-xt autosampler	CTC Analytics AG (PAL™)
QTrap® 5500 mass spectrometer	AB Sciex™ Ltd.

II.12.10.2. DETECTION SYSTEMS

detection system	producer / supplier
ABI 3730 DNA Analyzer	Applied Biosystems®
AxioImager Z1/ApoTome confocal microscope	Carl Zeiss AG
+ AxioCam MRm camera	Carl Zeiss AG
AxioPhot epifluorescence microscope	Carl Zeiss AG
AxioVert 40 CFL inverse microscope	Carl Zeiss AG
BioVision gel documentation system	PeqLab Biotechnologie GmbH
Cary®50 UV-Visible spectrophotometer	Varian, Inc.
Fusion FX7	Vilber Lourmat GmbH
GloMax®-Multi Detection System	Promega GmbH
+ Dual Injector System	Promega GmbH
NanoDrop™ ND-1000	PeqLab Biotechnologie GmbH
Odyssey® Infrared Imaging System	LI-COR® Biosciences GmbH
RF-5000 fluorimeter	Shimadzu Scientific Instruments, Inc.
Safire II plate reader	Tecan Group Ltd.
Synergy 2 Multi-Mode Microplate reader	BioTek Instruments, Inc.
UV/Vis spectrophotometer DU®530	Beckman Coulter, Inc.

II.12.10.3. CENTRIFUGES, INCUBATORS, SHAKERS, AND LAMINAR FLOWS

centrifuge	producer
Avanti® J-20 + JA-10, JA-18, and JS-4.3 rotors	Beckman Coulter, Inc.
Centrifuge 5415 D	Eppendorf AG
Concentrator 5301	Eppendorf AG
Hettich Universal 32R	Hettich Lab Technology GmbH
Hettich Rotanta 3500	Hettich Lab Technology GmbH
Optima™MAX ultracentrifuge + MLA-80, TLA-55 rotors	Beckman Coulter, Inc.
UniVapo 150 ECH + Vaccucenter vacuum pump	UniEquip GmbH

incubator / shaker	producer / supplier
CAT RM 5 roller mixer	CAT M. Zipperer GmbH
Duomax 1030	Heidolph GmbH & Co. KG
Gyrotory® water bath shaker (model G76)	New Brunswick Scientific GmbH
Heraeus® Function Line incubator	Heraeus Instruments GmbH
Innova 4230 refrigerated benchtop incubator shaker	New Brunswick Scientific GmbH
Innova CO-170 CO_2 incubator	New Brunswick Scientific GmbH
LD79 test-tube rotator	Labinco laboratory equipment
Rotamax 120	Heidolph GmbH & Co. KG

laminar flow	producer / supplier
Microflow Biological Safety Cabinet	Bioquell UK Ltd.
+ DITABIS HLC Compact aspiration systems AC 04	Ditabis AG

II.12.10.4. OTHER EQUIPMENT

device, glassware, resource	producer / supplier
accu-jet® pro	Brand® GmbH & Co. KG
Assistant® glass test tubes (100x16 mm)	Karl Hecht GmbH & Co KG
Barnstead™ E-Pure™ Ultrapure Water Purification Systems	Thermo Fisher Scientific Inc.
Cell Homogenizer with 10 μm clearance	Isobiotech
Cellometer Auto T4 Plus	PeqLab Biotechnologie GmbH
CoolCell® LX	BioCision LLC.
Criterion™ cell	Bio-Rad Laboratories GmbH
DURAN® baffled conical flasks (50-1000 ml)	Schott AG
DURAN® beaker glasses (50-2000 ml)	Schott AG
DURAN® conical flasks (100-300 ml)	Schott AG
DURAN® glass bottles (50-2000 ml)	Schott AG
GelAir™ Drying System	Bio-Rad Laboratories GmbH
GenePulser II	Bio-Rad Laboratories GmbH
Harvard Pump 11 Plus Single Syringe	Harvard Apparatus
Kimax® baffled conical flasks (250 ml)	Kimble Chase LLC.
Luer Lock gas tight syringes (1 ml)	Supelco® Co. LLC.
μMACS Separator	Miltenyi Biotec GmbH
MagnaRack™ Magnetic Separation Rack	Invitrogen™
Microman® pipettes (10 μl, 100 μl, 1000 μl)	Gilson® AG
Mini-PROTEAN® cell	Bio-Rad Laboratories GmbH
Mini-Sub® Cell GT cell	Bio-Rad Laboratories GmbH
Multipette® Plus dispenser	Eppendorf AG
Multipette® Xstream electronic dispenser	Eppendorf AG
PERMAQ® Compact 270 reverse osmosis	BTW Wassertechnik GmbH
Pipetman® Classic pipettes (10 μl, 20 μl, 200 μl, 1000 μl)	Gilson® AG
Positive Pressure-96 Processor	Waters GmbH
+ 96-Well Tabless Tube Holder	Phenomenex®, Inc.
PowerPac™ 200 Power Supply	Bio-Rad Laboratories GmbH
PowerPac™ 300 Power Supply	Bio-Rad Laboratories GmbH
PowerPac™ 3000 Power Supply	Bio-Rad Laboratories GmbH
Precellys® 24 tissue homogenizer	Bertin Technologies SAS
+ Cryolys temperature controller	Bertin Technologies SAS
Quartz SUPRASIL cuvette, 10 mm path (3500 μl)	Hellma® GmbH & Co. KG
Quartz SUPRASIL UV/Vis cuvettes, 10 mm path (400 μl)	Hellma® GmbH & Co. KG
RoboCycler® 96 thermal cycler	Stratagene®
Scotsman AF80 ice flaker	Scotsman Ice Systems Frimont S.P.A.
Sub-Cell® GT Cell	Bio-Rad Laboratories GmbH
Trans-Blot® SD semi-dry transfer cell	Bio-Rad Laboratories GmbH
Ultrasonic cleaner (bath)	VWR® LLC.
VacElut 20 Manifold	Varian, Inc.
+ Vacuum pump, Type: AEPF63BL-4-SO	Atma
Vacuum manifold multiscreen	Merck Millipore
VARIOKLAV 25 T steam sterilizer	HP Medizintechnik GmbH
VirSonic 475 sonicator with ultrasonic converter CL4	Virtis
Visiprep™ 24DL vacuum manifold	Supelco® Co. LLC.
+ Vacucenter vacuum pump	KNF Neuberger

II.12.11. CONSUMABLES

consumable	producer / supplier
12 % Criterion TGX precast midi gels	Bio-Rad Laboratories GmbH
96 DeepWell™ PP plates (MS)	Nunc®
96-well plates (PCR) + strips of 8 domed caps	Thermo Scientific
Capillary Pistons for Microman® (10 µl, 100 µl, 1000 µl)	Gilson® AG
Cellometer counting chambers	Nexcelom Bioscience LLC.
CELLSTAR® cell culture flasks (25 cm^2, 75 cm^2)	Greiner Bio-One Internat. GmbH
centrifuge tubes (15 ml, 50 ml)	Sarstedt AG & Co.
Combitips / advanced (100 µl – 25 ml)	Eppendorf AG
cover slips (22x22 mm, 24x24 mm, 24x60 mm)	Carl Roth® GMBH + CO. KG
Crimp µ-vials (350 µl)	Glastechnik Gräfenroda GmbH
CryoTubes (1.8 ml)	Nunc®
Diamond® tips Towerpack™ (10 µl, 200 µl, 1000 µl)	Gilson® AG
Eppendorf tubes (1.5 ml, 2 ml, 5 ml)	Eppendorf AG
F96 MicroWell™ white polystyrene plates	Nunc®
Fast-Read 102® counting chambers	Biosigma
Gas permeable seals (adhesive plate seal)	Thermo Scientific
GelAir™ cellophane	Bio-Rad Laboratories GmbH
Gel Blotting Paper GB003	Whatman®
GenePulser/MicroPulser 0.2 cm gap electroporation cuvettes	Bio-Rad Laboratories GmbH
glass vials (2000 µl)	Agilent Technologies, Inc.
Immobilon® FL PVDF membrane	Merck Millipore
micro vials PP (1.1 ml, 32 x 12 mm) with cap PU	Zinsser Analytic GmbH
MicroWell™ 96-Well optical-bottom plates	Nunc®
MN Square-well blocks (96 wells, 2.1 ml)	Macherey-Nagel GmbH & Co. KG
Falcon® Multiwell™ plates (6-well, 12-well, 24-well)	BD Biosciences
CELLSTAR® serological pipettes (5 ml, 10 ml, 25 ml, 50 ml)	Greiner Bio-One Internat. GmbH
Parafilm® M	Bemis® Inc.
Precellys® ceramic kit 1.4/2.8 mm 2.0 ml tubes	PeqLab Biotechnologie GmbH
Quick-Seal polypropylene tube (8 ml)	Beckman Coulter, Inc.
semi-micro disposable PS cuvettes	Brand® GmbH & Co. KG
Snap-On Cap polypropylene tubes (1.5 ml)	Beckman Coulter, Inc.
SuperFrost Plus microscope slides	Thermo Scientific
TipOne filtered tips (10 µl, 20 µl, 200 µl, 1000 µl)	Starlab International GmbH
Tissue culture dishes, 96 x 21 mm	TPP Techno Plastic Products AG
TPP cell scrapers, 240 mm long	TPP Techno Plastic Products AG

II.12.12. DATABASES AND SOFTWARE

database / program / algorithm	publisher/ producer / link
32 Karat software	Beckman Coulter, Inc.
Accelrys Draw (Version 4.2)	Accelrys, Inc.
AKR superfamily homepage	//www.med.upenn.edu/akr [20]
Alternative Splice Site Predictor – ASSP	//wangcomputing.com/assp/index [234]
Analyst® 1.6 software	AB Sciex™ Ltd.
AxioVision Rel. 4.8	Carl Zeiss AG
BioEdit Sequence Alignment Editor (Version 7.2.5)	Tom Hall [259]
BLAST® Basic Local Alignment Search Tool (NIH)	//blast.ncbi.nlm.nih.gov
Cary WinUV software	Varian, Inc.
CDC/NCHS	//www.cdc.gov/nchs/fastats/default.htm
Cellometer software	Nexcelom Bioscience LLC.

database / program / algorithm	publisher/ producer / link
CKSAAP_UbSite	//protein.cau.edu.cn/cksaap_ubsite [250, 251]
Destatis	//www.destatis.de/EN/FactsFigures.html
Ensembl Genome Browser (archive before release 75)	//www.ensembl.org/index.html
Eurostat	//ec.europa.eu/eurostat/statistics-explained/ index.php
Excel 2010, 2013	Microsoft® Cooperation
ExPASy ProtParam tool	//web.expasy.org/protparam
Fusion (Version 15.18)	Vilber Lourmat GmbH
Gen5 (Version 1.11)	BioTek Instruments, Inc.
GPS-SUMO	//sumosp.biocuckoo.org/online.php [248, 249]
Illustrator CS5, CS6	Adobe Systems GmbH
iPSORT Prediction	//ipsort.hgc.jp [237]
KinasePhos 2.0	//kinasephos2.mbc.nctu.edu.tw [241]
MEGA6: Molecular Evolutionary Genetics Analysis V6	//www.megasoftware.net [23]
Metabion Biocalculators	//www.metabion.com/support
MitoProt II (v1.101)	//ihg.gsf.de/ihg/mitoprot.html [235]
ND-1000 (Version: V3.1.0)	PeqLab Biotechnologie GmbH
NetGene2 Server	//www.cbs.dtu.dk/services/NetGene2 [233]
NetGlycate 1.0 Server	//www.cbs.dtu.dk/services/NetGlycate [244]
NetNGlyc 1.0 Server	//www.cbs.dtu.dk/services/NetNGlyc [245]
NetOGlyc 4.0 Server	//www.cbs.dtu.dk/services/NetOGlyc [246]
NetPhos 2.0 Server	//www.cbs.dtu.dk/services/ NetPhos [242]
NetPhosK 1.0 Server	//www.cbs.dtu.dk/services/ NetPhosK [243]
Photoshop CS5, CS6	Adobe Systems GmbH
PrediSi	//www.predisi.de/home.html [236]
PSORT II	//psort.hgc.jp/form2.html
RCSB – PDB Protein Workshop 4.2.0 (MBT)	//www.rcsb.org/pdb [260]
RCSB – Protein Data Bank (PDB)	//www.rcsb.org/pdb [261]
SDR superfamily web page	//www.sdr-enzymes.org [122]
SigmaPlot 12.0	Systat Software, Inc.
SignalP 4.1 Server	//www.cbs.dtu.dk/services/SignalP [238]
Sulfinator	//web.expasy.org/sulfinator [247]
SUMOplot	//www.abgent.com/sumoplot
TAL effector Nucleotide Targeter 2.0 algorithm	//www.cornell.edu
TargetP 1.1 Server	//www.cbs.dtu.dk/services/TargetP [239, 240]
TotalChrom Workstation (Version 6.3.2)	PerkinElmer®, Inc.
UbPred: predictor of protein ubiquitination sites	//www.ubpred.org [252]
UniGene (NCBI)	//www.ncbi.nlm.nih.gov/unigene
UniProtKB (database + alignment tool)	//www.uniprot.org/uniprot
Vector NTI Advance® (Version 11.5.2)	Life Technologies
WHO	//www.who.int/topics/mortality
Word 2010, 2013	Microsoft® Cooperation
XFluorSafireII (Version: V4.62n) software	Tecan Group Ltd.

III. Results

III.1. Characterization of the human Aldo-Keto Reductase 1B subfamily member 15 (AKR1B15)

III.1.1. *AKR1B15* transcript analysis

The starting point for the closer characterization of AKR1B15 was a paper published by Salabei *et al.* in 2011 annotating a novel human *AKR1B* subfamily member, *AKR1B15*, on Chr. 7q33: 134,549136-134,579875 for the first time [22].

Whereas that publication described only one transcript covering ten exons (Ensembl transcript *AKR1B15-201* [ENST00000423958.1]; in the following referred to as *AKR1B15.1*) which encodes for a 316 amino acid residues covering protein, an Ensembl and NCBI database search revealed a second possible transcript covering twelve exons (Ensembl transcript *AKR1B15-001* [ENST00000457545.2]; in the following referred to as *AKR1B15.2*) which encodes for a protein of 344 amino acid residues. Analysis of the intron-exon structure of both *AKR1B15* transcripts showed that *AKR1B15.1* and *AKR1B15.2* differ only in their first exons (*AKR1B15.1*: exon 1 and *AKR1B15.2:* exon 1-3) and share all other exons [Figure III-1].

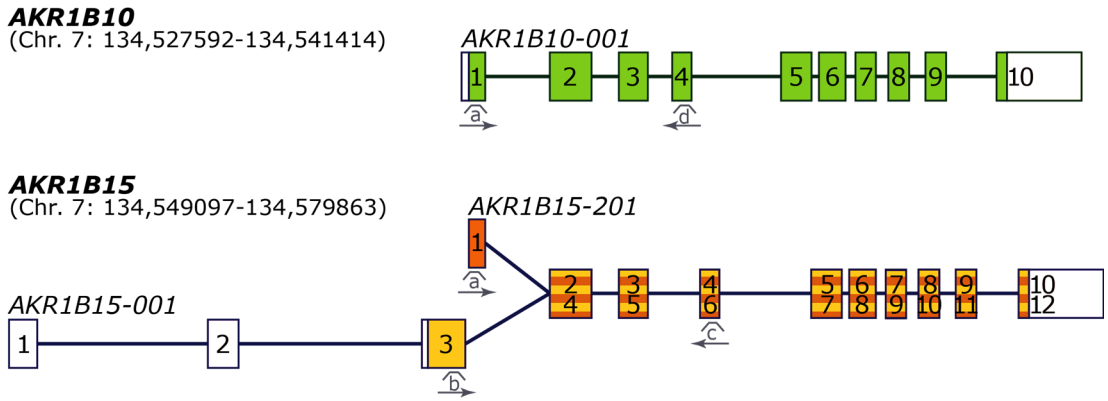

Figure III-1: The two *AKR1B15* transcript variants differ in their first exons.
Shown are the schematic intron-exon structures of *AKR1B10* and *AKR1B15* according to the transcripts described in the Ensemble database. For *AKR1B15*, two transcripts differing in their first exons are specified: a shorter ten exons covering transcript (*AKR1B15-201*; in the following referred to as *AKR1B15.1*) and a longer twelve exons covering one (*AKR1B15-001*; in the following referred to as *AKR1B15.2*).
Exons of *AKR1B10* are colored in green, alternative exons of *AKR1B15.1* and *AKR1B15.2* in orange and yellow, respectively, and common exons of the both *AKR1B15* variants in orange-yellow striped pattern. Untranslated regions are shown in white. Introns are displayed as straight lines. Primer binding sites for transcript analyses are indicated by brackets and arrows and are named by lower cases. The primers used were: # 2714 (a), # 2715 (b), # 2713 (c), and # 2716 (d).

III.1.1.1. Results from *in silico* *AKR1B15* splice site prediction

Using the Alternative Splice Site Predictor (ASSP) or the NetGene2 Server, the splice site predictions showed that the reported intron-exon structures are widely predicted by the applied algorithms [Table III-1]. Thus, the varying *AKR1B15* transcripts most probably result from an alternative splicing of the first exons and/or an alternative transcription start.

For the prediction of splice sites by the ASSP, position specific score matrices were used [234]. The resulting score values represent the reliability of the predicted splice sites and increase with the certainty of prediction. Here, an acceptor site cutoff score of 4.0 and a donor site cutoff score of 6.0 were chosen. Both minimize the false positive splice site predictions to 10 %, whereas up to 30 % false negative predictions were possible. In contrast, splice site predictions using the NetGene2 Server depict confidence values. This confidence values are calculated from neural network prediction scores [233]. Confidence values of 0.2 to 0.95 and 0.5 to 0.95 represent nearly all true acceptor sites and donor sites, respectively, whereas values higher than 0.95 represent highly confident splice sites. Predictions with high confidence include only very few false positive predictions but miss about 50 % of true positive sites. In contrast, nearly all true splice sites include nearly every splice site but also more false positive splice sites.

Table III-1: Splice sites in the *AKR1B15* gene and their prediction by the Alternative Splice Site Predictor and NetGene2 Server.

AKR1B			**splice sites in *AKR1B15*** (position within *AKR1B15* gene)		**prediction of splice sites** (acceptor site / donor site)	
15.2 exon		***15.1*** exon	**acceptor site** (intron → exon)	**donor site** (exon → intron)	**ASSP** (score)	**NetGene2** (confidence)
1	/	-	600	714	- / -	- / 0.63
2	/	-	8200	8324	5.7 / 10.2	0.33 / 0.61
3	/	-	16062	16234	10.3 / 13.1	**1.00** / 0.63
-	/	1	16945	17011	- / 6.9	- / 0.71
4	/	2	19622	19790	10.8 / 6.4	**0.95** / 0.60
5	/	3	20877	20994	11.9 / 7.4	**0.97** / 0.70
6	/	4	23068	23146	7.9 / 10.7	0.32 / 0.93
7	/	5	26884	27007	7.6 / 13.0	0.34 / 0.94
8	/	6	27285	27392	9.7 / 11.1	0.94 / 0.87
9	/	7	27813	27895	10.6 / 12.4	0.49 / 0.51
10	/	8	28427	28511	10.5 / 15.2	0.82 / **0.99**
11	/	10	29168	29251	14.1 / 11.4	**0.97** / **0.95**
12	/	11	30971	31340	11.6 / -	0.82 / -

Listed are the positions of splice sites in the *AKR1B15* gene as well as the respective score values of the prediction by the Alternative Splice Site Predictor (ASSP) using an acceptor and donor site cutoff of 4.0 and 6.0, respectively, and confidence values of the prediction by the NetGene2 Server. "Acceptor sites" of the first exons, which most probably agree with the transcription start of *AKR1B15* transcripts, are highlighted in red and high confident splice sites (> 95 %) are highlighted in bold.

Both splice site prediction tools predicted the reported splice sites in *AKR1B15.1* and *AKR1B15.2* partly with high confidence. The only exception was the splice donor site of the untranslated exon 1 of *AKR1B15.2* which was not predicted by the ASSP. In addition, the "acceptor sites" of the first exons of *AKR1B15.1* and *AKR1B15.2* (red in Table III-1) were neither predicted by the ASSP nor by the NetGene2 Server. If *AKR1B15.1* and *AKR1B15.2* would share the same 5′ UTR and the difference in the transcripts would result only from an alternative splicing of exon 1 and exon 3, respectively, the acceptor site of exon 1 of *AKR1B15.1* should have been predicted. Since no transcription starts are predicted by the splice site algorithms and no 5′ UTR is known for *AKR1B15.1*, there is a probability that both transcripts use different promoters. However, just variable translation starts could also be possible.

III.1.1.2. Design of *AKR1B15* transcript specific primers

To analyze the abundance of *AKR1B15* transcripts in biological samples, transcript specific primer pairs needed to be established. Since *AKR1B15.1* and *AKR1B10* possess 95 % sequence identity on mRNA level and *AKR1B15.1* and *AKR1B15.2* differ only in exon 1 and exon 1-3, respectively, the establishment of specific primer pairs was a challenging task. Therefore, regions with highest diversity between the *AKR1B15* variants and between *AKR1B15.1* and *AKR1B10* were selected for primer annealing sites [VI.4]. The primer pairs depicted in Figure III-1 and listed in Table II-10 showed high specificity for the respective transcript when tested on plasmids encoding for AKR1B10, AKR1B15.1, and AKR1B15.2 [Figure III-2]. In addition, the sequencing of semi-quantitative RT-PCR products from reactions with BeWo cell line cDNA verified the specificity of the primer pairs.

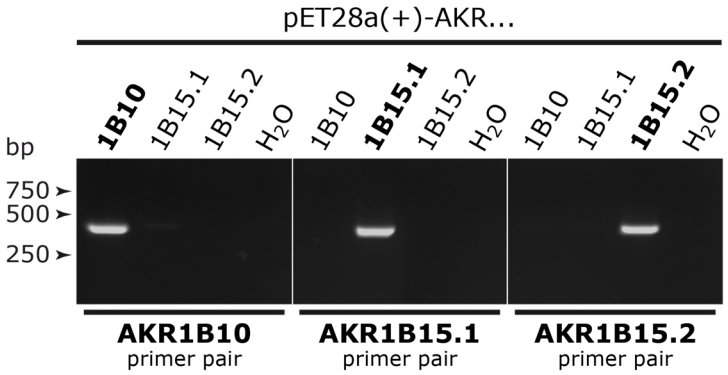

Figure III-2: The established transcript specific primer pairs act specifically in control PCR reactions.
Shown are the PCR products from control reactions with transcript specific primer pairs and different plasmid templates demonstrating a high specificity of the established primer pairs. The reactions were performed with 1 ng plasmid template (pET28a(+)-AKR1B10 (1B10), pET28a(+)-AKR1B15.1 (1B15.1), or pET28a(+)-AKR1B15.2 (1B15.2)) and transcript specific primer pairs (AKR1B10: # 2714 + # 2716, AKR1B15.1: # 2714 + # 2713, or AKR1B15.2: # 2715 + # 2713) in a final concentration of 200 nM each, using 30 cycles and an annealing temperature of 57 °C.

III.1.1.3. TRANSCRIPT ANALYSIS IN HUMAN TISSUES AND CELL LINES

After having specific primer pairs for the human *AKR1B15.1*, *AKR1B15.2*, and *AKR1B10* transcripts, transcript analysis in human tissues was first performed by semi-quantitative RT-PCR using a panel of total RNA tissue extracts.

Here, it was found that both *AKR1B15* transcript variants occur *in vivo*. Both *AKR1B15* variants are mainly expressed in adipose tissue, skeletal muscle, thymus, thyroid gland, and reproductive tissues, such as ovary, placenta, prostate, and testis [Figure III-3A]. Thus, compared with *AKR1B10*, the *AKR1B15* transcripts possessed a more distinct expression pattern [Figure III-3A]. In most tissues expressing both *AKR1B15* transcript variants, *AKR1B15.1* showed a higher abundance than *AKR1B15.2* did. The only tissues where the signal intensities of *AKR1B15.2* exceeded that of *AKR1B15.1* were skeletal muscle and thyroid gland [Figure III-3A]. Although the abundance of both *AKR1B15* transcripts in *AKR1B15* expressing tissues was quite low – 38 cycles were used for the amplification of *AKR1B15* and *AKR1B10* transcripts compared with 25 cycles used for the amplification of *GAPDH* transcripts which served as control – both *AKR1B15* transcript variants exceeded the amount of the ubiquitously expressed and overall higher abundant *AKR1B10* in placenta [Figure III-3A]. Thereby, placenta displayed the tissue with the highest levels of both *AKR1B15* transcripts. The presence of both *AKR1B15* transcript variants in adipose tissue and placenta was verified by semi-quantitative RT-PCR on cDNA of the preadipocyte cell strain SGBS and the placental cell line BeWo [Figure III-3A].

Because semi-quantitative RT-PCR gives only rough information about the abundance of transcripts, our cooperation partner Oleg Barski (University of Louisville, KY, USA) analyzed the relative amounts of transcripts in selected human tissues (adipose tissue, heart, skeletal muscle, thymus, ovary, placenta, prostate, testis, and uterus) by qPCR within our cooperative work. For this, he used the same set of transcript specific primers as used in the semi-quantitative RT-PCR, a 3-step protocol, and human *HPRT1*, *GAPDH*, and *18S-RNA* as housekeeping genes (published in Weber *et al.* [262]). Figure III-3B summarizes the results from the qPCR experiments by showing the relative abundances of *AKR1B15.1*, *AKR1B15.2*, and *AKR1B10* transcripts in different tissues, based on the abundance of *AKR1B15.1* in placenta. These relative abundances confirmed the results from the semi-quantitative RT-PCR. Compared with *AKR1B15*, the expression of *AKR1B10* was higher in all tissues tested, however, with the exception of placenta [Figure III-3B]. Considering the expression levels of *AKR1B15.1* and *AKR1B15.2*, the qPCR results verified highest expression levels for both transcripts in placenta. In placenta, *AKR1B15.1* was 3-fold and 17-fold higher abundant when compared with *AKR1B15.2* and *AKR1B10*, respectively. Regarding the levels of *AKR1B15.1* expression in different tissues, as mentioned above, placenta possessed the highest levels (100 %) followed by adipose tissue (17 %), testis (10 %), skeletal muscle (2 %), and prostate (1 %). When looking at the relative expression levels of *AKR1B15.2* in different tissues placenta (100 %) was followed by adipose tissue (16 %), skeletal muscle (9 %), testis (3 %), and prostate (1 %). All other tissues analyzed had *AKR1B15* transcript levels below 1 % of that occurring in placenta. As already indicated by the results from semi-quantitative RT-PCR experiments, the amount of *AKR1B15.2* exceeded that of *AKR1B15.1* in skeletal muscle by a factor of approximately 1.4, whereas all other tissues analyzed showed higher levels of *AKR1B15.1* expression [Figure III-3B].

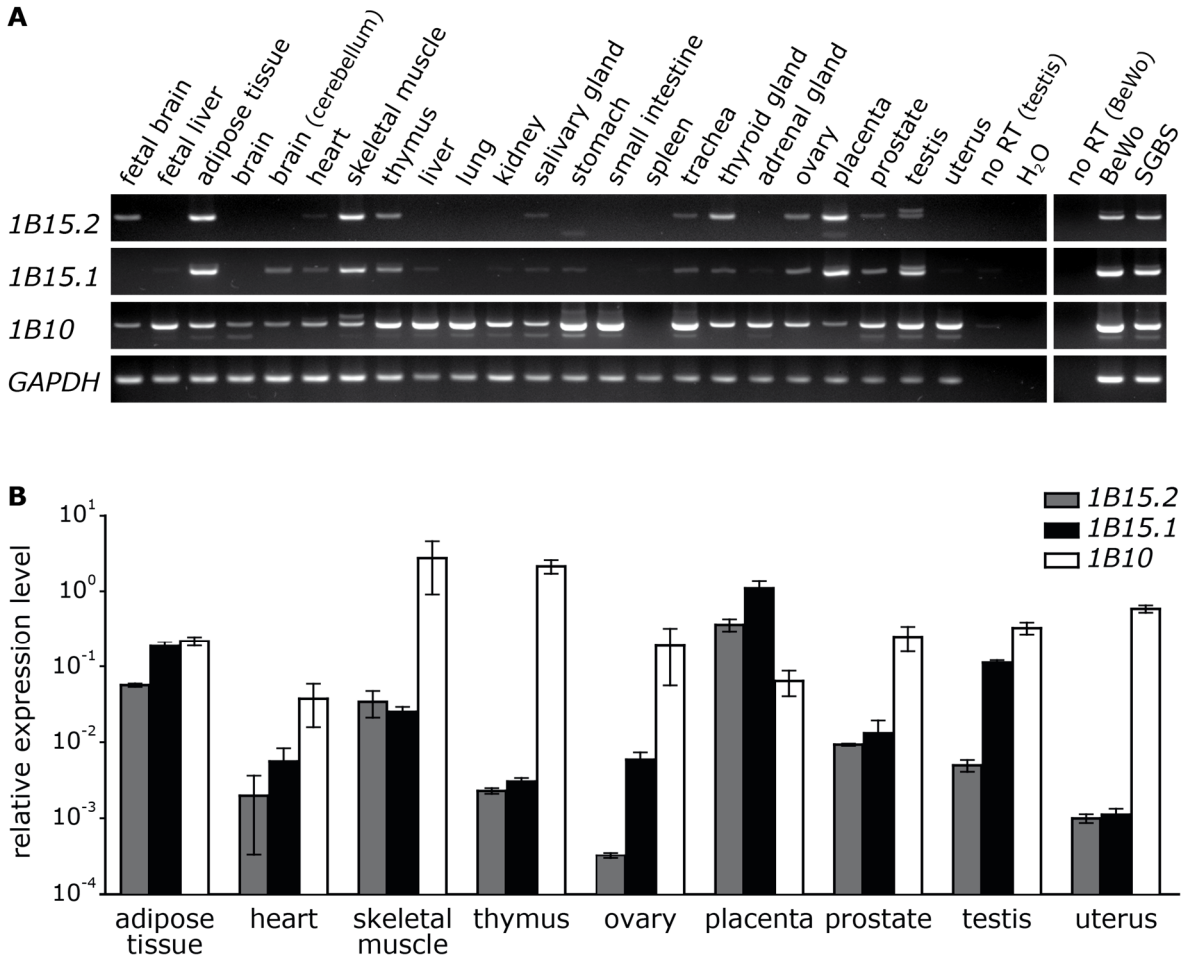

Figure III-3: Both *AKR1B15* transcripts are expressed *in vivo* and show highest expression levels in tissues related to steroid metabolism and signaling.
(A) Tissue distribution of *AKR1B15.1* (*1B15.1*), *AKR1B15.2* (*1B15.2*), and *AKR1B10* (*1B10*) analyzed by semi-quantitative RT-PCR. The reactions were performed with 50 ng of reverse transcribed human RNA samples and the transcript specific primer pairs for *AKR1B15.1* (# 2714 + # 2713), *AKR1B15.2* (# 2715 + # 2713), or *AKR1B10* (# 2714 + # 2716). Reactions with the human *GAPDH* primer pair # 1727 + # 1728 or with non-reverse transcribed RNA (no RT) samples served as loading or negative controls, respectively. **(B)** Relative expression levels of *AKR1B15.1* (*1B15.1*), *AKR1B15.2* (*1B15.2*), and *AKR1B10* (*1B10*) in selected tissues determined by Oleg Barski (University of Louisville, KY, USA) in qPCR experiments. The transcript specific C_T values, resulting from reactions with the same set of transcript specific primers as listed in (A), were first normalized to the average C_T value of the three housekeeping genes (human *GAPDH*, *HPRT*, and *18S RNA*) and then divided by the level of *AKR1B15.1* expression in placenta to calculate the relative expression levels (already published in Weber *et al.* [262]).

All in all, the *AKR1B15* transcript analysis studies demonstrated that both *AKR1B15* variants, *AKR1B15.1* and *AKR1B15.2*, are expressed *in vivo*, thereby, showing the highest levels in tissues which are related to steroid metabolism and signaling, like placenta, adipose tissue, or skeletal muscle.

III.1.2. Generation of monoclonal antibodies against AKR1B15

The previous chapter showed the expression of *AKR1B15* on RNA level *in vivo* by detecting both *AKR1B15* transcript variants in several tissues as well as in the SGBS cell strain and BeWo cell line. However, expression of a gene on RNA level does not necessarily implicate that the RNA is translated into protein.

Since an existing polyclonal antibody against a peptide corresponding to a C-terminal epitope present in both AKR1B15 isoforms [Figure III-4] was found to be not suited to detect endogenous AKR1B15.1 and AKR1B15.2 unambiguously, due to nonspecific detection of other proteins, monoclonal anti-AKR1B15 antibodies were generated in order to check whether *AKR1B15* is expressed also on protein level *in vivo*.

These monoclonal antibodies were generated in cooperation with the group around Dr. Elisabeth Kremmer (Monoclonal Antibody Unit at the Helmholtz Zentrum München), who performed the immunization of rats and mice, the hybridization of immune cells, the primary selection of clones via differential ELISAs, and, after the clones were verified by western blot analysis in our lab, the final establishment of positive clones.

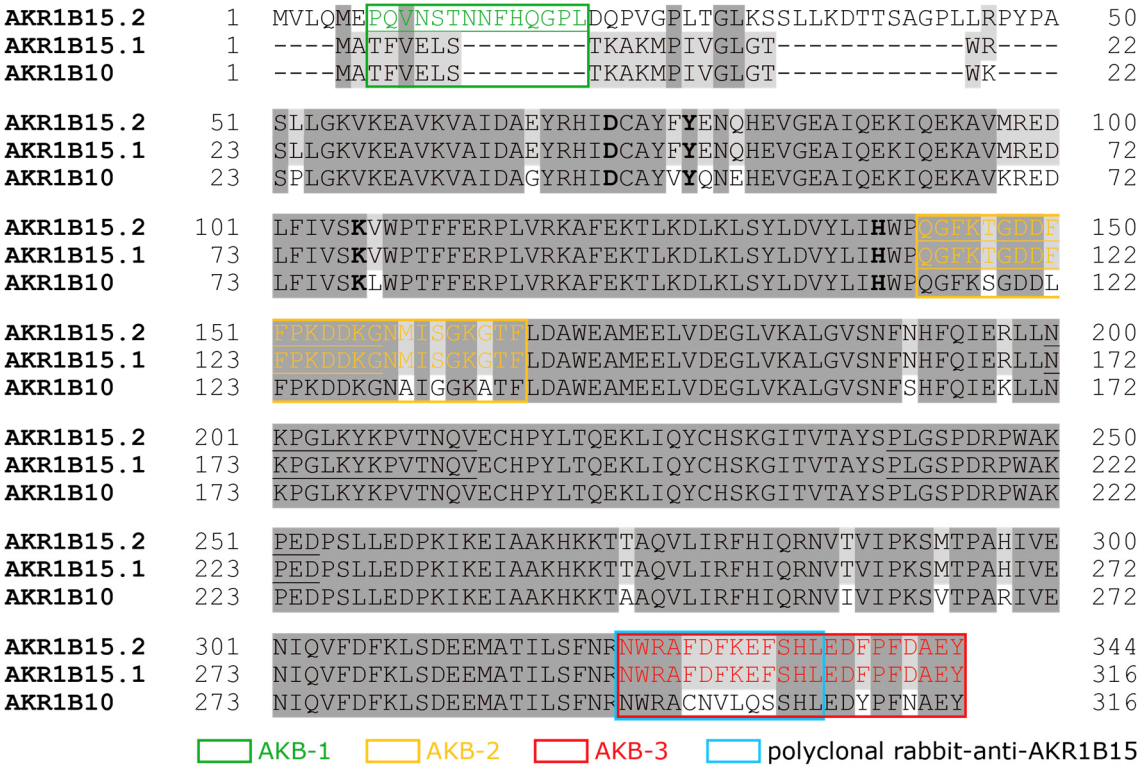

Figure III-4: Alignment of AKR1B15 isoforms and AKR1B10 showing the epitopes used for the generation of the monoclonal antibodies.
The epitopes of AKB-1, AKB-2, and AKB-3 antibodies are highlighted and framed in green, orange, and red, respectively. The epitope used for the generation of the polyclonal rabbit-anti-AKR1B15 antibody is framed in blue. The peptides recommended by the immunogenicity blot are underlined and the residues of the catalytic tetrad are highlighted in bold.

III.1.2.1. TARGET SEQUENCES FOR THE GENERATION OF MONOCLONAL ANTI-AKR1B15 ANTIBODIES

Since the human AKR1B15 isoforms (especially the AKR1B15.1 isoform) share high amino acid sequence identity to the human AKR1B10 protein, with highest diversity in the C-terminal amino acid sequence of the proteins, three AKR1B15 peptides (AKB-1, AKB-2, and AKB-3) possessing highest amino acid sequence diversity when compared to AKR1B10 as well as immunogenic potential were used for immunization of rats and mice [Figure III-4].

As far as possible, the peptides were selected according to the output of the immunogenicity plot (AKB-1 and first 16 amino acids of AKB-2). However, since the immunogenicity plot recommended mainly epitopes of the AKR1B15 isoforms which are identical to amino acid sequences found in AKR1B10, an additional peptide (AKB-3) corresponding to the C-terminus of the AKR1B15 isoforms, which differs strongly between the AKR1B15 proteins and AKR1B10, was chosen.

The immunization of Lou/c rats and C57BL/6 mice with AKB-1, AKB-2, or AKB-3 peptides yielded 67 putative positive clones after the initial selection via differential ELISA [Figure III-5]. The majority of these monoclonal antibody clones derived from rats (58 clones from rats versus nine clones from mice). In accordance with the results from the initial screening of the AKR1B15 sequence for immunogenic peptides [data not shown], most of the clones resulted from the immunization of rats with the AKB-2 peptide (35 clones). In contrast, the immunization rounds with the AKB-1 and AKB-3 peptides resulted in only 24 and eight clones, respectively. Here, no AKB-3 monoclonal antibody clone was received from mice.

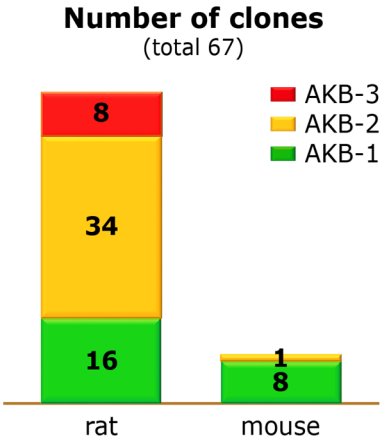

Figure III-5: Immunization of Lou/c rats and C57BL/6 mice led to a total of 67 putative positive monoclonal antibody clones.

III.1.2.2. ANALYSIS OF PUTATIVE POSITIVE MONOCLONAL ANTIBODIES

In order to identify specific positive clones recognizing only the AKR1B15 isoforms but not AKR1B10, the supernatants from putative positive monoclonal antibody clones [VI.3] were tested via Western blotting [Figure III-6]. Antigens for these analyses were dilutions of *E. coli* BL21 (DE3) lysates expressing AKR1B10 (38.2 kDa), AKR1B15.1 (38.7 kDa), or AKR1B15.2 (41.7 kDa) from the respective pET28a(+) expression plasmids. Since the initial antibody solution resulted from non-established clones and thus might also include less selective antibodies of other classes or subclasses, subclass specific secondary antibodies needed to be used for the identification of specific positive clones. Due to the selected cloning sites in the pET28a(+) plasmid, the expressed AKRs carried an N-terminal His_6 tag increasing the molecular weight of the proteins by approximately 2 kDa and allowing for the detection of the expressed proteins via a polyclonal rabbit-anti-His antibody, too [Figure III-6G].

In the initial Western blot analysis one murine clone (29D4) against the AKB-1 peptide was identified which produced antibodies with high affinity to the AKR1B15.2 protein, only [Figure III-6A]. All other clones targeting the AKB-1 peptide possessed very low affinity to AKR1B15.2 and showed, if at all, only very weak signals in Western blots [data not shown]. Three rat clones (7B1, 9A5, and 19E5) against the AKB-2 peptide were selective for the AKR1B15 isoforms [Figure III-6B-D], although the huge majority of AKB-2 clones, like the exemplarily shown rat clone 23H6 [Figure III-6E], could not distinguish between AKR1B15 proteins and AKR1B10. In addition, all rat clones resulting from the immunization with the C-terminal AKB-3 peptide reacted very nonspecifically and recognized various proteins in the *E. coli* cell lysates [Figure III-6F].

The obvious presence of multiple protein bands per lane – also in Western blots with identified specific antibodies – resulted from the use of crude recombinant expression culture lysates. Here, the strong overexpression of the AKR1B15 isoforms and AKR1B10 in *E. coli* and the downstream processing lead to partial protein truncations or degradations, which were also detected by the antibodies as protein bands with lower molecular weight.

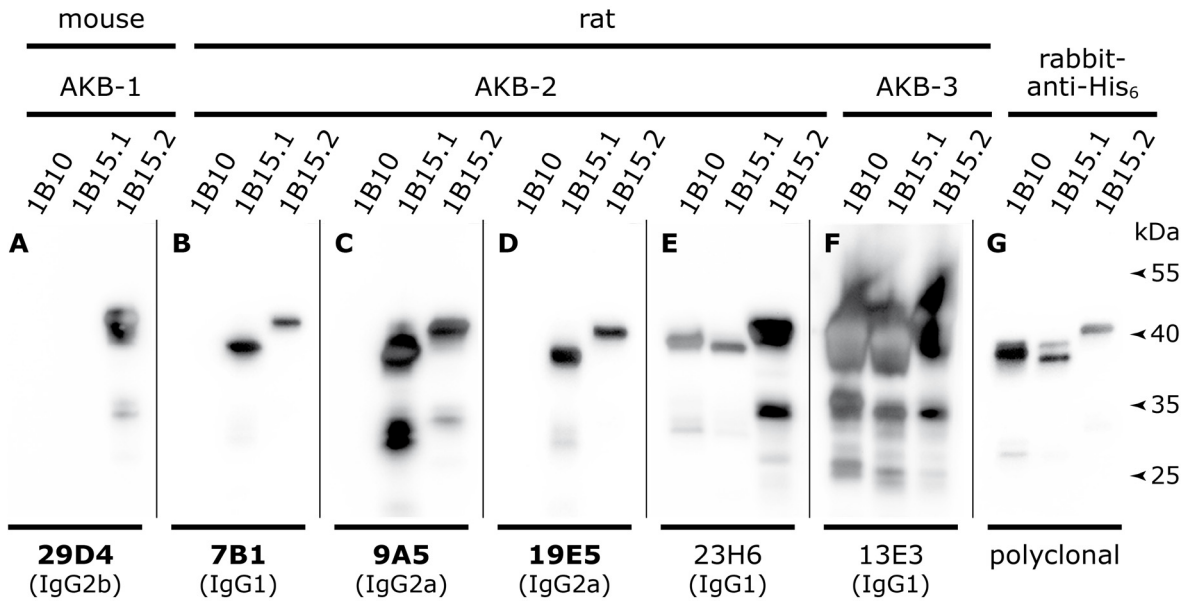

Figure III-6: Antibodies of one mouse-anti-AKB-1 clone and three rat-anti-AKB-2 clones recognized selectively AKR1B15.2 and both AKR1B15 isoforms in *E. coli* BL21 lysates, respectively.
Shown are selected Western blots for the identification of clones producing AKR1B15 specific monoclonal antibodies.
Western blots were performed with total *E. coli* BL21 (DE3) cell lysates expressing either N-terminally His_6-tagged AKR1B10 (1B10), AKR1B15.1 (1B15.1), or AKR1B15.2 (1B15.2). Supernatants of primary hybridoma clones – mouse-anti-AKB-1 clone 29D4 **(A)**, rat-anti-AKB-2 clones 7B1 **(B)**, 9A5 **(C),** 19E5 **(D)**, and 23H6 **(E)**, as well as rat-anti-AKB-3 clone 13E3 **(F)** – served as primary antibodies (the respective antibody subclasses are given in brackets) and were diluted 1:10 in 0.5 % milk solution. The detection was performed via HRP-conjugated subclass specific secondary antibodies (1:1000 in 0.5 % milk solution) and ECL substrate. The detection of the His_6 tag of expressed proteins by the polyclonal rabbit-anti-His primary antibody **(G)** served as control.
Specific and affine clones against AKR1B15.2 **(A)** and both AKR1B15 isoforms **(B-D)** are highlighted in bold.

III.1.2.3. Analysis of established monoclonal antibodies concerning specificity and sensitivity

The established monoclonal rat-anti-AKR1B15 (AKB-2) antibodies (clones 7B1, 9A5, and 19E5) as well as the monoclonal mouse-anti-AKR1B15.2 (AKB-1) antibody clone 29D4 were additionally tested for their specificity against other human AKRs [Figure III-7].

For this, Western blots were performed with *E. coli* BL21 (DE3) cell lysates expressing N-terminally His_6-tagged human AKR1A1, AKR1B1, AKR1B10, AKR1B15.1, AKR1B15.2, AKR1C3, or AKR6A3 proteins (all expressed from pET28a(+) vectors).

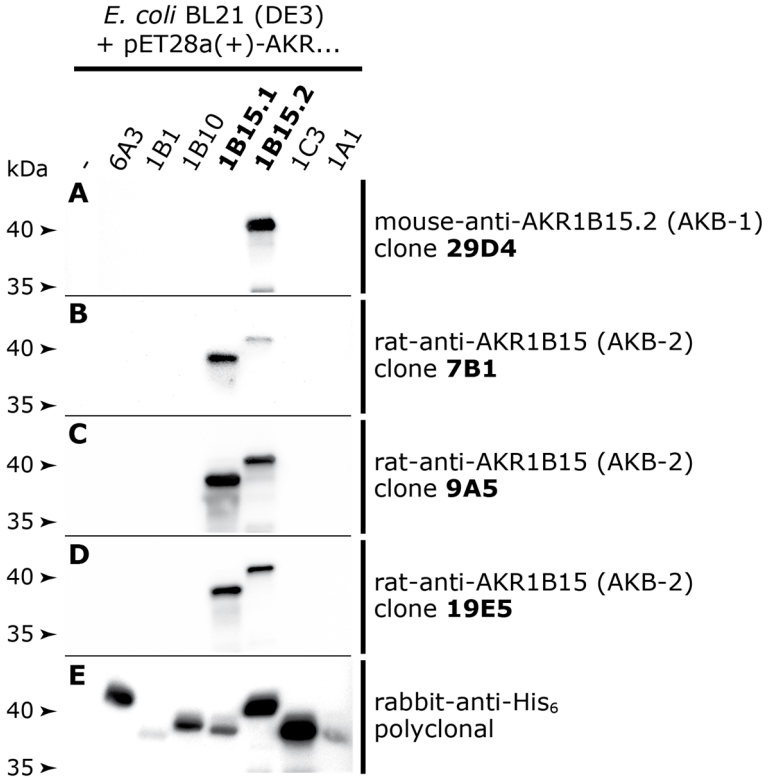

Figure III-7: The identified specific anti-AKR1B15 antibodies acted also selectively when tested against further human AKRs expressed in *E. coli* BL21.

The illustrated Western blots were performed with equal amounts of non-transformed *E. coli* BL21 (DE3) lysates (-) and *E. coli* BL21 (DE3) lysates expressing either N-terminally His_6-tagged AKR6A3 (6A3), AKR1B1 (1B1), AKR1B10 (1B10), AKR1B15.1 (1B15.1), AKR1C3 (1C3), or AKR1A1 (1A1). Supernatants of established hybridoma clones – mouse-anti-AKR1B15.2 (AKB-1) clone 29D4 **(A)** and rat-anti-AKR1B15 (AKB-2) clones 7B1 **(B)**, 9A5 **(C)**, and 19E5 **(D)** – and the polyclonal rabbit-anti-His antibody **(E)**, which served as control for the expression of the human AKRs in the *E. coli* BL21 (DE3), were used in a dilution of 1:10 (monoclonal primary antibodies) and 1:1000 (polyclonal primary antibody) in 0.5 % milk solution, respectively. The detection was performed via HRP-conjugated subclass specific (in case of monoclonal antibodies) or IgG class specific (in case of polyclonal antibodies) secondary antibodies (1:1000 in 0.5 % milk solution) and ECL substrate chemiluminescence.

The Western blot using the polyclonal rabbit-anti-His antibody showed that all AKRs were expressed in the respective *E. coli* lysates, however, in different amounts [Figure III-7E].

The preselected monoclonal antibodies revealed high specificity and recognized only the respective AKR1B15 isoform(s) [Figure III-7A-D]. Blots with supernatants of the AKB-1 clone 29D4 and AKB-2 clone 9A5 showed the highest chemiluminescence intensities, whereas the AKB-2 clone 7B1 showed the lowest. Thus, compared to the other antibody clones, the clones 29D4 and 9A5 produced antibodies with higher affinity to the AKR1B15 isoforms (or just higher antibody levels) allowing for the detection of lower AKR1B15 amounts

The monoclonal rat-anti-AKR1B15 clone 9A5 antibody acts specifically even in presence of high amounts of AKR1B10 because no luminescence signals could be detected in Western blots on a serial dilution of purified AKR1B10 [data not shown].

III.1.2.4. Analysis of established antibodies with HEK-293 lysates

The monoclonal anti-AKR1B15 antibodies were primarily generated to detect endogenous AKR1B15 isoforms in human cell and tissue samples. Therefore, the specific monoclonal antibodies were also tested on lysates of HEK-293 cells overexpressing untagged AKR1B15.1 or AKR1B15.2 proteins. For comparison reasons, the already existing affinity purified polyclonal rabbit-anti-AKR1B15 antibody, which was seen to be not specific enough to detect endogenous AKR1B15 in the past, was additionally included in the test.

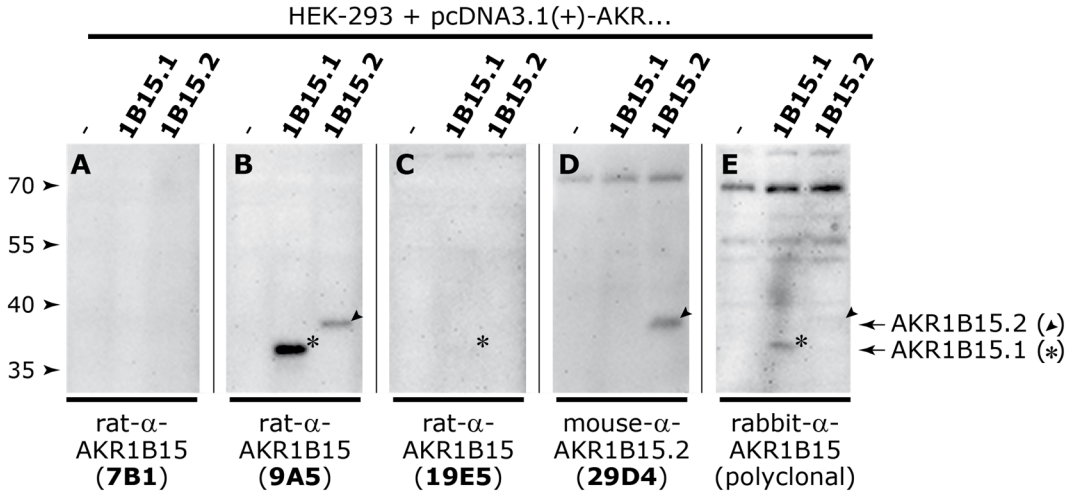

Figure III-8: The rat-anti-AKR1B15 clone 9A5 antibody supernatant recognizes specifically both AKR1B15 isoforms with good sensitivity when overexpressed in HEK-293 cells.
Shown are Western blots analyzing the specificity and sensitivity of monoclonal anti-AKR1B15 antibody supernatants with HEK-293 lysates.
The Western blots were performed with equal amounts of either non-transfected HEK-293 cell lysates (-) or lysates of HEK-293 cells either transiently transfected with pcDNA3.1(+)-AKR1B15.1 (1B15.1) or pcDNA3.1(+)-AKR1B15.2 (1B15.2). Supernatant dilutions (1:25) of the established hybridoma clones (rat-anti-AKR1B15 clones 7B1 **(A)**, 9A5 **(B)**, and 19E5 **(C)**, or mouse-anti-AKR1B15.2 clone 29D4 **(D)**) or a dilution (1:1000) of the affinity purified polyclonal rabbit-anti-AKR1B15 **(E)** in 0.5 % milk solution served as primary antibody solutions. The detection was performed via chemiluminescence after incubation with the respective HRP-conjugated secondary antibodies and ECL substrate.

Here, it was also seen that the monoclonal antibodies showed high specificity for the respective AKR1B15 isoform(s), whereas the polyclonal rabbit-anti-AKR1B15 antibody cross-reacted with proteins of the HEK-293 background, too [Figure III-8]. The signal intensities varied strongly between the antibody supernatants tested and were comparable to the results received from Western blots with *E. coli* BL21 (DE3) lysates [III.1.2.3]. Both AKR1B15 isoforms and the longer AKR1B15.2 isoform were detectable with the rat-anti-AKR1B15 clone 9A5 [Figure III-8B] and mouse-anti-AKR1B15.2 clone 29D4 [Figure III-8D] antibodies, respectively. In contrast, the rat-anti-AKR1B15 clone 19E5 antibody supernatant detected only the higher abundant shorter AKR1B15.1 isoform with very low intensity [Figure III-8C], whereas the rat-anti-AKR1B15 clone 7B1 antibody supernatant did not detect any AKR1B15 isoform [Figure III-8A], indicating a low affinity to AKR1B15 isoforms or a low concentration of antibodies in the supernatant.

As a result, the monoclonal antibody supernatants of the rat-anti-AKR1B15 clone 9A5 recognizing both AKR1B15 isoforms and the mouse-anti-AKR1B15.2 clone 29D4 detecting only AKR1B15.2 were used for further expression analysis.

III.1.3. Subcellular localization of AKR1B15 isoforms

Most members of the AKR superfamily, like AKR1B10 (sharing 91 % amino acid sequence identity with AKR1B15.1), localize intracellular to the cytosol. In order to fathom the subcellular localization of the two AKR1B15 isoforms, immunocytochemical analyses and *in silico* predictions were carried out.

III.1.3.1. Subcellular localization of full length AKR1B15 isoforms

Subcellular localization studies with HeLa cells overexpressing N- and C-terminally myc-tagged AKR1B15 isoforms showed that both N-terminally myc-tagged AKR1B15 isoforms, AKR1B15.1 and AKR1B15.2, colocalize with the cytosol [Figure III-9A, B]. A cytosolic localization was also determined for the C-terminally myc-tagged AKR1B15.2 [Figure III-9D, F, H]. In contrast, AKR1B15.1 carrying a C-terminal myc tag colocalized surprisingly with mitochondria [Figure III-9C, E, G].

Since it was found that the location of the fused myc tag within the protein influenced the subcellular localization of AKR1B15.1 – cytosolic versus mitochondrial – localization studies were also performed with untagged AKR1B15 isoforms. These studies dealt with two questions: First, what are the subcellular localizations of untagged AKR1B15 isoforms and second, are the generated monoclonal rat-anti-AKR1B15 (AKB-2) antibodies also functional in immunocytochemical analyses. The subcellular localization studies with untagged proteins revealed that, comparable to the C-terminally myc-tagged AKR1B15 isoforms, untagged AKR1B15.1 colocalizes to mitochondria [Figure III-10A, C, E], whereas untagged AKR1B15.2 is a cytosolic protein [Figure III-10B, D, F]. Thus, the mitochondrial localization of AKR1B15.1 was verified.

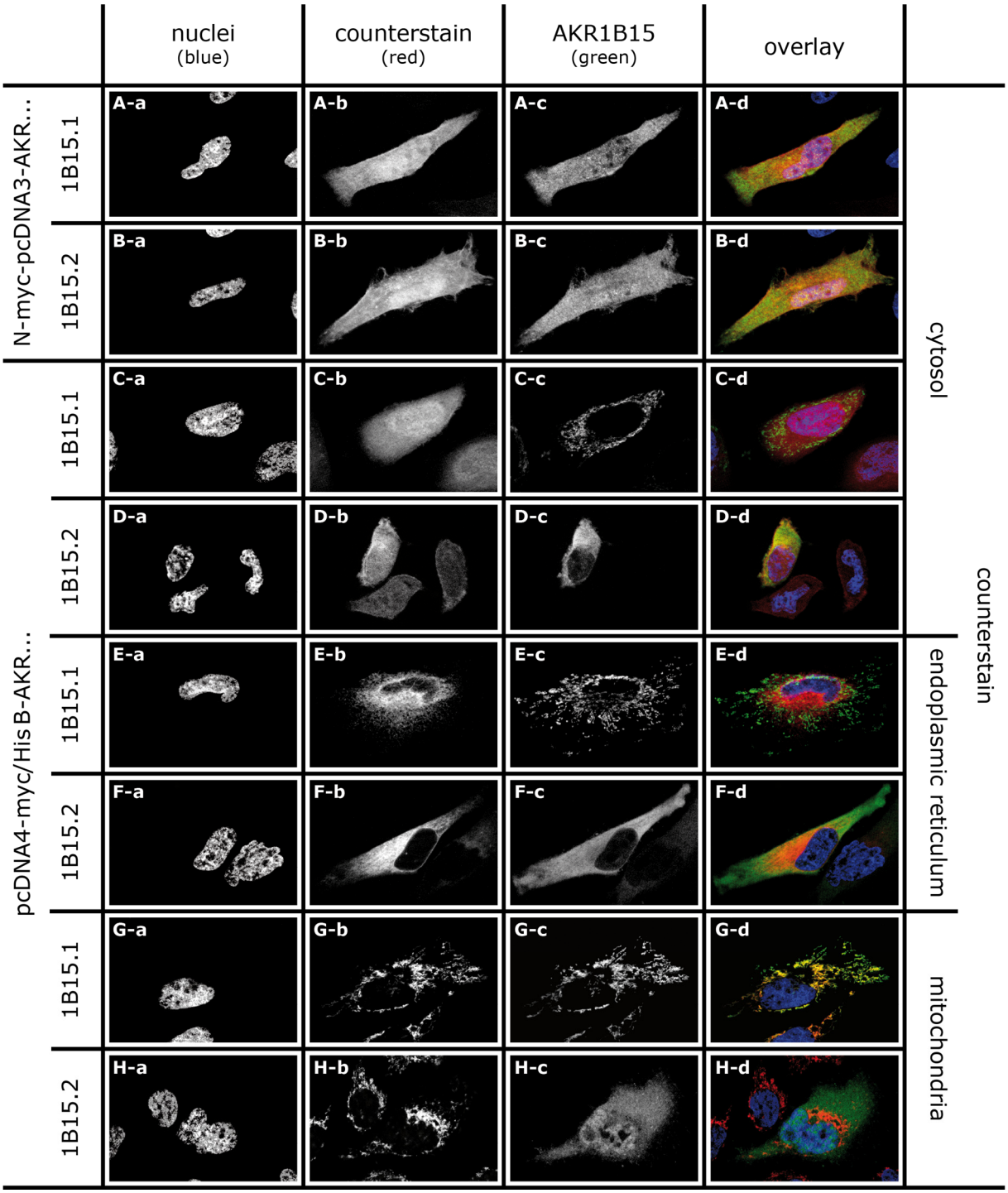

Figure III-9: Immunocytochemical subcellular localization studies with myc-tagged AKR1B15 isoforms revealed a surprising mitochondrial localization of C-terminally myc-tagged AKR1B15.1.
Shown are representative results from subcellular localization studies with N- or C-terminally myc-tagged AKR1B15 isoforms. HeLa cells were transiently transfected with N-myc-pcDNA3-AKR1B15.1 **(A),** N-myc-pcDNA3-AKR1B15.2 **(B)**, pcDNA4-myc/His B-AKR1B15.1 **(C, E, G)**, or pcDNA4-myc/His B-AKR1B15.2 **(D, F, H)** in order to express N-terminally myc-tagged **(A-B)** or C-terminally myc-tagged proteins **(C-H)**. Nuclei were stained using Hoechst 33342 dye **(a)**; counterstaining of the cytosol or endoplasmic reticulum was performed via the co-transfection of pCMV DsRed-Express2 or pDsRed2-ER, respectively, whereas mitochondria were counterstained by vital stain using MitoTracker Orange CMTMRos **(b)**; myc-tagged AKR1B15 isoforms were stained using mouse-anti-myc / AlexaFluor 488 goat-anti-mouse antibodies **(c)**. The overlay of individual stains **(d)** shows nuclei in blue, counterstains in red, AKR1B15 in green, and colocalization in yellow.

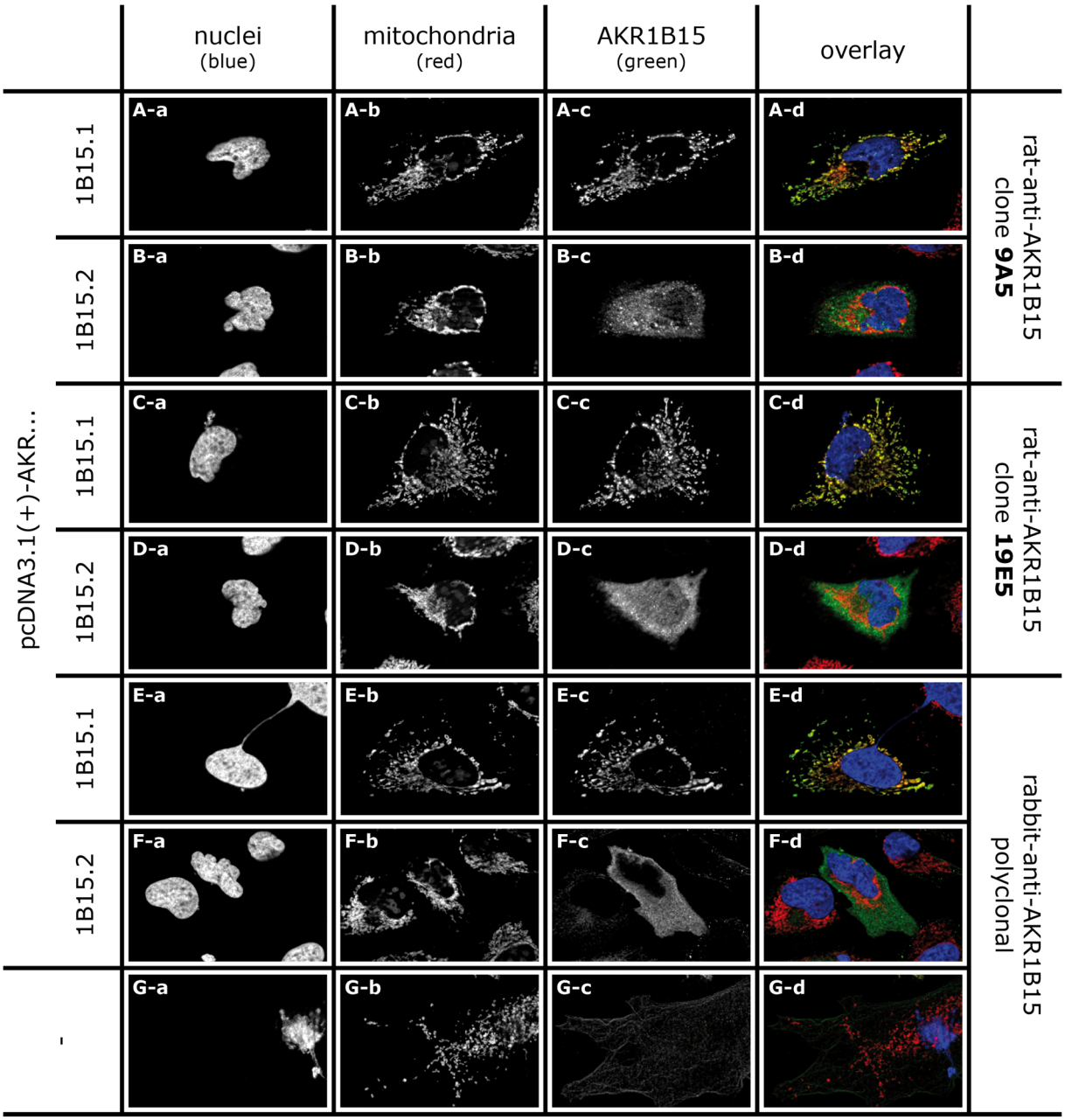

Figure III-10: Immunocytochemical subcellular localization studies with untagged AKR1B15 isoforms verified the mitochondrial and cytosolic localization of AKR1B15.1 and AKR1B15.2, respectively.
Shown are representative results from subcellular localization studies with untagged AKR1B15 isoforms. HeLa cells were transiently transfected with either pcDNA3.1(+)-AKR1B15.1 **(A, C, E)** or pcDNA3.1(+)-AKR1B15.2 **(B, D, F)** in order to express untagged AKR1B15 isoforms. Non-transfected HeLa cells served as control **(G)**. Nuclei were stained using Hoechst 33342 dye **(a)**; mitochondria were stained using MitoTracker Orange CMTMRos **(b)**; untagged AKR1B15 isoforms were stained using either the monoclonal rat-anti-AKR1B15 clone 9A5 **(A, B)** or clone 19E5 **(C, D)** primary antibody supernatants and AlexaFluor 488 goat-anti-rat secondary antibody pairs or the polyclonal rabbit-anti-AKR1B15 **(E-G)** primary antibody and AlexaFluor 488 goat-anti-rabbit secondary antibody pair **(c)**. The overlay of individual stains **(d)** shows nuclei in blue, mitochondria in red, AKR1B15 in green, and colocalization in yellow.

In addition, it could be seen that the generated monoclonal rat-anti-AKR1B15 clone 9A5 and clone 19E5 antibodies also work in immunocytochemical analyses by possessing sufficient affinity and low background [Figure III-10A-D]. Since the monoclonal antibodies were not existent at the beginning of these studies, the affinity purified polyclonal rabbit-anti-AKR1B15 antibody was also included in these analyses. Although this antibody recognized both AKR1B15 isoforms in the subcellular localization studies when overexpressed in HeLa cells [Figure III-10E, F], it gave also quite strong background signals resembling structures of the cytoskeleton [Figure III-10G]. These observations were in accord with the results gained from Western blotting experiments [III.1.2.4].

In conclusion, whereas most AKRs, including the longer AKR1B15 isoform AKR1B15.2, are cytosolic proteins, AKR1B15.1 seems to be the first (human) AKR1 family member localizing to mitochondria.

III.1.3.2. *IN SILICO* SUBCELLULAR LOCALIZATION PREDICTION

Immunocytochemistry revealed an unexpected mitochondrial localization of AKR1B15.1. Although it is known that *in silico* subcellular localization predictions are error prone, different subcellular prediction algorithms (TargetP 1.1 Server, SignalP 4.1 Server, PrediSi, iPSORT, PSORT II, and MitoProt II) were used for the prediction of signal peptides or signal cleavage sites in AKR1B15.1 and the subcellular localization of AKR1B15.1 in order to underline the results gained from immunocytochemistry and to get an idea of key amino acid residues in AKR1B15.1 responsible for its mitochondrial localization. For comparison reasons, sequences of AKR1B15.2 and AKR1B10 were also included in the *in silico* analyses.

The TargetP 1.1 Server, SignalP 4.1 Server, iPSORT, and MitoProt II prediction algorithms did not predict any signal peptides or signal cleavage sites in the three proteins. However, a cleavage site with a score of 0.185 at position 26 of AKR1B15.1 was predicted by PrediSi. Although that score was quite low and arguable, it was significantly higher compared with the scores of cleavage sites predicted for AKR1B15.2 (score of 0.074 at position 41) and AKR1B10 (score of 0.056 at position 221). When looking at the subcellular localization predictions, the TargetP 1.1 Server predicted no mitochondrial localization or secretory signal in AKR1B15.1, AKR1B15.2, and AKR1B10. The same was true for the PSORT II prediction algorithm which predicted a cytosolic localization for all three proteins. MitoProt II predicted a mitochondrial localization of AKR1B15.1, AKR1B15.2, and AKR1B10 with a probability of 15.5 %, 0.8 %, and 12.0 %, respectively, very slightly promoting the results from the immunocytochemical analyses. In contrast, the iPSORT algorithm definitely predicted a mitochondrial targeting peptide in AKR1B15.1 but not in AKR1B15.2 and AKR1B10 by regarding the sequence of the first 30 amino acids. Thus, the iPSORT algorithm was the only prediction tool which clearly underlined the mitochondrial localization of AKR1B15.1, though AKR1B15.1 misses a distinct signal peptide. In addition, iPSORT indicated a crucial role of the N-terminal amino acid residues in AKR1B15.1 for its subcellular localization. However, the *in silico* predictions represented per se just a poor tool to verify subcellular localizations.

The detailed outputs of predictions are listed in the appendix [VI.5].

III.1.3.3. EFFECT OF N-TERMINI ON THE SUBCELLULAR LOCALIZATION

The localization studies with myc-tagged and untagged AKR1B15 isoforms as well as iPSORT predictions demonstrated that the N-terminal amino acid sequence of AKR1B15.1 is responsible for its mitochondrial localization. To verify these results and identify amino acid residues important for the mitochondrial localization of AKR1B15.1 and the cytosolic localization of the highly identical AKR1B10, N-terminal sequence stretches of AKR1B10, AKR1B15.1, and AKR1B15.2 were N-terminally fused to AcGFP and these fusion proteins were analyzed for their subcellular localization by confocal microscopy [Figure III-11, Figure III-12].

The analyses showed that fusion proteins consisting of the first 38 amino acid residues (Met1-Ala38) of AKR1B15.1 and AKR1B10 fused to AcGFP [Figure III-11] colocalized with mitochondria and the cytosol, respectively [Figure III-12A, D]. A cytosolic localization was also seen for the N-terminus of AKR1B15.2 (Met1-Ala66) fused to AcGFP [Figure III-12E]. This reflected the earlier results from localization studies with full length proteins.

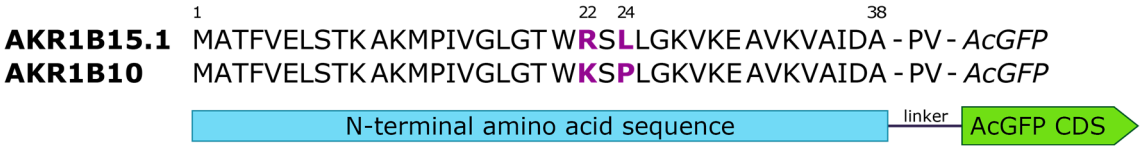

Figure III-11: The N-terminal amino acid sequences (Met1-Ala38) of AKR1B15.1 and AKR1B10 differ in only two amino acid residues.
Shown are the alignment of the N-terminal amino acid sequence (Met1-Ala38) in AKR1B15.1 and in AKR1B10 as well as a schematic illustration of the N-terminal sequence – AcGFP fusion proteins.
The two differing amino acid residues in the N-terminal sequence of AKR1B15.1 and AKR1B10 at positions 22 and 24 are highlighted in purple.

As illustrated in Figure III-4 and Figure III-11, AKR1B15.1 and AKR1B10 differ in only two amino acid residues within the first 38 amino acid residues: Arg22 and Leu24 in AKR1B15.1 compared to Lys22 and Pro24 in AKR1B10.

To analyze which of the two differing amino acid residue is responsible for the cytosolic localization of AKR1B10 or, contrary, the mitochondrial localization of AKR1B15.1, Lys22 and Pro24 in the N-terminal peptide (Met1-Ala38) of AKR1B10 were separately mutated to the AKR1B15 equivalents Arg22 and Leu24, respectively. Here, it was seen that the K22R mutation in the sequence of AKR1B10 had no effect on the cytosolic localization of the fusion protein [Figure III-12B]. In contrast, the P24L mutation changed the localization of the fusion protein towards mitochondrial [Figure III-12C]. Thus, a single amino acid residue exchange, namely P24L, in AKR1B10 was sufficient to shift the localization of AKR1B10 from the cytosol to mitochondria.

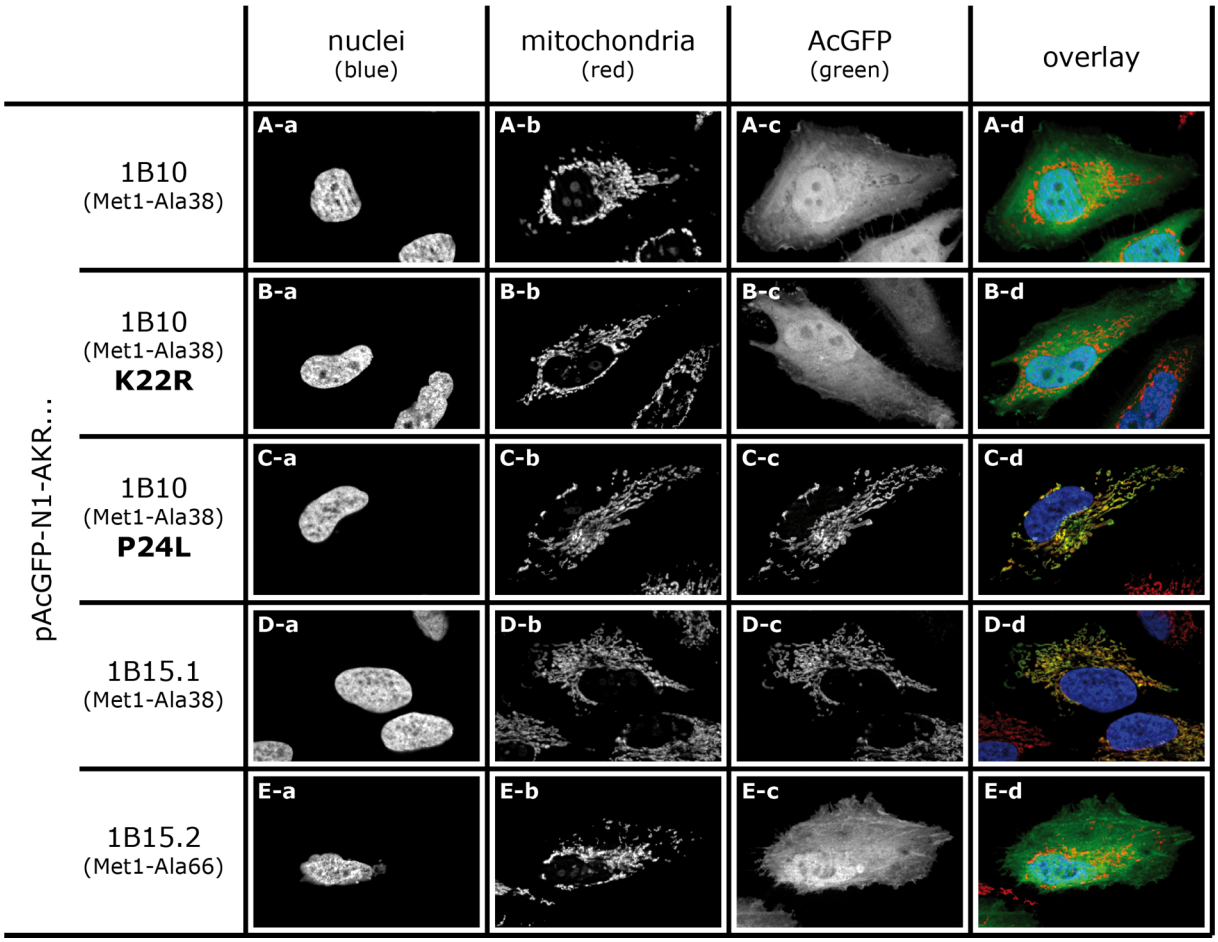

Figure III-12: Subcellular localization studies with N-terminal sequence with AcGPF fusion proteins identified Leu24 in AKR1B15.1 versus Pro24 in AKR1B10 as key amino acid residues responsible for their mitochondrial versus cytosolic localization, respectively.
Shown are representative results from subcellular localization studies with N-terminal AKR1B10 and AKR1B15 sequences fused to AcGFP. HeLa cells were transiently transfected with pAcGFP-N1-AKR1B10 (Met1-Ala38) **(A)**, pAcGFP-N1-AKR1B10 (Met1-Ala38) K22R **(B)**, pAcGFP-N1-AKR1B10 (Met1-Ala38) P24L **(C)**, pAcGFP-N1-AKR1B15.1 (Met1-Ala38) **(D)**, or pAcGFP-N1-AKR1B15.2 (Met1-Ala66) **(E)** in order to express N-terminal sequence – AcGFP fusion proteins. Nuclei were stained using Hoechst 33342 dye **(a)**; mitochondria were counterstained by vital stain using MitoTracker Orange CMTMRos **(b)**; fusion proteins were visualized via AcGFP fluorescence **(c)**. The overlay of individual stains **(d)** shows nuclei in blue, counterstains in red, AcGFP fusion proteins in green, and colocalization in yellow.

In conclusion, localization studies with the AKR1B15.1 N-terminus (Met1-Ala38) fused to AcGFP verified the mitochondrial subcellular localization of AKR1B15.1. In addition, Leu24 in AKR1B15.1 versus Pro24 in AKR1B10 was identified to be responsible for the mitochondrial and cytosolic localization of AKR1B15.1 and AKR1B10, respectively.

III.1.4. Enzymatic activity of AKR1B15 isoforms

In 2011 only a minor enzymatic activity of the human AKR1B15.1 with typical AKR substrates, such as DL-glyceraldehyde or 4-nitro-benzaldehyde, was detected [22].

Enzymatic activity assays with equal amounts of newly purified AKR1B15.1 (according to II.5.1) or AKR1B10 (provided by Oleg Barski) confirmed the poor enzymatic activity of AKR1B15.1 with the typical AKR substrate DL-glyceraldehyde [Figure III-13]. Thus, the reduction of DL-glyceraldehyde to the respective alcohol by AKR1B15.1 was very slow ($v_{0\,(5\,mM)} \approx 1\ min^{-1}$). For comparison, the AKR1B10 control revealed a much better enzymatic activity with DL-glyceraldehyde ($v_{0\,(5\,mM)} \approx 37\ min^{-1}$) and oxidized all NADPH cofactor within 1 min [Figure III-13].

This arose the question if there are other compounds which are better substrates of AKR1B15.

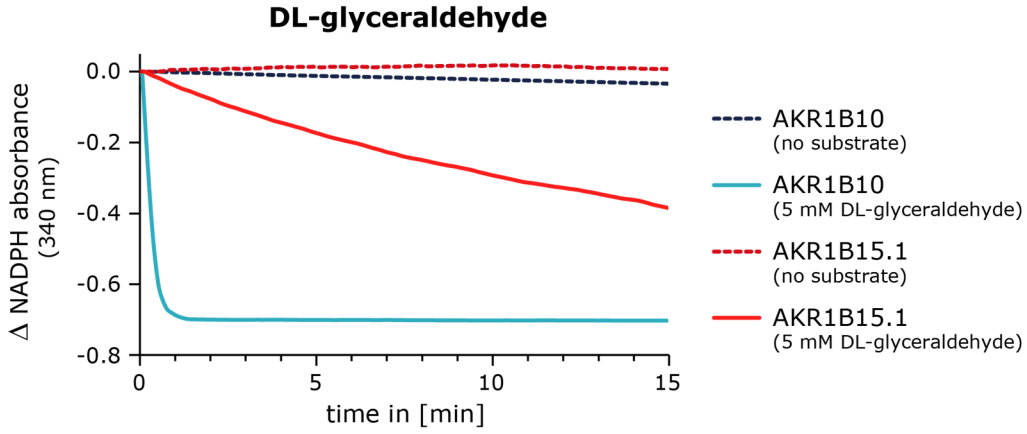

Figure III-13: AKR1B15.1 shows by far lower enzymatic activity with DL-glyceraldehyde than AKR1B10 does.
Illustrated are exemplary time courses of comparative enzymatic reactions with purified AKR1B10 or AKR1B15.1 and the typical AKR substrate DL-glyceraldehyde. The enzymatic reactions were carried out at 37 °C with 6 µM purified enzyme, 100 µM NADPH cofactor, and 5 mM DL-glyceraldehyde substrate in reaction buffer. The reduction of substrate was monitored at 340 nm via the decrease in NADPH absorption as described in II.8.2.3.

III.1.4.1. Identification of AKR1B15 substrates

Since both AKR1B15 isoforms are mainly expressed in steroid related tissues [III.1.1.3], at first, steroids were tested for being substrates of the human AKR1B15 isoforms. The initial tests covered compounds belonging to different classes of steroid hormones, like gestagens, androgens, estrogens, and glucocorticoids. For this, activity assays were performed with HEK-293 cells overexpressing AKR1B15.1 or AKR1B15.2 (after the transient transfection with pIRES-hrGFP-1α-AKR1B15.1 or pIRES-hrGFP-1α-AKR1B15.2, respectively), ^{3}H-labeled steroids, and the respective cofactors (NADPH for reductive reactions and $NADP^{+}$ for oxidative reactions) in reaction buffer.

Table III-2: Results from AKR1B15 substrate identification reactions using ^{3}H-labeled steroids.

class	steroid	cofactor	substrate of AKR1B15.1	substrate of AKR1B15.2
gestagens	progesterone	NADPH	no	no
androgens	testosterone (T)	NADP^{+}	**yes**	no
	Δ4-androstenedione (Δ4-Ae)	NADPH	**yes**	no
	dehydroepiandrosterone (DHEA)	NADPH	**yes**	no
	dihydrotestosterone (DHT)	NADP^{+}	**yes**	no
	3α,17β-androstanediol (A-diol)	NADP^{+}	**yes**	no
	androsterone (AN)	NADPH	**yes**	no
estrogens	17α-estradiol	NADP^{+}	no	no
	17β-estradiol (E2)	NADP^{+}	**yes**	no
	estrone (E1)	NADPH	**yes**	no
glucocorticoids	cortisol	NADP^{+}	no	no
	cortisone	NADPH	no	no
	corticosterone	NADP^{+}	no	no
	11-dehydrocorticosterone	NADPH	no	no

Activity tests were performed with 10^{6} HEK-293 cells which were transiently transfected with either pIRES-hrGFP-1α-AKR1B15.1 or pIRES-hrGFP-1α-AKR1B15.2, 0.5 µl ^{3}H-labeled steroid, as well as 300 µM or 350 µM NADPH or NADP^{+} cofactor in reaction buffer, respectively. The incubation time of reactions at 37 °C varied from 1-2 h.

Within these first screens it was found that AKR1B15.1 reduces or oxidizes androgens and estrogens. In contrast, neither progesterone (gestagen) nor corticosteroids were substrates of AKR1B15.1 [Table III-2]. In addition to the biologically occurring androgens, AKR1B15.1 was also able to reduce the fluorogenic Δ4-androstenedione substitute 8-acetyl-2,3,5,6-tetrahydro-1H,4H-11-oxa-3a-aza-benzo[de]anthracen-10-one [221], herein called fluorogenic substrate. Thus, in enzymatic activity assays containing AKR1B15.1, NADPH, and the fluorogenic substrate a clear increase in product fluorescence (λ_{ex}: 440 nm, λ_{em}: 510 nm) was detectable [Figure III-14]. The reduction of the fluorogenic substrate, which represents a good model substrate for androgens in enzymatic activity screens, verified the class of androgens as AKR1B15.1 substrates.

On the other hand, AKR1B15.2 showed no enzymatic activity with any steroidal substrate tested [Table III-2, Figure III-14].

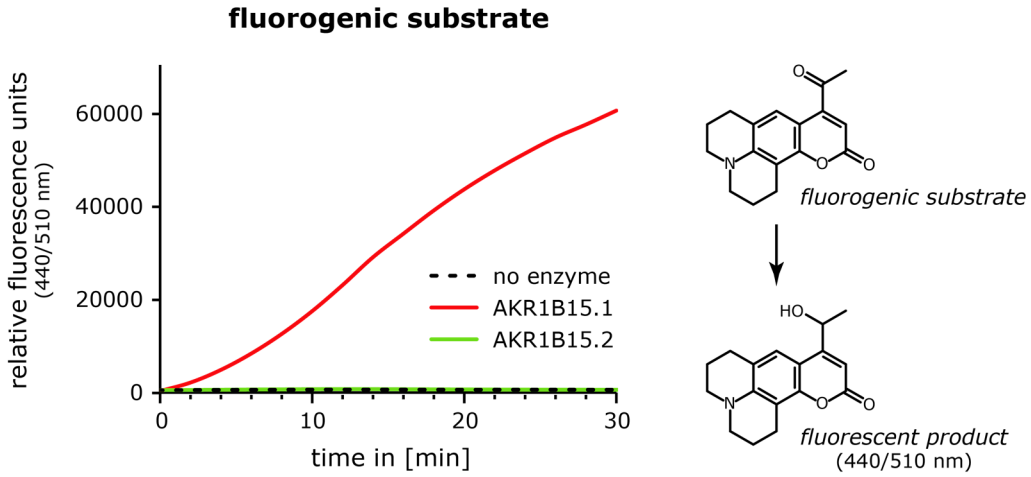

Figure III-14: AKR1B15.1, but not AKR1B15.2, reduces a fluorogenic Δ4-androstenedione substitute model substrate.
Illustrated are exemplary time courses of enzymatic activity assays with purified AKR1B15 isoforms and the fluorogenic substrate 8-acetyl-2,3,5,6-tetrahydro-1H,4H-11-oxa-3a-aza-benzo[de]anthracen-10-one [221]. The reductive enzymatic reactions were performed at 37 °C with 600 nM purified His_6-tagged AKR1B15.1 or AKR1B15.2, up to 4 µM fluorogenic substrate, and 20 µM NADPH in reaction buffer. The formation of the fluorescent product was monitored at λ_{ex} = 440 nm and λ_{em} = 510 nm.

In addition to steroids, compounds which are present in mitochondria, like free fatty acids (e.g., oxaloacetic acid and 2-oxo-butyric acid) or their CoA conjugates (e.g., acetoacetyl-CoA, methylmalonyl-CoA, succinyl-CoA, 3-hydroxy-butyryl-CoA, and 3-hydroxy-3-methyl-glutaryl-CoA), were analyzed for being substrates of AKR1B15.1. For this, either NADPH absorption (λ = 340 nm) or NADPH fluorescence (λ_{ex} = 340 nm, λ_{em} = 450 nm) were used as read-out.

The resulting curves from the kinetics with potential mitochondrial substrates of AKR1B15.1 are illustrated in Figure III-15. Reactions using NADPH fluorescence as well as NADPH absorption as read-out identified acetoacetyl-CoA which belongs to the class of 3-keto-acyl-CoA conjugates as a substrate of AKR1B15.1 [Figure III-15A, C]. Since the carboxylic

acid CoA conjugates methylmalonyl-CoA and succinyl-CoA were not reduced by AKR1B15.1 [Figure III-15A], the reduction of acetoacetyl-CoA was most probably at the C3 position of the acyl chain resulting in 3-hydroxy-butyryl-CoA. The reverse reaction showed a slight increase in NADPH fluorescence, suggesting that AKR1B15.1 could also be able to oxidize 3-hydroxy-butyryl-CoA [Figure III-15B]. Reactions containing 3-hydroxy-3-methyl-glutaryl-CoA or unconjugated short-chain 2-keto fatty acids (2-oxo-butyric acid and oxaloacetic acid) as substrates revealed only changes in NADPH fluorescence or absorption which were comparable to the negative controls lacking in substrate [Figure III-15B, C].

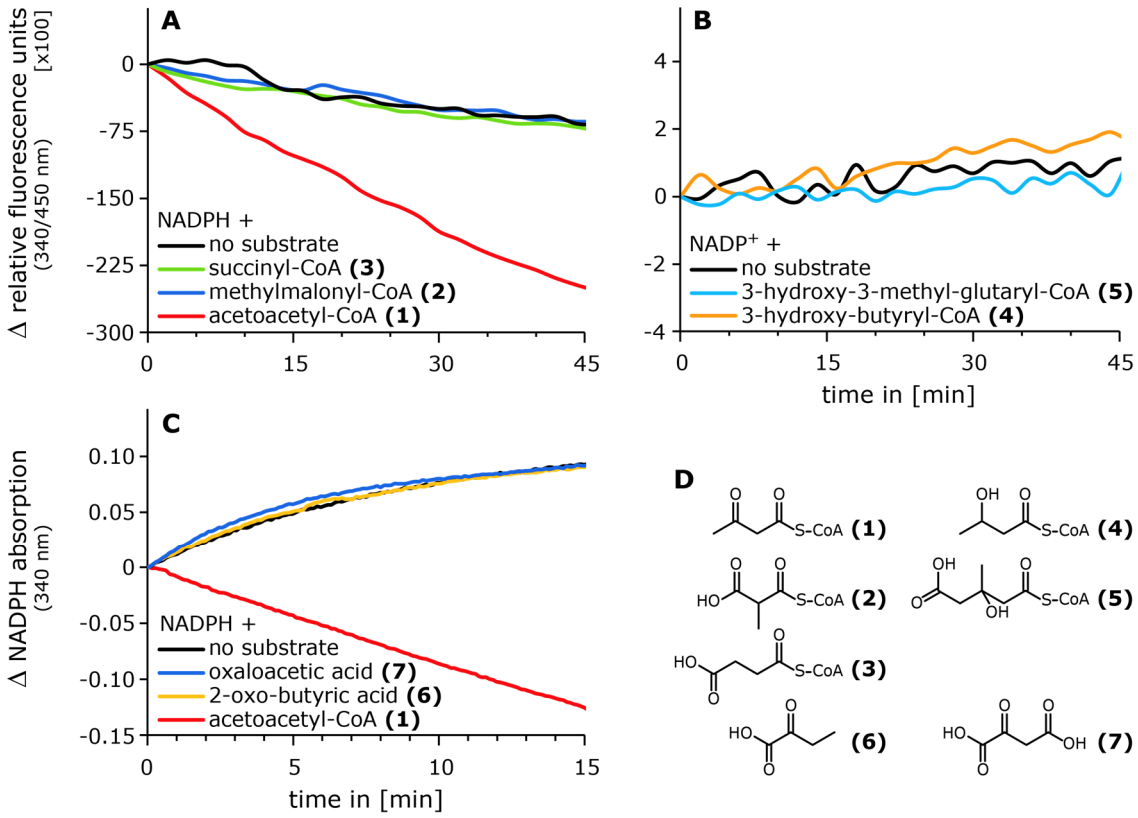

Figure III-15: AKR1B15.1 possesses enzymatic activity with the non-steroidal mitochondrial substrate acetoacetyl-CoA.
Shown are results from enzymatic activity assays for the identification of potential mitochondrial substrates of AKR1B15.1, using NADPH fluorescence or absorption as read-out.
(A, B) Kinetics monitoring the change in NADPH fluorescence by reductive **(A)** or oxidative **(B)** reactions. The reactions were performed according to II.8.2.2 at 37 °C and contained 600 nM purified AKR1B15.1, 100 µM potential substrate, and 20 µM NADPH or $NADP^+$, respectively, in reaction buffer. **(C)** Kinetics monitoring the decrease in NADPH absorption by reductive reactions. The reactions were performed according to II.8.2.3 at 37 °C and contained 6 µM purified AKR1B15.1, 500 µM potential substrate, and 100 µM NADPH in reaction buffer. **(D)** Chemical structures of the tested substrates: acetoacetyl-CoA **(1)**, methylmalonyl-CoA **(2)**, succinyl-CoA **(3)**, 3-hydroxy-butyryl-CoA **(4)**, 3-hydroxy-3-methyl-glutaryl-CoA **(5)**, 2-oxo-butyric acid **(6)**, and oxaloacetic acid **(7)**.

When the longer AKR1B15.2 isoform was tested with the "mitochondrial" substrates, again no substrate of AKR1B15.2 could be identified [data not shown].

Finally, retinoids (all-trans retinal and all-trans retinol) which represent good substrates for especially AKR1B10 [29] were tested for being substrates of the AKR1B15 isoforms. The initial screens were performed with HEK-293 cells overexpressing AKR1B15.1 or AKR1B15.2. Although the initial results suggested that AKR1B15.1 possesses low enzymatic activity with retinoids, these findings were quite doubtful since non-transfected HEK-293 cell controls exhibited already quite strong background activities (up to 15 % conversion) with those retinoids [Figure III-16B, C, E]. However, the reduction of all-trans retinal and oxidation of all-trans retinol by AKR1B15.1 was clearly visible in activity assays with the purified enzyme [Figure III-16D, E].

Like with all other substrates tested, AKR1B15.2 did not show any enzymatic activity with retinoids either [Figure III-16B, C, E; data not shown].

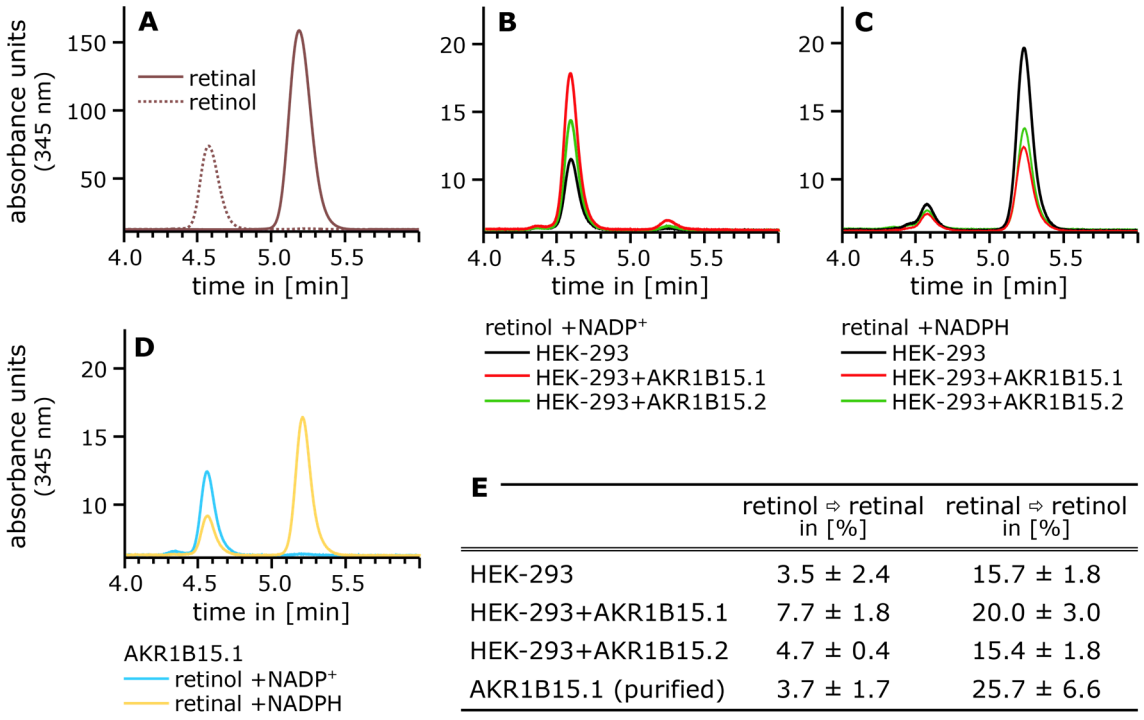

E

	retinol ⇨ retinal in [%]	retinal ⇨ retinol in [%]
HEK-293	3.5 ± 2.4	15.7 ± 1.8
HEK-293+AKR1B15.1	7.7 ± 1.8	20.0 ± 3.0
HEK-293+AKR1B15.2	4.7 ± 0.4	15.4 ± 1.8
AKR1B15.1 (purified)	3.7 ± 1.7	25.7 ± 6.6

Figure III-16: AKR1B15.1, but not AKR1B15.2, possesses enzymatic activity with the retinoids all-trans retinal and all-trans retinol.
Shown are exemplary results from enzymatic activity assays with AKR1B15 isoforms and retinoids (according to II.8.2.4).
(A) Chromatographic separation of all-trans retinol (retinol, t_R = 4.58 min) and all-trans retinal (retinal, t_R = 5.22 min) reference samples. **(B, C)** Representative chromatograms resulting from activity assays with 10^6 HEK-293 cells (black trace) or HEK-293 cells overexpressing either AKR1B15.1 (red trace) or AKR1B15.2 (green trace) after transient transfection with pIRES-hrGFP-1α-AKR1B15.1 or pIRES-hrGFP-1α-AKR1B15.2, respectively. The oxidation of all-trans retinol **(B)** and the reduction of all-trans retinal **(C)** was carried out at 37 °C for 2 h. **(D)** Representative chromatograms resulting from activity assays with 1.1 µg purified AKR1B15.1. The oxidation of all-trans retinol (blue trace) and reduction of all-trans retinal (yellow trace) was performed at 37 °C for 1 h. **(E)** Summary of results from activity tests with AKR1B15 isoforms and retinoids. Given are the average conversions of retinoids ± SD, which were calculated from the areas under the curve ratios of triplicates.

In summary, AKR1B15.1 catalyzes redox reactions on androgens and estrogens. Beside these C19 and C18 steroids, AKR1B15.1 reduces at least short-chain 3-keto-acyl-CoA conjugates, like acetoacetyl-CoA, and oxidizes most probably also short-chain 3-hydroxy-acyl-CoA conjugates. In contrast, 2/3-keto- or 2/3-hydroxy-acyl chains with additional carboxylic groups and/or lacking the bulky CoA conjugate are no substrates of AKR1B15.1. Finally, retinoids, represented here by all-trans retinol and all-trans retinal, are further substrates of AKR1B15.1.

Although AKR1B15.2 differs from AKR1B15.1 only in the first 50 amino acid residues and possesses all residues of the catalytic tetrad, no enzymatic activity was seen for AKR1B15.2 with the herein tested compounds [Figure III-4].

III.1.4.2. COFACTOR PREFERENCE OF AKR1B15 ISOFORMS SUBSTRATES

Enzymes of the AKR superfamily are known to prefer the phosphorylated nicotinamide adenine dinucleotides NADPH and $NADP^+$ as cofactors. To test whether this is also true for the two AKR1B15 isoforms AKR1B15.1 and AKR1B15.2, activity assays with different cofactors (NADPH, NADH, $NADP^+$, and NAD^+) in concentrations up to 1050 µM as well as cofactor titration studies with these cofactors were performed.

HEK-293 cells overexpressing AKR1B15.1 after transient transfection with pIRES-hrGFP-1α-AKR1B15.1 and non-transfected HEK-293 cells (negative controls) were used in the assays analyzing the cofactor preference via enzymatic activities. By analyzing the reduction and oxidation of ^{3}H-labeled steroids in presence of NAD(P)H and $NAD(P)^+$ cofactors, respectively, it was found that AKR1B15.1 strongly prefers NADP(H) cofactors and does not catalyze reductive reactions in the presence of up to 1050 µM NADH [Figure III-17A]. Although the results gained from oxidative reactions with NAD^+ were inconsistent, it seemed more likely that AKR1B15.1 does not use NAD^+ either because a quite high activity was also seen in the non-transfected HEK-293 negative controls [data not shown]. Since no substrate could have been identified for AKR1B15.2 in earlier assays, this isoform was not included in these activity assays.

Cofactor titration studies using the quenching of protein fluorescence due to the binding of cofactor as read-out verified the results from the enzymatic activity assays [Figure III-17]. By titrating $NADP^+$ or NADPH cofactor solutions to purified His_6-tagged AKR1B15.1 it was seen that $NADP^+$ and NADPH bind to the enzyme with a dissociation constant K_d of 60 nM and 58 nM, respectively [Figure III-17B]. The maximum quenching was about 25-26 %, and the high R^2 values (0.997-0.999) showed that the model used for the calculation of the K_d fitted well. In contrast, titration of NAD^+ and NADH (up to 40 µM final concentration) showed a maximum quenching below 3 % and R^2 values below 0.900. This indicated that the non-phosphorylated nicotinamide adenine dinucleotides do not readily bind to the enzyme and it is unlikely that they are used as cofactors for redox reactions catalyzed by AKR1B15.1.

In further titration studies performed by Oleg Barski it was seen that neither $NADP^+$ nor NADPH binds to AKR1B15.2 [data not shown]. The inability of AKR1B15.2 to bind cofactors would explain the lack in enzymatic activity detected above [III.1.4.1].

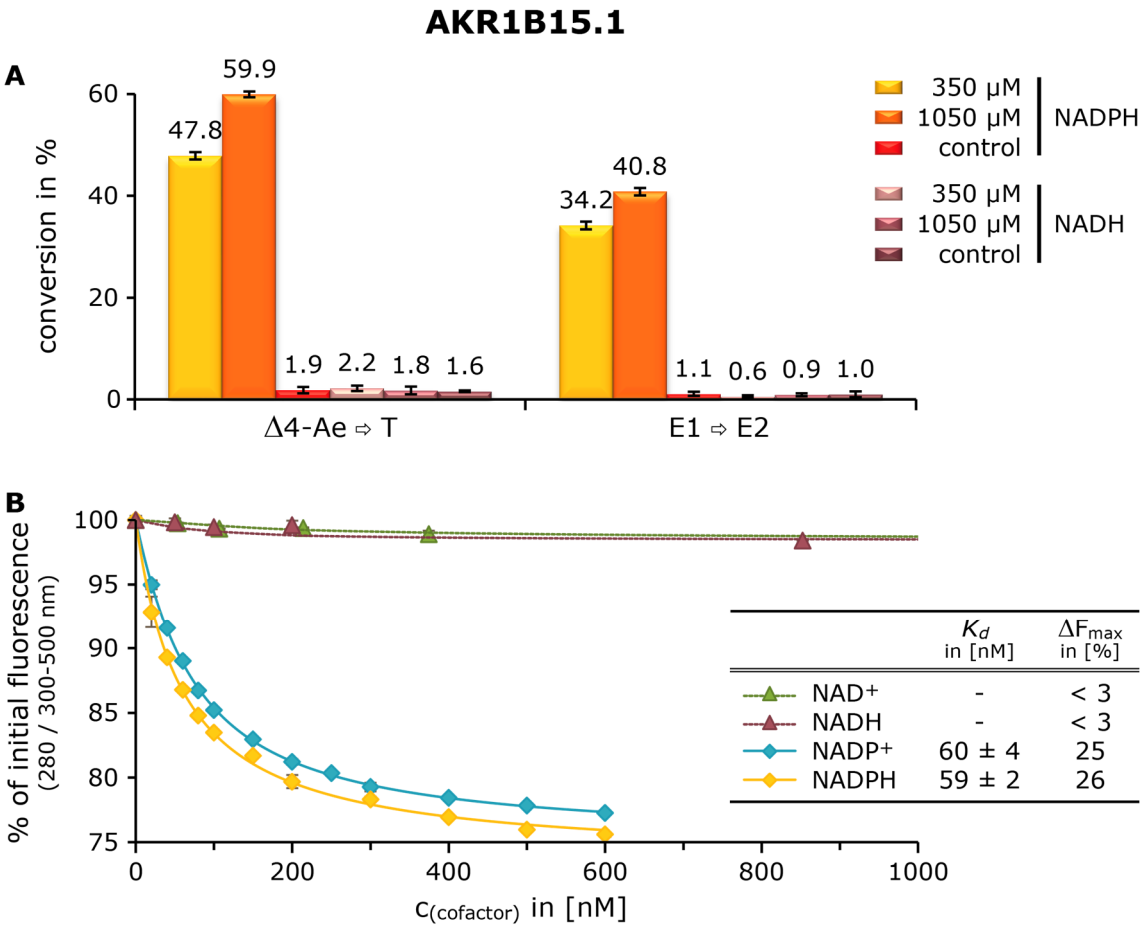

Figure III-17: AKR1B15.1 features a strong cofactor preference by binding exclusively the phosphorylated nicotinamide adenine dinucleotide cofactors NADPH and NADP+.
(A) Results from reductive activity assays with either HEK-293 cells overexpressing AKR1B15.1 after transient transfection with pIRES-hrGFP-1α-AKR1B15.1 (350 µM and 1050 µM) or non-transfected HEK-293 cells (control). The reactions contained 10^6 HEK-293 cells, 20 nM ^{3}H-labeled steroid, and 350 µM or 1050 µM cofactor (NADPH or NADH). Given are the average conversion of steroids ± SD per cofactor and concentration of reactions with transiently transfected HEK-293 in triplicates as well as the average conversion of steroids ± SD per cofactor (considering both cofactor concentrations) in unique reactions with non-transfected HEK-293 cells after an incubation at 37 °C for 1 h. **(B)** Results from cofactor titration studies with purified His_6-tagged AKR1B15.1. The graph shows the relative AKR1B15.1 protein fluorescence (mean of repeated measurements ± SD normalized by the initial protein fluorescence intensity at maximum peak height) in dependence of the amount of titrated cofactor. The dissociation constants K_d were calculated by fitting the quadratic Morison equation [Equation II-2] to the data.
Δ4-Ae, Δ4-androstenedione; ΔF_{max}, maximum quenching in protein fluorescence; E1, estrone, E2, 17β-estradiol; K_d, dissociation constant; T, testosterone.

Thus, AKR1B15.1 exhibits strong cofactor selectivity for phosphorylated nicotinamide adenine dinucleotide cofactors by binding solely NADPH and NADP+ with a K_d in the lower nanomolar range. In contrast, AKR1B15.2 is not able to bind any nicotinamide adenine dinucleotide cofactors, explaining its enzymatic inactivity.

III.1.4.3. Position selectivity of AKR1B15.1 with steroidal substrates

The enzymatic activity assays with androgens and estrogens for the identification of AKR1B15 substrates targeted only the C17 position of the steroid nucleus [III.1.4.1]. In assays using 17α-estradiol and 17β-estradiol as substrates, it was found that AKR1B15.1 catalyzes solely oxidative reactions at the C17β position of the steroid nucleus and thus exhibits 17β-hydroxysteroid dehydrogenase activity [Figure III-18B, Table III-2].

In order to analyze whether AKR1B15.1 is selective for reactions on the C17(β) position of the steroid nucleus or if it exhibits an additional 3α/β-hydroxysteroid dehydrogenase activity, enzymatic activity tests with ^{3}H-labeled androgens carrying either a keto group on C17(β) position and a hydroxyl group on C3 position (e.g., androsterone and DHEA) or vice versa (e.g., DHT) were carried out. In assays with 10^{6} HEK-293 cells overexpressing AKR1B15.1, the respective ^{3}H-labeled androgen and either 300 µM NADPH or 350 µM $NADP^{+}$ were incubated at 37 °C for 2-3 h. In doing so, either the C3(α/β) or the C17(β) position was targeted for redox reactions, as exemplarily shown for androsterone (AN) in Figure III-18A. In these assays, an enzymatic activity of AKR1B15.1 was only visible in reactions targeting the C17(β) position of the steroid nucleus [Figure III-18B].

Thus, AKR1B15.1 shows high position selectivity and possesses solely 17β-hydroxysteroid dehydrogenase activity but no 3(α/β)-hydroxysteroid dehydrogenase activity.

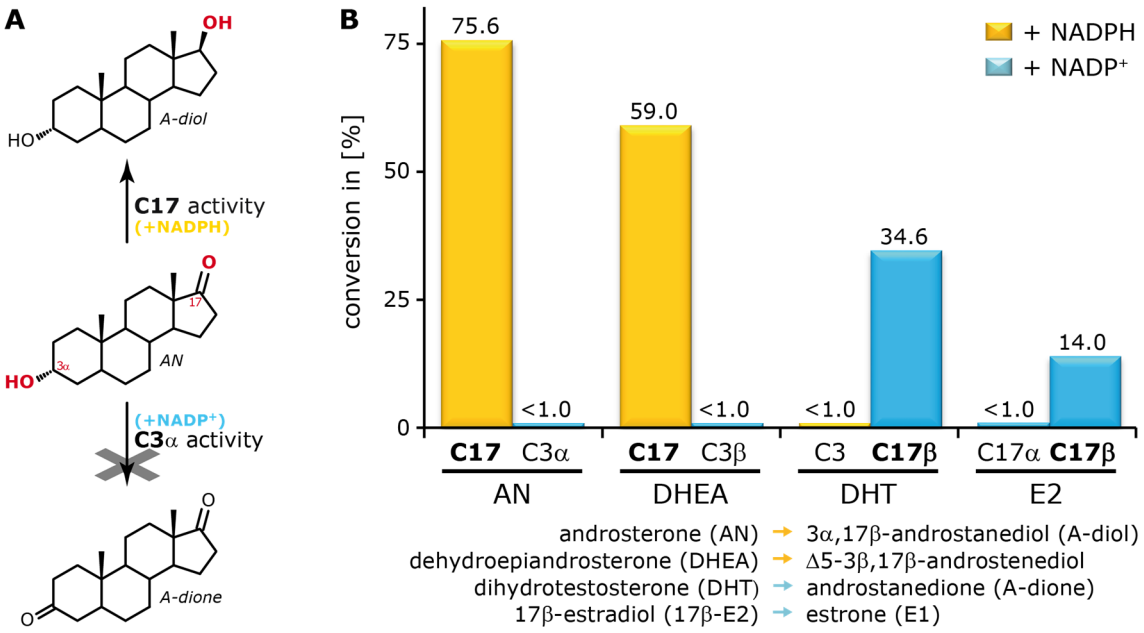

Figure III-18: AKR1B15.1 features solely 17β-hydroxysteroid dehydrogenase activity with steroids. Illustrated are the principle of enzymatic assays analyzing the position selectivity of AKR1B15.1 in redox reactions with steroids and their results.
(A) Assay set-up principle for the analysis of the position selectivity of AKR1B15.1 on the example of androsterone. **(B)** Representative results in % of conversion at the C17 or C3 position of the steroid nucleus. The activity assays were performed at 37 °C for 2-3 h with 10^{6} HEK-293 cells overexpressing AKR1B15.1 (from pIRES-hrGFP-1α-AKR1B15.1), ^{3}H-labeled steroids (10-30 nM), and either 300 µM NADPH (yellow bars) or 350 µM $NADP^{+}$ (blue bars) in reaction buffer.
A-diol, 3α,17β-androstanediol; A-dione, androstanedione; AN, androsterone; DHEA, dehydroepiandrosterone; DHT, dihydrotestosterone; E1, estrone; E2, estradiol.

III.1.4.4. KINETIC PARAMETERS OF AKR1B15.1

As described above, C18 and C19 steroids (estrogens and androgens), 3-keto-acyl-CoA conjugates (acetoacetyl-CoA), as well as retinoids (all-trans retinal and all-trans retinol) were identified as substrates of AKR1B15.1. Since our group is/was mainly interested in the sex steroid and fatty acid metabolism, the kinetic parameters of AKR1B15.1 were determined for androgens, estrogens, and acetoacetyl-CoA.

First, the relative apparent reaction velocities of AKR1B15.1 with steroids were analyzed. For this, reactions contained either 10^6 HEK-293 cells overexpressing AKR1B15.1 or 90 nmol purified AKR1B15.1, 20 nM ^{3}H-labeled steroid, and the respective cofactor. In both reaction set-ups, AKR1B15.1 preferred reductive reactions over oxidative ones. In addition, the enzymatic reaction velocities (initial turnover rates v_0) with androgenic substrates were faster than those with estrogenic substrates. The results of time course activity assays with the purified enzyme are illustrated in Figure III-19.

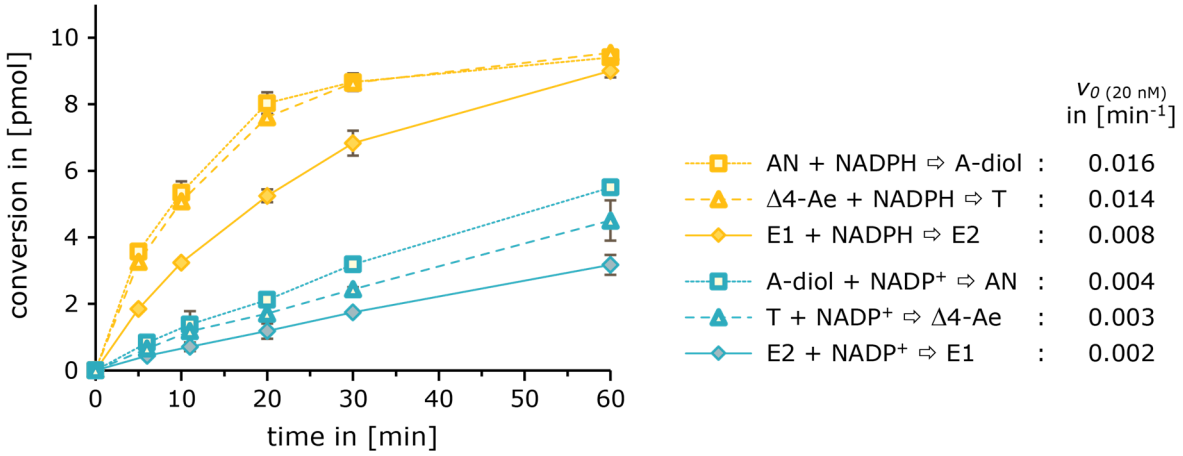

Figure III-19: AKR1B15.1 strongly prefers the reduction of steroids over their oxidation.
Shown are the results from time course activity assays for the comparison of apparent reaction velocities of AKR1B15.1 with steroids. The reduction (yellow symbols) or oxidation (blue symbols) of androgens (open symbols) and estrogens (filled symbols) was carried out in reactions containing 90 nmol purified AKR1B15.1, initial 20 nM ^{3}H-labeled steroids (20 nM correspond to 10 pmol steroid per reaction), and 300 µM NADPH or 325 µM $NADP^+$, respectively. The curves illustrate the average of conversion ± SD in triplicates measured per time point and steroid. The initial reaction velocities (expressed as initial turnover rates) were determined from the linear phase (0-5 min) of the time curves.
AN, androsterone; A-diol, 3α,17β-androstanediol; Δ4-Ae, Δ4-androstenedione; E1, estrone; E2, 17β-estradiol; T, testosterone, $v_{0\,(20\,nM)}$, initial turnover rate using 20 nM substrate.

Finally, the Michaelis constant K_M, the maximum turnover rate k_{cat}, as well as the catalytic efficiency k_{cat}/K_M of AKR1B15.1 were determined for reactions with different steroids and acetoacetyl-CoA. For this, either activity assays with ^{3}H-labeled steroids or with unlabeled acetoacetyl-CoA were carried out using purified His_6-tagged ARK1B15.1 in concentrations of either 50 nM or 6 µM, respectively. The results are listed in Table III-3.

Here, it can be seen that AKR1B15.1 possessed the highest affinity to steroids by exhibiting K_M values for "oxidized" steroids in the low micromolar range (K_M = 1.9-2.8 µM) and 3- to 6-fold higher K_M values for the respective "reduced" steroids (K_M = 7.1-19.2 µM) [Table III-3].

These affinities were comparable with the K_M values received from activity assays with HEK-293 cells overexpressing AKR1B15.1 [data not shown]. In comparison to steroids, AKR1B15.1 showed a lower affinity to the 3-keto-acyl-CoA conjugate acetoacetyl-CoA (K_M = 63.4 µM) [Table III-3]. With either substrate, the kinetic parameters were calculated via the Michaelis-Menten equation, although a quite high enzyme concentration (6 µM) was used in activity assays with acetoacetyl-CoA. However, the assumption of a Michaelis-Menten kinetic was valid, since AKR1B15.1 exhibited a K_M value for acetoacetyl-CoA which was more than 10-fold higher compared to the enzyme concentration [263, 264].

Regarding the reaction velocity of AKR1B15.1 with different substrates it could be seen that the reduction of androgens (k_{cat} = 1.13-1.68 min^{-1}) was faster than the reduction of estrone (k_{cat} = 0.96 min^{-1}) and that generally reductive reactions were approximately 2-fold faster than the respective reverse, oxidative reaction [Table III-3]. The k_{cat} of acetoacetyl-CoA (0.49 min^{-1}) was comparable to the k_{cat} of the AKR1B15.1 steroidal substrate with the slowest turnover rate: 17β-estradiol (k_{cat} = 0.50 min^{-1}) [Table III-3]. Here it needs to be mentioned that it is assumed that, due to the purification process, only a portion of the purified enzyme was properly folded and that the actual k_{cat} was most probably much higher than the determined apparent k_{cat} listed in Table III-3.

The calculated catalytic efficiencies (k_{cat} / K_M) were in accordance with the results gained from the time course experiments [Figure III-19]. AKR1B15.1 showed the highest k_{cat} / K_M values with androsterone and Δ4-androstenedione (approx. 0.6 µM^{-1} min^{-1}), whereas the k_{cat} / K_M with 17β-estradiol (0.055 µM^{-1} min^{-1}) was only 10 % of the androgen efficiencies [Table III-3]. Acetoacetyl-CoA was the substrate with the lowest k_{cat} / K_M (0.008 µM^{-1} min^{-1}), which was only 1.3 % of the efficiency with androsterone [Table III-3].

In summary, AKR1B15.1 is a predominantly reductive enzyme showing highest enzymatic activities with androgens followed by estrogens and acetoacetyl-CoA.

Table III-3: Kinetic parameters of AKR1B15.1.

	substrate	K_M [µM]	k_{cat} [min^{-1}]	k_{cat} / K_M [µM^{-1} min^{-1}]
reductive reactions	androsterone	2.77 ± 0.13	1.68 ± 0.03	0.606
	Δ4-androstenedione	1.87 ± 0.18	1.13 ± 0.03	0.604
	DHEA	6.03 ± 0.61	2.54 ± 0.13	0.421
	estrone	2.54 ± 0.42	0.96 ± 0.06	0.378
	acetoacetyl-CoA	63.40 ± 7.40	0.49 ± 0.02	0.008
oxidative reactions	3α,17β-androstanediol	19.18 ± 2.34	3.00 ± 0.24	0.156
	testosterone	7.06 ± 1.51	0.63 ± 0.06	0.089
	17β-estradiol	9.06 ± 1.21	0.50 ± 0.03	0.055
	3-hydroxy-butyryl-CoA	n.d.	n.d.	-

Given are kinetic parameter values ± error of the fit. The values were calculated by fitting the data of activity assays to the Michaelis-Menten equation (SigmaPlot 12.0: "Hyperbola, Single Rectangular, 2 Parameter"). For this, activity assays were performed with either 50 nM purified AKR1B15.1 and ^{3}H-labeled (+ unlabeled) steroids or 6 µM purified AKR1B15.1 and acetoacetyl-CoA.
K_M, Michaelis constant; k_{cat}, maximum turnover rate; k_{cat} / K_M, catalytic efficiency; n.d., not determined.

III.1.5. DETECTION OF ENDOGENOUS AKR1B15 ISOFORMS

Chapter III.1.1.3 demonstrated that *AKR1B15* is expressed on RNA level in distinct human tissues as well as in the BeWo cell line and the SGBS cell strain. In addition, the subcellular localization studies showed that AKR1B15.1 is a mitochondrial protein whereas AKR1B15.2 is a cytosolic one [III.1.3]. To analyze whether the RNA is translated into protein *in vivo* and to verify the mitochondrial localization of AKR1B15.1 in an immunocytochemical independent manner, different approaches were performed.

III.1.5.1. WESTERN BLOTTING WITH HUMAN TOTAL TISSUE AND CELL LYSATES

In the first instance, the abundance of AKR1B15 isoforms in different total protein tissues lysates (adipose tissue, placenta, prostate, testis, skeletal muscle, and thymus) as well as total cell lysates (BeWo and SGBS) on protein level was analyzed by Western blotting. For this, the monoclonal rat-anti-AKR1B15 clone 9A5 and mouse-anti-AKR1B15.2 clone 29D4 antibody supernatants were used as primary antibodies.

The Western blots, performed with the monoclonal rat-anti-AKR1B15 clone 9A5 and mouse-anti-AKR1B15.2 clone 29D4 primary antibodies, revealed no bands via ECL detection [data not shown] but showed some more or less intense bands via the more sensitive infrared fluorescence (IR) detection, using the Licor technology [Figure III-20]. Exemplary results gained from Western blots with total tissue and cell lysates using IR-dye labeled secondary antibodies are shown in Figure III-20.

Although AKR1B15.1 and AKR1B15.2 were easily detectable when transiently overexpressed in HEK-293 cells (AKR1B15.1/15.2) by using the monoclonal rat-anti-AKR1B15 clone 9A5 and goat-anti-rat-AlexaFluor 790 antibody pair, either no protein bands or protein bands with a divergent molecular weight were visible in tissues [Figure III-20B]. Here, the overexpressed AKR1B15.1 appeared as double band possessing a more intense band at the expected 36.5 kDa and a weaker 0.5-1 kDa smaller side band. The rat-anti-AKR1B15 clone 9A5 primary antibody acted quite specifically in the HEK-293 cell background since, with the exception of one endogenous protein of approximately 45 kDa, no further endogenous protein bands were visible in HEK-293 cell samples [Figure III-20B]. No protein bands corresponding to the molecular weight of the in HEK-293 cells overexpressed, untagged AKR1B15 isoforms were detectable in tissue samples [Figure III-20B]. Adipose tissue and placenta samples revealed one to three very weak signals. Among the tissues tested, skeletal muscle showed the most prominent signals at approximately 20 kDa and 45 kDa and some weaker signals at approximately 33 kDa, 35 kDa, and 42 kDa. The 20 kDa band, which is far from the expected molecular weight of the AKR1B15 isoforms, could be found in both placenta and skeletal muscle samples [Figure III-20B]. In contrast, the approximately 35 kDa and 45 kDa bands in the skeletal muscle sample were also visible in the control blot (without primary antibody) and negative control (HEK-293), respectively, and thus seemed unlikely to correspond to an AKR1B15 protein band [Figure III-20A, B].

The monoclonal mouse-anti-AKR1B15.2 clone 29D4 and IRDye 800CW goat-anti-mouse antibody pair which should specifically detect the longer AKR1B15.2 isoform recognized, beside the overexpressed AKR1B15.2 (approx. 40 kDa), several endogenous proteins in both tissue lysates and HEK-293 cell lysates [Figure III-20C]. Some of these signals were also present in the blots detected via the monoclonal rat-anti-AKR1B15 clone 9A5 antibody and secondary goat-anti-rat-AlexaFluor 790 antibody pair but also in the IRDye 800CW goat-anti-mouse antibody control blot (without primary antibody) and differed from the expected molecular weight for AKR1B15.2 [Figure III-20B, C, D].

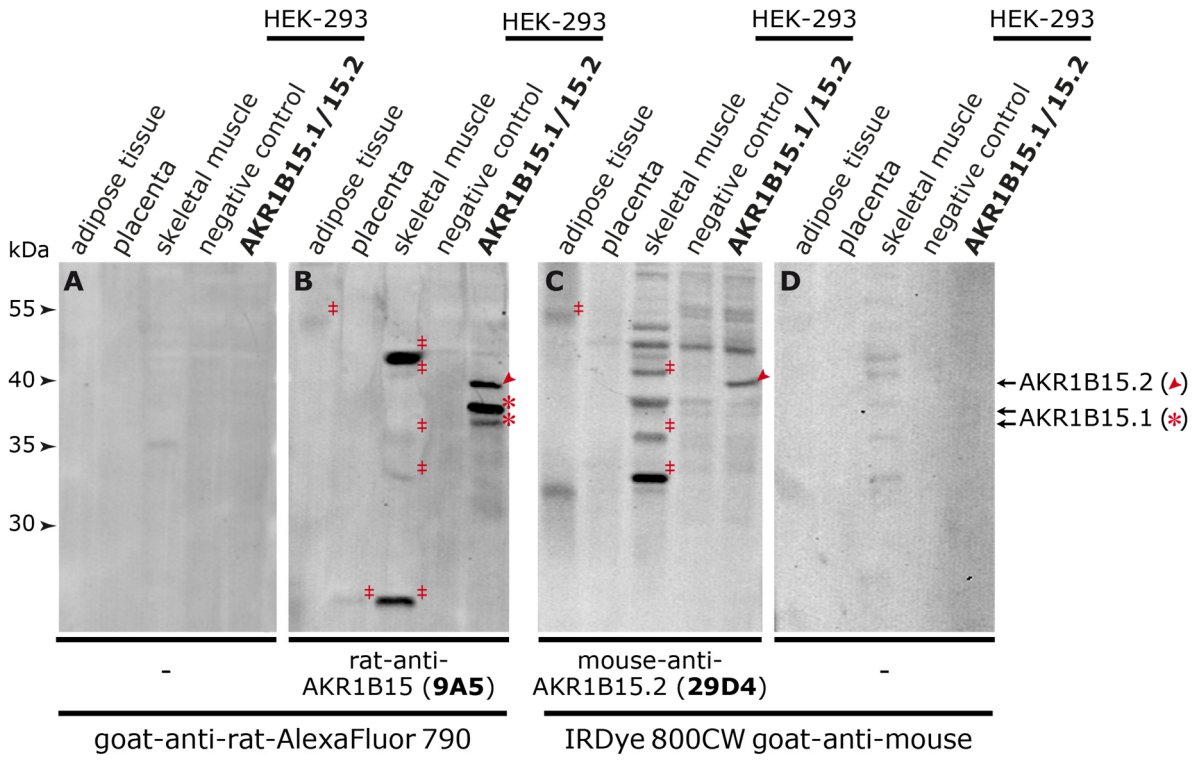

Figure III-20: The existence of endogenous AKR1B15 isoforms *in vivo* can only be speculated by Western blot analysis of total human tissue samples.
Shown are exemplary Western blots for the detection of endogenous AKR1B15 isoforms in human tissue samples. The Western blots were performed with total tissue lysate samples of human adipose tissue, placenta, and skeletal muscle. Lysates of non-transfected HEK-293 cells (negative control) and a mixture of HEK-293 cells transiently transfected with either pcDNA3.1-AKR1B15.1 or pcDNA3.1-AKR1B15.2 (AKR1B15.1/15.2) served as negative and positive controls, respectively. **(A, D)** Controls without primary antibody for the identification of nonspecific secondary antibody signals. The control membranes were only incubated in the respective secondary antibody dilution: goat-anti-rat-AlexaFluor 790 (1:200000) **(A)** or IRDye 800CW goat-anti-mouse (1:20000) **(D)**. **(B, C)** Membranes incubated with primary and secondary antibodies for the detection of endogenous AKR1B15 isoforms. For the detection of both AKR1B15 isoforms, the membranes were stained via the monoclonal rat-anti-AKR1B15 clone 9A5 primary antibody dilution (1:25) and the respective goat-anti-rat-AlexaFluor 790 secondary antibody dilution (1:200000) **(B)**. The longer AKR1B15.2 was selectively detected by the monoclonal mouse-anti-AKR1B15.2 clone 29D4 primary (1:25 diluted) and the IRDye 800CW goat-anti-mouse secondary antibody (1:20000 diluted) pair **(C)**.
Protein bands which possibly resulted from endogenous AKR1B15 isoforms are marked by double daggers; overexpressed AKR1B15.1 and AKR1B15.2 protein bands are marked by stars and arrow heads, respectively.

So far, none of the protein bands resulting from the Western blots with the monoclonal rat-anti-AKR1B15 clone 9A5 and mouse-anti-AKR1B15.2 clone 29D4 antibodies could have been directly assigned to the AKR1B15 isoforms in total tissue and cell lysates because none of the detected signals did accord with the theoretical molecular weight of AKR1B15.1 or AKR1B15.2 and the signals of the overexpressed AKR1B15 isoforms [Figure III-20, data not shown]. However, due to the high specificity of the monoclonal rat-anti-AKR1B15 clone 9A5 antibody and the assumption that the antibodies were simply not sensitive enough to detect endogenous AKR1B15 isoforms in the crowded environment of total tissue lysates, the rat-anti-AKR1B15 clone 9A5 antibody was further used in Western blots with enriched samples.

III.1.5.2. Prediction of post-translational modification sites in AKR1B15 isoforms

Since it was not possible to ambiguously detect endogenous AKR1B15 isoforms in human total tissue or cell lysates, both AKR1B15 isoform sequences were analyzed *in silico* for sites of post-translational modifications, perhaps preventing or diminishing the binding of antibodies or shifting the molecular weight of the endogenous isoforms.

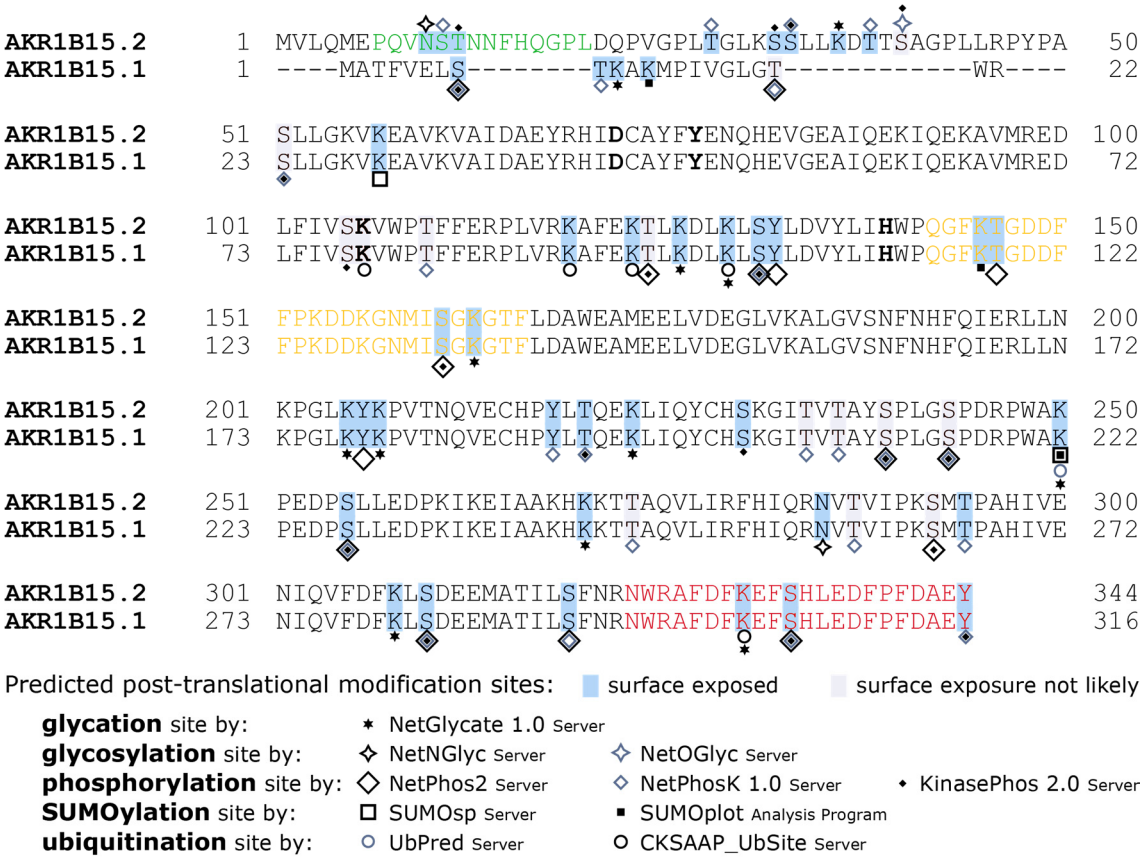

Figure III-21: Several post-translational modification sites are predicted in AKR1B15 isoforms.
Summarized are the results from *in silico* predictions of post-translational modification sites in AKR1B15 isoforms.
Please note that the prediction of residues which are surface exposed is based on the structure of the highly related AKR1B10. Residues of the catalytic tetrad are highlighted in bold. The epitopes targeted by AKB-1, AKB-2, and AKB-3 antibodies are colored in green, yellow, and red, respectively.

Here it was found that various phosphorylation sites as well as some glycation, SUMOylation, and ubiquitination sites are predicted for the AKR1B15 isoforms [Figure III-21]. Although predicted, a glycosylation of the proteins seems unlikely since no signal peptide for ER or Golgi apparatus import was detectable in any of both isoforms. In addition, no sulfation site was predicted by the Sulfinator server (ExPASy). Based on the structure of the highly identical AKR1B10, a portion of the predicted post-translational modification sites do not face the surface, e.g., the catalytic Lys106 and Lys78 in AKR1B15.2 and AKR1B15.1, respectively [Figure III-21, highlighted in bright gray]. Thus, these sites represent most probably false positive predictions. However, some predicted sites are located within the epitopes targeted by the generated antibodies and might prevent the binding of antibodies to the AKR1B15 isoforms. Yet, the presence of post-translational modifications within the endogenous AKR1B15 isoforms needs to be analyzed by molecular biological methods in the future.

III.1.5.3. Western blotting with enriched mitochondria from BeWo cell line

Despite the fact that the rat-anti-AKR1B15 clone 9A5 antibody was not very useful for the detection of endogenous AKR1B15 isoforms in total cell or tissue lysates (probably due to a limited sensitivity), it was also used in Western blots with enriched mitochondria which were isolated from BeWo cell line cultures. These Western blots pursued more or less two objectives: Primary, the detection of endogenous AKR1B15 isoforms in enriched fractions and secondary, the verification of the mitochondrial subcellular localization of AKR1B15.1.

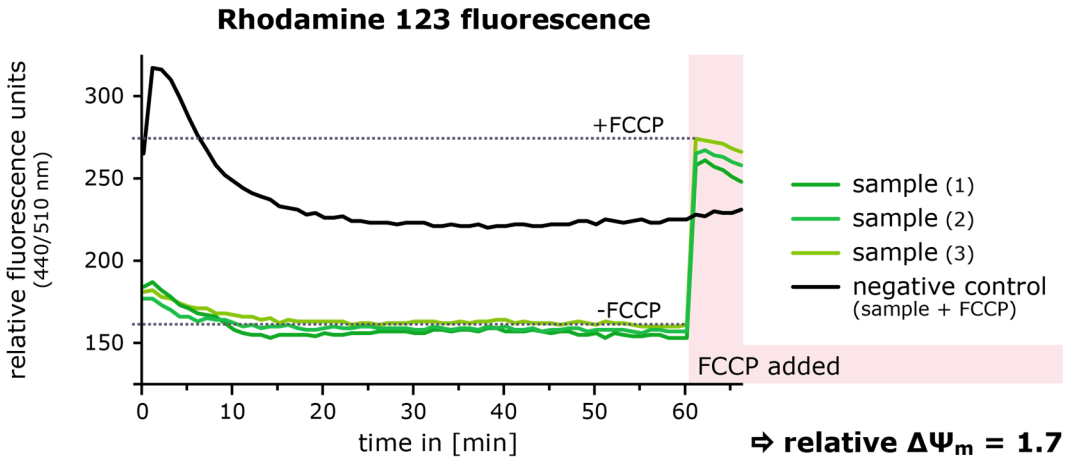

Figure III-22: The procedure for the isolation of mitochondria from BeWo cell line cultures yielded sound mitochondria.
Shown are exemplary Rhodamine 123 fluorescence time curves for the determination of the integrity of isolated BeWo mitochondria via the relative membrane potential $\Delta\Psi_m$.
The relative membrane potential of 50 ng isolated mitochondria (protein mass) was calculated according to Equation II-4 from the intensity of Rhodamine 123 fluorescence prior (-FCCP) and after (+FCCP) the decoupling of the respiratory chain by the addition of FCCP in technical triplicates. Immediate addition of FCCP at the beginning of the measurements served as negative control.
FCCP, carbonyl cyanide-4-(trifluoromethoxy)-phenylhydrazone.

Five confluent cultures in 75 cm^2 culture flasks were required to harvest a total number of $2x10^7$ BeWo cells, which were needed per isolation batch. The procedure described in II.3.4 resulted in a mitochondrial fraction of 360 µg protein per $2x10^7$ BeWo cells. The integrity of the mitochondrial fraction was analyzed via the membrane potential of intact mitochondria using Rhodamine 123 fluorescence quenching. Figure III-22 illustrates that the mitochondrial fraction (9000x*g* pellet) contained intact mitochondria with sufficient purity by showing a relative membrane potential $\Delta\Psi_m$ of 1.7.

Western blots with the 800x*g* and 9000x*g* pellets, resulting from the isolation of mitochondria from BeWo cells, demonstrated the endogenous existence of AKR1B15.1 and AKR1B15.2 on protein level in the BeWo cell line [Figure III-23]. Here, both AKR1B15 isoforms could be detected in the 800x*g* pellet (including nuclei, unbroken cells, and cell debris) as well as the 9000x*g* pellet (including mitochondria) by using the monoclonal rat-anti-AKR1B15 clone 9A5 supernatant and the polyclonal goat-anti-rat-AlexaFluor 790 antibody as primary and secondary antibody, respectively [Figure III-23B].

As a result, both *AKR1B15* transcripts, *AKR1B15.1* and *AKR1B15.2*, are translated into low amounts of protein *in vivo* since weak protein bands were detected in Western blots with BeWo cell fractions. The fact that both AKR1B15 isoforms were only visible in enriched fractions but not in total protein tissue lysate could be explained by a poor expression of *AKR1B15*, which was also seen on RNA level [III.1.1.3], and a reduced sensitivity of the monoclonal antibodies due to possible post-translational modifications at the epitope sites.

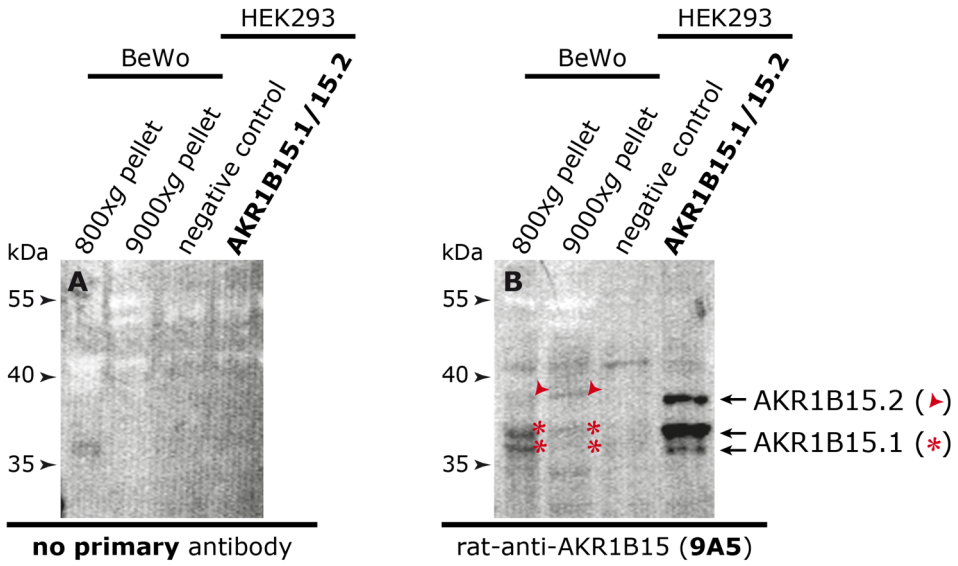

Figure III-23: Endogenous AKR1B15.1 and AKR1B15.2 could be detected in BeWo cell fractions.
Shown are Western blots for the detection of endogenous AKR1B15 isoforms. The Western blots were carried out with fractions (800x*g* and 9000x*g* pellets) resulting from the isolation of mitochondria from BeWo cells. Lysates of non-transfected HEK-293 cells (negative control) and a mixture of HEK-293 cells transiently transfected with pcDNA3.1-AKR1B15.1 or pcDNA3.1-AKR1B15.2 (AKR1B15.1/15.2) served as negative and positive control, respectively. Membranes were stained using either only the goat-anti-rat-AlexaFluor 790 secondary antibody in a final dilution of 1:200000 **(A)** or the monoclonal rat-anti-AKR1B15 clone 9A5 primary (1:25 diluted) and goat-anti-rat-AlexaFluor 790 secondary antibody (1:200000 diluted) pair **(B)**.

III.1.6. PROPERTIES OF THE AKR1B15.1 S8R MUTANT

In 2012, Calvo *et al.* presented that a mutation in the *AKR1B15* gene was linked to an *in utero* lethal mitochondrial phenotype with impaired complex I function [265]. The authors reported that a T→G substitution would be responsible for an exchange of arginine to serine at position 8 of the AKR1B15.1 isoform leading to the AKR1B15.1 S8R mutant.

To investigate how this mutation could explain the lethal phenotype, the subcellular localization and the enzymatic activity of the AKR1B15.1 S8R mutant were determined. In immunocytochemical subcellular localization studies on HeLa cells overexpressing N- and C-terminally myc-tagged as well as untagged full length AKR1B15.1 S8R it was seen that the AKR1B15.1 S8R mutant showed subcellular localizations comparable with the wild type enzyme: N-terminally myc-tagged AKR1B15.1 S8R localized to the cytosol, whereas the C-terminally myc-tagged as well as the untagged protein colocalized with mitochondria [Figure III-24, data not shown]. In addition, no huge differences between wild type and mutant AKR1B15.1 were seen in the predictions resulting from the *in silico* analysis on the subcellular localizations of the proteins [VI.5].

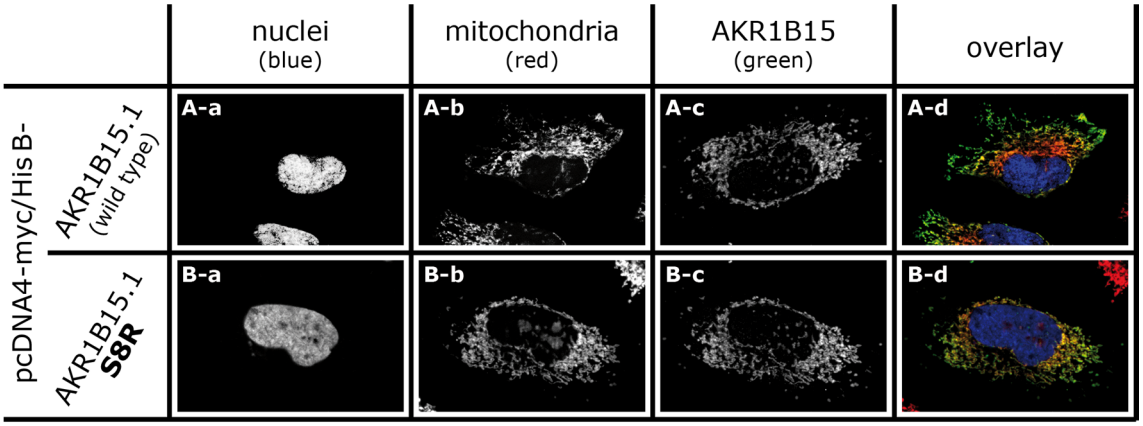

Figure III-24: Immunocytochemical studies revealed no differences in the subcellular localization of the AKR1B15.1 S8R mutant and the wild type enzyme.
Shown are exemplary results from subcellular localization studies with C-terminally myc-tagged AKR1B15.1 and AKR1B15.1 S8R proteins. HeLa cells were transiently transfected with either pcDNA4-myc/His B-AKR1B15.1 **(A)** or pcDNA4-myc/His B-AKR1B15.1 S8R **(B)** in order to express C-terminally myc-tagged wild type AKR1B15.1 or mutant AKR1B15.1 S8R, respectively. Nuclei were stained using Hoechst 33342 dye **(a)**; mitochondria were vital-stained using MitoTracker Orange CMTMRos **(b)**; myc-tagged AKR1B15 isoforms were stained using mouse-anti-myc / AlexaFluor 488 goat-anti-mouse antibodies **(c)**. The overlay of individual stains **(d)** shows nuclei in blue, counterstains in red, AKR1B15 in green, and colocalization in yellow.

Initial activity assays using HEK-293 cells overexpressing differently tagged AKR1B15.1 or AKR1B15.1 S8R proteins (N- and C-terminally myc-tagged or untagged proteins) with the ^{3}H-labeled steroids estrone and Δ4-androstenedione as substrates indicated no differences in enzymatic activities between the wild type and the mutant enzyme [data not shown]. To verify the indicated equivalent enzymatic properties of AKR1B15.1 and AKR1B15.1 S8R, Michaelis-Menten kinetics for the comparison of Michaelis constants K_M for estrogens were

performed. The enzymatic reactions were conducted with HEK-293 cells overexpressing either untagged wild type AKR1B15.1 or untagged mutant AKR1B15.1 S8R (after transient transfection with pcDNA3.1(+)-AKR1B15.1 or pcDNA3.1(+)-AKR1B15.1(S8R), respectively), the respective ^{3}H-labeled (+ unlabeled) estrogen as well as the appropriate cofactor. Here, both enzymes, the wild type AKR1B15.1 and the mutant AKR1B15.1 S8R, revealed similar K_M values for the reduction of estrone (2.9 µM and 3 µM, respectively) and comparable K_M values for the oxidation of 17β-estradiol (6.6 µM and 9.3 µM, respectively) [Figure III-25].

Thus, since the mutant AKR1B15.1 S8R also colocalizes with mitochondria and possesses enzymatic activities which are comparable with the wild type AKR1B15.1 enzyme, the lethal mitochondrial phenotype of the AKR1B15.1 S8R mutant [265] cannot be explained by an altered subcellular localization or enzymatic activity, as hypothesized in the beginning.

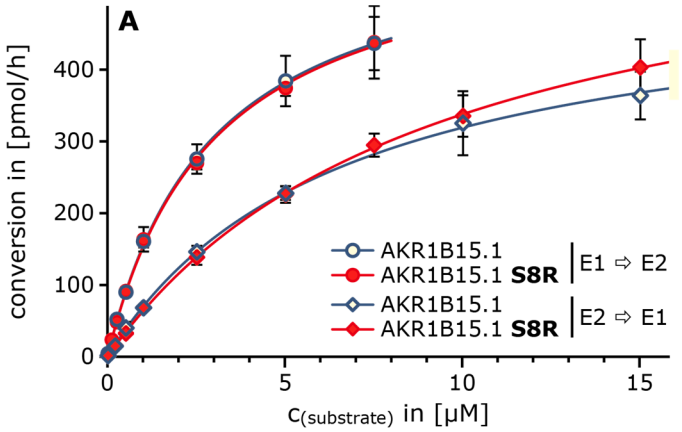

B

	K_M in [µM]
estrone (E1):	
AKR1B15.1	2.9
AKR1B15.1 **S8R**	3.0
estradiol (E2):	
AKR1B15.1	6.6
AKR1B15.1 **S8R**	9.3

Figure III-25: Enzymatic activity assays revealed that the enzymatic activity of the AKR1B15.1 S8R mutant is comparable with that of the wild type AKR1B15.1.
Michaelis-Menten kinetics were used for the comparison of enzymatic activities of the wild type AKR1B15.1 and the AKR1B15.1 S8R mutant. The reactions contained 10^6 HEK-293 cells transiently transfected with either pcDNA3.1-AKR1B15.1 or pcDNA3.1-AKR1B15.1 S8R (overexpressing untagged wild type AKR1B15.1 or untagged mutant AKR1B15.1 S8R, respectively), 20 nM ^{3}H-labeled steroid and up to 15 µM unlabeled steroid, as well as 300-325 µM NADP(H).
(A) Shown are the average reduction ± SD of estrone (circles) and oxidation ± SD of 17β-estradiol (diamonds) by the wild type AKR1B15.1 (blue symbols and lines) and the mutant AKR1B15.1 S8R (red symbols and lines) in reaction triplicates blotted against the steroid concentration and the respective curves of the Michaelis-Menten fit. **(B)** Determined K_M values of AKR1B15.1 and AKR1B15.1 S8R for estrone and 17β-estradiol. The K_M values were calculated from the average conversion of estrogens via Michaelis-Menten fit ("Hyperbola, Single Rectangular, 2 Parameter") using the SigmaPlot 12.0 software.
E1, estrone; E2, 17β-estradiol; K_M, Michaelis constant.

III.1.7. Generation of TALENs for AKR1B15 knock-outs in cell lines/strains via TALEN technology

A gene knock-out is a good tool to get an idea of the role of gene products with unknown or unclear function *in vivo*. In order to elucidate the physiological role of the AKR1B15 isoforms, the genome editing Transcription Activator-Like Effector Nucleases (TALEN) technology

should be applied for the selective knock-out of AKR1B15 in different cell lines/strains (e.g., BeWo or SGBS cells), followed by the analysis of the resulting phenotype. For this, diverse preparatory work was necessary to provide functional TALENs and pre-selection tools.

III.1.7.1. Design and cloning of TALENs

TALENs effecting the expression of AKR1B15.1, AKR1B15.2, or both AKR1B15 isoforms on protein level were designed by the TAL effector Nucleotide Targeter 2.0 algorithm, using the settings described in II.9.1. Since the N-terminal sequences of AKR1B15.1 and AKR1B15.2 are encoded by different exons, the diverging exons (exon 1 of *AKR1B15.1* and exon 3 of *AKR1B15.2*; see also Figure III-1 and VI.4) were used as input sequences for the selective knock-out of the respective AKR1B15 isoform. In contrast, the first common exon of the *AKR1B15.1* and *AKR1B15.2* transcripts (exon 2 and exon 4, respectively) was selected as input sequence for the simultaneous knock-out of both AKR1B15 isoforms. These selections were made by assuming that frameshifts in the translated exons of the *AKR1B15* variants, which might occur due to an incorrect repair of the genomic double-strand break caused by functional TALENs, lead to non-functional proteins. The detailed results from the design of the respective TALENs are listed in VI.6.

The cloning of TALEN effector plasmids was initially performed according to a protocol (Golden_Gate_TALEN_assembly _v5.doc) established at the Voytas lab and provided by Addgene. Since this procedure did not yield any positive clones after the first cloning step, the protocol was optimized within this thesis. Following the modified protocol (see II.9.2), all RVD sequences listed in the appendix [VI.6] could be cloned into pcGoldyTALEN target vectors, resulting in the respective effector plasmids listed in Table III-4.

In order to the identify and enrich cells transiently co-transfected with both TALEN effector plasmids and thus ease the preselection of cells with a potential AKR1B15 knock-out, beside the unmodified effector plasmids encoding for the appropriate RVD sequences fused to the *Fok*I nuclease, effector plasmids encoding additionally for a selection marker (either the fluorescent proteins AcGFP or DsRed or the cell surface protein ΔLNGFR) under the control of a CMV promoter should be generated [Table III-4]. The cloning of these selection markers into the target vector pcGoldyTALEN or the effector plasmids pcGoldyTALEN-AKR1B15-E2(26)_TAL1 and _TAL2 was quite difficult and did not result in positive clones using the *Afl*III/*Afl*II or *Afl*III/*Bgl*II restriction sites and a conventional cloning procedure [data not shown]. The same was true for applying the In-Fusion cloning kit method at the *Afl*III restriction site [data not shown]. However, using the *Dra*III restriction site for the cloning of selection marker via the In-Fusion technology, positive clones were received for the target vector pcGoldyTALEN-AcGFP (but not for pcGoldyTALEN-DsRed) as well as for the effector plasmids pcGoldyTALEN-AcGFP-AKR1B15-E2(26)_TAL1, pcGoldyTALEN-DsRed-AKR1B15-E2(26)_TAL2, and pcGoldyTALEN-ΔLNGFR-AKR1B15-E2(26)_TAL2. Thus, four out of five selection marker containing constructs were successfully cloned.

Here, it needs to be mentioned that a generation of the pcGoldyTALEN-ΔLNGFR target vector was not reasonable because the ΔLNFGR selection marker insert possesses multiple *Bsm*BI restriction sites destroying the modified target vector within the second cloning step (Golden Gate Reaction #2) of the TALEN assembly.

Table III-4: Generated TALEN effector plasmids for the (selective) knock-out of either AKR1B15.1 (1B15.1), AKR1B15.2 (1B15.2), or both AKR1B15 isoforms (1B15).

TALEN target	effector plasmid	selection marker
AKR1B15.2 (1B15.2)	pcGoldyTALEN-**AKR1B15.2(66)_TAL1**	-
	pcGoldyTALEN-**AKR1B15.2(66)_TAL2**	-
	pcGoldyTALEN-**AKR1B15.2(67)_TAL1**	-
	pcGoldyTALEN-**AKR1B15.2(67)_TAL2**	-
AKR1B15.1 (1B15.1)	pcGoldyTALEN-**AKR1B15.1(36)_TAL1**	-
	pcGoldyTALEN-**AKR1B15.1(36)_TAL2**	-
	pcGoldyTALEN-**AKR1B15.1(40)_TAL1**	-
	pcGoldyTALEN-**AKR1B15.1(40)_TAL2**	-
AKR1B15 (1B15)	pcGoldyTALEN-**AKR1B15-E2(25)_TAL1**	-
	pcGoldyTALEN-**AKR1B15-E2(25)_TAL2**	-
	pcGoldyTALEN-**AKR1B15-E2(26)_TAL1**	-
	pcGoldyTALEN-ΔLNGFR-**AKR1B15-E2(26)_TAL1**	ΔLNGFR
	pcGoldyTALEN-AcGFP-**AKR1B15-E2(26)_TAL1**	AcGFP
	pcGoldyTALEN-**AKR1B15-E2(26)_TAL2**	-
	pcGoldyTALEN-DsRed-**AKR1B15-E2(26)_TAL2**	DsRed

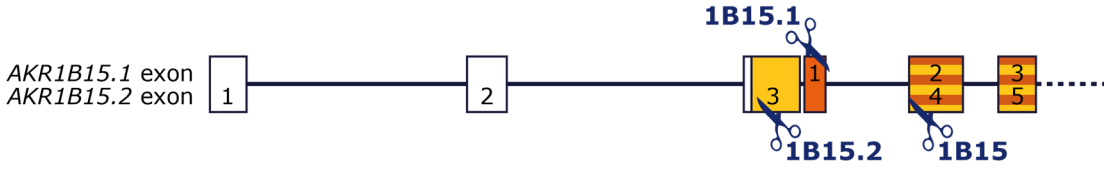

The image shows the approximate location of the TALEN target site (scissors) within the schematic intron-exon structure of *AKR1B15*. Alternative exons encoding for AKR1B15.1 and AKR1B15.2 are colored in orange and yellow, respectively, and common exons in orange-yellow striped pattern.

III.1.7.2. Analysis of AKR1B15 TALEN efficiencies

After the successful cloning of AKR1B15 TALEN constructs, the TALEN pairs were tested for their efficiency using a β-galactosidase reporter system as described in II.9.4. This system uses pCMV-Duplirep reporter plasmids for the determination of TALEN efficiencies. The reporter plasmids carry the coding sequences for both an inactive truncated (Met1-Leu135) and an active complete β-galactosidase which are separated by the respective TALEN or ZFN target sequence. Because of the stop codon downstream the sequence encoding for the N-terminal β-galactosidase fragment, only the inactive protein fragment was made in the original Duplirep plasmids. However, upon homologous recombination due to DNA double-strand breaks via efficient TALEN or ZFN pairs the stop codon is eliminated and the coding sequence for the active whole β-galactosidase is expressed. Hence, the β-galactosidase activity in cell lysates can be used as read-out for the occurrence of double-strand breaks due to dimerized nucleases (*Fok*I or ZFN) and thus for the determination of the TALEN or ZFN efficiency. Besides, the co-transfection of pCMV-hLuci, expressing a humanized luciferase, permits to normalize the determined β-galactosidase activity for the cell number and transfection efficiency via the respective luciferase expression level which is reflected in luciferase activity. The TALEN efficiency is expressed as ratio between

the β-galactosidase luminescence (normalized by the luciferase luminescence) in samples with cell lysates transiently transfected with a TALEN pair in addition to the appropriate pCMV-Duplirep reporter plasmid and the β-galactosidase luminescence (normalized by the luciferase luminescence) in the respective negative control, not including any TALEN pair.

Within the initial analysis of TALEN efficiencies all TALEN pairs not carrying a selection marker on the effector plasmid were tested by the use of different transfection methods (Lipofectamine 3000, ViaFect, and electroporation). Although the overall results were comparable between all transfection methods applied, most of the HEK-293 cells died during the electroporation process [data not shown]. Cells lipofected with either Lipofectamine 3000 or ViaFect did not differ significantly in their cell viability and luminescence signal intensities [data not shown]. Concerning the efficiency of TALEN pairs it was seen that all TALEN pairs targeting exon 1 of *AKR1B15.1* (AKR1B15.1(36) and AKR1B15.1(40)) or exon 3 of *AKR1B15.2* (AKR1B15.2(66) and AKR1B15.2(67)) [Table III-4] did not reveal sufficient efficiencies [data not shown]. In contrast, the TALEN pairs designed for the knock-out of both AKR1B15 isoforms (AKR1B15-E2(25) and AKR1B15-E2(26)) by binding to exon 2 and exon 4 of *AKR1B15.1* and *AKR1B15.2*, respectively, possessed very good efficiencies, which exceeded that determined for an approved ZFN pair (pCAG-Rab-ZFN effector plasmid pair) serving as positive control [data not shown]. No difference in TALEN efficiency could be detected between TALEN pairs targeting the same region of the *AKR1B15* gene [data not shown]. This was not surprising since these TALEN pairs bind to almost identical DNA sequences, merely shifted by one to two bases [VI.6].

A second analysis of TALEN efficiencies [Figure III-26], this time using only the ViaFect transfection reagent (because of the easier handling compared with Lipofectamine 3000) and selected TALEN effector plasmid pairs with or without selection marker [Table III-4], verified the results received within the initial analyses.

Like in the initial tests, the TALEN pairs AKR1B15.1(40) or AKR1B15.2(67), designed for the knock-out of either AKR1B15.1 or AKR1B15.2, showed only low efficiencies by possessing +TALEN/-TALEN (+/-) ratios of 1.9 or 2.9, respectively [Figure III-26C, D]. In contrast, the efficiencies of the TALEN pairs targeting the first common exon of *AKR1B15.1* and *AKR1B15.2* (AKR1B15-E2(26)) revealed good efficiencies (+/- ratios of 16.7, 56.8, or 74.2) and exceeded again the efficiency of the pCAG-Rab-ZFN pair positive control (+/- ratio of 8.2). Due to the higher normalized β-galactosidase luminescence (expressed as β-galactosidase/ luciferase luminescence ratio), the expression of pcGoldyTALEN-AKR1B15-E2(26) TALEN pair plasmids also encoding for selection markers (ΔLNGFR / DsRed or AcGFP / DsRed) seemed to possess higher efficiencies when compared with the plasmids encoding for the TALEN pair only [Figure III-26C, D]. However, looking at the raw values of luciferase and β-galactosidase luminescence [Figure III-26A, B] it can easily be seen that the higher efficiencies resulted from the normalization of the β-galactosidase signals by the respective luciferase signals. Here, the additional expression of selection markers was associated with a strong decrease in luciferase luminescence, whereas the β-galactosidase luminescence intensities remained quite constant. The drop in luciferase luminescence intensities could be explained by reduced luciferase expression levels in samples containing selection marker modified pcGoldyTALEN-AKR1B15-E2(26) TALEN pairs due to the higher number of CMV promoters (six instead of four), the cell machinery had to deal with.

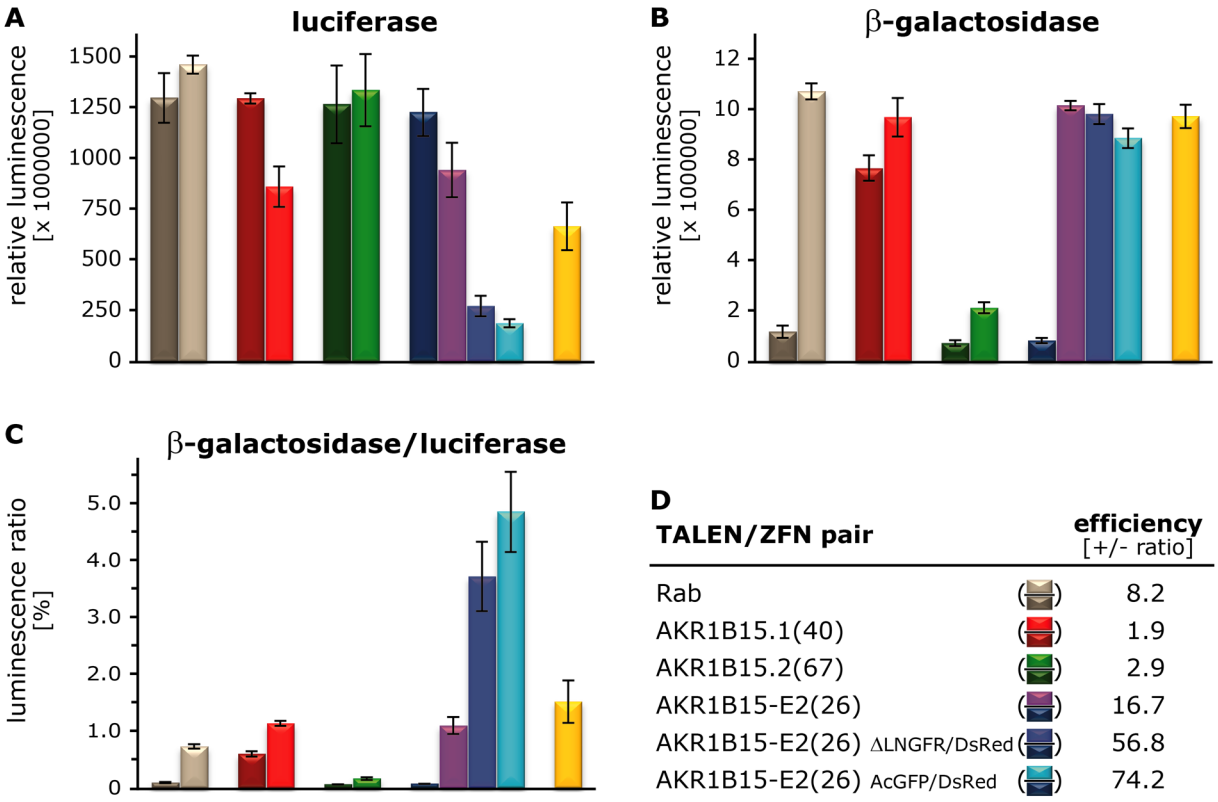

D

TALEN/ZFN pair	efficiency [+/- ratio]
Rab	8.2
AKR1B15.1(40)	1.9
AKR1B15.2(67)	2.9
AKR1B15-E2(26)	16.7
AKR1B15-E2(26) ΔLNGFR/DsRed	56.8
AKR1B15-E2(26) AcGFP/DsRed	74.2

E

pCMV-Duplirep	pcGoldyTALEN- (TAL) or pCAG- (ZFN) pair	pCMV-	control
Rab:	-	hLuci	neg
Rab:	Rab-ZFN-A + Rab-ZFN-B	hLuci	(pos)
AKR1B15.1:	-	hLuci	neg
AKR1B15.1:	AKR1B15.1(40)_TAL1 + AKR1B15.1(40)_TAL2	hLuci	-
AKR1B15.2:	-	hLuci	neg
AKR1B15.2:	AKR1B15.2(67)_TAL1 + AKR1B15.2(67)_TAL2	hLuci	-
AKR1B15-E2:	-	hLuci	neg
AKR1B15-E2:	AKR1B15-E2(26)_TAL1 + AKR1B15-E2(26)_TAL2	hLuci	-
AKR1B15-E2:	ΔLNGFR-AKR1B15-E2(26)_TAL1 + DsRed-AKR1B15-E2(26)_TAL2	hLuci	-
AKR1B15-E2:	AcGFP-AKR1B15-E2(26)_TAL1 + DsRed-AKR1B15-E2(26)_TAL2	hLuci	-
-	-	hLuci + βGal	pos

Figure III-26: The AKR1B15-E2(26) TALEN pairs designed for the simultaneous knock-out of both AKR1B15 isoforms possess good TALEN efficiencies, whereas the efficiencies of TALEN pairs for the isoform specific knock-outs are insufficient.

The efficiencies of AKR1B15 TALEN pairs were determined via the level of active β-galactosidase and luciferase expression. For this, HEK-293 cells were transiently transfected via ViaFect with different plasmid combinations and analyzed as described in II.9.4.2 and II.9.4.3, respectively.

(A) Luciferase activity in samples. Illustrated are average relative luciferase luminescence ± SD in combined lysates of equally transfected cells, which were used for the normalization of β-galactosidase signals. **(B)** β-galactosidase activity in samples. Illustrated are relative β-galactosidase luminescence ± SD in combined lysates of equally transfected cells, which were used as read-out for the occurrence of DNA double-strand breaks. **(C)** Normalized β-galactosidase activities (expressed as β-galactosidase/luciferase luminescence ratios) in samples. Shown are the average luminescence ratios ± SD of equally transfected lysates. **(D)** Efficiencies of AKR1B15 TALEN pairs. Listed are the calculated efficiencies (+/- ratios) of AKR1B15 TALEN pairs and the Rab reporter system, which were calculated from the normalized β-galactosidase activities. For this, the luminescence ratios of lysates expressing TALEN or ZFN pairs (+) were divided by the luminescence ratios of the respective negative controls (-). **(E)** Assignment of luminescence results and summary of transfected plasmids per sample for the determination of TALEN efficiencies. Samples not co-transfected with TALEN or ZFN pairs served as negative controls (neg) and samples transfected with pCMV-βGal served as positive control (pos), whereas the pCAG-Rab-ZFN pair served as positive control for nuclease efficiency ((pos)).

III.1.7.3. ENRICHMENT OF CELLS VIA *ΔLNGFR* EXPRESSION

This thesis dealt with the preparatory work necessary for the preselection of cells, based on the BeWo cell line or SGBS cell strain, with potential AKR1B15 knock-outs in future. Beside the generation of efficient TALENs, this preparatory work included also the evaluation of the selection marker ΔLNGFR for the preselection of transiently transfected cells. Here, it should be analyzed if the overexpression of the surface protein domain of the low-affinity nerve growth factor receptor (ΔLNGFR) from CMV-*ΔLNGFR* modified pcGoldyTALEN effector plasmids, like the pcGoldyTALEN-ΔLNGFR-AKR1B15-E2(26)_TAL1, is a potent tool for the enrichment of cells, which were transiently transfected with ΔLNGFR encoding plasmids, via the MACSelect LNGFR system.

In a first step, BeWo and SGBS cells were analyzed on RNA level for the endogenous expression of the *LNGFR* gene, encoding for the full length low-affinity nerve growth factor (LNGFR), which would if translated into protein interfere with the enrichment of transfected cells via MACS sorting.

For this, semi-quantitative RT-PCR using an endogenous *LNGFR* specific primer pair was performed on total RNA samples, isolated from BeWo and SGBS cells as well as placenta and adipose tissue. Because *LNGFR* is expressed in brain, total brain RNA served as positive control. Figure III-27 shows that *LNGFR* was expressed at similar levels in the three total tissue samples. In contrast, the *LNGFR* expression in the BeWo cell line was clearly reduced and not detectable in the SGBS cell strain, although comparable total RNA amounts were analyzed.

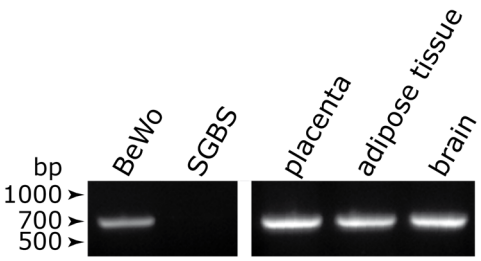

Figure III-27: The BeWo cell line, but not the SGBS cell strain, shows endogenous *LNGFR* expression.
The endogenous expression of *LNGFR* in cell lines/strains and tissues was analyzed by semi-quantitative RT-PCR, using 50 ng cDNA and a primer pair (# 2853 + # 2854) specific for the amplification of full length *LNGFR* transcripts.

Because it was seen that *LNGFR* was expressed in the BeWo cell line *in vivo*, it was analyzed whether this endogenous background expression would impair the enrichment of transfected BeWo cells via MACS selection. For this, BeWo cells were co-transfected with either pCMV DsRed-Express2 and pAcGFP-N1 **(2)**, pMACS-ΔLNGFR and pAcGFP-N1 **(3)**, or pcGoldyTALEN-ΔLNGFR-AKR1B15-E2(26)_TAL1 and pAcGFP-N1 **(4)**. Non-transfected BeWo cells **(1)** served as negative control. The cells were cultured for two days before BeWo cells expressing the surface protein domain of the low-affinity nerve growth factor receptor on protein level were enriched via the MACSelect LNGFR system.

Prior to the selection, transfection and co-transfection efficiencies were estimated from the portion of cells showing AcGFP fluorescence **(2-4)** and both DsRed as well as AcGFP fluorescence **(2)**, respectively. Here it was seen that only approximately 10-15 % of the BeWo cells were successfully transfected with pAcGFP-N1 and 7-10 % were co-transfected with pCMV DsRed-Express2 and pAcGFP-N1. These low transfection efficiencies were in accord with previous transfection studies using the BeWo cell line [data not shown].

The efficiency of MACS selection was primarily analyzed by cell counting. The determination of BeWo cell numbers in the fractions resulting from the MACSelect LNGFR selection showed that BeWo cells transiently transfected with ΔLNGFR encoding plasmids **(3, 4)** could be significantly enriched by a factor of three to four when compared with non-transfected cells **(1)** or cells transiently transfected with pCMV DsRed-Express2 and pAcGFP-N1 **(2)** via this selection/enrichment process [Figure III-28A]. Thereby, the total number of detached cells (total) was in general echoed by the sum of cells counted in the flow-through (FT), the combined wash, and the enriched fractions. It was possible to subculture MACSelect LNGFR enriched BeWo cells. However, since a large number of dead cells floated in the medium the day after selection and the number of selected cells was only approximately doubled after seven days [Figure III-28A], the subcultivation was linked to quite high cell deficits.

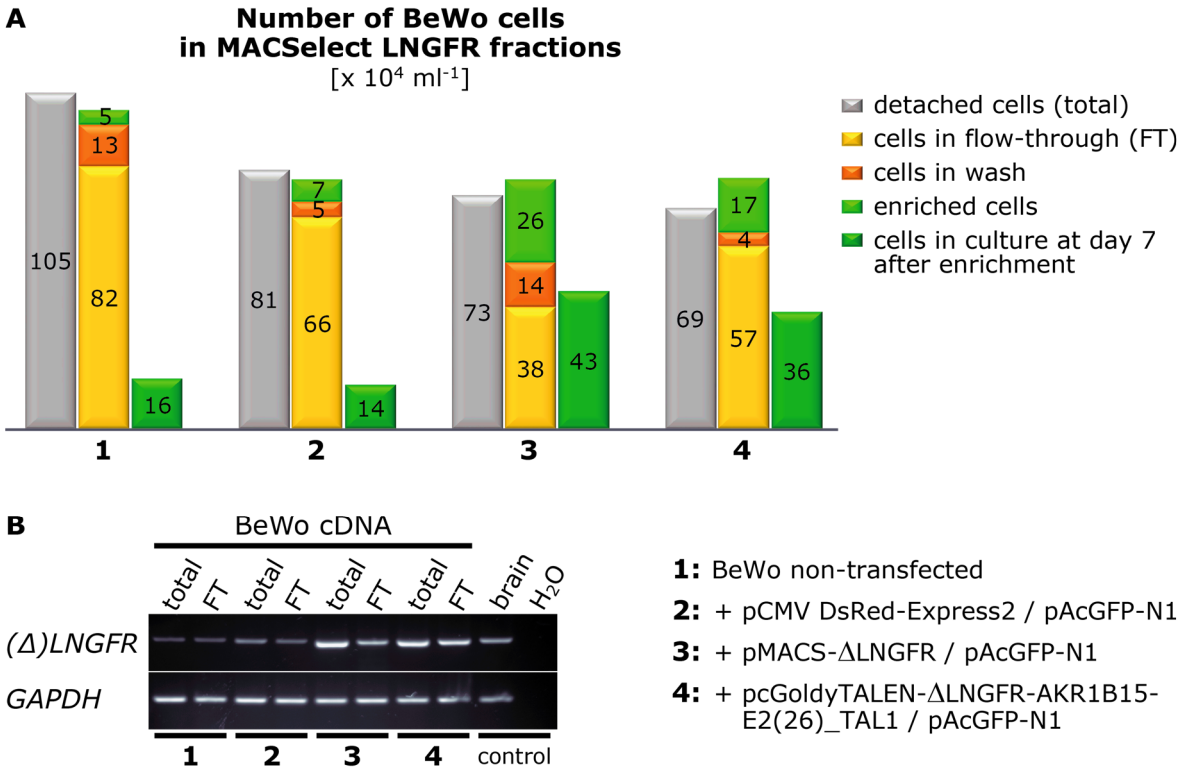

Figure III-28: BeWo cells overexpressing *ΔLNGFR* can be enriched by the MACSelect LNGFR system. Shown are the results from the selection process of transfected BeWo cells via the MACSelect LNGFR system. The MACSelect LNGFR system was tested on 10 cm dish cultures of either non-transfected BeWo cells **(1)** or BeWo cells transiently co-transfected with pCMV DsRed-Express2 and pAcGFP-N1 **(2)**, pMACS-ΔLNGFR and pAcGFP-N1 **(3)**, or pcGoldyTALEN-ΔLNGFR-AKR1B15-E2(26)_TAL1 and pAcGFP-N1 **(4)** via ViaFect.
(A) Number of BeWo cells in different fractions resulting from the selection/enrichment process using the MACSelect LNGFR system. Cells were counted after detachment (gray bars), in fractions of the selection/enrichment process (yellow, orange, and bright green bars), and after cultivation of enriched cells in 10 cm dishes for seven days (dark green bars). **(B)** Semi-quantitative RT-PCR products from reactions with equal amounts of total RNA isolated from detached cells (total) or cells of the flow-through (FT) using the primer pair # 2994 and # 2995. Human brain total RNA and H_2O samples served as positive and negative controls, respectively, whereas the amplification of human *GAPDH* (primer pair: # 1727 + # 1728) served as input control.

In addition, the enrichment of BeWo cells overexpressing *ΔLNGFR* was also analyzed on RNA level. To estimate the combined mRNA levels of endogenous *LNGFR* and exogenous *ΔLNGFR* in detached cells or cells of the flow-through fraction, semi-quantitative RT-PCR analysis was performed. Here, comparable but low *(Δ)LNGFR* amplification product levels were detected in reactions containing reverse-transcribed total RNA samples from detached non-transfected cells (total **1**) or from detached cells transiently co-transfected with pCMV DsRed-Express2 / pAcGFP-N1 (total **2**), which represented the endogenous *LNGFR* expression in BeWo cells [Figure III-28B]. On the other hand, the amount of *(Δ)LNGFR* amplification products was considerably increased in samples of detached cells transiently co-transfected with pMACS-ΔLNGFR / pAcGFP-N1 (total **3**) or pcGoldyTALEN-ΔLNGFR-AKR1B15-E2(26)_TAL1 / pAcGFP-N1 (total **4**), indicating the overexpression of exogenous *ΔLNGFR* in these samples [Figure III-28B]. Similar *LNGFR* transcript levels were found in samples of detached and flow-through cells of BeWo cultures which did not overexpress *ΔLNGFR* (total & FT **1**, **2**). However, the amount of *(Δ)LNGFR* amplification products was clearly reduced in reactions containing reverse-transcribed total RNA samples from flow-through fractions of BeWo cultures which overexpressed *ΔLNGFR* (FT **3**, **4**) when compared with those containing samples of the respective detached cells (total **3**, **4**) [Figure III-28B].

Thus, although the BeWo cell line expresses endogenous *LNGFR* at a low level, it was possible to enrich BeWo cells overexpressing *ΔLNGFR* after transient transfection with *ΔLNGFR* expression plasmids via the MACSelect LNGFR procedure. Similarly, however without the background of endogenous *LNGFR* expression, it was also feasible to enrich/ select SGBS cells which were transiently transfected with a *ΔLNGFR* overexpressing plasmid, like pcGoldyTALEN-AKR1B15-E2(26)_TAL1 (data not shown).

In summary, whereas tested TALEN pairs for the selective knock-out of either AKR1B15.1 or AKR1B15.2 did not reveal sufficient efficiencies, it was possible to generate an efficient TALEN pair for the simultaneous knock-out of both protein isoforms in cell culture. Furthermore, BeWo and SGBS cells overexpressing *ΔLNGFR* (the coding sequence for a C-terminally truncated human cell surface receptor which was beside the coding sequences for the fluorescent proteins AcGFP and DsRed successfully introduced into pcGoldyTALEN effector plasmids as marker for transfected cells) could be enriched by MACSelect LNGFR selection. However, optimization of the transfection method (especially for BeWo cells) as well as the MACSelect LNGFR selection process is still needed to facilitate the improved generation and selection of TALEN modified cells.

III.2. Expression and purification of the human 17β-Hydroxysteroid Dehydrogenase type 12 (17β-HSD12)

III.2.1. Expression of human *HSD17B12* in *Pichia Pastoris* (*P. pastoris*)

The recombinant expression of human *HSD17B12* followed by protein purification was aimed to clarify the biological functions of human 17β-HSD12 *in vitro*. Since 17β-HSD12 is classified as transmembrane protein colocalizing with the endoplasmic reticulum (ER), a eukaryotic expression system, namely the *P. pastoris* strains KM71 and X33, was chosen.

For recombinant expression, the coding sequence of the human *HSD17B12* combined with a C-terminally fused TEV protease recognition site was cloned into the yeast expression vector pPICZ-A. As a result, the generated pPICZ-A-HSD17B12 plasmid construct encodes for the human 17β-HSD12 protein fused to a C-terminal His_6 tag which can be cleaved by the TEV protease [Figure IV-4]. The PCR analysis of either crude cell lysates or isolated genomic DNA from different *P. pastoris* clones using the *AOX1* primer pair (# 2282 + # 2283) after the electroporation with pPICZ-A-HSD17B12 showed that only one out of ten potential positive clones of the *P. pastoris* KM71 and X33 strains recombined the linearized plasmid into the genome [data not shown]. Western blot analysis and enzymatic activity assays analyzing the reduction of estrone (E1) into 17β-estradiol (E2) with *P. pastoris* KM71 – pPICZ-A-HSD17B12 or *P. pastoris* X33 – pPICZ-A-HSD17B12 expression cultures showed that both strains expressed enzymatically active 17β-HSD12 [Table III-5, Figure III-29, Figure III-30]. Though, both *P. pastoris* strains expressed only little amounts of His_6-tagged 17β-HSD12 which were not obviously visible by Coomassie staining [Figure III-29A]. Despite the generally low expression, it seemed that the expression was more efficient in the *P. pastoris* KM71 strain compared with the wild type *P. pastoris* strain X33. However, up to now, *HSD17B12* could only be successfully expressed in cultures of up to 100 ml, whereas the upscaling of expression cultures resulted in a strongly reduced or absent expression of *HSD17B12* from pPICZ-A-HSD17B12.

Table III-5: Enzymatic activities of *P. pastoris* – pPICZ-A-HSD17B12 expression cultures.

P. pastoris	**E1 ⇨ E2** in [%]
KM71	< 1
KM71 pPICZ-A-HSD17B12	81.8
X33 pPICZ-A-HSD17B12	8.5

Activity tests were carried out in reactions containing cell pellets of 2 ml 48 h expression cultures ($OD_{600} \approx 10$), 50 nM ^{3}H-labeled estrone, and 300 mM NADPH in reaction buffer. Given is the conversion of estrone (E1) into 17β-estradiol (E2) in reactions after an incubation at 37 °C for 5 h.

III.2.2. SOLUBILIZATION OF HUMAN 17β-HSD12 FROM *P. PASTORIS* EXPRESSION CULTURES

Western blot analysis of fractions resulting from the lysis of cell pellets from *P. pastoris* X33 – pPICZ-A-HSD17B12 and *P. pastoris* KM71 – pPICZ-A-HSD17B12 expression cultures without the addition of any detergent showed that the overexpressed 17β-HSD12 was partly found as "soluble" protein in the supernatant fraction of lysates, thereby, possessing the anticipated molecular weight of the His_6-tagged protein (38.3 kDa) [Figure III-29B, Figure III-30A]. Up to now, it has been unclear whether 17β-HSD12 was appeared in the supernatant fraction as soluble protein or implemented in microsomes. However, as expected for membrane proteins, the majority of 17β-HSD12 was found as non-soluble protein in the pellet fractions. For any reasons, beside the protein band of anticipated molecular weight, a second His_6-tagged 17β-HSD12 band with lower molecular weight (approx. 31 kDa) showed up in the pellet fraction of lysates, too [Figure III-29B, Figure III-30A]. Whereas no 17β-HSD12 was detectable in the supernatant after the spheroblasting process, washing of spheroblasts with 1 M sorbitol lead to some release of soluble 17β-HSD12 into the wash fraction [Figure III-29].

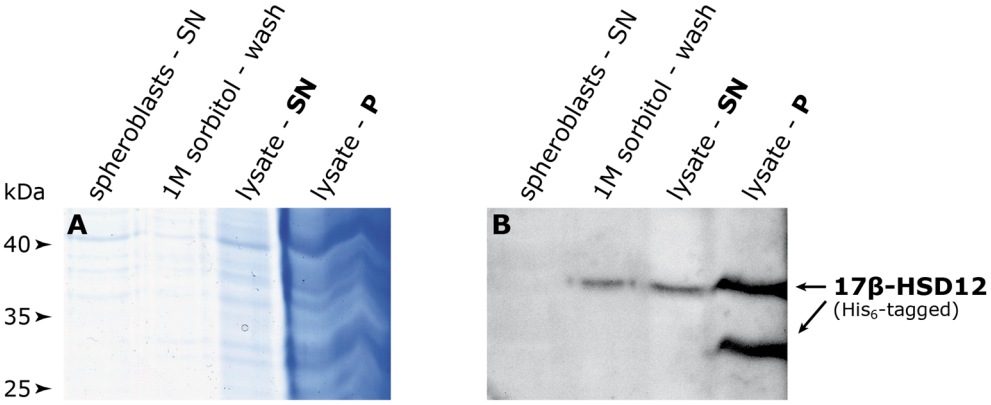

Figure III-29: Little amounts of "soluble" His_6-tagged 17β-HSD12 can be detected in the supernatants of *P. pastoris* X33 – pPICZ-A-HSD17B12 expression culture lysates via Western blotting.
Shown are exemplary results from the detection of His_6-tagged 17β-HSD12 in fractions resulting from the lysis of *P. pastoris* X33 – pPICZ-A-HSD17B12 expression cultures in MilliQ-H_2O+PI (according to II.5.2.1) via Coomassie staining and Western blotting.
(A) Coomassie stained SDS-PAGE mini gel with equal volumes of fraction samples loaded. **(B)** Western blot with equal volumes of fractions using mouse-anti-His (1:4000) and HRP-conjugated goat-anti-mouse (1:10000) antibodies.
P, pellet (resuspended in 2 ml); SN, supernatant (10 ml); wash, supernatant from the washing step (10 ml).

As mentioned above, when the spheroblasts were resuspended in MilliQ-H_2O and lysed via freeze-thaw cycles His_6-tagged 17β-HSD12 was already detectable in the soluble supernatant fraction of *P. pastoris* – pPICZ-A-HSD17B12 expression culture spheroblasts. Using *P. pastoris* KM71 – pPICZ-A-HSD17B12 spheroblasts it was additionally seen that these supernatants contained enzymatically active 17β-HSD12 by catalyzing the reduction of estrone (E1) in enzymatic activity assays with ^3H-labeled steroids [Figure III-30A, B].

However, since the majority of His_6-tagged 17β-HSD12 was found to appear as non-soluble protein when overexpressed in *P. pastoris*, several non-ionic detergents were tested in respect of their potential for increasing the amount of soluble and enzymatically active 17β-HSD12.

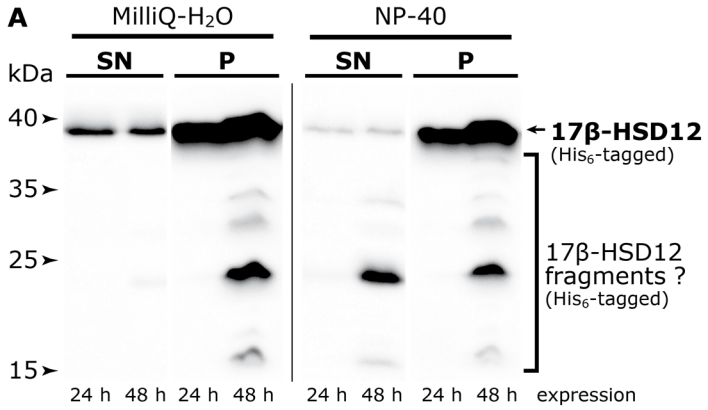

B

E1 ⇨ E2 in [%]	SN
spheroblast lysis in:	
MilliQ-H_2O (24 h)	37.6
MilliQ-H_2O (48 h)	38.2
2 % NP-40 (24 h)	< 1
2 % NP-40 (48 h)	1.5

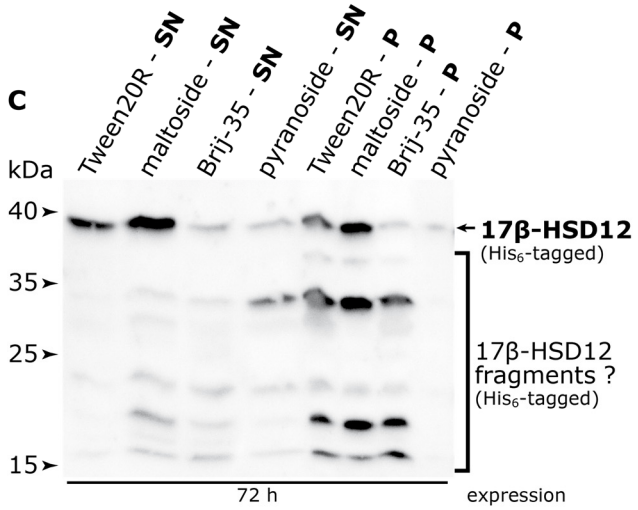

D

E1 ⇨ E2 in [%]	SN	P
harvest	18.9	
spheroblast lysate	44.3	11.8
solubilization of spheroblast lysate pellet in:		
1 % Tween20R	< 1	8.1
1 % maltoside	< 1	< 1
1 % Brij-35	1.5	6.9
1 % pyranoside	< 1	< 1

Figure III-30: The non-ionic detergent Brij-35 is able to solubilize enzymatically active 17β-HSD12.
Shown are results from Western blotting and enzymatic activity assays analyzing the solubilization of enzymatically active 17β-HSD12 with different detergents. For this, equal volumes of supernatant and pellet (resuspended in a comparable volume buffer) samples, resulting from solubilization experiments with pellets of *P. pastoris* KM71 – pPICZ-A-HSD17B12 expression cultures (as described in II.5.2.1), were analyzed via Western blotting (using the mouse-anti-His (1:5000) primary and HRP-conjugated goat-anti-mouse (1:15000) secondary antibody pair) and enzymatic activity assays (using 20 nM ^{3}H-labeled estrone as substrate and 300 µM NADPH as cofactor).
(A, B) Western blot **(A)** and enzymatic activities (reduction of estrone within 5 h) **(B)** with fractions from the simultaneous lysis and solubilization of spheroblasts in absence (MilliQ-H_2O) and in presence of 2 % NP-40 detergent (2 % NP-40). The analyzed fractions resulted from a final centrifugation step at 450 x *g* and 4 °C for 2 min. **(C, D)** Western blot **(C)** and enzymatic activities (reduction of estrone within 6 h) **(D)** with fractions from the successive lysis and solubilization of spheroblasts. The analyzed fractions resulted from the solubilization of spheroblast lysate pellets (after ultracentrifugation) using different detergents and a final ultracentrifugation step at 55000 x *g* and 4 °C for 30 min.
E1, estrone; E2, 17β-estradiol; maltoside, dodecyl-β-D-maltoside; pyranoside, 2,6-dimethyl-4-heptyl-β-D-maltopyranoside; P, pellet; SN, supernatant.

A first experiment examined the solubilization properties of the detergent NP-40. Although the use of 2 % NP-40 solution within the spheroblasts lysis step promoted the solubilization of His_6-tagged 17β-HSD12 (especially those fragments of smaller molecular weight), the resulting supernatants were only marginally enzymatically active [Figure III-30A, B]. This means that 2 % NP-40 in MilliQ-H_2O was not suitable for the solubilization of His_6-tagged 17β-HSD12 from *P. pastoris* expression cultures because it destroyed the enzymatic activity of solubilized 17β-HSD12.

In order to identify detergents which mediate the solubilization of enzymatically active His_6-tagged 17β-HSD12, pellets resulting from spheroblast lysates of *P. pastoris* KM71 – pPICZ-A-HSD17B12 expression cultures were resuspended, split, and treated with either 1 % Tween20R, 1 % dodecyl-β-D-maltoside (maltoside), 1 % Brij-35, or 1 % 2,6-dimethyl-4-heptyl-β-D-maltopyranoside (pyranoside) in solubilization buffer [II.5.2.1].

Here, it was found that all four non-ionic detergents possessed the potential to solubilize 17β-HSD12 by showing similar full length 17β-HSD12 signal intensities in both the resulting soluble supernatant fraction and the remaining insoluble pellet fraction in Western blots [Figure III-30C]. However, although the initial spheroblast lysate pellet was enzymatically active (approx. 12 % E1 ⇨ E2 conversion) in activity assays with ^{3}H-labeled estrone (E1) as substrate, no enzymatic activity was detectable in the supernatant and pellet fractions of samples treated with dodecyl-β-D-maltoside or 2,6-dimethyl-4-heptyl-β-D-maltopyranoside [Figure III-30D]. The pellet fractions resulting from the solubilization of 17β-HSD12 from the spheroblast lysate pellets with Tween20R or Brij-35 were able to catalyze the reduction of estrone (approx. 8 % and 7 % E1 ⇨ E2 conversion, respectively) [Figure III-30D]. The same was true for the supernatant fraction of the pellet treated with Brij-35, which revealed a clear traceable but very low (about 1.5 % E1 ⇨ E2 conversion) enzymatic activity [Figure III-30D] This low activity was in accord with the little amount of the full length 17β-HSD12 protein in the fraction, already detected by Western blotting [Figure III-30C]. In contrast, no clear enzymatic activity was seen in the supernatant fraction of Tween20R treated pellets, indicating that, despite showing good solubilization properties, Tween20R negatively affected the enzymatic activity of solubilized 17β-HSD12 [Figure III-30D].

The additionally tested detergents Anameg-7, MEGA-8, n-octyl-β-D-glucopyranoside, and sodium cholate showed no clear solubilizing properties [data not shown].

All in all, the four detergents 2,6-dimethyl-4-heptyl-β-D-maltopyranoside, dodecyl-β-D-maltoside, Brij-35, and Tween20R revealed good solubilization capabilities for 17β-HSD12 from pellets of spheroblast lysates. Tween20R and Brij-35 reduced the overall enzymatic activity of the resulting pellets and supernatants with estrone by approximately 20-25 %, whereas 2,6-dimethyl-4-heptyl-β-D-maltopyranoside and dodecyl-β-D-maltoside abolished the activity of 17β-HSD12 completely. Despite the fact that only the supernatant of Brij-35 treated pellets catalyzed the reduction of estrone and that Tween20R seemed to impair the enzymatic activity of solubilized 17β-HSD12, both detergents, Tween20R and Brij-35, were further analyzed in terms of solubilizing enzymatically active 17β-HSD12.

III.2.3. PURIFICATION OF HUMAN 17β-HSD12 FROM *P. PASTORIS* EXPRESSION CULTURES VIA THE HIS$_6$ TAG

First tests revealed that little amounts of enzymatically active 17β-HSD12 were detectable in the supernatant of centrifuged lysates of *P. pastoris* – pPICZ-A-HSD17B12 expression culture spheroblasts, although no detergent was added [Figure III-29, Figure III-30].

Because of this 17β-HSD12 was initially purified via its fused His$_6$ tag without the addition of any detergent (see II.5.2.2 - method A) from the supernatant of 17β-HSD12 overexpressing *P. pastoris* KM71 cell lysates **(+)** after ultracentrifugation (UC$_1$-SN) [Figure III-31]. In Western blots using the mouse-anti-His primary and HRP-conjugated goat-anti-mouse secondary antibody pair as well as in enzymatic activity assays using ^{3}H-labeled estrone (E1) as substrate it was seen that enzymatically active full length His$_6$-tagged 17β-HSD12 (molecular size approx. 38 kDa) bound to the HisTrap HP column since no clear His$_6$ tag signals and enzymatic activities were detectable in the flow-through (FT) and wash (W) fractions [Figure III-31]. The elution with 300 mM imidazole revealed that the majority of full length 17β-HSD12 was found in the first (EL$_1$) and second (EL$_2$) elution fraction [Figure III-31A]. Proportional to the full length His$_6$-tagged 17β-HSD12 protein amount detected in the Western blot fractions, the enzymatic activity was by far higher in the EL$_2$ fraction (53.6 % E1 ⇨ E2 conversion) when compared with the EL$_1$ fraction (7.8 % E1 ⇨ E2 conversion) [Figure III-31B]. Although weak signals corresponding to the size of full length His$_6$-tagged 17β-HSD12 were also visible in the third (EL$_3$) and fourth (EL$_4$) elution fraction, no enzymatic activity was measureable in those fractions [Figure III-31]. In addition to the full length His$_6$-tagged 17β-HSD12, a more prominent second His$_6$-tagged protein signal at approximately 20 kDa was detectable in the second to fourth elution fraction [Figure III-31A]. Since this signal band was missing in the purified supernatant (UC$_1$-SN) but was present in the *P. pastoris* KM71 – pPICZ-A-HSD17B12 expression culture lysate (total) and the pellets of the ultracentrifuged lysates (UC$_1$-P), the occurring signal band might represent an insoluble and inactive His$_6$-tagged 17β-HSD12 degradation product [Figure III-31A].

The solubilization of the lysate pellet resulting from the first ultracentrifugation step (UC$_1$-P) with either 1 % Brij-35 or 1 % Tween20R which was followed by a second ultracentrifugation step for the separation of soluble and insoluble His$_6$-tagged 17β-HSD12 showed that full length 17β-HSD12 but also smaller fragments could be found in the supernatant (UC$_2$-SN) after the second ultracentrifugation step, though, the majority of full length His$_6$-tagged 17β-HSD12 remained in the insoluble pellet fraction (UC$_2$-P) [Figure III-31A]. Although the two detergents revealed no clear difference in their solubilizing capability, a huge difference was again seen in the enzymatic activity of supernatants resulting from Brij-35 and Tween20R treated samples (UC$_2$-SN). Here, 27.6 % of estrone could be converted by the addition of the UC$_2$ supernatant sample resulting from the Brij-35 treated UC$_1$ pellet, whereas the respective UC$_2$ pellet as well as the supernatant and pellet of the Tween20R treated sample reduced only 3-4 % of the estrone [Figure III-31B].

The control samples from non-transformed *P. pastoris* KM71 lysates **(-)** did neither show signals in Western blots nor possessed enzymatic activity [Figure III-31].

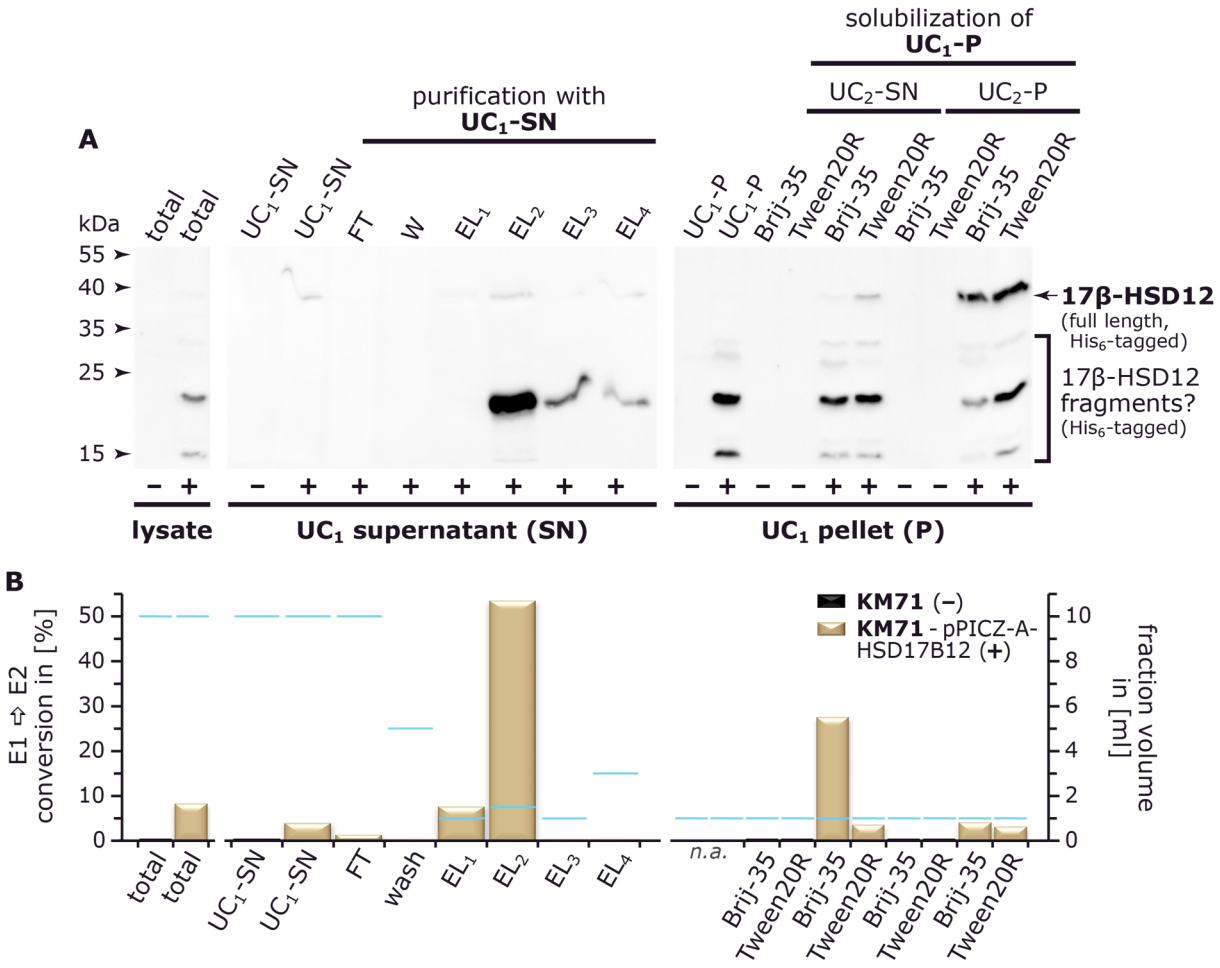

Figure III-31: Enzymatically active His$_6$-tagged 17β-HSD12 can be purified from the detergent-free supernatant of ultracentrifuged *P. pastoris* KM71 – pPICZ-A-HSD17B12 expression culture spheroblasts lysate and, by using the non-ionic detergent Brij-35, solubilized from the remaining pellet.

Shown are 17β-HSD12 amounts and enzymatic activities in fractions resulting from the detergent-free purification of His$_6$-tagged 17β-HSD12 from supernatants of ultracentrifuged *P. pastoris* KM71 – pPICZ-A-HSD17B12 lysates and its solubilization from the remaining ultracentrifugation pellet by using the non-ionic detergents Brij-35 and Tween20R. Pellets from 50 ml *P. pastoris* KM71 – pPICZ-A-HSD17B12 48 h expression cultures were processed as described in II.5.2.2 - method A and fractions from the purification as well as from the solubilization reactions were analyzed by Western blotting and enzymatic activity tests. Non-transformed *P. pastoris* KM71 cultures served as negative controls. Within each approach (purification and solubilization of 17β HSD12), equal sample volumes were applied in the analyses. **(A)** Results from Western blots with fractions using the mouse-anti-His (1:5000) primary and HRP-conjugated goat-anti-mouse (1:15000) secondary antibody pair. **(B)** Results from activity tests with fractions analyzing the reduction of 20 nM ^{3}H-labeled estrone in presence of 300 µM NADPH overnight (bars). The blue lines indicate the total volume of the respective fractions.

–, *P. pastoris* KM71 culture; +, *P. pastoris* KM71 – pPICZ-A-HSD17B12 48 h expression culture; E1, estrone; E2, 17β-estradiol; EL$_1$, first elution fraction (1 ml); EL$_2$, second elution fraction (1.5 ml); EL$_3$, third elution fraction (1 ml); EL$_4$, fourth elution fraction (3 ml); FT, flow-through fraction (10 ml); n.a., not analyzed; UC$_1$-P, pellet resulting from the first ultracentrifugation step (1 ml); UC$_1$-SN, supernatant resulting from the first ultracentrifugation step (10 ml); UC$_2$-P, pellet resulting from the second ultracentrifugation step (1 ml); UC$_2$-SN, supernatant resulting from the second ultracentrifugation step (1 ml); wash, wash fraction (5 ml).

An optimization of the purification method aimed to augment the yield of purified and enzymatically active recombinant human 17β-HSD12. Because it was seen previously that Brij-35 is able to solubilize enzymatically active His_6-tagged 17β-HSD12, two alternative procedures adding Brij-35 to spheroblasts at a very early stage of purification were tested (see II.5.2.2 - method B). These two Brij-35 containing purification methods combined the detergent mediated lysis of spheroblasts and the solubilization of 17β-HSD12 prior to the purification of His_6-tagged 17β-HSD12 in order to increase the amount of 17β-HSD12 in the soluble fraction of *P. pastoris* lysates and thus the yield of purified 17β-HSD12 as well as to accelerate the process and thus reduce a possible loss in enzymatic activity. The capabilities of these Brij-35 containing purification methods were again analyzed by Western blotting and enzymatic activity assays with fractions gained from the purification of His_6-tagged 17β-HSD12 from *P. pastoris* KM71 – pPICZ-A-HSD17B12 55 h expression cultures by using Econo-Pac columns with Ni Sepharose resin bed [Figure III-32].

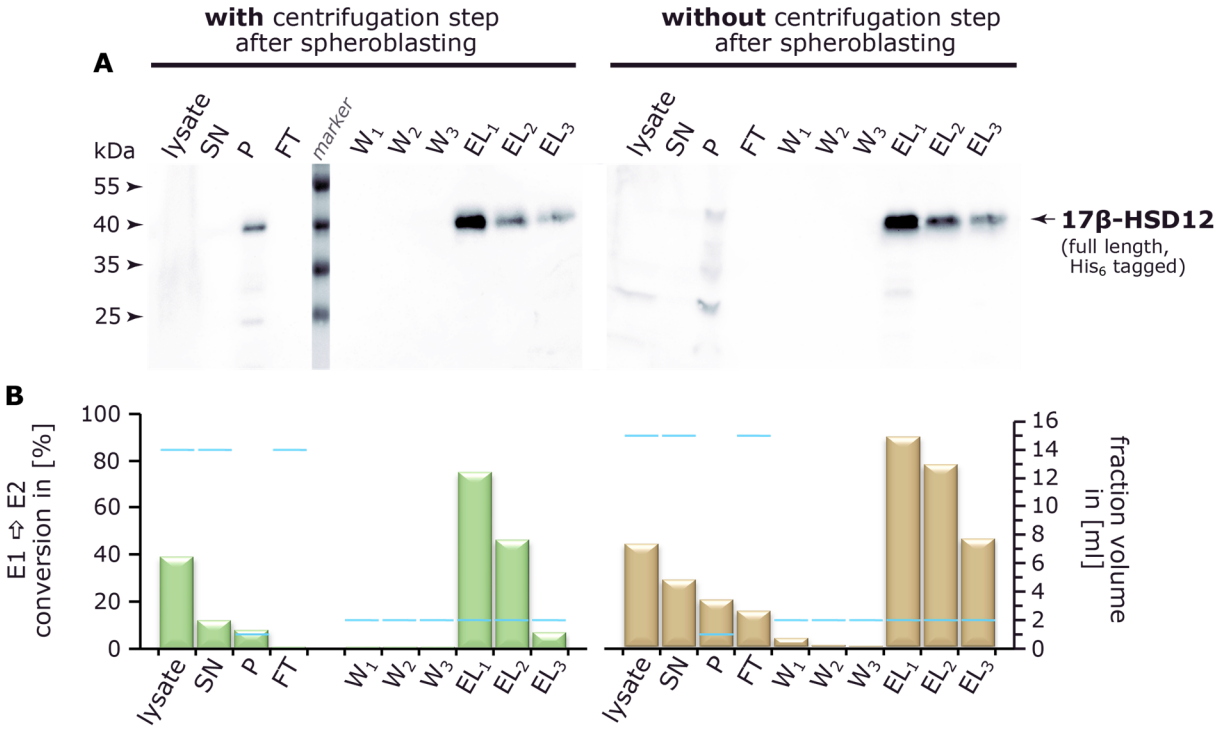

Figure III-32: Enzymatically active His_6-tagged 17β-HSD12 can be purified from *P. pastoris* KM71 – pPICZ-A-HSD17B12 expression cultures by two alternative Brij-35 containing purification procedures combining the lysis of spheroblasts and the solubilization of 17β-HSD12.

Shown are 17β-HSD12 amounts and enzymatic activities in fractions resulting from the purification of His_6-tagged 17β-HSD12 from *P. pastoris* KM71 – pPICZ-A-HSD17B12 expression cultures via two alternative Brij-35 containing purification procedures, combining the lysis of spheroblasts and the solubilization of 17β-HSD12. Pellets from 2x100 ml *P. pastoris* KM71 – pPICZ-A-HSD17B12 55 h expression cultures were processed as described in II.5.2.2 - method B and equal volumes of fraction samples were analyzed by Western blotting and activity assays. **(A)** Results from Western blots with fractions using the rabbit-anti-His (1:3000) primary and HRP-conjugated goat-anti-rabbit (1:5000) secondary antibody pair. **(B)** Results from enzymatic activity tests with fractions analyzing the reduction of 20 nM ^{3}H-labeled estrone in presence of 300 µM NADPH overnight (bars). The blue lines indicate the total volume of the respective fractions.

E1, estrone; E2, 17β-estradiol; EL_1, first elution fraction (2 ml); EL_2, second elution fraction (2 ml); EL_3, third elution fraction (2 ml); FT, flow-through fraction (15 ml); marker, PageRuler Prestained Protein Ladder; SN, supernatant (15 ml); P, pellet (1 ml); W_1, first wash fraction (2 ml); W_2, second wash fraction (2 ml); W_3, third wash fraction (2 ml).

The Western blots showed that generally only very weak full length His_6-tagged 17β-HSD12 signals were detectable in the lysates and the supernatants (SN) after an ultracentrifugation step, whereas more intense signals were visible in the 15-times concentrated pellet (P) fractions [Figure III-32A]. In addition, clearly enriched full length His_6-tagged 17β-HSD12 signals were seen in all elution fractions (EL_1 to EL_3) but not in the flow-through (FT) and wash (W) fractions [Figure III-32A]. The insertion of an extra centrifugation step at 40 x *g* and 4 °C for 3 min after the spheroblasting reaction revealed no obvious differences in the yield of 17β-HSD12 on protein level as seen in Western blots [Figure III-32A]. Though, it seemed that the intensity of signals at and below the molecular weight of full length His_6-tagged 17β-HSD12 was a little bit higher in fractions resulting from the purification without the additional centrifugation step [Figure III-32A]. However, looking at the enzymatic activity determined in the fractions with ^3H-labeled estrone (E1) as substrate, a clear difference was seen between the two procedures. Although not detectable in Western blotting, significant amounts of enzymatically active 17β-HSD12 were found in the flow-through (FT) and first wash (W_1) fractions (15.4 % and 3.8 % E1 ⇨ E2 conversion, respectively) using the procedure without an additional centrifugation step after the spheroblasting [Figure III-32B]. Generally, the enzymatic activities found in the elution fractions corresponded to the intensities of full length His_6-tagged 17β-HSD12 detected in Western blots [Figure III-32]. In principle, elution fractions resulting from the purification without an additional centrifugation step after spheroblasting exhibited higher activities when compared with the respective fractions of the additionally centrifuged spheroblasts (46.3-90.4 % versus 7.1-75.3 % E1 ⇨ E2 conversion) [Figure III-32B]. Moreover, the extra centrifugation step seemed to result in losses in enzymatic activities measured in the supernatant and pellet fractions (12.3 % and 8.1 % E1 ⇨ E2 conversion, respectively, versus 39.2 % E1 ⇨ E2 conversion in the lysate). Contrary, the purification process of the additionally centrifuged lysates was easier because the plugging of the Ni Sepharose resin bed was reduced and it seemed to yield eluates with higher purity [data not shown]. All in all, by considering the total volumes of fractions, a clear but not closer ascertained enrichment of 17β-HSD12 on protein and enzymatic activity level was seen in the elution fractions with both purification method variants.

In summary, it was possible to purify enzymatically active His_6-tagged 17β-HSD12 from the *P. pastoris* expression system, however, with yet unsettled purity. Although the expression of pPICZ-A-HSD17B12 was slightly higher in the *P. pastoris* KM71 strain when compared with the wild type X33 strain, the overall expression level was very low and the protein product only visible via Western blotting. Different purification procedures showed that small amounts of 17β-HSD12 occur in the soluble supernatant after ultracentrifugation and that the yield of soluble and enzymatically active 17β-HSD12 could be increased by the addition of 1 % Brij-35 for the lysis of spheroblasts. Up to now, the upscaling of small scale expression cultures and purification batches in order to produce and purify higher amounts of 17β-HSD12, respectively, have not been successful. Thus, it was not possible to perform extensive activity assays with purified 17β-HSD12 for its closer enzymatic characterization because the yields of 17β-HSD12 from small-scale approaches were too low.

III.3. METHOD DEVELOPMENT FOR THE ANALYSIS OF VITAMIN D METABOLITES IN BIOLOGICAL SAMPLES

The analysis of different vitamin D metabolites in biological samples is an important tool for the diagnosis of deficiencies and diseases, like chronic kidney diseases, but also for the monitoring of therapies and cellular pathways. Although numerous commercial vitamin D assays are available, these assays concentrate generally only on one or two metabolites and show often missing specificity (e.g., ELISAs). Thus, an in-house vitamin D analysis method being suitable for the simultaneous detection/quantification of various vitamin D metabolites in biological samples was developed and established within this thesis.

III.3.1. DEVELOPMENT OF A HPLC-UV METHOD FOR THE ANALYSIS OF VITAMIN D_3 METABOLITES

In a first step, a HPLC method for the separation of several biologically relevant vitamin D_3 metabolites coupled to UV absorption detection was developed. For this, a technical note of Phenomenex for the separation of vitamin D metabolites on a reversed phase column formed the basis of this HPLC-UV method. The basic method was optimized in terms of sensitivity, background, separation of vitamin D_3 metabolites, peak shape, and run time.

In order to achieve the highest detection sensitivity, the UV absorption of eluting vitamin D_3 metabolites was monitored at 265 nm which corresponded to the absorption maximum in the absorption spectra of vitamin D_3 dissolved in ethanol [Figure III-33C].

The optimization process revealed that the solvent composition of the sample loaded onto the column is critical for the separation of 24,25-$(OH)_2$-D_3 and 1α,25-$(OH)_2$-D_3 because too high proportions of methanol led to the broadening of early eluting peaks [data not shown]. In addition, too low proportions (< 50 %) of methanol in the sample solvent affected the solubility of vitamin D_3 metabolites, where especially the nonpolar vitamin D_3 tended to precipitate [data not shown]. In addition, the use of a 5 mM ammonium acetate, 0.1 % formic acid, and 80 % methanol in MilliQ-H_2O pre-mixture instead of 5 mM ammonium acetate and 0.1 % formic acid in MilliQ-H_2O as mobile phase A together with 5 mM ammonium acetate and 0.1 % formic acid in methanol as mobile phase B reduced the height of ghost peaks occurring at the stepwise gradient transitions.

After the optimization of the sample solvent composition and volume, the injection volume, as well as the HPLC gradient, the resulting final HPLC-UV method (described in II.11.2) allowed for a well baseline separation of 24,25-$(OH)_2$-D_3 (peak 1), 1α,25-$(OH)_2$-D_3 (peak 2), 25-(OH)-D_3 (peak 3), 1α-(OH)-D_3 (peak 4), and vitamin D_3 (peak 5) on a Kinetex 2.6 µm C18 100 Å 50 mm x 4.6 mm HPLC column [Figure III-33A, B]. Under these conditions the two enantiomers (24S)-24,25-$(OH)_2$-D_3 and (24R)-24,25-$(OH)_2$-D_3 showed equal chromatographic properties and were not distinguishable in chromatography [data not shown].

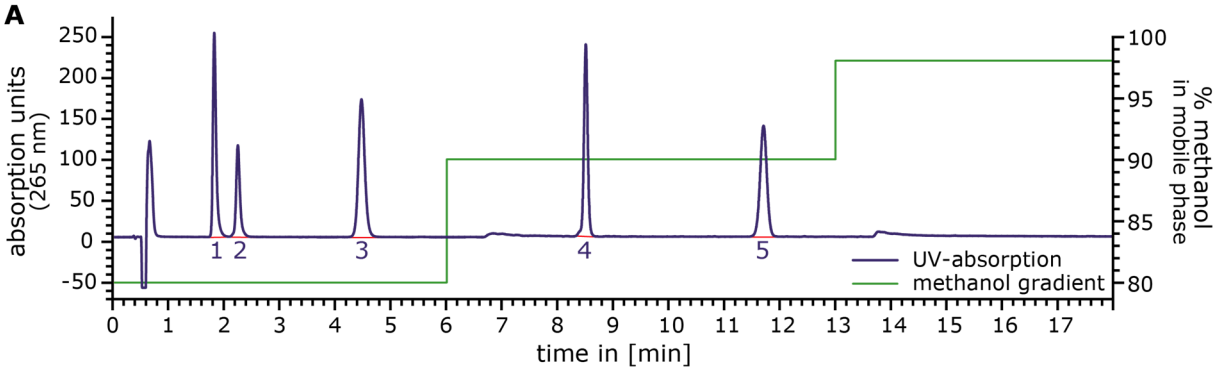

B

peak	compound	retention time [min]	load [ng]	peak area [µV·s]	peak area [%]
1	24,25-$(OH)_2$-D_3	1.8	400	1025178	19.6
2	1α,25-$(OH)_2$-D_3	2.3	200	544255	10.4
3	25-(OH)-D_3	4.5	400	1365936	26.2
4	1α-(OH)-D_3	8.5	400	1117599	21.4
5	vitamin D_3	11.7	400	1169982	22.4

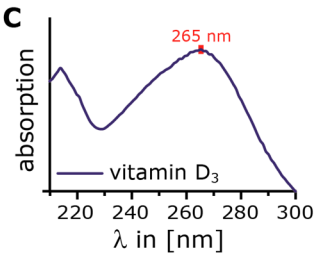

Figure III-33: Analysis of vitamin D_3 metabolites by HPLC-UV: The optimized HPLC coupled to UV detection method enables the detection of five baseline separated vitamin D_3 metabolites.
(A) Representative chromatogram illustrating the separation of vitamin D_3 metabolite reference mixes (blue trace) on a Kinetex 2.6 µm C18 100 Å 50 mm x 4.6 mm column with SecurityGuard Standard C18 4 mm x 2 mm cartridge via the final HPLC method coupled to UV detection [II.11.2] and the applied two-step methanol gradient (green line). **(B)** Retention times, injected amounts (load) and resulting peak areas (in µV·s and % of total area under the curve) of analyzed vitamin D_3 metabolites. **(C)** Absorption spectra of vitamin D_3 in ethanol.

Dilutions of reference vitamin D_3 metabolites in 50 % methanol in MilliQ-H_2O (10 $^{ng}/_{ml}$ to 10 $^{µg}/_{ml}$) showed a linear behavior of the resulting areas under the curves of peaks within the tested concentration range ($R^2 > 0.9993$). Thus, the established HPLC-UV method was able to quantify amounts of down to 0.5 ng of the respective vitamin D_3 metabolite reference sample loaded onto the column [data not shown]. Thereby, the solutions were stable for at least four days at 4 °C or room temperature [data not shown].

As a result, the HPLC-UV method could be theoretically used for the analysis of high abundant vitamin D_3 metabolites in biological samples, like 25-(OH)-D_3 in plasma or serum (< 30 $^{ng}/_{ml}$). However, since this method is not sensitive enough for the detection of low abundant vitamin D_3 metabolites, like the biologically active 1α,25-$(OH)_2$-D_3, and it seemed that the sample preparation process is associated with a loss of vitamin D_3 metabolites as well as the fact that matrix impurities could interfere with their detection, its application in the analysis of vitamin D_3 metabolites in biological samples is limited.

III.3.2. Development of a radioactive HPLC method for the analysis of ^{3}H-labeled Vitamin D_3 metabolites

Since UV detection is too little sensitive and interference-prone for the analysis of vitamin D_3 metabolites in biological samples, the established HPLC-UV method was adopted to a HPLC system with scintillation detector.

The method transfer required the adjustment of the mobile phase gradient used for the chromatographic separation of vitamin D_3 metabolites as ^{3}H-labeled samples were applied to the HPLC system solved in methanol containing 2 % formic acid. This direct application of SPE eluates reduced the hands-on time and avoided evaporation and reconstitution or dilution steps, which are generally problematic with radioactive samples. Using a HPLC system with in-line scintillation and UV detectors it was found that loading the samples with 30 % aqueous phase (mobile phase A: 0.05 % formic acid in MilliQ-H_2O) and 70 % organic phase (mobile phase B: 5 mM ammonium acetate and 0.1 % formic acid in methanol) followed by an adopted gradient ensured the baseline separation of 24,25-$(OH)_2$-D_3 and 1α,25-$(OH)_2$-D_3.

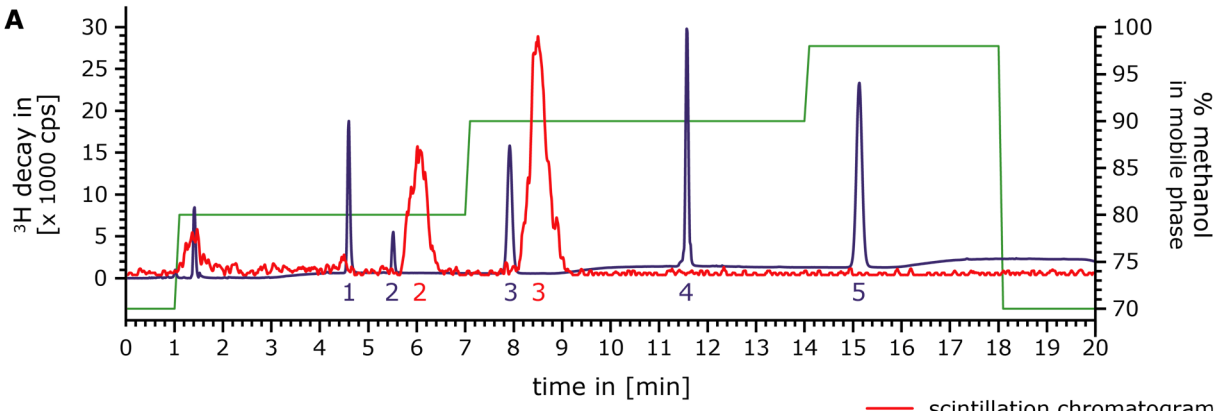

B

peak	compound	t_R (peak width) in [min] UV detection	^{3}H detection
1	24,25-$(OH)_2$-D_3	4.6 (0.2)	-
2	1α,25-$(OH)_2$-D_3	5.5 (0.2)	6.1 (0.8)
3	25-(OH)-D_3	7.9 (0.2)	8.5 (0.9)
4	1α-(OH)-D_3	11.5 (0.2)	-
5	vitamin D_3	15.1 (0.2)	-

Figure III-34: Analysis of vitamin D_3 metabolites by radioactive HPLC: The adopted HPLC coupled to scintillation detection (and in-line UV detection) method enables theoretically the baseline separation of all vitamin D_3 metabolites included, despite a strong peak broadening due to the scintillation detector. **(A)** Representative chromatogram illustrating the separation of unlabeled and ^{3}H-labeled vitamin D_3 metabolites via the final HPLC method for ^{3}H-labeled vitamin D_3 metabolites [II.11.2.2] on a Kinetex 2.6 µm C18 100 Å 50 mm x 4.6 mm column with SecurityGuard Standard C18 4 mm x 2 mm cartridge and the applied two-step methanol gradient (green line). The retention of metabolites was monitored by an in-line UV (blue trace) and scintillation detector (red trace). Please note that the left y-axis represents ^{3}H-decay signal intensities monitored by the scintillation detector in counts per second (cps), whereas no scaling is shown for UV absorption signals. **(B)** List of corresponding peak numbers, retention times (t_R), and peak widths of analyzed vitamin D_3 metabolites.

Figure III-34 shows a representative chromatogram from the separation of vitamin D_3 metabolites by applying the radioactive HPLC method described in II.11.2.2. Here, the unlabeled reference standards 24,25-$(OH)_2$-D_3 (peak 1), 1α,25-$(OH)_2$-D_3 (peak 2), 25-(OH)-D_3 (peak 3), 1α-(OH)-D_3 (peak 4), and vitamin D_3 (peak 5) eluted baseline separated and with good peak shapes (peak width at basis: 0.2 min) in the in-line UV detector chromatogram from the Kinetex 2.6 µm C18 100 Å 50 mm x 4.6 mm column [Figure III-34, blue trace]. In contrast, the chromatogram resulting from the downstream scintillation detector revealed quite broad peak shapes (peak width at basis: 0.8-0.9 min) for the analyzed, commercially available ^{3}H-labeled vitamin D_3 metabolites 1α,25-$(OH)_2$-D_3 (peak 2) and 25-(OH)-D_3 (peak 3) [Figure III-34, red trace]. This broadening of peaks in the scintillation chromatogram could be attributed to the mixing process with the scintillation liquid. The in-line arrangement of the UV detector and scintillation detector resulted in monitored shifts between retention times of unlabeled and ^{3}H-labeled vitamin D_3 metabolites (time shift: 0.6 min). As the retention time shift is constant, this in-line set-up could allow for the identification of peaks belonging to commercially unavailable ^{3}H-vitamin D_3 metabolites.

Dilution series indicated that the detection limit of this method was approximately 80 pg (= approx. 0.03 µCi) for ^{3}H-labeled 1α,25-$(OH)_2$-D_3 and 25-(OH)-D_3 [data not shown].

Although the established radioactive HPLC method is more sensitive than the method with UV detection and thus enables the detection of vitamin D_3 metabolites at biological relevant levels, the use of this method is limited due to the need of radioactive (^{3}H)-labeled analytes. In addition, it was seen that the mixing chamber of the scintillation detector led to a 4- to 5-fold peak broadening and, even though 24,25-$(OH)_2$-D_3 and 1α,25-$(OH)_2$-D_3 are theoretically individually analyzable (computed peak resolution: > 1), the poor resolution due to broad peaks in combination with the possible presence of additional hydroxylation products, which could occur very likely, would make the analysis of these two important metabolites more difficult.

III.3.3. Development of a LC-MS/MS method for the analysis of Vitamin D metabolites

The previous chapters showed that an analysis of vitamin D metabolites in biological samples via UV absorption detection at 265 nm or ^{3}H-mediated scintillation detection is only limited applicable because UV detection has low sensitivity and scintillation detection requires the analysis of radioactive (^{3}H)-labeled vitamin D compounds which are sparsely available.

In order to have a sensitive and all-purpose method for the analysis of vitamin D metabolites in biological samples, like cells and media from cell culture experiments (or serum, plasma, and tissue samples), a LC-MS/MS vitamin D method, which simultaneously detects the most important vitamin D_3 metabolites (24,25-$(OH)_2$-D_3, 1α,25-$(OH)_2$-D_3, 25-(OH)-D_3, 1α-(OH)-D_3, and vitamin D_3) as well as additional vitamin D_2 metabolites (1α,25-$(OH)_2$-D_2, 25-(OH)-D_2, and vitamin D_2), was established and partially validated.

III.3.3.1. Optimization of MRM parameters for the MS/MS detection of vitamin D metabolites

First, the multiple reaction monitoring (MRM) parameters for the detection of vitamin D metabolites using a QTrap 5500 mass spectrometer with electrospray ionization (ESI) in positive mode were "optimized" via infusion and flow injection analysis (FIA) experiments [II.11.2.3]. Here, it should be mentioned that, although initially positive and negative modes were tested for few vitamin D_3 metabolites, in accord with numerous already published LC-MS/MS methods the signal intensities were much higher in positive mode. Thus, the positive mode was exclusively used for the optimization of MRMs.

Infusion experiments with single vitamin D metabolites in appropriate dilutions and known Q_1 mother ion masses [m/z] were carried out in order to identify the MRMs of a compound with the highest intensities and the best MRM specific MS/MS parameters (collision cell exit potential, collision energy, declustering potential, and entrance potential). In order to increase the specificity of MRMs, daughter ions with less than - 40 m/z difference to the mother ion mass, which often correspond to dehydration products (up to - 2 H_2O), or below a minimum daughter ion mass of 60 m/z were excluded. Here, multiple MRMs, however, with partly strongly differing intensities, could be identified per metabolite. In general, a preliminary MS/MS method was built for each metabolite using the three most intense MRMs. Some metabolites, such as 25-(OH)-D_3 and 1α-(OH)-D_3 or (24S)-24,25-$(OH)_2$-D_3, (24R)-24,25-$(OH)_2$-D_3, and 1α,25-$(OH)_2$-D_3, shared the same MRM transitions with similar MS/MS parameters. This reduced the number of MRMs which had to be monitored but required a good chromatographic separation of those metabolites prior to MS/MS analysis.

The source parameters (curtain gas, collision gas, ion spray voltage, temperature, ion source gas 1, and ion source gas 2) were optimized in FIA experiments with single vitamin D metabolites using the preliminary MS/MS method and 0.05 % formic acid in 80 % methanol (± 0.15 mM lithium acetate) as mobile phase. Since the source parameters are not variable between different MRMs within one method, the final source parameters for the vitamin D MS/MS method were selected with respect to two aspects. First, those parameter settings were chosen, which were the best common values for all vitamin D metabolites. Second, the common parameters were adjusted with respect to the optimized settings determined for the highest ionization of the poorly detectable 1α,25-$(OH)_2$-D_3, which had higher priority.

The results of these MRM parameter optimizations are listed in Table II-30 [II.11.2.3] and in the appendix [VI.8].

III.3.3.2. Adaptation of the HPLC method for the MS/MS analysis of vitamin D metabolites

The initially developed HPLC methods for the separation of vitamin D_3 metabolites revealed two major drawbacks. First, the total run times (including equilibration, separation, and washing steps) of the HPLC methods coupled to UV and scintillation detection last 23 min and 22 min, respectively, which strongly reduced the capability of high-throughput analysis. And second, the quite high flow rate of 1 $^{ml}/_{min}$ diluted the eluting compounds and influenced their ionization in MS/MS detection negatively.

To overcome dilution effects because of a high flow rate in MS/MS detection, vitamin D metabolites were separated at a lower flow rate of 300 µl/min on a Kinetex 2.6 µm C18 column with a diameter of 2.1 mm (Kinetex 2.6 µm C18 100 Å 50 mm x 2.1 mm; instead of 4.6 mm). The smaller volume of this Kinetex column in combination with a faster mobile phase gradient resulted in a shorter run time [II.11.2.3], whereby the most hydrophobic vitamin D_3 metabolites, 1α-(OH)-D_3 (peak 4) and vitamin D_3 (peak 5), eluted at 5.4 min and 6.0 min, respectively, but the peaks corresponding to 24,25-$(OH)_2$-D_3 (peak 1; t_R = 1.8 min) and 1α,25-$(OH)_2$-D_3 (peak 2; t_R = 2.3 min) remained baseline separated [Figure III-35]. Thereby, the two 24,25-$(OH)_2$-D_3 enantiomers, (24S)-24,25-$(OH)_2$-D_3 and (24R)-24,25-$(OH)_2$-D_3, were again not distinguishable and were, thus, not further differentiated. For the chromatography it was again of importance that the extracted metabolites and reference samples were applied to the column dissolved in 65-70 % methanol. At higher methanol concentrations (e.g., 100 % methanol) peaks representing 24,25-$(OH)_2$-D_3, 1α,25-$(OH)_2$-D_3, and 25-(OH)-D_3 showed very strong fronting and reduced peak heights making a baseline separation of 24,25-$(OH)_2$-D_3 and 1α,25-$(OH)_2$-D_3 as well as an analysis of the aforementioned metabolites impossible [Figure III-38F]. The same was true for the vitamin D_2 metabolites 1α,25-$(OH)_2$-D_2 and 25-(OH)-D_2 [Figure III-38F], which were together with vitamin D_2 later implemented into the vitamin D LC-MS/MS method.

Although vitamin D metabolites could be well baseline separated on the Kinetex 2.6 µm C18 100 Å 50 mm x 2.1 mm column within 8 min using the established LC-MS/MS method, the total run time per sample was about 18 min. The quite long total run time resulted from a preceding equilibration step (5 min), which assured stable retention times t_R of vitamin D metabolites, as well as an additional LC wash method (5 min), which minimized potential (autosampler) carry-overs and protected the column.

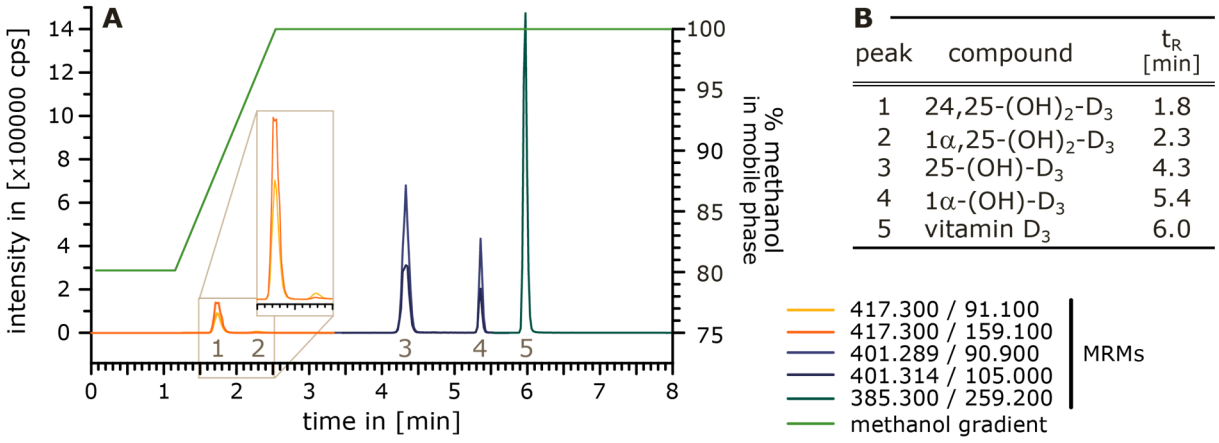

B

peak	compound	t_R [min]
1	24,25-$(OH)_2$-D_3	1.8
2	1α,25-$(OH)_2$-D_3	2.3
3	25-(OH)-D_3	4.3
4	1α-(OH)-D_3	5.4
5	vitamin D_3	6.0

Figure III-35: Detection of vitamin D_3 metabolites via LC-MS/MS: The ionization and detectability of 1α,25-$(OH)_2$-D_3 in ESI positive mode without the addition of supplements is very poor.
(A) Representative chromatogram illustrating the separation of vitamin D_3 metabolites on a Kinetex 2.6 µm C18 100 Å 50 mm x 2.1 mm column with SecurityGuard Standard C18 4 mm x 2 mm cartridge via an initial HPLC method using 0.05 % formic acid in MilliQ-H_2O as mobile phase A and 0.1 % formic acid in methanol as mobile phase B as well as the applied methanol gradient (green line). The reference mix contained each vitamin D_3 metabolite in a concentration of 0.5 µM in 67 % methanol in MilliQ-H_2O (corresponding to 4 ng of each vitamin D_3 metabolite loaded on the column). **(B)** List of retention times (t_R) of analyzed vitamin D_3 metabolites.

Casetta *et al.* reported that the addition of lithium ions to the mobile phase could promote the ionization of the poorly detectable 1α,25-$(OH)_2$-D_3 by forming stable lithium adducts [266].

Using a mobile phase A without lithium ions, like exemplarily shown in Figure III-35 and Figure III-36A, C, the ionization of the biologically important and interesting 1α,25-$(OH)_2$-D_3 by protonation $(M+H)^+$ was very poor. The same was true for the vitamin D_2 derivative 1α,25-$(OH)_2$-D_2, which was together with 25-(OH)-D_2 and vitamin D_2 from now on also included in the analyzable vitamin D metabolite panel. However, a mobile phase A supplemented with lithium acetate, which did not influence the retention times and peak shapes, promoted the ionization of these compounds by forming almost exclusively stable positively charged lithium adducts $(M+Li)^+$ [Figure III-36B, D; Figure III-37]. Thus, the detection limits of 1α,25-$(OH)_2$-D_3 and 1α,25-$(OH)_2$-D_2 lithium adduct MRMs (Q_1 [m/z] = $(M+Li)^+$ = approx. 423 and 435, respectively) was below 4 pg of the respective dihydroxylated vitamin D metabolite reference sample loaded on the column (column load). In comparison, peaks of protonated 1α,25-$(OH)_2$-D_3 and 1α,25-$(OH)_2$-D_2 mother ion MRMs (Q_1 [m/z] = $(M+H)^+$ = approx. 417 and 429, respectively) exceeded, in the absence of lithium ions in the mobile phase, only the background levels and were, thus, only detectable if at least 400 pg metabolite were loaded on the column [Figure III-36A, C; Figure III-37]. Although the ionization and detectability of 24,25-$(OH)_2$-D_3 in the absence of lithium ions (Q_1 [m/z] = $(M+H)^+$ = approx. 417) was about 10- to 20-fold higher when compared with 1α,25-$(OH)_2$-D_3, the addition of lithium acetate to the mobile phase A affected also positively the ionization of 24,25-$(OH)_2$-D_3 by forming stable lithium adducts with this metabolite (Q_1 [m/z] = $(M+Li)^+$ = approx. 423), too. As a result, the detection limit of 24,25-$(OH)_2$-D_3 reference samples was decreased from approximately 20 pg column load (for $(M+H)^+$ without lithium ions) to less than 2 pg (for $(M+Li)^+$ with lithium ions) [Figure III-36, Figure III-37]. Unlike 1α,25-$(OH)_2$-D_3, beside lithium adducts, protonated 24,25-$(OH)_2$-D_3 mother ions could also be detected in the presence of lithium ions, however, with much lower intensity. In contrast, only a minor portion of vitamin D_3 and vitamin D_2 formed stable lithium adducts in the presence of lithium ions, which is indicated by marginally reduced peak areas of protonated mother ion MRMs (Q_1 [m/z] = $(M+H)^+$ = approx. 385 and 397, respectively) and much lower intensities of vitamin D_2 peaks monitoring its lithium adducts (Q_1 [m/z] = $(M+Li)^+$ = approx. 403) when compared with the respective protonated mother ions (Q_1 [m/z] = $(M+H)^+$ = approx. 397) [Figure III-37]. This led to a detection limit of less than 1 pg column load for protonated vitamin D_3 and vitamin D_2 mother ion MRMs. 25-(OH)-D_3, 1α-(OH)-D_3, and 25-(OH)-D_2 displayed intermediates. Here, only a portion of the loaded metabolites formed stable lithium adducts in the presence of lithium ions. In the case of 25-(OH)-D_3 and 1α-(OH)-D_3 similar intensities of protonated and lithium adduct MRMs (Q_1 [m/z] = $(M+H)^+$ = approx. 401 and Q_1 [m/z] = $(M+Li)^+$ = approx. 407, respectively) were detected. However, these intensities were much below the intensities observed for the protonated mother ion MRMs (Q_1 [m/z] = $(M+H)^+$ = approx. 401) in the absence of lithium ions [Figure III-36, Figure III-37]. Thus, the detection limits were approximately 20 pg and 2 pg column load using a mobile phase with and without lithium acetate, respectively. Similar to 25-(OH)-D_3, the intensity of protonated 25-(OH)-D_2 mother ion MRMs (Q_1 [m/z] = $(M+H)^+$ = approx. 413) were strongly reduced in analyses with lithium ions. But here, the lithium adduct MRM 419.323/361.300 exceeded the signal intensities of protonated 25-(OH)-D_2 MRMs occurring in the absence of lithium ions by more than 10-fold and revealed a detection limit of approximately 2 pg column load.

When looking at Figure III-37 it seems that in some cases lithium adducts of vitamin D metabolites could be detected even if no lithium acetate was supplemented. Since the areas of those peaks were proportionally very little, the occurrence of those adducts were most likely artificial and resulted from higher background signals. However, a leaching of lithium ions from glass surfaces or linings could not be excluded.

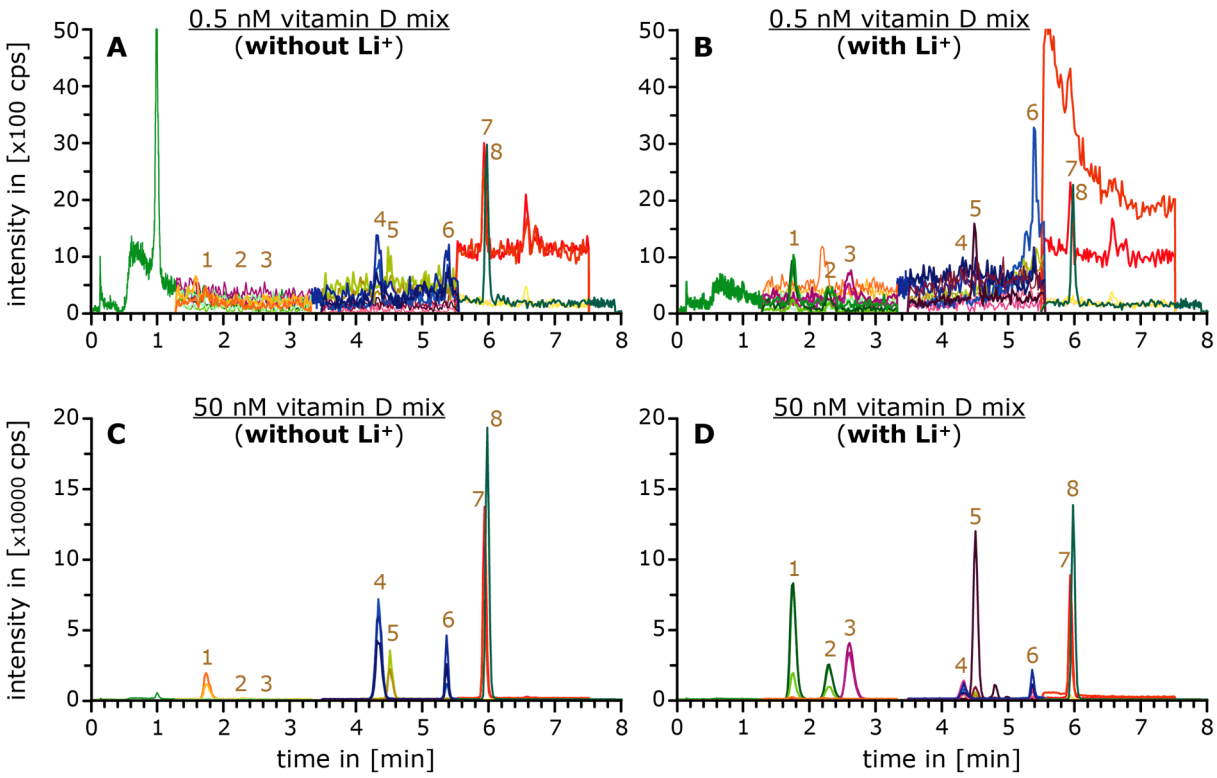

E

	peak	retention time [min]	MRM (Q_1 / Q_3) H^+ adducts	MRM (Q_1 / Q_3) Li^+ adducts
24,25-$(OH)_2$-D_3	1	1.8	417.300 / 91.100	423.174 / 91.000
1α,25-$(OH)_2$-D_3	2	2.3	417.300 / 159.100	423.323 / 77.000
				423.174 / 128.000
25-(OH)-D_3	4	4.3	401.289 / 90.900	407.326 / 90.900
1α-(OH)-D_3	6	5.4	401.314 / 105.000	407.185 / 105.000
			401.300 / 159.200	
vitamin D_3	8	6.0	385.300 / 259.200	
1α,25-$(OH)_2$-D_2	3	2.7	429.373 / 90.900	435.314 / 91.000
			429.373 / 79.000	435.314 / 77.100
25-(OH)-D_2	5	4.5	413.332 / 91.000	419.323 / 361.300
			413.332 / 105.000	419.323 / 77.000
vitamin D_2	7	5.9	397.325 / 91.100	403.300 / 91.000
			397.325 / 105.000	403.300 / 77.100

Figure III-36: The addition of lithium ions to the mobile phase enhances the ionization and detectability of dihydroxylated vitamin D metabolites through the formation of stable lithium adducts.
(A-D) Representative chromatograms illustrating the separation of vitamin D metabolites on a Kinetex 2.6 µm C18 100 Å 50 mm x 2.1 mm column with SecurityGuard Standard C18 4 mm x 2 mm cartridge and their detectability via the final HPLC method [II.11.2.3] without **(A, C)** and with **(B, D)** 0.15 mM lithium acetate in the mobile phase A. The analyses were performed on the same day using the same reference mixes which contained each vitamin D metabolite in a concentration of 0.5 nM **(A, B)** or 50 nM **(C, D)** (correspond to approx. 4 pg or 400 pg of each vitamin D metabolite loaded onto the column, respectively). **(E)** List of retention times and monitored MRMs of analyzed vitamin D metabolites.

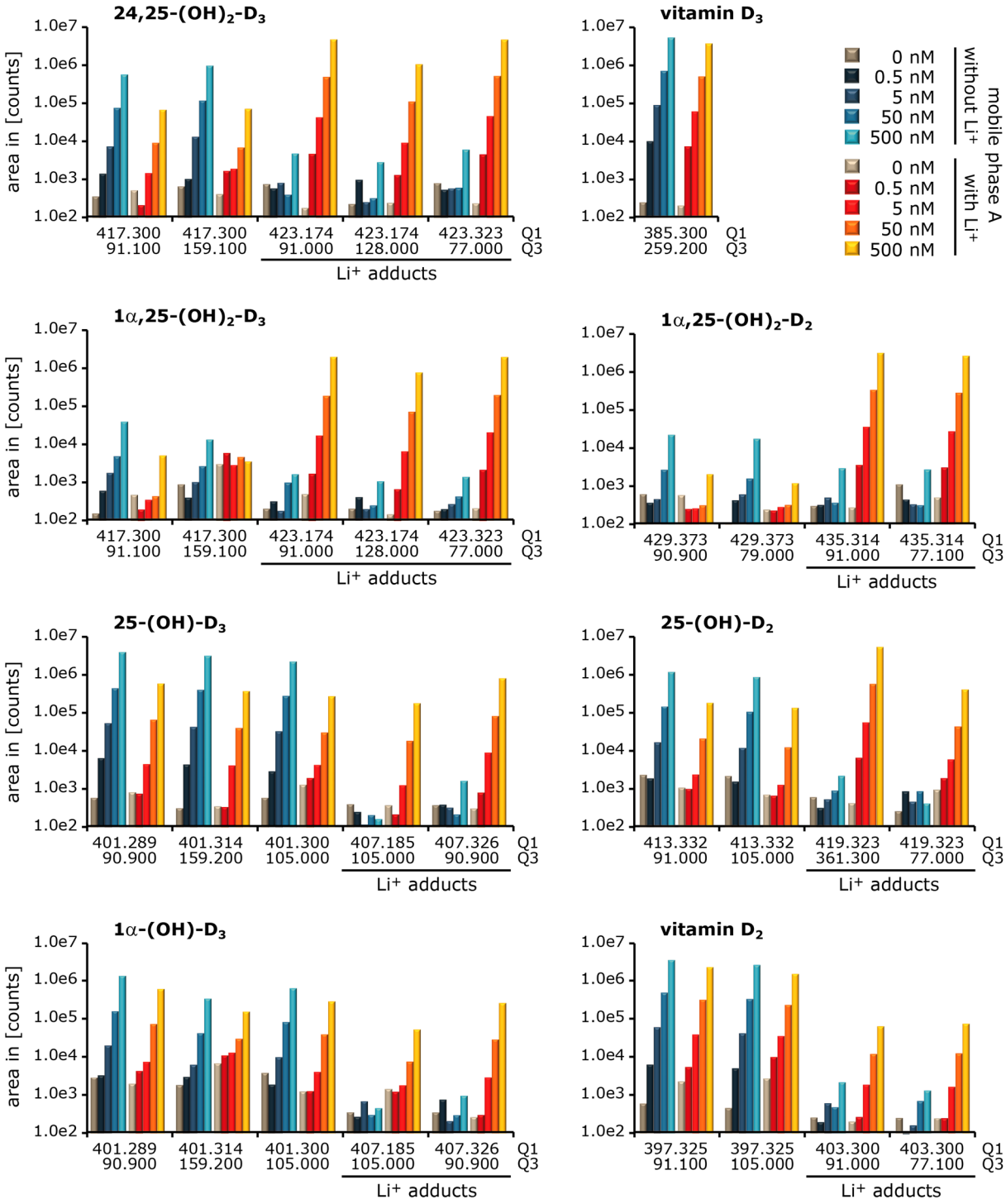

Figure III-37: The comparison of protonated and lithium adduct MRM peak areas demonstrates a clear benefit by the addition of lithium ion with respect to the overall sensitivity of the LC-MS/MS method.
Shown are raw peak areas of various MRMs monitored per vitamin D metabolite in logarithmic scale. The peak areas resulted from the analysis of vitamin D reference mix samples containing each metabolite in a concentration of 0.5-500 nM (correspond to approx. 4 pg - 4 ng vitamin D metabolite loaded on the column), after their separation on a Kinetex 2.6 µm C18 100 Å 50 mm x 2.1 mm column with SecurityGuard Standard C18 4 mm x 2 mm cartridge using the final HPLC method without (blue bars) and with (red-yellow bars) 0.15 mM lithium acetate in the mobile phase A [II.11.2.3, VI.8].
Please note that, although no lithium acetate was supplemented (blue bars), it seemed that lithium adducts could be detected. However, these areas were proportionally very small and thus could also result from stronger background signals. In addition, it cannot be excluded that lithium ions dissolved away from glass surfaces or linings.

In summary, the established HPLC method using 0.15 mM lithium acetate and 0.05 % formic acid in MilliQ-H_2O as mobile phase A and 0.1 % formic acid in methanol as mobile phase B allowed for a sensitive detection (in the low picogram range) of vitamin D metabolites. Thereby, the addition of lithium ions to the mobile phase A increased significantly the detectability of the biologically low abundant vitamin D metabolites 1α,25-$(OH)_2$-D_3 and 1α,25-$(OH)_2$-D_2. In contrast, 25-(OH)-D_3 formed only partially stable lithium adducts which was associated with similar portions of protonated and lithium adduct mother ions and resulted, thus, in an suboptimal but still acceptable decrease in the signal intensities of 25-(OH)-D_3 MRMs when lithium ions were present. However, the positive effect of lithium ions on the detectability of the generally low abundant 1α,25-$(OH)_2$-D_3 and 1α,25-$(OH)_2$-D_2 outweighs the unfavorable effect for the high abundant 25-(OH)-D_3 by far. Although a multitude of MRMs of the respective vitamin D metabolites were considered in the adaptation of the HPLC method [VI.8], only MRMs with highest signal intensities were used for the final validation of the vitamin D LC-MS/MS method (see II.11.2.3 and III.3.5).

III.3.4. Extraction of vitamin D metabolites from cell culture samples

The established vitamin D LC-MS/MS method was primarily intended for the analysis of vitamin D metabolites in cell culture samples. Since an appropriate sample preparation is a good option to concentrate metabolites prior to their measurement but also to reduce interferences within the LC-MS/MS analysis, a sample preparation procedure (including the harvest of cells and the solid phase extraction of vitamin D metabolites from cell culture samples) was established and optimized.

III.3.4.1. Optimizing and testing of solid phase extraction (SPE)

Literature recommended the use of Strata-X 30 µm polymeric reversed phase solid phase extraction cartridges for the extraction of vitamin D metabolites from biological samples. Therefore, a solid phase extraction (SPE) protocol providing highest recovery and "purity" rates was established for Strata-X cartridges. Because predominantly samples with low amounts of vitamin D metabolites should be analyzed and too high capacities of the cartridge sorbent materials might reduce the recovery of those compounds in low amounts, Strata-X 30 µm cartridges with a capacity of 30 $^{mg}/_{ml}$ were selected.

Initial tests analyzing the recovery of applied 25-(OH)-D_3 and vitamin D_3 metabolites with respect to the kind and volume of the elution solvent by HPLC coupled to UV detection (HPLC-UV) showed that the recommended eluent 2 % formic acid in methanol (according to the Strata-X protocol published by Phenomenex) was the most suitable one since it was good to handle, easy to evaporate, and showed higher recovery rates when compared with 100 % methanol, 100 % acetonitrile, or 100 % acetic acid. In addition, elution with two times 150-200 µl 2 % formic acid in methanol resulted in higher recovery rates when compared with a single elution step using 350-400 µl [data not shown].

Having these optimized elution parameters, different conditions for sample loading and washing steps were tested. In assays analyzing the presence of vitamin D metabolites in the flow-through or wash fractions of the SPE and the "purity" of eluates under various conditions by LC-MS/MS, it was found that no vitamin D metabolites were detectable in the flow-through, even if the vitamin D metabolite reference solutions (7.5 ng = approx. 18 pmol of each metabolite) loaded on the preconditioned SPE cartridges (conditioned with 1 ml methanol followed by 1 ml MilliQ-H_2O according to the manufacturer's recommendation) contained up to 52 % methanol in MilliQ-H_2O [Figure III-38A]. The same was true for the successive washing steps using 1 ml 50 % methanol in MilliQ-H_2O or 500 µl 55 % methanol in MilliQ-H_2O [Figure III-38B, C] following the initial washing steps with 1 ml 10 % methanol in MilliQ-H_2O and 1 ml 30 % methanol in MilliQ-H_2O [data not shown]. In contrast, the eluates exhibited all vitamin D metabolites analyzed [Figure III-38E]. However, the MRM signal intensities of the more hydrophobic vitamin D metabolites 1α-(OH)-D_3, vitamin D_2, and vitamin D_3 in the eluates were strongly reduced when compared with the intensities of the equivalent evaporated and reconstituted original reference mixtures (loading control) [Figure III-38D]. Thus, although the best elution conditions were tested in the beginning, these metabolites were highly retained by the column sorbent and, as a result, showed only a poor recovery from the SPE procedure (see also III.3.5.8).

In accord with the results gained from the analysis of vitamin D_3 metabolites by HPLC-UV, reconstitution of eluates or loading controls in 100 % methanol in combination with the vitamin D LC-MS/MS method lead to a strong peak broadening and reduced peak height. These effects were most pronounced among the "rather hydrophilic" vitamin D metabolites 24,25-$(OH)_2$-D_3 (t_R = 1.8 min), 1α,25-$(OH)_2$-D_3 (t_R = 2.3 min), 1α,25-$(OH)_2$-D_2 (t_R = 2.7 min), 25-(OH)-D_3 (t_R = 4.3 min), as well as 25-(OH)-D_2 (t_R = 4.5 min) but were also marginally visible with 1α-(OH)-D_3 (t_R = 5.4 min), vitamin D_3 (t_R = 6.0 min), and vitamin D_2 (t_R = 5.9 min) [Figure III-38F]. As illustrated in Figure III-38, the SPE with vitamin D metabolites using the Strata-X 33 µm polymeric reversed phase (30 $^{mg}/_{ml}$) tubes yielded sufficient pure samples when applying higher amounts of vitamin D metabolites. Though, analysis of blank samples or low concentrated vitamin D reference mixture samples with and without SPE showed that the extraction process was associated with clearly increased background signals when compared with the reconstituted SPE omitted reference materials [Figure III-39]. These background signals were most prominent within the first four minutes and impaired especially the detection of 24,25-$(OH)_2$-D_3 and 1α,25-$(OH)_2$-D_3 but also 25-(OH)-D_2 and 1α-(OH)-D_3. Here, solely the background peak of the 1α-(OH)-D_3 MRM 401.289/90.900, appearing next to the 1α-(OH)-D_3 peak itself, could be referred to the formic acid used within the SPE process [data not shown]. Since all other solvent compounds could be excluded as sources for the remaining background peaks, it was assumed that compounds (e.g., plasticizer) were dissolved out of the cartridge material during the extraction process which interfered with some MRMs monitored for the analysis of vitamin D metabolites.

Since the established SPE procedure was aimed for the sample preparation of cell culture samples, it was also tested with spiked cell and medium samples. The SPE procedure covering the washing steps with 1 ml of each 10 %, 30 %, and 50 % methanol in MilliQ-H_2O and the elution with 350 µl 2 % formic acid in methanol yielded extracts of sufficient purity from spiked cells, comparable to those resulting from the extraction of reference samples without cellular matrix [data not shown]. However, a fourth washing step using 500 µl 55 % methanol in MilliQ-H_2O was necessary for the preparation of extracts from cell culture

medium since tests with supplemented medium (containing phenol red as indicator) showed that a final washing step with 1 ml 50 % methanol in MilliQ-H_2O was not sufficient to totally rinse out phenol red which was also retained by the SPE sorbent material under aqueous conditions [data not shown]. The final SPE method is summarized in Figure III-43.

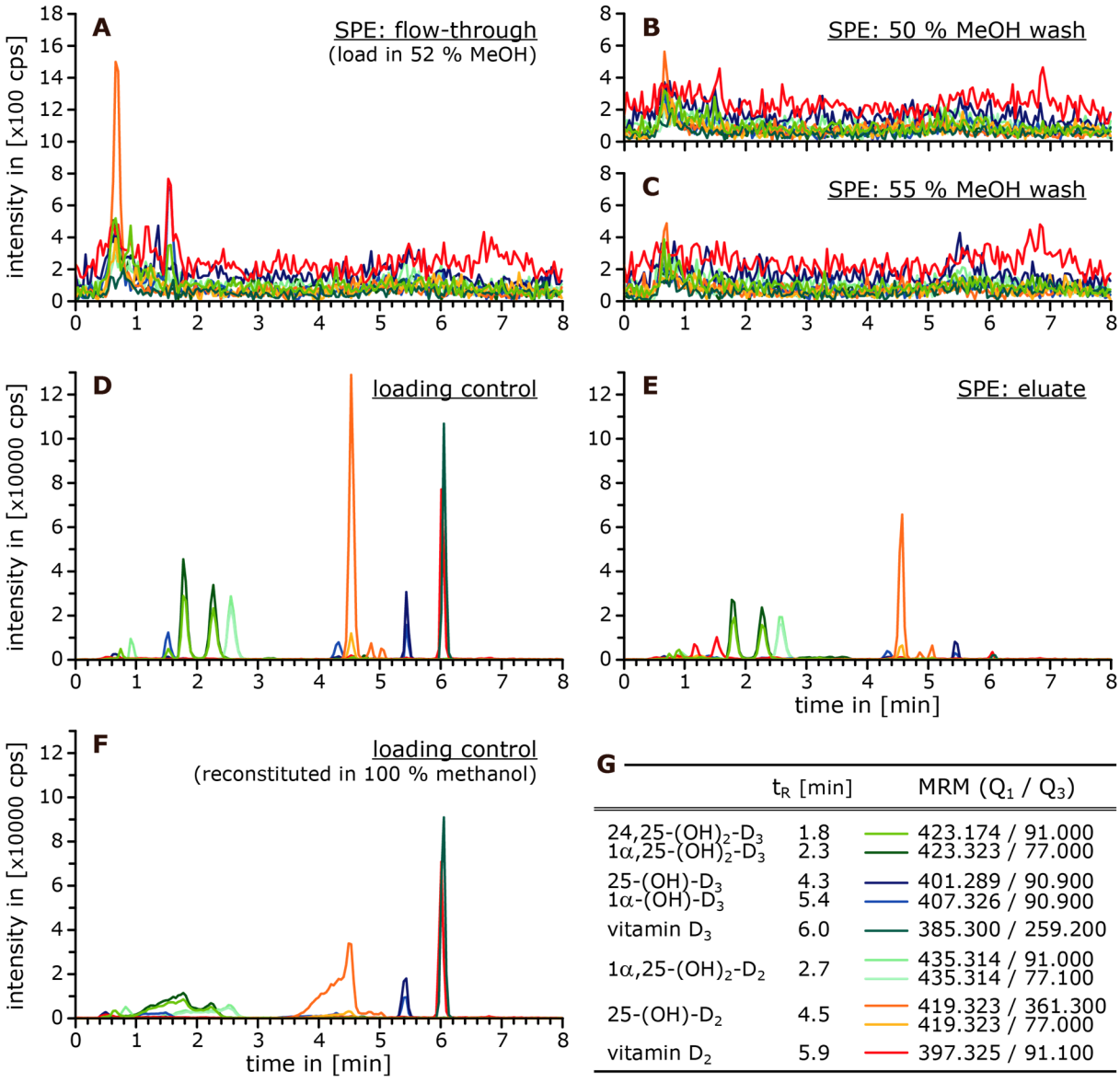

Figure III-38: The developed solid phase extraction procedure using the Strata-X 30 µm sorbent ensures the extraction of vitamin D metabolites without any losses in the flow-through and wash fractions.
Shown are representative chromatograms from the analysis of vitamin D metabolites in fractions of the solid phase extraction (SPE) process **(A-C, E)** and in unprocessed reference samples **(D, F)**. SPE of a mixture of vitamin D metabolites (7.5 ng = approx. 18 pmol of each metabolite) in a total volume of 1250 µl 52 % methanol in MilliQ-H_2O was performed with Strata-X 30 µm 30 $^{mg}/_{ml}$ cartridges as described in II.11.1.4. All fractions were collected, evaporated, and reconstituted in 100 µl methanol and 50 µl MilliQ-H_2O before the SPE flow-through **(A)**, SPE 50 % methanol wash **(B)**, SPE 55 % methanol wash **(C)**, as well as SPE elution **(E)** fractions were analyzed via LC-MS/MS for the occurrence of vitamin D metabolites (according to II.11.2.3). For comparison reasons unprocessed reference samples were additionally analyzed. For this, mixtures of 7.5 ng of each vitamin D metabolite were evaporated and reconstituted in either 100 µl methanol plus 50 µl MilliQ-H_2O **(D)** or 100 % methanol **(F)**. MRMs and retention times (t_R) of the analyzed vitamin D metabolites are listed in **(G)**.

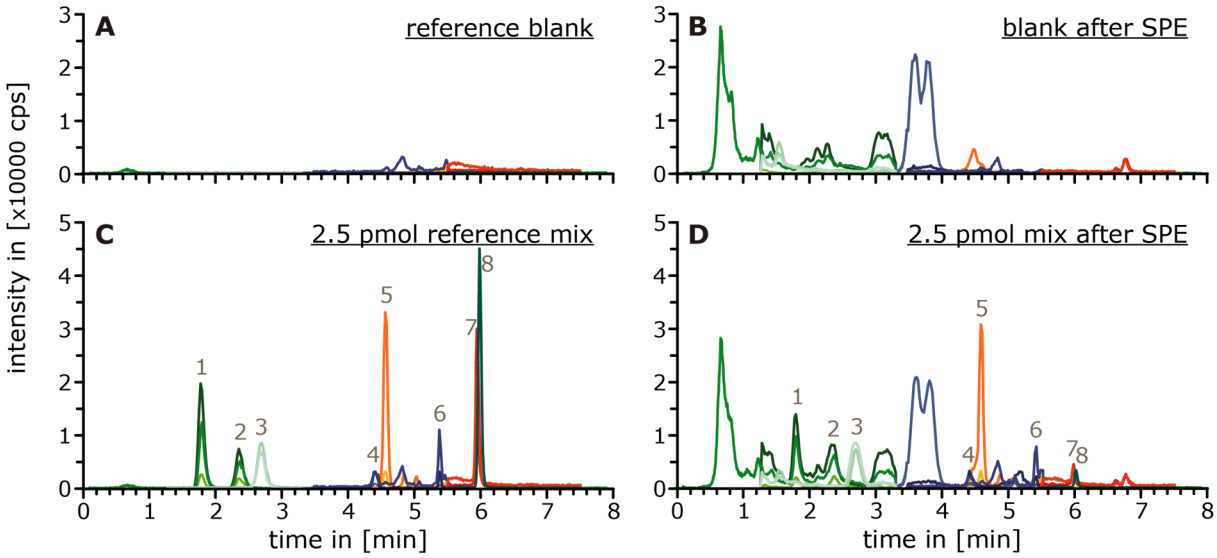

E

	peak	MRM (Q_1 / Q_3)		
24,25-$(OH)_2$-D_3	1	423.174 / 91.000	423.174 / 128.000	423.323 / 77.000
1α,25-$(OH)_2$-D_3	2	423.174 / 91.000	423.174 / 128.000	423.323 / 77.000
1α,25-$(OH)_2$-D_2	3	435.314 / 77.100	435.314 / 91.000	
25-(OH)-D_3	4	401.289 / 90.900	407.185 / 105.000	407.326 / 90.900
25-(OH)-D_2	5	419.323 / 77.000	419.323 / 361.300	
1α-(OH)-D_3	6	401.289 / 90.900	407.185 / 105.000	407.326 / 90.900
vitamin D_2	7	397.325 / 91.100	397.325 / 105.000	
vitamin D_3	8	385.300 / 259.200		

Figure III-39: The SPE process increases background signals in vitamin D LC-MS/MS analysis.
Samples were either only evaporated **(A, C)** or SPE processed [II.11.1.4] **(B, D)** and reconstituted in 100 µl methanol plus 50 µl MilliQ-H_2O before they were analyzed via the final LC-MS/MS method [II.11.2.3].
(A) Chromatogram resulting from the evaporation and reconstitution of 350 µl 2 % formic acid in methanol (reference blank). **(B)** Chromatogram resulting from the SPE eluate of 52 % methanol in MilliQ-H_2O (blank). **(C)** Chromatogram resulting from the evaporation and reconstitution of a mixture of 2.5 pmol vitamin D metabolite each (reference mix) in 350 µl 2 % formic acid in methanol. **(D)** Chromatogram resulting from the SPE eluate of a mixture of 2.5 pmol vitamin D metabolite each (mix) in 52 % methanol in MilliQ-H_2O. **(E)** List of monitored MRMs of vitamin D metabolites and peak numbers.

III.3.4.2. Testing of suitable cell harvest protocols

Three different cell harvest methods were compared regarding the highest detectable signal intensities of vitamin D metabolites (24,25-$(OH)_2$-D_3, 1α,25-$(OH)_2$-D_3, and 25-(OH)-D_3) in harvested cells (and medium).

HaCaT cells were used for the testing of cell harvest methods with respect to the detectability or signal intensity of vitamin D metabolites in the downstream LC-MS/MS analysis because these cells were easy to culture and represented a suitable model cell line for vitamin D metabolism. For this, HaCaT cells were cultured in serum-free DMEM medium for 48 h. Prior to cell harvest, the culture medium was replaced by serum-free DMEM supplemented with the most "hydrophilic" vitamin D_3 metabolites, 24,25-$(OH)_2$-D_3, 1α,25-$(OH)_2$-D_3, and 25-(OH)-D_3, in a final concentration of 0.5 µM each. The cells were incubated therein for 30 min to allow the uptake of the vitamin D metabolites into the cells. Afterwards, the

medium supernatant was collected and the cell layers were washed once with PBS before the cells were harvested by either trypsinization, scraping with PBS, or scraping with methanol in MilliQ-H_2O (MeOH/H_2O) mixtures. Finally, the vitamin D metabolites were extracted from medium or cell samples by SPE and analyzed via LC-MS/MS [Figure III-40].

LC-MS/MS analysis of vitamin D_3 metabolites in HaCaT cells and medium supernatants showed clear differences in MRM intensities and raw peak areas between cells which were harvested by either trypsinization or scraping with PBS and those which were harvested by successive scraping with 60 % and 40 % methanol in MilliQ-H_2O (MeOH/H_2O). As depicted in Figure III-41A, compared with trypsinization or scraping with PBS, cell scraping with the MeOH/H_2O mixtures resulted in significantly higher 24,25-$(OH)_2$-D_3, 1α,25-$(OH)_2$-D_3, and 25-(OH)-D_3 signal intensities (peak areas) in cells. This effect was more pronounced for the more hydrophilic, dihydroxylated vitamin D_3 metabolites 24,25-$(OH)_2$-D_3 and 1α,25-$(OH)_2$-D_3 (> 20-fold and > 15-fold higher versus trypsinized cells or > 15-fold and > 9.5-fold higher versus PBS scraped cells, respectively) than for the monohydroxylated vitamin D_3 metabolite 25-(OH)-D_3 (> 5-fold or > 4-fold higher versus trypsinized or PBS scraped cells, respectively) [Figure III-41B]. Thereby, a divergent uptake of metabolites from the medium could almost certainly be excluded because no significant metabolite differences were detectable in the respective medium supernatants of the harvested cells [Figure III-41A].

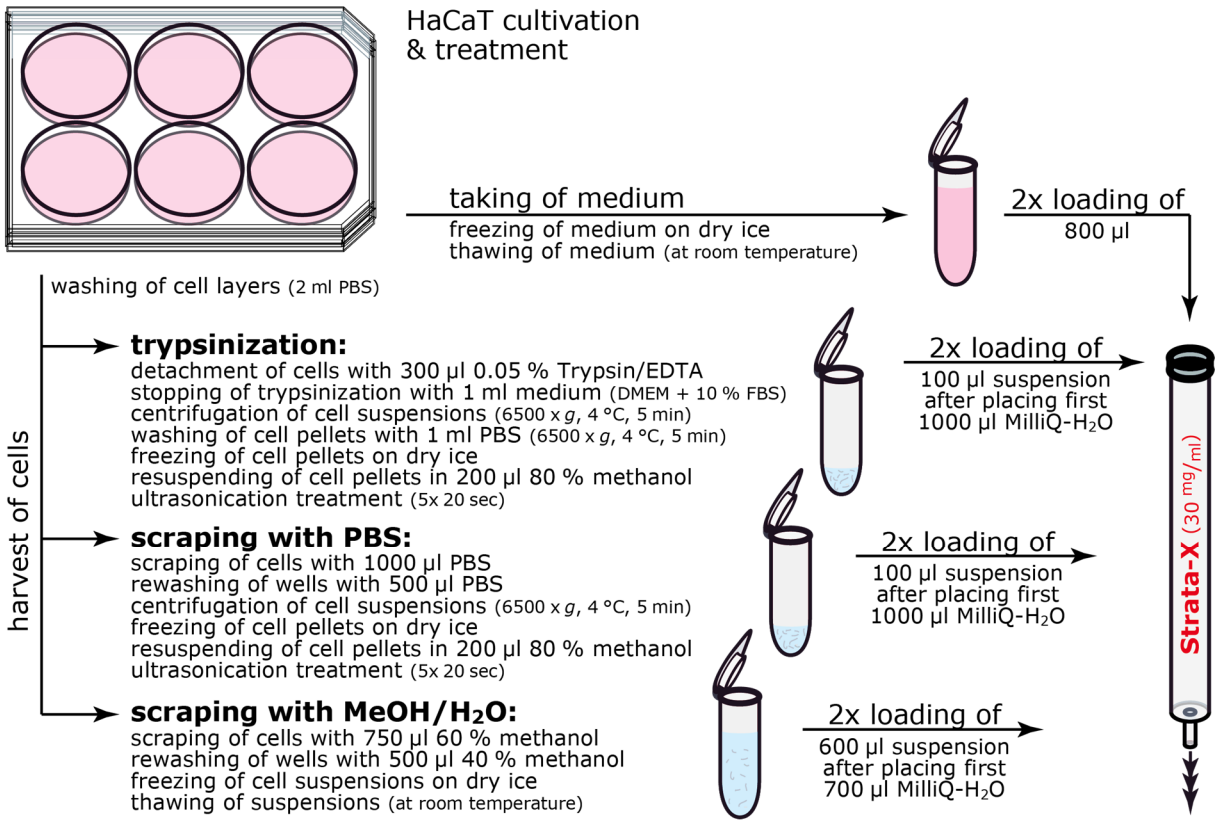

Figure III-40: Illustration of the procedures used for the comparison of vitamin D metabolite signal intensities in HaCaT cells by LC-MS/MS analysis in dependence of the applied harvest method.
$2x10^5$ HaCaT cells were cultured per well of a 6-well plate in 2 ml serum-free DMEM medium for 48 h before the medium was replaced by 2 ml serum-free DMEM supplemented with 0.5 µM 24,25-$(OH)_2$-D_3, 1α,25-$(OH)_2$-D_3, and 25-(OH)-D_3. After an incubation period of 30 min, medium supernatants and cells were processed as illustrated. Final extracts resulting from SPE [II.11.1.4] were analyzed by LC-MS/MS [II.11.2.3].

The varying ratios between the different vitamin D_3 metabolites could be explained by the loss of cells in centrifugation steps and/or the loss of metabolites from leaky cells. Leakage of vitamin D metabolites from damaged cells (due to physical stress during the trypsinization or scraping with PBS) concerns especially hydrophilic metabolites because of their water solubility. Thus, whereas the more "hydrophilic" vitamin D metabolites of leaky cells could accumulate in the aqueous supernatant, more hydrophobic compounds should be stronger retained by cell debris and, therefore, be higher abundant in the pellet after centrifugation.

Within this cell harvest evaluation, the harvested cell samples were diluted in MilliQ-H_2O for the solid phase extraction of vitamin D metabolites. However, later, when cultured cells were processed, this dilution step was not necessary since the scraping with MeOH/H_2O harvest method yield samples for SPE in 52 % methanol in MilliQ-H_2O and it was shown that at this concentration vitamin D metabolites bind completely to the Strata-X sorbent (see III.3.4.1).

In conclusion, the scraping of cells with MeOH/H_2O provided the most sensitive and an easy applicable, quite fast, as well as fail-safe cell harvest method for the analysis of vitamin D metabolites in cultured cells.

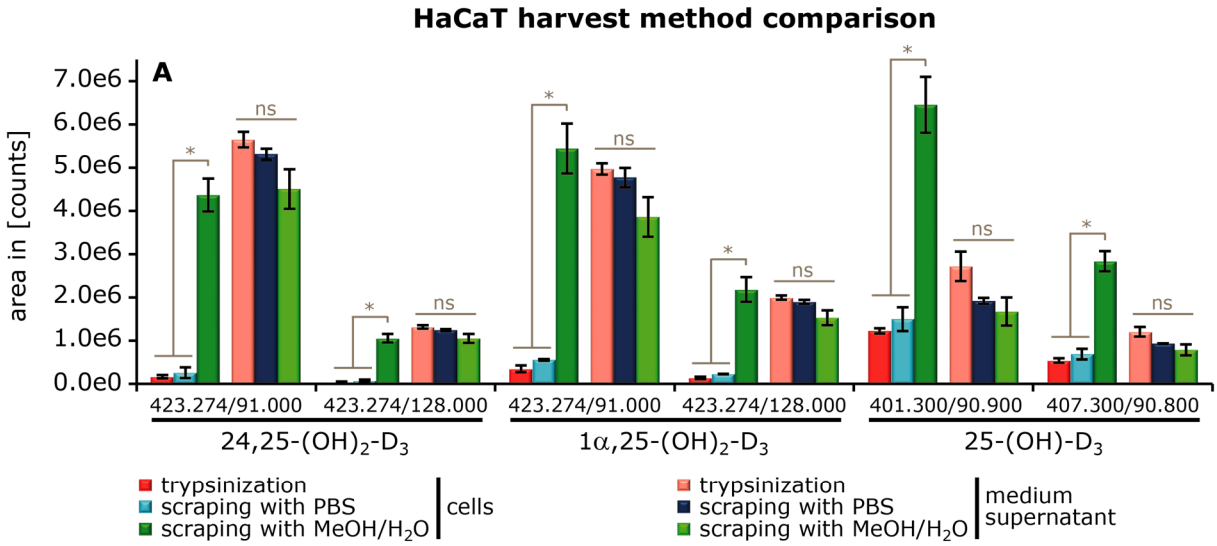

B

ratio (cells)	24,25-$(OH)_2$-D_3		1α,25-$(OH)_2$-D_3		25-(OH)-D_3	
	423.274/91.000	423.274/128.000	423.274/91.000	423.274/128.000	401.300/90.900	407.300/90.800
MeOH/H_2O *vs.* trypsinization	26.0	22.7	15.5	15.5	5.3	5.2
MeOH/H_2O *vs.* PBS	16.9	15.2	9.8	9.6	4.3	4.1

Figure III-41: Scraping of cells with methanol in MilliQ-H_2O mixtures is the most efficient cell harvest method for the analysis of vitamin D metabolites in cultured cells.
Cell harvest methods were evaluated via the comparison of raw peak areas of vitamin D metabolites in differently harvested cell samples. For this, HaCaT cells were treated with 24,25-$(OH)_2$-D_3, 1α,25-$(OH)_2$-D_3, and 25-(OH)-D_3, each in a final concentration of 0.5 µM in serum-free DMEM, for 30 min. Medium was collected and cells were harvested as described in Figure III-40 before medium and cell samples were processed via SPE [II.11.1.4] and analyzed via LC-MS/MS [II.11.2.3].
(A) Average raw peak areas ± SD per metabolite MRM and harvest method in cell or medium triplicates. The statistical significance of peak area variations in dependence of the cell harvest method was determined by Kruskal-Wallis test (*, $p < 0.05$; ns, not significant). **(B)** Ratios of vitamin D metabolite peak areas for differently harvested cells. The ratios were calculated for the analyzed MRMs by dividing the average peak areas of MeOH/H_2O scraped (MeOH/H_2O) cells by the respective average peak area of trypsinized (trypsinization) or PBS scraped (PBS) cells.

III.3.4.3. IMBEDDING AN INTERNAL STANDARD: 25-(OH)-D_2 [25,26,27-$^{13}C_3$]

In order to reduce variations due to heterogeneities within harvest, extraction, and/or LC-MS/MS processes, a stable isotope labeled internal standard (IS), namely the three times ^{13}C-labeled vitamin D_2 derivative 25-(OH)-D_2 [25,26,27-$^{13}C_3$], was implemented in the analysis of vitamin D metabolites.

As expected, the internal standard co-eluted with its unlabeled equivalent 25-(OH)-D_2 and possessed identical ionization properties [Figure III-42A]. However, due to its three ^{13}C labels, the signals of the IS 25-(OH)-D_2 [25,26,27-$^{13}C_3$] (M = 415 g/mol) were well distinguishable from those of the unlabeled 25-(OH)-D_2 (M = 412 g/mol) in mass spectrometric analyses. By adding the IS within the cell harvest process, not only ionization artefacts but also harvest, storage, and extraction deviations could be corrected. IS dilution studies showed that the addition of 30 ng or 40 ng 25-(OH)-D_2 [25,26,27-$^{13}C_3$] per cell or medium sample, respectively, resulted in good quantifiable signal intensities, in the range of 25-(OH)-D_3 MRM signal intensities from harvested cells which were treated with 0.5 µM or 2 µM 25-(OH)-D_3 for 90 min and below the non-linear detector range [Figure III-42B, C; data not shown for medium]. The addition of 30-40 ng 25-(OH)-D_2 [25,26,27-$^{13}C_3$] as IS did not impair the analysis of other vitamin D metabolites in cell culture samples [data not shown] and enabled the comparison of relative or absolute vitamin D levels in different samples by minimizing harvest or ionization artefacts and promoting stable and reproducible results (see III.3.5).

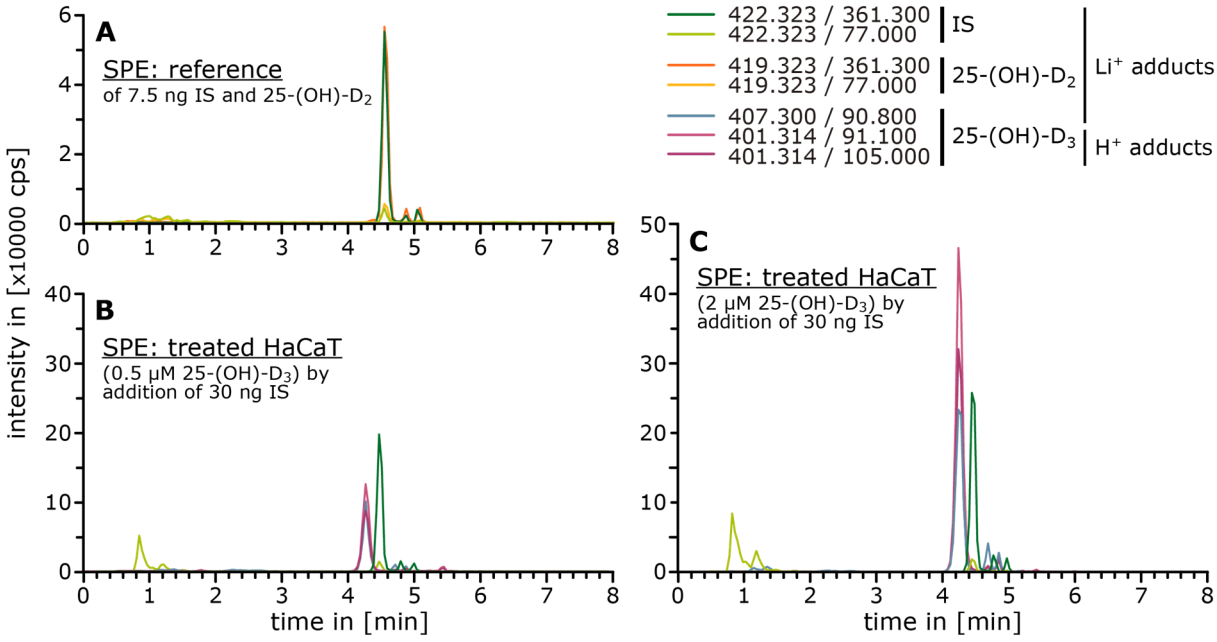

Figure III-42: The addition of 30 ng 25-(OH)-D_2 [25,26,27-$^{13}C_3$] as internal standard within the cell harvest process was found to be suited for the quantitative analysis of vitamin D metabolites in cells.
(A) Representative chromatogram from the LC-MS/MS analysis of SPE processed samples containing a mixture of 7.5 ng 25-(OH)-D_2 [25,26,27-$^{13}C_3$] (IS) and 7.5 ng 25-(OH)-D_2 in 52 % methanol in MilliQ-H_2O. **(B, C)** Representative chromatograms from the LC-MS/MS analysis of SPE processed HaCaT cell samples which were incubated with 0.5 µM **(B)** or 2 µM **(C)** 25-(OH)-D_3 for 90 min and afterwards harvested by consecutive scraping with 750 µl 60 % methanol in MilliQ-H_2O supplemented with 30 ng IS and 500 µl 40 % methanol in MilliQ-H_2O. SPE and LC-MS/MS analysis were performed according to established procedures described in II.11.1.4 and II.11.2.3, respectively.

III.3.4.4. FINAL METHOD FOR CELL CULTURE SAMPLE PREPARATION

Figure III-43 summarizes the established sample preparation procedure for the analysis of vitamin D metabolites in cell culture samples. Please note that, although initially established for cell culture samples, the described SPE procedure was also applicable to mouse tumor samples and human plasma samples in pilot experiments (see III.3.6.2 and III.3.6.3).

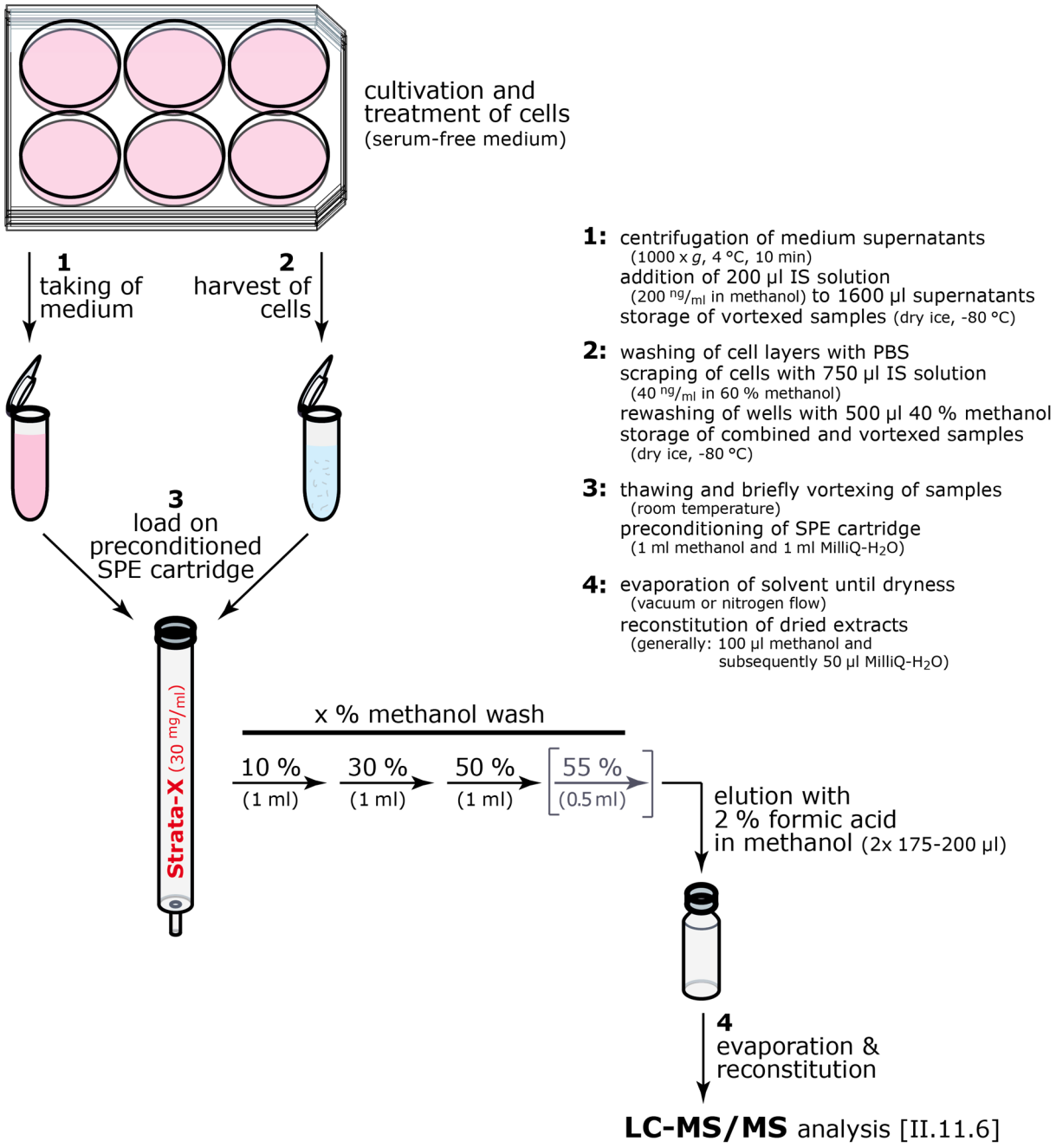

Figure III-43: Sample preparation procedure for the analysis of samples from cell culture experiments. Summarized are the steps of the final method for the preparation of cell culture samples for LC-MS/MS analysis. The internal standard (IS) 25-(OH)-D_2 [25,26,27-$^{13}C_3$] is already added within the harvest process and Strata-X 33 µm polymeric reversed phase (30 mg/ml) tubes are used for the SPE. The 55 % methanol wash step within the SPE procedure is only necessary with medium samples (indicated by a squared bracket) in order to reduce the amount of phenol red and possibly other compounds in the eluate.

III.3.5. VALIDATION OF THE VITAMIN D LC-MS/MS METHOD FOR CELL CULTURE SAMPLES

The previous chapters described the establishment of a solid phase extraction (SPE) based sample preparation method and a subsequent LC-MS/MS analysis method for the analysis of vitamin D metabolites in cell culture samples. In order to objectively characterize the capabilities of the established methods in more detail, the final vitamin D LC-MS/MS method (covering the SPE sample preparation process and the LC-MS/MS analysis process) was basically validated for cell culture samples, especially with regard to its limits of detection (LODs) and quantification (LOQs), linearity, selectivity, reproducibility, precision, recovery, and stability.

The different validation parameters were determined from the analysis of the either unprocessed or SPE processed vitamin D reference mix samples as well as vitamin D spiked and subsequently SPE processed cell culture samples (covering ASZ001, HaCaT, $Ptch^{WT}$, or $Ptch^{-/-}$ cells and DMEM or 154CF media [Table II-31]) via LC-MS/MS using a scheduled MRM detection as described in II.11.3. Thereby, each prepared sample was measured twice: first, on the day of sample preparation (day 0) and second, six days after the sample preparation and first measurement (day 6).

III.3.5.1. DESIGN OF A QUANTIFICATION METHOD FOR VITAMIN D METABOLITES

In chapter III.3.4.1 it was shown that the SPE process resulted in increased background peak intensities when compared with the direct injection of reference mixes. In order to maximize the selectivity of the vitamin D LC-MS/MS method, with the exception of vitamin D_3, two to three different MRM transitions were monitored per metabolite [Table III-6]. Considering the respective sensitivity (metabolite signal intensities vs. background intensities) as well as the linearity and accuracy of the MRMs, one to two MRMs were defined as quantifier, whereas the others were used as qualifier [Table III-6]. Although merely the quantifier MRMs were used for the quantification of the respective vitamin D metabolites, only those vitamin D metabolite signals were considered to be specific and were quantified which featured peaks of both quantifier and qualifier MRMs.

Peak areas of quantifier MRMs were used for the generation of calibration curves as well as the relative and absolute quantification of vitamin D metabolites in samples. For this, the peak areas of vitamin D metabolite quantifier MRMs were normalized to (divided by) the peak area of the internal standard (IS: 25-(OH)-D_2 [25,26,27-$^{13}C_3$]) quantifier MRM (422.323/ 361.300) in the respective sample. The calibration curves used for the quantification of vitamin D metabolites in cell culture samples were generated from triplicates of SPE processed vitamin D reference mixes (1-100 pmol) in 1.25 ml 52 % methanol in MilliQ-H_2O supplemented with 30 ng IS [II.11.3]. For this, the normalized peak areas of the quantifier MRMs in the reference sample were plotted against the amount of vitamin D metabolite in the respective sample and the calibration equation was determined by fitting the data points (> LOQ) to a straight line (linear fit) without any weighting.

Table III-6: Qualifier and quantifier MRMs used for the detection / quantification of vitamin D metabolites in cell culture samples.

metabolite	MRM			adduct	quantifier	qualifier
	Q_1	/	Q_3			
24,25-$(OH)_2$-D_3	423.174	/	91.000	Li^+	X	
	423.174	/	128.000	Li^+	X	
	423.323	/	77.000	Li^+		X
1α,25-$(OH)_2$-D_3	423.174	/	91.000	Li^+	X	
	423.174	/	128.000	Li^+	X	
	423.323	/	77.000	Li^+		X
25-(OH)-D_3	401.289	/	90.900	H^+		X
	407.185	/	105.000	Li^+		X
	407.326	/	90.900	Li^+	X	
1α-(OH)-D_3	401.289	/	90.900	H^+	X	
	407.185	/	105.000	Li^+		X
	407.326	/	90.900	Li^+	X	
vitamin D_3	385.300	/	259.200	H^+	X	
1α,25-$(OH)_2$-D_2	435.314	/	91.000	Li^+	X	
	435.314	/	77.100	Li^+		X
25-(OH)-D_2	419.323	/	361.300	Li^+	X	
	419.323	/	77.000	Li^+		X
vitamin D_2	397.325	/	91.100	H^+	X	
	397.325	/	105.100	H^+		X
internal standard (IS) 25-(OH)-D_2 [25,26,27-$^{13}C_3$]	419.323	/	361.300	Li^+	X	
	419.323	/	77.000	Li^+		X

Generally quantifier MRMs with best sensitivities (represented by highest signal intensities and signal-to-noise ratios) were used for the quantification of vitamin D metabolites, however, only if the respective qualifier MRM was also detectable.

III.3.5.2. LIMITS OF DETECTION (LOD) AND QUANTIFICATION (LOQ)

Previous chapters showed that the SPE process applied within the sample preparation for vitamin D LC-MS/MS analysis resulted in higher background signals when compared with unprocessed samples [III.3.4.1]. Thus, SPE processed reference solutions were used for the determination of the limits of detection (LODs) and limits of quantification (LOQs) of the vitamin D LC-MS/MS method. Although the generated quantification method considers normalized peak areas, the peak heights of quantifier MRM signals were taken to determine the LOD and LOQ of the respective vitamin D metabolite quantifier. According to published procedures, two slightly varying algorithms, herein after referred to as "blank" and "blank & low", were applied for the assessment of LOD and LOQ values [267, 268].

Using the first algorithm (blank), the LOD and LOQ values were calculated from the average noise (SD) of blank sample replicates (SD_{blank}). The LOD was set to 3.3x SD_{blank}, whereas the LOQ was defined as 3x LOD corresponding to 10x SD_{blank} [268].

The second algorithm (blank & low) considered the peak heights of blank and low amount samples for the determination of LOD and LOQ values. The LOD was calculated according to Equation III-1 by choosing a confidence interval of 95 % [267, 268]. The LOQ was again defined as 3x LOD [268].

$$y_{LOD} = \overline{y}_{blank} + t_{(n,\,0.95)} \cdot \left(SD_{blank} + SD_{sample}\right) / \sqrt{n}$$

Equation III-1: Blank & low algorithm used for the calculation of LOD peak heights by considering blank and low amount samples. y_{LOD}, minimum peak height for peak detection; $\bar{y}_{blank}$, mean peak height of blank samples; $t_{(n,\,0.95)}$, t-distribution quantiles at 0.95 % confidence level; SD_{blank}, average noise of blank samples; SD_{sample}, standard deviation of peak heights of low concentrated sample replicates; n, number of replicates.

Both algorithms revealed LOD and LOQ values for the analyzed quantifier MRMs of different vitamin D metabolites at similar levels [Table III-7]. However, the blank & low algorithm, which considers additionally the variation in peak heights of low concentrated samples (1 pmol), was more stringent. By calculating the LOD of vitamin D metabolites from the average noise of blank samples (blank), the detection limit of each metabolite in the original sample was equal or below 1 pmol [Table III-7]. This was also true for most LOD values determined by the blank & low algorithm, however, with the exception of the LODs ascertained for the 1α,25-(OH)$_2$-D$_3$ MRM 423.174/91.000 and both 1α-(OH)-D$_3$ MRMs which were about 1.5 pmol and 1.5-2 pmol, respectively [Table III-7].

Table III-7: LOD and LOQ of the established vitamin D LC-MS/MS method.

metabolite	MRM			LOD [pmol]		LOQ [pmol]	
	Q_1	/	Q_3	blank	blank & low	blank	blank & low
24,25-(OH)$_2$-D$_3$	423.174	/	91.000	**< 0.5**	**< 0.5**	**0.5**	**0.5**
24,25-(OH)$_2$-D$_3$	423.174	/	128.000	**< 1.0**	**< 1.0**	**1.0**	**1.0**
1α,25-(OH)$_2$-D$_3$	423.174	/	91.000	1.0	**1.5**	3.5	**5.0**
1α,25-(OH)$_2$-D$_3$	423.174	/	128.000	**< 1.0**	**< 1.0**	1.5	**2.5**
25-(OH)-D$_3$	407.326	/	90.900	**< 1.0**	**< 1.0**	1.5	**2.0**
1α-(OH)-D$_3$	401.289	/	90.900	1.0	**1.5**	2.5	**4.0**
1α-(OH)-D$_3$	407.326	/	90.900	1.0	**2.0**	3.0	**4.5**
vitamin D$_3$	385.300	/	259.200	< 0.5	**< 1.0**	0.5	**1.0**
1α,25-(OH)$_2$-D$_2$	435.314	/	91.000	**< 0.5**	**< 0.5**	**0.5**	**0.5**
25-(OH)-D$_2$	419.323	/	361.300	**< 0.5**	**< 0.5**	**0.5**	**0.5**
vitamin D$_2$	397.325	/	91.100	< 0.5	**1.0**	**1.0**	**1.0**

The listed LODs and LOQs of the vitamin D LC-MS/MS method for different vitamin D quantifier MRMs refer to vitamin D amounts in the original SPE processed reference mix sample. LOD and LOQ values were either determined from the average noise of blank sample replicates (blank) or from blank and low amount sample replicates (blank & low) by determining the standard deviation of peak heights with blank samples or applying Equation III-1, respectively. The resulting LOD and LOQ peak heights were correlated to the vitamin D metabolite amount in the respective reference samples. More stringent LOD and LOQ values, which were used in the following validation process, are highlighted in bold.

The LOQ was defined as three times the peak height of the LOD, hence, the resulting limits of quantification of the method for vitamin D metabolites were in the range between 0.5 pmol for 24,25-$(OH)_2$-D_3 (MRM 423.174/91.000), 1α,25-$(OH)_2$-D_2 (MRM 435.314/91.000), or 25-(OH)-D_2 (MRM 419.323/361.300) and 5 pmol for 1α,25-$(OH)_2$-D_3 (MRM 423.174/91.000) in the original sample [Table III-7].

III.3.5.3. SELECTIVITY OF THE LC-MS/MS METHOD

As mentioned in III.3.4.1, the SPE sample preparation process was linked to increased background signals in LC-MS/MS analysis which impaired the detection of some vitamin D metabolite MRM peaks with low intensity. Besides the monitoring of quantifier and qualifier MRMs for one metabolite (see III.3.5.1), stable and defined retention times of metabolites within the chromatographic separation ensure the selective detection and quantification of all vitamin D metabolites. In order to evaluate the selectivity of the vitamin D LC-MS/MS method, the variability in retention times of peaks belonging to the same metabolite was analyzed. Here it was seen that the average retention times t_R of all vitamin D metabolites (considering peaks above LOD of all MRMs per analyte) with all analyzed matrices (reference mixes with and without SPE processing as well as SPE processed cell culture samples) were very stable and showed only very small (< 1 %) overall intraday and interday coefficients of variation ($CV_{(intraday)}$ and $CV_{(interday)}$, respectively) [Table III-8].

Thus, the herein demonstrated robust chromatography enables together with the selected quantifier and qualifier MRMs the selective detection of vitamin D metabolites by the established vitamin D LC-MS/MS method.

Table III-8: Intra- and interday variability of retention times of vitamin D metabolites.

metabolite	t_R [min]		$CV_{(intraday)}$ [%]		$CV_{(interday)}$ [%]
	day 0	day 6	day 0	day 6	day 0 & 6
24,25-$(OH)_2$-D_3	1.81 ± 0.01	1.82 ± 0.01	0.68	0.49	0.67
1α,25-$(OH)_2$-D_3	2.39 ± 0.02	2.39 ± 0.01	0.82	0.54	0.72
25-(OH)-D_3	4.43 ± 0.02	4.42 ± 0.01	0.42	0.26	0.37
1α-(OH)-D_3	5.40 ± 0.02	5.39 ± 0.01	0.34	0.20	0.31
vitamin D_3	6.01 ± 0.01	5.99 ± 0.01	0.23	0.09	0.24
1α,25-$(OH)_2$-D_2	2.71 ± 0.02	2.72 ± 0.01	0.78	0.47	0.65
25-(OH)-D_2	4.59 ± 0.02	4.58 ± 0.01	0.33	0.16	0.28
vitamin D_2	5.97 ± 0.01	5.95 ± 0.01	0.24	0.08	0.25
internal standard	4.59 ± 0.01	4.58 ± 0.01	0.31	0.16	0.28

The listed average retention time ± SD for vitamin D metabolites was determined from the analysis of LC-MS/MS chromatograms of in total 90 samples, containing different amounts of metabolites (1-100 pmol) in different matrices [II.11.3]. Please note that the retention times of peaks belonging to the same compound but resulting from different MRMs were combined. The intra- and interday coefficients of variation were calculated according to Equation III-2.
CV, coefficient of variation; day 0, samples analyzed on the day of sample preparation; day 6, samples analyzed once more six days after sample preparation; t_R, retention time.

$$CV = SD \cdot 100\ \% / mean$$

Equation III-2: Calculation of coefficients of variation.
Intraday CVs based on the SDs and arithmetic means of values measured within one day (day 0 or day 6), whereas SDs and arithmetic means of all measured samples (day 0 and day 6) were used for interday CVs.
CV, coefficient of variation; SD, standard deviation.

III.3.5.4. INJECTION REPRODUCIBILITY

In order to analyze the stability and robustness of the LC-MS/MS apparatus set-up, the injection reproducibility, which mirrors both the constant injection of sample and the equal ionization of metabolites, was determined. For this, aliquots of the same unprocessed vitamin D reference mix (containing 5 pmol of each vitamin D metabolite and 30 ng internal standard in a final reconstitution volume of 225 µl) was injected six times and the coefficients of variation (CVs) were determined from the peak areas for each metabolite quantifier MRM.

Table III-9: Injection reproducibility of the established vitamin D LC-MS/MS method.

metabolite	adduct	MRM			average peak area [counts]	SD [counts]	CV [%]
		Q_1	/	Q_3			
24,25-$(OH)_2$-D_3	Li^+	423.174	/	91.000	1.45×10^5	2.97×10^3	2.0
24,25-$(OH)_2$-D_3	Li^+	423.174	/	128.000	3.35×10^4	8.93×10^2	2.7
1α,25-$(OH)_2$-D_3	Li^+	423.174	/	91.000	6.76×10^4	5.97×10^3	8.8
1α,25-$(OH)_2$-D_3	Li^+	423.174	/	128.000	2.43×10^4	1.80×10^3	7.4
1α,25-$(OH)_2$-D_2	Li^+	435.314	/	91.000	1.35×10^5	2.64×10^3	2.0
25-(OH)-D_3	Li^+	407.326	/	90.900	2.56×10^4	2.25×10^3	8.8
25-(OH)-D_2	Li^+	419.323	/	361.300	2.17×10^5	2.41×10^4	11.1
1α-(OH)-D_3	H^+	401.289	/	90.900	5.10×10^4	2.15×10^3	4.2
1α-(OH)-D_3	Li^+	407.326	/	90.900	1.18×10^4	1.23×10^3	10.4
vitamin D_2	H^+	397.325	/	91.100	1.89×10^5	5.89×10^3	3.1
vitamin D_3	H^+	385.300	/	259.200	2.73×10^5	4.88×10^3	1.8
internal standard	Li^+	422.323	/	361.300	4.37×10^6	4.43×10^5	10.2

Given are the average peak areas, their standard deviations (SD), as well as their coefficients of variation (CV) of different vitamin D metabolite MRMs after six repeated injections of one reference vitamin D mix solution. The reference mix contained 5 pmol of each vitamin D metabolite and 30 ng IS (25-(OH)-D_2 [25,26,27-$^{13}C_3$]) which were reconstituted in a final volume of 225 µl.

The CVs of peak areas ranged between 1.8 % and 11.1 %, with the majority of peaks possessing CVs below 10 % [Table III-9]. MRMs detecting lithium adducts of vitamin D metabolites (particularly those of 1α-(OH)-D_3 (407.326/90.900), 25-(OH)-D_2 (419.323/361.300),

and the internal standard (422.323/361.300) having CVs > 10 %) showed generally a tendency toward higher CVs [Table III-9]. Moreover, 25-(OH)-D_3, which formed protonated (Q_1 [m/z] = $(M+H)^+$ = 401.289) and lithium adduct (Q_1 [m/z] = $(M+Li)^+$ = 407.326) mother ions in a similar range, revealed a clear negative correlation between the peak areas of both MRMs [data not shown]. Thus, the ionization of vitamin D metabolites, especially the formation of stable lithium adducts, but not a variation in the injected volumes seemed to have the biggest influence on the variability in vitamin D LC-MS/MS analyses. All in all, the established LC-MS/MS method set-up features sufficient robustness by exhibiting mostly CVs in the unnormalized peak areas below 10 %.

III.3.5.5. LINEARITY OF THE QUANTIFICATION METHOD

The introduced vitamin D LC-MS/MS quantification method [III.3.5.1] assumed a linear dependency between peak areas and metabolite amounts. To check if this is true for all vitamin D metabolites and at which amount range, linear regression analyses with SPE processed standard calibration curves were performed.

The regression analyses revealed that all calibration curve equations which considered vitamin D amounts between LOD and 100 pmol in the original sample possessed correlation coefficients r close to 1 [Table III-10]. In addition, only random patterns were seen in the respective residual plots [data not shown]. These results confirmed a linear relationship between normalized peak areas and the amount of vitamin D metabolites (between LOD and at least 100 pmol) and thus the eligibility of the applied quantification method.

Table III-10: Linearity of the established vitamin D quantification method.

metabolite	adduct	MRM			linear range [pmol]	r	
		Q_1	/	Q_3		day 0	day 6
24,25-$(OH)_2$-D_3	Li^+	423.174	/	91.000	0.5 – 100	0.9967	0.9995
24,25-$(OH)_2$-D_3	Li^+	423.174	/	128.000	1.0 – 100	0.9970	0.9993
1α,25-$(OH)_2$-D_3	Li^+	423.174	/	91.000	5.0 – 100	0.9994	0.9994
1α,25-$(OH)_2$-D_3	Li^+	423.174	/	128.000	2.5 – 100	0.9993	0.9992
25-(OH)-D_3	Li^+	407.326	/	90.900	2.0 – 100	0.9966	0.9975
1α-(OH)-D_3	H^+	401.289	/	90.900	4.0 – 100	0.9983	0.9956
1α-(OH)-D_3	Li^+	407.326	/	90.900	4.5 – 100	0.9963	0.9984
vitamin D_3	H^+	385.300	/	259.200	1.0 – 100	0.9928	0.9742
1α,25-$(OH)_2$-D_2	Li^+	435.314	/	91.000	0.5 – 100	0.9973	0.9995
25-(OH)-D_2	Li^+	419.323	/	361.300	0.5 – 100	0.9996	0.9995
vitamin D_2	H^+	397.325	/	91.100	1.0 – 100	0.9962	0.9824

Given are the minimum linear range and the linear correlation coefficient r of the respective linear calibration curve equation. The curves were generated from the peak areas of quantifier MRMs using triplicates of SPE processed vitamin D reference mix dilutions above LOQ as calibration standards and analyzing these standards on the day of sample preparation (day 0) and once again after six days storage at 4 °C (day 6).

III.3.5.6. PRECISION OF THE LC-MS/MS METHOD

Another parameter representing the robustness of a method is its precision. Therefore, the intraday and interday precisions of the vitamin D LC-MS/MS method in the quantification of vitamin D metabolites in different matrices were determined. These precisions are an indicator for the statistical variability of measurements due to random errors within the entire method (including the steps in sample preparation via SPE and LC-MS/MS analysis) without considering the accuracy of the values.

The precision of the method was determined for each metabolite quantifier MRM in different matrices (SPE processed reference solutions, spiked cells, or spiked media) considering all vitamin D metabolite levels (1-100 pmol) analyzed. In order to describe the precisions in an amount independent manner for the entire quantifiable range, the precisions were calculated by normalizing the determined amount of vitamin D metabolite in one sample by the arithmetic average of amount (= 100 %) determined in replicates (triplicates) belonging to the same amount level. Due to this normalization (mean of all normalized data equals 100 %), the respective precision, which was expressed as coefficient of variation CV, corresponded to the standard deviation SD of the normalized amounts [Equation III-3].

$$CV = SD = \sqrt{\left(\sum\left(\frac{a_{n,m}}{\bar{a}_n} - 1\right)^2\right) / (n-1)} \cdot 100\ \%$$

Equation III-3: Calculation of the precision of the vitamin D LC-MS/MS method, expressed by the coefficient of variation of normalized vitamin D amounts determined in samples.
The precisions of the method were expressed as CVs and calculated for each quantifier MRM and matrix used. To cover the entire vitamin D amount range, the determined amounts in single samples were normalized to (divided by) the respective arithmetic average of the amounts determined in all replicates of the same amount level and matrix. Due to this normalization (mean of each level and of all samples equals 100 %), the determined CVs corresponded to the SDs of all normalized amounts [Equation III-2].
a, determined amount in one sample; ā, determined average amount in replicates of the same theoretical amount; CV, coefficient of variation; m, replicate of n; n, amount level, SD, standard deviation.

The intraday precision of the method with solid phase extracted reference samples (SPE) was quite high for all vitamin D metabolites when analyzed on the day of sample preparation (day 0) since the normalized amounts of all metabolites revealed an intraday variation $CV_{(intraday)}$ below 10 % at day 0 [Table III-11]. This high precision was still observable for the more "hydrophilic" vitamin D metabolites 24,25-$(OH)_2$-D_3, 1α,25-$(OH)_2$-D_3, 1α,25-$(OH)_2$-D_2, 25-(OH)-D_3, and 25-(OH)-D_2 when analyzed once more six days after the SPE and the first measurement (day 6) [Table III-11]. In contrast, at day 6 the precision was slightly reduced for the more hydrophobic vitamin D metabolite 1α-(OH)-D_3 ($CV_{(intraday)} \leq 18$ %) and very poor for the most hydrophobic vitamin D_2 and vitamin D_3 ($CV_{(intraday)} > 57$ %) [Table III-11], which could be explained by a possible precipitation of the more hydrophobic metabolites due to a probable evaporation of methanol during the storage of the extracts at 4 °C for six days.

Table III-11: Intraday precision of the vitamin D LC-MS/MS method for quantifier MRMs of vitamin D metabolites in different matrices.

metabolite adduct		$CV_{(intraday)}$ [%]						
		SPE	in cells				in media	
			HaCaT	ASZ001	$Ptch^{WT}$	$Ptch^{-/-}$	DMEM	154CF
24,25-$(OH)_2$-D_3 + Li^+	**day 0**	5.1	5.6	8.2	3.3	13.7	13.2	14.4
	day 6	6.9	8.9	4.8	5.5	8.7	12.7	17.0
1α,25-$(OH)_2$-D_3 + Li^+	**day 0**	3.6	4.9	4.8	3.3	13.2	8.0	17.9
	day 6	3.0	4.2	6.3	5.2	14.7	15.5	15.6
1α,25-$(OH)_2$-D_2 + Li^+	**day 0**	6.7	5.4	10.8	3.5	19.7	13.3	13.8
	day 6	3.4	7.1	6.1	6.5	13.1	16.2	15.5
25-(OH)-D_3 + Li^+	**day 0**	4.5	3.9	8.4	3.9	8.8	6.8	13.9
	day 6	3.3	3.5	7.6	9.4	4.1	7.2	13.8
25-(OH)-D_2 + Li^+	**day 0**	2.6	3.7	6.2	5.8	6.2	10.5	8.3
	day 6	3.0	4.4	4.7	4.9	5.1	12.3	8.1
1α-(OH)-D_3 + Li^+	**day 0**	8.1	15.7	13.5	35.1	17.6	19.0	21.7
	day 6	15.9	22.3	74.2	49.9	38.9	33.4	12.3
1α-(OH)-D_3 + H^+	**day 0**	7.7	17.9	13.8	21.4	13.7	18.0	22.5
	day 6	18.0	27.7	38.5	51.3	40.6	19.0	20.0
vitamin D_2 + H^+	**day 0**	9.1	5.8	14.7	13.8	20.2	26.9	24.6
	day 6	57.4	21.2	63.9	77.8	70.2	52.0	72.7
vitamin D_3 + H^+	**day 0**	7.8	8.4	13.1	21.6	18.9	35.0	24.7
	day 6	64.1	32.5	65.5	85.5	82.0	55.1	65.1

The listed intraday coefficients of variation ($CV_{(intraday)}$) represent the standard deviation SD of normalized amounts in at least six (up to 21) samples, which were analyzed by LC-MS/MS either on the day (day 0) or once more six days after the first analysis (day 6). To cover the precision of different amounts of vitamin D metabolites in the samples, the CVs were calculated from normalized amounts according to Equation III-3. $CVs_{(intraday)}$ > 20 %, indicating metabolites (quantifier MRMs) with low precision, are highlighted in grey.

Similar results for the precision of the method for the quantification of vitamin D metabolites were obtained in the cells which were spiked with 2.5-10 pmol of each vitamin D metabolite after cell harvest. Here, it was seen that, with the exception of the $Ptch^{-/-}$ cell line which revealed a higher intraday variability ($CV_{(intraday)}$: 8-20 %) in the normalized amounts of dihydroxylated vitamin D metabolites, the intraday precision for the more "hydrophilic" vitamin D metabolites 24,25-$(OH)_2$-D_3, 1α,25-$(OH)_2$-D_3, 1α,25-$(OH)_2$-D_2, 25-(OH)-D_3, and 25-(OH)-D_2 was quite high by showing generally $CVs_{(intraday)}$ below 10 % at day 0 and day 6 [Table III-11]. Like seen for the SPE processed reference samples, though more pronounced, the precision of 1α-(OH)-D_3, vitamin D_2, and vitamin D_3 in cells was lower when compared with the more "hydrophilic" metabolites. Thus, the intraday variability of these metabolites in cells ranged between 6 % and 35 % at day 0 or 21 % and 86 % at day 6 [Table III-11].

The analysis of vitamin D metabolites in media, which were spiked with 2.5-10 pmol of each vitamin D metabolite, was less precise. Again no clear difference was seen in the intraday variability of the dihydroxylated and 25-monohydroxylated vitamin D metabolites in media

between day 0 and day 6 ($CV_{(intraday)}$: 7-18 %), although the determined variabilities were increased when compared to those seen with cells [Table III-11]. An intermediate intraday precision of the LC-MS/MS method was seen for quantifier MRMs of 1α-(OH)-D_3 in spiked media at day 0 and day 6 ($CV_{(intraday)}$: 12-33 %), whereas the intraday variation for vitamin D_2 and vitamin D_3 was more than 24 % at day 0 ($CV_{(intraday)}$: 24-35 %) and approximately twice as high at day 6 ($CV_{(intraday)}$: 52-73 %) [Table III-11].

Because the intraday precisions of the LC-MS/MS method for 1α-(OH)-D_3, vitamin D_2, and vitamin D_3 were already quite low in samples analyzed at day 6 [Table III-11], the interday precisions, which were expressed as interday coefficients of variation $CV_{(interday)}$, were only determined for the more "hydrophilic" and robust quantifiable vitamin D metabolites 24,25-$(OH)_2$-D_3, 1α,25-$(OH)_2$-D_3, 1α,25-$(OH)_2$-D_2, 25-(OH)-D_3, and 25-(OH)-D_2 [Table III-12]. It was seen that, with the exception of three values (highlighted in dark red in Table III-12), in general, the interday precisions were slightly reduced when compared with the respective intraday precisions [Table III-11, Table III-12]. The interday precisions in the analysis of solid phase extracted reference mixes (SPE) as well as of samples with HaCaT and $Ptch^{WT}$ cell matrix were again high ($CV_{(interday)} < 11$ %). Whereas the precision of the majority of metabolites was acceptable in the ASZ001 and $Ptch^{-/-}$ cell line ($CV_{(interday)}$: 6-15 % and 5-22 %, respectively), the analysis of vitamin D metabolites in media showed once more higher interday variabilities ($CV_{(interday)} > 10$ %) [Table III-12]. Here, it is noticeable that 25-(OH)-D_3 and 25-(OH)-D_2, which behave most similar to the internal standard in the LC-MS/MS analysis, generally possessed the highest interday precisions [Table III-12].

Table III-12: Day 0 versus day 6 interday precision of the vitamin D LC-MS/MS method for selected less hydrophobic vitamin D metabolites in different matrices.

metabolite (Li^+ adduct)		**$CV_{(interday)}$ [%]**						
		SPE	**in cells**				**in media**	
			HaCaT	ASZ001	$Ptch^{WT}$	$Ptch^{-/-}$	DMEM	154CF
24,25-$(OH)_2$-D_3	**day 0 & 6**	10.7	7.8	12.2	7.5	15.2	16.5	24.9
1α,25-$(OH)_2$-D_3	**day 0 & 6**	4.1	6.7	8.1	6.6	17.1	35.3	35.6
1α,25-$(OH)_2$-D_2	**day 0 & 6**	5.7	9.7	14.8	9.4	21.7	20.1	20.5
25-(OH)-D_3	**day 0 & 6**	4.9	5.1	10.6	5.1	5.2	10.2	10.7
25-(OH)-D_2	**day 0 & 6**	6.3	4.6	5.8	6.1	5.6	11.4	15.9

The listed interday coefficients of variation ($CV_{(interday)}$) represent the standard deviation SD of normalized amounts in at least two times six (up to 21) samples, which were analyzed on the day and once more six days after SPE (day 0 & 6). To cover the precision of different amounts of vitamin D metabolites in the samples, the CVs were again calculated from normalized amounts according to Equation III-3.
$CVs_{(interday)} > 20$ %, indicating a low precision, are highlighted in grey, whereas $CVs_{(interday)}$ smaller than the respective $CV_{(intraday)}$ at day 6 are highlighted in dark red.

All in all, the determined intra- and interday precisions of the LC-MS/MS method for the more "hydrophilic" vitamin D metabolites 24,25-$(OH)_2$-D_3, 1α,25-$(OH)_2$-D_3, 1α,25-$(OH)_2$-D_2, 25-(OH)-D_3, and 25-(OH)-D_2 were quite good and meet widely FDA criteria. In contrast, for the more hydrophobic 1α-(OH)-D_3, vitamin D_3, and vitamin D_2, the measurements were only sufficient precise when these metabolites were analyzed on the day of sample preparation.

III.3.5.7. RECOVERY OF THE INTERNAL STANDARD 25-(OH)-D_2 [25,26,27-$^{13}C_3$]

Since the internal standard (IS) 25-(OH)-D_2 [25,26,27-$^{13}C_3$] was present in each sample at equal amount and thus offered a quite big data set for analysis, IS peak areas were used to determine the recovery of the IS in reference mixes after SPE, in processed cells, or in processed media. This raw analysis enabled an initial estimate of the influence of different matrices on the recovery of vitamin D metabolites. For the determination of the internal standard recovery from the SPE process, the mean IS (MRM 422.323/361.300) peak area of solid phase extracted reference mix samples was divided by the mean peak area of unprocessed reference mix samples. The internal standard recovery from cells or media was calculated in a similar manner, however, the respective mean peak areas of cells or media were referred to the mean peak area of SPE processed reference samples, respectively.

In this analysis it was seen that neither the SPE process nor the cellular matrix of HaCaT, ASZ001, $Ptch^{WT}$, or $Ptch^{-/-}$ cells had an influence on the recovery of the IS by showing recovery rates of 100 ± 20 % [Table III-13]. The low variability of IS peak areas in reference mix samples and cell samples demonstrated again the robustness of the method. In contrast, both DMEM and 154CF medium as sample matrix revealed recovery rates below 20 % which represented a very poor and insufficient recovery [Table III-13]. Although a loss of IS within the processing of medium samples cannot be entirely excluded, a quite strong suppression of the internal standard MRM 422.323/361.300 within the MS/MS analysis of medium samples is much more likely.

Table III-13: Recovery of the internal standard in different matrices.

	internal standard recovery [%]						
	from SPE process	**from cells**				**from media**	
		HaCaT	ASZ001	$Ptch^{WT}$	$Ptch^{-/-}$	DMEM	154CF
day 0	98	109	114	102	108	18	11
day 6	111	103	112	80	80	14	8

The recovery of the internal standard (IS) 25-(OH)-D_2 [25,26,27-$^{13}C_3$] (MRM 422.323/361.300) was calculated from the average raw peak areas by normalizing SPE processed reference mix samples to unprocessed reference mix samples (recovery from SPE process) or by normalizing processed cell or media samples to SPE processed reference mix samples (recovery from cells and media, respectively). Please note that the coefficients of variation of the raw peak area means were in the range of 8-14 % for unprocessed and SPE processed reference mix samples as well as cellular samples, whereas media samples had a significantly higher variation (25-38 %).

III.3.5.8. RECOVERY OF VITAMIN D METABOLITES

The recovery of vitamin D metabolites was analyzed with respect to two approaches: First, to determine the recovery of different vitamin D metabolites from the SPE process itself and second, by analyzing the recovery of vitamin D metabolites in different matrices, to ascertain the accuracy of the LC-MS/MS (quantification) method.

In the first approach, the loss of vitamin D metabolites due to the SPE process was determined by comparing the levels of vitamin D metabolites in solid phase extracted reference mix samples with those in directly applied reference mix samples [Equation III-4].

$$\text{recovery [\%]} = \left(\frac{\bar{a}_{1(\text{SPE-RM})}}{\bar{a}_{1(\text{RM})}} + \frac{\bar{a}_{2(\text{SPE-RM})}}{\bar{a}_{2(\text{RM})}} + \cdots + \frac{\bar{a}_{n(\text{SPE-RM})}}{\bar{a}_{n(\text{RM})}} \right) \cdot 100\ \% \,/\, n$$

Equation III-4: Calculation of the recovery of vitamin D metabolites from the SPE process.
The recovery rates were calculated from the average amounts of vitamin D metabolites measured in triplicates per level ($\bar{a}_1$, $\bar{a}_2$, ..., $\bar{a}_n$) and based on the calibration curves generated with solid phase extracted reference mixes.
SPE-RM, SPE processed reference mix sample; RM, unprocessed reference mix sample; n, number of levels considered.

The analysis of both the averaged raw peak areas [data not shown] and the corresponding calculated amounts of metabolites [Table III-14] demonstrated clearly that the recovery of the hydrophobic metabolites vitamin D_2 and vitamin D_3 from the SPE process was quite poor (recovery of 16 % and 10 %, respectively). In contrast, mono- and dihydroxylated vitamin D metabolites possessed recovery rates of more than 72 % in samples measured at day 0 and 59 % in those measured once more at day 6, with highest recovery rates (approx. 100 %) found for the 25-hydroxyvitamin D metabolites 25-(OH)-D_3 and 25-(OH)-D_2 [Table III-14]. As a result, if at all, only little amounts of mono- and dihydroxylated vitamin D metabolites are lost due to the applied SPE procedure, whereas high losses (90-80 %) were observed for vitamin D_2 and vitamin D_3. The strongly reduced abundance of these compounds in the extracts was most probably due to a strong retention by the Strata-X SPE sorbent and limited the detectability of vitamin D_2 and vitamin D_3 in processed biological samples.

Table III-14: Recovery of vitamin D metabolites from the SPE process.

metabolite adduct		recovery from SPE [%]	
		day 0	day 6
24,25-$(OH)_2$-D_3	+ Li^+	72 ± 6	59 ± 4
1α,25-$(OH)_2$-D_3	+ Li^+	92 ± 4	72 ± 5
1α,25-$(OH)_2$-D_2	+ Li^+	85 ± 7	71 ± 8
25-(OH)-D_3	+ Li^+	100 ± 11	92 ± 3
25-(OH)-D_2	+ Li^+	96 ± 8	96 ± 4
1α-(OH)-D_3	+ Li^+/H^+	79 ± 12	72 ± 15
vitamin D_2	+ H^+	16 ± 3	10 ± 3
vitamin D_3	+ H^+	10 ± 3	6 ± 3

Given are the mean recovery rates ± SD of vitamin D metabolites from the SPE process. SPE processed and unprocessed reference mix samples were measured on the day of sample preparation (day 0) or once again after six days (day 6) and the recovery rates were calculated according to Equation III-4.

In a second approach, the influence of the sample matrix on the recovery of vitamin D metabolites from different cell lines (HaCaT, ASZ001, $Ptch^{WT}$, and $Ptch^{-/-}$) as well as media (DMEM and 154CF) was analyzed by comparing the levels of vitamin D metabolites in processed spiked matrices and solid phase extracted reference mix samples [Table III-15]. In doing so, the recovery of vitamin D metabolites in cell lines and culture media represented the accuracy of the vitamin D LC-MS/MS (quantification) method for those metabolites with different matrices.

Table III-15: Recovery of vitamin D metabolites in cell lines and media as a measure for the accuracy of the vitamin D LC-MS/MS (quantification) method with different matrices.

metabolite adduct		recovery / accuracy at day 0 [%]					
		in cells				in media	
		HaCaT	ASZ001	$Ptch^{WT}$	$Ptch^{-/-}$	DMEM	154CF
24,25-$(OH)_2$-D_3	+ Li^+	94 ± 9	91 ± 9	100 ± 4	92 ± 14	107 ± 28	118 ± 20
1α,25-$(OH)_2$-D_3	+ Li^+	92 ± 5	97 ± 5	98 ± 2	94 ± 7	97 ± 7	176 ± 25
1α,25-$(OH)_2$-D_2	+ Li^+	85 ± 9	82 ± 6	93 ± 8	89 ± 21	111 ± 17	205 ± 29
25-(OH)-D_3	+ Li^+	100 ± 3	93 ± 4	102 ± 4	96 ± 3	76 ± 16	100 ± 15
25-(OH)-D_2	+ Li^+	92 ± 1	89 ± 3	88 ± 2	91 ± 1	74 ± 8	81 ± 4
1α-(OH)-D_3	+ Li^+	91 ± 4	79 ± 15	38 ± 1	57 ± 23	358 ± 10	403 ± 48
1α-(OH)-D_3	+ H^+	58 ± 31	92 ± 17	114 ± 15	108 ± 32	196 ± 26	202 ± 49
vitamin D_2	+ H^+	82 ± 18	85 ± 12	76 ± 9	82 ± 21	833 ± 99	1467 ± 328
vitamin D_3	+ H^+	72 ± 12	81 ± 12	90 ± 8	83 ± 21	928 ± 76	1511 ± 363

metabolite adduct		recovery / accuracy at day 6 [%]					
		in cells				in media	
		HaCaT	ASZ001	$Ptch^{WT}$	$Ptch^{-/-}$	DMEM	154CF
24,25-$(OH)_2$-D_3	+ Li^+	84 ± 18	92 ± 14	113 ± 3	106 ± 6	128 ± 11	131 ± 31
1α,25-$(OH)_2$-D_3	+ Li^+	87 ± 18	106 ± 13	110 ± 11	111 ± 5	189 ± 31	378 ± 76
1α,25-$(OH)_2$-D_2	+ Li^+	77 ± 13	81 ± 19	90 ± 7	91 ± 10	137 ± 10	243 ± 7
25-(OH)-D_3	+ Li^+	95 ± 6	96 ± 8	82 ± 29	98 ± 2	87 ± 8	90 ± 5
25-(OH)-D_2	+ Li^+	93 ± 3	90 ± 1	92 ± 4	90 ± 3	76 ± 9	87 ± 8
1α-(OH)-D_3	+ Li^+	67 ± 37	47 ± 15	48 ± 6	63 ± 6	412 ± 42	364 ± 62
1α-(OH)-D_3	+ H^+	68 ± 29	88 ± 23	203 ± 30	180 ± 10	334 ± 26	509 ± 147
vitamin D_2	+ H^+	60 ± 37	90 ± 33	203 ± 80	304 ± 113	1998 ± 183	2005 ± 763
vitamin D_3	+ H^+	52 ± 36	88 ± 33	252 ± 109	251 ± 86	2183 ± 124	1944 ± 601

Given are the mean recovery rates ± SD of vitamin D metabolites in different cell lines and culture media [Table II-31], which represent also the accuracy of the (quantification) method. The recovery rates in samples measured on the day of sample preparation (recovery / accuracy at day 0) or once again six days after the first measurement (recovery / accuracy at day 6) were in principle calculated according to Equation III-4, however, with the exception that the amounts determined in cell or media matrices were divided by the amounts determined in SPE processed reference mixes.
Inadequate recoveries / accuracies of less than 70 % and more than 130 % are highlighted in gray.

Here, it was seen that at day 0 in general adequate recovery rates or accuracies (70-115 %) were obtained with cells as matrix [Table III-15]. With the exception of 1α-(OH)-D_3, no substantial differences in the recovery rates of vitamin D metabolites were seen between the different cell lines [Table III-15]. Compared with ASZ001, $Ptch^{WT}$, and $Ptch^{-/-}$ cells, HaCaT cells revealed strongly reduced recovery rates when considering the protonated 1α-(OH)-D_3 MRM 401.289/90.900 (approx. 100 % vs. 58 %). Vice versa, $Ptch^{WT}$ and $Ptch^{-/-}$ cells showed diminished recovery rates (38 % and 57 %, respectively) for the 1α-(OH)-D_3 lithium adduct MRM 407.326/90.900. Looking at the recoveries in spiked cell lines analyzed by LC-MS/MS six days after SPE (day 6), no obvious changes in any vitamin D metabolite recovery levels were detected with the ASZ001 cell matrix. The same was true for the more "hydrophilic" vitamin D metabolites (24,25-$(OH)_2$-D_3, 1α,25-$(OH)_2$-D_3, 1α,25-$(OH)_2$-D_2, 25-(OH)-D_3, and 25-(OH)-D_2) eluting within the first 5 min with the HaCaT, $Ptch^{WT}$, and $Ptch^{-/-}$ cell matrices. However, for the more hydrophobic metabolites 1α-(OH)-D_3, vitamin D_2, and vitamin D_3, reduced recovery rates were detected with the HaCaT cell matrix, whereas about 2-fold increased recovery rates were found with $Ptch^{WT}$ or $Ptch^{-/-}$ cell matrices at day 6. The later changes were not detectable in the respective blank samples (unspiked cells) when analyzed once more six days after SPE and the first measurement [data not shown].

In spiked medium samples, only 25-(OH)-D_3 and 25-(OH)-D_2 possessed acceptable recovery rates at day 0 and day 6 [Table III-15]. Although, at least at day 0, the more "hydrophilic" vitamin D metabolites 24,25-$(OH)_2$-D_3, 1α,25-$(OH)_2$-D_3, and 1α,25-$(OH)_2$-D_2 revealed recovery rates of about 100 % in DMEM medium, the levels of the more hydrophobic metabolites (1α-(OH)-D_3, vitamin D_2, and vitamin D_3) were 2- to 10-fold overestimated [Table III-15]. The recovery rates of vitamin D metabolites were even worse with 154CF medium as matrix, as the majority of vitamin D metabolites were already more than 2- to 15-fold overestimated at day 0 [Table III-15]. At day 6, the observed recovery rates of metabolites which do not elute in close proximity to the internal standard (IS) 25-(OH)-D_2 [25,26,27-$^{13}C_3$] were even more increased (up to 22-fold) in all medium samples [Table III-15].

The fact that 25-(OH)-D_3 and 25-(OH)-D_2 exhibited good to sufficient recovery rates / accuracies in both cell and medium samples was not surprising because the ^{13}C-labeled 25-(OH)-D_2 [25,26,27-$^{13}C_3$] (used as IS for the normalization of peak areas prior to the determination of vitamin D metabolites amounts) co-elutes with the unlabeled 25-(OH)-D_2 and elutes within 0.2 min next to 25-(OH)-D_3. Thus, a potential suppression or enhancement of the detectability of analytes due to matrix compounds co-eluting with the analytes are more adequately eliminated by the normalization to the IS.

III.3.5.9. Stability of vitamin D metabolites in cell culture samples

A comparison of day 0 (on the day of sample preparation) and day 6 (six days after the first measurement) analyses could reveal differences in the stability of the analyzed vitamin D metabolites. By regarding the precision ($CV_{(intraday)}$ and $CV_{(interday)}$: < 20 %) and the accuracy (recovery: 80-120 %) of vitamin D metabolites in SPE processed vitamin D reference mixes and spiked cells [Table III-11, Table III-12, Table III-15], the quantification results for the more "hydrophilic" dihydroxylated and 25-monohydroxylated vitamin D metabolites seemed to be quite stable with the reconstituted solid phase extracts for at least six days. In

contrast, quite high variabilities ($CV_{(intraday)}$: > 50 %) and low accuracies (recovery: < 60 % or > 200 %) were seen for the hydrophobic non-hydroxylated vitamin D metabolites vitamin D_3 and vitamin D_2 at day 6 [Table III-11, Table III-15]. The accurate and reliable quantification of the 1α-monohydroxylated 1α-(OH)-D_3 depended strongly on the recorded MRM transition (401.289/90.900 or 407.326/90.900 for protonated or lithium adduct mother ions, respectively) and the sample matrix. Whereas the quantification of both MRMs was consistent over six days in the SPE processed reference samples [Table III-14], in spiked $Ptch^{WT}$ and $Ptch^{-/-}$ cell lines only the quantification of 1α-(OH)-D_3 lithium adducts resulted in a similar recovery upon storage for six days, though, the accuracy was poor [Table III-15]. In contrast, the quantification of the protonated 1α-(OH)-D_3 mother ion MRM showed high reproducibility and accuracy in ASZ001 cells but only low accuracy in HaCaT cells [Table III-15].

III.3.5.10. SUMMARY OF THE VALIDATION RESULTS

The validation of the established vitamin D LC-MS/MS method showed that the limit of detection (LOD) and limit of quantification (LOQ) for all vitamin D metabolites in SPE processed samples depended on the MRM monitored and was below 2 pmol and 5 pmol of vitamin D metabolite in the initial reference mix and spiked cell samples, respectively [III.3.5.2]. Thereby, the linearity of the method ranged between the LOQ and at least 100 pmol [III.3.5.5]. The LC-MS/MS analysis of samples within 24 h after sample preparation (day 0) revealed a high precision of the method for all vitamin D metabolites analyzed [III.3.5.6]. However, the precision of the method with samples stored for six days at 4 °C after SPE and the first measurement depended strongly on the polarity of the metabolite [III.3.5.6]. As a result, the quantification of more "hydrophilic" vitamin D metabolites 24,25-$(OH)_2$-D_3, 1α,25-$(OH)_2$-D_3, 1α,25-$(OH)_2$-D_2, 25-(OH)-D_3, and 25-(OH)-D_2 was quite stable and showed a high precision even at day 6. In contrast, 1α-(OH)-D_3, vitamin D_2, and vitamin D_3 revealed a clearly reduced stability and precision when analyzed once more after storage for six days [III.3.5.6, III.3.5.9]. The loss of vitamin D metabolites due to the SPE process varied between the different metabolites [III.3.5.8]. Here, in experiments with reference vitamin D mixes, the recovery rates of the mono- and dihydroxylated vitamin D metabolites from the SPE ranged between 72 % (24,25-$(OH)_2$-D_3) and 100 % (25-(OH)-D_3 or 25-(OH)-D_2). However, less than 20 % of applied non-hydroxylated vitamin D metabolites could be eluted from the Strata-X 33 µm polymeric reversed phase (30 $^{mg}/_{ml}$) cartridge. Like the precision of the method, the accuracies (recoveries) of all determined vitamin D metabolites in reference mixes and spiked cells were quite good (± 20 %) at day 0 but at day 6 decreased accuracies (± 30-200 %) were seen for the hydrophobic metabolites 1α-(OH)-D_3, vitamin D_2, and vitamin D_3 [III.3.5.8].

Whereas vitamin D metabolites behaved quite similar in reference and spiked cell samples, the stability, precision and recovery of metabolites were worse in spiked medium. Because strongly decreased peak intensities of vitamin D metabolites, e.g., of the IS [III.3.5.7], were observed in medium samples, the poor performance of the method with medium as matrix could have resulted from ion suppression effects and/or problems in the SPE, which did not occur in the reference samples used for the generation of the calibration curves.

25-(OH)-D_3 and 25-(OH)-D_2, which eluted from the Kinetex 2.6 µm C18 column either in close proximity of or together with the internal standard (IS) 25-(OH)-D_2 [25,26,27-$^{13}C_3$],

showed the highest precision, accuracy and stability in the validation of the established vitamin D LC-MS/MS method with all kinds of matrices. Thus, the embedding of additional IS for dihydroxylated and non-hydroxylated vitamin D metabolites would certainly improve the quantification of these metabolites with respect to precision and accuracy in future.

In summary, the established vitamin D method is suitable for the quantification of vitamin D metabolites in cell samples from cell culture experiments. However, although it was possible to detect all vitamin D metabolites in medium samples within the validation process, the quantification of these metabolites in medium was very error prone and needs further optimization and validation.

III.3.6. Biological application of the vitamin D LC-MS/MS method

III.3.6.1. Detection of vitamin D_3 metabolites in cell culture samples

Please note that the analysis of cell culture experiments was not performed with the validated scheduled vitamin D LC-MS/MS method, which includes the optimized MRMs for all metabolites, but with individual LC-MS/MS methods monitoring continuously the optimized MRMs of selected relevant vitamin D metabolites [Table II-30]. Using these modified vitamin D LC-MS/MS methods it was possible to detect the uptake and conversion of vitamin D_3 metabolites by cultured cells in samples of various cell culture experiments performed by Benedikt Linder (Tumor Genetics Group, UMG) in Göttingen [253].

The results of two of these experiments are exemplarily shown in Figure III-44. The murine BCC cell line ASZ001 as well as the murine fibroblast cell line $Ptch^{WT}$ were treated with either 2 μM 25-(OH)-D_3 [Figure III-44A-C] or 10 μM vitamin D_3 [Figure III-44D-G] for up to 6 h and harvested according to the established procedure. After shipment to Munich, the uptake of the respective vitamin D_3 metabolite and the generation of successive dihydroxyvitamin D_3 or mono- and dihydroxyvitamin D_3 metabolites were determined by LC-MS/MS. Here, the experiments were not analyzed by absolute but relative quantification. For this, the sum of monitored MRM peak areas per analyte were divided by the sum of IS peak areas in the samples. To gain fold changes, the IS standardized peak areas of vitamin D_3 metabolites at different time points were normalized to the respective peak areas at the time point zero.

It was seen that ASZ001 and $Ptch^{WT}$ cells took up 25-(OH)-D_3 and vitamin D_3 within the first 30 min [Figure III-44A, D]. In addition, both cell lines were able to metabolize the applied vitamin D precursors. Thus, the treatment of cells with 25-(OH)-D_3 caused a clear gain in 24,25-$(OH)_2$-D_3 levels, which was more pronounced in the ASZ001 cell line than in the $Ptch^{WT}$ cell line [Figure III-44B]. In contrast, only low amounts of the major biologically active vitamin D_3 metabolite 1α,25-$(OH)_2$-D_3 were produced from the precursor [Figure III-44C]. When treated with vitamin D_3, both cell lines exhibited a continuous increase in 25-(OH)-D_3 levels [Figure III-44E], which was, though to a far lesser extent, further hydroxylated to 24,25-$(OH)_2$-D_3 or 1α,25-$(OH)_2$-D_3 [Figure III-44F, G].

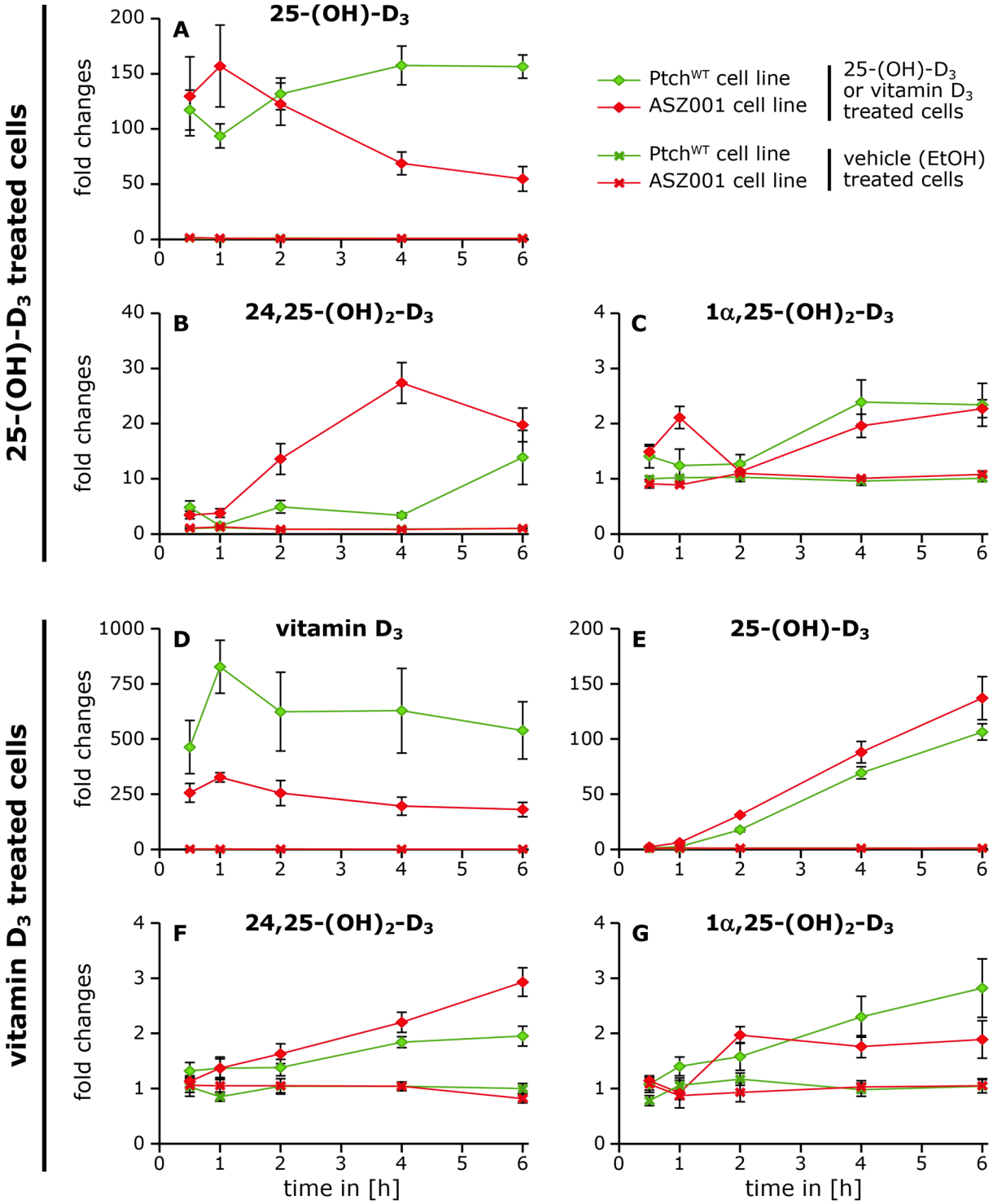

Figure III-44: ASZ001 and Ptch^{WT} cells take up and metabolize vitamin D metabolites.
Time-course experiments analyzing the uptake and metabolism of vitamin D metabolites in cells were performed by Benedikt Linder (Tumor Genetics Group, UMG) in Göttingen and analyzed via a modified vitamin D LC-MS/MS method in Munich [253]. For this, cells of the BCC cell line ASZ001 (red) or fibroblast cell line Ptch^{WT} (green) were treated with either 2 µM 25-(OH)-D$_3$ **(A-C)** or 10 µM vitamin D$_3$ **(D-G)** for up to six hours. The fold changes of vitamin D$_3$ metabolites in the cells were determined by dividing the average IS standardized peak areas (sum of metabolite MRMs) of vitamin D$_3$ metabolites in samples of the respective time point by those in samples of the time point zero. Shown are the fold changes in average relative peak areas of 25-(OH)-D$_3$ **(A, E)**, 24,25-(OH)$_2$-D$_3$ **(B, F)**, 1α,25-(OH)$_2$-D$_3$ **(C, G)**, and vitamin D$_3$ **(D)** from triplicates ± standard error of the mean (SEM). Diamonds represent data of vitamin treated samples, whereas vehicle ethanol (EtOH) treated control samples are indicated by crosses.

Other experiments concentrated on the metabolism of vitamin D_3 metabolites in different cell lines, such as the murine BCC cell line ASZ001 or the human keratinocyte cell line HaCaT, in the presence of the CYP inhibitor itraconazole (ITZ) [253].

For this, the detection of ITZ (MRMs: 705.203/256.000 and 705.203/392.200) first had to be implicated into the vitamin D LC-MS/MS method. Initial tests with reference solutions showed that ITZ can be extracted from samples by applying the established SPE method for vitamin D metabolites [data not shown]. In addition, ITZ possessed a low bonding power on the Kinetex 2.6 µm C18 100 Å 50 mm x 2.1 mm column (t_R = 1.22 min) but a high ionization capability [Figure III-45A, B, data not shown]. However, since the analysis of ITZ was only secondary in these approach, the method for the determination of ITZ in biological samples by LC-MS/MS was not further validated with respect to, e.g., limits of detection and quantification, linearity, precision, recovery, or recovery with different matrices, allowing only for a relative quantification of ITZ with unknown reliability.

One application of the enhanced vitamin D LC-MS/MS method was the detection and relative quantification of 1α,25-$(OH)_2$-D_3 (and ITZ) in ASZ001 and HaCaT cells treated for 6 h with vehicle/solvent (ethanol and DMSO for 1α,25-$(OH)_2$-D_3 and ITZ, respectively) and either 100 nM 1α,25-$(OH)_2$-D_3 or 1 µM ITZ or with a combination of 1 µM ITZ and 100 µM 1α,25-$(OH)_2$-D_3. Beside the cells, the respective medium supernatants were analyzed as well. Figure III-45 shows representative chromatograms from the analysis of ASZ001 and HaCaT cells treated with either 1 µM ITZ and 100 nM 1α,25-$(OH)_2$-D_3 (ITZ / 1α,25-$(OH)_2$-D_3) or vehicle (solvent control). Here, it could be seen that ITZ (t_R = 1.22 min, peak 1) as well as 1α,25-$(OH)_2$-D_3 (t_R = 2.24 min, peak 2) were taken up by both cell lines [Figure III-45A, B].

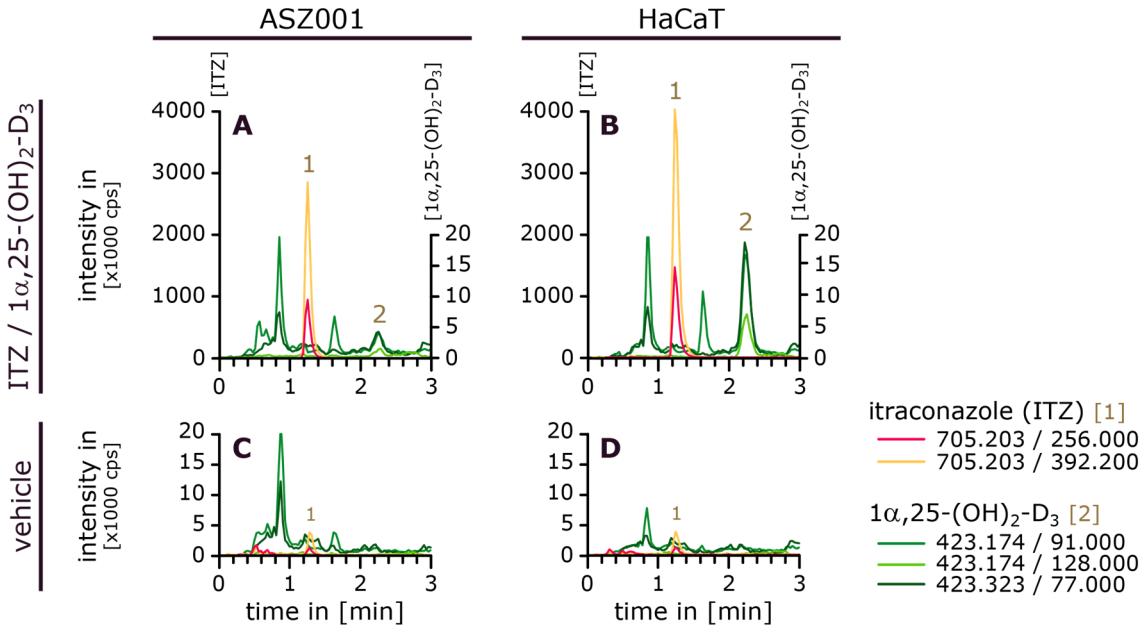

Figure III-45: Itraconazole can be detected in cells via an enhanced vitamin D LC-MS/MS method. Illustrated are representative chromatograms of samples resulting from the treatment of ASZ001 and HaCaT cells with 1α,25-$(OH)_2$-D_3 / itraconazole (ITZ) or vehicle by Benedikt Linder (Tumor Genetics Group, UMG) in Göttingen [253]. The cells of the murine BCC cell line ASZ001 **(A, C)** and the human keratinocyte cell line HaCaT **(B, D)** were treated with either 100 nM 1α,25-$(OH)_2D_3$ and 1 µM ITZ (1α,25-$(OH)_2D_3$ / ITZ) **(A, B)** or with the ethanol and DMSO solvent mixture (vehicle) **(C, D)** for 6 h. The harvested cells were processed and analyzed via a modified vitamin D LC-MS/MS method monitoring continuously optimized MRMs for selected vitamin D metabolites and ITZ.

No 1α,25-$(OH)_2$-D_3 signals but surprisingly small ITZ peaks were detectable in the solvent controls [Figure III-45C, D]. Since the intensities of ITZ signals were very low (< 0.2 %) in the control samples when compared with the intensities in the 1 µM ITZ treated cell samples and as the peaks were not present in every control or in cells of other experiments which were not treated with ITZ, it was assumed that the ITZ signals in the respective control samples resulted from cross-contaminations within the harvest or extraction process.

For the biological analysis of this experiment, the relative quantities of 1α,25-$(OH)_2$-D_3 and ITZ in differently treated ASZ001 or HaCaT cells were calculated by normalizing the average IS standardized peak areas of the either mono or combination treated samples to those of the respective solvent controls. The results are summarized in Figure III-46.

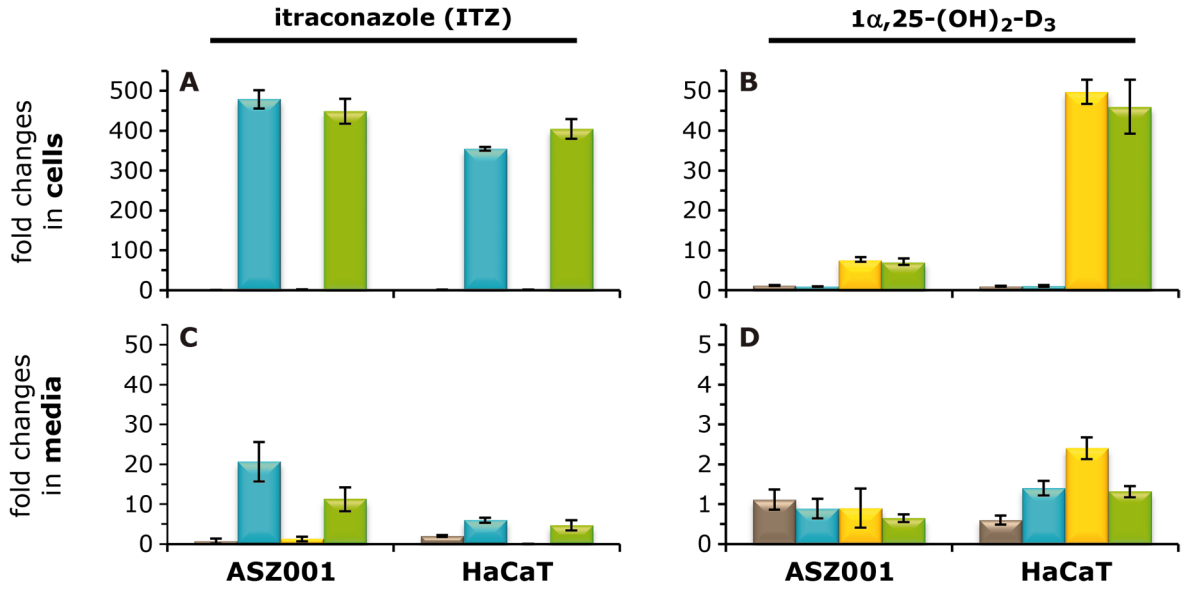

E

treatment	IS normalized peak areas ± SEM of ITZ [x10⁻¹]		1α,25-$(OH)_2$-D_3 [x10⁻³]	
	ASZ001	HaCaT	ASZ001	HaCaT
DMSO + EtOH	0.1 ± 0.1	0.2 ± 0.1	2.1 ± 0.3	2.3 ± 0.3
1 µM ITZ + EtOH	69.3 ± 3.3	90.5 ± 1.2	1.5 ± 0.2	2.3 ± 0.5
DMSO + 100 nM 1α,25-$(OH)_2$-D_3	0.2 ± 0.1	0.3 ± 0.1	13.9 ± 1.1	115.0 ± 7.0
1 µM ITZ + 100 nM 1α,25-$(OH)_2$-D_3	64.9 ± 4.5	103.2 ± 6.3	13.0 ± 1.4	106.4 ± 15.7

Figure III-46: Treatment of ASZ001 or HaCaT cells with 1 µM itraconazole has not effect on relative intracellular 1α,25-$(OH)_2$-D_3 levels.
Illustrated are the relative 1α,25-$(OH)_2$-D_3 and itraconazole (ITZ) levels in cell culture samples from experiments analyzing the effect of ITZ on the metabolism of 1α,25-$(OH)_2$-D_3 in ASZ001 and HaCaT cell lines. The cells were treated for 6 h with either pure vehicle mixture (DMSO + EtOH), 1 µM ITZ (1 µM ITZ + EtOH), 100 nM 1α,25-$(OH)_2$-D_3 (DMSO + 100 nM 1α,25-$(OH)_2$-D_3), or a combination of 1 µM ITZ and 100 nM 1α,25-$(OH)_2$-D_3 (1 µM ITZ + 100 nM 1α,25-$(OH)_2$-D_3) by Benedikt Linder (Tumor Genetics Group, UMG) in Göttingen [253]. The medium supernatants and cells were harvested and shipped to Munich, where cells and media were processed and analyzed via a modified vitamin D LC-MS/MS method continuously monitoring MRMs for selected vitamin D metabolites and ITZ [Table II-30].
(A-D) Average fold changes ± the standard error of the mean (SEM) of ITZ **(A, C)** and 1α,25-$(OH)_2$-D_3 **(B, D)** in ASZ001 or HaCaT cells **(A, B)** as well as culture medium **(C, D)** were based on the average peak area in the respective control samples without ITZ and 1α,25-$(OH)_2$-D_3, respectively, and were calculated from IS standardized peak areas. **(E)** Assignment of treatment and list of IS normalized peak areas ± SEM in cells used for the calculation of fold changes.

It could be seen that the treatment with ITZ (± 1α,25-$(OH)_2$-D_3) led to huge fold changes of ITZ peak areas (> 350-fold) in both cell lines [Figure III-46A]. Significant fold changes were also detected in 1α,25-$(OH)_2$-D_3 peak areas when the cells were treated with 1α,25-$(OH)_2$-D_3 (± ITZ) [Figure III-46B]. The determined fold changes of 1α,25-$(OH)_2$-D_3 signals in the HaCaT cell line (> 45-fold) clearly exceeded those in the ASZ001 cell line (> 7-fold) [Figure III-46B], whereas similar fold changes in ITZ signals were calculated for ASZ001 and HaCaT cells [Figure III-46A]. However, when considering the raw IS standardized peak areas, it could be seen that HaCaT cells revealed higher apparent levels in both ITZ and 1α,25-$(OH)_2$-D_3 signals [Figure III-46E]. In addition, no differences in 1α,25-$(OH)_2$-D_3 peak areas were seen between DMSO solvent treated and ITZ treated cells [Figure III-46B], indicating that the treatment with 1 µM ITZ does not significantly influence/impair the metabolism of 1α,25-$(OH)_2$-D_3 in cultured cells.

Although earlier experiments as well as the validation of the vitamin D LC-MS/MS method demonstrated that the quantification of vitamin D metabolites in culture media (using 154CF medium for the ASZ001 cells and DMEM for the HaCaT cells [Table II-31]) was very error prone and only possible if high amounts of vitamins were applied, the respective media supernatants were additionally analyzed. Significant residues of ITZ were detectable in media supernatants which were initially supplemented with 1 µM ITZ [Figure III-46C]. In contrast, no clear 1α,25-$(OH)_2$-D_3 signals could be monitored in any supernatant analyzed [Figure III-46D], although 1α,25-$(OH)_2$-D_3 was measurable in the originally applied media containing 100 nM 1α,25-$(OH)_2$-D_3 [data not shown]. Here, it should be noticed that all 1α,25-$(OH)_2$-D_3 peak areas analyzed in medium supernatants represented integrated baseline peaks, not showing any differences between treated and untreated medium samples (fold changes of approx. 1).

III.3.6.2. Detection of vitamin D metabolites and itraconazole (ITZ) in mouse tumor samples

The non-validated itraconazole (ITZ) implemented vitamin D LC-MS/MS method was also used for the analysis of ASZ001 allograft tumor samples resulting from NMRI-*Foxn1*^{nu} nude mice treated with vehicle, ITZ, 1α,25-$(OH)_2$-D_3, or a combination of ITZ and 1α,25-$(OH)_2$-D_3 for 30 days. The generation of allografts, treatment of mice and isolation of allograft tumors were performed by Benedikt Linder (Tumor Genetics Group, UMG) in Göttingen [253]. The question of this experiment was whether ITZ has the potential to penetrate the allograft tumors and if the adjunction with ITZ and 1α,25-$(OH)_2$-D_3 would increase the level of 1α,25-$(OH)_2$-D_3 in the allograft tumors compared to the sole 1α,25-$(OH)_2$-D_3 treatment.

The isolated tumors were processed according to a non-validated, newly generated sample preparation method for tumors (described in II.11.1.2) and the reconstituted extracts were analyzed via a modified enhanced vitamin D LC-MS/MS method monitoring continuously the MRMs of dihydroxylated vitamin D_3 metabolites, 1α,25-$(OH)_2$-D_2, and ITZ [II.11.2.3]. In contrast to all other analyses which used 25-(OH)-D_2 [25,26,27-$^{13}C_3$] as IS, here, the vitamin D_2 metabolite 1α,25-$(OH)_2$-D_2 was included as loading control. For this, defined amounts of 1α,25-$(OH)_2$-D_2 (10 ng IS per 100 mg tumor sample) were added to weighted tumor samples prior to their processing.

The mass spectrometric analysis of the tumor samples isolated either from vehicle, ITZ, 1α,25-(OH)$_2$-D$_3$, or ITZ and 1α,25-(OH)$_2$-D$_3$ (ITZ / 1α,25-(OH)$_2$-D$_3$) treated mice showed that only 1α,25-(OH)$_2$-D$_2$, which was added to all tumor samples as loading control prior to tumor sample preparation, was traceable in all samples analyzed [Figure III-47]. ITZ peaks (t_R = 1.2 min) were solely detectable in tumors resulting from ITZ [data not shown] or (ITZ / 1α,25-(OH)$_2$-D$_3$) treated mice [Figure III-47B]. This demonstrated that ITZ had penetrated the allograft tumors. Although the continuous monitoring of MRMs allowing for the detection of dihydroxylated vitamin D$_3$ metabolites resulted in multiple peaks in mouse tumors, no difference was seen between tumor samples of vehicle and 1α,25-(OH)$_2$-D$_3$ treated mice. In addition, the peaks of all three monitored MRMs for 1α,25-(OH)$_2$-D$_3$ did not simultaneously show up at the expected retention time t_R of 2.2 min. Thus, no 1α,25-(OH)$_2$-D$_3$ was detectable in tumor samples of 1α,25-(OH)$_2$-D$_3$ [data not shown] or ITZ / 1α,25-(OH)$_2$-D$_3$ treated mice [Figure III-47B]. This was not surprising since mice were treated with 100 ng 1α,25-(OH)$_2$-D$_3$ per kg body weight which corresponded to 10 pmol per mouse in maximum. Because it can be supposed that 1α,25-(OH)$_2$-D$_3$ was distributed all over the organism, only a small portion would had penetrated the allograft tumors. Moreover, some of the applied 1α,25-(OH)$_2$-D$_3$ was most probably catabolized *in vivo*, even in the presence of the CYP inhibitor ITZ. As a result, the levels of 1α,25-(OH)$_2$-D$_3$ in the tumors were most likely below the detection limit.

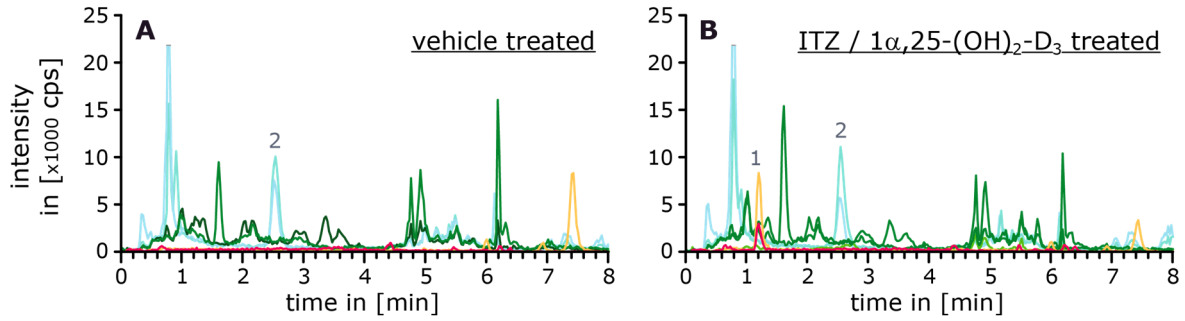

C

MRM (Q_1 / Q_3)	metabolite	t_R [min]	peak
423.174 / 91.000	24,25-(OH)$_2$-D$_3$	1.72	n.d.
423.174 / 128.000	1α,25-(OH)$_2$-D$_3$	2.25	n.d.
423.323 / 77.000			
435.314 / 77.100	1α,25-(OH)$_2$-D$_2$	2.54	2
435.314 / 91.000			
705.203 / 256.000	itraconazole (ITZ)	1.19	1
705.203 / 392.200			

Figure III-47: Itraconazole penetrates mouse allograft tumors and can be detected in tumor samples of itraconazole treated mice, whereas 1α,25-(OH)$_2$-D$_3$ is not detectable in any tumor sample.
ASZ001 allograft tumors of NMRI-*Foxn1*^{nu} nude mice treated with either vehicle, ITZ (100 $^{mg}/_{kg}$ body weight, three times a week), 1α,25-(OH)$_2$-D$_3$ (100 $^{ng}/_{kg}$ body weight, daily), or a combination of ITZ and 1α,25-(OH)$_2$-D$_3$ (ITZ / 1α,25-(OH)$_2$-D$_3$) for 30 days were prepared by Benedikt Linder (Tumor Genetics Group, UMG) in Göttingen [253]. The tumors were shipped to Munich, in collaboration with Benedikt Linder processed according to II.11.1.2, and analyzed by a modified vitamin D LC-MS/MS method monitoring continuously MRMs of dihydroxylated vitamin D$_3$ metabolites, 1α,25-(OH)$_2$-D$_2$, and ITZ [Table II-30]. Substances were only considered to be present in the sample, when all monitored MRMs (quantifier and qualifier MRMs) per substance showed a peak at the respective retention time.
(A, B) Representative chromatograms resulting from the analysis of control tumor samples from vehicle treated mice **(A)** or tumor samples from ITZ / 1α,25-(OH)$_2$-D$_3$ treated mice **(B)**, respectively. **(C)** List of monitored MRMs of selected vitamin D metabolites and ITZ, their retention time, and peak labels.
n.d., not detected; t_R, retention time.

Despite the insufficient performance in the detection of 1α,25-$(OH)_2$-D_3 in allograft tumor samples, not allowing for the analysis of the effect of ITZ on 1α,25-$(OH)_2$-D_3 levels *in vivo*, the established tumor extraction procedure and ITZ expanded vitamin D LC-MS/MS method is a useful method for the detection of ITZ in tumor samples/tissues.

III.3.6.3. Detection of vitamin D metabolites in human plasma

The primary purpose of the developed vitamin D LC-MS/MS method was the detection and analysis of vitamin D metabolites in cell culture samples. However, since some vitamin D metabolites are associated with various human diseases and are supposed to possess a great therapeutic potential, the levels of different vitamin D metabolites in the easy available human plasma are of particular interest in the field of research, too.

In order to have an idea whether the established vitamin D LC-MS/MS method has the potential to analyze vitamin D metabolites in human plasma, varying volumes of human plasma (50-500 µl) were analyzed.

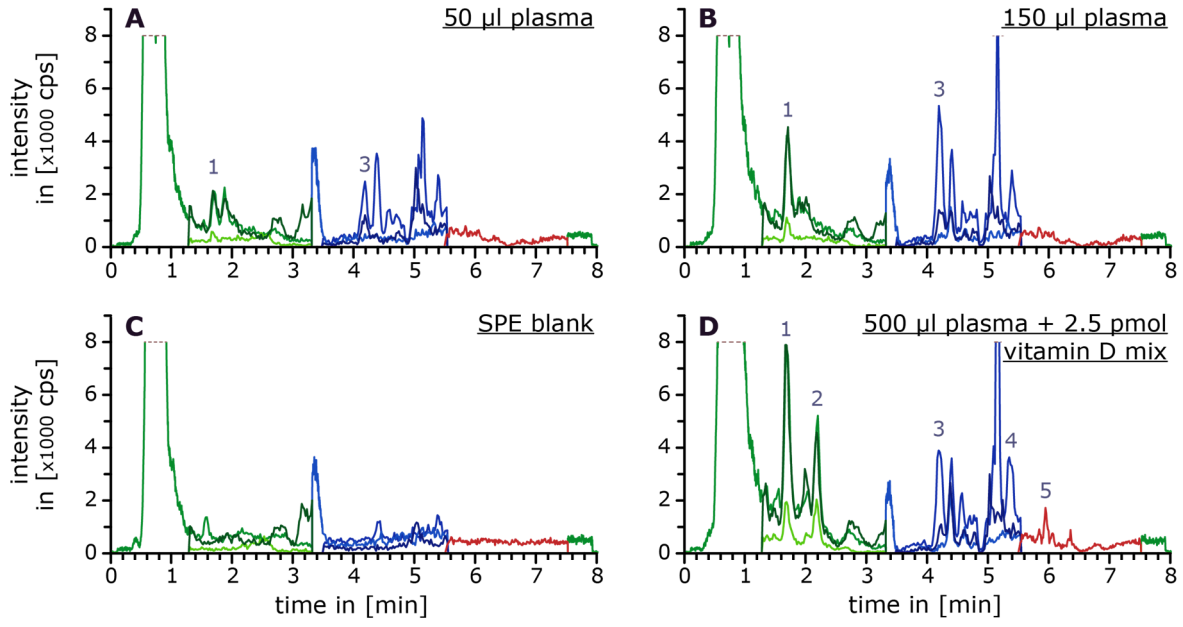

E

peak		MRM (Q_1 / Q_3)		
24,25-$(OH)_2$-D_3	1	423.174 / 91.000	423.174 / 128.000	423.323 / 77.000
1α,25-$(OH)_2$-D_3	2	423.174 / 91.000	423.174 / 128.000	423.323 / 77.000
25-(OH)-D_3	3	401.289 / 90.900	407.185 / 105.000	407.326 / 90.900
1α-(OH)-D_3	4	401.289 / 90.900	407.185 / 105.000	407.326 / 90.900
vitamin D_3	5	385.300 / 259.200		

Figure III-48: Endogenous 24,25-$(OH)_2$-D_3 and 25-(OH)-D_3 can be detected in human plasma by using the established vitamin D LC-MS/MS method.
Different volumes of human plasma were applied for the extraction of vitamin D metabolites according to II.11.1.3 and analyzed via LC-MS/MS (scheduled detection of vitamin D MRMs).
(A-D) The shown chromatograms illustrate isolated traces of vitamin D_3 metabolite MRMs resulting from the analysis of 50 µl plasma **(A)**, 150 µl plasma **(B)**, 60 % methanol blank **(C)**, and 500 µl plasma spiked with 2.5 pmol of each vitamin D metabolite **(D)**. **(E)** The table lists the attribution of traces to considered MRMs as well as of peak numbers to vitamin D_3 metabolites.

For this, a solid phase extraction method (described in II.11.1.3), which was similar to that established for the extraction of vitamin D metabolites from cells, and the for cell culture samples validated vitamin D LC-MS/MS method [II.11.2.3] were applied. By this means, endogenous 24,25-$(OH)_2$-D_3 and 25-(OH)-D_3 could be detected in human plasma samples, even with an applied plasma sample volume of as small as 50 µl [Figure III-48]. In contrast, the vitamin D_3 metabolites 1α,25-$(OH)_2$-D_3, 1α-(OH)-D_3, and vitamin D_3 or the vitamin D_2 metabolites 1α,25-$(OH)_2$-D_2, 25-(OH)-D_2, and vitamin D_2 were only detectable in a spiked plasma sample (500 µl plasma spiked with 2.5 pmol of each analyzed vitamin D metabolite) [Figure III-48D, data not shown]. The fact that no vitamin D_3 was detectable in human plasma samples was quite surprising. However, the demonstrated strong retention (90 %) of vitamin D_3 by the Strata-X SPE sorbent [Table III-14] in combination with possibly lower vitamin D_3 levels or ionization properties when compared with 24,25-$(OH)_2$-D_3 or 25-(OH)-D_3 could explain its missing detectability in the samples.

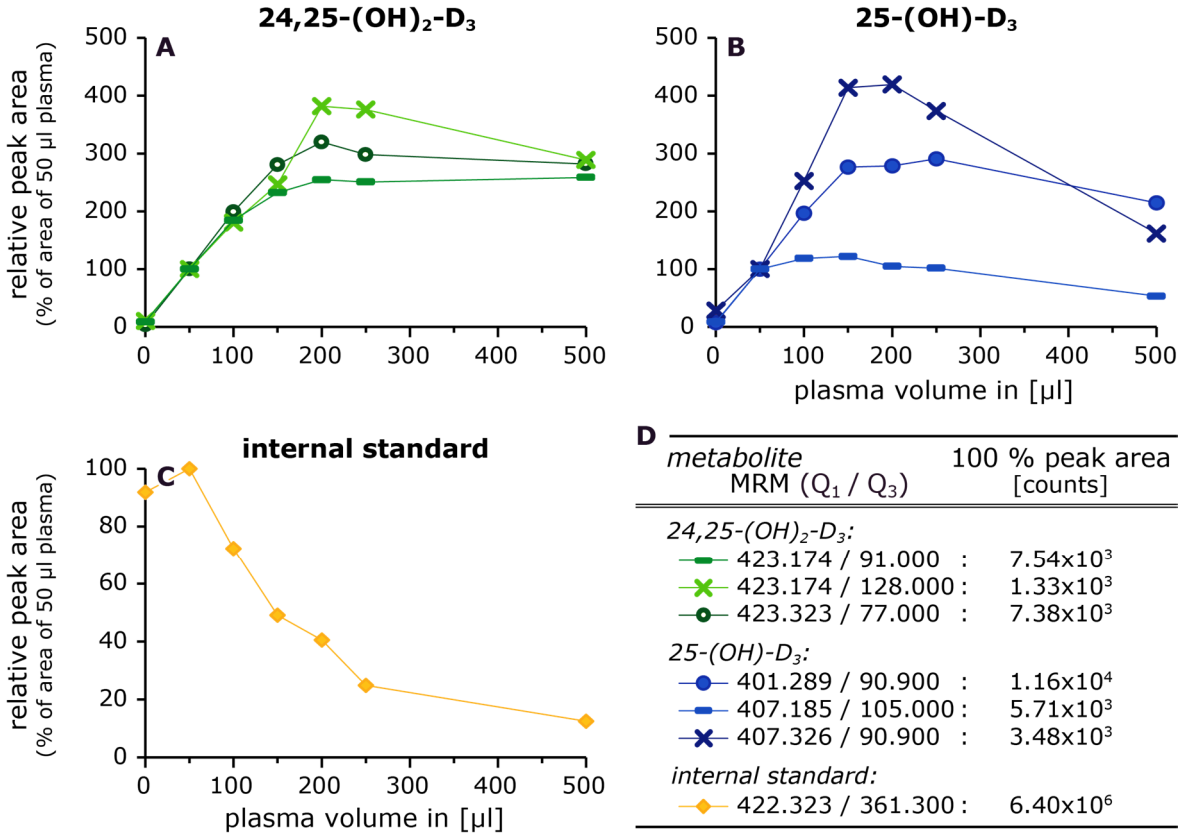

Figure III-49: The analysis of different human plasma volumes demonstrated a negative relationship between peak areas and the plasma volume applied.
Shown are normalized peak areas of 24,25-$(OH)_2$-D_3 and 25-(OH)-D_3 MRMs as well as of the equally spiked internal standard (25-(OH)-D_2 [25,26,27-$^{13}C_3$]) in dependence of the volume of the human plasma applied. Different volumes (50 µl, 100 µl, 150 µl, 200 µl, 250 µl, and 500 µl) of plasma were processed according to II.11.1.3 and analyzed by LC-MS/MS [II.11.2.3]. The peak areas of quantifier and qualifier MRMs of the detectable vitamin D metabolites 24,25-$(OH)_2$-D_3 and 25-(OH)-D_3 as well as those of the quantifier MRM of the internal standard were normalized to the respective peak area of the 50 µl plasma sample (= 100 %).
(A-C) Shown are the relative peak areas of 24,25-$(OH)_2$-D_3 **(A)**, 25-(OH)-D_3 **(B)**, and the internal standard **(C)** plotted against the volume of human plasma applied. **(D)** List of MRMs and determined peak areas in the 50 µl plasma sample which were set to 100 % for the calculation of relative peak areas in the different plasma volumes analyzed.

When increasing volumes (50 µl, 100 µl, 150 µl, 200 µl, 250 µl, and 500 µl) of human plasma were closer analyzed, ascending 24,25-$(OH)_2$-D_3 and 25-(OH)-D_3 MRM peak heights and peak areas, were observed in samples resulting from low plasma volumes (50-150 µl), which positively correlated with the applied plasma volume [Figure III-49A, B; data not shown]. However, at plasma volumes of more than 200 µl only decreasing peak areas and heights could be detected [Figure III-49A, B; data not shown]. In addition, the signal intensities of the internal standard 25-(OH)-D_2 [25,26,27-$^{13}C_3$], which was added to the plasma samples in equal amounts, decreased steadily with increasing plasma volumes applied [Figure III-49C]. As a result, the internal standard peak area of the 150 µl and 500 µl plasma sample was approximately 50 % and 10 % of that detected in the 50 µl plasma sample, respectively [Figure III-49C]. The negative relationship between internal standard signal intensities and applied plasma volumes could explain the reduced 24,25-$(OH)_2$-D_3 and 25-(OH)-D_3 peak areas and heights when bigger plasma volumes were processed and analyzed within the experiment, and perhaps the missing detectability of further, lower abundant vitamin D metabolites. In this regard, possible matrix effects, like increased ion suppression in MS/MS analysis or significant losses within the protein precipitation and/or SPE steps due to higher amounts of matrix compounds, could outweigh the expected gain in signal intensities of low abundant metabolites when larger plasma volumes were analyzed. However, the exact reason for the observed signal suppression with bigger plasma volumes is yet unclear.

All in all, the for cell culture samples validated vitamin D LC-MS/MS method represented a good basis method for the analysis of vitamin D metabolites in human plasma. Whether the observed decrease in vitamin D signal intensities with bigger volumes analyzed are because of higher ion suppressions due to the increased portion of plasma matrix in the LC-MS/MS analysis or because of losses within the sample preparation process (resulting from the precipitation step or from an overloading of the SPE column sorbent) and if the optimization of these parameters allows for the detection of further vitamin D metabolites in human plasma needs to be clarified in future.

IV. Discussion

IV.1. Human *AKR1B15*: A gene encoding for two isoforms with different characteristics

The work on the characterization of the novel human aldo-keto reductase *AKR1B15* (gene and gene products) within this thesis was started shortly after its first annotation and initial characterization by Salabei *et al.* in 2011 [22]. Since the AKR1B15 protein showed only little catalytic activity with typical AKR substrates in these initial experiments [22], the authors contacted our lab to help answering the question of substrate specificity, especially with respect to steroids. However, it was realized that a more comprehensive analysis would be needed to elucidate the biological role of *AKR1B15*. Thus, several further analyses were performed which, altogether, gave some hints for the protein's *in vivo* function.

IV.1.1. Expression of two variants *in vivo*

In 2011, Salabei *et al.* reported a novel gene locus *tcag7.1260*, named *AKR1B15*, on the human chromosome 7q33 encoding for an enzyme with little enzymatic activity [22].

Although this initial publication recorded only one *AKR1B15* transcript (Ensembl transcript *AKR1B15-201* [ENST00000423958.1]; here referred to as *AKR1B15.1*) encoding for a 316 amino acids long AKR with 91 % sequence identity towards the well described human AKR1B10 enzyme [22], database search revealed a second transcript (Ensembl transcript *AKR1B15-001* [ENST00000457545.2]; here referred to as *AKR1B15.2*) which encodes for a 344 amino acids long protein. In accordance with the guidelines for the nomenclature of alternatively spliced AKRs, the shorter AKR1B15 isoform was named AKR1B15.1 and the longer one AKR1B15.2 [269]. The splice variants *AKR1B15.1* (10 exons) and *AKR1B15.2* (12 exons) differ only in the first and first three exons, respectively, and share all following exons, including those encoding for the catalytic tetrad. Thereby, the alternative splicing of the first exons in the *AKR1B15* variants leads to a N-terminal amino acid sequence in AKR1B15.2 differing from all other AKRs and being prolonged when compared with other AKR1 family members. Using transcript specific primers, it was shown that both *AKR1B15* transcript variants are expressed in human tissues. However, whereas the expression of the closely related *AKR1B10* is ubiquitous [61], both *AKR1B15* variants reveal a more distinct expression pattern. Here, the expression of both *AKR1B15* transcripts is mainly concentrated on tissues which are linked to sex steroid metabolism and signaling, like reproductive organs (especially ovary, placenta, and testis) as well as adipose tissue, skeletal muscle, and thymus [270–275]. The expression of *AKR1B15* in placenta and adipose tissue could be verified by the detection of both transcripts in the placental choriocarcinoma cell line BeWo and the fibroblastic preadipocyte cell strain SGBS, respectively.

Expression of a gene on mRNA level does not imply that the transcribed mRNA is translated into a functional protein, even if the mRNA contains an open reading frame as it is the case for both *AKR1B15* transcripts. Due to the high intron-exon structure and sequence analogy between *AKR1B15* and *AKR1B10* genes and transcripts, respectively, it could be assumed that *AKR1B15* represents a pseudogene of *AKR1B10*. Thus, *AKR1B15* might merely be expressed on mRNA level *in vivo* and might fulfill mRNA mediated physiological functions. One example of such a pseudogene is *PTENP1* which acts in a protein-coding independent manner in the suppression of tumor growth [276]. Thereby, the transcripts of the tumor suppressor *PTEN* and its pseudogene *PTENP1* compete for the binding of *PTEN*-targeting miRNAs resulting in increased levels of the tumor suppressor PTEN [276]. Within this thesis, it was shown that *AKR1B15* most likely does not represent a pseudogene of *AKR1B10* since endogenous AKR1B15.1 and AKR1B15.2 could be detected in BeWo cell fractions by Western blotting. Thus, both *AKR1B15* mRNA transcripts are translated into proteins in the BeWo cell line *in vivo*. However, in the Western blots, the endogenous AKR1B15 isoforms could only be detected in low amounts in the 800x*g* and 9000x*g* pellet fractions resulting from the isolation process of mitochondria from BeWo cells and corresponding to the enriched cell debris/ unbroken cells and crude mitochondria fractions, respectively, but not in total cell lysates or total human tissue (adipose tissue, skeletal muscle, placenta, prostate, testis, and thymus) lysates.

Various reasons might explain the ambiguous detection of endogenous AKR1B15 isoforms in total cell or tissue lysates by Western blotting using the herein newly generated monoclonal rat-anti-AKR1B15 clone 9A5 (AKB-2) primary antibody. First, different algorithms predicted four post-translational modification sites within the AKB-2 epitope in AKR1B15.1 (Lys117, Thr118, Ser133, and Lys135) and AKR1B15.2 (Lys145, Thr146, Ser161, and Lys163) [Figure III-21]. Thereby, Thr118 and Ser133 (AKR1B15.1 numbering) are predicted to be phosphorylated and correspond to two out of five amino acid residues that differ between the AKR1B15 isoforms and AKR1B10, whereas Lys117 and Lys135 (AKR1B15.1 numbering) are predicted to be SUMOylated and glycated, respectively, and locate next to those residues different in the AKR1B15 isoforms and AKR1B10 [Figure III-4, Figure III-21]. Thus, the predicted post-translationally modified amino acid residues are very likely targeted by the specific antibodies against the AKB-2 peptide. Since the antibodies were, however, produced against unmodified peptides, post-translational modifications within the AKB-2 epitope could strongly reduce the affinity or completely prevent the binding of the specific antibody to the epitope. Second, both AKR1B15 isoforms might be present at very low protein levels and escape the detection as the established antibodies possess only a limited sensitivity. Low protein levels of AKR1B15 isoforms in human tissues or cell lines could easily be assumed because of the low to moderate abundance of *AKR1B15* transcripts in the respective total RNA samples, although several studies reported that the mRNA levels and the respective protein levels in human samples often do not directly correlate [277, 278]. Although the stability of both *AKR1B15* transcripts and AKR1B15 isoforms has not been analyzed till now, a reduced mRNA stability and/or increased protein turnover rate due to lysosomal degradation but also proteasomal degradation might also explain the low AKR1B15 protein levels detected [279–281]. Both AKR1B15 isoforms exhibit some predicted ubiquitination and SUMOylation sites [Figure III-21]. As a result, low protein levels due to an increased proteasomal degradation of the mitochondrial and the cytosolic AKR1B15 isoform after polyubiquitination (Lys48 linked ubiquitin chain) are supposable. On the other hand, the protection from proteolysis by monoubiquitination, SUMOylation, or other post-

translational modifications could also be possible [282–286]. However, the real occurrence of post-translational modifications in the AKR1B15 isoforms *in vivo* and the true reasons for their poor detectability in human cell and tissue samples expressing *AKR1B15* on RNA level need to be clarified in future projects.

IV.1.2. TWO ISOFORMS WITH DIFFERENT SUBCELLULAR LOCALIZATION

This thesis demonstrated that the human *AKR1B15* gene encodes for two protein isoforms, AKR1B15.1 and AKR1B15.2, *in vivo*. These two isoforms differ in their N-terminal sequences (amino acid residues Met1-Arg22 in AKR1B15.1 and Met1-Ala50 in AKR1B15.2) but share the same sequence in the downstream 294 amino acids, including those belonging to the catalytic tetrad.

Subcellular localization studies showed that AKR1B15.2 is a cytosolic protein, whereas AKR1B15.1 reveals an unexpected colocalization with mitochondria. The mitochondrial localization of the AKR1B15.1 isoform was surprising since AKRs, including the highly identical AKR1B10, are generally considered to be cytosolic proteins [36, 287]. In addition, although iPSORT predicted a mitochondrial localization for AKR1B15.1, no obvious mitochondrial localization sequence or other signal peptide could be identified for both AKR1B15 isoforms by other prediction tools. The inconsistency between the results from *in silico* predictions and experimental analyses for the subcellular localization of AKR1B15.1 was not surprising because those *in silico* predictions are very hypothetical and do often not agree with *in vivo* localizations [288]. In most cases, N-terminal amino acid sequences (presequences) determine the mitochondrial localization of proteins by forming positively charged amphiphilic α-helices which interact with the translocase complex of the outer membrane (TOM complex) [289]. Whereas the mitochondrial AKR1B15.1 and the cytosolic AKR1B15.2 reveal a high diversity in their N-terminal sequences, AKR1B15.1 and the highly identical but cytosolic AKR1B10 differ only in two amino acid residues within the first 30 amino acids (Arg22 and Leu24 in AKR1B15.1 compared with Lys22 and Pro24 in AKR1B10 [Figure IV-1]).

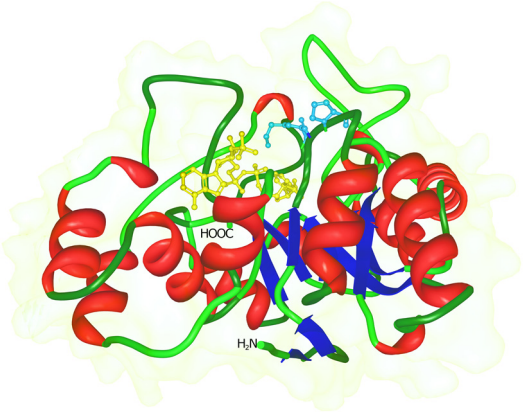

Figure IV-1: Leu22 and Pro24 are located within a turn structure in AKR1B15.
Shown is the crystal structure of AKR1B10 in complex with $NADP^+$ and tolrestat according to Gallego *et al.* (PDB: 1ZUA) [29].
The two amino acid residues Lys22 and Pro24, which are substituted by Arg22 and Leu24 in AKR1B15.1, respectively, are illustrated in ball-and-stick style and highlighted in bright blue. $NADP^+$ is colored in yellow, whereas tolrestat is hidden.

Subcellular localization studies with N-terminal sequences of AKR1B15 and AKR1B10 fused to AcGFP demonstrated that the stretch of the first 38 amino acids of AKR1B15.1 is sufficient to target AKR1B15.1 (here AcGFP) to mitochondria. In addition, Leu24 in the N-terminus of AKR1B15.1 was identified as the amino acid residue responsible for the different subcellular localizations of AKR1B15.1 and AKR1B10 since the single amino acid exchange Pro24Leu, but not Lys22Arg, in the N-terminal sequence of AKR1B10 shifted the localization of the respective AcGFP fusion protein towards mitochondria. The dependency of the mitochondrial subcellular localization of AKR1B15.1 on Leu24 (replaced by Pro24 in the cytosolic AKR1B10) was not surprising since proline and leucine residues differ clearly in their characteristics and proline residues are known to represent helix breaker (as can be seen in the N-terminal structure of AKR1B10 [Figure IV-1]) [290–292]. Lysine and arginine residues, however, share similar physicochemical properties and an exchange of these two amino acid residues preserves widely the characteristics of proteins [292]. Here, it needs to be mentioned that shorter AKR1B15.1 N-termini (Met1-Gly26 or Met1-Glu30) fused to AcGFP showed incomplete mitochondrial and partial cytosolic localization [data not shown], although the iPSORT algorithm predicted a mitochondrial subcellular localization for AKR1B15.1 by considering exclusively the first 30 amino acid residues. The more diffuse localization pattern could be explained by the fact that the *Age*I restriction site used for the cloning of N-termini into the pAcGFP-N1 vector encoded for a proline on the second amino acid position downstream the N-terminal sequence [Figure III-11]. As described above, this proline most probably disturbed the localization signal and led to the artificial localization of shorter AKR1B15.1 N-termini-AcGFP fusion proteins. In contrast, the length of N-terminal sequences of AKR1B15.2 and AKR1B10 had no influence on the cytosolic localization of the respective fusion proteins with AcGFP [data not shown] since AcGFP as well as AKR1B15.2 and AKR1B10 are cytosolic proteins anyway.

The mitochondrial subcellular localization of AKR1B15.1 found by immunocytochemistry was confirmed by Western blotting. Here, endogenous AKR1B15.1 could be detected in the 800x*g* and 9000x*g* pellets resulting from BeWo cell homogenates processed for the isolation of mitochondria. The 800x*g* pellet included the nuclear fraction, unbroken cells and cell debris, as well as residues of the supernatant, and the 9000x*g* pellet represented the crude mitochondrial fraction [216, 293]. In contrast to the results gained from *in silico* prediction and immunocytochemistry, indicating a cytosolic localization of AKR1B15.2 *in vivo*, in Western blots, endogenous AKR1B15.2 was primarily found in the 9000x*g* pellet of BeWo cell homogenates but not in the 9000x*g* supernatant, as expected for cytosolic proteins. These inconsistent localization results for AKR1B15.2 could be explained by a strong association with subcellular compartments, e.g., lysosomes or microsomes, which are likely to be present in the 9000x*g* pellet as well [216, 293]. However, this issue needs clarification in the future.

Like mentioned above, the majority of AKRs are soluble cytosolic proteins. Prior to the annotation of AKR1B15, only one human AKR belonging to the aflatoxin reductase family, the AKR7A2, had been reported to be associated with mitochondria in the neuroblastoma cell line SH-SY5Y. Its rat ortholog, though, showed a localization to the Golgi apparatus [105, 294]. Assuming that the arguable mitochondrial localization of the human AKR7A2 is true, AKR1B15.1 is at least the first human AKR1 family member which colocalizes to mitochondria. At the moment, it is unknown whether AKR1B15.1 is associated with the outer or inner membrane or it is located within the intermembrane or matrix space. Calvo *et al.* reported that the S8R mutation in AKR1B15.1 was linked to a lethal mitochondrial

phenotype with impaired complex I activity [265]. Thus, a possible association of AKR1B15.1 with the inner membrane could be supposed. However, the actual exact localization of AKR1B15.1 in the mitochondria remains to be determined (e.g., by using immunogold electron microscopy) as well as the biological relevance of two AKR1B15 isoforms with different subcellular distribution.

IV.1.3. TWO ISOFORMS WITH DIFFERENT ENZYMATIC PROPERTIES

When the *AKR1B15* gene was annotated in 2011 [22], nothing was known about the substrate preferences and enzymatic properties of both AKR1B15 isoforms. This thesis demonstrated that AKR1B15.1 is an enzymatically active protein using C18 and C19 steroids (androgens and estrogens, respectively), 3-keto-acyl-CoA conjugates (acetoacetyl-CoA), as well as retinoids as substrates, whereas AKR1B15.2 seems to be enzymatically inactive. Thereby, AKR1B15.1 represents a predominantly reductive enzyme which catalyzes redox reactions exclusively in the presence of NADPH or $NADP^+$ as cofactors.

These general enzymatic properties of AKR1B15.1 are in accord with other AKRs, which largely catalyze the reduction of a broad substrate spectrum and prefer NADPH as cofactor [26, 27, 35, 37, 295]. Monitoring of protein fluorescence quenching in cofactor titration studies demonstrated that solely NADP(H) – but not NAD(H) – bind to AKR1B15.1 as cofactors with a dissociation constant K_d of approximately 60 nM, which is within the range or below the K_d values published for other AKRs [14, 108, 220, 296–300]. In contrast, no clear binding of any nicotinamide adenine dinucleotide cofactor (neither NADP(H) nor NAD(H)) was observable for AKR1B15.2. The lack in cofactor binding would explain the missing enzymatic activity of AKR1B15.2 with various substrates. Compared to the enzymatically active AKR1B15.1 isoform, AKR1B15.2 possesses a prolonged and divergent N-terminal amino acid sequence, which could impede the entry of cofactors to the binding sites by partially or completely closing the entrance cleft. In addition, it could also impair the cofactor binding itself. Structural and sequence analyses of various AKRs in the past showed that the sites responsible for cofactor binding are quite conserved within the majority of AKRs [24, 26]. Beside the amino acid residues located in the center of AKR proteins, which are present in both AKR1B15 isoforms, an additional site located rather N-terminally (Gly19, Thr20, Trp21, Lys22 in AKR1B10) is described for the interaction with NAD(P)(H) cofactors [24, 26, 300]. Comparison of sequences revealed that the huge majority of AKRs, including AKR1B15.1, exhibit a conserved glycine at position 19 as well as a tryptophan or phenylalanine and lysine or arginine residue at positions 21 and 22 (AKR1B10 numbering), respectively. However, no similar motif could be found in the prolonged N-terminal amino acid sequence of AKR1B15.2. Instead, AKR1B15.2 possesses a P-Y-P-A motif at the corresponding positions [data not shown]. Thus, a stable binding of NADP(H) by AKR1B15.2 might be prevented by different structural and physicochemical properties of the special N-terminal sequence in AKR1B15.2. Besides, until now it is unclear whether the lack in cofactor binding is an intrinsic feature of the AKR1B15.2 protein itself or an extrinsic effect due to an improper folding within the artificial expression systems and the downstream purification process. However, since an enzymatic activity was not only missing in AKR1B15.2 purified from *E. coli* but also after its overexpression in the mammalian HEK-293 system, where proteins

usually fold properly, the missing binding capability of cofactors by AKR1B15.2 seems to be most probably an intrinsic effect.

Like mentioned above, AKR1B15.1 is a predominantly reductive enzyme. Salabei *et al.* demonstrated that, although it shares 91 % amino acid identity with AKR1B10, AKR1B15.1 possesses only minor enzymatic activity with the typical AKR substrates DL-glyceraldehyde and 4-nitrobenzaldehyde [45]. Studies concerning the identification of biologically relevant AKR1B15.1 substrates within this thesis confirmed a poor activity with DL-glyceraldehyde in comparison to AKR1B10. Instead, androgenic and estrogenic steroids (but not progesterone or glucocorticoids), 3-keto-acyl-CoA conjugates, as well as retinoids were identified to be potent substrates of AKR1B15.1, and this might be of biological importance.

Michaelis-Menten kinetics showed that the K_M for "oxidized" 17-ketoandrogens and estrone ranged between 1.9 μM and 2.8 μM. In contrast, about 3- to 6-fold higher K_M values were determined for the corresponding "reduced" 17β-hydroxysteroids. Similar ratios between "oxidized" and "reduced" substrates were seen in the respective catalytic efficiencies k_{cat}/K_M, which were in principal higher with androgens than with estrogens. Thereby, AKR1B15.1 possesses K_M values for 17-ketosteroids which are in the range of those of reductive human 17β-HSDs, e.g., the SDR superfamily members 17β-HSD1, 17β-HSD7, and 17β-HSD12 or the AKR superfamily member AKR1C3 [72, 97, 139, 161, 301, 302]. Whereas the human AKR1C3 (also known as 17β-HSD5 or 3α-HSD2) possesses trifunctional enzymatic activities by acting on position C3(α), C17(β), and C20(α) of steroid nuclei [89, 90], AKR1B15.1 features a high position selectivity and catalyzes exclusively redox reactions at position C17(β) of androgens and estrogens. Although AKR1B15.1 shows only poor catalytic efficiencies with steroids (k_{cat}/K_M: approx. 0.6 $\mu M^{-1} \cdot min^{-1}$ for reductive reactions) when compared to the catalytic efficiency of the cytosolic human 17β-HSD1 with estrone (k_{cat}/K_M: approx. 11600 μM^{-1} min^{-1}), the catalytic efficiencies of AKR1B15.1 are at least 50-fold and 15-fold higher than those of the human 17β-HSD7 and AKR1C3, respectively [72, 161, 302]. Thus, AKR1B15.1 should be classified as a novel human 17β-HSD group member. Looking at the enzymatic properties of the highly identical human AKR1B10 with steroids, Endo *et al.* reported an inhibition of AKR1B10 by androgens and estrogens [303]. The inhibitory effect of steroids on AKR1B10 contrasts to observations made within this thesis, where purified AKR1B10 was able to catalyze redox reactions on androgens and estrogens in the nanomolar range [data not shown]. However, in these reactions the overall enzymatic activity of AKR1B10 with steroids was lower when compared to AKR1B15.1 [data not shown]. In addition, AKR1B10 preferred the oxidation of steroids over their reduction [data not shown]. Thus, the reported apparent inhibition of AKR1B10 by androgens and estrogens might have resulted from higher affinities to and much slower reaction velocities with C18 and C19 steroids (possibly because of substrate inhibition) when compared to pyridine-3-aldehyde, used as AKR1B10 substrate in the assays [303]. Though, at the moment, these assumptions are only of theoretical nature and need to be validated by determining K_M and k_{cat} values for the conversion of steroids by AKR1B10 in future.

In addition to steroids, AKR1B15.1 was also able to catalyze the reduction of acetoacetyl-CoA into 3-hydroxy-butyryl-CoA with K_M and k_{cat} values of approximately 63 μM and 0.5 min^{-1}, respectively. Compared to the catalytic parameters of AKR1B15.1 with steroids, the K_M with acetoacetyl-CoA is much higher, while the k_{cat} seems to be reduced. However, the diminished k_{cat} could also result from the altered experimental set-up [304]. On the other hand, the higher K_M does not per se preclude acetoacetyl-CoA as biologically relevant substrate of AKR1B15.1

because its cellular levels are many times higher than those of steroids. Nevertheless, other human enzymes using acetoacetyl-CoA as substrate (e.g., cytosolic acetoacetyl-CoA thiolase or HMG-CoA synthase) have clearly lower K_M values [305–307]. In the assays using NADPH absorption as read-out, no definite oxidation of 3-hydroxy-butyryl-CoA into acetoacetyl-CoA was seen. Although not obviously visible, it is supposed that this oxidative reaction could also be catalyzed by AKR1B15.1, however, similar to the oxidation of steroids, to a much lesser extent, ranging at the sensitivity limit of the detection method. In addition, there were slight evidences that AKR1B15.1 can reduce 3-keto-palmitoyl-CoA into 3-hydroxy-palmitoyl-CoA and thus is able to catalyze not only the reduction of acetoacetyl-CoA but also the reduction of longer chain 3-keto-acyl-CoA conjugates into the respective 3-hydroxy-acyl-CoA conjugates [data not shown]. Though, this question remains to be addressed in future. No enzymatic activity of AKR1B15.1 was seen in assays using succinyl-, methylmalonyl-, or 3-hydroxy-3-methyl-glutaryl-CoA conjugates as well as unconjugated acetoacetic acid or 2-oxo-butyric acid as substrates. This demonstrated that neither thioesters or carboxylic groups nor keto groups next to charged carboxylic groups can be reduced by AKR1B15.1. Whereas it was initially thought that substrates of AKR1B15.1 need a bulky ring system for their proper orientation within the active site pocket, Giménez-Dejoz *et al.* published that AKR1B15.1 reduces also unconjugated short and medium chain mono- or dicarbonyls [300]. In addition, they confirmed the enzymatic activity of AKR1B15.1 with retinoids, seen also in experiments within this thesis, and demonstrated that compared to steroids and all-trans retinal (alias all-trans retinaldehyde), 9-cis-retinaldehyde (K_M = 0.16 μM) is a more potent substrate of AKR1B15.1 [300].

This thesis as well as the activities reported by Giménez-Dejoz *et al.* demonstrate a high diversity in the identified AKR1B15.1 substrates. This was not surprising because a broad substrate spectrum was already previously seen for other AKRs and SDRs belonging to the 17β-HSD family. For example, similar to AKR1B15.1, the human SDRs 17β-HSD3, 17β-HSD4, 17β-HSD10, and 17β-HSD12 catalyze beside redox reactions on sex steroids also reactions on 3-keto-acyl-CoA conjugates [129]. Furthermore, AKR1C3, the only human AKR superfamily member classified as 17β-HSD up to now, catalyzes not only redox reactions on sex steroids but also the reduction of prostaglandins [72, 94]. Though, no activity with 3-keto-acyl-CoA conjugates has been reported for AKR1C3 so far.

In contrast to the observations made within this thesis in which AKR1B10 showed in parallel enzymatic activity assays a 35-fold higher activity with DL-glyceraldehyde than AKR1B15.1 did, Giménez-Dejoz *et al.* reported for AKR1B15.1 a 2-fold higher catalytic efficiency with DL-glyceraldehyde when compared to that of AKR1B10 [300]. At the moment it is hard to say which result represents the truth since the catalytic efficiencies of AKR1B10 and AKR1B15.1 with DL-glyceraldehyde were not determined simultaneously in [300] and the catalytic efficiencies of AKR1B10 published by different research groups differed already by a factor of three [300, 303]. The approximately 10-fold higher maximum turnover rate (k_{cat}) of AKR1B15.1 with DL-glyceraldehyde in the hands of Giménez-Dejoz *et al.* in comparison to the rough determined turnover rate at 5 mM DL-glyceraldehyde (v_{5mM}) within this thesis could be explained by differences in the protein expression and purification method applied. Whereas Gimenéz-Dejoz *et al.* expressed *AKR1B15.1* upon coexpression of chaperones in *E. coli* and purified native folded AKR1B15.1 monomers from the expression cultures [300], AKR1B15.1 used in enzymatic assays within this thesis was purified from inclusion bodies after overexpression in the classical *E.coli* BL21 (DE3) expression system. The purification of

AKR1B15.1 from inclusion bodies included a denaturing solubilization step using 1 % N-lauroylsarcosine and 2 % Triton X-100 detergents in buffer, followed by an on-column IMAC purification and refolding step. Thereby, the refolding was enabled by the washing-off of Triton X-100 and the stepwise reduction of N-lauroylsarcosine to a final concentration of 0.1 % in the eluate. For the determination of the kinetic parameters, it was supposed that the enzyme was pure and properly folded. However, the presence of protein oligomers or impurities after the IMAC and desalting purification protocol could not be excluded. In addition, usually only a portion of proteins are properly refolded within the refolding process and thus enzymatically active [308–310]. Another factor which might had affected the enzymatic activity of AKR1B15.1 was the use of the detergent N-lauroylsarcosine (alias sarkosyl) itself. Different studies in the past showed that N-lauroylsarcosine negatively influences the activity of various enzymes, e.g., that of the mycobacterial trehalose-phosphate phosphatase (TPP) or horse glutathione S-transferase (GST) [311–313].

Taking all facts together, it is assumed that, in fact, the maximum turnover rates (k_{cat}) and, hence, enzymatic activities of AKR1B15.1 with all substrates are many times higher than that determined within this thesis. As a result, the catalytic efficiencies of AKR1B15.1 *in vivo* are underestimated and thus the enzymes' physiological importance might be undervalued. However, the assumption of a possible underestimation of the catalytic efficiencies of AKR1B15.1 needs to be verified in future by using an expression system which allows for the expression of soluble AKR1B15.1 without any refolding or detergent treatment (e.g., *E. coli* BL21 (DE3) coexpressing different chaperones) and a more efficient purification method.

IV.1.4. WHAT PROVOKES THE SEVERE PHENOTYPE OF THE AKR1B15.1 S8R MUTANT?

In 2012, the AKR1B15.1 S8R mutant was correlated to a lethal fetal phenotype with multiple pterygium syndrome, severe fetal hydrops, and intrauterine growth restriction linked to a markedly impaired complex I activity in liver [265]. However, analysis of the subcellular localization of the AKR1B15.1 S8R mutant and its enzymatic activities with steroids within this thesis did not reveal any remarkable differences between the mutant and wild type enzymes.

Because only mitochondrial encoded and a subset of nuclear encoded genes were targeted in the next-generation sequencing approach used by Calvo *et al*., it is hard to say whether the described lethal phenotype was solely based on the reported single nucleotide substitution (T→G) in the *AKR1B15* gene leading to the exchange of serine by arginine at position 8 of AKR1B15.1 [265]. Thus, by using the targeted next-generation sequencing approach, Calvo *et al.* might have missed so far unknown gene variants which could also play a role in mitochondrial diseases [314]. For example, targeted next-generation sequencing studies (e.g., analyzing only the exome of individuals or known cytogenetic regions) missed a causal gene variant in patients with amyotrophic lateral sclerosis-frontotemporal dementia (ALS-FTD) and allowed initially only for the discovery of a founder haplotype on Chr. 9p21 within the Finnish population [314, 315]. However, a study analyzing this region in more detail was able to identify an expansion of a hexanucleotide in the first intron of the human *C9ORF72*

gene as monogenic cause of the disease in the Finnish but also in the outbred European population [316].

On the other hand, the observed mitochondrial phenotype does not necessarily have to result from an altered subcellular localization or enzymatic activity of the AKR1B15.1 S8R mutant. The fact that the *in silico* analysis of post-translational modification sites in AKR1B15 isoforms predicted a phosphorylation site at Ser8 in the wild type AKR1B15.1 [III.1.5.2] provoked a new hypothesis for the molecular basis of the AKR1B15.1 S8R phenotype. According to the crystal structure of the highly identical human AKR1B10, the putatively phosphorylated amino acids Ser8 and Thr9 define a hairpin between two β-strands [29]. The resulting N-terminal β-sheet is a common motif among AKR1B family members and creates the bottom of the α/β-barrel structure [27, 29, 317]. If Ser8 is phosphorylated in the wild type AKR1B15.1, the enzyme will be negatively charged at that position, whereas the S8R mutant cannot be phosphorylated and is positively charged because of the serine to arginine substitution. The significant changes in physicochemical properties at position 8 could destroy the hairpin structure and, thereby, the N-terminal β-sheet by altering the backbone structure itself but also reversing potential repulsive interactions between phosphorylated Ser8 and Thr9 into attractive ones [292]. In addition, the importance of phosphorylated serines in direct protein-protein interactions with, e.g., 14-3-3 proteins but also other protein domains has been shown in several previous studies [318, 319]. Thus, a probable structural change in the N-terminal region of AKR1B15.1 S8R but also the reversed charge on Ser8 itself might affect potential protein-protein interactions (e.g., possible interactions with complex I of the respiratory chain) and, thereby, lead to the described phenotype. However, this is only hypothesized and needs to be investigated in future by protein-protein interaction studies.

Without any knowledge of enzymatic activities or protein-protein interactions, a functional assessment of intact mitochondria could also help to elucidate possible effects of the S8R mutation in AKR1B15.1 on mitochondria functions, explaining the lethal mitochondrial phenotype with impaired complex I activity in liver [265]. Preliminary results from pilot studies analyzing the ATP synthesis rates by mitochondria isolated from HEK-293 cells cultured under low (approx. 6 mM) or high (approx. 25 mM) glucose conditions revealed no clear correlations between samples from non-transfected cells and from cells overexpressing either untagged wild type AKR1B15.1 or untagged mutant AKR1B15.1 S8R [data not shown]. Although this pilot studies partially showed differences in the ATP synthesis rates between different samples, the interpretation of those was quite difficult since the results were very variable, most probably because of varying transfection efficiencies and/or the sensitive but error prone assay used. In addition, substrates for complex activities were in excess and thus substrate-related effects due to the mutation could be hidden.

In summary, although some hypotheses arose, it is nebulous why the S8R mutation in AKR1B15.1 caused a severe mitochondrial phenotype with impaired complex I activity in liver [265]. Further studies are needed to clarify whether AKR1B15 affects directly the activity of complex I, like supposed from the observations made by Calvo *et al.* in 2012, or whether it controls or regulates, for example, the import and export of mitochondrial substrates or the mitochondrial redox homeostasis.

IV.1.5. Hypotheses for the biological roles of AKR1B15 isoforms *in vivo*

At the moment the biological role of AKR1B15.1 can only be hypothesized. Considering the colocalization of AKR1B15.1 with mitochondria, the cellular compartment where primarily the oxidative phosphorylation, the citric cycle, the β-oxidation of fatty acids, and parts of the urea cycle but also the first steps (from cholesterol to pregnenolone) of the steroid synthesis take place [198, 320], a physiologically relevant reduction of sex steroids and 3-keto-acyl-CoA conjugates by AKR1B15.1 *in vivo* seems unlikely. However, although a physiological role of AKR1B15.1 in mitochondria appears implausible at first sight (mitochondria are known to produce acetoacetyl-CoA for the citric cycle by β-oxidation of fatty acids instead of to use acetoacetyl-CoA for reductive anabolic reactions and AKR1B15.1 is not able to catalyze redox reactions on gestagens the only sex steroids synthesized in mitochondria), the results of this thesis in combination with updated mitochondrial activities reported in literature ended up in some hypotheses for possible actions and targets of AKR1B15.1 in mitochondria. These hypotheses are basically summarized in Figure IV-2 and discussed below.

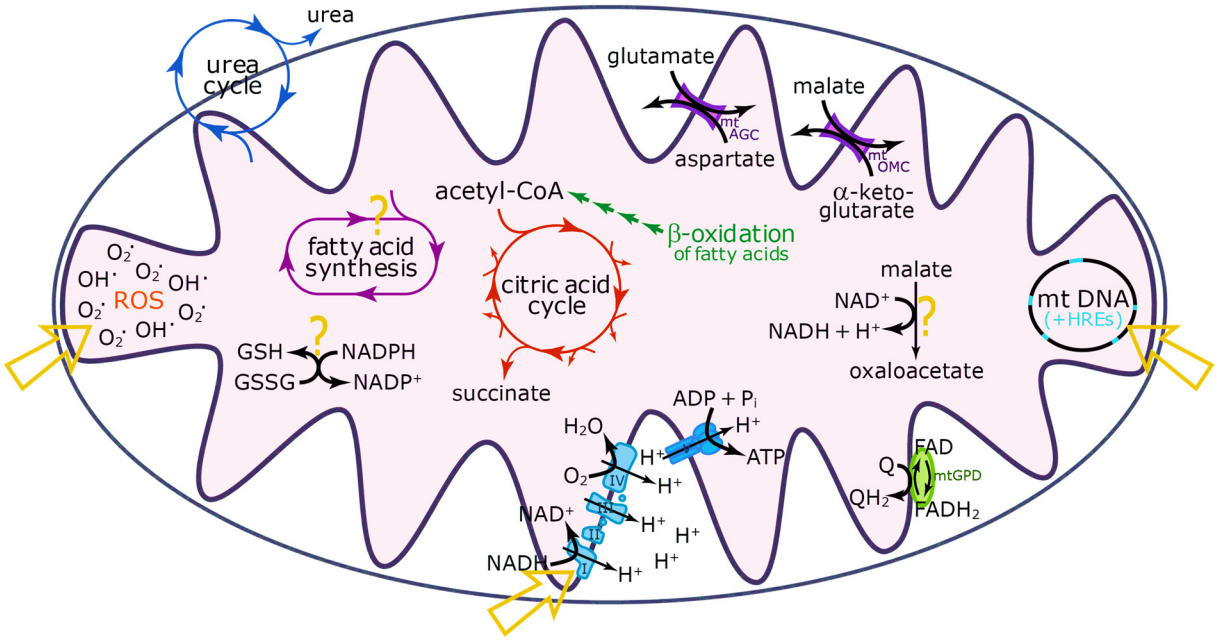

Figure IV-2: Hypothetical physiological targets of AKR1B15.1 action in mitochondria.
The currently hypothesized potential functions of AKR1B15.1 in mitochondria cover the modulation of mitochondrial gene expression via mitochondrial hormone receptors and hormone responsive elements (HREs), the warranty of a proper complex I function, as well as the regulation of the amount of reactive oxygen species (ROS) in mitochondria, e.g., by effecting the glutathione system or malate/glutamate pathways. In addition, the reduction of 3-keto-acyl ACP conjugates by AKR1B15.1 in mitochondria and thus a physiological role in mitochondrial fatty acid synthesis is also possible. Thereby, the biological role of AKR1B15.1 might be accomplished either by its enzymatic activity or by its interaction with and effect on yet unknown proteins.
AGC, aspartate-glutamate carrier; GPD, glycerol-3-phosphate dehydrogenase; mt, mitochondrial; mtOMC, 2-oxoglutarate-malate carrier.

One possible function of AKR1B15.1 is the generation of highly biologically active androgens and estrogens in mitochondria. Several studies have shown that estrogenic, androgenic, as well as glucocorticoid receptors (ERα, ERβ, AR, and GR) and the respective hormone response elements (HREs) occur in the mitochondrial matrix and genome, respectively, and that steroidal signaling in mitochondria effects mitochondrial functions [321–325]. Among the 17β-HSDs only 17β-HSD8 and the short-chain L-3-hydroxy-acyl-CoA dehydrogenase 17β-HSD10 localize to the mitochondria, too [162, 166]. However, compared to AKR1B15.1, these mitochondrial 17β-HSDs possess lower affinities to estrogens or androgens and catalyze predominately the oxidation and thus the inactivation of sex steroids [163, 167]. Because AKR1B15.1 is a predominantly reductive enzyme, AKR1B15.1 might be responsible for the activation of steroid signaling in mitochondria by regulating the presence of the higher potent 17β-estradiol or testosterone in mitochondria which can effect the expression of mitochondrial genes (e.g., *COX1* or *COX2*) [Figure IV-2] or the activity of mitochondrial ion channels (e.g., the mitochondrial Ca^{2+} uniporter or the mitochondrial ATP-sensitive K^+ channel) [326–328]. In addition, previous studies demonstrated that 17β-estradiol influences the functionality and the successive aging of mitochondria by reducing the amount of reactive oxygen species (ROS) in mitochondria [329]. A role of AKR1B15.1 in the regulation of ROS levels in mitochondria is supposable [Figure IV-2]. Calvo *et al.* reported a lethal fetal phenotype with impaired complex I activity due to a homozygous mutation in the *AKR1B15* gene encoding for the AKR1B15.1 S8R mutant [265]. This is insofar of interest as previous studies indicated complex I as substantial mitochondrial source of ROS, whose ROS production depended on its activity, the mitochondrial NAD(P)H/$NAD(P)^+$ ratios, and protonmotive forces [330–332]. In mitochondria, ROS are not only generated by members of the respiratory chain (especially complex I and complex III) but result also from other mitochondrial pathways, like the β-oxidation of fatty acids or reactions catalyzed by the mitochondrial NADPH oxidase, glycerol-3-phosphate dehydrogenase (mtGPD), α-keto-glutarate dehydrogenase, and other proteins [331, 333, 334]. Thereby, the mitochondrial glutathione/thioredoxin system, which is connected to the mitochondrial redox state and NAD(P)H/$NAD(P)^+$ pool, is an important pathway for the elimination of continuously produced ROS in mitochondria, and a dysfunction of these systems is responsible for an impaired ROS homeostasis and an increased export of ROS to the cytosol [335–337]. Although there is a controversy on the effects of high cellular ROS levels on cell senescence, aging, and lifespan in model systems [337], augmented ROS production by the complex I was reported to be linked to increased cell senescence and accelerated aging *in vivo* [338]. In this context, Yashin *et al.* reported an intronic single nucleotide polymorphism (SNP) in the *AKR1B15* gene having a small effect on human longevity [339]. In addition, *in silico* analysis of the *AKR1B15* promoter indicated some binding sites for nuclear transcription factors, e.g., AP-1, NF-κB, Nrf2, and p53 [data not shown], which are involved in ROS signaling and homeostasis [337]. These facts might support a current hypothesis assuming a possible physiological interaction between AKR1B15.1 and the respiratory chain complex I function and/or a role of AKR1B15.1 in the generation or elimination of mitochondrial ROS [Figure IV-2].

Besides steroids, AKR1B15.1 catalyzes also the reduction of acetoacetyl-CoA. Although no conclusive enzymatic activity was seen with 3-keto-palmitoyl-CoA, it is supposed that not only acetoacetyl-CoA but also long-chain 3-keto-acyl-CoA conjugates can be reduced into the respective 3-hydroxy-acyl-CoA conjugates by AKR1B15.1. The reduction of 3-keto-acyl-CoA conjugates in mitochondria seems implausible since a key process in mitochondria is the

reverse reaction, namely the β-oxidation of fatty acids. However, mitochondria harbor also the reductive enzymes of the mitochondrial fatty acid synthesis type II (mtFAS II) pathway [Table I-5] which is mainly responsible for the *de novo* synthesis of octanoic acid (the precursor for the synthesis of the vital lipoic acid) but also longer chain (up to C14 or C16) fatty acids in mitochondria [183–185]. In addition, by exhibiting total NADPH/$NADP^+$ and NADH/NAD^+ ratios of about 30 and 0.15-0.5 in rat liver mitochondria, respectively, the environment of the mitochondrial matrix is rather reductive than oxidative, especially when compared to the respective cytosolic ratios [340]. The importance of the mitochondrial fatty acid synthesis with respect to the mitochondrial functions (including respiration) and integrity was demonstrated in several studies covering mammalian, fungal, and yeast model system organisms [183–185]. Previous studies indicated that the reduction of 3-keto-acyl-CoA conjugates within the human mtFAS II pathway is carried out by a 17β-HSD8/CBR4 heterotetramer in a rather NADH dependent manner [162]. Because AKR1B15.1 catalyzed the NADPH dependent reduction of acetoacetyl-CoA to 3-hydroxy-butyryl-CoA *in vitro* and, compared to the NADH/NAD^+ ratio, the NADPH/$NADP^+$ ratio is quite high in mitochondria, a direct involvement of AKR1B15.1 in the mitochondrial fatty acid elongation process *in vivo* might be possible [Figure IV-2]. This hypothesis is supported by the determined K_M value of AKR1B15.1 for acetoacetyl-CoA (K_M = 63.4 μM) which is much lower in comparison to the respective K_M of the yeast mitochondrial 3-oxoacyl-ACP reductase OAR1p (K_M = 815.8 μM) and the fact that the highly identical cytosolic AKR1B10 was reported to modulate the lipid synthesis in cells [71, 341].

Although not closer characterized within this thesis, AKR1B15.1 possesses good enzymatic activity with retinoids [300] and might, therefore, play a potential role in retinoid signaling. In addition, *in silico* promoter analyzes revealed numerous binding motifs for homeobox transcription factors [data not shown]. As a result, it is also possible that AKR1B15.1 is involved in developmental processes *in vivo*, which would explain the severe fetal phenotype of the AKR1B15.1 S8R mutant as well.

In contrast to the mitochondrial AKR1B15.1, the supposed cytosolic AKR1B15.2 was found to be an enzymatically inactive protein. If AKR1B15.2 actually plays a role *in vivo* can just be presumed. Some proteins belonging to the AKR family, like the frog lens ϱ-crystallines (AKR1C10a and AKR1C10b) as well as the members of the AKR6 family (voltage-gated K^+ channel β-subunits), possess no or only low catalytic efficacies and fulfill rather structural, regulatory, or chaperone-like actions than enzymatic functions [107, 342]. Such a structural, regulatory, or modulatory physiological function might also be possible for AKR1B15.2 (maybe caused by its prolonged N-terminal amino acid sequence). Indeed, a non-enzymatic function cannot be excluded for AKR1B15.1, either. As a result, AKR1B15.1 might possibly modulate the activity of the complex I of the respiratory chain in an enzyme independent manner via direct protein-protein interactions.

However, to clarify the functions of both AKR1B15 isoforms *in vivo*, further studies covering, e.g., enzymatic activity, mitochondrial function, and metabolomic analyses of cells upon *AKR1B15* overexpression or knock-out in addition to in-depth promoter analyses, and protein-protein interactions have to be conducted in future.

IV.2. HUMAN 17β-HSD12: ON THE WAY TO EFFICIENT PROTEIN PURIFICATION AND CHARACTERIZATION

There is a lasting disagreement about the physiological function of 17β-HSD12, as both a role in fatty acid metabolism and steroid metabolism have been reported [139, 140].

Although there are evident indications that human 17β-HSD12 plays an important role in the elongation of (very) long fatty acids *in vivo*, at the moment, a probable (additional) function in sex steroid metabolism cannot be completely excluded [139, 140, 145]. A good possibility to clarify this question is the in-depth characterization of the human 17β-HSD12, which demands the purified enzyme. Since 17β-HSD12 is considered to be a membrane-bound protein which is anchored via three putative transmembrane helixes (predicted to cover the amino acid residues at positions 4-12, 182-202, and 271-291; however, the domain covering the positions 182-202 is questionable because it includes two amino acid residues of the catalytic tetrad) to the membrane of the endoplasmic reticulum (ER) [Figure IV-3], the purification of native and soluble enzyme is a challenging task [140].

```
  1  MESALPAAGFLYWVGAGTVAYLALRISYSLFTALRVWGVGNEAGVGPGLGEWAVVTGSTD  60
 61  GIGKSYAEELAKHGMKVVLISRSKDKLDQVSSEIKEKFKVETRTIAVDFASEDIYDKIKT 120
121  GLAGLEIGILVNNVGMSYEYPEYFLDVPDLDNVIKKMININILSVCKMTQLVLPGMVERS 180
181  KGAILNISSGSGMLPVPLLTIYSATKTFVDFFSQCLHEEYRSKGVFVQSVLPYFVATKLA 240
241  KIRKPTLDKPSPETFVKSAIKTVGLQSRTNGYLIHALMGSIISNLPSWIYLKIVMNMNKS 300
301  TRAHYLKKTKKN                                                  312
```

Figure IV-3: Particular amino acid residues in the sequence of 17β-HSD12.
Amino acid residues of the catalytic tetrad, the GxxxGxG cofactor binding motif, and the endoplasmic reticulum retention/retrieval signal sequence are shown in bold and are colored in red, blue, and green, respectively. The three putative helical transmembrane domains are indicated by serrated underlines and amino acid residues encoded by codons with different usage frequencies in human and *P. pastoris* are highlighted by yellow background.

IV.2.1. SOLUBILIZATION OF 17β-HSD12 EXPRESSED IN *P. PASTORIS*

Previous studies demonstrated that the yeast *Pichia pastoris* (*P. pastoris*) is an useful tool for the expression of heterologous proteins, including integral membrane proteins of the ER or other compartments, in high amounts [343–345]. This was also seen within this thesis, where it was possible to express and roughly purify (or at least enrich) enzymatically active 17β-HSD12.

By using a *P. pastoris* expression system comprising an expression construct which encodes for a C-terminally myc- and His_6-tagged 17β-HSD12 [Figure IV-4], a small portion of the overexpressed 17β-HSD12 was found as enzymatically active protein in the supernatant of

detergent-free cell lysates after an ultracentrifugation step at 125000 x *g*, representing usually the soluble, non-microsomal fraction [346, 347].

This surprising outcome might have resulted from a partial masking of the ER retention signal sequence (KxKxx in transmembrane proteins) by the C-terminal TEV protease recognition sequence (TEV site) and the following myc and His_6 tags [Figure IV-4] [348–351]. On the other hand, an insufficient fractionation could have also been responsible for the presence of 17β-HSD12 in the supernatant.

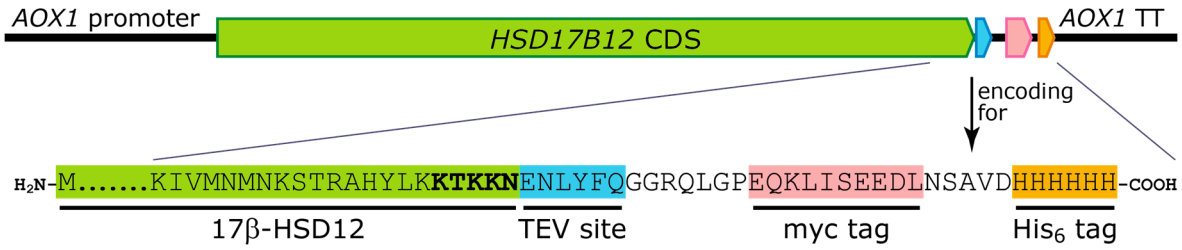

Figure IV-4: Illustration of the 17β-HSD12 encoding region of the *HSD17B12* expression construct in *P. pastoris* and the resulting protein product.
Shown are a schematic overview over the structure of the *HSD17B12* expression construct and the detailed C-terminal sequence of the His_6-tagged 17β-HSD12 expression product, possibly masking the C-terminal ER retention motiv (KTKKN, highlighted in bold) of the untagged protein.
Regions encoding for or representing amino acids of the untagged 17β-HSD12 protein are colored in green, whereas those of the TEV protease recognition sequence (TEV site), the additional myc tag, and the His_6 tag are colored in blue, rose, and orange, respectively.
AOX1 promoter, *AOX1* promoter region; *AOX1* TT, *AOX1* transcription termination region.

Though, the vast majority of overexpressed 17β-HSD12 was detected in the non-soluble pellet fraction of lysates. Using the non-ionic detergent Brij-35, it was possible to solubilize enzymatically active 17β-HSD12 from the ultracentrifugation pellets, whereas all other detergents tested showed either only poor solubilization properties (Anameg-7, MEGA-8, n-octyl-β-D-glucopyranoside, and sodium cholate) or good solubilization properties but a strong decrease in enzymatic activity (2,6-dimethyl-4-heptyl-β-D-glycopyranoside, dodecyl-β-D-maltoside, and Tween20R). The diverse solubilization properties of different detergents on different proteins as well as an impairment of enzymatic activities in the presence of various detergents have been reported in several studies in the past and are difficult to predict in advance [352–354]. However, in general, non-ionic detergents, like NP-40, Tween20R, or Brij-35, are considered to be mild detergents hardly affecting the activities of solubilized proteins. Thus, the loss in enzymatic activity of 17β-HSD12 when using 2 % NP-40 or 1 % Tween20R in the solubilization buffer could be a matter of too high detergent levels during the solubilization but also within the enzymatic assays, which could impair the enzyme function either by destroying enzyme structures or inhibiting enzyme activities. For example, Susa *et al.* demonstrated that the phosphatidylinositol 3-kinase (PI3K) activity was strongly reduced in 3T3 fibroblast lysates containing 0.01-1 % NP-40 and that the kinase activity could be revived at higher dilutions (< 0.001 %) of the detergent [355]. Srinivasulu and Rao showed that the enzymatic activity of the soybean lipoxygenase L1 was stronger affected by Tween20R than by Brij-35 at detergent concentrations above 1 mM (equivalent to

approx. 0.1 %) [356], which was in accord with the observations made for 17β-HSD12 within this thesis. Furthermore, the effects of one detergent on different proteins are variable and hardly predictable. Woeltje *et al.*, for example, revealed that the solubilization of the mitochondrial carnitine O-palmitoyltransferase 2 from the inner membrane of isolated rat mitochondria with a buffer system containing 1 % Tween20R led to a considerably reduced activity of the enzyme [357]. In contrast, Pérez-Rosés *et al.* showed that Tween20R increases the enzymatic activity of the human myeloperoxidase in a final concentration ranging from 0.005 % to at least 0.5 % [358].

IV.2.2. LIMITATIONS OF *P. PASTORIS* AS EXPRESSION SYSTEM FOR HUMAN PROTEINS

Not only solubilization of enzymatically active human 17β-HSD12 but also its expression in the heterologous expression system *P. pastoris* in high amounts was problematic within this thesis.

As illustrated in Figure IV-3, more than 60 % of the amino acid residues of the human 17β-HSD12 protein chain are encoded by codons with different bias in *P. pastoris*. Multiple reports showed that the synonymous codon usage bias as well as the C+G content within coding sequences significantly influence the protein yield in heterologous but also homologous expression systems [343, 359–361]. Thus, Sinclair and Choy, for example, were able to highly increase the production of the human glucocerebrosidase in *P. pastoris* by optimizing the codon usage and C+G content of the human coding sequence with respect to the ones frequent in their heterologous expression system [362]. To overcome the low yields of recombinant 17β-HSD12 in *P. pastoris*, which could not be increased by simply upscaling the volume of expression cultures, a codon optimized expression plasmid was generated. However, because of occurring transfection and recombination problems, up to now, this construct could not have been successfully inserted into *P. pastoris* strains [data not shown].

Another point which needs to be considered when analyzing the properties of recombinant 17β-HSD12 are the post-translational modifications introduced by the *P. pastoris* expression system. Unlike *E. coli*, *P. pastoris* is able to insert most of the post-translational modifications occurring in human (membrane) proteins, like phosphorylation, glycosylation, lipidation, disulfide bonds, or modifications affecting proteolytic processing [344, 351]. Among others, post-translational glycosylations of proteins are known to affect protein folding, stability, as well as biological activity. For example, the 11β-dehydrogenase activity of recombinant rat 11β-HSD1 was reduced by approximately 50 % due to the treatment of TK$^-$ 143B expression cultures (human osteosarcoma cells infected with recombinant vaccinia virus) with tunicamycin, a compound which inhibits post-translational N-glycosylation [363]. Although yeast species, like *P. pastoris* and *S. cerevisiae*, modify recombinant proteins by N- and O-linked glycosylations, the structures of these post-translational glycosylations differ generally from the multiple types appearing in humans/mammals [246, 343, 344, 364]. Thereby, in particular *S. cerevisiae* but to a lesser extent also the here used *P. pastoris* show especially in the Golgi apparatus a tendency to hypermannosylation which could possibly alter the characteristics and activities of either secreted recombinant proteins or recombinant proteins retrieved to the ER [343, 344, 365].

An expression of human membrane proteins in mammalian or human cell lines, which provide a native environment for the translation, folding, and post-translational modification of proteins, could circumvent the problems resulting from the heterologous *P. pastoris* expression system, covering, e.g., low expression levels due to altered codon usage bias and potentially modified activity due to divergent glycosylation pattern [344, 351]. However, previous papers and reviews reported with few exceptions a generally low expression of membrane proteins, even in homologous expression systems [351, 366]. This was also seen for the human 17β-HSD12 within this thesis. Here, only quite low protein levels could be detected in Western blots after overexpression in the homologous HEK-293 expression system, using cells which were either transiently or stably transfected with a *HSD17B12* expression construct [data not shown]. Thus, the amount of the membrane-bound human 17β-HSD12 in expression cultures seems to be limited *per se*. This makes the production of high 17β-HSD12 protein yields for subsequent purification a challenging task.

IV.2.3. How to clarify the physiological role of 17β-HSD12 in human in future?

Because of the poor expression of 17β-HSD12 on protein level in *P. pastoris* and additional very high losses within the solubilization and purification steps, which were even more pronounced by upscaling the expression cultures, the yield of sufficient purified and active protein was quite low and did not allow for a deeper characterization of the primarily enzymatic properties of 17β-HSD12 within this thesis.

To increase the yield of 17β-HSD12 through the *P. pastoris* expression system, the successful electroporation, recombination, and expression of the codon optimized pPICZ-A-HSD17B12 expression constructs is the minimum demand for the future. Although 17β-HSD12 is predicted to be a membrane protein, its expression as secreted protein (e.g., via an α-mating factor signal sequence) should also be considered because it would allow for an easier purification procedure in the absence of any detergent, however, only in the case of the expression of soluble protein in medium. The use of engineered *P. pastoris* strains, as described by the group of Contreras, could minimize hypermannosylation and instead add more complex glycan structures occurring naturally in mammals [344, 365, 367, 368]. Thus, the expression of soluble and native folded proteins could be supported. Another possibility to circumvent low protein yields and hypermannosylation represents the baculovirus-mediated recombinant expression of human *HSD17B12* in insect cell lines. In the past, several human or mammalian membrane-bound proteins have been successfully expressed in *Spodoptera frugiperda* derived cell lines and subsequently purified from them [344, 369]. Those proteins do not show hypermannosylation but offer paucimannosidic instead of complex, terminally sialylated N-glycan structures [370]. The preparatory work for the expression of 17β-HSD12 in insect cells via baculoviruses, namely the cloning of *HSD17B12* into pFastBac vectors encoding for N- or C-terminally His_6-tagged 17β-HSD12 as well as the generation of the respective recombinant bacmids for baculovirus production, had already been successfully performed within this thesis [data not shown]. Thus, the baculovirus-insect cells expression system could be a sound alternative to the *P. pastoris* expression system for the purification of high amounts of functional 17β-HSD12 in close future.

Having pure and active 17β-HSD12 in sufficient amounts, comparative activity assays, using (very) long chain 3-keto-acyl-CoA conjugates (e.g., 3-keto-palmitoyl-CoA) and steroids (e.g., estrone) as substrates and NADPH fluorescence/absorption as read-out, could be performed in order to identify its preferred substrate spectrum.

Beside activity assays with purified enzyme, different analyses with intact cells or cell lysates overexpressing *HSD17B12* could also help to determine the actual biological role(s) of 17β-HSD12 *in vivo*. Thus, co-immunoprecipitation experiments, using HEK-293 cells stably transfected with a *HSD17B12* expression construct and in case of a targeted approach HEK-293 cells transiently transfected with expression plasmids encoding for the proteins of interest (e.g., ELOVLs, HACDs, TECR, SCD5, HMGCR, …) followed by Western blotting or in case of an untargeted approach mass spectrometry-based proteomics, could reveal interaction partners of 17β-HSD12. The identified interaction partners could then point to the physiological functions of the enzyme. Determination of the topology of 17β-HSD12 in the ER membrane – facing the lumen of the ER or the cytosol – is another optional experiment to get and support an idea concerning its real function. This approach was already applied by other groups addressing other ER membrane-bound SDRs, like 17β-HSD3 or RoDH1 [143, 371], and could be performed with the stable-transfected HEK-293 cells, too.

IV.3. Vitamin D analysis: Monitoring the vitamin D status in biological samples

Another part of this thesis covered the development and validation of an analytical method for the simultaneous quantification of up to eight different vitamin D metabolites, namely 24,25-$(OH)_2$-D_3, 1α,25-$(OH)_2$-D_3, 1α,25-$(OH)_2$-D_2, 25-(OH)-D_3, 25-(OH)-D_2, 1α-(OH)-D_3, vitamin D_3, and vitamin D_2. The final method comprises a solid phase extraction (SPE) based sample preparation procedure and the subsequent analysis of vitamin D metabolites by high-performance liquid chromatography coupled to tandem mass spectrometry (LC-MS/MS) and is validated for cells (and medium) resulting from cell culture experiments. This basic method was more or less successfully applied to biological samples, like cell culture samples, human plasma, or mouse tumor samples.

The method development started with analytical methods using high-performance liquid chromatography coupled to UV detection (HPLC-UV) or scintillation detection (radioactive HPLC). However, these methods were not further validated because they exhibited strong limitations. Thus, the HPLC-UV method possessed only a limited sensitivity (approx. 0.5 ng column load), whereas the radioactive HPLC method exhibited a good sensitivity (approx. 80 pg column load) but showed only a poor chromatographic resolution (due to broad peak shapes) as well as a strong restriction in the spectrum of analyzable vitamin D metabolites (due to a poor availability of various ^{3}H-labeled vitamin D compounds) and biological samples (treatment with ^{3}H-labeled compounds necessary).

Since the latter both methods were not further considered for the routine quantification of vitamin D metabolites in biological samples, they are not further discussed here.

IV.3.1. ADVANTAGES AND LIMITATIONS OF THE DEVELOPED VITAMIN D LC-MS/MS METHOD

As already mentioned above, this thesis included also the development and validation of a SPE based sample preparation method and a method for the simultaneous analysis of up to eight different vitamin D metabolites (24,25-$(OH)_2$-D_3, 1α,25-$(OH)_2$-D_3, 25-(OH)-D_3, 1α-(OH)-D_3, vitamin D_3, 1α,25-$(OH)_2$-D_2, 25-(OH)-D_2, and vitamin D_2) by LC-MS/MS in biological samples (primarily cells) resulting from cell culture experiments.

In the past, numerous research laboratories and companies have developed various assays for the quantification of vitamin D metabolites in serum or plasma samples. The established methods based on different technologies, such as manual binding-protein assays (BPAs), automated competitive binding-protein assays (CBPAs), chemiluminescent immunoassays (CLIAs), enzyme-linked immunoassays (ELISAs), radioimmunoassays (RIAs), and high-performance liquid chromatography (HPLC) coupled to ultraviolet wavelength absorption (HPLC-UV) or tandem mass spectrometry (LC-MS/MS) detection [372–374]. However, a huge majority of the vitamin D profiling methods described in literature concentrate only on the detection and quantification of 25-(OH)-D metabolites because of their use in clinics to assess the vitamin D status in individuals [374–376]. In addition, binding-protein assay and immunoassay based methods widely exhibit limited selectivity and do often cross-react with other vitamin D metabolites which represents a grave disadvantage compared to the usually highly selective LC-MS/MS methods [374, 377]. Hence, several studies comparing different routinely available methodologies showed that the outcomes of the assays differ significantly and that LC-MS/MS based assays are the most reliable, accurate, and reproducible methods to measure the vitamin D status in serum or plasma [378–380].

In order to analyze endogenous or exogenous impacts on the vitamin D metabolism, a simultaneous, specific, and accurate ascertainment of different vitamin D metabolites, like the endogenous vitamin D_3 and the exogenous vitamin D_2 as well as their downstream hydroxylation products, is of importance. Although some published LC-MS/MS methods feature the quantification of four to five mono- or dihydroxylated vitamin D metabolites in serum or plasma samples [377, 381–383], no method has been reported for the simultaneous analysis of vitamin D_3, 25-(OH)-D_3, 1α-(OH)-D_3, 1α,25-$(OH)_2$-D_3, 24,25-$(OH)_2$-D_3, vitamin D_2, 25-(OH)-D_2, as well as 1α,25-$(OH)_2$-D_2 in cells or medium of cell culture experiments. The simultaneous analysis of those vitamin D metabolites via the herein developed and for cell culture samples basically validated LC-MS/MS method is beneficial compared to other published vitamin D methods mentioned above, especially with respect to the analysis of activities of enzymes (CYPs) involved in the vitamin D pathway in cell culture experiments. Another advantage of this new vitamin D LC-MS/MS method is the absence of any chemical derivatization step which accelerates and simplifies the sample preparation procedure.

The final vitamin D LC-MS/MS method was in principle validated for both cells and media supernatants resulting from cell culture experiments. However, only cells showed good recoveries (accuracies) and precisions within the validation process. With medium samples, in contrast, the method showed very poor performance and allowed merely for the detection but not for the reliable quantification of higher amounts of vitamin D metabolites (see also IV.3.2), limiting the use of this method, for example, in the analysis of the release of vitamin D metabolites from cells into medium.

Although the established vitamin D method was predominantly validated for cells, revealing generally an adequate sensitivity for the detection of vitamin D metabolites in cells (mostly < 400 $^{pg}/_{sample}$), it is assumed that its limits of detection (LODs) and quantification (LOQs) for most vitamin D metabolites are below or in the range of those of other vitamin D LC-MS/MS methods having not included a chemical derivatization step with PTAD (4-phenyl-1,2,4-triazoline-3,5-dione) [377]. Thus, this new vitamin D LC-MS/MS method should have the capability to measure physiological levels of vitamin D metabolites in blood samples, however, with the exception of the biologically very low abundant 1α,25-$(OH)_2$-D_3 and 1α,25-$(OH)_2$-D_2 which are in general below 100 $^{pg}/_{ml}$ in serum or plasma [384, 385]. The addition of lithium acetate to the aqueous mobile phase during the optimization process of the herein established vitamin D LC-MS/MS method improved strongly the ionization of 24,25-$(OH)_2$-D_3, 1α,25-$(OH)_2$-D_3, and 1α,25-$(OH)_2$-D_2 via the generation of stable lithium adducts. An enhanced sensitivity by lithium ions was already reported by Casetta *et al.* and Yuan *et al.* [266, 386]. But, in contrast to their published LC-MS/MS methods, the vitamin D LC-MS/MS method generated within this thesis was not able to reach LODs and LOQs in the low picomolar range. The higher limits of the herein newly generated method are most likely due to the more stringent selection of monitored MRM transitions, which, unlike MRMs selected by Casetta *et al.* and Yuan *et al.* [266, 386], did not allow for the detection of MRMs resulting from the removal of one to three water molecules in the fragmentation process, and the sample preparation method applied, which strongly increased the background signals (see IV.3.2). Thus, in order to increase the detectability of especially low abundant vitamin D compounds in future, it should be considered to refine the utilized MRM transitions by incorporating those which loose up to three water molecules because this could result in a vitamin D LC-MS/MS method with higher sensitivity but still sufficient selectivity [387, 388]. The addition of lithium acetate to the mobile phase A affected the sensitivity for 25-(OH)-D_3 adversely because only a portion of 25-(OH)-D_3 formed stable lithium adducts, leading to a reduction of signal intensities for the single transitions. Yet, the limits of the 25-(OH)-D_3 quantifier MRM (407.326/91.900) were adequate to analyze 25-(OH)-D_3 at physiological levels. An additional Diels-Alder derivatization with Cookson-type reagents (like PTAD) within the sample preparation process would have been able to lower the LODs and LOQs of all vitamin D metabolites (especially 1α,25-$(OH)_2$-D_3) and to circumvent the problems resulting from unstable lithium adducts [389, 390]. As a result, several groups published LC-MS/MS methods which were sensitive enough to analyze physiological amounts of 1α,25-$(OH)_2$-D_3 and other vitamin D metabolites after extraction and derivatization with Cookson-type reagents [381, 389–393]. However, the derivatization with those reagents could also be a problematic issue within the analysis of vitamin D metabolites because the reaction is strongly quenched by aprotic solvents, like water or methanol, and generally generates two epimers which appear as two eluting peaks under chiral LC separation conditions [389], complicating their analysis. A quenching of the derivatization reaction by aprotic solvent compounds was most probably the reason for the failure of initial attempts to derivatize vitamin D metabolites with PTAD during the method development [data not shown]. In addition, the sample preparation as well as the chromatographic separation and MS/MS analysis was optimized for non-derivatized vitamin D metabolites. Because the addition of lithium ions to the LC mobile phase provided sufficient sensitivity for the analysis of the metabolism of vitamin D compounds in cell culture experiments, which was the primary aim of the herein developed method, the derivatization of vitamin D compounds was not further addressed within this thesis; especially as the delayed inclusion of an derivatization step

would have been associated with a modified and prolonged sample preparation method, an adaptation of MRMs, and most notably a need for further optimization of the LC method in order to separate, e.g., 24,25-$(OH)_2$-D_3 and 1α,25-$(OH)_2$-D_3, which would be even more difficult when vitamin D epimers should be analyzed in future, too.

The vitamin D LC-MS/MS developed within this thesis was not aimed for the discrimination between vitamin D metabolites and their C3 epimers. Thus, it does not include any chiral resolution. Previous studies revealed that the C3 epimerization of mono- or dihydroxylated vitamin D metabolites is another pathway for the catabolism of vitamin D metabolites in infant and adult individuals as well as in experiments with cultured cells [202–205]. C3 epimers of vitamin D metabolites possess generally lower binding affinities to the VDR receptor and are, therefore, regarded to have lower biological activities than their respective non-epimerized counterparts [202, 394]. Since vitamin D metabolites and their C3 epimers are hydroxylated by the same CYPs within the vitamin D pathway [202], the distinctive analysis of vitamin D epimers seems not to be very important for the detection of CYP activities in cell culture experiments (like aimed in this thesis). However, Ouweland *et al.* reported a 30-40 % higher ionization efficiency for 3-epi-25-(OH)-D_3 when compared with 25-(OH)-D_3 [395]. Since the quantification method of the herein newly described vitamin D method does not consider any C3 epimers in the calibration curves, the negligence of C3 stereoisomers could result in an overestimation of the actual 25-(OH)-D_3 and most probably other vitamin D metabolites in biological samples. This is particularly of importance when analyzing blood samples of patients in order to assess their vitamin D status. Thus, to ensure the proper assessment of vitamin D levels in humans, the possible existence of those epimers should be considered which is not feasible by the novel non-chiral vitamin D LC-MS/MS method developed within this thesis.

IV.3.2. Critical issues in sample preparation and vitamin D analysis

The sample preparation via solid phase extraction (SPE) has been a critical step for the analysis of vitamin D metabolites in biological samples. As illustrated in chapter III.3.4.1, the SPE step increased the background signals by more than 10-fold resulting in higher LODs and LOQs of especially 24,25-$(OH)_2$-D_3, 1α,25-$(OH)_2$-D_3, and 1α,25-$(OH)_2$-D_2. The higher background intensities in SPE treated samples could be explained by contaminants introduced during the SPE process. Here, most probably because of the strong acidic organic elution conditions (2 % formic acid in methanol), polyethylene glycols (PEGs), plasticizers (e.g., phthalates) and/or anti-oxidants of diverse molecular weights might have leached from the Strata-X polypropylene tubes and thus contaminated the elution fraction [396–398]. In addition, ambient laboratory air, like the nitrogen flow of the overpressure device, as well as solvents or reagents could also have been sources of impurities [396, 397, 399]. Currently, it is hypothesized that the leaching of additives in the Strata-X tubes and maybe the used formic acid, which is also stored in plastic bottles, are responsible for the quite high background signals. The use of Teflon-coated tubes could minimize the introduced impurities. However, such tubes have not been available for the required StrataX matrices and could, thus, not be tested within this thesis.

Another critical point linked with the SPE concerns the recovery of vitamin D compounds from the SPE process, especially that of vitamin D_2 (16 ± 3 %) and vitamin D_3 (10 ± 3 %). Whereas the recovery of SPE processed reference samples was between 70 % and 100 % for hydroxylated vitamin D metabolites when compared with non-processed reference samples, quite low values were observed for the hydrophobic vitamin D_2 and vitamin D_3 (10-15 %). The later compounds were strongly retained by the Strata-X polymeric reversed phase sorbent, although the elution was performed in two steps with 2 % formic acid in methanol, representing a quite harsh organic solvent. A strong retention of vitamin D_2 and vitamin D_3 by the Oasis HLB sorbent, which is comparable to the Strata-X sorbent, was reported by Aronov *et al.* [389]. In addition, Moreno and Salvadó showed that the recovery of vitamin D_3 from SPE using a C18 reversed phase sorbent and different organic solvents for elution was mostly only about 20-40 % but also that it could be increased to 78 % by applying chloroform as eluent [400]. Priego Capote *et al.* compared C8 and C18 reversed phase sorbents and indicated that the C8 reversed phase in combination with the SPE eluent isopropanol is the best SPE system for fat-soluble vitamins including vitamin D_2 and vitamin D_3 [401]. Thus, the use of a C8 reversed phase (such as in Strata C8 tubes) instead of the Strata-X reversed phase sorbent could be an alternative to increase the recovery of vitamin D_2 and vitamin D_3 from the SPE process in future. Another option would be the extraction of vitamin D metabolites by liquid-liquid extraction (LLE) instead of SPE. Adamec *et al.* reported a fast and easy but quite crude LLE method with high recoveries for all vitamin D compounds [402]. Besides, several other groups introduced more complex LLE procedures which included at least one additional protein precipitation step [377, 382, 401, 403]. However, because non-automated LLE is often laborious, more error prone, and hardly high-throughput compatible, it was no option for the method development here.

The validation of the created vitamin D LC-MS/MS method revealed quite good recoveries (in general 80-115 % accuracy) and precisions (in general < 22 % variability) for all vitamin D metabolites in different cell line matrices when sample preparation (SPE) and LC-MS/MS analysis were performed on the same day (day 0). In this context it should be noticed that samples prepared for the validation of the method with cellular matrices were spiked with vitamin D metabolites after the harvest process and shipment to our lab, whereas, according to the established cell harvest procedure [II.11.1.1], the internal standard (IS) was already added during the cell harvest. Consequently, a possible loss of the IS during the cell harvest (loss at sample collection) was not considered when these samples were spiked subsequently with constant amounts of vitamin D metabolites and could have led to discrepancies within the normalization and quantification process, maybe resulting in diminished recoveries and precisions of vitamin D metabolites in harvested cells. Thus, the real accuracies and precisions of the vitamin D LC-MS/MS method could be even better than revealed here with the here used validation set-up. Still, the validation parameters met widely the FDA criteria for the bioanalytical method validation [404]. However, when the SPE processed samples were analyzed once again after the storage at 4 °C for six days (day 6), the recovery and precision for the more hydrophobic vitamin D metabolites (1α-(OH)-D_3, vitamin D_3, and vitamin D_2) were much worse (50-300 % accuracy and < 40 % variability). When looking at the recoveries and precisions of vitamin D metabolites in medium samples, it was seen that, although media were simultaneously spiked with the IS and different amounts of vitamin D mixes, the validation parameters were mostly quite bad. This fact can be explained by the occurrence of high ion suppression (and in rare cases enhancement) effects due to coeluting matrix compounds and the use of only a single internal standard, 25-(OH)-D_2 [25,26,27-$^{13}C_3$],

which possibly is another problematic matter in the herein generated vitamin D method. Negative effects of matrix compounds on the ionization of analytes within LC-MS/MS analysis, especially in the electrospray ionization (ESI) mode, have been elucidated in multiple studies and are summarized in several reviews [405–408]. Within this thesis, the incidence of ion suppression due to cellular or medium matrices in the LC-MS/MS analysis of cell or medium samples had not been systematically analyzed. However, quite high ion suppression effects were seen for medium samples, indicated by a strong decrease in signal intensities of the IS (10-20 % of the intensity of references without medium matrix) but also by lower overall signal intensities in medium samples when compared to cell samples. In the validation of the vitamin D LC-MS/MS method with medium samples, only 25-(OH)-D_2 and 25-(OH)-D_3, which elute with and in close proximity to the single IS, respectively, showed acceptable recoveries and precisions at day 0 and day 6. In contrast, all other vitamin D compounds eluting from the LC column with more than one minute distance to the IS, especially those with higher retention times (1α-(OH)-D_3, vitamin D_2, or vitamin D_3), showed by far less accuracies and precisions (200-1500 % or 300-2200 % accuracy and 20-35 % or 20-70 % precision at day 0 or day 6, respectively). The poor validation results for vitamin D metabolites not eluting close to the IS can be explained by variable ion suppression levels occurring during the chromatographic separation due to the coelution of suppressive matrix components.

One option to compensate for the differing ionization levels represents the use of one matching IS for every analyte [405, 407]. Stable isotope labeled (SIL) analytes are the best choice for IS [409]. Here, the application of three times ^{13}C-labeled IS can circumvent possible errors associated with the use of deuterated IS because deuterated compounds tend to deuterium-hydrogen exchanges under harsh conditions and often show isotope effects which are reflected by an altered behavior in chromatography and ionization [409, 410]. The reported similar performance of ^{13}C-labeled and unlabeled analytes in LC-MS/MS analysis was also seen within this thesis on the example of the only included IS (25-(OH)-D_2 [25,26,27-$^{13}C_3$]) and 25-(OH)-D_2 [Figure III-42A]. The inclusion of solely one IS into the generated LC-MS/MS method, as mentioned above, resulted from a limited availability of ^{13}C-labeled vitamin D metabolites at the beginning of the method development. Although the use of this single IS was largely sufficient for the accurate and precise quantification of vitamin D metabolites in cells (at least at day 0), the addition of at least two more internal standards, one eluting together with dihydroxylated and one eluting together with non-hydroxylated vitamin D metabolites, could further improve this method (especially when medium samples are analyzed) by fairly abolishing variable effects resulting from ion suppression but also from the sample preparation and chromatography [406, 409]. Now, at the end of this thesis, respective standards would be easily available on the market (e.g., 1α,25-$(OH)_2$-D_3 [25,26,27-$^{13}C_3$] and vitamin D_3 [25,26,27-$^{13}C_3$], both sold by Sigma-Aldrich) and could be embedded into the method, too. Another option to compensate for ion suppression and thus to increase the detectability, accuracy, and precision of vitamin D metabolites in especially medium samples represents a change in the sample preparation method [405, 406]. For example, generally less ion suppression by matrix compounds was reported in samples prepared by advanced LLE than in those prepared by SPE [411–413]. However, in dependence of the analytes of interest, the use of another or the combination of different SPE sorbents could already reduce matrix interferences as well [412].

Finally, the stability of analytes or their quantification in the samples could also be a critical point in LC-MS/MS analysis. The comparison of vitamin D levels in SPE processed samples measured on the same day of sample preparation (day 0) and once more after six days (day 6) showed especially for the more hydrophobic vitamin D metabolites discrepancies. When compared to day 0, the overall precision of the method for 1α-(OH)-D_3, vitamin D_2, and vitamin D_3 was clearly reduced in all samples at day 6. In addition, the validation process demonstrated a reduced accuracy within the quantification of 1α-(OH)-D_3, vitamin D_2, and vitamin D_3 in the HaCaT, $Ptch^{WT}$, and $Ptch^{-/-}$ cell matrices at day 6 by revealing diminished (with HaCaT cells) or about 2-3 times higher recoveries (with $Ptch^{WT}$ and $Ptch^{-/-}$ cells) of these metabolites. At the moment, the actual reason for this can only be hypothesized. Previous studies showed that vitamin D metabolites are greatly stable, even if they are exposed to extreme conditions, as long as they are protected from intense light exposure [382, 414]. Thus, no significant changes in the levels of 25-(OH)-D_2 and 25-(OH)-D_3 were detectable in serum samples which had been stored protected from light at variable ambient temperatures (between 5 °C and 30 °C) for up to eight days or which passed through up to five freeze-thaw cycles when compared to those of once thawed and immediately processed serum samples [414]. The same was true for dihydroxylated vitamin D_3 metabolites in plasma samples which were stored protected from light at 4 °C for one week [382]. Because of the detected stability of vitamin D metabolites [382, 414], a degradation of vitamin D metabolites as cause for significantly lower or higher vitamin D levels, for example, in samples with cellular matrices, seems unlikely; although at first sight a spontaneous dehydroxylation of hydroxylated vitamin D metabolites during the storage at 4 °C as reason for increased vitamin D_2 and vitamin D_3 levels could be assumed. In addition, the observed differences in the determined amounts of hydrophobic vitamin D metabolites between day 0 and day 6 might had also resulted from instable matrix compounds. Thus, during the storage at 4 °C, matrix compounds coeluting with vitamin D metabolites could have changed and could have possibly enhanced or suppressed the ionization of the IS and/or other vitamin D metabolites. Finally, the evaporation of small amounts of methanol, which was used as organic solvent for the reconstitution of evaporated eluates after SPE, during the storage of processed samples could be another factor possibly explaining the observed changes in the amounts of especially more hydrophobic vitamin D compounds between the day 0 and day 6 measurements. Although the applied IS allows for the correction of evaporation deficits and, therefore, more concentrated samples at day 6, an evaporation of predominantly methanol could negatively affect the solubility of the hydrophobic 1α-(OH)-D_3, vitamin D_2, and vitamin D_3, leading possibly even to the precipitation of those compounds. In that way changed solutions might also be the reason for the higher variations seen in both SPE processed reference mix samples and spiked cell culture samples at day 6. Though, the actual reasons for the poor accuracy of especially 1α-(OH)-D_3, vitamin D_2, and vitamin D_3 in most cell lines (HaCaT, $Ptch^{WT}$, and $Ptch^{-/-}$), when analyzed once more six days after the first measurement, remain unknown.

In summary, the herein developed and validated SPE and vitamin D LC-MS/MS method enables the reliable quantification of all vitamin D metabolites in various cell lines (HaCaT, ASZ001, $Ptch^{WT}$, and $Ptch^{-/-}$), at least when analyzed on the day of sample preparation. Since only the quantification of 24,25-$(OH)_2$-D_3, 1α,25-$(OH)_2$-D_3, 1α,25-$(OH)_2$-D_2, 25-(OH)-D_3, and 25-(OH)-D_2 exhibited sufficient precisions and accuracies in repeated measurements six days after the first analysis, solely these more "hydrophilic" vitamin D metabolites can be reliably quantified in resurveys within up to at least one week after sample preparation. The

quantification of vitamin D metabolites in culture media samples, however, is generally very error prone. Thus, in media, the validated method can only be used for the detection but not for the quantification of vitamin D metabolites.

IV.3.3. APPLICABILITY OF THE VITAMIN D LC-MS/MS METHOD WITHIN THE IN-HOUSE METABOLOMIC ANALYSES POOL

The aim of the vitamin D method development within this thesis was to generate a method for the simultaneous analysis of different vitamin D metabolites in samples resulting primary from cell culture experiments. As discussed above, the generated and validated vitamin D method, which covers a SPE sample preparation method and a LC-MS/MS based analysis method, showed sufficient sensitivity and accuracy for the analysis/quantification of eight different vitamin D metabolites in cells. However, its performance was quite poor with culture media samples. Thus, the established vitamin D method represents an adequate method for the quantification of 24,25-$(OH)_2$-D_3, 1α,25-$(OH)_2$-D_3, 1α,25-$(OH)_2$-D_2, 25-(OH)-D_3, 25-(OH)-D_2, 1α-(OH)-D_3, vitamin D_3, and vitamin D_2 in cultured cells (having already the potential to be included into the in-house metabolomics portfolio). In addition, pilot studies showed that it is also a basic method for the detection of the higher abundant vitamin D metabolites 24,25-$(OH)_2$-D_3 and 25-(OH)-D_3 in human plasma samples. However, further optimization and validation of this novel method is necessary to provide a valuable robust in-house tool for the routine high-throughput analysis of the chosen vitamin D metabolites in different kinds of matrices in future.

As indicated above, different optimization options could significantly improve the vitamin D LC-MS/MS method. In a first step, the integration of additional internal standards, which are now easily available, like 1α,25-$(OH)_2$-D_3 [25,26,27-$^{13}C_3$] and vitamin D_3 [25,26,27-$^{13}C_3$] for early and late eluting vitamin D metabolites, respectively, would increase the robustness, precision, and accuracy of the vitamin D LC-MS/MS analysis by reducing ionization effects due to coeluting matrix compounds [405, 407]. In addition, different factors could be further optimized in order to improve the LODs and LOQs of the method. Beside an adaptation of the monitored MRMs within the LC-MS/MS method, including also mass transitions which detect the removal of one to three water molecules [387, 388], an optimization or modification of the sample preparation procedure should be considered, too. A change of the SPE sorbent and tube materials (e.g. using a C8 sorbent and inert Teflon-coated tubes) and/or SPE solvents could most likely improve the recovery of especially vitamin D_3 and vitamin D_2 from the SPE process, probably increase the poor recovery of all vitamin D metabolites from medium samples, and possibly reduce the background signals introduced by the present SPE procedure. Regarding the analysis of vitamin D metabolites in plasma samples, the sample preparation needs to be optimized, particularly with respect to the optimal plasma volume applied and an optional protein precipitation step. Furthermore, it should be evaluated if the above mentioned optimizations are sufficient to detect and quantify even low abundant vitamin D metabolites, like 1α,25-$(OH)_2$-D_3 or 1α,25-$(OH)_2$-D_2, in plasma/serum samples at physiological levels. If not, a derivatization of vitamin D metabolites with PTAD or other Cookson-type reagents, as reported by several other groups [381, 389–391, 393], could be another option in order to provide an adequately sensitive method for the routine analysis of

vitamin D metabolites at low levels. However, the insertion of an additional derivatization step demands also the modification and optimization of other processes, such as the sample preparation procedure, the chromatographic separation, and the mass spectrometric parameters. As already mentioned, previous studies showed that vitamin D metabolites and their respective C3 epimers have different biological activities and analytical properties [202, 394, 395]. Thus, the distinct analysis of vitamin D and 3-epi vitamin D metabolites, which would increase the analytical power of the in-house vitamin D method, should also be taken into consideration for further optimization options of the vitamin D LC-MS/MS method. The chromatographic separation of these epimers could be achieved by the use of chiral HPLC columns (e.g., a Kinetex PFP HPLC column from Phenomenex or a Zorbax SB CN HPLC column from Agilent) instead of the here used Kinetex C18 HPLC column [377, 383, 415] or by an acetylation of the C3 hydroxyl group allowing for the discrimination between C3 epimers on a C18 reversed phase column [416]. In this context, it should be noted that a Diels-Alder derivatization of vitamin D metabolites with Cookson-type reagents generally complicates the LC analysis of vitamin D stereoisomers since the derivatization reaction generates an additional chiral center [389].

In conclusion, the herein developed and validated vitamin D LC-MS/MS method represents already an appropriate routineously applicable method for the quantification of up to eight different vitamin D metabolites in cells. The implementation of the optimizations outlined above, however, should result in a more powerful method allowing for the sensitive and reliable analysis of vitamin D metabolites in additional biological matrices, such as culture medium, blood plasma or serum, and tissues, which then could be included in the in-house metabolomics portfolio in the future, too.

V. REFERENCES

[1] *Bericht zum Krebsgeschehen in Deutschland 2016.* (2016) Berlin

[2] Nichols, M., Townsend, N., Scarborough, P., and Rayner, M. (2013) Trends in age-specific coronary heart disease mortality in the European Union over three decades: 1980–2009. *Eur. Heart J.* **34**, 3017–3027

[3] Finegold, J. A., Asaria, P., and Francis, D. P. (2013) Mortality from ischaemic heart disease by country, region, and age: Statistics from World Health Organisation and United Nations. *Int. J. Cardiol.* **168**, 934–945

[4] Nowbar, A. N., Howard, J. P., Finegold, J. A., Asaria, P., and Francis, D. P. (2014) 2014 Global geographic analysis of mortality from ischaemic heart disease by country, age and income: Statistics from World Health Organisation and United Nations. *Int. J. Cardiol.* **174**, 293–298

[5] Townsend, N., Wilson, L., Bhatnagar, P., Wickramasinghe, K., Rayner, M., and Nichols, M. (2016) Cardiovascular disease in Europe: epidemiological update 2016. *Eur. Heart J.*, 1–14

[6] Siegel, R. L., Miller, K. D., and Jemal, A. (2016) Cancer statistics, 2016. *CA. Cancer J. Clin.* **66**, 7–30

[7] Malvezzi, M., Carioli, G., Bertuccio, P., Rosso, T., Boffetta, P., Levi, F., La Vecchia, C., and Negri, E. (2016) European cancer mortality predictions for the year 2016 with focus on leukaemias. *Ann. Oncol. Off. J. Eur. Soc. Med. Oncol.* **27**, 725–731

[8] *Global Cancer Facts & Figures 3rd Edition* (2015) Atlanta

[9] Berry, J. D., Dyer, A., Cai, X., Garside, D. B., Ning, H., Thomas, A., Greenland, P., Van Horn, L., Tracy, R. P., and Lloyd-Jones, D. M. (2012) Lifetime Risks of Cardiovascular Disease. *N. Engl. J. Med.* **366**, 321–329

[10] Rendic, S., and Guengerich, F. P. (2012) Contributions of human enzymes in carcinogen metabolism. *Chem. Res. Toxicol.* **25**, 1316–1383

[11] Pludowski, P., Holick, M. F., Pilz, S., Wagner, C. L., Hollis, B. W., Grant, W. B., Shoenfeld, Y., Lerchbaum, E., Llewellyn, D. J., Kienreich, K., and Soni, M. (2013) Vitamin D effects on musculoskeletal health, immunity, autoimmunity, cardiovascular disease, cancer, fertility, pregnancy, dementia and mortality—A review of recent evidence. *Autoimmun. Rev.* **12**, 976–989

[12] Schwab, U., Lauritzen, L., Tholstrup, T., Haldorssoni, T., Riserus, U., Uusitupa, M., and Becker, W. (2014) Effect of the amount and type of dietary fat on cardiometabolic risk factors and risk of developing type 2 diabetes, cardiovascular diseases, and cancer: a systematic review. *Food Nutr. Res.* **58**

[13] DeBerardinis, R. J., and Chandel, N. S. (2016) Fundamentals of cancer metabolism. *Sci. Adv.* **2**, e1600200

[14] Penning, T. M. (2015) The aldo-keto reductases (AKRs): Overview. *Chem. Biol. Interact.* **234**, 236-246

[15] Oppermann, U. C. T., Filling, C., and Jörnvall, H. (2001) Forms and functions of human SDR enzymes. *Chem. Biol. Interact.* **130**, 699–705

[16] Nebert, D. W., Wikvall, K., and Miller, W. L. (2013) Human cytochromes P450 in health and disease. *Philos. Trans. R. Soc. B Biol. Sci.* **368**

[17] Verzoni, E., Grassi, P., Ratta, R., Niger, M., De Braud, F., Valdagni, R., and Procopio, G. (2016) Safety of long-term exposure to abiraterone acetate in patients with castration-resistant prostate cancer and concomitant cardiovascular risk factors. *Ther. Adv. Med. Oncol.* **8**, 323–330

[18] Chrusciel, P., Rysz, J., and Banach, M. (2014) Defining the role of trimetazidine in the treatment of cardiovascular disorders: some insights on its role in heart failure and peripheral artery disease. *Drugs* **74**, 971–980

[19] Mindnich, R. D., and Penning, T. M. (2009) Aldo-keto reductase (AKR) superfamily: genomics and annotation. *Hum. Genomics* **3**, 362–370

[20] Hyndman, D., Bauman, D. R., Heredia, V. V, and Penning, T. M. (2003) The aldo-keto reductase superfamily homepage. *Chem. Biol. Interact.* **143-144**, 621–631

[21] Jez, J. M., Flynn, T. G., and Penning, T. M. (1997) A new nomenclature for the aldo-keto reductase superfamily. *Biochem. Pharmacol.* **54**, 639–647

[22] Salabei, J. K., Li, X.-P., Petrash, J. M., Bhatnagar, A., and Barski, O. A. (2011) Functional expression of novel human and murine AKR1B genes. *Chem. Biol. Interact.* **191**, 177–184

[23] Tamura, K., Stecher, G., Peterson, D., Filipski, A., and Kumar, S. (2013) MEGA6: Molecular Evolutionary Genetics Analysis version 6.0. *Mol. Biol. Evol.* **30**, 2725–2729

[24] Jez, J. M., Bennett, M. J., Schlegel, B. P., Lewis, M., and Penning, T. M. (1997) Comparative anatomy of the aldo-keto reductase superfamily. *Biochem. J.* **326**, 625–636

[25] Ellis, E. M. (2002) Microbial aldo-keto reductases. *FEMS Microbiol. Lett.* **216**, 123–131

[26] Sanli, G., Dudley, J. I., and Blaber, M. (2003) Structural biology of the aldo-keto reductase family of enzymes: catalysis and cofactor binding. *Cell Biochem. Biophys.* **38**, 79–101

[27] Barski, O. A., Tipparaju, S. M., and Bhatnagar, A. (2008) The aldo-keto reductase superfamily and its role in drug metabolism and detoxification. *Drug Metab. Rev.* **40**, 553–624

[28] Sengupta, D., Naik, D., and Reddy, A. R. (2015) Plant aldo-keto reductases (AKRs) as multi-tasking soldiers involved in diverse plant metabolic processes and stress defense: A structure-function update. *J. Plant Physiol.* **179**, 40–55

[29] Gallego, O., Ruiz, F. X., Ardèvol, A., Domínguez, M., Alvarez, R., de Lera, A. R., Rovira, C., Farrés, J., Fita, I., and Parés, X. (2007) Structural basis for the high all-trans-retinaldehyde reductase activity of the tumor marker AKR1B10. *Proc. Natl. Acad. Sci.* **104**, 20764–20769

[30] Kondo, K. H., Kai, M. H., Setoguchi, Y., Eggertsen, G., Sjöblom, P., Setoguchi, T., Okuda, K. I., and Björkhem, I. (1994) Cloning and expression of cDNA of human delta 4-3-oxosteroid 5 beta-reductase and substrate specificity of the expressed enzyme. *Eur. J. Biochem.* **219**, 357–363

[31] Di Costanzo, L., Drury, J. E., Penning, T. M., and Christianson, D. W. (2008) Crystal structure of human liver Delta4-3-ketosteroid 5beta-reductase (AKR1D1) and implications for substrate binding and catalysis. *J. Biol. Chem.* **283**, 16830–16839

[32] Chen, M., Drury, J. E., Christianson, D. W., and Penning, T. M. (2012) Conversion of human steroid 5β-reductase (AKR1D1) into 3β-hydroxysteroid dehydrogenase by single point mutation E120H: example of perfect enzyme engineering. *J. Biol. Chem.* **287**, 16609–16622

[33] Bohren, K. M., Grimshaw, C. E., and Gabbay, K. H. (1992) Catalytic effectiveness of human aldose reductase. Critical role of C-terminal domain. *J. Biol. Chem.* **267**, 20965–20970

[34] Schlegel, B. P., Jez, J. M., and Penning, T. M. (1998) Mutagenesis of 3alpha-hydroxysteroid dehydrogenase reveals a "push-pull" mechanism for proton transfer in aldo-keto reductases. *Biochemistry* **37**, 3538–3548

[35] Jin, Y., and Penning, T. M. (2007) Aldo-keto reductases and bioactivation/detoxication. *Annu. Rev. Pharmacol. Toxicol.* **47**, 263–292

[36] Penning, T. M., and Drury, J. E. (2007) Human aldo-keto reductases: Function, gene regulation, and single nucleotide polymorphisms. *Arch. Biochem. Biophys.* **464**, 241–250

[37] Cooper, W. C., Jin, Y., and Penning, T. M. (2007) Elucidation of a complete kinetic mechanism for a mammalian hydroxysteroid dehydrogenase (HSD) and identification of all enzyme forms on the reaction coordinate: the example of rat liver 3alpha-HSD (AKR1C9). *J. Biol. Chem.* **282**, 33484–33493

[38] Wermuth, B., Münch, J. D., and von Wartburg, J. P. (1977) Purification and properties of NADPH-dependent aldehyde reductase from human liver. *J. Biol. Chem.* **252**, 3821–3828

[39] Wermuth, B., and Monder, C. (1983) Aldose and aldehyde reductase exhibit isocorticosteroid reductase activity. *Eur. J. Biochem.* **131**, 423–426

[40] O'Connor, T., Ireland, L. S., Harrison, D. J., and Hayes, J. D. (1999) Major differences exist in the function and tissue-specific expression of human aflatoxin B1 aldehyde reductase and the principal human aldo-keto reductase AKR1 family members. *Biochem. J.* **343**, 487–504

[41] Palackal, N. T., Burczynski, M. E., Harvey, R. G., and Penning, T. M. (2001) Metabolic activation of polycyclic aromatic hydrocarbon trans-dihydrodiols by ubiquitously expressed aldehyde reductase (AKR1A1). *Chem. Biol. Interact.* **130-132**, 815–824

[42] Hankes, L. V, Politzer, W. M., Touster, O., and Anderson, L. (1969) Myo-inositol catabolism in human pentosurics: the predominant role of the glucuronate-xylulose-pentose phosphate pathway. *Ann. N. Y. Acad. Sci.* **165**, 564–576

[43] Barski, O. A., Papusha, V. Z., Ivanova, M. M., Rudman, D. M., and Finegold, M. J. (2005) Developmental expression and function of aldehyde reductase in proximal tubules of the kidney. *Am. J. Physiol. Renal Physiol.* **289**, F200–F207

[44] Reddy, C. C., Swan, J. S., and Hamilton, G. A. (1981) myo-Inositol oxygenase from hog kidney. I. Purification and characterization of the oxygenase and of an enzyme complex containing the oxygenase and D-glucuronate reductase. *J. Biol. Chem.* **256**, 8510–8518

[45] Penning, T. M. (2014) Human aldo-keto reductases and the metabolic activation of polycyclic aromatic hydrocarbons. *Chem. Res. Toxicol.* **27**, 1901–1917

[46] Morrison, A. D., Clements, R. S., Travis, S. B., Oski, F., and Winegrad, A. I. (1970) Glucose utilization by the polyol pathway in human erythrocytes. *Biochem. Biophys. Res. Commun.* **40**, 199–205

[47] Penning, T. M., and Drury, J. E. (2007) Human aldo–keto reductases: Function, gene regulation, and single nucleotide polymorphisms. *Arch. Biochem. Biophys.* **464**, 241–250

[48] Ko, B. C., Ruepp, B., Bohren, K. M., Gabbay, K. H., and Chung, S. S. (1997) Identification and characterization of multiple osmotic response sequences in the human aldose reductase gene. *J. Biol. Chem.* **272**, 16431–16437

[49] Gabbay, K. H. (1975) Hyperglycemia, polyol metabolism, and complications of diabetes mellitus. *Annu. Rev. Med.* **26**, 521–536

[50] Ramana, K. V. (2011) Aldose reductase: new insights for an old enzyme. *Biomol. Concepts* **2**, 103–114

[51] Tang, W. H., Martin, K. A., and Hwa, J. (2012) Aldose reductase, oxidative stress, and diabetic mellitus. *Front. Pharmacol.* **3**, 87

[52] Srivastava, S. K., Ramana, K. V, and Bhatnagar, A. (2005) Role of aldose reductase and oxidative damage in diabetes and the consequent potential for therapeutic options. *Endocr. Rev.* **26**, 380-392

[53] Vander Jagt, D. L., Robinson, B., Taylor, K. K., and Hunsaker, L. A. (1992) Reduction of trioses by NADPH-dependent aldo-keto reductases. Aldose reductase, methylglyoxal, and diabetic complications. *J. Biol. Chem.* **267**, 4364–4369

[54] Vander Jagt, D. L., Kolb, N. S., Vander Jagt, T. J., Chino, J., Martinez, F. J., Hunsaker, L. A., and Royer, R. E. (1995) Substrate specificity of human aldose reductase: identification of 4-hydroxynonenal as an endogenous substrate. *Biochim. Biophys. Acta* **1249**, 117–126

[55] Srivastava, S., Chandra, A., Ansari, N. H., Srivastava, S. K., and Bhatnagar, A. (1998) Identification of cardiac oxidoreductase(s) involved in the metabolism of the lipid peroxidation-derived aldehyde-4-hydroxynonenal. *Biochem. J.* **329**, 469–475

[56] Srivastava, S., Spite, M., Trent, J. O., West, M. B., Ahmed, Y., and Bhatnagar, A. (2004) Aldose reductase-catalyzed reduction of aldehyde phospholipids. *J. Biol. Chem.* **279**, 53395–53406

[57] Kabututu, Z., Manin, M., Pointud, J.-C., Maruyama, T., Nagata, N., Lambert, S., Lefrançois-Martinez, A.-M., Martinez, A., and Urade, Y. (2009) Prostaglandin F2alpha synthase activities of aldo-keto reductase 1B1, 1B3 and 1B7. *J. Biochem.* **145**, 161–168

[58] Nagata, N., Kusakari, Y., Fukunishi, Y., Inoue, T., and Urade, Y. (2011) Catalytic mechanism of the primary human prostaglandin F2α synthase, aldo-keto reductase 1B1 - prostaglandin D2 synthase activity in the absence of NADP(H). *FEBS J.* **278**, 1288–1298

[59] Bresson, E., Lacroix-Pépin, N., Boucher-Kovalik, S., Chapdelaine, P., and Fortier, M. A. (2012) The Prostaglandin F Synthase Activity of the Human Aldose Reductase AKR1B1 Brings New Lenses to Look at Pathologic Conditions. *Front. Pharmacol.* **3**, 98

[60] Cao, D., Tat Fan, S., and Chung, S. S. M. (1998) Identification and characterization of a novel human aldose reductase-like gene. *J. Biol. Chem.* **273**, 11429–11435

[61] Hyndman, D. J., and Flynn, T. G. (1998) Sequence and expression levels in human tissues of a new member of the aldo-keto reductase family. *Biochim. Biophys. Acta* **1399**, 198–202

[62] Crosas, B., Hyndman, D. J., Gallego, O., Martras, S., Parés, X., Flynn, T. G., and Farrés, J. (2003) Human aldose reductase and human small intestine aldose reductase are efficient retinal reductases: consequences for retinoid metabolism. *Biochem. J.* **373**, 973–979

[63] Gallego, O., Belyaeva, O. V, Porté, S., Ruiz, F. X., Stetsenko, A. V, Shabrova, E. V, Kostereva, N. V, Farrés, J., Parés, X., and Kedishvili, N. Y. (2006) Comparative functional analysis of human medium-chain dehydrogenases, short-chain dehydrogenases/reductases and aldo-keto reductases with retinoids. *Biochem. J.* **399**, 101–109

[64] Martin, H.-J., Breyer-Pfaff, U., Wsol, V., Venz, S., Block, S., and Maser, E. (2006) Purification and characterization of AKR1B10 from human liver: role in carbonyl reduction of xenobiotics. *Drug Metab. Dispos.* **34**, 464–470

[65] Martin, H.-J., and Maser, E. (2009) Role of human aldo-keto-reductase AKR1B10 in the protection against toxic aldehydes. *Chem. Biol. Interact.* **178**, 145–150

[66] Zhong, L., Shen, H., Huang, C., Jing, H., and Cao, D. (2011) AKR1B10 induces cell resistance to daunorubicin and idarubicin by reducing C13 ketonic group. *Toxicol. Appl. Pharmacol.* **255**, 40–47

[67] Fukumoto, S., Yamauchi, N., Moriguchi, H., Hippo, Y., Watanabe, A., Shibahara, J., Taniguchi, H., Ishikawa, S., Ito, H., Yamamoto, S., Iwanari, H., Hironaka, M., Ishikawa, Y., Niki, T., Sohara, Y., Kodama, T., Nishimura, M., Fukayama, M., Dosaka-Akita, H., and Aburatani, H. (2005) Overexpression of the aldo-keto reductase family protein AKR1B10 is highly correlated with smokers' non-small cell lung carcinomas. *Clin. Cancer Res.* **11**, 1776–1785

[68] Heringlake, S., Hofdmann, M., Fiebeler, A., Manns, M. P., Schmiegel, W., and Tannapfel, A. (2010) Identification and expression analysis of the aldo-ketoreductase1-B10 gene in primary malignant liver tumours. *J. Hepatol.* **52**, 220–227

[69] Matsunaga, T., Wada, Y., Endo, S., Soda, M., El-Kabbani, O., and Hara, A. (2012) Aldo-Keto Reductase 1B10 and Its Role in Proliferation Capacity of Drug-Resistant Cancers. *Front. Pharmacol.* **3**, 5

[70] Yan, R., Zu, X., Ma, J., Liu, Z., Adeyanju, M., and Cao, D. (2007) Aldo-keto reductase family 1 B10 gene silencing results in growth inhibition of colorectal cancer cells: Implication for cancer intervention. *Int. J. Cancer* **121**, 2301–2306

[71] Wang, C., Yan, R., Luo, D., Watabe, K., Liao, D.-F., and Cao, D. (2009) Aldo-keto reductase family 1 member B10 promotes cell survival by regulating lipid synthesis and eliminating carbonyls. *J. Biol. Chem.* **284**, 26742–26748

[72] Penning, T. M., Burczynski, M. E., Jez, J. M., Hung, C. F., Lin, H. K., Ma, H., Moore, M., Palackal, N., and Ratnam, K. (2000) Human 3alpha-hydroxysteroid dehydrogenase isoforms (AKR1C1-AKR1C4) of the aldo-keto reductase superfamily: functional plasticity and tissue distribution reveals roles in the inactivation and formation of male and female sex hormones. *Biochem. J.* **351**, 67–77

[73] Rižner, T. L., and Penning, T. M. (2014) Role of aldo-keto reductase family 1 (AKR1) enzymes in human steroid metabolism. *Steroids* **79**, 49–63

[74] Jin, Y., Mesaros, A. C., Blair, I. A., and Penning, T. M. (2011) Stereospecific reduction of 5β-reduced steroids by human ketosteroid reductases of the AKR (aldo-keto reductase) superfamily: role of AKR1C1-AKR1C4 in the metabolism of testosterone and progesterone via the 5β-reductase pathway. *Biochem. J.* **437**, 53–61

[75] Burczynski, M. E., Harvey, R. G., and Penning, T. M. (1998) Expression and characterization of four recombinant human dihydrodiol dehydrogenase isoforms: oxidation of trans-7,8-dihydroxy-7,8-dihydrobenzo[a]pyrene to the activated o-quinone metabolite benzo[a]pyrene-7,8-dione. *Biochemistry* **37**, 6781–6790

[76] Nishizawa, M., Nakajima, T., Yasuda, K., Kanzaki, H., Sasaguri, Y., Watanabe, K., and Ito, S. (2000) Close kinship of human 20alpha-hydroxysteroid dehydrogenase gene with three aldo-keto reductase genes. *Genes Cells* **5**, 111–125

[77] Graham, J. D., and Clarke, C. L. (1997) Physiological action of progesterone in target tissues. *Endocr. Rev.* **18**, 502–519

[78] Miller, W. L., and Auchus, R. J. (2011) The molecular biology, biochemistry, and physiology of human steroidogenesis and its disorders. *Endocr. Rev.* **32**, 81–151

[79] Belelli, D., and Lambert, J. J. (2005) Neurosteroids: endogenous regulators of the GABA(A) receptor. *Nat. Rev. Neurosci.* **6**, 565–575

[80] Burczynski, M. E., Sridhar, G. R., Palackal, N. T., and Penning, T. M. (2001) The reactive oxygen species--and Michael acceptor-inducible human aldo-keto reductase AKR1C1 reduces the alpha,beta-unsaturated aldehyde 4-hydroxy-2-nonenal to 1,4-dihydroxy-2-nonene. *J. Biol. Chem.* **276**, 2890–2897

[81] Matsunaga, T., Hojo, A., Yamane, Y., Endo, S., El-Kabbani, O., and Hara, A. (2013) Pathophysiological roles of aldo-keto reductases (AKR1C1 and AKR1C3) in development of cisplatin resistance in human colon cancers. *Chem. Biol. Interact.* **202**, 234–242

[82] Trauger, J. W., Jiang, A., Stearns, B. A., and LoGrasso, P. V (2002) Kinetics of allopregnanolone formation catalyzed by human 3alpha-hydroxysteroid dehydrogenase type III (AKR1C2). *Biochemistry* **41**, 13451–13459

[83] Rižner, T. L., Lin, H. K., Peehl, D. M., Steckelbroeck, S., Bauman, D. R., and Penning, T. M. (2003) Human type 3 3alpha-hydroxysteroid dehydrogenase (aldo-keto reductase 1C2) and androgen metabolism in prostate cells. *Endocrinology* **144**, 2922–2932

[84] Stolz, A., Hammond, L., Lou, H., Takikawa, H., Ronk, M., and Shively, J. E. (1993) cDNA cloning and expression of the human hepatic bile acid-binding protein. A member of the monomeric reductase gene family. *J. Biol. Chem.* **268**, 10448–10457

[85] Hara, A., Matsuura, K., Tamada, Y., Sato, K., Miyabe, Y., Deyashiki, Y., and Ishida, N. (1996) Relationship of human liver dihydrodiol dehydrogenases to hepatic bile-acid-binding protein and an oxidoreductase of human colon cells. *Biochem. J.* **313**, 373–376

[86] Khanna, M., Qin, K. N., Wang, R. W., and Cheng, K. C. (1995) Substrate specificity, gene structure, and tissue-specific distribution of multiple human 3alpha-hydroxysteroid dehydrogenases. *J. Biol. Chem.* **270**, 20162–20168

[87] Russell, D. W. (2003) The enzymes, regulation, and genetics of bile acid synthesis. *Annu. Rev. Biochem.* **72**, 137–174

[88] Dufort, I., Rheault, P., Huang, X.-F., Soucy, P., and Luu-The, V. (1999) Characteristics of a Highly Labile Human Type 5 17β-Hydroxysteroid Dehydrogenase. *Endocrinology* **140**, 568–574

[89] Penning, T. M., Burczynski, M. E., Jez, J. M., Lin, H. K., Ma, H., Moore, M., Ratnam, K., and Palackal, N. (2001) Structure-function aspects and inhibitor design of type 5 17beta-hydroxysteroid dehydrogenase (AKR1C3). *Mol. Cell. Endocrinol.* **171**, 137–149

[90] Griffin, L. D., and Mellon, S. H. (1999) Selective serotonin reuptake inhibitors directly alter activity of neurosteroidogenic enzymes. *Proc. Natl. Acad. Sci. U. S. A.* **96**, 13512–13517

[91] Lin, H. K., Jez, J. M., Schlegel, B. P., Peehl, D. M., Pachter, J. A., and Penning, T. M. (1997) Expression and characterization of recombinant type 2 3alpha-hydroxysteroid dehydrogenase (HSD) from human prostate: demonstration of bifunctional 3alpha/17beta-HSD activity and cellular distribution. *Mol. Endocrinol.* **11**, 1971–1984

[92] Penning, T. M., and Byrns, M. C. (2009) Steroid hormone transforming aldo-keto reductases and cancer. *Ann. N. Y. Acad. Sci.* **1155**, 33–42

[93] Byrns, M. C., Mindnich, R., Duan, L., and Penning, T. M. (2012) Overexpression of aldo-keto reductase 1C3 (AKR1C3) in LNCaP cells diverts androgen metabolism towards testosterone resulting in resistance to the 5α-reductase inhibitor finasteride. *J. Steroid Biochem. Mol. Biol.* **130**, 7–15

[94] Suzuki-Yamamoto, T., Nishizawa, M., Fukui, M., Okuda-Ashitaka, E., Nakajima, T., Ito, S., and Watanabe, K. (1999) cDNA cloning, expression and characterization of human prostaglandin F synthase 1. *FEBS Lett.* **462**, 335–340

[95] Matsuura, K., Shiraishi, H., Hara, A., Sato, K., Deyashiki, Y., Ninomiya, M., and Sakai, S. (1998) Identification of a principal mRNA species for human 3alpha-hydroxysteroid dehydrogenase isoform (AKR1C3) that exhibits high prostaglandin D2 11-ketoreductase activity. *J. Biochem.* **124**, 940–946

[96] Ricciotti, E., and FitzGerald, G. A. (2011) Prostaglandins and inflammation. *Arterioscler. Thromb. Vasc. Biol.* **31**, 986–1000

[97] Byrns, M. C., Jin, Y., and Penning, T. M. (2011) Inhibitors of type 5 17β-hydroxysteroid dehydrogenase (AKR1C3): overview and structural insights. *J. Steroid Biochem. Mol. Biol.* **125**, 95–104

[98] Charbonneau, A., and Luu-The, V. (2001) Genomic organization of a human 5beta-reductase and its pseudogene and substrate selectivity of the expressed enzyme. *Biochim. Biophys. Acta* **1517**, 228–235

[99] Lemonde, H. A., Custard, E. J., Bouquet, J., Duran, M., Overmars, H., Scambler, P. J., and Clayton, P. T. (2003) Mutations in SRD5B1 (AKR1D1), the gene encoding delta(4)-3-oxosteroid 5beta-reductase, in hepatitis and liver failure in infancy. *Gut* **52**, 1494–1499

[100] Clayton, P. T. (2011) Disorders of bile acid synthesis. *J. Inherit. Metab. Dis.* **34**, 593–604

[101] Chen, W.-D., and Zhang, Y. (2012) Regulation of aldo-keto reductases in human diseases. *Front. Pharmacol.* **3**, 35

[102] Ireland, L. S., Harrison, D. J., Neal, G. E., and Hayes, J. D. (1998) Molecular cloning, expression and catalytic activity of a human AKR7 member of the aldo-keto reductase superfamily: evidence that the major 2-carboxybenzaldehyde reductase from human liver is a homologue of rat aflatoxin B1-aldehyde reductase. *Biochem. J.* **332**, 21–34

[103] Knight, L. P., Primiano, T., Groopman, J. D., Kensler, T. W., and Sutter, T. R. (1999) cDNA cloning, expression and activity of a second human aflatoxin B1-metabolizing member of the aldo-keto reductase superfamily, AKR7A3. *Carcinogenesis* **20**, 1215–1223

[104] Bodreddigari, S., Jones, L. K., Egner, P. A., Groopman, J. D., Sutter, C. H., Roebuck, B. D., Guengerich, F. P., Kensler, T. W., and Sutter, T. R. (2008) Protection against aflatoxin B1-induced cytotoxicity by expression of the cloned aflatoxin B1-aldehyde reductases rat AKR7A1 and human AKR7A3. *Chem. Res. Toxicol.* **21**, 1134–1142

[105] Lyon, R. C., Johnston, S. M., Watson, D. G., McGarvie, G., and Ellis, E. M. (2007) Synthesis and catabolism of gamma-hydroxybutyrate in SH-SY5Y human neuroblastoma cells: role of the aldo-keto reductase AKR7A2. *J. Biol. Chem.* **282**, 25986–25992

[106] Picklo, M. J., Olson, S. J., Hayes, J. D., Markesbery, W. R., and Montine, T. J. (2001) Elevation of AKR7A2 (succinic semialdehyde reductase) in neurodegenerative disease. *Brain Res.* **916**, 229-238

[107] Weng, J., Cao, Y., Moss, N., and Zhou, M. (2006) Modulation of voltage-dependent Shaker family potassium channels by an aldo-keto reductase. *J. Biol. Chem.* **281**, 15194–15200

[108] Tipparaju, S. M., Barski, O. A., Srivastava, S., and Bhatnagar, A. (2008) Catalytic mechanism and substrate specificity of the beta-subunit of the voltage-gated potassium channel. *Biochemistry* **47**, 8840–8854

[109] McCormack, K., McCormack, T., Tanouye, M., Rudy, B., and Stühmer, W. (1995) Alternative splicing of the human Shaker K+ channel beta 1 gene and functional expression of the beta 2 gene product. *FEBS Lett.* **370**, 32–36

[110] Leicher, T., Roeper, J., Weber, K., Wang, X., and Pongs, O. (1996) Structural and functional characterization of human potassium channel subunit beta 1 (KCNA1B). *Neuropharmacology* **35**, 787–795

[111] Sewing, S., Roeper, J., and Pongs, O. (1996) Kv beta 1 subunit binding specific for shaker-related potassium channel alpha subunits. *Neuron* **16**, 455–463

[112] Leicher, T., Bähring, R., Isbrandt, D., and Pongs, O. (1998) Coexpression of the KCNA3B gene product with Kv1.5 leads to a novel A-type potassium channel. *J. Biol. Chem.* **273**, 35095–35101

[113] Bähring, R., Milligan, C. J., Vardanyan, V., Engeland, B., Young, B. A., Dannenberg, J., Waldschutz, R., Edwards, J. P., Wray, D., and Pongs, O. (2001) Coupling of voltage-dependent potassium channel inactivation and oxidoreductase active site of Kvbeta subunits. *J. Biol. Chem.* **276**, 22923–22929

[114] Li, Y., Um, S. Y., and McDonald, T. V (2006) Voltage-gated potassium channels: regulation by accessory subunits. *Neuroscientist* **12**, 199–210

[115] Tipparaju, S. M., Liu, S.-Q., Barski, O. A., and Bhatnagar, A. (2007) NADPH binding to beta-subunit regulates inactivation of voltage-gated K(+) channels. *Biochem. Biophys. Res. Commun.* **359**, 269–276

[116] Pan, Y., Weng, J., Cao, Y., Bhosle, R. C., and Zhou, M. (2008) Functional coupling between the Kv1.1 channel and aldoketoreductase Kvbeta1. *J. Biol. Chem.* **283**, 8634–8642

[117] Pongs, O., and Schwarz, J. R. (2010) Ancillary subunits associated with voltage-dependent K+ channels. **90**, 755–796

[118] Nishinaka, T., Azuma, Y., Ushijima, S., Miki, T., and Yabe-Nishimura, C. (2003) Human testis specific protein: a new member of aldo-keto reductase superfamily. *Chem. Biol. Interact.* **143-144**, 299–305

[119] Azuma, Y., Nishinaka, T., Ushijima, S., Soh, J., Katsuyama, M., Lu, H.-P., Kawata, M., Yabe-Nishimura, C., and Miki, T. (2004) Characterization of htAKR, a novel gene product in the aldo-keto reductase family specifically expressed in human testis. *Mol. Hum. Reprod.* **10**, 527–533

[120] Persson, B., and Kallberg, Y. (2013) Classification and nomenclature of the superfamily of short-chain dehydrogenases/reductases (SDRs). *Chem. Biol. Interact.* **202**, 111–115

[121] Bhatia, C., Oerum, S., Bray, J., Kavanagh, K. L., Shafqat, N., Yue, W., and Oppermann, U. (2015) Towards a systematic analysis of human short-chain dehydrogenases/reductases (SDR): Ligand identification and structure-activity relationships. *Chem. Biol. Interact.* **234**, 114–125

[122] Persson, B., Kallberg, Y., Bray, J. E., Bruford, E., Dellaporta, S. L., Favia, A. D., Duarte, R. G., Jörnvall, H., Kavanagh, K. L., Kedishvili, N., Kisiela, M., Maser, E., Mindnich, R., Orchard, S., Penning, T. M., Thornton, J. M., Adamski, J., and Oppermann, U. (2009) The SDR (short-chain dehydrogenase/reductase and related enzymes) nomenclature initiative. *Chem. Biol. Interact.* **178**, 94–98

[123] Kavanagh, K. L., Jörnvall, H., Persson, B., and Oppermann, U. (2008) The SDR superfamily: functional and structural diversity within a family of metabolic and regulatory enzymes. *Cell. Mol. Life Sci.* **65**, 3895–3906

[124] Filling, C., Berndt, K. D., Benach, J., Knapp, S., Prozorovski, T., Nordling, E., Ladenstein, R., Jörnvall, H., and Oppermann, U. (2002) Critical residues for structure and catalysis in short-chain dehydrogenases/reductases. *J. Biol. Chem.* **277**, 25677–25684

[125] Negri, M., Recanatini, M., and Hartmann, R. W. (2010) Insights in 17beta-HSD1 enzyme kinetics and ligand binding by dynamic motion investigation. *PLoS One* **5**, e12026

[126] Kallberg, Y., Oppermann, U., Jörnvall, H., and Persson, B. (2002) Short-chain dehydrogenases/reductases (SDRs). *Eur. J. Biochem.* **269**, 4409–4417

[127] Kavanagh, K. L., Klimacek, M., Nidetzky, B., and Wilson, D. K. (2002) The structure of apo and holo forms of xylose reductase, a dimeric aldo-keto reductase from Candida tenuis. *Biochemistry* **41**, 8785–8795

[128] Jörnvall, H., Persson, B., Krook, M., Atrian, S., Gonzàlez-Duarte, R., Jeffery, J., and Ghosh, D. (1995) Short-chain dehydrogenases/reductases (SDR). *Biochemistry* **34**, 6003–6013

[129] Mindnich, R., Möller, G., and Adamski, J. (2004) The role of 17beta-hydroxysteroid dehydrogenases. *Mol. Cell. Endocrinol.* **218**, 7–20

[130] Marchais-Oberwinkler, S., Henn, C., Möller, G., Klein, T., Negri, M., Oster, A., Spadaro, A., Werth, R., Wetzel, M., Xu, K., Frotscher, M., Hartmann, R. W., and Adamski, J. (2011) 17β-Hydroxysteroid dehydrogenases (17β-HSDs) as therapeutic targets: protein structures, functions, and recent progress in inhibitor development. *J. Steroid Biochem. Mol. Biol.* **125**, 66–82

[131] Peltoketo, H., Luu-The, V., Simard, J., and Adamski, J. (1999) 17beta-hydroxysteroid dehydrogenase (HSD)/17-ketosteroid reductase (KSR) family; nomenclature and main characteristics of the 17HSD/KSR enzymes. *J. Mol. Endocrinol.* **23**, 1–11

[132] Adamski, J., and Jakob, F. J. (2001) A guide to 17beta-hydroxysteroid dehydrogenases. *Mol. Cell. Endocrinol.* **171**, 1–4

[133] Moeller, G., and Adamski, J. (2006) Multifunctionality of human 17beta-hydroxysteroid dehydrogenases. *Mol. Cell. Endocrinol.* **248**, 47–55

[134] Moeller, G., and Adamski, J. (2009) Integrated view on 17beta-hydroxysteroid dehydrogenases. *Mol. Cell. Endocrinol.* **301**, 7–19

[135] Geissler, W. M., Davis, D. L., Wu, L., Bradshaw, K. D., Patel, S., Mendonca, B. B., Elliston, K. O., Wilson, J. D., Russell, D. W., and Andersson, S. (1994) Male pseudohermaphroditism caused by mutations of testicular 17beta-hydroxysteroid dehydrogenase 3. *Nat. Genet.* **7**, 34–39

[136] Marijanovic, Z., Laubner, D., Moller, G., Gege, C., Husen, B., Adamski, J., and Breitling, R. (2003) Closing the gap: identification of human 3-ketosteroid reductase, the last unknown enzyme of mammalian cholesterol biosynthesis. *Mol. Endocrinol.* **17**, 1715–1725

[137] Filling, C., Keller, B., Hirschberg, D., Marschall, H.-U., Jörnvall, H., Bennett, M. J., and Oppermann, U. (2008) Role of short-chain hydroxyacyl CoA dehydrogenases in SCHAD deficiency. *Biochem. Biophys. Res. Commun.* **368**, 6–11

[138] Yang, S.-Y., He, X.-Y., and Miller, D. (2007) HSD17B10: a gene involved in cognitive function through metabolism of isoleucine and neuroactive steroids. *Mol. Genet. Metab.* **92**, 36–42

[139] Luu-The, V., Tremblay, P., and Labrie, F. (2006) Characterization of type 12 17beta-hydroxysteroid dehydrogenase, an isoform of type 3 17beta-hydroxysteroid dehydrogenase responsible for estradiol formation in women. *Mol. Endocrinol.* **20**, 437–443

[140] Moon, Y.-A., and Horton, J. D. (2003) Identification of two mammalian reductases involved in the two-carbon fatty acyl elongation cascade. *J. Biol. Chem.* **278**, 7335–7343

[141] Sakurai, N., Miki, Y., Suzuki, T., Watanabe, K., Narita, T., Ando, K., Yung, T. M. C., Aoki, D., Sasano, H., and Handa, H. (2006) Systemic distribution and tissue localizations of human 17beta-hydroxysteroid dehydrogenase type 12. *J. Steroid Biochem. Mol. Biol.* **99**, 174–181

[142] Mindnich, R., Haller, F., Halbach, F., Moeller, G., Hrabé de Angelis, M., and Adamski, J. (2005) Androgen metabolism via 17beta-hydroxysteroid dehydrogenase type 3 in mammalian and non-mammalian vertebrates: comparison of the human and the zebrafish enzyme. *J. Mol. Endocrinol.* **35**, 305–316

[143] Legeza, B., Balázs, Z., Nashev, L. G., and Odermatt, A. (2013) The microsomal enzyme 17β-hydroxysteroid dehydrogenase 3 faces the cytoplasm and uses NADPH generated by glucose-6-phosphate dehydrogenase. *Endocrinology* **154**, 205–213

[144] Day, J. M., Foster, P. A., Tutill, H. J., Parsons, M. F. C., Newman, S. P., Chander, S. K., Allan, G. M., Lawrence, H. R., Vicker, N., Potter, B. V. L., Reed, M. J., and Purohit, A. (2008) 17beta-hydroxysteroid dehydrogenase Type 1, and not Type 12, is a target for endocrine therapy of hormone-dependent breast cancer. *Int. J. cancer* **122**, 1931–1940

[145] Haller, F. (2011) Multifunctionality in the enzyme family of 17beta-hydroxysteroid dehydrogenases. *Tech. Univ. München*, Dissertation

[146] Bellemare, V., Laberge, P., Noël, S., Tchernof, A., and Luu-The, V. (2009) Differential estrogenic 17beta-hydroxysteroid dehydrogenase activity and type 12 17beta-hydroxysteroid dehydrogenase expression levels in preadipocytes and differentiated adipocytes. *J. Steroid Biochem. Mol. Biol.* **114**, 129–134

[147] Puranen, T., Poutanen, M., Ghosh, D., Vihko, R., and Vihko, P. (1997) Origin of substrate specificity of human and rat 17beta-hydroxysteroid dehydrogenase type 1, using chimeric enzymes and site-directed substitutions. *Endocrinology* **138**, 3532–3539

[148] Haller, F., Moman, E., Hartmann, R. W., Adamski, J., and Mindnich, R. (2010) Molecular framework of steroid/retinoid discrimination in 17beta-hydroxysteroid dehydrogenase type 1 and photoreceptor-associated retinol dehydrogenase. *J. Mol. Biol.* **399**, 255–267

[149] Wu, L., Einstein, M., Geissler, W. M., Chan, H. K., Elliston, K. O., and Andersson, S. (1993) Expression cloning and characterization of human 17beta-hydroxysteroid dehydrogenase type 2, a microsomal enzyme possessing 20alpha-hydroxysteroid dehydrogenase activity. *J. Biol. Chem.* **268**, 12964–12969

[150] Suzuki, T., Sasano, H., Andersson, S., and Mason, J. I. (2000) 3beta-hydroxysteroid dehydrogenase/delta5->4-isomerase activity associated with the human 17beta-hydroxysteroid dehydrogenase type 2 isoform. *J. Clin. Endocrinol. Metab.* **85**, 3669–3672

[151] Adamski, J., Normand, T., Leenders, F., Monté, D., Begue, A., Stéhelin, D., Jungblut, P. W., and de Launoit, Y. (1995) Molecular cloning of a novel widely expressed human 80 kDa 17 beta-hydroxysteroid dehydrogenase IV. *Biochem. J.* **311**, 437–443

[152] Jiang, L. L., Kobayashi, A., Matsuura, H., Fukushima, H., and Hashimoto, T. (1996) Purification and properties of human D-3-hydroxyacyl-CoA dehydratase: medium-chain enoyl-CoA hydratase is D-3-hydroxyacyl-CoA dehydratase. *J. Biochem.* **120**, 624–632

[153] Jiang, L. L., Kurosawa, T., Sato, M., Suzuki, Y., and Hashimoto, T. (1997) Physiological role of D-3-hydroxyacyl-CoA dehydratase/D-3-hydroxyacyl-CoA dehydrogenase bifunctional protein. *J. Biochem.* **121**, 506–513

[154] Suzuki, Y., Jiang, L. L., Souri, M., Miyazawa, S., Fukuda, S., Zhang, Z., Une, M., Shimozawa, N., Kondo, N., Orii, T., and Hashimoto, T. (1997) D-3-hydroxyacyl-CoA dehydratase/D-3-hydroxyacyl-CoA dehydrogenase bifunctional protein deficiency: a newly identified peroxisomal disorder. *Am. J. Hum. Genet.* **61**, 1153–1162

[155] Dieuaide-Noubhani, M., Asselberghs, S., Mannaerts, G. P., and Van Veldhoven, P. P. (1997) Evidence that multifunctional protein 2, and not multifunctional protein 1, is involved in the peroxisomal beta-oxidation of pristanic acid. *Biochem. J.* **325**, 367–373

[156] Möller, G., Leenders, F., van Grunsven, E. G., Dolez, V., Qualmann, B., Kessels, M. M., Markus, M., Krazeisen, A., Husen, B., Wanders, R. J., de Launoit, Y., and Adamski, J. (1999) Characterization of the HSD17B4 gene: D-specific multifunctional protein 2 / 17beta-hydroxysteroid dehydrogenase IV. *J. Steroid Biochem. Mol. Biol.* **69**, 441–446

[157] Biswas, M. G., and Russell, D. W. (1997) Expression cloning and characterization of oxidative 17beta- and 3alpha-hydroxysteroid dehydrogenases from rat and human prostate. *J. Biol. Chem.* **272**, 15959–15966

[158] Huang, X. F., and Luu-The, V. (2000) Molecular characterization of a first human 3(alpha->beta)-hydroxysteroid epimerase. *J. Biol. Chem.* **275**, 29452–29457

[159] Chetyrkin, S. V, Hu, J., Gough, W. H., Dumaual, N., and Kedishvili, N. Y. (2001) Further characterization of human microsomal 3alpha-hydroxysteroid dehydrogenase. *Arch. Biochem. Biophys.* **386**, 1–10

[160] Belyaeva, O. V, Chetyrkin, S. V, Clark, A. L., Kostereva, N. V, SantaCruz, K. S., Chronwall, B. M., and Kedishvili, N. Y. (2007) Role of microsomal retinol/sterol dehydrogenase-like short-chain dehydrogenases/reductases in the oxidation and epimerization of 3alpha-hydroxysteroids in human tissues. *Endocrinology* **148**, 2148–2156

[161] Törn, S., Nokelainen, P., Kurkela, R., Pulkka, A., Menjivar, M., Ghosh, S., Coca-Prados, M., Peltoketo, H., Isomaa, V., and Vihko, P. (2003) Production, purification, and functional analysis of recombinant human and mouse 17beta-hydroxysteroid dehydrogenase type 7. *Biochem. Biophys. Res. Commun.* **305**, 37–45

[162] Chen, Z., Kastaniotis, A. J., Miinalainen, I. J., Rajaram, V., Wierenga, R. K., and Hiltunen, J. K. (2009) 17beta-hydroxysteroid dehydrogenase type 8 and carbonyl reductase type 4 assemble as a ketoacyl reductase of human mitochondrial FAS. *FASEB J.* **23**, 3682–3691

[163] Ohno, S., Nishikawa, K., Honda, Y., and Nakajin, S. (2008) Expression in E. coli and tissue distribution of the human homologue of the mouse Ke 6 gene, 17beta-hydroxysteroid dehydrogenase type 8. *Mol. Cell. Biochem.* **309**, 209–215

[164] Gamble, M. V, Shang, E., Zott, R. P., Mertz, J. R., Wolgemuth, D. J., and Blaner, W. S. (1999) Biochemical properties, tissue expression, and gene structure of a short chain dehydrogenase/ reductase able to catalyze cis-retinol oxidation. *J. Lipid Res.* **40**, 2279–2292

[165] Wang, J., Chai, X., Eriksson, U., and Napoli, J. L. (1999) Activity of human 11-cis-retinol dehydrogenase (Rdh5) with steroids and retinoids and expression of its mRNA in extra-ocular human tissue. *Biochem. J.* **338**, 23–27

[166] Shafqat, N., Marschall, H.-U., Filling, C., Nordling, E., Wu, X.-Q., Björk, L., Thyberg, J., Mårtensson, E., Salim, S., Jörnvall, H., and Oppermann, U. (2003) Expanded substrate screenings of human and Drosophila type 10 17beta-hydroxysteroid dehydrogenases (HSDs) reveal multiple specificities in bile acid and steroid hormone metabolism: characterization of multifunctional 3alpha/7alpha/7beta/17beta/20beta/21-HSD. *Biochem. J.* **376**, 49–60

[167] He, X. Y., Merz, G., Mehta, P., Schulz, H., and Yang, S. Y. (1999) Human brain short chain L-3-hydroxyacyl coenzyme A dehydrogenase is a single-domain multifunctional enzyme. Characterization of a novel 17beta-hydroxysteroid dehydrogenase. *J. Biol. Chem.* **274**, 15014–15019

[168] Brereton, P., Suzuki, T., Sasano, H., Li, K., Duarte, C., Obeyesekere, V., Haeseleer, F., Palczewski, K., Smith, I., Komesaroff, P., and Krozowski, Z. (2001) Pan1b (17betaHSD11)-enzymatic activity and distribution in the lung. *Mol. Cell. Endocrinol.* **171**, 111–117

[169] Chai, Z., Brereton, P., Suzuki, T., Sasano, H., Obeyesekere, V., Escher, G., Saffery, R., Fuller, P., Enriquez, C., and Krozowski, Z. (2003) 17 beta-hydroxysteroid dehydrogenase type XI localizes to human steroidogenic cells. *Endocrinology* **144**, 2084–2091

[170] Fujimoto, Y., Itabe, H., Sakai, J., Makita, M., Noda, J., Mori, M., Higashi, Y., Kojima, S., and Takano, T. (2004) Identification of major proteins in the lipid droplet-enriched fraction isolated from the human hepatocyte cell line HuH7. *Biochim. Biophys. Acta* **1644**, 47–59

[171] Horiguchi, Y., Araki, M., and Motojima, K. (2008) Identification and characterization of the ER/lipid droplet-targeting sequence in 17beta-hydroxysteroid dehydrogenase type 11. *Arch. Biochem. Biophys.* **479**, 121–130

[172] Liu, S., Huang, C., Li, D., Ren, W., Zhang, H., Qi, M., Li, X., and Yu, L. (2007) Molecular cloning and expression analysis of a new gene for short-chain dehydrogenase/reductase 9. *Acta Biochim. Pol.* **54**, 213–218

[173] Su, W., Wang, Y., Jia, X., Wu, W., Li, L., Tian, X., Li, S., Wang, C., Xu, H., Cao, J., Han, Q., Xu, S., Chen, Y., Zhong, Y., Zhang, X., Liu, P., Gustafsson, J.-Å., and Guan, Y. (2014) Comparative proteomic study reveals 17β-HSD13 as a pathogenic protein in nonalcoholic fatty liver disease. *Proc. Natl. Acad. Sci. U. S. A.* **111**, 11437–11442

[174] Lukacik, P., Keller, B., Bunkoczi, G., Kavanagh, K. L., Kavanagh, K., Lee, W. H., Hwa Lee, W., Adamski, J., and Oppermann, U. (2007) Structural and biochemical characterization of human orphan DHRS10 reveals a novel cytosolic enzyme with steroid dehydrogenase activity. *Biochem. J.* **402**, 419–427

[175] Smith, S., Witkowski, A., and Joshi, A. K. (2003) Structural and functional organization of the animal fatty acid synthase. *Prog. Lipid Res.* **42**, 289–317

[176] Jakobsson, A., Westerberg, R., and Jacobsson, A. (2006) Fatty acid elongases in mammals: their regulation and roles in metabolism. *Prog. Lipid Res.* **45**, 237–249

[177] Leonard, A. E., Pereira, S. L., Sprecher, H., and Huang, Y.-S. (2004) Elongation of long-chain fatty acids. *Prog. Lipid Res.* **43**, 36–54

[178] Kihara, A. (2012) Very long-chain fatty acids: elongation, physiology and related disorders. *J. Biochem.* **152**, 387–395

[179] Tehlivets, O., Scheuringer, K., and Kohlwein, S. D. (2007) Fatty acid synthesis and elongation in yeast. *Biochim. Biophys. Acta* **1771**, 255–270

[180] Ohno, Y., Suto, S., Yamanaka, M., Mizutani, Y., Mitsutake, S., Igarashi, Y., Sassa, T., and Kihara, A. (2010) ELOVL1 production of C24 acyl-CoAs is linked to C24 sphingolipid synthesis. *Proc. Natl. Acad. Sci. U. S. A.* **107**, 18439–18444

[181] Ikeda, M., Kanao, Y., Yamanaka, M., Sakuraba, H., Mizutani, Y., Igarashi, Y., and Kihara, A. (2008) Characterization of four mammalian 3-hydroxyacyl-CoA dehydratases involved in very long-chain fatty acid synthesis. *FEBS Lett.* **582**, 2435–2440

[182] Houten, S. M., Violante, S., Ventura, F. V, and Wanders, R. J. A. (2015) The biochemistry and physiology of mitochondrial fatty acid β-oxidation and its genetic disorders. *Annu. Rev. Physiol.* **78**, 23–44

[183] Witkowski, A., Joshi, A. K., and Smith, S. (2007) Coupling of the de novo fatty acid biosynthesis and lipoylation pathways in mammalian mitochondria. *J. Biol. Chem.* **282**, 14178–14185

[184] Hiltunen, J. K., Schonauer, M. S., Autio, K. J., Mittelmeier, T. M., Kastaniotis, A. J., and Dieckmann, C. L. (2009) Mitochondrial fatty acid synthesis type II: more than just fatty acids. *J. Biol. Chem.* **284**, 9011–9015

[185] Hiltunen, J. K., Autio, K. J., Schonauer, M. S., Kursu, V. A. S., Dieckmann, C. L., and Kastaniotis, A. J. (2010) Mitochondrial fatty acid synthesis and respiration. *Biochim. Biophys. Acta* **1797**, 1195-1202

[186] Joshi, A. K., Zhang, L., Rangan, V. S., and Smith, S. (2003) Cloning, expression, and characterization of a human 4′-phosphopantetheinyl transferase with broad substrate specificity. *J. Biol. Chem.* **278**, 33142–33149

[187] Abu-Elheiga, L., Brinkley, W. R., Zhong, L., Chirala, S. S., Woldegiorgis, G., and Wakil, S. J. (2000) The subcellular localization of acetyl-CoA carboxylase 2. *Proc. Natl. Acad. Sci. U. S. A.* **97**, 1444–1449

[188] Kaushik, V. K., Kavana, M., Volz, J. M., Weldon, S. C., Hanrahan, S., Xu, J., Caplan, S. L., and Hubbard, B. K. (2009) Characterization of recombinant human acetyl-CoA carboxylase-2 steady-state kinetics. *Biochim. Biophys. Acta* **1794**, 961–967

[189] Loeffen, J. L., Triepels, R. H., van den Heuvel, L. P., Schuelke, M., Buskens, C. A., Smeets, R. J., Trijbels, J. M., and Smeitink, J. A. (1998) cDNA of eight nuclear encoded subunits of NADH:ubiquinone oxidoreductase: human complex I cDNA characterization completed. *Biochem. Biophys. Res. Commun.* **253**, 415–422

[190] Zhang, L., Joshi, A. K., and Smith, S. (2003) Cloning, expression, characterization, and interaction of two components of a human mitochondrial fatty acid synthase. Malonyl-transferase and acyl carrier protein. *J. Biol. Chem.* **278**, 40067–40074

[191] Schneider, R., Brors, B., Bürger, F., Camrath, S., and Weiss, H. (1997) Two genes of the putative mitochondrial fatty acid synthase in the genome of Saccharomyces cerevisiae. *Curr. Genet.* **32**, 384–388

[192] Feng, D., Witkowski, A., and Smith, S. (2009) Down-regulation of mitochondrial acyl carrier protein in mammalian cells compromises protein lipoylation and respiratory complex I and results in cell death. *J. Biol. Chem.* **284**, 11436–11445

[193] Schonauer, M. S., Kastaniotis, A. J., Hiltunen, J. K., and Dieckmann, C. L. (2008) Intersection of RNA processing and the type II fatty acid synthesis pathway in yeast mitochondria. *Mol. Cell. Biol.* **28**, 6646–6657

[194] Ghayee, H. K., and Auchus, R. J. (2007) Basic concepts and recent developments in human steroid hormone biosynthesis. *Rev. Endocr. Metab. Disord.* **8**, 289–300

[195] Cai, C., and Balk, S. P. (2011) Intratumoral androgen biosynthesis in prostate cancer pathogenesis and response to therapy. *Endocr. Relat. Cancer* **18**, R175–R182

[196] Mostaghel, E. A. (2014) Beyond T and DHT - novel steroid derivatives capable of wild type androgen receptor activation. *Int. J. Biol. Sci.* **10**, 602–613

[197] Payne, A. H., and Hales, D. B. (2013) Overview of steroidogenic enzymes in the pathway from cholesterol to active steroid hormones. *Endocr. Rev.* **25**, 947–970

[198] Miller, W. L. (2013) Steroid hormone synthesis in mitochondria. *Mol. Cell. Endocrinol.* **379**, 62–73

[199] Prosser, D. E., and Jones, G. (2004) Enzymes involved in the activation and inactivation of vitamin D. *Trends Biochem. Sci.* **29**, 664–673

[200] Lehmann, B. (2005) The vitamin D3 pathway in human skin and its role for regulation of biological processes. *Photochem. Photobiol.* **81**, 1246–1251

[201] Nebert, D. W., and Russell, D. W. (2002) Clinical importance of the cytochromes P450. *Lancet* **360**, 1155–1162

[202] Kamao, M., Tatematsu, S., Hatakeyama, S., Sakaki, T., Sawada, N., Inouye, K., Ozono, K., Kubodera, N., Reddy, G. S., and Okano, T. (2004) C-3 epimerization of vitamin D3 metabolites and further metabolism of C-3 epimers: 25-hydroxyvitamin D3 is metabolized to 3-epi-25-hydroxyvitamin D3 and subsequently metabolized through C-1alpha or C-24 hydroxylation. *J. Biol. Chem.* **279**, 15897–15907

[203] Yazdanpanah, M., Bailey, D., Walsh, W., Wan, B., and Adeli, K. (2013) Analytical measurement of serum 25-OH-vitamin D_3, 25-OH-vitamin D_2 and their C3-epimers by LC-MS/MS in infant and pediatric specimens. *Clin. Biochem.* **46**, 1264–1271

[204] Cashman, K. D., Kinsella, M., Walton, J., Flynn, A., Hayes, A., Lucey, A. J., Seamans, K. M., and Kiely, M. (2014) The 3 epimer of 25-hydroxycholecalciferol is present in the circulation of the majority of adults in a nationally representative sample and has endogenous origins. *J. Nutr.* **144**, 1050–1057

[205] Aghajafari, F., Field, C. J., Rabi, D., Kaplan, B. J., Maggiore, J. A., O'Beirne, M., Hanley, D. A., Eliasziw, M., Dewey, D., Ross, S., and APrON Study Team (2016) Plasma 3-epi-25-hydroxycholecalciferol can alter the assessment of vitamin D status using the current reference ranges for pregnant women and their newborns. *J. Nutr.* **146**, 70–75

[206] Kanis, J. A. (1982) Vitamin D metabolism and its clinical application. *J. Bone Joint Surg. Br.* **64**, 542–560

[207] Dirks-Naylor, A. J., and Lennon-Edwards, S. (2011) The effects of vitamin D on skeletal muscle function and cellular signaling. *J. Steroid Biochem. Mol. Biol.* **125**, 159–168

[208] Chiang, K.-C., and Chen, T. C. (2013) The anti-cancer actions of vitamin D. *Anticancer. Agents Med. Chem.* **13**, 126–139

[209] Curtis, K. M., Aenlle, K. K., Roos, B. A., and Howard, G. A. (2014) 24R,25-dihydroxyvitamin D3 promotes the osteoblastic differentiation of human mesenchymal stem cells. *Mol. Endocrinol.* **28**, 644–658

[210] Lancaster, S. T., Blackburn, J., Blom, A., Makishima, M., Ishizawa, M., and Mansell, J. P. (2014) 24,25-Dihydroxyvitamin D3 cooperates with a stable, fluoromethylene LPA receptor agonist to secure human (MG63) osteoblast maturation. *Steroids* **83**, 52–61

[211] Schuster, I., and Bernhardt, R. (2007) Inhibition of cytochromes p450: existing and new promising therapeutic targets. *Drug Metab. Rev.* **39**, 481–499

[212] Wabitsch, M., Brenner, R. E., Melzner, I., Braun, M., Möller, P., Heinze, E., Debatin, K. M., and Hauner, H. (2001) Characterization of a human preadipocyte cell strain with high capacity for adipose differentiation. *Int. J. Obes. Relat. Metab. Disord.* **25**, 8–15

[213] Boukamp, P., Petrussevska, R. T., Breitkreutz, D., Hornung, J., Markham, A., and Fusenig, N. E. (1988) Normal keratinization in a spontaneously immortalized aneuploid human keratinocyte cell line. *J. Cell Biol.* **106**, 761–771

[214] Boukamp, P., Popp, S., Altmeyer, S., Hülsen, A., Fasching, C., Cremer, T., and Fusenig, N. E. (1997) Sustained nontumorigenic phenotype correlates with a largely stable chromosome content during long-term culture of the human keratinocyte line HaCaT. *Genes, Chromosom. Cancer* **19**, 201–214

[215] Wefers, B., Panda, S. K., Ortiz, O., Brandl, C., Hensler, S., Hansen, J., Wurst, W., and Kühn, R. (2013) Generation of targeted mouse mutants by embryo microinjection of TALEN mRNA. *Nat. Protoc.* **8**, 2355–2379

[216] Schmitt, S., Saathoff, F., Meissner, L., Schropp, E.-M., Lichtmannegger, J., Schulz, S., Eberhagen, C., Borchard, S., Aichler, M., Adamski, J., Plesnila, N., Rothenfusser, S., Kroemer, G., and Zischka, H. (2013) A semi-automated method for isolating functionally intact mitochondria from cultured cells and tissue biopsies. *Anal. Biochem.* **443**, 66–74

[217] Sawano, A., and Miyawaki, A. (2000) Directed evolution of green fluorescent protein by a new versatile PCR strategy for site-directed and semi-random mutagenesis. *Nucleic Acids Res.* **28**, e78

[218] Smith, L. M., Sanders, J. Z., Kaiser, R. J., Hughes, P., Dodd, C., Connell, C. R., Heiner, C., Kent, S. B., and Hood, L. E. (1986) Fluorescence detection in automated DNA sequence analysis. *Nature* **321**, 674–679

[219] Prober, J. M., Trainor, G. L., Dam, R. J., Hobbs, F. W., Robertson, C. W., Zagursky, R. J., Cocuzza, A. J., Jensen, M. A., and Baumeister, K. (1987) A system for rapid DNA sequencing with fluorescent chain-terminating dideoxynucleotides. *Science* **238**, 336–341

[220] Barski, O. A., Gabbay, K. H., Grimshaw, C. E., and Bohren, K. M. (1995) Mechanism of human aldehyde reductase: characterization of the active site pocket. *Biochemistry* **34**, 11264–11275

[221] Yee, D. J., Balsanek, V., and Sames, D. (2004) New tools for molecular imaging of redox metabolism: development of a fluorogenic probe for 3 alpha-hydroxysteroid dehydrogenases. *J. Am. Chem. Soc.* **126**, 2282–2283

[222] Zamzami, N., Métivier, D., and Kroemer, G. (2000) Quantitation of mitochondrial transmembrane potential in cells and in isolated mitochondria. *Methods Enzymol.* **322**, 208–213

[223] Baracca, A., Sgarbi, G., Solaini, G., and Lenaz, G. (2003) Rhodamine 123 as a probe of mitochondrial membrane potential: evaluation of proton flux through F0 during ATP synthesis. *Biochim. Biophys. Acta - Bioenerg.* **1606**, 137–146

[224] Cermak, T., Doyle, E. L., Christian, M., Wang, L., Zhang, Y., Schmidt, C., Baller, J. A., Somia, N. V, Bogdanove, A. J., and Voytas, D. F. (2011) Efficient design and assembly of custom TALEN and other TAL effector-based constructs for DNA targeting. *Nucleic Acids Res.* **39**, e82

[225] Ding, Q., Lee, Y.-K., Schaefer, E. A. K., Peters, D. T., Veres, A., Kim, K., Kuperwasser, N., Motola, D. L., Meissner, T. B., Hendriks, W. T., Trevisan, M., Gupta, R. M., Moisan, A., Banks, E., Friesen, M., Schinzel, R. T., Xia, F., Tang, A., Xia, Y., Figueroa, E., Wann, A., Ahfeldt, T., Daheron, L., Zhang, F., Rubin, L. L., Peng, L. F., Chung, R. T., Musunuru, K., and Cowan, C. A. (2013) A TALEN genome-editing system for generating human stem cell-based disease models. *Cell Stem Cell* **12**, 238–251

[226] Wefers, B., Meyer, M., Ortiz, O., Hrabé de Angelis, M., Hansen, J., Wurst, W., and Kühn, R. (2013) Direct production of mouse disease models by embryo microinjection of TALENs and oligodeoxynucleotides. *Proc. Natl. Acad. Sci. U. S. A.* **110**, 3782–3787

[227] Miller, J. C., Tan, S., Qiao, G., Barlow, K. A., Wang, J., Xia, D. F., Meng, X., Paschon, D. E., Leung, E., Hinkley, S. J., Dulay, G. P., Hua, K. L., Ankoudinova, I., Cost, G. J., Urnov, F. D., Zhang, H. S., Holmes, M. C., Zhang, L., Gregory, P. D., and Rebar, E. J. (2011) A TALE nuclease architecture for efficient genome editing. *Nat. Biotechnol.* **29**, 143–148

[228] Li, T., Huang, S., Jiang, W. Z., Wright, D., Spalding, M. H., Weeks, D. P., and Yang, B. (2011) TAL nucleases (TALNs): hybrid proteins composed of TAL effectors and FokI DNA-cleavage domain. *Nucleic Acids Res.* **39**, 359–372

[229] Weterings, E., and van Gent, D. C. (2004) The mechanism of non-homologous end-joining: a synopsis of synapsis. *DNA Repair (Amst).* **3**, 1425–1435

[230] Chapman, J. R., Taylor, M. R. G., and Boulton, S. J. (2012) Playing the end game: DNA double-strand break repair pathway choice. *Mol. Cell* **47**, 497–510

[231] Cong, L., Zhou, R., Kuo, Y.-C., Cunniff, M., and Zhang, F. (2012) Comprehensive interrogation of natural TALE DNA-binding modules and transcriptional repressor domains. *Nat. Commun.* **3**, 968

[232] Streubel, J., Blücher, C., Landgraf, A., and Boch, J. (2012) TAL effector RVD specificities and efficiencies. *Nat. Biotechnol.* **30**, 593–595

[233] Brunak, S., Engelbrecht, J., and Knudsen, S. (1991) Prediction of human mRNA donor and acceptor sites from the DNA sequence. *J. Mol. Biol.* **220**, 49–65

[234] Wang, M., and Marín, A. (2006) Characterization and prediction of alternative splice sites. *Gene* **366**, 219–227

[235] Claros, M. G., and Vincens, P. (1996) Computational method to predict mitochondrially imported proteins and their targeting sequences. *Eur. J. Biochem.* **241**, 779–786

[236] Hiller, K., Grote, A., Scheer, M., Münch, R., and Jahn, D. (2004) PrediSi: prediction of signal peptides and their cleavage positions. *Nucleic Acids Res.* **32**, W375–W379

[237] Bannai, H., Tamada, Y., Maruyama, O., Nakai, K., and Miyano, S. (2002) Extensive feature detection of N-terminal protein sorting signals. *Bioinformatics* **18**, 298–305

[238] Petersen, T. N., Brunak, S., von Heijne, G., and Nielsen, H. (2011) SignalP 4.0: discriminating signal peptides from transmembrane regions. *Nat. Methods* **8**, 785–786

[239] Nielsen, H., Engelbrecht, J., Brunak, S., and von Heijne, G. (1997) Identification of prokaryotic and eukaryotic signal peptides and prediction of their cleavage sites. *Protein Eng.* **10**, 1–6

[240] Emanuelsson, O., Nielsen, H., Brunak, S., and von Heijne, G. (2000) Predicting Subcellular Localization of Proteins Based on their N-terminal Amino Acid Sequence. *J. Mol. Biol.* **300**, 1005-1016

[241] Wong, Y.-H., Lee, T.-Y., Liang, H.-K., Huang, C.-M., Wang, T.-Y., Yang, Y.-H., Chu, C.-H., Huang, H.-D., Ko, M.-T., and Hwang, J.-K. (2007) KinasePhos 2.0: a web server for identifying protein kinase-specific phosphorylation sites based on sequences and coupling patterns. *Nucleic Acids Res.* **35**, W588–W594

[242] Blom, N., Gammeltoft, S., and Brunak, S. (1999) Sequence and structure-based prediction of eukaryotic protein phosphorylation sites. *J. Mol. Biol.* **294**, 1351–1362

[243] Blom, N., Sicheritz-Pontén, T., Gupta, R., Gammeltoft, S., and Brunak, S. (2004) Prediction of post-translational glycosylation and phosphorylation of proteins from the amino acid sequence. *Proteomics* **4**, 1633–1649

[244] Johansen, M. B., Kiemer, L., and Brunak, S. (2006) Analysis and prediction of mammalian protein glycation. *Glycobiology* **16**, 844–853

[245] Gupta, R., Jung, E., and Brunak, S. (2004) Prediction of N-glycosylation sites in human proteins. *(in Preparation).*

[246] Steentoft, C., Vakhrushev, S. Y., Joshi, H. J., Kong, Y., Vester-Christensen, M. B., Schjoldager, K. T.-B. G., Lavrsen, K., Dabelsteen, S., Pedersen, N. B., Marcos-Silva, L., Gupta, R., Bennett, E. P., Mandel, U., Brunak, S., Wandall, H. H., Levery, S. B., and Clausen, H. (2013) Precision mapping of the human O-GalNAc glycoproteome through SimpleCell technology. *EMBO J.* **32**, 1478–1488

[247] Monigatti, F., Gasteiger, E., Bairoch, A., and Jung, E. (2002) The Sulfinator: predicting tyrosine sulfation sites in protein sequences. *Bioinformatics* **18**, 769–770

[248] Ren, J., Gao, X., Jin, C., Zhu, M., Wang, X., Shaw, A., Wen, L., Yao, X., and Xue, Y. (2009) Systematic study of protein sumoylation: Development of a site-specific predictor of SUMOsp 2.0. *Proteomics* **9**, 3409–3412

[249] Zhao, Q., Xie, Y., Zheng, Y., Jiang, S., Liu, W., Mu, W., Liu, Z., Zhao, Y., Xue, Y., and Ren, J. (2014) GPS-SUMO: a tool for the prediction of sumoylation sites and SUMO-interaction motifs. *Nucleic Acids Res.* **42**, W325–W330

[250] Chen, Z., Chen, Y.-Z., Wang, X.-F., Wang, C., Yan, R.-X., and Zhang, Z. (2011) Prediction of ubiquitination sites by using the composition of k-spaced amino acid pairs. *PLoS One* **6**, e22930

[251] Chen, Z., Zhou, Y., Song, J., and Zhang, Z. (2013) hCKSAAP_UbSite: improved prediction of human ubiquitination sites by exploiting amino acid pattern and properties. *Biochim. Biophys. Acta* **1834**, 1461–1467

[252] Radivojac, P., Vacic, V., Haynes, C., Cocklin, R. R., Mohan, A., Heyen, J. W., Goebl, M. G., and Iakoucheva, L. M. (2010) Identification, analysis, and prediction of protein ubiquitination sites. *Proteins Struct. Funct. Bioinforma.* **78**, 365–380

[253] Linder, B. (2015) Interaction of the Hedgehog and vitamin D receptor signaling pathways in Patched associated cancers. *Georg-August-Universität Göttingen*, Dissertation

[254] Lehmann, B. (1997) HaCaT cell line as a model system for vitamin D3 metabolism in human skin. *J. Invest. Dermatol.* **108**, 78–82

[255] Aszterbaum, M., Epstein, J., Oro, A., Douglas, V., LeBoit, P. E., Scott, M. P., and Epstein, E. H. (1999) Ultraviolet and ionizing radiation enhance the growth of BCCs and trichoblastomas in patched heterozygous knockout mice. *Nat. Med.* **5**, 1285–1291

[256] So, P.-L., Langston, A. W., Daniallinia, N., Hebert, J. L., Fujimoto, M. A., Khaimskiy, Y., Aszterbaum, M., and Epstein, E. H. (2006) Long-term establishment, characterization and manipulation of cell lines from mouse basal cell carcinoma tumors. *Exp. Dermatol.* **15**, 742–750

[257] Nitzki, F., Zibat, A., König, S., Wijgerde, M., Rosenberger, A., Brembeck, F. H., Carstens, P.-O., Frommhold, A., Uhmann, A., Klingler, S., Reifenberger, J., Pukrop, T., Aberger, F., Schulz-Schaeffer, W., and Hahn, H. (2010) Tumor stroma-derived Wnt5a induces differentiation of basal cell carcinoma of Ptch-mutant mice via CaMKII. *Cancer Res.* **70**, 2739–2748

[258] Uhmann, A., Niemann, H., Lammering, B., Henkel, C., Hess, I., Nitzki, F., Fritsch, A., Prüfer, N., Rosenberger, A., Dullin, C., Schraepler, A., Reifenberger, J., Schweyer, S., Pietsch, T., Strutz, F., Schulz-Schaeffer, W., and Hahn, H. (2011) Antitumoral effects of calcitriol in basal cell carcinomas involve inhibition of hedgehog signaling and induction of vitamin D receptor signaling and differentiation. *Mol. Cancer Ther.* **10**, 2179–2188

[259] Hall, T. A. (1999) BioEdit: a user-friendly biological sequence alignment editor and analysis program for Windows 95/98/NT. *Nucl. Acids. Symp. Ser.* **41**, 95–98

[260] Moreland, J. L., Gramada, A., Buzko, O. V, Zhang, Q., and Bourne, P. E. (2005) The Molecular Biology Toolkit (MBT): a modular platform for developing molecular visualization applications. *BMC Bioinformatics* **6**, 21

[261] Berman, H. M., Westbrook, J., Feng, Z., Gilliland, G., Bhat, T. N., Weissig, H., Shindyalov, I. N., and Bourne, P. E. (2000) The Protein Data Bank. *Nucleic Acids Res.* **28**, 235–242

[262] Weber, S., Salabei, J. K., Moller, G., Kremmer, E., Bhatnagar, A., Adamski, J., and Barski, O. A. (2015) Aldo-Keto Reductase 1B15 (AKR1B15): a mitochondrial human aldo-keto reductase with activity towards steroids and 3-keto-acyl-CoA conjugates. *J. Biol. Chem.* **290**, 6531–6545

[263] Morrison, J. F. (1969) Kinetics of the reversible inhibition of enzyme-catalysed reactions by tight-binding inhibitors. *Biochim. Biophys. Acta - Enzymol.* **185**, 269–286

[264] Schnell, S. (2014) Validity of the Michaelis-Menten equation--steady-state or reactant stationary assumption: that is the question. *FEBS J.* **281**, 464–472

[265] Calvo, S. E., Compton, A. G., Hershman, S. G., Lim, S. C., Lieber, D. S., Tucker, E. J., Laskowski, A., Garone, C., Liu, S., Jaffe, D. B., Christodoulou, J., Fletcher, J. M., Bruno, D. L., Goldblatt, J., DiMauro, S., Thorburn, D. R., and Mootha, V. K. (2012) Molecular diagnosis of infantile mitochondrial disease with targeted next-generation sequencing. *Sci. Transl. Med.* **4**, 118ra10

[266] Casetta, B., Jans, I., Billen, J., Vanderschueren, D., and Bouillon, R. (2010) Development of a method for the quantification of 1alpha,25(OH)$_2$-vitamin D3 in serum by liquid chromatography tandem mass spectrometry without derivatization. *Eur. J. Mass Spectrom. (Chichester, Eng).* **16**, 81–89

[267] Linnet, K., and Kondratovich, M. (2004) Partly nonparametric approach for determining the limit of detection. *Clin. Chem.* **50**, 732–740

[268] Mani, D. R., Abbatiello, S. E., and Carr, S. A. (2012) Statistical characterization of multiple-reaction monitoring mass spectrometry (MRM-MS) assays for quantitative proteomics. *BMC Bioinformatics* **13**, S9

[269] Barski, O. A., Mindnich, R., and Penning, T. M. (2013) Alternative splicing in the aldo-keto reductase superfamily: implications for protein nomenclature. *Chem. Biol. Interact.* **202**, 153–158

[270] Mayes, J. S., and Watson, G. H. (2004) Direct effects of sex steroid hormones on adipose tissues and obesity. *Obes. Rev.* **5**, 197–216

[271] Brown, M. (2008) Skeletal muscle and bone: effect of sex steroids and aging. *Adv. Physiol. Educ.* **32**, 120–126

[272] Sato, K., and Iemitsu, M. (2015) Exercise and sex steroid hormones in skeletal muscle. *J. Steroid Biochem. Mol. Biol.* **145**, 200–205

[273] Sasson, S., and Mayer, M. (1981) Effect of androgenic steroids on rat thymus and thymocytes in suspension. *J. Steroid Biochem.* **14**, 509–517

[274] Kuhl, H., Gross, M., Schneider, M., Weber, W., Mehlis, W., Stegmüller, M., and Taubert, H.-D. (1983) The effect of sex steroids and hormonal contraceptives upon thymus and spleen of intact female rats. *Contraception* **28**, 587–601

[275] Dulos, G. J., and Bagchus, W. M. (2001) Androgens indirectly accelerate thymocyte apoptosis. *Int. Immunopharmacol.* **1**, 321–328

[276] Poliseno, L., Salmena, L., Zhang, J., Carver, B., Haveman, W. J., and Pandolfi, P. P. (2010) A coding-independent function of gene and pseudogene mRNAs regulates tumour biology. *Nature* **465**, 1033–1038

[277] Anderson, L., and Seilhamer, J. (1997) A comparison of selected mRNA and protein abundances in human liver. *Electrophoresis* **18**, 533–537

[278] Greenbaum, D., Colangelo, C., Williams, K., and Gerstein, M. (2003) Comparing protein abundance and mRNA expression levels on a genomic scale. *Genome Biol.* **4**, 117.1–117.8

[279] Hargrove, J., and Schmidt, F. (1989) The role of mRNA and protein stability in gene expression. *FASEB J* **3**, 2360–2370

[280] Pratt, J. M. (2002) Dynamics of protein turnover, a missing dimension in proteomics. *Mol. Cell. Proteomics* **1**, 579–591

[281] Ciechanover, A. (2005) Proteolysis: from the lysosome to ubiquitin and the proteasome. *Nat. Rev. Mol. Cell Biol.* **6**, 79–87

[282] Hochstrasser, M. (1996) Ubiquitin-dependent protein degradation. *Annu. Rev. Genet.* **30**, 405–439

[283] Lecker, S. H., Goldberg, A. L., and Mitch, W. E. (2006) Protein degradation by the ubiquitin-proteasome pathway in normal and disease states. *J. Am. Soc. Nephrol.* **17**, 1807–1819

[284] Heo, J.-M., and Rutter, J. (2011) Ubiquitin-dependent mitochondrial protein degradation. *Int. J. Biochem. Cell Biol.* **43**, 1422–1426

[285] Melchior, F. (2000) SUMO--nonclassical ubiquitin. *Annu. Rev. Cell Dev. Biol.* **16**, 591–626

[286] Zhao, J. (2007) Sumoylation regulates diverse biological processes. *Cell. Mol. Life Sci.* **64**, 3017–3033

[287] Ma, J., Yan, R., Zu, X., Cheng, J.-M., Rao, K., Liao, D.-F., and Cao, D. (2008) Aldo-keto reductase family 1 B10 affects fatty acid synthesis by regulating the stability of acetyl-CoA carboxylase-alpha in breast cancer cells. *J. Biol. Chem.* **283**, 3418–3423

[288] Keller, B., Meier, M., and Adamski, J. (2009) Comparison of predicted and experimental subcellular localization of two putative rat steroid dehydrogenases from the short-chain dehydrogenase/reductase protein superfamily. *Mol. Cell. Endocrinol.* **301**, 43–46

[289] Habib, S. J., Neupert, W., and Rapaport, D. (2007) Analysis and prediction of mitochondrial targeting signals. *Methods Cell Biol.* **80**, 761–781

[290] Alías, M., Ayuso-Tejedor, S., Fernández-Recio, J., Cativiela, C., and Sancho, J. (2010) Helix propensities of conformationally restricted amino acids. Non-natural substitutes for helix breaking proline and helix forming alanine. *Org. Biomol. Chem.* **8**, 788–792

[291] Lam, C.-W., Yuen, Y.-P., Cheng, W.-F., Chan, Y.-W., and Tong, S.-F. (2006) Missense mutation Leu72Pro located on the carboxyl terminal amphipathic helix of apolipoprotein C-II causes familial chylomicronemia syndrome. *Clin. Chim. Acta.* **364**, 256–259

[292] Betts, M. J., and Russell, R. B. (2003) in *Bioinformatics for Geneticists* (Barnes, M. R., and Gray, I. C., eds.) pp. 289–316, John Wiley & Sons, Ltd, Chichester, UK

[293] Brega, A., and Baglioni, C. (1971) A Study of Mitochondrial Protein Synthesis in Intact HeLa Cells. *Eur. J. Biochem.* **22**, 415–422

[294] Kelly, V. P., Sherratt, P. J., Crouch, D. H., and Hayes, J. D. (2002) Novel homodimeric and heterodimeric rat gamma-hydroxybutyrate synthases that associate with the Golgi apparatus define a distinct subclass of aldo-keto reductase 7 family proteins. *Biochem. J.* **366**, 847–861

[295] Flynn, T. G. (1982) Aldehyde reductases: Monomeric NAPDH-dependent oxidoreductases with multifunctional potential. *Biochem. Pharmacol.* **31**, 2705–2712

[296] Tarle, I., Borhani, D. W., Wilson, D. K., Quiocho, F. A., and Petrash, J. M. (1993) Probing the active site of human aldose reductase. Site-directed mutagenesis of Asp-43, Tyr-48, Lys-77, and His-110. *J. Biol. Chem.* **268**, 25687–25693

[297] Jez, J. M., Schlegel, B. P., and Penning, T. M. (1996) Characterization of the substrate binding site in rat liver 3alpha-hydroxysteroid/dihydrodiol dehydrogenase. The roles of tryptophans in ligand binding and protein fluorescence. *J. Biol. Chem.* **271**, 30190–30198

[298] Kubiseski, T. J., and Flynn, T. G. (1995) Studies on human aldose reductase. Probing the role of arginine 268 by site-directed mutagenesis. *J. Biol. Chem.* **270**, 16911–16917

[299] Davidson, W. S., and Flynn, T. G. (1979) Kinetics and mechanism of action of aldehyde reductase from pig kidney. *Biochem. J.* **177**, 595–601

[300] Giménez-Dejoz, J., Kolář, M. H., Ruiz, F. X., Crespo, I., Cousido-Siah, A., Podjarny, A., Barski, O. A., Fanfrlík, J., Parés, X., Farrés, J., and Porté, S. (2015) Substrate specificity, inhibitor selectivity and structure-function relationships of aldo-keto reductase 1B15: A novel human retinaldehyde reductase. *PLoS One* **10**, e0134506

[301] Puranen, T. J., Poutanen, M. H., Peltoketo, H. E., Vihko, P. T., and Vihko, R. K. (1994) Site-directed mutagenesis of the putative active site of human 17beta-hydroxysteroid dehydrogenase type 1. *Biochem. J.* **304**, 289–293

[302] Han, Q., Campbell, R. L., Gangloff, A., Huang, Y. W., and Lin, S. X. (2000) Dehydroepiandrosterone and dihydrotestosterone recognition by human estrogenic 17beta-hydroxysteroid dehydrogenase. C-18/C-19 steroid discrimination and enzyme-induced strain. *J. Biol. Chem.* **275**, 1105–1111

[303] Endo, S., Matsunaga, T., Mamiya, H., Ohta, C., Soda, M., Kitade, Y., Tajima, K., Zhao, H.-T., El-Kabbani, O., and Hara, A. (2009) Kinetic studies of AKR1B10, human aldose reductase-like protein: endogenous substrates and inhibition by steroids. *Arch. Biochem. Biophys.* **487**, 1–9

[304] Bisswanger, H. (2014) Enzyme assays. *Perspect. Sci.* **1**, 41–55

[305] Rokosz, L. L., Boulton, D. A., Butkiewicz, E. A., Sanyal, G., Cueto, M. A., Lachance, P. A., and Hermes, J. D. (1994) Human cytoplasmic 3-hydroxy-3-methylglutaryl coenzyme A synthase: expression, purification, and characterization of recombinant wild-type and Cys129 mutant enzymes. *Arch. Biochem. Biophys.* **312**, 1–13

[306] Haapalainen, A. M., Meriläinen, G., Pirilä, P. L., Kondo, N., Fukao, T., and Wierenga, R. K. (2007) Crystallographic and kinetic studies of human mitochondrial acetoacetyl-CoA thiolase: the importance of potassium and chloride ions for its structure and function. *Biochemistry* **46**, 4305–4321

[307] Puisac, B., Ramos, M., Arnedo, M., Menao, S., Gil-Rodríguez, M. C., Teresa-Rodrigo, M. E., Pié, A., de Karam, J. C., Wesselink, J.-J., Giménez, I., Ramos, F. J., Casals, N., Gómez-Puertas, P., Hegardt, F. G., and Pié, J. (2012) Characterization of splice variants of the genes encoding human mitochondrial HMG-CoA lyase and HMG-CoA synthase, the main enzymes of the ketogenesis pathway. *Mol. Biol. Rep.* **39**, 4777–4785

[308] Middelberg, A. P. J. (2002) Preparative protein refolding. *Trends Biotechnol.* **20**, 437–443

[309] Ho, J. G. S., and Middelberg, A. P. J. (2004) Estimating the potential refolding yield of recombinant proteins expressed as inclusion bodies. *Biotechnol. Bioeng.* **87**, 584–592

[310] Yang, Z., Zhang, L., Zhang, Y., Zhang, T., Feng, Y., Lu, X., Lan, W., Wang, J., Wu, H., Cao, C., and Wang, X. (2011) Highly efficient production of soluble proteins from insoluble inclusion bodies by a two-step-denaturing and refolding method. *PLoS One* **6**, e22981

[311] Klutts, S., Pastuszak, I., Edavana, V. K., Thampi, P., Pan, Y.-T., Abraham, E. C., Carroll, J. D., and Elbein, A. D. (2003) Purification, cloning, expression, and properties of mycobacterial trehalose-phosphate phosphatase. *J. Biol. Chem.* **278**, 2093–2100

[312] Kiefer, H. (2003) In vitro folding of alpha-helical membrane proteins. *Biochim. Biophys. Acta - Biomembr.* **1610**, 57–62

[313] Tao, H., Liu, W., Simmons, B. N., Harris, H. K., Cox, T. C., and Massiah, M. A. (2010) Purifying natively folded proteins from inclusion bodies using sarkosyl, Triton X-100, and CHAPS. *Biotechniques* **48**, 61–64

[314] Koboldt, D. C., Steinberg, K. M., Larson, D. E., Wilson, R. K., and Mardis, E. R. (2013) The next-generation sequencing revolution and its impact on genomics. *Cell* **155**, 27–38

[315] Laaksovirta, H., Peuralinna, T., Schymick, J. C., Scholz, S. W., Lai, S.-L., Myllykangas, L., Sulkava, R., Jansson, L., Hernandez, D. G., Gibbs, J. R., Nalls, M. A., Heckerman, D., Tienari, P. J., and Traynor, B. J. (2010) Chromosome 9p21 in amyotrophic lateral sclerosis in Finland: a genome-wide association study. *Lancet Neurol.* **9**, 978–985

[316] Renton, A. E., Majounie, E., Waite, A., Simón-Sánchez, J., Rollinson, S., Gibbs, J. R., Schymick, J. C., Laaksovirta, H., van Swieten, J. C., Myllykangas, L., Kalimo, H., Paetau, A., Abramzon, Y., Remes, A. M., Kaganovich, A., Scholz, S. W., Duckworth, J., Ding, J., Harmer, D. W., Hernandez, D. G., Johnson, J. O., Mok, K., Ryten, M., Trabzuni, D., Guerreiro, R. J., Orrell, R. W., Neal, J., Murray, A., Pearson, J., Jansen, I. E., Sondervan, D., Seelaar, H., Blake, D., Young, K., Halliwell, N., Callister, J. B., Toulson, G., Richardson, A., Gerhard, A., Snowden, J., Mann, D., Neary, D., Nalls, M. A., Peuralinna, T., Jansson, L., Isoviita, V.-M., Kaivorinne, A.-L., Hölttä-Vuori, M., Ikonen, E., Sulkava, R., Benatar, M., Wuu, J., Chiò, A., Restagno, G., Borghero, G., Sabatelli, M., Heckerman, D., Rogaeva, E., Zinman, L., Rothstein, J. D., Sendtner, M., Drepper, C., Eichler, E. E., Alkan, C., Abdullaev, Z., Pack, S. D., Dutra, A., Pak, E., Hardy, J., Singleton, A., Williams, N. M., Heutink, P., Pickering-Brown, S., Morris, H. R., Tienari, P. J., and Traynor, B. J. (2011) A hexanucleotide repeat expansion in C9ORF72 is the cause of chromosome 9p21-linked ALS-FTD. *Neuron* **72**, 257–268

[317] Wilson, D. K., Bohren, K. M., Gabbay, K. H., and Quiocho, F. A. (1992) An unlikely sugar substrate site in the 1.65 A structure of the human aldose reductase holoenzyme implicated in diabetic complications. *Science* **257**, 81–84

[318] Muslin, A. J., Tanner, J. W., Allen, P. M., and Shaw, A. S. (1996) Interaction of 14-3-3 with signaling proteins is mediated by the recognition of phosphoserine. *Cell* **84**, 889–897

[319] Tzivion, G., and Avruch, J. (2002) 14-3-3 proteins: active cofactors in cellular regulation by serine/threonine phosphorylation. *J. Biol. Chem.* **277**, 3061–3064

[320] Galluzzi, L., Kepp, O., Trojel-Hansen, C., and Kroemer, G. (2012) Mitochondrial control of cellular life, stress, and death. *Circ. Res.* **111**, 1198–1207

[321] Yang, S.-H., Liu, R., Perez, E. J., Wen, Y., Stevens, S. M., Valencia, T., Brun-Zinkernagel, A.-M., Prokai, L., Will, Y., Dykens, J., Koulen, P., and Simpkins, J. W. (2004) Mitochondrial localization of estrogen receptor beta. *Proc. Natl. Acad. Sci. U. S. A.* **101**, 4130–4135

[322] Pedram, A., Razandi, M., Wallace, D. C., and Levin, E. R. (2006) Functional estrogen receptors in the mitochondria of breast cancer cells. *Mol. Biol. Cell* **17**, 2125–2137

[323] Vasconsuelo, A., Milanesi, L., and Boland, R. (2013) Actions of 17β-estradiol and testosterone in the mitochondria and their implications in aging. *Ageing Res. Rev.* **12**, 907–917

[324] Gavrilova-Jordan, L. P., and Price, T. M. (2007) Actions of steroids in mitochondria. *Semin. Reprod. Med.* **25**, 154–164

[325] Demonacos, C. V, Karayanni, N., Hatzoglou, E., Tsiriyiotis, C., Spandidos, D. A., and Sekeris, C. E. (1996) Mitochondrial genes as sites of primary action of steroid hormones. *Steroids* **61**, 226–232

[326] Chen, J. Q., Delannoy, M., Cooke, C., and Yager, J. D. (2004) Mitochondrial localization of ERalpha and ERbeta in human MCF7 cells. *Am. J. Physiol. Endocrinol. Metab.* **286**, E1011–E1022

[327] Lobatón, C. D., Vay, L., Hernández-Sanmiguel, E., Santodomingo, J., Moreno, A., Montero, M., and Alvarez, J. (2005) Modulation of mitochondrial Ca(2+) uptake by estrogen receptor agonists and antagonists. *Br. J. Pharmacol.* **145**, 862–871

[328] Er, F., Michels, G., Gassanov, N., Rivero, F., and Hoppe, U. C. (2004) Testosterone induces cytoprotection by activating ATP-sensitive K+ channels in the cardiac mitochondrial inner membrane. *Circulation* **110**, 3100–3107

[329] Flynn, J. M., Dimitrijevich, S. D., Younes, M., Skliris, G., Murphy, L. C., and Cammarata, P. R. (2008) Role of wild-type estrogen receptor-beta in mitochondrial cytoprotection of cultured normal male and female human lens epithelial cells. *Am. J. Physiol. Endocrinol. Metab.* **295**, E637–E647

[330] Kussmaul, L., and Hirst, J. (2006) The mechanism of superoxide production by NADH:ubiquinone oxidoreductase (complex I) from bovine heart mitochondria. *Proc. Natl. Acad. Sci. U. S. A.* **103**, 7607–7612

[331] Murphy, M. P. (2009) How mitochondria produce reactive oxygen species. *Biochem. J.* **417**, 1–13

[332] Pryde, K. R., and Hirst, J. (2011) Superoxide is produced by the reduced flavin in mitochondrial complex I: a single, unified mechanism that applies during both forward and reverse electron transfer. *J. Biol. Chem.* **286**, 18056–18065

[333] Aon, M. A., Stanley, B. A., Sivakumaran, V., Kembro, J. M., O'Rourke, B., Paolocci, N., and Cortassa, S. (2012) Glutathione/thioredoxin systems modulate mitochondrial H_2O_2 emission: an experimental-computational study. *J. Gen. Physiol.* **139**, 479–491

[334] Genova, M. L., and Lenaz, G. (2015) The interplay between respiratory supercomplexes and ROS in aging. *Antioxid. Redox Signal.* **23**, 208–238

[335] Marí, M., Morales, A., Colell, A., García-Ruiz, C., and Fernández-Checa, J. C. (2009) Mitochondrial glutathione, a key survival antioxidant. *Antioxid. Redox Signal.* **11**, 2685–2700

[336] Garcia, J., Han, D., Sancheti, H., Yap, L.-P., Kaplowitz, N., and Cadenas, E. (2010) Regulation of mitochondrial glutathione redox status and protein glutathionylation by respiratory substrates. *J. Biol. Chem.* **285**, 39646–39654

[337] Davalli, P., Mitic, T., Caporali, A., Lauriola, A., and D'Arca, D. (2016) ROS, cell senescence, and novel molecular mechanisms in aging and age-related diseases. *Oxid. Med. Cell. Longev.* **2016**, 3565127

[338] Miwa, S., Jow, H., Baty, K., Johnson, A., Czapiewski, R., Saretzki, G., Treumann, A., and von Zglinicki, T. (2014) Low abundance of the matrix arm of complex I in mitochondria predicts longevity in mice. *Nat. Commun.* **5**, 3837

[339] Yashin, A. I., Wu, D., Arbeev, K. G., and Ukraintseva, S. V (2010) Joint influence of small-effect genetic variants on human longevity. *Aging (Albany. NY).* **2**, 612–620

[340] Williamson, D. H., Lund, P., and Krebs, H. A. (1967) The redox state of free nicotinamide-adenine dinucleotide in the cytoplasm and mitochondria of rat liver. *Biochem. J.* **103**, 514–527

[341] Zhang, Y., Ning, F., Li, X., and Teng, M. (2013) Structural insights into cofactor recognition of yeast mitochondria 3-oxoacyl-ACP reductase OAR1. *IUBMB Life* **65**, 154–162

[342] Fujii, Y., Watanabe, K., Hayashi, H., Urade, Y., Kuramitsu, S., Kagamiyama, H., and Hayaishi, O. (1990) Purification and characterization of rho-crystallin from Japanese common bullfrog lens. *J. Biol. Chem.* **265**, 9914–9923

[343] Daly, R., and Hearn, M. T. W. (2005) Expression of heterologous proteins in Pichia pastoris: a useful experimental tool in protein engineering and production. *J. Mol. Recognit.* **18**, 119–138

[344] Brondyk, W. H. (2009) Selecting an appropriate method for expressing a recombinant protein. *Methods Enzymol.* **463**, 131–147

[345] Ruf, A., Müller, F., D'Arcy, B., Stihle, M., Kusznir, E., Handschin, C., Morand, O. H., and Thoma, R. (2004) The monotopic membrane protein human oxidosqualene cyclase is active as monomer. *Biochem. Biophys. Res. Commun.* **315**, 247–254

[346] Tata, J. R. (1972) in *Subcellular Components - Preparation and Fractination* (Birnie, G. D., ed.) 2nd Ed., pp. 185–213, Butterworth & Co Ltd, London, UK

[347] Völkl, A. (2010) in *eLS* (Völkl, A., ed.), John Wiley & Sons Ltd, Chichester, UK

[348] Shin, J., Dunbrack, R. L., Lee, S., and Strominger, J. L. (1991) Signals for retention of transmembrane proteins in the endoplasmic reticulum studied with CD4 truncation mutants. *Proc. Natl. Acad. Sci. U. S. A.* **88**, 1918–1922

[349] Gaynor, E. C., te Heesen, S., Graham, T. R., Aebi, M., and Emr, S. D. (1994) Signal-mediated retrieval of a membrane protein from the Golgi to the ER in yeast. *J. Cell Biol.* **127**, 653–665

[350] Gande, S. L., Mariappan, M., Schmidt, B., Pringle, T. H., von Figura, K., and Dierks, T. (2008) Paralog of the formylglycine-generating enzyme--retention in the endoplasmic reticulum by canonical and noncanonical signals. *FEBS J.* **275**, 1118–1130

[351] Junge, F., Schneider, B., Reckel, S., Schwarz, D., Dötsch, V., and Bernhard, F. (2008) Large-scale production of functional membrane proteins. *Cell. Mol. Life Sci.* **65**, 1729–1755

[352] Savelli, G., Spreti, N., and Di Profio, P. (2000) Enzyme activity and stability control by amphiphilic self-organizing systems in aqueous solutions. *Curr. Opin. Colloid Interface Sci.* **5**, 111–117

[353] Privé, G. G. (2007) Detergents for the stabilization and crystallization of membrane proteins. *Methods* **41**, 388–397

[354] Sadaf, A., Cho, K. H., Byrne, B., and Chae, P. S. (2015) Amphipathic agents for membrane protein study. *Methods Enzymol.* **557**, 57–94

[355] Susa, M., Keeler, M., and Varticovski, L. (1992) Platelet-derived growth factor activates membrane-associated phosphatidylinositol 3-kinase and mediates its translocation from the cytosol. Detection of enzyme activity in detergent-solubilized cell extracts. *J. Biol. Chem.* **267**, 22951–22956

[356] Srinivasulu, S., and Rao, A. G. A. (1993) Kinetic and structural studies on the interaction of surfactants with lipoxygenase L1 from soybeans (Glycine max). *J. Agric. Food Chem.* **41**, 366–371

[357] Woeltje, K. F., Kuwajima, M., Foster, D. W., and McGarry, J. D. (1987) Characterization of the mitochondrial carnitine palmitoyltransferase enzyme system. II. Use of detergents and antibodies. *J. Biol. Chem.* **262**, 9822–9827

[358] Pérez-Rosés, R., Risco, E., Vila, R., Peñalver, P., and Cañigueral, S. (2015) Antioxidant activity of Tween-20 and Tween-80 evaluated through different in-vitro tests. *J. Pharm. Pharmacol.* **67**, 666–672

[359] Sharp, P. M., Cowe, E., Higgins, D. G., Shields, D. C., Wolfe, K. H., and Wright, F. (1988) Codon usage patterns in Escherichia coli, Bacillus subtilis, Saccharomyces cerevisiae, Schizosaccharomyces pombe, Drosophila melanogaster and Homo sapiens; a review of the considerable within-species diversity. *Nucleic Acids Res.* **16**, 8207–8211

[360] Gustafsson, C., Govindarajan, S., and Minshull, J. (2004) Codon bias and heterologous protein expression. *Trends Biotechnol.* **22**, 346–353

[361] Angov, E. (2011) Codon usage: nature's roadmap to expression and folding of proteins. *Biotechnol. J.* **6**, 650–659

[362] Sinclair, G., and Choy, F. Y. M. (2002) Synonymous codon usage bias and the expression of human glucocerebrosidase in the methylotrophic yeast, Pichia pastoris. *Protein Expr. Purif.* **26**, 96–105

[363] Agarwal, A. K., Tusie-Luna, M. T., Monder, C., and White, P. C. (1990) Expression of 11beta-hydroxysteroid dehydrogenase using recombinant vaccinia virus. *Mol. Endocrinol.* **4**, 1827–1832

[364] Gemmill, T. R., and Trimble, R. B. (1999) Overview of N- and O-linked oligosaccharide structures found in various yeast species. *Biochim. Biophys. Acta* **1426**, 227–237

[365] Hamilton, S. R., and Gerngross, T. U. (2007) Glycosylation engineering in yeast: the advent of fully humanized yeast. *Curr. Opin. Biotechnol.* **18**, 387–392

[366] Chaudhary, S., Pak, J. E., Pedersen, B. P., Bang, L. J., Zhang, L. B., Ngaw, S. M. M., Green, R. G., Sharma, V., and Stroud, R. M. (2011) Efficient expression screening of human membrane proteins in transiently transfected Human Embryonic Kidney 293S cells. *Methods* **55**, 273–280

[367] Vervecken, W., Kaigorodov, V., Callewaert, N., Geysens, S., De Vusser, K., and Contreras, R. (2004) In vivo synthesis of mammalian-like, hybrid-type N-glycans in Pichia pastoris. *Appl. Environ. Microbiol.* **70**, 2639–2646

[368] Wildt, S., and Gerngross, T. U. (2005) The humanization of N-glycosylation pathways in yeast. *Nat. Rev. Microbiol.* **3**, 119–128

[369] Aricescu, A. R., Lu, W., and Jones, E. Y. (2006) A time- and cost-efficient system for high-level protein production in mammalian cells. *Acta Crystallogr. D. Biol. Crystallogr.* **62**, 1243–1250

[370] Shi, X., and Jarvis, D. L. (2007) Protein N-glycosylation in the baculovirus-insect cell system. *Curr. Drug Targets* **8**, 1116–1125

[371] Wang, J., Bongianni, J. K., and Napoli, J. L. (2001) The N-terminus of retinol dehydrogenase type 1 signals cytosolic orientation in the microsomal membrane. *Biochemistry* **40**, 12533–12540

[372] Hollis, B. W., and Horst, R. L. (2007) The assessment of circulating 25(OH)D and 1,25$(OH)_2$D: where we are and where we are going. *J. Steroid Biochem. Mol. Biol.* **103**, 473–476

[373] Wallace, A. M., Gibson, S., de la Hunty, A., Lamberg-Allardt, C., and Ashwell, M. (2010) Measurement of 25-hydroxyvitamin D in the clinical laboratory: current procedures, performance characteristics and limitations. *Steroids* **75**, 477–488

[374] Le Goff, C., Cavalier, E., Souberbielle, J.-C., González-Antuña, A., and Delvin, E. (2015) Measurement of circulating 25-hydroxyvitamin D: A historical review. *Pract. Lab. Med.* **2**, 1–14

[375] Vogeser, M. (2010) Quantification of circulating 25-hydroxyvitamin D by liquid chromatography-tandem mass spectrometry. *J. Steroid Biochem. Mol. Biol.* **121**, 565–573

[376] Holick, M. F. (2009) Vitamin D status: measurement, interpretation, and clinical application. *Ann. Epidemiol.* **19**, 73–78

[377] Van den Ouweland, J. M. W., Vogeser, M., and Bächer, S. (2013) Vitamin D and metabolites measurement by tandem mass spectrometry. *Rev. Endocr. Metab. Disord.* **14**, 159–184

[378] Roth, H. J., Schmidt-Gayk, H., Weber, H., and Niederau, C. (2008) Accuracy and clinical implications of seven 25-hydroxyvitamin D methods compared with liquid chromatography-tandem mass spectrometry as a reference. *Ann. Clin. Biochem.* **45**, 153–159

[379] Enko, D., Fridrich, L., Rezanka, E., Stolba, R., Ernst, J., Wendler, I., Fabian, D., Hauptlorenz, S., and Halwachs-Baumann, G. (2014) 25-hydroxy-vitamin D status: limitations in comparison and clinical interpretation of serum-levels across different assay methods. *Clin. Lab.* **60**, 1541–1550

[380] Heijboer, A. C., Blankenstein, M. A., Kema, I. P., Buijs, M. M., Armas, L., Heaney, R., Bouvard, B., Annweiler, C., Salle, A., Beauchet, O., Chappard, D., Audran, M., Legrand, E., Thacher, T., Clarke, B., Justova, V., Starka, L., Wilczek, H., Pacovsky, V., Bouillon, R., Kerkhove, P., De, M., Gilbertson, T., Stryd, R., Vogeser, M., Wallace, A., Gibson, S., Hunty, A. de la, Lamberg-Allardt, C., Ashwell, M., Beastall, G., Rainbow, S., Stepman, H., Vanderroost, A., Van, U., Thienpont, L., Bouillon, R., Assche, F. Van, Baelen, H. Van, Heyns, W., Moor, P. De, Aarskog, D., Aksnes, L., Markestad, T., Rodland, O., Dick, I., Prince, R., Kelly, J., Ho, K., Hollis, B., Johnson, D., Hulsey, T., Ebeling, M., Wagner, C., Jeng, L., Yamshchikov, A., Judd, S., Blumberg, H., Martin, G., Ziegler, T., Tangpricha, V., Dahl, B., Schiodt, F., Ott, P., Wians, F., Lee, W., Balko, J., O'Keefe, G., Boutin, B., Galbraith, R., Arnaud, P., Bouillon, R., Baelen, H. Van, Moor, P. De, Speeckaert, M., Huang, G., Delanghe, J., Taes, Y., Arnaud, J., Constans, J., Koenig, K., Lindberg, J., Zerwekh, J., Padalino, P., Cushner, H., and Copley, J. (2012) Accuracy of 6 routine 25-hydroxyvitamin D assays: influence of vitamin D binding protein concentration. *Clin. Chem.* **58**, 543–548

[381] Ding, S., Schoenmakers, I., Jones, K., Koulman, A., Prentice, A., and Volmer, D. A. (2010) Quantitative determination of vitamin D metabolites in plasma using UHPLC-MS/MS. *Anal. Bioanal. Chem.* **398**, 779–789

[382] Wang, Z., Senn, T., Kalhorn, T., Zheng, X. E., Zheng, S., Davis, C. L., Hebert, M. F., Lin, Y. S., and Thummel, K. E. (2011) Simultaneous measurement of plasma vitamin D(3) metabolites, including 4β,25-dihydroxyvitamin D(3), using liquid chromatography-tandem mass spectrometry. *Anal. Biochem.* **418**, 126–133

[383] Baecher, S., Leinenbach, A., Wright, J. A., Pongratz, S., Kobold, U., and Thiele, R. (2012) Simultaneous quantification of four vitamin D metabolites in human serum using high performance liquid chromatography tandem mass spectrometry for vitamin D profiling. *Clin. Biochem.* **45**, 1491–1496

[384] Lips, P. (2007) Relative value of 25(OH)D and $1,25(OH)_2D$ measurements. *J. Bone Miner. Res.* **22**, 1668–1671

[385] Kennel, K. A., Drake, M. T., and Hurley, D. L. (2010) Vitamin D deficiency in adults: when to test and how to treat. *Mayo Clin. Proc.* **85**, 752–758

[386] Yuan, C., Kosewick, J., He, X., Kozak, M., and Wang, S. (2011) Sensitive measurement of serum 1α,25-dihydroxyvitamin D by liquid chromatography/tandem mass spectrometry after removing interference with immunoaffinity extraction. *Rapid Commun. Mass Spectrom.* **25**, 1241–1249

[387] Couchman, L., Benton, C. M., and Moniz, C. F. (2012) Variability in the analysis of 25-hydroxyvitamin D by liquid chromatography–tandem mass spectrometry: The devil is in the detail. *Clin. Chim. Acta* **413**, 1239–1243

[388] Volmer, D. A., Mendes, L. R. B. C., and Stokes, C. S. (2015) Analysis of vitamin D metabolic markers by mass spectrometry: current techniques, limitations of the "gold standard" method, and anticipated future directions. *Mass Spectrom. Rev.* **34**, 2–23

[389] Aronov, P. A., Hall, L. M., Dettmer, K., Stephensen, C. B., and Hammock, B. D. (2008) Metabolic profiling of major vitamin D metabolites using Diels-Alder derivatization and ultra-performance liquid chromatography-tandem mass spectrometry. *Anal. Bioanal. Chem.* **391**, 1917–1930

[390] Hedman, C. J., Wiebe, D. A., Dey, S., Plath, J., Kemnitz, J. W., and Ziegler, T. E. (2014) Development of a sensitive LC/MS/MS method for vitamin D metabolites: 1,25 dihydroxyvitamin $D_{2\&3}$ measurement using a novel derivatization agent. *J. Chromatogr. B. Analyt. Technol. Biomed. Life Sci.* **953-954**, 62–67

[391] Duan, X., Weinstock-Guttman, B., Wang, H., Bang, E., Li, J., Ramanathan, M., and Qu, J. (2010) Ultrasensitive quantification of serum vitamin D metabolites using selective solid-phase extraction coupled to microflow liquid chromatography and isotope-dilution mass spectrometry. *Anal. Chem.* **82**, 2488–2497

[392] Netzel, B. C., Cradic, K. W., Bro, E. T., Girtman, A. B., Cyr, R. C., Singh, R. J., Grebe, S. K. G., Vogeser, M., Seger, C., Dooley, K., Rauh, M., Etter, M., Eichhorst, J., Lehotay, D., Turpeinen, U., Itkonen, O., Ahola, L., Stenman, U., Minutti, C., Lacey, J., Magera, M., Hahn, S., McCann, M., Schultze, A., Lacey, J., Minutti, C., Magera, M., Tauscher, A., Casetta, B., McCann, M., Hsing, A., Stanczyk, F., Belanger, A., Schroeder, P., Chang, L., Falk, R., Fears, T., Hart, M. Van der, Hofland, C., Bosker, F., Boer, J. den, Westerink, B., Cremers, T., Faupel-Badger, J., Fuhrman, B., Xu, X., Falk, R., Keefer, L., Veenstra, T., Moal, V., Mathieu, E., Reynier, P., Malthiery, Y., Gallois, Y., Taib, J., Beattar, C., Birr, A., Lindenbaum, A., Boudou, P., Taieb, J., Mathian, B., Badonnel, Y., Lacroix, I., Mathieu, E., Potischman, N., Falk, R., Laiming, V., Siiteri, P., Hoover, R., Weiskopf, A., Vouros, P., Cunniff, J., Binderup, E., Bjorkling, F., Binderup, L., Higashi, T., Miura, K., Kitahori, J., Shimada, K., Higashi, T., Awada, D., Shimada, K., Higashi, T., Shimada, K., Toyo'oka, T., Cookson, R., Gupte, S., Stevens, I., Watts, C., Singh, R., Taylor, R., Reddy, G., Hollis, B., Grebe, S., Taylor, R., Grebe, S., Singh, R., Inczedy, J., Lengyel, T., Ure, A., Zeng, W., Musson, D., Fisher, A., Wang, A. Q., Aggarwal, K., Choe, L., and Lee, K. (2011) Increasing liquid chromatography-tandem mass spectrometry throughput by mass tagging: a sample-multiplexed high-throughput assay for 25-hydroxyvitamin D2 and D3. *Clin. Chem.* **57**, 431–440

[393] Ogawa, S., Kittaka, H., Shinoda, K., Ooki, S., Nakata, A., and Higashi, T. (2016) Comparative evaluation of new Cookson-type reagents for LC/ESI-MS/MS assay of 25-hydroxyvitamin D3 in neonatal blood samples. *Biomed. Chromatogr.* **30**, 938–945

[394] Molnár, F., Sigüeiro, R., Sato, Y., Araujo, C., Schuster, I., Antony, P., Peluso, J., Muller, C., Mouriño, A., Moras, D., and Rochel, N. (2011) 1α,25$(OH)_2$-3-epi-vitamin D3, a natural physiological metabolite of vitamin D3: its synthesis, biological activity and crystal structure with its receptor. *PLoS One* **6**, e18124

[395] Van den Ouweland, J. M. W., Beijers, A. M., and van Daal, H. (2014) Overestimation of 25-hydroxyvitamin D3 by increased ionisation efficiency of 3-epi-25-hydroxyvitamin D3 in LC–MS/MS methods not separating both metabolites as determined by an LC–MS/MS method for separate quantification of 25-hydroxyvitamin D3, 3-epi-25-hydroxyvitamin D3 and 25-hydroxyvitamin D2 in human serum. *J. Chromatogr. B* **967**, 195–202

[396] Ende, M., and Spiteller, G. (1982) Contaminants in mass spectrometry. *Mass Spectrom. Rev.* **1**, 29–62

[397] Williams, S. (2004) Ghost peaks in reversed-phase gradient HPLC: a review and update. *J. Chromatogr. A* **1052**, 1–11

[398] Keller, B. O., Sui, J., Young, A. B., and Whittal, R. M. (2008) Interferences and contaminants encountered in modern mass spectrometry. *Anal. Chim. Acta* **627**, 71–81

[399] Schlosser, A., and Volkmer-Engert, R. (2003) Volatile polydimethylcyclosiloxanes in the ambient laboratory air identified as source of extreme background signals in nanoelectrospray mass spectrometry. *J. Mass Spectrom.* **38**, 523–525

[400] Moreno, P., and Salvadó, V. (2000) Determination of eight water- and fat-soluble vitamins in multi-vitamin pharmaceutical formulations by high-performance liquid chromatography. *J. Chromatogr. A* **870**, 207–215

[401] Priego Capote, F., Jiménez, J. R., Granados, J. M. M., and de Castro, M. D. L. (2007) Identification and determination of fat-soluble vitamins and metabolites in human serum by liquid chromatography/triple quadrupole mass spectrometry with multiple reaction monitoring. *Rapid Commun. Mass Spectrom.* **21**, 1745–1754

[402] Adamec, J., Jannasch, A., Huang, J., Hohman, E., Fleet, J. C., Peacock, M., Ferruzzi, M. G., Martin, B., and Weaver, C. M. (2011) Development and optimization of an LC-MS/MS-based method for simultaneous quantification of vitamin D2 , vitamin D3 , 25-hydroxyvitamin D2 and 25-hydroxyvitamin D3. *J. Sep. Sci.* **34**, 11–20

[403] Xie, W., Chavez-Eng, C. M., Fang, W., Constanzer, M. L., Matuszewski, B. K., Mullett, W. M., and Pawliszyn, J. (2011) Quantitative liquid chromatographic and tandem mass spectrometric determination of vitamin D3 in human serum with derivatization: a comparison of in-tube LLE, 96-well plate LLE and in-tip SPME. *J. Chromatogr. B. Analyt. Technol. Biomed. Life Sci.* **879**, 1457–1466

[404] US Department of Health and Human services Food and Drug Administration. Center for Drug Evaluation and Research (CDER). Center for Veterinary medicine (CVM) (2001) Guidance for Industry, Bioanalytical Method Validation. *http://www.fda.gov/cvm*

[405] Annesley, T. M. (2003) Ion Suppression in Mass Spectrometry. *Clin. Chem.* **49**, 1041–1044

[406] Antignac, J.-P., de Wasch, K., Monteau, F., De Brabander, H., Andre, F., and Le Bizec, B. (2005) The ion suppression phenomenon in liquid chromatography–mass spectrometry and its consequences in the field of residue analysis. *Anal. Chim. Acta* **529**, 129–136

[407] Gosetti, F., Mazzucco, E., Zampieri, D., and Gennaro, M. C. (2010) Signal suppression/ enhancement in high-performance liquid chromatography tandem mass spectrometry. *J. Chromatogr. A* **1217**, 3929–3937

[408] Grebe, S. K., and Singh, R. J. (2011) LC-MS/MS in the clinical laboratory - Where to from here? *Clin. Biochem. Rev.* **32**, 5–31

[409] Vogeser, M., and Seger, C. (2010) Pitfalls associated with the use of liquid chromatography–tandem mass spectrometry in the clinical laboratory. *Clin. Chem.* **56**, 1234–1244

[410] Stokvis, E., Rosing, H., and Beijnen, J. H. (2005) Stable isotopically labeled internal standards in quantitative bioanalysis using liquid chromatography/mass spectrometry: necessity or not? *Rapid Commun. Mass Spectrom.* **19**, 401–407

[411] Bonfiglio, King, Olah, and Merkle (1999) The effects of sample preparation methods on the variability of the electrospray ionization response for model drug compounds. *Rapid Commun. Mass Spectrom.* **13**, 1175–1185

[412] Müller, C., Schäfer, P., Störtzel, M., Vogt, S., and Weinmann, W. (2002) Ion suppression effects in liquid chromatography-electrospray-ionisation transport-region collision induced dissociation mass spectrometry with different serum extraction methods for systematic toxicological analysis with mass spectra libraries. *J. Chromatogr. B. Analyt. Technol. Biomed. Life Sci.* **773**, 47–52

[413] Van Hout, M. W. J., Niederländer, H. A. G., de Zeeuw, R. A., and de Jong, G. J. (2003) Ion suppression in the determination of clenbuterol in urine by solid-phase extraction atmospheric pressure chemical ionisation ion-trap mass spectrometry. *Rapid Commun. Mass Spectrom.* **17**, 245–250

[414] Lewis, J. G., and Elder, P. A. (2008) Serum 25-OH vitamin D2 and D3 are stable under exaggerated conditions. *Clin. Chem.* **54**, 1931–1932

[415] Lensmeyer, G., Poquette, M., Wiebe, D., and Binkley, N. (2012) The C-3 epimer of 25-hydroxyvitamin D3 is present in adult serum. *J. Clin. Endocrinol. Metab.* **97**, 163–168

[416] Higashi, T., Suzuki, M., Hanai, J., Inagaki, S., Min, J. Z., Shimada, K., and Toyo'oka, T. (2011) A specific LC/ESI-MS/MS method for determination of 25-hydroxyvitamin D3 in neonatal dried blood spots containing a potential interfering metabolite, 3-epi-25-hydroxyvitamin D3. *J. Sep. Sci.* **34**, 725–732

VI. APPENDIX

VI.1. PUBLICATIONS, PRESENTATIONS, AND AWARDS

VI.1.1. SCIENTIFIC PUBLICATIONS

Giménez-Dejoz, J., **Weber**, **S.**, Porté, S., Barski, O. A., Adamski, J., Parés, X., and Farrés, J. (2016): Characterization of AKR1B16, a novel mouse aldo-keto reductase. *Chem. Biol. Interact.*, **Submitted**

Manz, J., Rodríguez, E., ElSharawy, A., Oesau, E.-M., Petersen, B.-S., Baurecht, H., Mayr, G., **Weber**, **S.**, Harder, J., Reischl, E., Schwarz, A., Novak, N., Franke, A., and Weidinger, S. (2016): Targeted resequencing and functional testing identifies low-frequency missense variants in the gene encoding GARP as significant contributors to atopic dermatitis risk. *J. Invest. Dermatol.*, **In Press**

Weber, **S.**, Salabei, J. K., Möller, G., Kremmer, E., Bhatnagar, A., Adamski, J., and Barski, O. A. (2015): Aldo-Keto Reductase 1B15 (AKR1B15): a Mitochondrial Human Aldo-Keto Reductase with Activity towards Steroids and 3-Keto-acyl-CoA Conjugates. *J. Biol. Chem.* **290**, 6531–6545

Linder, B., **Weber**, **S.**, Dittmann, K., Adamski, J., Hahn, H., and Uhmann, A. (2015): A functional and putative physiological role of calcitriol in Patched1 / Smoothened interaction. *J. Biol. Chem.* **290**, 19614–19628

Schmitt, S., Eberhagen, C., **Weber**, **S.**, Aichler, M., and Zischka, H. (2015): Isolation of Mitochondria from Cultured Cells and Liver Tissue Biopsies for Molecular and Biochemical Analyses. *Methods Mol. Biol.* **1295**, 87–97

VI.1.2. SCIENTIFIC PRESENTATIONS

Oral & poster presentation: 18th International Workshop Enzymology and Molecular Biology of Carbonyl Metabolism – Girona (2016)

Susanne Weber, Gabriele Möller, Alexander Cecil, Verena Häfner, Cornelia Prehn, Silke Becker, Maria Kugler, Oleg A. Barski, Jerzy Adamski: AKR1B15 – In search of the biological role of AKR1B15

Poster presentation: 3nd Congress on Steroid Research (CSR) – Chicago (2015)

Susanne Weber, Matthias Negri, Pauline Banachowicz, Sandrine Marchais-Oberwinkler, Gabriele Möller, Rolf W. Hartmann, Jerzy Adamski: Structure-function relationship of 17β-HSD type 2.

Oral & poster presentation: 3nd Congress on Steroid Research (CSR) – Chicago (2015)

Susanne Weber, Gabriele Möller, Sabine Schmitt, Oleg A. Barski, Jerzy Adamski: AKR1B15: Expression of two isoforms with different properties in vivo?

Oral & poster presentation: 17th International Workshop Enzymology and Molecular Biology of Carbonyl Metabolism – Poconos (2014)

Susanne Weber, Gabriele Möller, Elisabeth Kremmer, Aruni Bhatnagar, Oleg A. Barski, Jerzy Adamski: AKR1B15 – A Steroid and acyl-CoA Metabolizing Mitochondrial Enzyme.

Oral presentation: Internal workshop at Biocrates – Innsbruck (2013)

Susanne Weber: Assay Development for Profiling Vitamin D and its Metabolites.

Oral presentation: Retreat of the Institute of Experimental Genetics – Grassau (2013)

Susanne Weber, Joshua K. Salabei, Gabriele Möller, Aruni Bhatnagar, Jerzy Adamski, Oleg A. Barski: Annotation and characterization of human AKR1B15 – A novel player in lipid metabolism?

Poster presentation: 95th Endocrine Society's Annual Meeting (ENDO) – San Francisco (2013)

Susanne Weber, Joshua K. Salabei, Gabriele Möller, Aruni Bhatnagar, Oleg A. Barski, Jerzy Adamski: AKR1B15 – a novel human mitochondrial oxidoreductase participating in steroid metabolism.

Oral & poster presentation: 2nd Congress on Steroid Research (CSR) – Chicago (2013)

Susanne Weber, Joshua K. Salabei, Gabriele Möller, Aruni Bhatnagar, Jerzy Adamski, Oleg A. Barski: AKR1B15 – A novel human steroid-metabolizing enzyme.

Oral presentation: Lecture at the University of Louisville – Louisville (2012)

Susanne Weber, Joshua K. Salabei, Gabriele Möller, Aruni Bhatnagar, Jerzy Adamski, Oleg A. Barski: In Search of Function of AKR1B15.

Oral & poster presentation: 16th International Workshop Enzymology and Molecular Biology of Carbonyl Metabolism – Plön (2012)

Susanne Weber, Joshua K. Salabei, Gabriele Möller, Aruni Bhatnagar, Jerzy Adamski, Oleg A. Barski: In Search of Function of AKR1B15.

Oral presentation: Retreat of the Institute of Experimental Genetics – Grassau (2011)

Susanne Weber: Assay Development for Profiling Vitamin D and its Metabolites.

VI.1.3. SCIENTIFIC AWARDS

***Trainee Award** at the 18th International Workshop Enzymology and Molecular Biology of Carbonyl Metabolism – Girona (2016)*

AKR1B15 – In search of the biological role of AKR1B15

***Oral presentation Award** at the 3nd Congress on Steroid Research (CSR) – Chicago (2015)*

AKR1B15: Expression of two isoforms with different properties in vivo?

***Trainee Award** at the 17th International Workshop Enzymology and Molecular Biology of Carbonyl Metabolism – Poconos (2014)*

AKR1B15 – A Steroid and acyl-CoA Metabolizing Mitochondrial Enzyme

VI.2. ABBREVIATIONS

% ($^{v}/_{v}$)	percent volume per volume
% ($^{w}/_{v}$)	percent weight per volume
°C	degree Celsius
17α-E2	17α-estradiol
1α-(OH)-D_3	1α-hydroxyvitamin D_3
1α,25-$(OH)_2$-D_2	1α,25-dihydroxyvitamin D_2
1α,25-$(OH)_2$-D_3	1α,25-dihydroxyvitamin D_3; calcitriol
24,25-$(OH)_2$-D_3	24,25-dihydroxyvitamin D_3
25-(OH)-D_2	25-hydroxyvitamin D_2
25-(OH)-D_2 [25,26,27-$^{13}C_3$]	25-hydroxyvitamin D_2 (25,26,27-$^{13}C_3$), internal standard
25-(OH)-D_3	25-hydroxyvitamin D_3
^{3}H	tritium
4-HNE	4-hydroxy-2-nonenal
Å	angstrom
Ac	acetate
AcGFP	*Aequorea coerulescens* green fluorescent protein
ACN	acetonitrile
ACP	acyl-carrier-protein
A-diol	3α,17β-androstanediol
A-dione	androstanedione
AKR	aldo-keto reductase
Amp	ampicillin
AN	androsterone
AOX1	alcohol oxidase 1
ASZ001	murine BCC cell line
BCC	basal cell carcinoma
BeWo	human placental choriocarcinoma cell line
bp	base pair(s)
BSA	bovine serum albumin
BTS	BioTech Trade & Service GmbH
cDNA	coding DNA
CDS	coding double-stranded sequence
CIL	Cambridge Isotope Laboratories
CO_2	carbon dioxide
CoA	coenzyme A
C-ol	cortisol
C-one	cortisone
cps	counts per second
CYP	cytochrome P450
DHEA	dehydroepiandrosterone
DHT	dihydrotestosterone
DMSO	dimethyl sulfoxide
DNA	deoxyribonucleic acid

dNTP(s)	deoxynucleoside triphosphates: mix of ATP, GTP, TTP, and CTP
DsRed	*Discosoma sp.* red fluorescent protein
DTT	dithiothreitol
E. coli	*Escherichia coli*
E1	estrone
E2	17β-estradiol
EDTA	ethylene-diamine-tetraacetic acid, Titriplex III
EGTA	ethylene-glycol-tetraacetic acid
ER	endoplasmic reticulum
ESI	electrospray ionization
EtOH	ethanol
FAS I	fatty acid synthase/synthesis type I
FAS II	fatty acid synthesis type II
FBS	fetal bovine serum
FCCP	carbonyl cyanide-4-(trifluoromethoxy)-phenylhydrazone
FIA	flow injection analysis
FW	forward
h	hour(s)
HaCaT	human keratinocyte cell line
HCl	hydrochloric acid
HEK-293	human embryonic kidney-293 cell line
HeLa	human cervix adenocarcinoma cell line
HMGU	Helmholtz Zentrum München GmbH
HPLC	high performance liquid chromatography
HR	homologous recombination
HRP	horse radish peroxidase
HSD	hydroxysteroid dehydrogenase
IDG	Institute of Developmental Genetics (HMGU)
IEG	Institute of Experimental Genetics (HMGU)
IMAC	immobilized metal affinity chromatography
IMI	Institute of Molecular Immunology, Service Unit Monoclonal Antibodies (HMGU)
IPTG	isopropyl-β-D-thiogalactopyranosid
IR	infrared
IS	internal standard
ITZ	itraconazole
k_{cat}	maximum substrate turnover rate
K_M	Michaelis constant
k_{cat} / K_M	catalytic efficiency
Kan	kanamycin
KAR	3-keto-acyl-reductase
KOH	potassium hydroxide
KP_i	potassium phosphate buffer
LB	lysogeny broth
LC	liquid chromatography
LNGFR	low-affinity nerve growth factor receptor

LOD	limit of detection
LOQ	limit of quantification
m/z	mass-to-charge ratio
MeOH	methanol
MilliQ-H_2O	double deionized water
min	minute(s)
miRNA	microRNA
ml	milliliter
$^{ml}/_{min}$	milliliter per minute
MRM	multiple reaction monitoring
mRNA	messenger RNA
MS/MS	tandem mass spectrometry
mt	mitochondrial
NaP_i	sodium phosphate buffer
NEB	New England BioLabs, Inc.
NHEJ	non-homologous end joining
OD_{xxx}	optical density at xxx nm wavelength
P	progesterone or pellet
P. pastoris	*Pichia pastoris*
PAGE	polyacrylamide gel electrophoresis
PAH	polycyclic aromatic hydrocarbons
PBS	phosphate buffered saline
PCC	pump-controlled cell rupture system
PCR	polymerase chain reaction
PGD_2	prostaglandin D_2
$PGF_2(\alpha)$	prostaglandin $F_2(\alpha)$
PGH_2	prostaglandin H_2
PI	protease inhibitor (Complete mini EDTA-free)
$Ptch^{WT}$	murine fibroblast cell line (expressing wild type *Ptch*)
$Ptch^{-/-}$	murine *Ptch* deficient fibroblast cell line
RFU	relative fluorescence units
RNA	ribonucleic acid
rpm	rounds per minute
RT	reverse transcriptase
RV	reverse
RVD	repeat-variable di-residue
S. cerevisiae	*Saccharomyces cerevisiae*
SCFA	short-chain fatty acid
SD	standard deviation
SDR	short-chain dehydrogenase/reductase
SDS	sodium dodecyl sulfate
sec	second(s)
SEM	standard error of the mean
SGBS	human Simpson-Golabi-Behmel syndrome (SGBS) preadipocyte cell strain
SN	supernatant
Spec	spectinomycin

T	testosterone
TALEN	transcription activator-like effector nuclease
TEMED	tetramethylethylenediamine
Tes	2-{[1,3-dihydroxy-2-(hydroxymethyl)propan-2-yl]amino}-ethanesulfonic acid
Tet	tetracycline
t_R	retention time
Tris	tris(hydroxymethyl)aminomethane
U	unit(s)
U of L	University of Louisville, USA
UMG	University Medical Center Göttingen
UPenn	University of Pennsylvania, USA
V	volt
$v_{0\ (xx\ M)}$	initial turnover rate at xx M
(V)LCFA	(very) long-chain fatty acid
WT	wild type
x *g*	times acceleration of gravity
X-Gal	5-bromo-4-chloro-3-indolyl-β-D-galactopyranoside
YNB	yeast nitrogen base
YPD	yeast extract-peptone-dextrose
ZFN	Zinc-finger nuclease
Δ4-AE	Δ4-androstenedione
$\Delta\Psi_m$	mitochondrial membrane potential
$\varepsilon_{260\ nm}$	extinction coefficient at 260 nm
λ_{em}	emission wavelength
λ_{ex}	excitation wavelength
Ω	ohm

VI.3. Monoclonal antibody clones

#	clone	species	subclass	epitope
1	1D12	rat	IgG2c	AKB-2
2	1E6	rat	IgG2c	AKB-2
3	2D4	rat	IgG1	AKB-2
4	2D5	rat	IgG2c	AKB-2
5	2E5	rat	IgG2c	AKB-2
6	3D1	rat	IgG2c	AKB-2
7	3D12	rat	IgG2c	AKB-2
8	3G8	rat	IgG2c	AKB-2
9	3H9	rat	IgG2c	AKB-2
10	4A2	rat	IgG1	AKB-2
11	4C6	rat	IgG2c	AKB-2
12	5F1	rat	IgG2c	AKB-2
13	5H3	rat	IgG2c	AKB-2
14	7E2	rat	IgG2c	AKB-2
15	7F3	rat	IgG2c	AKB-2
16	9H6	rat	IgG2c	AKB-2
17	10E8	rat	IgG2c	AKB-2
18	11E3	rat	IgG2c	AKB-2
19	11F11	rat	IgG2c	AKB-2
20	12H4	rat	IgG2c	AKB-2
21	15D2	rat	IgG2c	AKB-2
22	15F2	rat	IgG2c	AKB-2
23	16E7	rat	IgG2c	AKB-2
24	17A4	rat	IgG2c	AKB-2
25	17H2	rat	IgG2c	AKB-2
26	19D12	rat	IgG2c	AKB-2
27	19E5	rat	IgG2a	AKB-2
28	20F10	rat	IgG2c	AKB-2
29	21D11	rat	IgG2c	AKB-2
30	21E2	rat	IgG2c	AKB-2
31	23H6	rat	IgG1	AKB-2
32	7F6	rat	IgG2c	AKB-1
33	1G11	rat	IgG1	AKB-3
34	10B7	rat	IgG1	AKB-3
35	19D3	rat	IgG2a	AKB-3
36	7B1	rat	IgG1	AKB-2
37	9A5	rat	IgG2a	AKB-2
38	18B7	rat	IgG2a	AKB-2
39	1C4	rat	IgG1	AKB-1
40	6C11	rat	IgG2B	AKB-1
41	7H1	rat	IgG1	AKB-1
42	8B11	rat	IgG2a	AKB-1
43	9E1	rat	IgG2a	AKB-1
44	10B1	rat	IgG1	AKB-1
45	10H6	rat	IgG1	AKB-1
46	11B1	rat	IgG2a	AKB-1
47	11E1	rat	IgG1	AKB-1
48	11E6	rat	IgG1	AKB-1
49	11F10	rat	IgG2a	AKB-1
50	13A6	rat	IgG2a	AKB-1
51	13B3	rat	IgG1	AKB-1
52	14G4	rat	IgG1	AKB-1
53	17E4	rat	IgG1	AKB-1
54	9E11	rat	IgG1	AKB-3
55	10A4	rat	IgG1	AKB-3
56	10A9	rat	IgG1	AKB-3
57	12B11	rat	IgG1	AKB-3
58	13E3	rat	IgG1	AKB-3
M1	26G6	mouse	IgG2a	AKB-2
M2	25F6	mouse	IgG2a	AKB-1
M3	29A4	mouse	IgG2a	AKB-1
M4	29D4	mouse	IgG2b	AKB-1
M5	31F6	mouse	IgG2a	AKB-1
M6	31G8	mouse	IgG2a	AKB-1
M7	32A8	mouse	IgG2b	AKB-1
M8	32E10	mouse	IgG2b	AKB-1
M9	32H4	mouse	IgG1	AKB-1

The specificity of monoclonal antibody clones was analyzed in Western blots using the crude monoclonal primary antibody supernatants and the respective HRP-conjugated subclass specific secondary antibodies in a dilution of 1:10 and 1:1000 in 0.5 % milk solution, respectively.

VI.4. Alignment of AKR1B15.1, AKR1B15.2, and AKR1B10 cDNA sequences

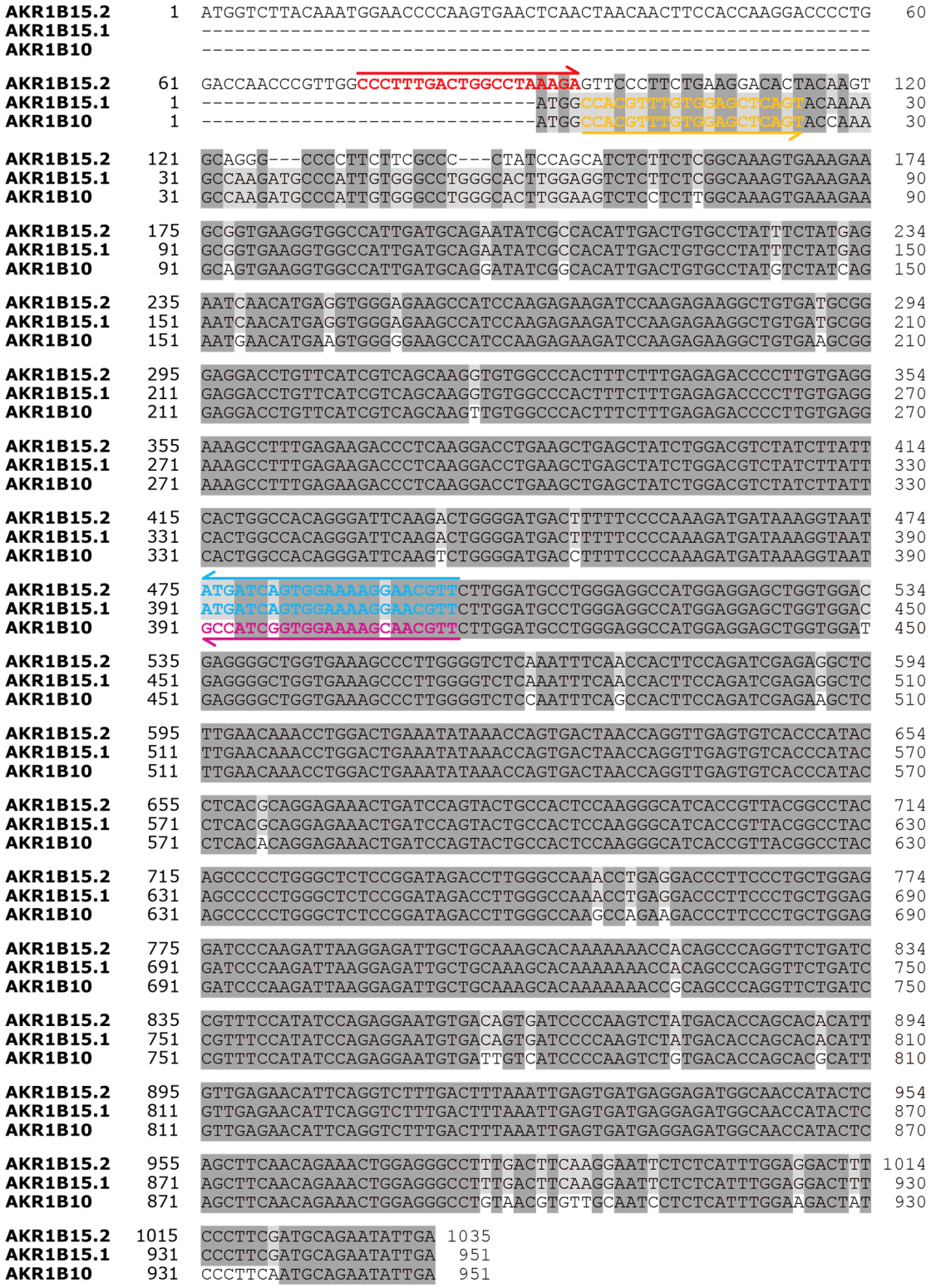

The annealing sites of the AKR1B15.1-TK-FW primer (# 2714) recognizing *AKR1B15.1* as well as *AKR1B10* transcripts are colored in yellow, the annealing site of the *AKR1B15.2* transcript specific AKR1B15.2-TK-FW primer (# 2715) in red, the annealing sites of the *AKR1B15* specific AKR1B15-TK-LocR1 primer (# 2713) in blue, and the annealing site of the *AKR1B10* specific AKR1B10-TK-RV primer (# 2716) in magenta.

VI.5. OUTPUTS FROM LOCALIZATION PREDICTIONS

VI.5.1. MITOPROT II (V1.101) PREDICTION

	cleavage site	**probability of export to mitochondria**
AKR1B15.1	not predictable	0.1550
AKR1B15.1 S8R	not predictable	0.3985
AKR1B15.2	not predictable	0.0080
AKR1B10	not predictable	0.1196
AKR1B10 P24L	not predictable	0.1455

VI.5.2. IPSORT PREDICTION

	signal peptide (hydropathy value ≥ 0.953)	**mitochondrial targeting peptide** (net charge value ≥ 0.083)	**indexing: AI1** pattern: 221121122 (ins/del ≤ 3)
AKR1B15.1	No (0.273)	**Yes** (0.100)	Match
AKR1B15.1 S8R	No (0.027)	**Yes** (0.133)	Match
AKR1B15.2	No (-1.233)	No (-0.067)	No match
AKR1B10	No (0.273)	No (0.100)	No match
AKR1B10 P24L	No (0.273)	No (0.100)	No match

AI1 index: 0 = DEGHKN, 1 = IR, 2 = ACFLMPQSTVWY.

VI.5.3. PSORT II PREDICTION

	predicted localization in [%]						
	cyto	**nucl**	**vacu**	**secr**	**Golgi**	**skel**	**mito**
AKR1B15.1	65.2	13.0	4.3	4.3	4.3	4.3	4.3
AKR1B15.1 S8R	65.2	13.0	4.3	4.3	4.3	4.3	4.3
AKR1B15.2	60.9	17.4	4.3	4.3	4.3	4.3	4.3
AKR1B10	65.2	26.1	4.3	4.3	0.0	0.0	0.0
AKR1B10 P24L	69.6	17.4	4.3	4.3	0.0	4.3	0.0

cyto, cytosolic protein; nucl, nuclear protein; vacu, vacuolar protein; secr, secretory protein; Golgi, protein of the Golgi apparatus; skel, cytoskeletal protein; mito, mitochondrial protein.

VI.5.4. PrediSi prediction

	cleavage site	secretion	score
AKR1B15.1	26	no	0.18529
AKR1B15.1 S8R	26	no	0.18529
AKR1B15.2	41	no	0.07361
AKR1B10	221	no	0.05592
AKR1B10 P24L	26	no	0.15140

VI.5.5. SignalP 4.1 Server

	signal peptide	score
AKR1B15.1	no	0.133
AKR1B15.1 S8R	no	0.137
AKR1B15.2	no	0.105
AKR1B10	no	0.120
AKR1B10 P24L	no	0.130

VI.5.6. TargetP 1.1 Server

	score			Loc	RC	TPlen
	mTP	**SP**	**other**			
AKR1B15.1	0.133	0.088	0.779	any other	2	no
AKR1B15.1 S8R	0.269	0.059	0.682	any other	3	no
AKR1B15.2	0.085	0.085	0.887	any other	1	no
AKR1B10	0.096	0.077	0.857	any other	2	no
AKR1B10 P24L	0.084	0.098	0.860	any other	2	no

mTP, mitochondrial target peptide/protein; SP, secretory protein; other, any other localization; Loc, predicted localization; RC, reliability class (1 and 5 indicate the strongest and lowest prediction level, respectively, depending on the difference between the highest and the second highest score); TPlen, predicted presequence length (cleaved amino acids).

VI.6. CONSTRUCTED *AKR1B15* TALEN PAIRS

TALEN knock-out	**AKR1B15.1**	
#	**(36)**	**(40)**
TAL1 (sense) RVD sequence	NH NH HD HD NI HD NH NG NG NG NH NG NH NH NI NH	NH NH HD HD NI HD NH NG NG NG NH NG NH NH NI NH HD NG HD NI
TAL2 (antisense) RVD sequence	NH HD HD HD NI NH NH HD HD HD NI HD NI NI NG NH NH NH HD NI	NH HD HD HD NI NH NH HD HD HD NI HD NI NI NG NH NH
target sense sequence (TAL1 - spacer - TAL2) (cut site: ¦)	T GGCCACGTTTGTGGAG ctcagtacaa¦aagccaaga TGCCCATTGTGGGCCTGGGC A	T GGCCACGTTTGTGGAGCTCA gtacaaaagc¦caagatgc CCATTGTGGGCCTGGGC A
off target counts	1 (*AKR1B10*)	1 (*AKR1B10*)

TALEN knock-out	**AKR1B15.2**	
#	**(66)**	**(67)**
TAL1 (sense) RVD sequence	HD NI NI HD NG NI NI HD NI NI HD NG NG HD HD NI HD HD NI	HD NI NI HD NG NI NI HD NI NI HD NG NG HD HD NI HD HD NI NI
TAL2 (antisense) RVD sequence	HD NI NI NI NH NH NH HD HD NI NI HD NH NH NH NG	HD NI NI NI NH NH NH HD HD NI NI HD NH NH NH
target sense sequence (TAL1 - spacer - TAL2) (cut site: ¦)	T CAACTAACAACTTCCACCA aggacccc¦tggacca ACCCGTTGGCCCTTTG A	T CAACTAACAACTTCCACCAA ggacccct¦ggaccaa CCCGTTGGCCCTTTG A
off target counts	-	-

TALEN knock-out	**AKR1B15-E2**	
#	**(25)**	**(26)**
TAL1 (sense) RVD sequence	NG NG NG HD NI NH NG HD NG HD NG NG HD NG HD	NG NG NG HD NI NH NG HD NG HD NG NG HD NG HD NH
TAL2 (antisense) RVD sequence	HD NI NI NG NH NH HD HD NI HD HD NG NG HD NI HD HD NH HD	HD NI NI NG NH NH HD HD NI HD HD NG NG HD NI HD HD NH
target sense sequence (TAL1 - spacer - TAL2) (cut site: ¦)	T TTTCAGTCTCTTCTC ggcaaagt¦gaaagaa GCGGTGAAGGTGGCCATTG A	T TTTCAGTCTCTTCTCG gcaaagtg¦aaagaag CGGTGAAGGTGGCCATTG A
off target counts	-	-

Results from the TAL effector Nucleotide Targeter 2.0 algorithm for the construction of TALENs knocking-out either AKR1B15.1 (AKR1B15.1), AKR1B15.2 (AKR1B15.2), or both AKR1B15 isoforms (AKR1B15-E2). Two TALEN pairs with lowest off target counts and highest NH levels were selected per knock-out target. Listed are RVD sequences of selected TAL1 (binds to sense strand) and TAL2 (binds to antisense strand) pairs as well as the respective target sequence, position of the double-strand break within the spacer sequence, and number of off targets recognized by the respective TALEN pair.

VI.7. PRIMERS

VI.7.1. VECTOR PRIMERS

int. #	**primer name** sequence (5′→ 3′)	($T_{annealing}$)	suitable for … vectors / plasmid constructs
# **1927**	**pET15b_rev** GCTAGTTATTGCTCAGCGGTG	(50-58 °C)	pET28a(+)
# **2051**	**T7_for** AATACGACTCACTATAGGG	(50-53 °C)	pcDNA3.1(+), N-myc-pcDNA3, pcDNA4-myc/His B, pET28a(+)
# **2228**	**pIRES-hrGFP-1α_rev** GTCCTTATCATCGTCGTCTT	(53 °C)	pIRES-hrGFP-1α
# **2229**	**pcDNA3_r** GGGCAAACAACAGATGGCTGGC	(51-58 °C)	pcDNA3.1(+), N-myc-pcDNA3
# **2230**	**pcDNA3_for2** AGAGAACCCACTGCTTACTGGCTTAT	(53-58 °C)	pcDNA3.1(+)
# **2282**	**5'-AOX1_fw** GACTGGTTCCAATTGACAAGC	(55-56 °C)	pPICZ-A
# **2283**	**3'-AOX1_rv** GCAAATGGCATTCTGACATCC	(55-56 °C)	pPICZ-A
# **2482**	**pcDNA4_rev** GGTGATGGTGATGATCGGTATG	(51 °C)	pcDNA4-myc/His B
# **2698**	**pCR8_F1** TTGATGCCTGGCAGTTCCCT	(52-54 °C)	pFUS-A/B
# **2699**	**pCR8_R1** CGAACCGAACAGGCTTATGT	(52-54 °C)	pFUS-A/B
# **2700**	**TAL_F1** TTGGCGTCGGCAAACAGTGG	(55-57 °C)	pcGoldyTALEN
# **2701**	**TAL_R2** GGCGACGAGGTGGTCGTTGG	(52-57 °C)	pcGoldyTALEN
# **2702**	**SeqTALEN_5-1** CATCGCGCAATGCACTGAC	(52-53 °C)	pcGoldyTALEN
# **2726**	**pTC14_F2** CAAGCCTGATTGGGAGAAAA	(52 °C)	TALEN module vectors
# **2727**	**pTC14_F1** CCTACTCAGGAGAGCGTTCA	(52 °C)	TALEN pLR plasmids
# **2776**	**pCMV-DsRed-FW** AATGTCGATACAACTCCGC	(52 °C)	pCMV-βGal, pCMV-Duplirep, pCMV-hLuci, pMACS-ΔLNGFR
# **2822**	**CMV-FW** CGCAAATGGGCGGTAGGCGTG	(59 °C)	pCMV-Duplirep reporter
# **3002**	**Goldy-Dra3-FW ST** TCAGCTCATTTTTTAACCAATAG	(54 °C)	pcGoldyTALEN (*Dra*III cloning site)

int. #	**primer name** sequence (5′→ 3′)	($T_{annealing}$)	suitable for … vectors / plasmid constructs
# **3003**	**Goldy-Dra3-RV ST** GTTCCGATTTAGTGCTTTACG	(54 °C)	pcGoldyTALEN (*Dra*III cloning site)
# **24436**	**T3-for** AATTAACCCTCACTAAAGGG	(53 °C)	pIRES-hrGFP-1α
# **61748**	**pAcGFPN1-for1_404** CGGTTTGACTCACGGGGATTTCCAAGTC	(57 °C)	pAcGFP-N1

Vector primers were used for sequencing or screening of plasmids. The listed annealing temperatures ($T_{annealing}$) represent temperatures applied in sequencing reactions using the BigDye3.1 Terminator v3.1 Cycle Sequencing Kit or colony screens using the lab-made House-*Taq* at which the primers worked well.

VI.7.2. CLONING PRIMERS

VI.7.2.1. CLONING OF FULL LENGTH PROTEIN ENCODING SEQUENCES

int. #	**primer name** sequence (5′→ 3′)	($T_{annealing}$)	cloning of… (feature)
# **2242**	**hsHSD17B12_EcoR1-FW** aaaagaattcATGGAGAGCGCTCTCCCCG	(58 °C)	human *HSD17B12* into pPICZ-A
# **2269**	**hsHSD17B12_TEV_Not1-RV_neu** ttttagcggccgcc*ctgaaaataaagattctc*GTTCTTCTTGGTTTTCTTCAGATAGTG	(58 °C)	human *HSD17B12* into pPICZ-A (contains C-terminal TEV protease recognition site)
# **2533**	**AKR1B15-344-Not1-FW** aaatggcggccgcaccatgggcagcagccat*catcatcatcatcac*agcagcggc*ctggtgccgcgcggcagcc*catATGGTCTTACAAATGGAACCCCAAGTGAACTCA	(53-57 °C)	human *AKR1B15.2* into pIRES-hrGFP-1α (contains N-terminal His_6 tag and thrombin recognition site)
# **2534**	**AKR1B15-Xho1-RV** aaagtcctcgagTCAATATTCTGCATCGAAGGGAAAGT	(53-57 °C)	human *AKR1B15.2* into pIRES-hrGFP-1α (*)
# **2541**	**AKR1B15-316-Hind3-FW** ttttaagcttATGGCCACGTTTGTGGAGCTC	(57-58 °C)	human *AKR1B15.1* into pcDNA4 – myc/His B
# **2542**	**AKR1B15-344-Hind3-FW** ttttaagcttATGGTCTTACAAATGGAACCCCA	(57-63 °C)	human *AKR1B15.2* into pcDNA3.1(+), pcDNA4-myc/His B
# **2543**	**AKR1B15-Not1-RV** ttttgcggccgctATATTCTGCATCGAAGGGAAAGT	(58 °C)	human *AKR1B15* into pcDNA4-myc/His B
# **2544**	**AKR1B15-316-Not1-FW** ttttgcggccgcaaGCCACGTTTGTGGAGCTC	(54-58 °C)	human *AKR1B15.1* into N-myc-pcDNA3 (without start codon)
# **2545**	**AKR1B15-344-Not1-FW** ttttgcggccgcaaGTCTTACAAATGGAACCCCA	(54-58 °C)	human *AKR1B15.2* into N-myc-pcDNA3 (without start codon)

int. #	**primer name** sequence (5′→ 3′)	($T_{annealing}$)	cloning of… (feature)
# **2546**	**AKR1B15-Xho1-RV** tttctcgagTCAATATTCTGCATCGAAGGGAAAGT	(54-63 °C)	human *AKR1B15* into cDNA3.1(+), N-myc-pcDNA3, pET28a(+)
# **2799**	**AKR1B15(344)-NdeI-FW** ttttcatATGGTCTTACAAATGGAACCCCAAG	(56 °C)	human *AKR1B15.2* into pET28a(+)
# **2883**	**AKR1A1-NdeI-FW** ttttcatATGGCGGCTTCCTGTGTTC	(60 °C)	human *AKR1A1* into pET28a(+)
# **2884**	**AKR1A1-XhoI-RV** ttttctcgagTCAGTACGGGTCATTAAAGGG	(60 °C)	human *AKR1A1* into pET28a(+)
# **2913**	**AKR1C3-XhoI-RV** ttttctcgagTTAATATTCATCTGAATATGGATAAT	(58 °C)	human *AKR1C3* into pET28a(+)
# **2914**	**AKR1C3-NdeI-FW-1** ttttcatATGGATTCCAAACACCAGTGTG	(58 °C)	human *AKR1C3* into pET28a(+)
# **2943**	**InFus-pLNGFR-Dra3-FW** agggcgatggcccacCCAGATATACGCGTTGACATTG	(55 °C)	CMV-*ΔLNGFR* into final pcGoldyTALEN constructs (In-Fusion technology)
# **2944**	**InFus-pLNGFR-Dra3-RV** agggtgatggttcacCTGCTATAATCAGCCATACCAC	(55 °C)	CMV-*ΔLNGFR* into final pcGoldyTALEN constructs (In-Fusion technology)
# **2945**	**InFus-pR-GFP-Dra3-FW** agggcgatggcccacGCTCACATGTTCTTTCCTGCG	(55 °C)	CMV-*DsRed* or CMV-*AcGFP* into pcGoldyTALEN constructs (In-Fusion technology)
# **2946**	**InFus-pR-GFP-Dra3-RV** agggtgatggttcacCAAACCACAACTAGAATGCAG TG	(55 °C)	CMV-*DsRed* or CMV-*AcGFP* into pcGoldyTALEN constructs (In-Fusion technology)

These cloning primers were used for the amplification of encoding sequences for cloning. The listed annealing temperatures ($T_{annealing}$) represent temperatures applied in reactions using the Phusion High-Fidelity DNA Polymerase or 2x CloneAmp HiFi PCR-Mix at which the primers worked well.
Protein encoding sequences in primers are shown in capital letters, restriction enzyme sites are underlined, and extra features are highlighted in italic.

VI.7.2.2. CLONING OF N-TERMINI ENCODING SEQUENCES INTO PACGFP-N1

int. #	**primer name** sequence (5′→ 3′)	($T_{annealing}$)	cloning of … into pAcGFP-N1
# **2541**	**AKR1B15-316-Hind3-FW** ttttaagcttATGGCCACGTTTGTGGAGCTC	(57 °C)	5′end of human *AKR1B15.1* or *AKR1B10*
# **2542**	**AKR1B15-344-Hind3-FW** ttttaagcttATGGTCTTACAAATGGAACCCCA	(57 °C)	5′end of human *AKR1B15.2*
# **2704**	**15l-RV-2** tttaccggTAGGCCAGTCAAAGGGCCAAC	(57 °C)	5′end of human *AKR1B15.2* (*) (encoding for Met1-Leu30)

int. #	**primer name** sequence (5′→ 3′)	($T_{annealing}$)	cloning of … into pAcGFP-N1
# **2705**	**15sl-RV-1** tttaccggTTCTTTCACTTTGCCGAGAAGAGA	(57 °C)	5′end of human *AKR1B15.1* or *AKR1B15.2* (*) (encoding for Met1-Glu30 or Met1-Glu58)
# **2707**	**10-RV-1** tttaccggTTCTTTCACTTTGCCAAGAGGAGA	(57 °C)	5′end of human *AKR1B10* (*) (encoding for Met1-Glu30)
# **2708**	**1015-RV-3** tttaccggTGCATCAATGGCCACCTTCAC	(57 °C)	5′end of human *AKR1B10*, *AKR1B15.1*, or *AKR1B15.2* (*) (encoding for Met1-Ala38 or Met1-Ala66)
# **2711**	**15s-RV-4** tttaccggTCCGAGAAGAGACCTCCAAGTGC	(57 °C)	5′end of human *AKR1B15.1* (*) (encoding for Met1-Gly26)

These cloning primers were used for the amplification of 5′ ends of transcripts encoding for N-terminal peptides of variable length. RV primers marked by (*) were also used in colony screens. The listed annealing temperatures ($T_{annealing}$) represent temperatures applied in amplification and screening reactions using the lab-made House-*Taq* at which the primers worked well.
Peptide encoding sequences in primers are shown in capital letters, restriction enzyme sites are underlined.

VI.7.2.3. CLONING OF TALEN TARGET SITES INTO PCMV-UNIV-DUPLIREP

int. #	**primer name** sequence (5′→ 3′)	cloning of … TAL1/TAL2 target site in pCMV-Univ-Duplirep
# **2816**	**AKR1B15.2_Sense** cgTCAACTAACAACTTCCACCAAGGACCCCTG GACCAACCCGTTGGCCCTTTGA	pcGoldyTALEN-AKR1B15.2(66), pcGoldyTALEN-AKR1B15.2(67)
# **2817**	**AKR1B15.2_AntiSense** TCAAAGGGCCAACGGGTTGGTCCAGGGGTCC TTGGTGGAAGTTGTTAGTTGA	pcGoldyTALEN-AKR1B15.2(66), pcGoldyTALEN-AKR1B15.2(67)
# **2818**	**AKR1B15.1_Sense** cgTGGCCACGTTTGTGGAGCTCAGTACAAAAG CCAAGATGCCCATTGTGGGCCTGGGCA	pcGoldyTALEN-AKR1B15.1(36), pcGoldyTALEN-AKR1B15.1(40)
# **2819**	**AKR1B15.1_AntiSense** TGCCCAGGCCCACAATGGGCATCTTGGCTTTT GTACTGAGCTCCACAAACGTGGCCA	pcGoldyTALEN-AKR1B15.1(36), pcGoldyTALEN-AKR1B15.1(40)
# **2820**	**AKR1B15-E2_Sense** cgTTTTCAGTCTCTTCTCGGCAAAGTGAAAGAA GCGGTGAAGGTGGCCATTGA	pcGoldyTALEN-AKR1B15-E2(25), pcGoldyTALEN-AKR1B15-E2(26)
# **2821**	**AKR1B15-E2_AntiSense** TCAATGGCCACCTTCACCGCTTCTTTCACTTTG CCGAGAAGAGACTGAAAA	pcGoldyTALEN-AKR1B15-E2(25), pcGoldyTALEN-AKR1B15-E2(26)

These cloning primers were used for the generation of double-stranded TALEN pair target sequences for cloning into pCMV-Univ-Duplirep vectors. Sense and AntiSense primer pairs were annealed via an incubation at 99 °C and slow cool down.
TALEN pair target sequences in primers are shown in capital letters, 5′-cg overhangs for directional cloning via *Bst*BI/*Nru*I cloning sites are underlined.

VI.7.3. SITE-DIRECTED MUTAGENESIS PRIMERS

int. #	**primer name** sequence (5′→ 3′)	($T_{annealing}$)	mutagenesis of … ⇨ mutant
# **2680**	**AKR1B15-short_Mut-S8R-FW** *Phos*-TTGTGGAGCTCAG**G**ACAAAAGCCAAG	(62 °C)	human AKR1B15.1 ⇨ Ser8Arg
# **2681**	**AKR1B15-short_Mut-S8R-RV** *Phos*-CTTGGCTTTTGT**C**CTGAGCTCCACAA	(62 °C)	human AKR1B15.1 ⇨ Ser8Arg
# **2919**	**10-P24L-Muta-FW** CTTGGAAGTCTC**T**TCTTGGCAAAG	(55 °C)	human AKR1B10 ⇨ Pro24Leu
# **2920**	**10-P24L-Muta-RV** CTTTGCCAAGA**A**GAGACTTCCAAG	(55 °C)	human AKR1B10 ⇨ Pro24Leu
# **2921**	**10-K22R-Muta-FW** GGCACTTGGA**G**GTCTCCTCTTG	(55 °C)	human AKR1B10 ⇨ Lys22Arg
# **2922**	**10-K22R-Muta-RV** CAAGAGGAGAC**C**TCCAAGTGCC	(55 °C)	human AKR1B10 ⇨ Lys22Arg

Site-directed mutagenesis primers were used for single nucleotide exchanges in open reading frames of plasmids. The listed annealing temperatures ($T_{annealing}$) represent temperatures applied in site-directed mutagenesis reactions using either the Phusion High-Fidelity DNA Polymerase or the QuikChange Lightning Site-Directed Mutagenesis Kit at which the primers worked well.
Phos- indicates a 5′-phosphorylation of the primers, sites of the nucleotide exchange are underlined and highlighted in bold.

VI.7.4. SEMI-QUANTITATIVE RT-PCR PRIMERS

int. #	**primer name** sequence (5′→ 3′)	($T_{annealing}$)	target gene transcript (feature)
# **1727**	**hGAPDH qRT rev 1** ATGACAAGCTTCCCGTTCT	(50 °C)	human *GAPDH* (house-keeper)
# **1728**	**hGAPDH qRT for 1** AGTCAACGGATTTGGTCGTA	(50 °C)	human *GAPDH* (house-keeper)
# **2713**	**AKR1B15-TK-LocR1** AACGTTCCTTTTCCACTGATCAT	(57 °C)	human *AKR1B15* (for both *AKR1B15* transcripts)
# **2714**	**AKR1B15.1-TK-FW** CCACGTTTGTGGAGCTCAGT	(57 °C)	human *AKR1B15.1* and *AKR1B10*
# **2715**	**AKR1B15.2-TK-FW** CCCTTTGACTGGCCTAAAGA	(57 °C)	human *AKR1B15.2*
# **2716**	**AKR1B10-TK-RV** AACGTTGCTTTTCCACCGATGGC	(57 °C)	human *AKR1B10*
# **2853**	**LNGFR_human_fw** AGGACAAGCAGAACACCGTG	(57 °C)	human *LNGFR* (for endogenous *LNGFR* transcripts)

int. #	**primer name** sequence (5′→ 3′)	($T_{annealing}$)	target gene transcript (feature)
# **2854**	**LNGFR_human_rev** GCAGAGCCGTTGAGAAGCTT	(57 °C)	human *LNGFR* (for endogenous *LNGFR* transcripts)
# **2994**	**LNGFR_MiltiRT_FW** CTGCAAAGCCTGCAACCTG	(55 °C)	human *LNGFR* (for endogenous *LNGFR* and exogenous pMACS-*ΔLNGFR* transcripts)
# **2995**	**LNGFR_MiltiRT_RV** GGGGTGTGGACCGTGTAATC	(55 °C)	human *LNGFR* (for endogenous *LNGFR* and exogenous pMACS-*ΔLNGFR* transcripts)

Semi-quantitative RT-PCR primers were used for the detection and rough quantification of transcripts in cDNA samples resulting from human tissues or cell lines. The listed annealing temperatures ($T_{annealing}$) for primers worked well in amplification reactions using the DreamTaq DNA Polymerase.

VI.7.5. OTHER PRIMERS

int. #	**primer name** sequence (5′→ 3′)	($T_{annealing}$)	application
# **2005**	**anchored_Oligo(dT)$_{18}$** TTTTTTTTTTTTTTTTTTNV		cDNA synthesis
# **2231**	**AKR1B15_5'_rev** AGGCCCACAATGGGCATCTT	(58 °C)	sequencing of 5′ cloning sites of human *AKR1B15.1* constructs
# **2232**	**AKR1B15_3'_for** AGCTTCAACAGAAACTGGAGGG	(58 °C)	sequencing of 3′ cloning sites of human *AKR1B15* constructs
# **2551**	**AKR1B15-RV-n2** CTCCAAATGAGAGAATTCCTTG	(51-52 °C)	screening of *AKR1B15* constructs
# **2592**	**AKR1B15-5'-RV-2** CCTTCACCGCTTCTTTCACT	(55 °C)	sequencing of 5′ cloning sites of human *AKR1B15* constructs
# **2991**	**3'DsRed-RV** CAGCTTGGAGTCCACGTA	(54 °C)	sequencing of CMV-*DsRed* marker (*)
# **2992**	**3'AcGFR-RV** GTGGTTATCGGGCAGCAG	(54 °C)	sequencing of CMV-*AcGFP* marker (*)
# **2993**	**3'LNGFR-RV** CATCACTGTGGTCACCAC	(54 °C)	sequencing of CMV-*ΔLNGFR* marker (*)
# **3035**	**3'DsRed-FW** ATCCACAAGGCGCTGAAG	(54 °C)	sequencing of 3′ cloning sites of *DsRed* constructs
# **3036**	**3'AcGFR-FW** CCGACAAGGCCAAGAATG	(54 °C)	sequencing of 3′ cloning sites of *AcGFP* constructs
# **3037**	**3'LNGFR-FW** ATTCCGACGAGGCCAACC	(54 °C)	sequencing of 3′ cloning sites of *ΔLNGFR* constructs

Except the cDNA synthesis primer # 2005, listed primers were used for the sequencing of cloning products. Internal RV primers marked by (*) were also used in colony screens. The given annealing temperatures ($T_{annealing}$) represent temperatures applied in sequencing reactions using the BigDye3.1 Terminator v3.1 Cycle Sequencing Kit or colony screens using the lab-made House-*Taq* at which the primers worked well.

VI.8. PARAMETERS OF MRMS USED WITHIN THE VITAMIN D LC-MS/MS METHOD DEVELOPMENT

compound	adduct	Q_1 [m/z]	Q_3 [m/z]	DP [V]	EP [V]	CE [V]	CXP [V]
24,25-$(OH)_2$-D_3 & 1α,25-$(OH)_2$-D_3	H^+	417.300	91.100	166	10	83	6
	H^+	417.300	159.100	120	10	31	20
	Li^+	**423.174**	**91.000**	**110**	**10**	**100**	**14**
	Li^+	**423.174**	**128.000**	**110**	**10**	**120**	**14**
	Li^+	**423.323**	**77.000**	**181**	**10**	**127**	**12**
25-(OH)-D_3 & 1α-(OH)-D_3	H^+	**401.289**	**90.900**	**101**	**10**	**79**	**12**
	H^+	401.300	159.200	61	15	31	20
	H^+	401.314	91.100	126	10	75	14
	H^+	401.314	105.000	126	10	73	14
	Li^+	**407.185**	**105.000**	**230**	**10**	**50**	**12**
	Li^+	**407.326**	**90.900**	**186**	**10**	**101**	**14**
vitamin D_3	H^+	**385.300**	**259.200**	**86**	**10**	**21**	**6**
1α,25-$(OH)_2$-D_2	H^+	429.373	90.900	171	10	87	10
	H^+	429.373	79.000	171	10	83	12
	Li^+	**435.314**	**91.000**	**141**	**10**	**99**	**14**
	Li^+	**435.314**	**77.100**	**141**	**10**	**123**	**6**
25-(OH)-D_2	H^+	413.332	91.000	131	10	81	10
	H^+	413.332	105.000	131	10	65	18
	Li^+	**419.323**	**361.300**	**181**	**10**	**35**	**26**
	Li^+	**419.323**	**77.000**	**181**	**10**	**127**	**12**
vitamin D_2	H^+	**397.325**	**91.100**	**61**	**10**	**83**	**10**
	H^+	**397.325**	**105.100**	**61**	**10**	**51**	**12**
	Li^+	403.300	91.000	171	10	103	14
	Li^+	403.300	77.100	171	10	121	12
internal standard (25-(OH)-D_2 [25,26,27-$^{13}C_3$])	Li^+	**422.323**	**361.300**	**181**	**10**	**35**	**26**
	Li^+	**422.323**	**77.000**	**181**	**10**	**127**	**12**

source = TurboSpray CUR = 40 CAD = Medium IS = 5500 TEM = 600 GS1 = 40 GS2 = 50

Optimized MRMs and ionization parameters used for the detection of vitamin D metabolites within this thesis. Please note that MRMs as well as the respective ionization parameters used in the final vitamin D LC-MS/MS method are highlighted in bold.

CAD, collision gas; CE, collision energy; CUR, curtain gas; CXP, collision cell exit potential; DP, declustering potential; EP, entrance potential; GS1, ion source gas 1; GS2, ion source gas 2; IS, ion spray voltage; source, ion source; TEM, temperature.

DANKSAGUNG (ACKNOWLEDGEMENTS)

Am Ende dieser Arbeit ist es Zeit DANKE zu sagen.

DANKE an all die Menschen, ohne die diese Doktorarbeit nicht zu dem geworden wäre, was sie heute ist.

In erster Linie DANKE ich meinem Doktorvater Prof. Jerzy Adamski für die Chance in seiner Gruppe über diese interessanten Themen zu promovieren. Dabei DANKE ich ihm vor allem für seine beispiellose Unterstützung – sei es finanzieller oder ideeller Natur. DANKE für sein in mich gesetztes Vertrauen sowie für die unvergleichlichen Freiheiten, die er mir gegeben hat, um erfolgreich in diesen Themengebieten zu forschen und meine Ergebnisse in der „weiten Welt“ zu präsentieren. Ebenso möchte ich Dr. Gabriele Möller für ihr stets offenes Ohr, ihre große Hilfsbereitschaft und ihre unzählbaren Hilfestellungen – sei es fachlicher, technischer oder organisatorischer Natur – danken. DANKE für die kritische Betrachtung und Prüfung meiner Pläne und Ergebnisse sowie für die Korrektur zahlreicher von mir verfasster Texte (inklusive dieser Doktorarbeit), aber auch für die gute Zusammenarbeit innerhalb des HSD17B2-Projekts. Ein weiterer Dank gilt meinen Thesis-Komitee Mitgliedern Dr. Cornelia Prehn und Prof. Johannes Beckers. DANKE für die guten Denkanstöße und Ratschläge innerhalb der Thesis-Komitee-Treffen.

Ein besonderes Dankeschön möchte ich an meine Kooperationspartner Dr. Oleg A. Barski und Dr. Benedikt Linder richten. Many thanks to Dr. Oleg A. Barski who initiated the AKR1B15 project and handed it over to me. THANK YOU for the fruitful cooperative work and numerous discussions, the time I could spend in Louisville, and especially for being a friend. Here, I would like to thank his wife Rita and his two kids Lisa and Sasha for housing me in their home and family, too. THANK YOU to Prof. Aruni Bhatnagar for hosting me in his group at the University of Louisville for two month and to his group members for the kind working atmosphere and support. Dr. Benedikt Linder und seinen früheren Vorgesetzten an der Universitätsmedizin Göttingen, Dr. Anja Uhmann und Prof. Heidi Hahn, möchte ich vor allem für die Initiierung und die gute Zusammenarbeit im Vitamin D Projekt danken. DANKE für all die Diskussionen und Vorschläge sowie für die bereitgestellten Proben und Zelllinien zur Etablierung der Vitamin D LC-MS/MS Methode. Darüber hinaus möchte ich mich auch bei Dr. Sabine Schmitt und PD Dr. Hans Zischka vom Institut für Molekulare Toxikologie und Pharmakologie des Helmholtz Zentrum München für ihre Beratung und Hilfe bei der Isolation von Mitochondrien aus Zellen und deren Funktionsanalyse, bei Dr. Elisabeth Kremmer (der ehemaligen Leitung der Serviceeinheit Monoklonale Antikörper am Institut für Molekulare Immunologie) für die Herstellung und Hilfe bei der Etablierung der monoklonalen Antikörper gegen AKR1B15 sowie bei Dipl.-Ing. Andreas Voss von der Abteilung Analytische Pathologie für die Hilfestellung bei der konfokalen Fluoreszenz-mikroskopie bedanken.

Natürlich empfinde ich auch große Dankbarkeit gegenüber meinen Wegbegleitern während meiner Doktorarbeit: den Postdocs, Doktoranden, technischen Assistenten, Studenten und Auszubildenden im Institut für Experimentelle Genetik (IEG/GAC) und in den Nachbargruppen. DANKE für das hervorragende Arbeitsklima und die unschätzbare Unterstützung in jeglicher Form. Hier möchte ich besonders Dr. Janina Tokarz aber auch den anderen Postdocs und Doktoranden für ihre Hilfsbereitschaft, die zahlreichen Diskussionen und ihre Freundschaft danken. Ein besonderes DANKE auch an die technischen Assistenten für die Gewährleistung reibungsloser Abläufe im Labor. Dabei empfinde ich vor allem gegenüber Bianca Eichner, Maria Kugler, Marion Schieweg und Gabriele Zieglmeier eine große Dankbarkeit, da ich stets auf ihre Hilfe vertrauen konnte falls ich „Manpower" benötigte. Ein weiterer Dank gilt meinen Bürokolleginnen und -kollegen: Silke Becker, Bianca Eichner, Katharina Faschinger, Maria Kugler, Patrick Pann und Sven Zukunft. DANKE für die heiteren Momente, für die sich entwickelten Freundschaften, für die Diskussionen, für die Antworten auf meine Fragen aber auch für das Ignorieren meiner Selbstgespräche. Auf diesem Weg möchte ich mich auch nochmal herzlichst bei „meinen" zahlreichen Studenten (Miriam Blei, Anna Rast, Aurelia Weber, Elisabeth Franz, Benedikt Herold, Heidi Hertlein, Fiona Rathmann, Stephan Hess, Verena Häfner) und Auszubildenden (Doris Knuff, Mareike Bamberger, Stefanie Bemelmann, Lisa Eidenschink, Milena Artmann, Lorenz Graser) für ihre tatkräftige Unterstützung bei meinen Forschungsprojekten bedanken. Ich hoffe, dass sie mit mir ebenso viele positive Erfahrungen sammeln konnten wie ich mit ihnen und dass sie die zumeist arbeitsintensive Zeit in guter Erinnerung behalten.

Schließlich bedanke ich mich aus tiefstem Herzen bei meiner allerliebsten Familie und meinen einzigartigen Freunden. DANKE für ihr Verständnis, für ihre seelische, moralische und organisatorische Unterstützung, für ihren uneingeschränkten Rückhalt aber auch für ihre Kritik. Ohne ihre Prägung wäre ich nicht der Mensch, der ich heute bin.

LEBENSLAUF (CURRICULUM VITAE)

NAME:	Susanne Weber
GEBURTSDATUM:	28.07.1980
GEBURTSORT:	Landshut, Deutschland
STAATSANGEHÖRIGKEIT:	deutsch

SCHULISCHE BILDUNG:

09/1986 - 07/1992:	Grundschule & Hauptschule Ergoldsbach
09/1992 - 07/1996:	Staatliche Realschule Neufahrn in NB (Zweig: Wirtschaft) **– Abschluss: Mittlere Reife**
09/2003 - 07/2005:	Staatliche Berufsoberschule Landshut (Zweig: Technik) **– Abschluss: Allgemeine Hochschulreif**e

BERUFLICHE AUSBILDUNG:

09/1996 - 07/1998:	Private Lehranstalt - staatlich anerkannt - für pharmazeutisch-technische Assistenten in München (schulische Ausbildung)
09/1998 - 03/1999:	St. Wolfgang-Apotheke in Essenbach (praktische Ausbildung)
03/1999:	Prüfung zur pharmazeutisch-technischen Assistentin (PTA) **– Abschluss: Staatlich geprüfte PTA**

UNIVERSITÄRE AUSBILDUNG:

10/2005 - 08/2008:	Studiengang Biochemie (B. Sc.) an der TU München Bachelor-Thesis: *Charakterisierung des Hsp110 Sse1p aus S. cerevisiae und Untersuchungen zur Luciferase-Rückfaltung mit Hsp40/Hsp70/Hsp90 aus S. cerevisiae* am Lehrstuhl für Biotechnologie – Prof. J. Buchner - der TU München **– Abschluss: Bachelor of Science in der Biochemie**
10/2008 - 08/2010:	Studiengang Biochemie (M. Sc.) an der TU München Master-Thesis: *Die Funktion des Bmpr1b in der Sehnerventwicklung* am Institut für Entwicklungsgenetik - Prof. J. Graw - des Helmholtz Zentrums München **– Abschluss: Master of Science in der Biochemie**

seit 09/2010:	Promotion im Bereich Biochemie Dissertation: *Charakterisierung der neuen humanen AKR1B15 und der enzymatischen Aktivitäten von 17β-HSD12 und CYPs* am Institut für Experimentelle Genetik - Prof. J. Adamski - des Helmholtz Zentrums München

BERUFLICHE TÄTIGKEITEN:

04/1999 - 08/2003:	Vollzeitanstellung als pharmazeutisch-technische Assistentin in der St. Michael-Apotheke in Landshut
09/2003 - 08/2013:	geringfügige Beschäftigung als pharmazeutisch-technische Assistentin in der St. Michael-Apotheke in Landshut
09/2010 - 09/2014:	Vollzeitanstellung zur Erlangung des Grades Dr. rer. nat. (Doktorand) am Institut für Experimentelle Genetik - Gruppe: Prof. Jerzy Adamski - des Helmholtz Zentrum Münchens
09/2014 - 09/2016:	Anstellung als wissenschaftliche Mitarbeiterin am Institut für Experimentelle Genetik - Gruppe: Prof. Jerzy Adamski - des Helmholtz Zentrum Münchens

AUSLANDSERFAHRUNG:

10/2012 - 12/2012:	Auslandsaufenthalt im Labor des Kooperationspartners Oleg Barski (PhD) / Prof. Aruni Bhatnagar am Diabetes and Obesity Center, School of Medicine, University of Louisville, KY, USA